Pandemic haiku from young scientists p. 22

Adipose tissue macrophages regulate fat storage pp. 24 & 74

Stable zeolites with large pores pp. 28 & 104

Science

$15
2 JULY 2021
SPECIAL ISSUE
sciencemag.org

AAAS

OUR PLASTICS DILEMMA

CALL FOR PAPERS

SPJ
SCIENCE PARTNER JOURNALS

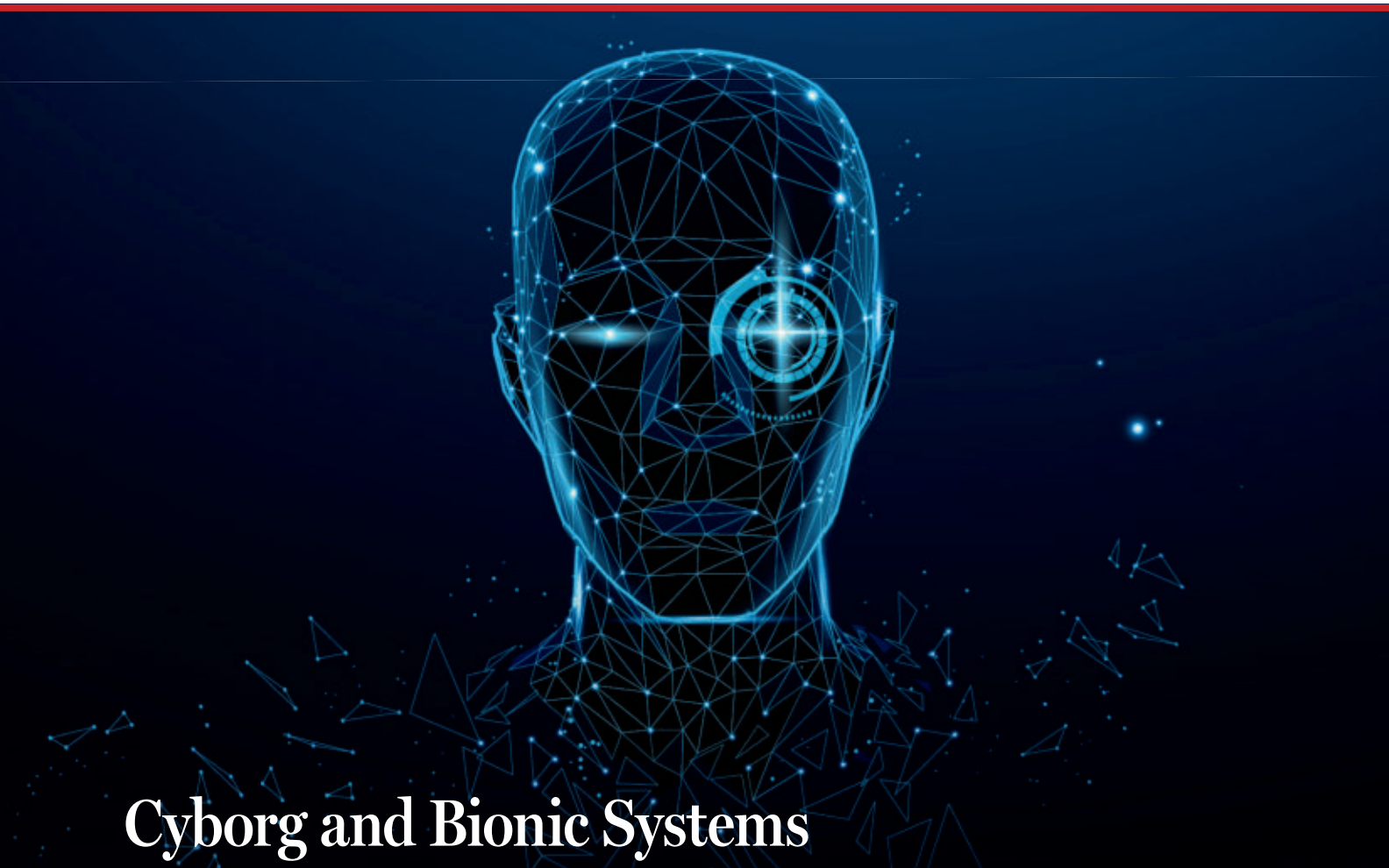

Cyborg and Bionic Systems

Cyborg and Bionic Systems is an online-only, Open Access journal published in affiliation with the **Beijing Institute of Technology (BIT)** and distributed by the **American Association for the Advancement of Science (AAAS).** The journal publishes original, peer-reviewed articles based on fundamental, applied science, or their interaction. C*yborg and Bionic Systems* promotes the knowledge interchange and hybrid system codesign between living beings and robotic systems. The journal also covers a wide range of fields related to cybernetic organisms (cyborg) and bionic systems (CBS), mainly including robotics, biomedical engineering and neuro-engineering.

Submit your research to *Cyborg and Bionic System* today!

Learn more at **spj.sciencemag.org/cbsystems**

The Science Partner Journal (SPJ) program was established by the American Association for the Advancement of Science (AAAS), the nonprofit publisher of the *Science* family of journals. The SPJ program features high-quality, online-only, Open Access publications produced in collaboration with international research institutions, foundations, funders and societies. Through these collaborations, AAAS furthers its mission to communicate science broadly and for the benefit of all people by providing top-tier international research organizations with the technology, visibility, and publishing expertise that AAAS is uniquely positioned to offer as the world's largest general science membership society.

Visit us at **spj.sciencemag.org**

@SPJournals **@SPJournals**

OPEN ACCESS

ARTICLE PROCESSING CHARGES WAIVED UNTIL JULY 2023

1848 SOCIETY

AAAS

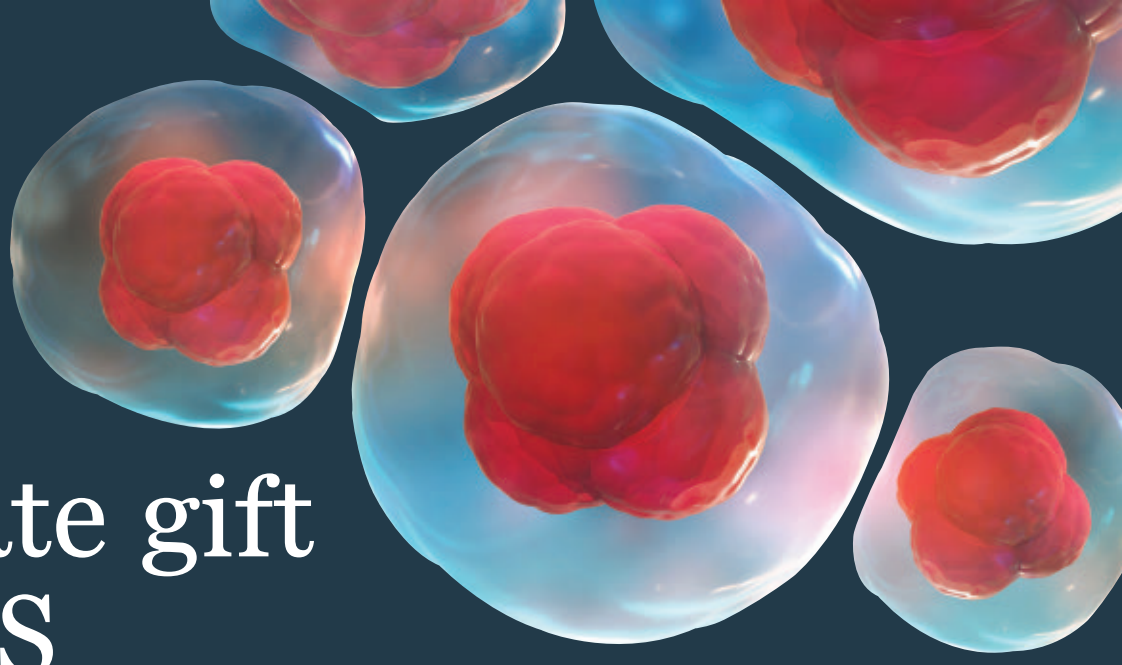

An estate gift to AAAS

Going all the way back to 1848, our founding year, the American Association for the Advancement of Science (AAAS) has been deeply committed to advancing science, engineering and innovation around the world for the benefit of all people.

Today, we are dedicated to advocating for science and scientific evidence to be fully and positively integrated into public policy and for the community to speak with one voice to advance science and engineering in the United States and around the world.

By making AAAS a beneficiary of your will, trust, retirement plan or life insurance policy, you will become a member of our 1848 Society and will help fuel our work on behalf of science and society – including publishing the world's most promising, innovative research in the *Science* family of journals and engaging in the issues that matter locally, nationally and around the world.

"As a teacher and instructor, I bear responsibility for the younger generations. If you have extra resources, concentrate them on organizations, like AAAS, that are doing work for all."

—Prof. Elisabeth Ervin-Blankenheim, 1848 Society member

If you intend to include AAAS in your estate plans, provide this information to your lawyer or financial adviser:

Legal Name: American Association for the Advancement of Science
Federal Tax ID Number: 53-0196568
Address: 1200 New York Avenue, NW, Washington, DC 20005

If you would like more information on making an estate gift to AAAS, cut out and return the form below or send an email to philanthropy@aaas.org. Additional details are also available online at **www.aaas.org/1848Society**.

AMERICAN ASSOCIATION FOR THE ADVANCEMENT OF SCIENCE

cut here

Yes, I would like more information about joining the AAAS 1848 Society.

1848 SOCIETY

AAAS

PLEASE CONTACT ME AT:

Name: _____

Address: _____

City: _____ State: _____ Zip code: _____ Country: _____

Email: _____ Phone: _____

RETURN THIS FORM TO:
AAAS Office of Philanthropy and Strategic Partnerships • 1200 New York Avenue, NW • Washington, DC 20005 USA

CONTENTS

2 JULY 2021 • VOLUME 373 • ISSUE 6550

SPECIAL SECTION

OUR PLASTICS DILEMMA

INTRODUCTION

34 A devil's bargain

NEWS

36 The plastic eaters *By W. Cornwall*

40 When plastics are precious *By S. Kean*

POLICY FORUM

43 A binding global agreement to address the life cycle of plastics *By N. Simon* et al.

PERSPECTIVES

47 The myth of historical bio-based plastics *By R. Altman*

49 Achieving a circular bioeconomy for plastics *By S. Kakadellis and G. Rosetto*

REVIEWS

51 Plastics in the Earth system *A. Stubbins* et al.

56 Plastic ingestion as an evolutionary trap: Toward a holistic understanding *R. G. Santos* et al.

61 The global threat from plastic pollution *M. MacLeod* et al.

66 Toward polymer upcycling—adding value and tackling circularity *L. T. J. Korley* et al.

ON THE COVER

Plastic waste is accumulating rapidly in our environment and will leave a geological signature like fossils or archaeological remains. Here, we see an illustrated record, not to scale, of a region's past and the plastic consumer waste that will eventually leave a permanent mark on Earth's history and carbon cycle. See p. 34. *Illustration: Sam Falconer*

SEE ALSO: REPORT p. 107; PODCAST; VIDEO

NEWS

IN BRIEF

8 News at a glance

IN DEPTH

11 'Dragon Man' may be an elusive Denisovan
Paleoanthropologists are both excited and puzzled by "wonderful skull" from China *By A. Gibbons*

12 Black-footed albatrosses find a new home across an ocean
International project offers a model for tricky translocation of seabirds threatened by rising sea level *By R. Pérez Ortega*

13 Ship gauges potential for catastrophic earthquake
Fault structures could reveal whether next rupture in Pacific Northwest will be a repeat of megaquake in 1700 *By P. Voosen*

15 Did a Chinese team 'obscure' early coronavirus sequences?
Preprint's claim inflames already divisive origin debate *By J. Cohen*

16 Gene editor injected into the body treats disease
In a first, CRISPR components infused into patients' blood shut down mutant gene in liver *By J. Kaiser*

FEATURES

17 A voice for the river
Jack Schmidt tells hard truths about how climate change will shrink the Colorado River, a lifeline for the Southwest. Will officials listen? *By E. Stokstad*

INSIGHTS

LETTERS

22 NextGen Voices: Pandemic haiku

PERSPECTIVES

24 An anti-obesity immunotherapy?
Adipose tissue–resident macrophages promote lipid storage in mice but can be stopped with antibody treatment
By C. J. O. O'Brien and A. Domingos
RESEARCH ARTICLE p. 74

25 Reengineering protein-phosphorylation switches
Phosphorylation circuits operate as logic gates that rapidly toggle a system between two stable states *By B. N. Kholodenko and M. Okada*
RESEARCH ARTICLE p. 75

PHOTO: MANDY BARKER

26 Small RNAs on the move in male germ cells
DNA in plant male meiocytes is methylated by intercellular small interfering RNAs
By R. A. Mosher
RESEARCH ARTICLE p. 76

28 New insight from an old concept for zeolites
Two supercage-based large-pore zeolites are potentially useful for industrial applications
By D. Xie
REPORT p. 104

29 Astrocytes control the critical period of circuit wiring
Astrocytes regulate the experience-dependent remodeling of brain circuits during development *By P. Kofuji and A. Araque*
RESEARCH ARTICLE p. 77

30 Finding genes that control body weight
DNA exome sequencing at scale reveals unknown human biology of adiposity
By G. S. H. Yeo and S. O'Rahilly
RESEARCH ARTICLE p. 73

BOOKS *ET AL.*

32 The peopling of the Pacific
An anthropologist traces the emergence of the rich and varied cultures of the Pacific islands
By C. J. Bae

33 When Einstein met Curie
Historical documents hint at a fulfilling friendship between the two physicists
By G. Farmelo

RESEARCH

IN BRIEF

70 From *Science* and other journals

RESEARCH ARTICLES

73 Human genomics
Sequencing of 640,000 exomes identifies *GPR75* variants associated with protection from obesity
P. Akbari et al.
RESEARCH ARTICLE SUMMARY; FOR FULL TEXT: DOI.ORG/10.1126/SCIENCE.ABF8683
PERSPECTIVE p. 30

74 Immunometabolism
Diet-regulated production of PDGFcc by macrophages controls energy storage *N. Cox* et al.
RESEARCH ARTICLE SUMMARY; FOR FULL TEXT: DOI.ORG/10.1126/SCIENCE.ABE9383
PERSPECTIVE p. 24

75 Synthetic biology
An engineered protein-phosphorylation toggle network with implications for endogenous network discovery *D. Mishra* et al.
RESEARCH ARTICLE SUMMARY; FOR FULL TEXT: DOI.ORG/10.1126/SCIENCE.AAV0780
PERSPECTIVE p. 25

76 Plant science
Nurse cell–derived small RNAs define paternal epigenetic inheritance in *Arabidopsis* *J. Long* et al.
RESEARCH ARTICLE SUMMARY; FOR FULL TEXT: DOI.ORG/10.1126/SCIENCE.ABH0556
PERSPECTIVE p. 26

77 Neurodevelopment
Astrocytes close the mouse critical period for visual plasticity *J. Ribot* et al.
PERSPECTIVE p. 29

82 Mesoscopic physics
Nontopological zero-bias peaks in full-shell nanowires induced by flux-tunable Andreev states *M. Valentini* et al.

REPORTS

88 Applied physics
Monolithic optical microlithography of high-density elastic circuits *Y.-Q. Zheng* et al.

95 Spectroscopy
Single-molecule laser nanospectroscopy with micro–electron volt energy resolution
H. Imada et al.

99 Applied optics
Laser soliton microcombs heterogeneously integrated on silicon
C. Xiang et al.

104 Zeolites
Synthesis of thermally stable SBT and SBS/SBT intergrowth zeolites
H. Lee et al.
PERSPECTIVE p. 28

107 Plastic pollution
The missing ocean plastic sink: Gone with the rivers *L. Weiss* et al.
OUR PLASTICS DILEMMA SECTION p. 34

111 Spatial genetics
Embryo-scale, single-cell spatial transcriptomics *S. R. Srivatsan* et al.

118 Enzyme structure
Crystal structure of a key enzyme for anaerobic ethane activation
C. J. Hahn et al.

DEPARTMENTS

6 Editorial
Shared blame for the opioid crisis
By H. Holden Thorp

7 Editorial
Director Lander, the time is now
By Omolola Eniola-Adefeso and Hana El-Samad

126 Working Life
Embracing my roots *By Sheila Teves*

Science Careers 122

A transplanted black-footed albatross chick with its Laysan albatross foster parent on Mexico's Guadalupe Island.

PHOTO: © GECI J.A. SORIANO

SCIENCE (ISSN 0036-8075) is published weekly on Friday, except last week in December, by the American Association for the Advancement of Science, 1200 New York Avenue, NW, Washington, DC 20005. Periodicals mail postage (publication No. 484460) paid at Washington, DC, and additional mailing offices.

Copyright © 2021 by the American Association for the Advancement of Science. The title SCIENCE is a registered trademark of the AAAS.

Domestic individual membership, including subscription (12 months): $165 ($74 allocated to subscription). Domestic institutional subscription (51 issues): $2148; Foreign postage extra: Air assist delivery: $98. First class, airmail, student, and emeritus rates on request. Canadian rates with GST available upon request, GST #125488122. Publications Mail Agreement Number 1069624. **Printed in the U.S.A.**
Change of address: Allow 4 weeks, giving old and new addresses and 8-digit account number. **Postmaster:** Send change of address to AAAS, P.O. Box 96178, Washington, DC 20090–6178. **Single-copy sales:** $15 each plus shipping and handling available from backissues.sciencemag.org; bulk rate on request. **Authorization to reproduce** material for internal or personal use under circumstances not falling within the fair use provisions of the Copyright Act can be obtained through the Copyright Clearance Center (CCC), www.copyright.com. The identification code for *Science* is 0036-8075. *Science* is indexed in the *Reader's Guide to Periodical Literature* and in several specialized indexes.

EDITORIAL

Shared blame for the opioid crisis

H. Holden Thorp
Editor-in-Chief, *Science* journals.
hthorp@aaas.org;
@hholdenthorp

As the COVID-19 pandemic recedes, it's time to turn attention back to the slow-moving and devastating epidemic caused by America's opioid crisis. For the last 10 years, around 15,000 annual deaths have been ascribed to prescription opioid overdoses. Add in deaths from all opioids, whether obtained by prescription or on the black market, and the total reaches almost 50,000. Black market fentanyl has played a big role, as well as a now notorious pharmaceutical called OxyContin, which is manufactured and sold by Purdue Pharma. The company's dysfunctional culture combined with complacent oversight by the US Food and Drug Administration (FDA), the research community, and the medical community led to this perfect storm—one we must learn from so that we can avoid a similar tragedy in the future.

Much outstanding reporting has been done about the OxyContin saga and the role of Purdue Pharma and the Sackler family, which owns and runs the company. Most recently, Patrick Radden Keefe has written a compelling version of the tale in his new book, *Empire of Pain*. The book centers mostly on the horrific business actions of the Sacklers, but given Keefe's detailed reporting, I asked him to help me understand why the scientists and physicians in the company couldn't stop the crisis earlier. "One of the real oddities of this story," he told me, "is the absence of whistleblowers. You would expect precisely what you describe, people to come forward, to quit in protest, to try and alert the authorities—and there's not a huge amount of that along the way." Keefe says the fact that Purdue was not a public company and that there was a high premium placed on loyalty to the Sackler family were key considerations. But he also cites an idealistic belief among company scientists that with OxyContin, they had cracked the code on managing pain. "These are drugs that we've known for thousands of years to have important therapeutic benefits but also really significant downsides," he said, "and I think that the hope and the ambition of Purdue was that they'd hacked it." Keefe was referring to the time-release aspect of OxyContin, which allowed Purdue to deliver much higher doses of opioid.

One telling episode in the company's history involves a chemical explosion at a Purdue manufacturing facility in New Jersey in 1995 that killed five people and injured dozens of others. All kinds of corners were cut in the interest of profits, creating a hazard that should have been foreseeable. Keefe said, "The family that owns the company and that was driving that push for profits accepts no responsibility whatsoever. They don't go to any funerals. They don't even make any expressions of regret... to me that was in a nutshell a story of the ways in which a relentless drive for profit can blind people to the seriously dangerous consequences of some of the risks that they're undertaking." This lack of safety culture at Purdue's factory apparently carried over to the whole organization.

> **"The OxyContin story is first and foremost a story of greed and hubris."**

The FDA also failed to address the situation. Though the drug was approved in 1995, it was not until 2009 that the FDA started warning about its dangerously addictive properties. David Kessler, who was the FDA commissioner when OxyContin was approved, was later quoted as saying that the destigmatization of opioids is "one of the great mistakes of modern medicine." Nevertheless, Keefe says that the FDA casually took Purdue at its word both in terms of the science and the marketing of the drug. It was 14 years after the drug was approved when FDA Commissioner Margaret Hamburg finally began to hold hearings and issue warnings about the dangers of the drug. Joshua Sharfstein, who was FDA's deputy commissioner at the time, said to me, "The FDA has to remember that it is the last line of defense against something horrible happening, and for a variety of reasons, the agency didn't play that role."

The OxyContin story is first and foremost a story of greed and hubris. But science bears some responsibility for failing to come forward but also for acceding to the view that science can solve anything. As Keefe surmised, "The original three Sackler brothers in the 1950s had this, I think, very American sense that if the chemistry is good enough, there's no human problem that cannot be fixed with a pill." For many scientists, this view can be just as intoxicating as an illicit drug.

–H. Holden Thorp

10.1126/science.abk1718

Director Lander, the time is now

The Biden administration's decision to elevate the Director of the White House Office of Science and Technology Policy (OSTP) to a cabinet-level position is a win for science. Eric Lander, confirmed in May by the Senate, is now advising the president on the scientific, engineering, and technological policies of the US government. As Dr. Lander carries out this task, we hope that he keeps in mind what President Biden asked him in a letter in January: "How can we guarantee that the fruits of science and technology are fully shared across America and among all Americans?"

The challenges ahead are formidable. The devastating health and economic impacts of two major crises—climate change and the COVID-19 pandemic—have revealed deep societal fault lines that prevent the United States from drawing on the talents of all Americans to tackle these problems. Thus, there is an urgent need for smart and socially minded policy-making.

If the fruits of science and technology are to be truly shared, they should be produced by all Americans. This cannot happen if the scientific enterprise tolerates insidious systemic racism and sexism. That membership in the US National Academies of Sciences, Engineering, and Medicine remains predominantly white and male speaks volumes. Such stark disparity also exists in federal institutions that support research and training in science, technology, engineering, and mathematics (STEM) and biomedicine. For example, National Institutes of Health (NIH) intramural senior investigators from underrepresented groups (Black, Hispanic, Alaska Native/American Indian) constitute only 5.1% (and women only 24%), and Black scientists remain 55% less likely than white scientists to receive NIH's extramural funding. This year, the agency announced that all NIH Institutes and Centers are now jointly focused on identifying and correcting structural racism. However, this acknowledgment of the problem is only a first step. For example, although funding research on health disparities through the new NIH UNITE initiative is important, it is essential to recognize that such initiatives will not solve racial inequality problems in science. A system that pigeonholes scientists into a narrow racial interest bin must be overhauled. Racially underrepresented scientists are as likely to put the first humans on Mars, for example, as they are to solve health disparity problems. Therefore, OSTP should work with all federal research agencies to eliminate bias throughout their systems and in existing and new funding programs.

> "...acknowledgment of the problem is only a first step."

A major charge placed on OSTP by President Biden is to ensure that science and technology flourish in America. This starts with making inclusive STEM education a priority, as many STEM classrooms at top US universities still lack students from underrepresented groups. Despite all the efforts to address education equity, the US educational system is still producing disproportionately fewer racially underrepresented Americans for jobs in science and engineering. For example, in 2019, Black, Hispanic, American Indian/Alaska Native, and Native Hawaiian/Other Pacific Islander groups received 4.4, 12.1, 0.4, and 0.2% of engineering bachelor's degrees, respectively. This underrepresentation is most stark for Blacks, who make up 14% of "Gen Z" (6 to 24 years old). Similarly, women accounted for only 22.5% of engineering bachelor's degrees in 2019. Left uncorrected, the negative impact on the US technical workforce size and innovation will be vast, as students of color will soon represent nearly 48% of high school graduates. Moreover, COVID-19 pandemic hardships might cause an exodus of women and racially underrepresented role models—those most affected by the pandemic—from STEM, setting back already lagging equity efforts.

Concomitantly, leadership within national funding agencies and at federally funded universities must change. These positions cannot remain the privilege of white men--only 14% of higher education administration are non-white despite their 38% representation in the population. Women and non-white scientists cannot continue to be given junior fellowships, only to be derailed from professional advancement later by majority gatekeepers. A cultural change is also needed to retain those in the STEM career pipeline. Accountability systems for discrimination, sexism, racism, and harassment need overhauls—their burden cannot continue to crush and end the careers of victims and truth-tellers.

The answer to President Biden's question to Director Lander is clear: OSTP must guide the administration toward policies that mandate all stakeholders to attract, nurture, and promote the best and brightest across all populations in the United States. The steps toward implementing these policies will be hard. Nevertheless, the American people are ready, and the time is now.

–Omolola Eniola-Adefeso and Hana El-Samad

Omolola Eniola-Adefeso is the University Diversity and Social Transformation Professor in Chemical Engineering and a professor of Biomedical Engineering and Macromolecular Sciences at the University of Michigan, Ann Arbor, MI, USA. lolaa@umich.edu

Hana El-Samad is the Kuo Family Endowed Professor and vice-chair in the Department of Biochemistry and Biophysics at the University of California, San Francisco, CA, USA. hana.el-samad@ucsf.edu

10.1126/science.abk1976

NEWS

> "It is impossible to look at these findings and not see a reflection of the systemic racism in the U.S."
>
> **Duke University health services researcher Lesley Curtis**, to NPR, on life expectancy declines from 2018 to 2020: 3.9 years for Hispanic Americans, 3.3 for Black Americans, and 1.4 for white Americans.

IN BRIEF

Edited by **Kelly Servick**

Children in Uganda tuned in to radio lessons last month after rising COVID-19 rates prompted school closures.

PHOTO: NICHOLAS KAJOBA/XINHUA/GETTY IMAGES

COVID-19

Third pandemic wave threatens Africa

At least a dozen countries across Africa are facing a steep rise in coronavirus infections, pushing hospitals in several countries to their limits. The highly infectious Delta variant of SARS-CoV-2 is largely driving the increase; it has been documented in at least 14 African countries. Liberia, Rwanda, Namibia, and the Democratic Republic of the Congo all reported record numbers of new COVID-19 cases this week, as countries across the continent were reporting more than 30,000 new cases each day, racing toward the previous peak from early January. At the same time, the continent is facing an acute shortage of vaccines, with less than 1% of the population vaccinated. Officials at the World Health Organization said 18 African countries had used more than 80% of their vaccine stocks, and eight countries had exhausted their supplies.

Black holes eat neutron stars

ASTROPHYSICS | Gravitational wave astronomers have twice spotted a black hole consuming a neutron star, researchers with the Laser Interferometer Gravitational-Wave Observatory (LIGO) in the United States and the Virgo Observatory in Italy announced this week. LIGO and Virgo had previously spotted dozens of pairs of black holes spiraling together and two pairs of merging neutron stars—including one that set off a spectacular explosion seen by telescopes of all kinds in 2017. Astronomers saw no similar explosions from the newly detected black hole-neutron star mergers, either because they were too far away or because the black holes swallowed the neutron stars whole, a possibility that could put a damper on hopes that such a collision might someday lay bare the innards of a neutron star.

Say 'recycling,' not plagiarism

RESEARCH INTEGRITY | Although researchers have valid reasons to reuse their text across papers—in literature

reviews or methods descriptions, for example—peers often frown on this practice as "self-plagiarism." Some oversight bodies, including the Committee on Publication Ethics, have considered the practice acceptable in some circumstances. This week, the Text Recycling Research Project, based at Duke University and funded by the U.S. National Science Foundation, released new guidance on the finer points, drawing on advice from journal publishers and other specialists. The document describes when the practice is both ethical and legal and how to present reused text transparently. One aim is to ease the workload of authors who are currently forced to reword passages unnecessarily, purely to avoid the appearance of self-plagiarism, says project leader Cary Moskovitz.

National academy ousts biologist

SCIENTIFIC COMMUNITY | The U.S. National Academy of Sciences (NAS) last week expelled evolutionary biologist Francisco Ayala from its ranks 3 years after he was found to have sexually harassed women colleagues. Ayala resigned from the University of California, Irvine, in 2018 after a university investigation found him guilty of sexual harassment. Ayala declined to comment on NAS's action, but has denied the allegations against him, which included making sexually suggestive comments and inviting a junior professor to sit on his lap. Women who filed complaints with the university over Ayala's behavior applauded the move, but charged that NAS's process was too slow. Ayala is the second NAS member to be ousted over sexual harassment allegations since the academy revised its bylaws 2 years ago to allow members to be removed if they violate its code of conduct.

China declared malaria-free

PUBLIC HEALTH | The World Health Organization (WHO) on 30 June certified China as free of malaria, making it the 40th country—and the most populous one by far—to gain that status. In the 1940s, China had an estimated 30 million malaria cases and 300,000 deaths annually, but antimalarial drugs, insecticides, and other countermeasures brought cases to zero in 2017. Along the way, pharmaceutical chemist Tu Youyou bagged a Nobel Prize for isolating a powerful malaria drug, artemisinin, in sweet wormwood (*Artemisia annua*), a plant used in traditional Chinese medicine. "China's ability to think outside the box served the country well in its own response to malaria," Pedro Alonso, director of WHO's Global Malaria Programme, said in a statement this week. The last three countries awarded WHO's malaria-free status were El Salvador, in February, and Algeria and Argentina, both in 2019.

A new citation metric, by field

PUBLISHING | The controversial journal impact factor will be supplemented by a new metric that allows accurate comparisons of journal citation rates in different disciplines, its creator, Clarivate Analytics, said last week. The Journal Citation Indicator (JCI), released on 30 June as part of Clarivate's 2021 update to its Journal Citation Reports database, covers a wider range of journals, measured over a longer time period, than the company's existing impact factor. The impact metric captures how many citations a journal accumulated per article published over a 2-year period; the new metric is an average that attempts to take into account the substantially different rates of publication and citation in different fields, according to Clarivate. The

BY THE NUMBERS

267 million

People worldwide who live on land less than 2 meters above sea level—areas at greatest flood risk from sea level rise. Researchers predict an increase to 410 million people by 2100. (*Nature Communications*)

250–350 million years

Estimated age of the universe at "cosmic dawn," when the first stars switched on, based on new telescope observations of the most distant known galaxies. (*Monthly Notices of the Royal Astronomical Society*)

Weights from Tiryns, in Bronze Age Greece, weighed about the same as their counterparts elsewhere in Europe and in the Middle East.

PHOTO: N. IALONGO *ET AL., PNAS* **118**, E2105873118 (2021)

ARCHAEOLOGY

Ancient weights reveal Europe's first common market

Merchants of the Bronze Age faced a problem still familiar today: how to know you're getting what you pay for. Historians have long assumed that standard weights—used to measure and trade goods of equivalent value—were handed down from on high, first created by a king or religious authority to collect taxes or tribute. But a new study suggests that more than 3000 years ago, informal networks of merchants established a standardized weight system that started in Mesopotamia and spread across Europe. Researchers analyzed weights from previously excavated sites spanning nearly 5000 kilometers. More than 2000 of the weights—crafted over 2000 years—weighed nearly the same amount: between 8 and 10.5 grams, they report this week in the *Proceedings of the National Academy of Sciences*. They propose that as traders compared weights at each meeting, a standard emerged, forming the first known common Eurasian market.

JCI is a step forward but has important limitations, says Henk Moed, a bibliometrician at the Sapienza University of Rome. He says that, like impact factors, the new metric will be problematic if applied to individual researchers.

Prize funds pandemic prevention

PUBLIC HEALTH | In its inaugural award ceremony last week, a coalition of public, private, and philanthropic organizations known as the Trinity Challenge gave out a total of $8 million to eight projects focused on preventing the next pandemic. Launched in September 2020 with support from 42 organizations including the Bill & Melinda Gates Foundation, Google, GlaxoSmithKline, and Imperial College London, the challenge recognizes projects that use data and analytics to respond to health emergencies. The $1.8 million grand prize went to a project called Participatory One Health Disease Detection, which aims to help farmers in Asia and Africa identify and report sick livestock via a mobile app to prevent the spread of disease among animals and to humans. Second place prizes of $1.4 million each will support an effort to help health authorities in West Africa forecast emerging diseases and a project that uses artificial intelligence to spot infectious disease outbreaks using routine blood tests.

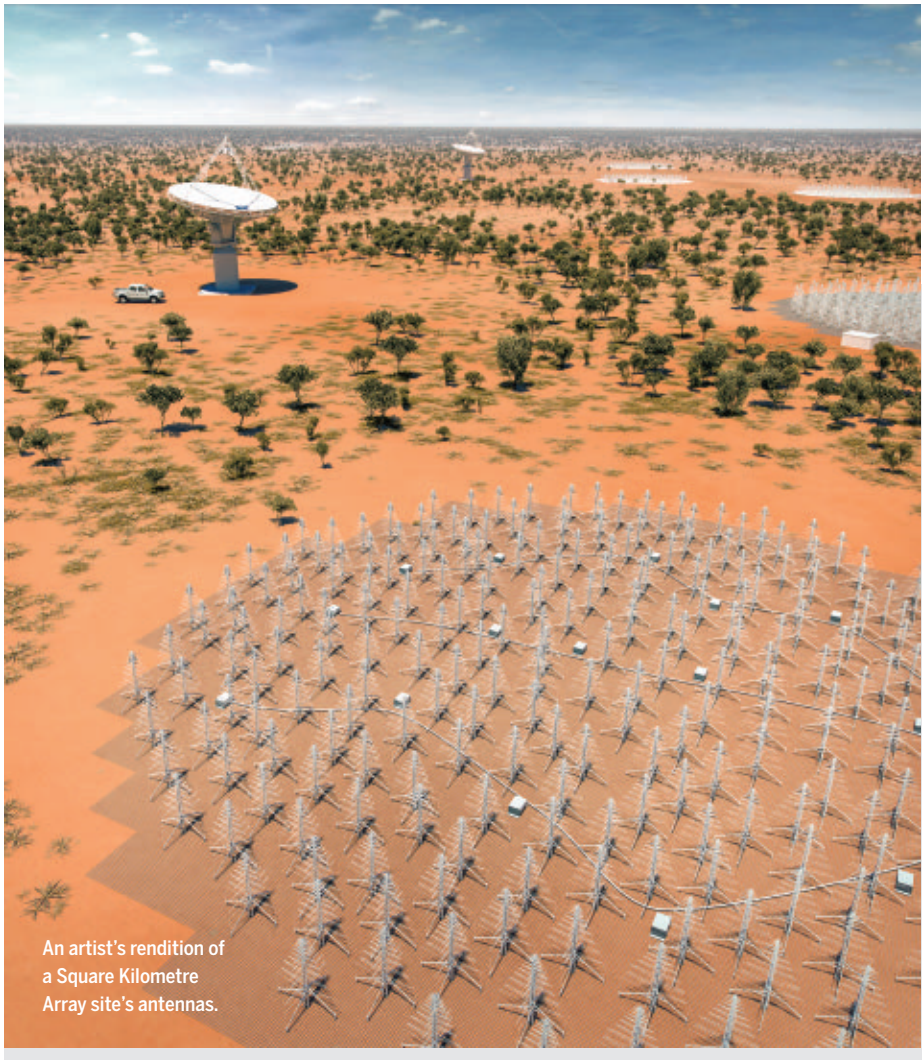

An artist's rendition of a Square Kilometre Array site's antennas.

ILLUSTRATION: SKA ORGANISATION

ASTRONOMY

Green light for giant radio array

Representatives from seven member nations this week gave the go-ahead to start construction later this year on the world's biggest scientific instrument: the twin telescope networks of the Square Kilometre Array (SKA). Once complete in 2028, the nearly €2 billion SKA will comprise hundreds of radio dishes scattered across South Africa and thousands of wire antennas in Western Australia. Combining the signals from this vast array of detectors will give astronomers unprecedented sensitivity and resolution as they search for the universe's first stars and galaxies and seek to understand gravity and cosmic magnetism. The green light means the U.K.-based SKA Observatory can begin to award industrial contracts.

New radiation limit endorsed

SPACE SCIENCE | An expert panel at the U.S. National Academies of Sciences, Engineering, and Medicine (NASEM) is encouraging NASA to push forward with a proposed change to limits on radiation exposure that would place women astronauts on equal footing with their male counterparts. Current standards limit astronauts to a radiation level that increases their risk of exposure-induced death by 3%, a metric that varies based on age and sex. A change under consideration at NASA, endorsed in a NASEM report released last week, would limit all astronauts to 600 millisieverts of radiation over their careers. The report also proposes a color-coded system to communicate the risks of longer missions and proposes that astronauts sign a waiver if a mission is expected to exceed their radiation limit.

House backs boost for research

SCIENCE POLICY | The U.S. House of Representatives this week overwhelmingly approved two bills that would authorize massive spending increases at the National Science Foundation (NSF) and the Department of Energy's Office of Science. H.R. 2225 calls for more than doubling NSF's annual budget of $8.5 billion to $17.9 billion by 2026, and H.R. 3593 would give the Office of Science a 63% boost, to $11.1 billion, over the same period. The bills represent a slimmer alternative to the sprawling and more costly one passed last month by the Senate to address the growing scientific, economic, and military threat of China. Science lobbyists generally prefer the House bills' approach to tightening research security and correcting the uneven geographic distribution of funding. Reconciling these competing visions could take months, and separate legislation will be needed to determine the 2022 budgets for each agency.

SCIENCEMAG.ORG/NEWS
Read more news from *Science* online.

A massive, remarkably complete skull from China may reveal the long-sought face of a Denisovan, a kind of ancient human known chiefly from DNA.

PHOTOS: XIJUN NI

PALEOANTHROPOLOGY

'Dragon Man' may be an elusive Denisovan

Paleoanthropologists are both excited and puzzled by "wonderful skull" from China

By **Ann Gibbons**

Almost 90 years ago, Japanese soldiers occupying northern China forced a Chinese man to help build a bridge across the Songhua River in Harbin. While his supervisors weren't looking, he found a treasure buried in the riverbank: a remarkably complete human skull. He wrapped up the heavy cranium and lowered it into a well to hide it from the Japanese. Today, the skull is finally coming out of hiding as "Dragon Man," the newest member of the human family, who lived more than 146,000 years ago.

In three papers in the year-old journal *The Innovation*, paleontologist Qiang Ji of Hebei GEO University and his team describe the skull and argue it represents a new species that is a sister group to *Homo sapiens*, even closer kin to us than were the Neanderthals. Other researchers question that idea. But they suspect the large skull, which the team calls *H. longi* (*long* means dragon in Mandarin), has an equally exciting identity: It may be the long-sought skull of a Denisovan, an elusive human relative from Asia known chiefly from DNA. "It's a wonderful skull; I think it's the best skull of a Denisovan that we'll ever have," says paleoanthropologist Jean-Jacques Hublin of the Max Planck Institute for Evolutionary Anthropology.

The stunning fossil was brought to light by the bridge builder's grandchildren, who retrieved it from the well after their grandfather told them about it on his deathbed. They donated it to the Geoscience Museum at Hebei GEO University. (The family asked to remain anonymous.) But the man died without saying precisely where he had found the fossil, leaving the researchers uncertain of its geological context.

So Ji enlisted several researchers to help date the skull. Geochronologist Rainer Grün of Griffith University, Nathan, in Australia and colleagues linked strontium isotopes in sediment crust from its nasal cavities to a 9-meter layer of sediments around the bridge, which they dated to between 138,000 and 309,000 years ago. Uranium series dating on the bone itself gives it a minimum age of 146,000 years.

Next, the researchers tried to identify the skull. Paleontologist Xijun Ni of the Chinese Academy of Sciences and Hebei GEO University, who led the effort, was initially puzzled: The massive skull held a brain comparable in size to that of modern humans. But it couldn't be a member of *H. sapiens* because it had larger, almost square eye sockets, thick brow ridges, and a wide mouth, and its one remaining molar was huge. So Ni compared 55 traits of the skull—including its length, brow size, and dental features—with those of 95 other fossilized skulls, jaws, or teeth from the genus *Homo* from around the world. A computer model then sorted the fossils into family trees, and the tree that fit best with the data had four main clusters. The new skull nestled in a cluster with several other skulls from China's Middle Pleistocene, 789,000 to 130,000 years ago. Within that cluster, the new skull was most closely related to a jawbone from Xiahe Cave on the Tibetan Plateau.

> **"I think it probably is a Denisovan."**
> **Chris Stringer**, Natural History Museum

Ni says the entire cluster of Chinese fossils was closer to early *H. sapiens* than the Neanderthals in the sample were. "Our discovery suggests that the new lineage we identified that includes *Homo longi* is the actual sister group of *H. sapiens*," he

told *Science*. If so, Dragon Man and his kin would displace Neanderthals as modern humans' closest known relative.

Ni says he chose to publish in the little-known journal *The Innovation*, part of the Cell family of journals, "because they promised that they can handle our submissions very fast and will respect our choice of novel research methods." Others are less respectful. "When I saw this analysis, I nearly fell off my chair," Hublin says. He and others question how the team concluded that the skull—which lacks a lower jaw—is closely related to the Xiahe lower jaw.

They also question Li's overall classification of the skull as a new lineage, close to modern humans. "It's premature to name a new species, especially a fossil with no context, with contradictions in the data set," says María Martinón-Torres, a paleoanthropologist at CENIEH, the national center for research on human evolution in Spain. Paleoanthropologist Marta Mirazón Lahr of the University of Cambridge calls the find fascinating, but says she's "skeptical of the statements about humans' long-lost sister lineage."

Instead, she and others say, Dragon Man is probably a Denisovan, an extinct cousin of the Neanderthals. To date, the only clearly identified Denisovan fossils are a pinkie bone, teeth, and a bit of skull bone from Denisova Cave in Siberia, where Denisovans lived off and on from 280,000 to 55,000 years ago. But the enormous, "weird" molar from the new skull fits with the molars from Denisova, says Bence Viola, a paleoanthropologist at the University of Toronto, who analyzed the Denisova fossils with Hublin. The link with the Xiahe Cave jawbone, if correct, would strengthen the case, as a protein from that fossil as well as ancient DNA in the sediments of the cave strongly suggest it was a Denisovan.

The authors concede that their critics have a point. "I think it probably is a Denisovan," says Chris Stringer, a paleoanthropologist at London's Natural History Museum and co-author on two of the papers. DNA analysis of the new skull could resolve the issue. But the team says it does not want to risk destroying the tooth or other bone to get DNA or protein.

If the new skull is indeed from a Denisovan, the team's claim to have found the closest human ancestor would crumble. DNA studies have established that Denisovans and Neanderthals formed sister groups, more closely related to each other than to *H. sapiens*. But Dragon Man would still be a landmark fossil. Viola hopes researchers can analyze its DNA, so that "I can finally look into the eyes of a Denisovan." ■

Researchers hope this black-footed albatross chick, settling in on Guadalupe Island, will return here to breed.

CONSERVATION BIOLOGY

Black-footed albatrosses find a new home across an ocean

International project offers a model for tricky translocation of seabirds threatened by rising sea level

By **Rodrigo Pérez Ortega**

On the morning of 16 June, Snowflake spread its wings and let the strong, cold wind of Guadalupe Island help it take a first flight away from its nest. But this was not the first time the young black-footed albatross had soared above the North Pacific Ocean: Five months before, as an egg, Snowflake had been flown more than 6000 kilometers on a commercial airline—in economy plus seating—from Midway Atoll northwest of Hawaii to the remote Guadalupe Island in Mexico.

Snowflake's own flight, just 3 days before World Albatross Day, marked a milestone in a binational project of the United States and Mexico, aimed at keeping the birds safe from the rising sea levels that threaten their survival. On Midway, they "were destined to drown," says Julio Hernández Montoya, a conservation biologist with the nonprofit Island Ecology and Conservation Group (GECI), who helped lead the effort.

Now, with nesting sites on higher ground, the albatross will be more resilient to environmental threats, says Axel Moehrenschlager of the Calgary Zoo. "One of the things that's really, crucially wonderful is that you're putting more eggs in more baskets," he says. Moehrenschlager, who chairs the translocation specialist group at the International Union for Conservation of Nature (IUCN), calls the project "potentially groundbreaking." Three projects have moved albatrosses within the United States and Japan. But this first transfer of a seabird species between nations "is exactly the type of approach that we need on a global level," he says.

He and other conservation scientists caution that translocations are not first-line interventions for saving species—but sometimes, they are the only option. In the past 30 years, he notes, there has been a 30-fold increase in translocations of species ranging from corals to elephants.

Albatrosses, top predators in the ocean's food chain, can spend years without touching land and fly thousands of kilometers in search of food. But they return every year to mate and nest in the islands where they were born. About 95% of the world's black-footed albatrosses (*Phoebastria nigripes*) nest in the Hawaiian islands; Midway Atoll, in a remote part of the state, is home to close to 21,600 breeding pairs, about one-third of the global breeding population.

PHOTO: © GECI/J.A. SORIANO

These 3-kilogram seabirds nest on low-lying sandy beaches—vulnerable to sea level rise and flooding. During a 2011 tsunami, 30,000 albatross nests were lost on three atolls, says Eric VanderWerf, a bird biologist with the nonprofit Pacific Rim Conservation. IUCN lists the seabirds, as well as their close cousin, the Laysan albatross, as near-threatened. A 2015 study estimated that a 2-meter sea level rise and storm waves—possible in the next century under many climate change scenarios—would flood up to 91% of black-footed albatross nests on the Eastern Island of Midway Atoll.

"It is alarming that the rate of habitat loss could really impact them," says Michelle Hester, a seabird biologist at Oikonos, a nonprofit that studies Pacific ecosystems.

VanderWerf teamed up with colleagues from GECI to move black-footed albatross eggs and chicks from Midway to Guadalupe Island, a reserve some 260 kilometers off Mexico's Baja California Peninsula where the species and other seabirds once nested. The Mexican nonprofit has been working on the island for the past 20 years to eradicate invasive species, first removing nearly 50,000 goats and then eliminating nearly 1500 feral cats.

"It fills us with astonishment and joy."
Julio Hernández Montoya, GECI

Hernández Montoya's team had previously tried to get black-footed albatrosses to nest on the island by attracting them with decoys and recorded courtship sounds, but none that visited settled in. At a meeting in 2016 on Oahu, scientists from Pacific Rim and GECI got the idea of reestablishing a new colony in the Mexican island by moving the birds' eggs and chicks before they imprinted on their Hawaiian location; once imprinted, the birds would return there to breed. VanderWerf's team had already successfully relocated black-footed and Laysan albatrosses' eggs and chicks from Midway to Oahu, a higher island in Hawaii. (The two species live and nest close to each other, have somewhat similar behaviors, and face the same environmental threats, including sea level rise and plastics pollution.)

Meanwhile, on Guadalupe, Hernández Montoya's team had been monitoring a growing native colony of Laysan albatrosses, keeping it safe from remaining feral cats on a fenced-off, predator-free peninsula.

After years of planning, dozens of permits from both countries, half a million dollars in funding from several nongovernmental organizations, and extra complications from the COVID-19 pandemic, the teams finally chose 21 black-footed albatross eggs from Midway in January and flew them to Guadalupe Island. There, they met their foster parents: experienced Laysan albatross pairs whose eggs had not been fertilized or had broken. Eighteen Midway eggs hatched in February.

The new parents fed and cared for their adopted offspring, but there's no guarantee the young black-footed albatrosses will learn behaviors specific to their species, such as courtship behavior. But that appears to be innate. To encourage natural behavior, the team planted decoys and played recorded black-footed albatross vocalizations.

Worried about how well Laysan parents would care for the imported eggs, the team repeated the journey across the Pacific in February with 12 1-month-old, fluffy black-footed chicks. Nine reached the island safely. GECI's team hand-reared them and again exposed the chicks to decoys and recorded vocalizations of their species. Scientists monitor the chicks daily until their ash-gray fluff gives way to adult feathers and they fly away; so far, three have done so. Previous research showed that 93% of hand-reared albatross chicks fledged, although there are no data yet on breeding success.

Hester notes that artificially forming a new seabird colony is difficult and has rarely been accomplished. Translocating birds is "a specialized skill," she says, and the work may offer lessons for projects on other birds. "Albatrosses are a really good species to start with," she says, because they tolerate people, nest on land, and take fostering well.

This project's international cooperation sets a precedent, says Brad Keitt, a seabird biologist with the American Bird Conservancy. "That was a big, bold step made by governments and regulatory agencies."

So far, the team is thrilled. "This was a complicated project," VanderWerf says. "Doing all that in the midst of the pandemic … I still can't believe we did it." The effort "was quite a feat," Hernández Montoya says. "It fills us with astonishment and joy."

VanderWerf says the teams are talking about moving other seabirds, perhaps the black-vented shearwater and Leach's storm petrel, to Guadalupe or other Mexican islands that had been "a seabird paradise" until invasive predators arrived. With those predators gone, the islands "have a lot of potential."

As the rest of Snowflake's fellows take wing, the team is planning to bring 80 more black-footed albatross eggs to Guadalupe Island in the next few years. But they won't know how well the project works until Snowflake and the rest of the first batch return in 5 years to start looking for mates. "It will be an important moment when those birds come back," VanderWerf says. ■

MARINE SEISMOLOGY

Ship gauges potential for catastrophic earthquake

Fault structures could reveal whether next rupture in Pacific Northwest will be a repeat of megaquake in 1700

By **Paul Voosen**

At the Cascadia subduction zone, which has generated some of North America's greatest earthquakes, the silence is deafening. Lying off the Pacific Northwest, where a plate of ocean crust dives beneath North America and into the mantle, Cascadia is best known for a mammoth magnitude 9 earthquake in 1700 that sent a tsunami all the way to Japan. But in modern times, it has been ominously quiet, with almost none of the small, daily earthquakes that are common at other subduction zones. Stress building up at the fault seemingly has had no release. "It's just way, way, way too quiet," says Chris Goldfinger, a marine geologist at Oregon State University, Corvallis.

Last month, however, that silence was shattered with the arrival of the *Marcus G. Langseth*, a research vessel that is generating miniearthquakes of its own in a 2-month campaign. On the ship, owned by Columbia University and funded by the U.S. National Science Foundation, scientists use an airgun to blast sound through the water, sending waves into the crust below. A long chain of hydrophones trailing the ship catches echoes from the innards of the 1300-kilometer-long Cascadia fault (see map, p. 14). Other receivers, dropped on the ocean floor and scattered across coastal farmland and woods, listen for reflections from the deeper parts of the fault, which slopes east, down under the coast.

The resulting pictures of the fault, sharper than any collected before, could show whether its silence is cause for alarm. "We've been waiting for this moment for quite a few years," says Kelin Wang, a geophysicist at the Geological Survey of Canada.

Cascadia's quiet has long been taken to mean the fault is entirely locked, with the edge of the North American continental plate stuck to the subducting Juan de Fuca oceanic plate as it plunges by about 4 centimeters a year. As the continental plate flexes and builds up stress, Cascadia could be headed toward a megaquake like the one in 1700, when the fault ruptured along its entire length, from north of Vancouver, Canada, to south of Portland, Oregon. Such a quake would inundate the coast with a wave up to 30 meters high, liquefy soil under cities, and likely claim thousands of lives.

Large quakes have struck Cascadia every 500 years or so, and building codes in the Pacific Northwest are based on a worst case scenario. But without a modern example of the 1700 strike, no one knows for certain whether the next Cascadia quake will rupture the entire fault again, says Lydia Staisch, a geologist at the U.S. Geological Survey. "It really fuels mystery."

Movement captured by GPS stations in recent years offers some reassurance, suggesting the part of the fault off central Oregon is creeping, releasing some stress without earthquakes. Paleoseismologists have also found evidence that many of the large quakes in the past 10,000 years did not rupture the whole fault. Rough patches along the fault may split it into segments, acting as "gates" that can stop a rupture in its tracks. Fuzzy images from previous imaging campaigns hinted at potential gates: eroded undersea mountains on the oceanic plate or faults in the continental plate. Decisively identifying these structures would firm up the idea of Cascadia's segmentation—and lower the odds of large, catastrophic earthquakes, says Suzanne Carbotte, a Columbia marine geophysicist who is leading the cruise.

The imaging might also gauge another dimension of a future rupture: how close to the surface it might extend. Scientists thought subduction zone ruptures could not slip all the way up to the ocean floor because the water-logged clays of the upper crust are too weak to build up strain. But the 2011 Tohoku undersea earthquake in Japan punched through to the sea floor, causing the devastating tsunami that triggered the Fukushima nuclear disaster. Images of sediments trapped in Cascadia's trench, where the plates meet, could reveal layering that would indicate how often past ruptures have reached the surface.

Those kilometers-thick piles of sediments could hold clues to another potential catastrophe. The researchers will be looking for pockets of gas trapped in the sediments, which might make them liable to collapse during an earthquake in tsunami-forming submarine landslides. And measuring how quickly the airgun waves travel through sediments across the region will improve early warning systems that predict how quickly earthquake waves will arrive at a given place and how damaging they will be, says Harold Tobin, director of the Pacific Northwest Seismic Network, who helped expand an alert system called ShakeAlert to the Pacific Northwest this spring (*Science*, 2 November 2018, p. 514).

Fundamental insights into how subduction zones work could emerge, too. About 15 years ago, seismometers in the Cascadia region began to pick out a small shudder—as subtle as the rumble of a passing train—lasting for several weeks. The noise turned out to come from the depths of the fault, where the rock is so hot the plates transition from locked to smooth sliding.

Some scientists believe the rumble, which has been detected every year or so, stems from "slow slip"—an earthquake in slow motion. Similar events preceded Tohoku, as well as a 2014 magnitude 8.2 earthquake in Chile, suggesting slow slip events can add stresses to locked parts of the fault and trigger major quakes. But other scientists tie the tremors to noise generated as rising water is expelled from hot minerals in the slab. The 800 seismic receivers deployed on land should add 3D detail to this deepest part of the fault, helping resolve this debate, says Emilie Hooft, a marine geophysicist at the University of Oregon. That is, if the teams can recover the receivers, with their stored data, from across 130,000 square kilometers after a summer's worth of plant growth, she says. "Our challenge now will be to find them."

It's not the only hurdle the seismic campaign has faced, Carbotte says, speaking to *Science* from the *Langseth* as huge swells buffeted it. During the airgun shots small chase boats scurry to drive off whales and dolphins, in an effort to protect them from potential hearing damage. And early in the cruise, fishing gear got tangled in the 15-kilometer-long hydrophone cable. Then, she says, "we actually lost it" when the cable broke in rough weather. They found the tail buoy quickly, but lost several days bringing the line back on board and switching to a 12-kilometer cable.

Later this month, calm will once again return to Cascadia. It will take researchers years to stitch together all the data collected by the cruise. But once they do, if they get lucky, something in those images may shout out why this subduction zone, compared with all others, stays so hushed. "That's hanging out there as a great big question mark," Goldfinger says. "People are still tiptoeing about it." ■

Perilous slope

A research ship, zigzagging up the coast of the Pacific Northwest, is building a picture of the eerily quiet Cascadia subduction zone by firing seismic shots into the water and capturing reflections from under the sea floor. More than 800 receivers on land will help image deeper parts of the fault, which last ruptured more than 300 years ago in a magnitude 9 earthquake.

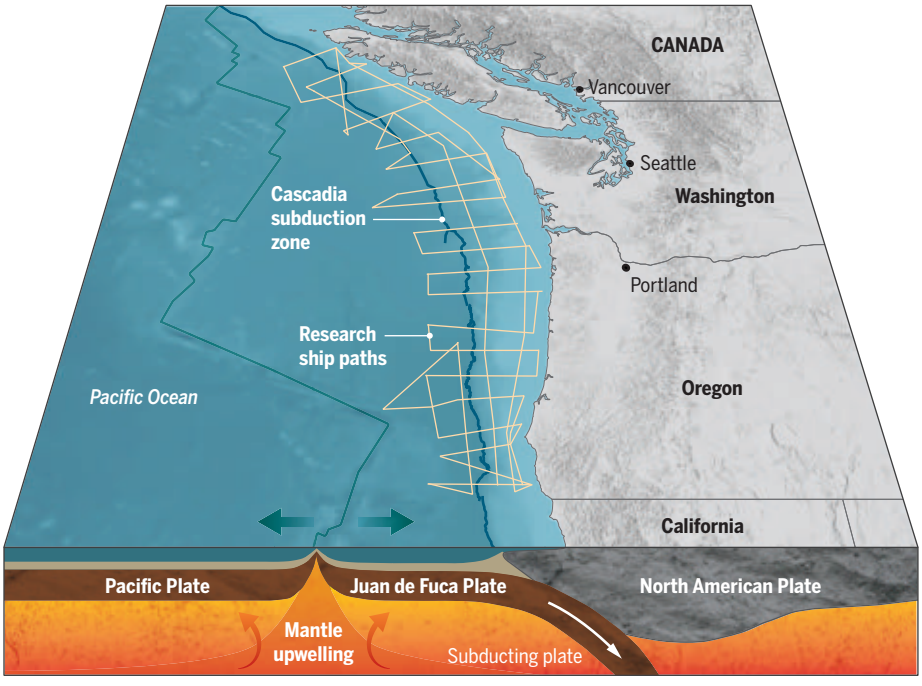

CREDITS: (GRAPHIC) K. FRANKLIN/*SCIENCE*; (DATA) KATHLEEN CANTNER/AMERICAN GEOSCIENCES INSTITUTE

PHOTO: KYODO/AP IMAGES

Many of the first COVID-19 cases were linked to a seafood market (center) in Wuhan, China, but a new analysis suggests a different strain of SARS-CoV-2 caused early cases elsewhere.

COVID-19

Did a Chinese team 'obscure' early coronavirus sequences?

Preprint's claim inflames already divisive origin debate

By **Jon Cohen**

In a world starved for data to clarify the origin of COVID-19, a study claiming to have unearthed early sequences of SARS-CoV-2 that were deliberately hidden was bound to ignite a sizzling debate. Last week a preprint by evolutionary biologist Jesse Bloom of the Fred Hutchinson Cancer Research Center asserted that Chinese researchers sampled viruses from some of the first COVID-19 patients in Wuhan, China, posted the viral sequences to a National Institutes of Health (NIH) database, and then later had the genetic information removed to "obscure their existence."

The uproar over the preprint led Senator Josh Hawley (R–MO) to demand answers from NIH on why the agency agreed to "purge" the data and to call for an investigation into the matter. Even for some scientists, Bloom's work reinforced suspicions that the Chinese government has tried to hide how the pandemic started. "This is a creative and rigorous approach to investigating the provenance of SARS-CoV-2," says Ian Lipkin, a microbiologist at Columbia University's Mailman School of Public Health. "There may have been active suppression of epidemiological and sequence data needed to track its origin."

But critics of Bloom's bioRxiv preprint call his detective work much ado about nothing, because the Chinese scientists later published the viral information in a different form, and the recovered sequences may add little to the origin hunt. "The idea that the group was trying to hide something is farcical," says evolutionary biologist Andrew Rambaut at the University of Edinburgh.

Bloom says he has no bias toward a particular origin hypothesis for SARS-CoV-2, and he agrees that the 13 partial sequences he recovered don't resolve whether the virus originally jumped to humans from an unknown animal or somehow leaked from a Wuhan virology center. "I don't think this bolsters either the lab origin or zoonosis hypothesis."

Science's COVID-19 reporting is supported by the Heising-Simons Foundation.

Chinese health officials on 31 December 2019 tied the Huanan Seafood Market in Wuhan to an outbreak of an "unexplained pneumonia," but within a month it had become clear that many of the earliest COVID-19 cases had no link to the market. Bloom, who studies viral evolution, set out to investigate early cases after a controversial report on the pandemic's origin issued in March by a joint commission of Chinese and foreign researchers overseen by the World Health Organization. The report deemed it "extremely unlikely" that SARS-CoV-2 escaped from a lab; Bloom helped organize a much-discussed letter, cosigned by 17 other scientists, criticizing that conclusion and calling for further investigation.

Bloom wanted to do his own analyses of the viruses detected in the earliest cases, which led him to a list of all SARS-CoV-2 sequences submitted before 31 March 2020 to the Sequence Read Archive (SRA), an NIH database. But when he checked the SRA for one of the listed projects, he couldn't find its sequences. Googling some of the project's information, he found a study, led by Ming Wang from Wuhan University's Renmin Hospital, that had been posted as a preprint on 6 March 2020 on medRxiv and published in June of that year in *Small*, a journal little known to virologists. That paper lists some of the earliest COVID-19 patients in Wuhan and the specific mutations in their viruses, but doesn't give the full sequence data. Further internet sleuthing led Bloom to discover that the SRA backs up its information in Google's Cloud platform, and a search there turned up files containing some of the Wang team's earlier data submissions.

The *Small* paper mentions no corrections to the viral sequences that might explain why they were removed from the SRA, which led Bloom to conclude that "the trusting structures of science have been abused to obscure sequences relevant to the early spread of SARS-CoV-2 in Wuhan." (In the wake of criticisms of the initial preprint, Bloom toned down this sentence and other accusatory language.) Bloom acknowledges SARS-CoV-2 sequences can be derived from the data in the *Small* paper, but he says most virologists expect to be able to download whole viral genomes from a database like the SRA.

Several authors of the *Small* paper did not reply to requests for comment, but NIH last week noted in a statement that it removed the SRA sequences at the request of the submitting investigator, who the agency says holds the rights to the data. Bloom added NIH's email exchange to his revised preprint. "I have submitted an updated version of this SRA data to another website," reads a 15 June email sent to NIH from a Wuhan University researcher whose name was redacted. Yet Bloom says he cannot find the sequences in any other virology database.

Bloom asserts that because the deleted sequences lack three mutations seen in COVID-19 cases linked to the seafood market, the patient viruses Wang's team analyzed more likely represent a progenitor SARS-CoV-2. But Rambaut says the differences Bloom highlighted are too few to distinguish the "roots" of the SARS-CoV-2 family tree.

Leaving aside the meaning of the sequences Bloom found, the demonstration that researchers can potentially find "new" SARS-CoV-2 data in the cloud is an exciting advance and may prompt similar sleuthing, says genomicist Sudhir Kumar of Temple University, who has also analyzed early SARS-CoV-2 sequences. "Many people feel that there is a lot more Chinese data out there, and they don't have access to it." ■

BIOMEDICINE

Gene editor injected into the body treats disease

In a first, CRISPR components infused into patients' blood shut down mutant gene in liver

By **Jocelyn Kaiser**

The gene editor CRISPR excels at fixing disease mutations in lab-grown cells. But using CRISPR to treat most people with genetic disorders requires clearing an enormous hurdle: getting the molecular scissors into the body and having it slice DNA in the tissues where it's needed. Now, in a medical first, researchers have injected a CRISPR drug into the blood of people born with a disease that causes fatal nerve and heart disease and shown that in three of them it nearly shut off production of a toxic protein by their livers.

Although it's too soon to know whether the CRISPR treatment will ease the symptoms of the disease, known as transthyretin amyloidosis, the preliminary data reported last week are generating excitement about what could be a one-time, lifelong treatment. "These are stunning results," says gene editing researcher and cardiologist Kiran Musunuru of the University of Pennsylvania, who was not involved in the trial. "It exceeds all my expectations."

The work also marks a milestone in the race to develop treatments based on messenger RNA (mRNA), the protein-building instructions naturally made by cells. Synthetic mRNAs power two COVID-19 vaccines being given to millions of people to fight the coronavirus pandemic, and many companies are working on other mRNA vaccines and drugs. The new treatment includes an mRNA encoding Cas, a DNA-cutting enzyme that is one of CRISPR's two components.

It "begins the convergence of the fields of CRISPR and mRNA," says cardiovascular researcher Kenneth Chien of the Karolinska Institute, a co-founder of Moderna, which makes one of the COVID-19 vaccines and is also developing mRNA drugs.

The CRISPR clinical trial aims to deactivate a mutated gene that causes liver cells to churn out misfolded forms of a protein called transthyretin (TTR), which build up on nerves and the heart and lead to pain, numbness, and heart disease. The resulting condition is relatively rare, and an approved drug, patisiran, can stabilize it. But researchers at veteran biotech Regeneron Pharmaceuticals and startup Intellia Therapeutics saw it as a good proof of principle for their experimental CRISPR treatment.

Last year, researchers used CRISPR to turn on a fetal form of hemoglobin to correct sickle cell disease or a related condition in several people (*Science*, 11 December 2020, p. 1254). The treatment required removing a patient's diseased blood stem cells, modifying them with CRISPR in a dish, and then infusing them back. A trial testing a direct injection of a virus encoding CRISPR's components into the eye to treat a condition that causes blindness is also underway. But treating most other genetic diseases means injecting CRISPR's components, or genetic instructions for them, into the blood and having the therapy target an organ or tissue—a huge challenge, but potentially easier in the liver, which sops up foreign particles.

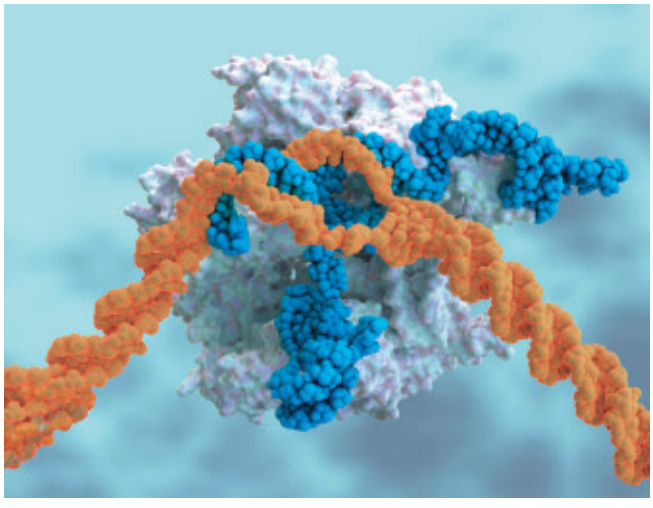

A new CRISPR-based treatment for a deadly rare disease contains a messenger RNA encoding a DNA-cutting enzyme (white) and another RNA (blue) that guides the enzyme to a specific gene sequence (orange).

In the CRISPR trial, four men and two women with transthyretin amyloidosis between ages 46 and 64 were injected with a lipid particle carrying two different RNAs: the mRNA for Cas and a guide RNA to direct the enzyme to the gene for TTR. After Cas makes its cut, the cell's DNA repair machinery heals the break, but imperfectly, knocking out the activity of the gene.

After 28 days, three men given the higher of two doses of the treatment had an 80% to 96% drop in TTR levels, on par or better than the average of 81% with patisiran, the team reported last week in *The New England Journal of Medicine*. "The data are extremely encouraging," says trial leader Julian Gillmore of University College London, who also presented the study at the online annual meeting of the Peripheral Nerve Society. "It could be potentially the first curative treatment for this hereditary disabling and life-threatening disease," says neurologist David Adams of the University of Paris-Saclay, who led trials for patisiran. (That drug is a kind of RNA that silences TTR production temporarily, meaning it must be injected regularly.)

It may take months for patients receiving the CRISPR treatment to see their symptoms lessen, but they reported few short-term side effects. Problems could surface over time: CRISPR can potentially make cuts in the wrong DNA location (and in the wrong cells), triggering cancer or other problems. But the lipid-encased mRNA approach is potentially safer than using viruses to ferry genes for a gene editor, a tried-and-true approach others are pursuing for systemic treatments. Those genes can persist in cells, continuing to make the gene editor long after it has done its job. In contrast, "The beauty of mRNA is that it is gone afterwards," Chien says.

The study paves the way for modifying the liver with CRISPR to treat other diseases, either by knocking out a gene or—more challenging—modifying it with the help of a DNA template. The latter approach could also be used to turn the liver into a factory for making an enzyme needed elsewhere in body.

Jennifer Doudna of the University of California, Berkeley, who shared a Nobel Prize last year for developing the gene editor CRISPR from a bacterial immune system and co-founded Intellia, sees even bigger prospects. The new work, she says, is "a critical first step in being able to inactivate, repair, or replace any gene that causes disease, anywhere in the body." ■

IMAGE: ELLA MARU STUDIO/SCIENCE SOURCE

Jack Schmidt shooting rapids on Utah's Green River, a tributary of the Colorado River.

PHOTO: WAYNE WURTSBAUGH

A VOICE FOR THE RIVER

Jack Schmidt tells hard truths about how climate change will shrink the Colorado River, a lifeline for the Southwest. Will officials listen?

By **Erik Stokstad**

On a spring morning in 1996, then–Interior Secretary Bruce Babbitt stood at Glen Canyon Dam, a concrete bulwark in Arizona that holds back the Colorado River to form Lake Powell. During a live broadcast on the *Today* show, a popular national TV program, Babbitt opened valves to unleash an unprecedented experimental flood into the Grand Canyon just downstream. As onlookers applauded, water gushed from gaping outlet pipes. Babbitt called the experiment, which was testing one way of restoring Grand Canyon ecosystems damaged by the dam, the start of "a new era" in environmental management.

Jack Schmidt was underwhelmed by the scene. He had spent years helping design the controversial experiment—which cost electric utilities nearly $3 million in lost revenue—and fighting to launch it. But compared with the natural deluges that raged down the canyon before the dam was completed in 1963, he remarked to a *Los Angeles Times* reporter, "This is a pretty wimpy flood."

That verdict was typical of Schmidt, a river scientist at Utah State University who thinks big and speaks candidly. During his long research career, he has played a major role in revealing how the Colorado River functions, and how forces—natural and human—are reshaping and often damaging it. Despite his bluntness, Schmidt is a go-to expert for stakeholders and policymakers. He has taken them on river trips to explain key research findings, drawing graphs in the sand. And with other researchers, Schmidt has catalyzed far-reaching changes in how government agencies manage the Colorado River system, a critical source of water shared by seven states and Mexico.

"Jack looms very large in both the science and the policy of the Colorado River," says Gordon Grant, a hydrologist and geomorphologist with the U.S. Forest Service in Oregon. "He's not afraid to push back on the water managers and he's not afraid to push back on the environmental groups," says Tom Buschatzke, director of the Arizona Department of Water Resources. "He's willing to use science to try to find practical solutions."

As a warming climate reduces the river's flow, Schmidt, 70, is making what could be his most important push to shape the fate of his beloved waterway. He and his colleagues are working to inject a dose of scientific reality into public debate over water resources that, the team says, is too often clouded by wishful or outdated thinking. The biggest delusion: that there will be enough water in a drier future to satisfy all the demands from cities, farmers, power producers, and others, while still protecting sensitive ecosystems and endangered species. The hard truth, according to long-term scenarios produced by Schmidt and his colleagues, is that some users will have to consume less water, and that policymakers will face agonizing choices sure to produce winners and losers.

Those are messages that many players aren't eager to hear, especially states planning to drain more water from the river to fuel growth. But Schmidt says he and his colleagues simply want everyone to understand the potentially divisive trade-offs. "We ask provocative and uncomfortable questions," he says.

The moment is ripe, as a record-breaking drought provides a taste of what more climate change could bring. Last month, Lake Mead, a second massive reservoir downstream from Lake Powell, dropped to its lowest level ever. At the same time, government officials are beginning a 5-year process of renegotiating several key agreements over use and management of the river's water. They have sought Schmidt's views. "We had Jack and his team present to our leadership because of the high regard we hold for their research," says Katrina Grantz, assistant regional director of the Upper Colorado Basin for the federal Bureau of Reclamation, which operates many major dams.

Some see Schmidt's tell-it-as-it-is approach as critical to developing realistic policies. "Jack is never afraid to speak the truth, according to what the research is saying," says Mike Fiebig of American Rivers, an environmental group that Schmidt advises. And, he adds, Schmidt will speak "to whoever is listening."

FOR A CONTINENTAL-SCALE river, the Colorado is not very big, but it has an outsize importance. Rising in the Rocky Mountains, its muddy water has always been crucial to the development of the arid West. In 1931, the Hoover Dam created what is still North America's largest reservoir, Lake Mead. The dam's 17 turbines generate electricity that lights Los Angeles, Las Vegas, and other cities, and also powers pumps that lift river water over mountains and into southern California. Engineers built hundreds of kilometers of canals to carry the water to cities and farmers. In Colorado, they constructed numerous tunnels, including one below the continental divide, to deliver water to Denver. Today, more than 40 million people in seven states and many Native American tribes rely on the Colorado River.

The water has long been worth fighting over. In 1922, in a bid to prevent conflicts, states in the watershed divided the rights to nearly 20 cubic kilometers of water, which they assumed was only part of the river's annual flow. The compact gave half of the water to the lower basin, where cities and farms, especially in California and Arizona, have long used about twice as much water as consumers in the upper basin. It promised the other half to the upper basin, so that states including Colorado and Utah could develop in the future. A follow-on agreement in 1944 gave water to Mexico, where the river's last drops barely trickle into the sea.

Lawyers and politicians spent decades disputing the terms of the original compact, parts of which remain contested. Meanwhile, it became ever clearer that the compact rested on flawed assumptions, because it was struck when the region was abnormally wet. After 1933, the Colorado River carried considerably less water on average for the next 5 decades (see chart, p. 20). The past 2 decades have seen another decline, as the region endures its worst dry spell in 1250 years; flows have been about 19% less than the entire 20th century average. Climate models suggest an additional 30% decline by 2050, as precipitation continues to decrease and the atmosphere warms. The heat dries the soil and causes plants to transpire more, reducing the runoff efficiency—the fraction of precipitation that reaches the river.

The impacts are impossible to miss. From the air, bathtub rings of white stone encircle Lake Mead, which has been less than 40% full since 2015, as well as Lake Powell, which has been below 50% capacity since 2013. Boat ramps have been extended to help keep a large recreational industry afloat. Farmers in multiple states are expecting cutbacks in water deliveries next year. Nevada is launching new conservation measures, including a ban on using Colorado River water to irrigate lawns after 2026.

In some states, the shrinking river has only intensified claims on its flow. "It's our water," Utah State Senator Don Ipson (R) proclaimed in March. He was urging his colleagues to support a bill, now awaiting the governor's signature, that creates a new commission to advocate for the state's right to develop future water supplies.

Such assertive political jockeying highlights the challenge facing negotiators. They must grapple with key agreements that expire in just 5 years, as well as an inexorably changing climate. "All of that," says water

Lifeline for the Southwest

The Colorado River supplies water to farms and cities both within and outside the basin, such as Denver and Los Angeles. Two major dams store water, provide recreation, and generate power.

CREDITS: (MAP) N. DESAI/*SCIENCE*; (DATA) COLORADO RIVER BASIN GIS OPEN DATA PORTAL

Water gushes from Glen Canyon Dam's outlet pipes in 2012 to create an artificial flood, one of several intended to help rebuild sandbars in the Grand Canyon.

policy expert Brad Udall of Colorado State University, Fort Collins, "has combined into this slow-moving trainwreck."

SCHMIDT GREW UP far from the Colorado in suburban New Jersey. He first glimpsed southwestern landscapes in undergraduate geology classes at Bucknell University in Pennsylvania. An encounter with famed river scientist Luna Leopold during his master's work at the University of California, Berkeley, inspired his passion for natural resource issues. He went on to a Ph.D. at Johns Hopkins University, studying water policy and how rivers reshape landscapes with one of the field's top experts, Gordon "Reds" Wolman.

Soon he was immersed in a conflict over the Colorado River that had begun in the 1970s, not long after Glen Canyon Dam was completed. The barrier nearly doubled the storage capacity for water, but it dramatically changed river conditions in the Grand Canyon. It cut off supplies of sediment that had created vast sandbars, for example, and released clear, cold water that allowed introduced species, such as trout, to displace native fish adapted to warm, muddy flows. Sudden releases of water to meet electrical demand, an operation called hydropeaking, disturbed wildlife, plants, and thousands of rafters who float the canyon each year.

Environmental groups sued, demanding that the Bureau of Reclamation do more to protect the ecosystem. In response, in 1982 the federal government launched what became a $12 million research program to probe dam impacts. Schmidt was funded to study the Grand Canyon's sandbars, which river guides complained were shrinking, depriving them of camping spots.

Schmidt's research helped explain the losses, revealing how swirling water digs up sediment in certain places and drops it elsewhere. The work "really has been foundational for all the thinking about sandbar dynamics since," says Grant, who was a student alongside Schmidt at Johns Hopkins.

During a weeklong rafting trip studying erosion, Schmidt and others discussed what could be done to prevent the losses. By the light of a campfire, they drafted a "beach bill" in his field book, sketching out the kind of federal legislation that could safeguard the canyon's beaches.

A few years later, Bill Bradley, a Democratic senator from New Jersey, visited Middlebury College, where Schmidt was a faculty member. He and three students handed the senator a report they had written on sandbar erosion. Bradley took it with him when, the next month, he visited the canyon to see the problems for himself.

Bradley and other lawmakers were in the process of crafting their own bill, which became the Grand Canyon Protection Act of 1992. It helped set the stage for the experimental floods that began in 1996. The idea, developed by a small group of researchers including Schmidt, was that artificial floods could push sand downstream. Although Glen Canyon Dam blocks most of the sand that used to wash down the main river channel, tributaries below the dam still supply some. The floods would drop the sediment onto sandbars (*Science*, 10 December 2004, p. 1884). Dam operators weren't eager to cede control to the scientists, though. "Jack had to duke it out," Grant says.

The experimental floods have proved only modestly successful, in large part because the tributaries don't deliver enough sediment to make a huge difference. Rich Ingebretsen, co-founder of the Glen Can-

Severe drought

Average precipitation in the Southwest over the past 3 decades is much lower than before.

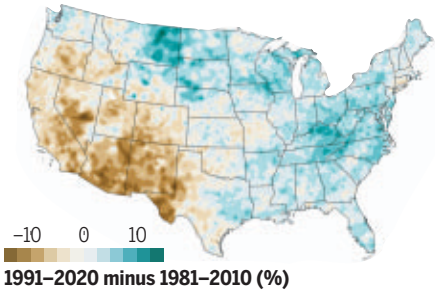

1991–2020 minus 1981–2010 (%)

CREDITS: (PHOTO) REUTERS/BOB STRONG; (MAP) COOPERATIVE INSTITUTE FOR SATELLITE EARTH SYSTEM STUDIES; (DATA) NATIONAL OCEANIC AND ATMOSPHERIC ADMINISTRATION

yon Institute, an environmental group, says the real significance of the first experiment was that dam operators now consider environmental impacts—and not just the needs of electric utilities, farmers, or recreational boaters—in deciding when and how much water to release. "It ushered in a new world," Ingebretsen says. "Environmentalists were now working with water managers for the first time in the history of the country."

POLICYMAKERS HAVE BEEN slower to grapple, at least publicly, with a question that extends far beyond the river's ecosystems and recreational opportunities: the limits of its ability to supply all the water the West wants, now and in the future.

Schmidt remained focused on river dynamics and developing strategies to lessen the impact of dams on ecosystems, first at Utah State and then, starting in 2011, as chief of the U.S. Geological Survey's Grand Canyon Monitoring and Research Center (GCMRC), which helps guide restoration and management efforts. Martin Doyle, who studies river science and policy at Duke University, says he was skeptical that Schmidt would thrive as a government official, in part based on his frank approach to peer-reviewing papers. "He always signed his reviews and it was always just brutal, because he wasn't tolerant of sloppy thinking." But Schmidt had remarkable success boosting his staff's morale and conditions for research, Doyle says. "He started to turn the GCMRC from a monitoring center to a science center."

One research goal was to figure out exactly when an experimental flood would most benefit ecosystems. "Jack had a huge influence," says Anne Castle, a fellow at the University of Colorado, Boulder, who oversaw water and science policy at the Department of the Interior from 2009 to 2014. "He cares about getting it right, that the river is managed in a way that reflects the best science available."

The experience at GCMRC also got Schmidt thinking about how regional water supply decisions, often made decades ago, could thwart plans to improve river management. For example, when his team participated in writing a new plan for operating the Glen Canyon Dam to make sandbars more stable and protect endangered fish such as the humpback chub, it learned it could not consider any changes that were inconsistent with existing water supply agreements. That was frustrating, Schmidt recalls: "Nobody really asked the question: What's the way to manage the [whole] system that's the best for Grand Canyon?"

AFTER SCHMIDT LEFT GCMRC to return to Utah State in 2014, he wanted to explore those possibilities—unhindered by political and institutional constraints. He set up an interdisciplinary research center, and 2 years ago pulled together an all-star team of water experts for the effort, called the Future of the Colorado River Project. Among the collaborators: Udall, a veteran of western water policy; Eric Kuhn, retired general manager of the Colorado River Water Conservation District, a planning agency, who provides a practical perspective; and Kevin Wheeler of the University of Oxford, a master of complex hydrological models.

The group has so far released six white papers. Some address technical matters, such as how to improve the models used to develop management policy for reservoirs. Others have scrutinized hot-button proposals, such as prioritizing water storage in Lake Mead and keeping less in Lake Powell. This proposal, called Fill Mead First, could be a first step toward dismantling Glen Canyon Dam and restoring the Grand Canyon. (Schmidt's team concluded the approach wouldn't save much water and would likely greatly perturb the downstream ecosystem.)

The latest installment, released in February, evaluated for the first time how rising temperatures and declining runoff might jeopardize the regional water supply. The white paper also looked at how demand might change in coming decades. Using the same computer model that the Bureau of Reclamation and state water agencies use, known as the Colorado River Simulation System, the team examined numerous scenarios, including how meager runoff could reduce water storage in Lake Powell and Lake Mead to critical levels. At one threshold dam turbines couldn't generate electricity. If levels fall even lower, the reservoirs can no longer release water to alleviate downstream shortages, leaving users at nature's mercy.

The modeling, done by Wheeler, showed reservoirs might dip into the danger zone by 2041, assuming the present drought persists. To maintain a degree of water security, the study found that upper basin users would have to cap consumption at a long-term average, and lower basin states might have to cut their use by as much as 40% by the 2050s. "Colorado River outlook darkens dramatically in new study," ran a headline in the *Arizona Daily Star*.

That is a "really bold and difficult upshot," Fiebig of American Rivers says. And although it's not news to veteran water experts, says Elizabeth Koebele, an environmental social scientist at the University of Nevada, Reno, "bringing that [message] into the broader policy conversation is pretty provocative now." The results mean the upper basin can't develop all of its water rights, Schmidt says. Making that scenario "completely transparent forces everybody to deal with it."

Not surprisingly, some groups argue the study is overly pessimistic. Amy Haas, executive director of the Upper Colorado River Commission, notes the white paper uses "obsolete" water demand forecasts from 2007. More recent forecasts predict lower demand, she says. (Schmidt says those numbers don't change the overall picture.)

The new abnormal

For the first third of the 20th century, the Colorado River supplied plentiful water on average, despite large annual fluctuations (top). Then water supply fell to a relatively constant level while use by cities and farms ramped up. Over the past 3 decades, climate change affected supply as rising air temperatures (bottom) increased water loss from soil and plants. Lower runoff efficiency means less rain and melted snow end up reaching the streams that feed the Colorado River.

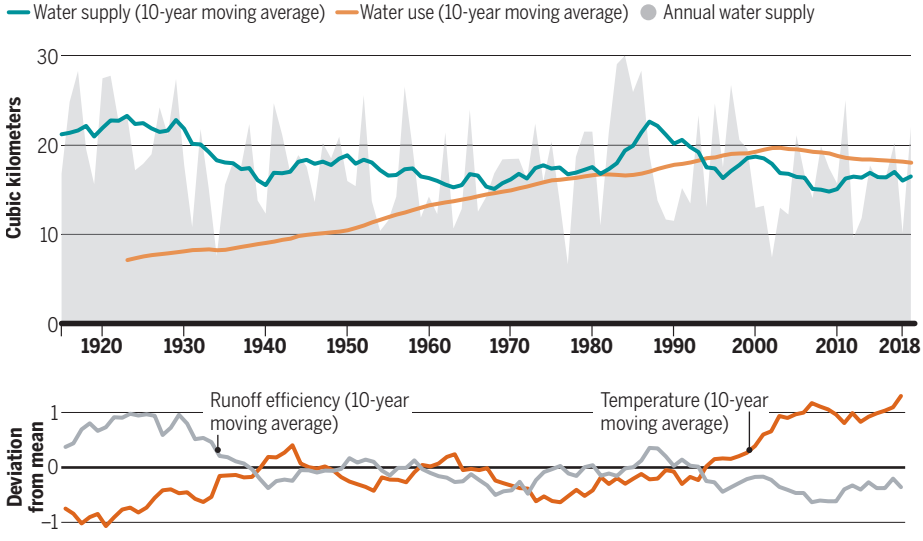

CREDITS: (GRAPHIC) N. DESAI/*SCIENCE*; (DATA, TOP TO BOTTOM) BUREAU OF RECLAMATION; MCCABE *ET AL.*, *EARTH INTERACTIONS*, 21 (10), 1–14, (2017); GREG MCCABE

Lake Mead last month fell to its lowest level since the Hoover Dam was built in 1936. Some 45 meters of shoreline have emerged since the reservoir was last full in 2000.

PHOTO: BRIDGET BENNETT/AFP VIA GETTY IMAGES

Average demand for water has not risen in recent decades in the upper basin, Schmidt notes, but that may shift, especially as coal-fired power plants close and agricultural practices shift. And more change may be in store if Native American tribes decide to assert their water rights and develop or market them outside of their reservations.

Buschatzke of the Arizona Department of Water Resources says the group's sobering scenarios are helpful for informing decision-making. "We understand what they're doing is pushing the envelope, rightly so for academia." But he says the department must create a water supply plan that is acceptable to diverse parties. Some lower basin groups are likely to oppose any plan that calls for cuts, he says, whereas conservation-minded advocates might push for even larger cuts.

Upper basin states, meanwhile, remain staunchly opposed to any notion of giving up future development. In Utah, which had the nation's fastest growing population over the past decade, despite having the second driest climate, officials want to build a 225-kilometer pipeline to tap more water from Lake Powell. They shrug off concerns about how that could affect downstream supplies. Critics of Utah's new water advocacy agency worry it will simply deny the reality of climate change as it attempts to protect the state's water rights. "The Utah State Legislature is still mired in an era of unreality," says Daniel McCool, a political scientist at the University of Utah. The state's recent moves amount to "a declaration of water war, frankly."

THE NEW ROUND OF NEGOTIATIONS over the Colorado compact will reveal just how far the parties are willing to go in acknowledging the potential worst case scenarios. "It's all coming to a head," Koebele says. "The extreme drought … is really highlighting that we do need to think more creatively." Some of the big ideas floated by Schmidt's group include new water accounting methods that span the entire basin, which would allow more flexible dam operations, and expand voluntary water banking and market exchanges of water rights.

Even as Schmidt works to highlight the risks of business as usual, he knows he may have to accept another difficult truth: that, in the end, people might once again decide to sacrifice the Colorado River ecosystems he treasures in order to get the water they want for cities, farms, and power.

Currently, environmental management programs—including some he helped design—mitigate some of the most severe impacts of existing dams and other infrastructure. But that won't suffice as climate change and new water demands take hold. "We can't solely rely on tweaking small aspects of reservoir operations to protect river ecosystems," he says. "We also have to consider how much water rivers need to remain healthy."

Schmidt would like that need to be a larger part of the upcoming negotiations. His own priority is to preserve the flows of rivers in the upper basin, which are wilder than the lower basin's highly engineered reaches. When pressed, he confesses to an "aesthetic and philosophical wish" for a return to vanishing and long-gone landscapes of the Colorado. But, "I also recognize it's such a complicated world that in most of those cases, it's perhaps impossible."

Still, Schmidt wants officials debating the future of the Colorado to know the region's vast and growing human presence is not the only thing at stake. Next month, he will lead scientists, water managers, tribal leaders, and other river stakeholders on a raft trip down the Green River, the longest headwaters tributary of the Colorado. During the 5-day trip, organized by his center at Utah State and American Rivers, Schmidt will use sandbars as classrooms, sharing what he and other researchers have learned about the fish, plants, sand, and dams. The goal, he says, is that "when people are sitting in those conference rooms making decisions about water supply, they have in the back of their mind what these rivers are all about." ■

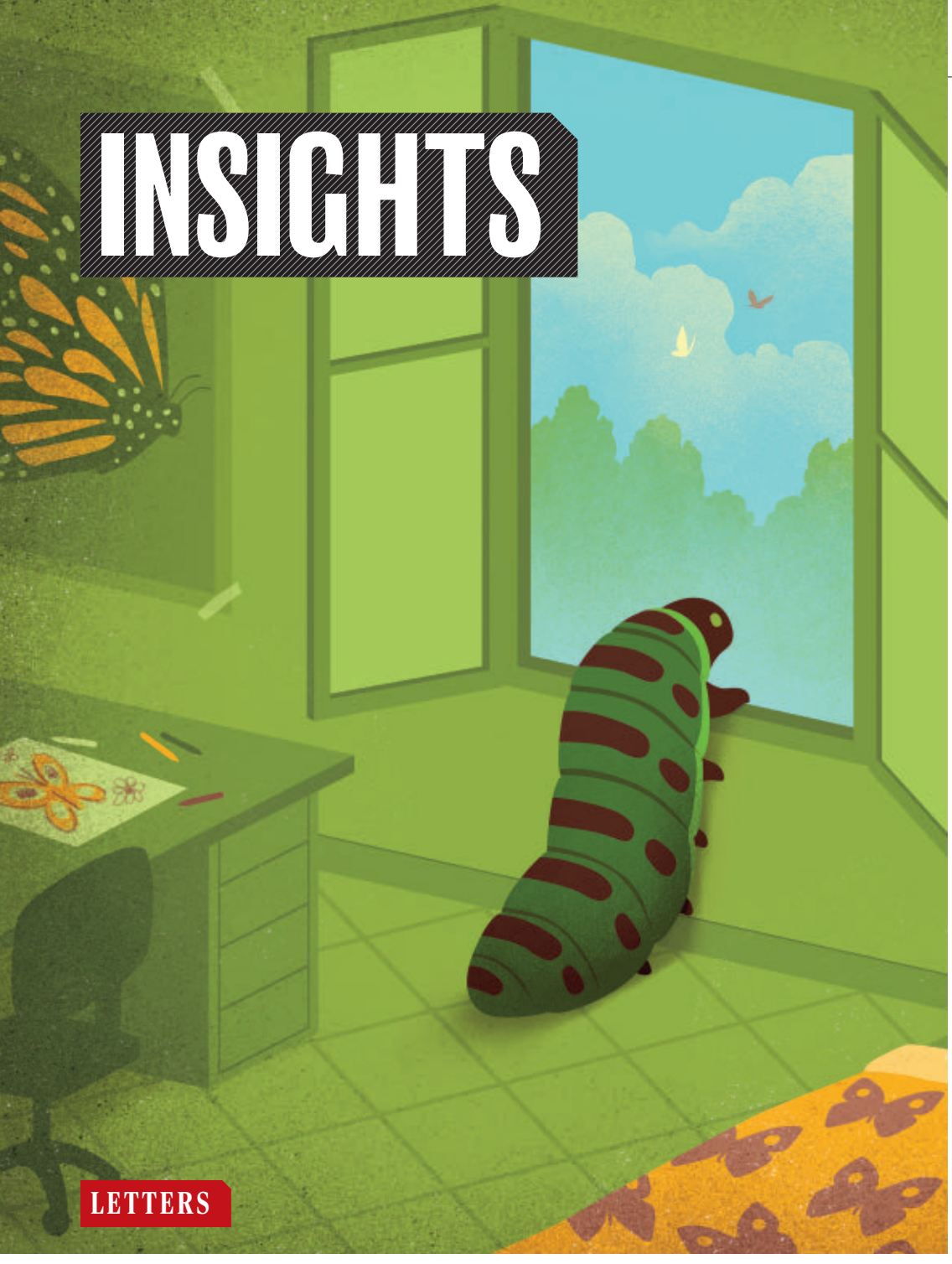

NEXTGEN VOICES

Pandemic haiku

As we look toward post-pandemic life, we wanted to take a moment to think back on how this experience affected scientists. We gave young scientists this challenge: **Write a haiku describing your career or field during the pandemic and your hopes for the future.** Read a selection of their responses here. Follow NextGen Voices on Twitter with hashtag #NextGenSci. Read previous NextGen Voices survey results at https://science.sciencemag.org/collection/nextgen-voices. **—Jennifer Sills**

Home

Work-life balance

"This is importa-"
"Mommy, I need a snack now"
It's all important
Karla K. Haack, USA

CPR

Lonely coffee break
Office plants have surely died
Colleagues catch up soon
Astrid Van Wilder, Belgium

Zoom meetings

Non-stop, but soon not
To the pajamas I love
Bittersweet goodbye
Dhruv Patel, USA

Reaction cookbooks

Exchanged flask for pot
Cookbook replaced lab notebook
Tasty test results
Shivani Patel, USA

Dimensions unknown

Theorists on Zoom
How tall are my co-workers?
Hold something for scale
Leo E. Chambers, USA

Online speech

Oops, camera's on!
Speech broadcast in full color
Pajamas exposed
Yuan Zhi, China

Passion with a lag

Online lab meetings
Heated debates but with lags
Victories lack oomph
Hikaru Katie Kotake, USA

Relevance

Infectious disease modeling

No one knew my field
Now all say "R naught"; I hope
They can forget soon
Akira Endo, UK

Symphony in silico

Genome surveillance,
Of the pathogens we fight
Predict, protect lives
Michael Strong, USA

Nano tackles COVID

Nanoscience sees
Nanoparticle stops spread
And nanotech cures
Shruti Sharma, USA

ILLUSTRATION: DAVIDE BONAZZI/SALZMANART

Experience and lessons
Hunting for measures
From history's disasters
To prevent the next
Jian Zhang, China

Lifesaving logistics
Vaccines delivered
Supply chain research crucial
Relevance maintained
Samuel Nathan Kirshner, Australia

911 calls me
A first responder
Vaccinators, SOS!
EMT role grows
Morgan Daly Dedyo, USA

PlasticMasks, LLC
Diverted to masks.
Made them better. No buyers.
Now back to rockets.
Adrian Tymes, USA

Psychology
Mental health declines
Psychologists in demand
Time to nourish souls
Sarita Kumari, India

Classroom

A chemist's life
Make sanitizer
Teach online classes daily
Dear vaccine, come soon
Matheus Pereira Postigo, Brazil

Pandemic teaching
What are breakout rooms?
Unstable connection. Ugh.
Chat with your neighbor!
Ashley Barbara Heim, USA

Pandemic education
Back to "normal" soon
Effort and innovation
Can we keep what works?
Rachel Yoho, USA

Classroom
Tall panes guard the desks
A cloudy inconvenience
I'll see clearly through
Elizabeth Aurora Chua, USA

(Emotionally) distanced
No classmates; black squares
Am I struggling alone
Or is it you, too?
Jasleen Gill, USA

Transitions

Impressions
New city, new lab
I still have not met my boss
Labmates became friends
Erica L. Gorenberg, USA

Grad school interview
I talk to my screen
Interview? Insanity?
We'll shake hands someday
Charlotte Ruth Mineo, USA

Colleagues
My friends, my peers, who?
Just pixels on a phone screen
I will meet them soon
Phoebe White, USA

2020 graduate
Dissertation done
Defense via zoom, success
Now to find a job?
Michele Fullarton, USA

Walk across the keyboard
Ding, inbox degree
Hug to pixel family
PhD? We'll see
Joseph Nicholas Rainaldi, USA

Introspection

Spring comes
Plants grow more slowly
During the long, harsh winter
But spring is coming
Marcela Viviana Nicola, Argentina

Circles and phases
Glimpse of crescent Moon
In between clouds passing by
Full Moon will soon come
Asli Pinar Tan, Turkey

Unpredictable
Could it be the air?
The doorknob or the salmon?
Maybe it is us
Hanafiah Fazhan, Malaysia

After a century
Corona looked in
And saw an epoch waiting
To take a deep breath
Archna Singh, India

Frozen in time
Like cells: Lonely, trapped
Encased: Paraffin prison
Yearning to be free
Joseph Chong, USA

Lab and Field

Germ-free mouse
Axenic before
The COVID pandemic, and
Axenic after
Martin Schwarzer, Czech Republic

The silent lab
Rusty blade, dry tube
Lie on dusty bench for months
Creak...the door opens
Bo Cao, China

Lab hands
Hands scrubbed red and raw
Tremble holding the pipette
Will grow steady soon
Charlotte Ruth Mineo, USA

Delivery delays
"Week to deliver"
Been a month but still not here
Reagent, hurry!
Anna Uzonyi, Israel

Separation anxiety
Lonely flask in lab
Searching for its scientist
United at last
Shivani Patel, USA

Waiting for pollen
Fieldwork is postponed
Recycling old datasets
Trees will bloom again
Raf Aerts, Belgium

Geology field work
No travel, just screens
Trading sunburn for eye strain
Sunscreen beats eye drops
Julie McDermott Griffin, USA

Spring melt date
Permits still on hold
I watch the snow melt swiftly
Alpine herbs still sleep
Andrea Tirrell, USA

Publishing

My PhD dissertation
Planned to finish my
Dissertation: home sweet home
But no place to write
Markus Vihma, Estonia

Missing persons
Where have you all gone?
My dearest peer reviewers
I want to publish
Man Kit Cheung, Hong Kong

Quarantine resolution
Could write a review
Maybe starting tomorrow
Or the day after
Andrea Mattiotti, Netherlands

New rotation
Nice! A break from work!
No. One per lab, come at night.
Revise. Resubmit.
Mark Allen Brimble, USA

Community

Silver lining
I'll appreciate
Bitter conference coffee
More than in the past
Jana Nickel, Germany

Photoshop wizard wanted
Annual photo
Was photoshopped together
Next year I won't blink
Leo E. Chambers, USA

All quiet on the western bench
Finally, it worked!
Is anyone here to see?
Solo dance, just me
Joseph Nicholas Rainaldi, USA

Insects
Their confined winter
I've experienced all year
Soon, fly together
Marie-Caroline Lefort, France

PhD's forage
Stomach cravings—ugh
There's no free food on campus
Bring back conferences!
Jan Kadlec, Israel

Essential work
Thank you very much
Cannot take you for granted
Campus bus driver
Ahmed Al Harraq, USA

Computation
Virtual carbons
With theoretical bonds
Soon, we synthesize
Sam Robert May, USA

Rise
No longer asking
"Who will sink and who will swim?"
Together we rise
Caitlin M. Aamodt, USA

10.1126/science.abk0461

PERSPECTIVES

METABOLISM

An anti-obesity immunotherapy?

Adipose tissue–resident macrophages promote lipid storage in mice but can be stopped with antibody treatment

By **Conan J. O. O'Brien** and **Ana Domingos**

Energy storage is a crucial physiological process for all metazoans, the mechanisms of which are at least partially conserved across the animal kingdom. Lipid-storing adipocytes, the major constituent cell type of adipose tissues, are specialized for the storage of energy in the form of lipid triglycerides. Macrophages are an evolutionarily conserved immune cell population and are the most abundant immunocyte in obese adipose tissue. Recruited monocyte-derived macrophages have long been implicated in promoting the adipose tissue inflammation and metabolic diseases associated with obesity. However, a defined role for adipose tissue–resident macrophages in energy storage has remained elusive. On page 74 of this issue, Cox *et al.* (*1*) demonstrate that adipose-resident macrophages—through a conserved mechanism—directly regulate energy storage in adipocytes through the mammalian platelet-derived growth factor *PDGFc* and its *Drosophila melanogaster* ortholog, PDGF- and VEGF-related factor 3 (*Pvf3*). This study introduces a new, macrophage-centered paradigm in metazoan energy storage.

Adipose tissue macrophages are a heterogeneous population with varied and diverse functions. They can be broadly categorized into either adipose tissue–resident macrophages or recruited bone marrow– and monocyte-derived macrophages. Tissue-resident macrophages are thought to be seeded during embryonic hematopoiesis and are transcriptionally distinct, long-lived, and self-renewing cells (*2*). Bone marrow–derived macrophages are recruited to adipose (and other) tissues in response to chemotactic and inflammatory signals—a process that is accelerated in obesity. Recruitment of these macrophages is dependent on expression of the C-C chemokine receptor type 2 (CCR2), which is necessary for monocyte egress from the bone marrow (*3*).

Studies in which CCR2 expression is disrupted indicate that these cells are responsible for adipose tissue inflammation, hepatic steatosis (fat accumulation in the liver), and the predisposition to type 2 diabetes, all of which are associated with obesity (*4*–*7*). However, CCR2 silencing in mice does not prevent weight gain or adipocyte hypertrophy in response to high-fat diet (HFD) feeding (*1*, *4*). By contrast, global macrophage (recruited and tissue-resident) depletion through strategies that target the colony-stimulating factor 1 (CSF1)–CSF1 receptor (CSF1R) axis results in reduced adipocyte and adipose tissue size (*1*, *8*, *9*), although these studies did not document food intake, so the effects could have been due to malaise and/or cachexia (muscle wasting). Nevertheless, collectively these findings indicate that CCR2-independent macrophages may play a role in the regulation of energy storage.

Building on these observations and capitalizing on the conserved evolutionary nature of macrophages, Cox *et al.* undertook a *D. melanogaster*–based screen, which revealed that hemocytes (macrophages in fruit flies) control lipid storage. The authors screened conserved macrophage-borne factors for effects on lipid storage, which led to the finding that macrophage-specific genetic ablation of *Pvf3* and fat-body cell–specific deletion of its receptor *Pvr* diminished lipid storage in *D. melanogaster* fat-body cells—the fruit fly equivalent of mammalian adipocytes.

Translating this finding to mice, Cox *et al.* showed that *Pdgfc* (the ortholog of *Pvf3*) was expressed most prominently in an embryo-derived subset of adipose tissue–resident macrophages. A different, non–*Pdgfc*-expressing CCR2-dependent macrophage subset was responsible for HFD-induced expression of proinflammatory genes. Tellingly, *Pdgfc* expression was also up-regulated upon HFD in a CSF1R-dependent and CCR2-independent manner. Macrophage-specific deletion of *Pdgfc* reduced white adipocyte tissue weight, adipocyte size, and lipid content in mice. Moreover, antibody-mediated PDGFcc (PDGFc forms a dimeric ligand) inhibition suppressed HFD-induced weight gain to amounts comparable to those observed in lean, normal diet–fed control mice—an effect mediated by diminished white adipose tissue size and adipocyte lipid content. Notably, the resistance to obesity was not mediated by reduced caloric intake, but rather increased energy expenditure in the anti–PDGFcc-treated mice, which gives a glimpse of the potential therapeutic relevance of this discovery. Treatment also enhanced brown adipose tissue thermogenesis and modestly increased liver lipid content, indicating that during treatment, as lipid storage in white adipocytes is inhibited, excess lipids are redirected to these sites for dissipation and storage of excess energy, respectively (see the figure).

Prior to this study, some may have contended that although macrophages are implicated in systemic inflammation and metabolic dysfunction in obesity, they likely

Targeting adipose tissue–resident macrophages

Adipose tissue–resident macrophages control lipid storage through the production of platelet-derived growth factor (PDGFcc), which induces lipid retention in white adipose tissue adipocytes in a paracrine manner, although the precise mechanism is unclear. Recruited macrophages are responsible for the inflammation that characterizes obese adipose tissue. Treatment of mice with PDGFcc antibodies restores homeostasis and reduces lipid storage and body weight, redirecting excess lipids mostly to thermogenesis.

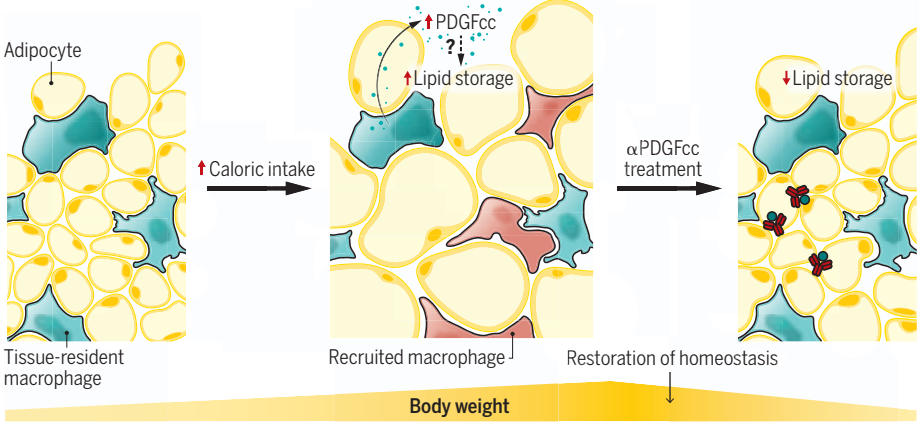

GRAPHIC: V. ALTOUNIAN/*SCIENCE*

Department of Physiology, Anatomy and Genetics, University of Oxford, Oxford, UK. Email: ana.domingos@dpag.ox.ac.uk

do not play causal roles (in organismal metabolism) owing to the lack of efficacy of anti-inflammatory therapies in preventing obesity (*10*, *11*). However, this is not the first study to implicate macrophages as causal in energy storage and HFD-induced weight gain. Adipose tissue–residing sympathetic neuron–associated macrophages contribute to obesity by importing and catabolizing norepinephrine (*12*), a lipolytic agent, in an inflammasome- and age-dependent manner (*13*). However, these macrophages likely do not mediate the effects seen in the study of Cox *et al.* because they do not express *Pdgfc* (*12*). Similarly, Tribbles homolog 1–deficient mice have impaired macrophage differentiation and exhibit metabolic syndrome and a lipodystrophic phenotype with reduced white adipose tissue mass (*14*).

The study of Cox *et al.* debunks the outdated M1-M2 model of macrophage polarization and promotes a model, at least in mice, in which adipose tissue–resident macrophages behave homeostatically to sense increased organismal nutritional status and promote energy storage, whereas the recruited macrophages are responsible for the inflammation and metabolic syndrome that characterize obesity. It will be fascinating to explore the extent to which this paradigm remains applicable in other tissues and inflammatory conditions. The biggest unanswered question centers on the extent to which the findings of Cox *et al.* will translate to humans. Single-cell RNA sequencing analysis indicates that human adipose tissue macrophages express PDGFC (*15*), although whether it performs the same function in humans as in mice is unknown. Future investigations should also probe the mechanism by which adipose tissue–resident macrophages sense nutritional status and the identity of the factors that prompt resident macrophages to express *Pdgfc* and promote energy storage. Nevertheless, this study has the potential to inform and inspire therapeutic strategies that could selectively and separately manipulate energy storage and the metabolic and inflammatory consequences of obesity. ■

REFERENCES AND NOTES

1. N. Cox *et al.*, *Science* **373**, eabe9383 (2021).
2. E. Gomez Perdiguero, F. Geissmann, *Nat. Immunol.* **17**, 2 (2016).
3. C.-L. Tsou *et al.*, *J. Clin. Invest.* **117**, 902 (2007).
4. S. P. Weisberg *et al.*, *J. Clin. Invest.* **116**, 115 (2006).
5. A. E. Obstfeld *et al.*, *Diabetes* **59**, 916 (2010).
6. J. Kim *et al.*, *Mol. Ther. Nucleic Acids* **5**, e280 (2016).
7. A. Ito *et al.*, *J. Biol. Chem.* **283**, 35715 (2008).
8. S. Wei *et al.*, *Immunobiology* **210**, 109 (2005).
9. C. Pridans *et al.*, *J. Immunol.* **201**, 2683 (2018).
10. O. Patsalos *et al.*, *Front. Pharmacol.* **11**, 481 (2020).
11. R. Poggioli *et al.*, *Obesity* **21**, E415 (2013).
12. R. M. Pirzgalska *et al.*, *Nat. Med.* **23**, 1309 (2017).
13. C. D. Camell *et al.*, *Nature* **550**, 119 (2017).
14. T. Satoh *et al.*, *Nature* **495**, 524 (2013).
15. X. Han *et al.*, *Nature* **581**, 303 (2020).

10.1126/science.abj5072

SYNTHETIC BIOLOGY

Reengineering protein-phosphorylation switches

Phosphorylation circuits operate as logic gates that rapidly toggle a system between two stable states

By **Boris N. Kholodenko**[1,2,3] *and* **Mariko Okada**[4]

Toggle switches and oscillations in cellular networks have been of scientific interest since the late 1990s (*1*–*4*). Synthetic biologists have strived to build similar input-output responses by constructing DNA-RNA-protein circuits (*1*). Engineering genetic circuits has seen successes, including a synthetic circadian clock with oscillation periods of hours (*5*) and genetic bistable toggle switches operating on time scales of tens of minutes to hours (*6*). On page 75 of this issue, Mishra *et al.* (*7*) report the design of a faster regulatory network in yeast comprising synthetic protein phosphorylation circuits that act as logic gates. Furthermore, the authors identified similar network motifs across known endogenous signaling pathways in yeast.

Phosphorylation-encoded switches and oscillators in protein networks operate quicker than genetic switches, but attempts to build these circuits synthetically have so far incorporated slower DNA logical operations (*8*). To attain rapid responses, optogenetics manipulations have been extensively employed. Indeed, different periods of light exposure triggered distinct enzyme activation kinetics, dynamics-dependent gene expression, and cell differentiation that are normally induced by growth factors and receptors in mammalian cells (*9*). However, no synthetic system has ever reproduced a logic gate that responds to signals on a time scale of seconds.

In digital electronics, logical gates are combined into integrated circuits to perform chains of operations that enable computer calculations. Mishra *et al.* constructed phosphorylation circuits that operate as logic gates (OR, NOT, and BUFFER) used in electronics. Each gate is built with several fusion proteins. The upstream protein receives an input signal and binds a downstream protein, which is the gate output. The input protein effector domain is a protein-phosphorylating enzyme (kinase) for an OR gate or a dephosphorylating enzyme (phosphatase) for a NOT gate. In an engineered circuit, two distinct fusion proteins receive different input signals, and both proteins share the same output protein. The synthetic NOT gate has a single input protein and a single output protein. After phosphorylation of an input fusion protein that has a phosphatase domain (PTP), the initially phosphorylated output protein is dephosphorylated, which eliminates signaling.

Mutual repression topology of two protein nodes or pathways in a circuit creates a toggle switch featuring two stable states—that is, either node is active when the other node is inactive (*10*–*12*). Mishra *et al.* built a bistable toggle switch using two paired OR and NOT gates and several BUFFER gates that formed mutual repression topology of the switch (see the figure). This occurs because a protein cascade (activated by sorbitol) phosphorylates a downstream protein that is a fusion of a PTP domain and osmotic stress sensor high osmolarity glycerol [HOG1, a mitogen-activated protein kinase (MAPK)] labeled with green fluorescent protein (GFP). Activated phospho-PTP-HOG1-GFP dephosphorylates another fusion protein called HOT-JH1 [high-osmolarity–induced transcription protein 1 (HOT1) and a catalytic domain of Janus kinase JAK 2 (JH1)]. In turn, the isopentenyl adenine (IP)–stimulated protein CRE1-HKRR$_{SLN1}$ [which consists of the *Arabidopsis thaliana* cytokinin receptor (CRE1)–histidine kinase response regulator fused to the intracellular effector domains SLN1 (HKRR^{SLN1})] activates a downstream protein, MAPK kinase kinase osmolarity two-component system protein 1 (SSK1) through a chain of protein phosphorylations (BUFFER) and prevents the activation of sorbitol-stimulated protein polymyxin B resistance protein 2 (PBS2, known as MAPK kinase). The two external inputs, sorbitol and IP, activate their cognate fusion proteins through the plasma membrane osmosensor high osmolarity signaling protein 1 (SHO1) and histidine kinase receptor, respectively. Nuclear localized PTP-HOG1-GFP was measured to characterize system behaviors. These two inputs switched the system between two stable states on a time scale of seconds.

[1]Systems Biology Ireland, School of Medicine and Medical Science, University College Dublin, Belfield, Dublin 4, Ireland. [2]Conway Institute of Biomolecular and Biomedical Research, University College Dublin, Ireland. [3]Department of Pharmacology, Yale University School of Medicine, New Haven, CT, USA. [4]Institute for Protein Research, Osaka University, Suita, Osaka 565-0871, Japan. Email: boris.kholodenko@ucd.ie; mokada@protein.osaka-u.ac.jp.

A fast, protein-only synthetic toggle network

A toggle bistable switch that contains two OR, BUFFER, or NOT gates creates a mutual repression topology in yeast cells (left). Changes in the concentration of input signals (sorbitol and isopentenyl adenine) rapidly control switches between the two stable states, which is monitored by the nuclear translocation of a fusion green fluorescent protein (right).

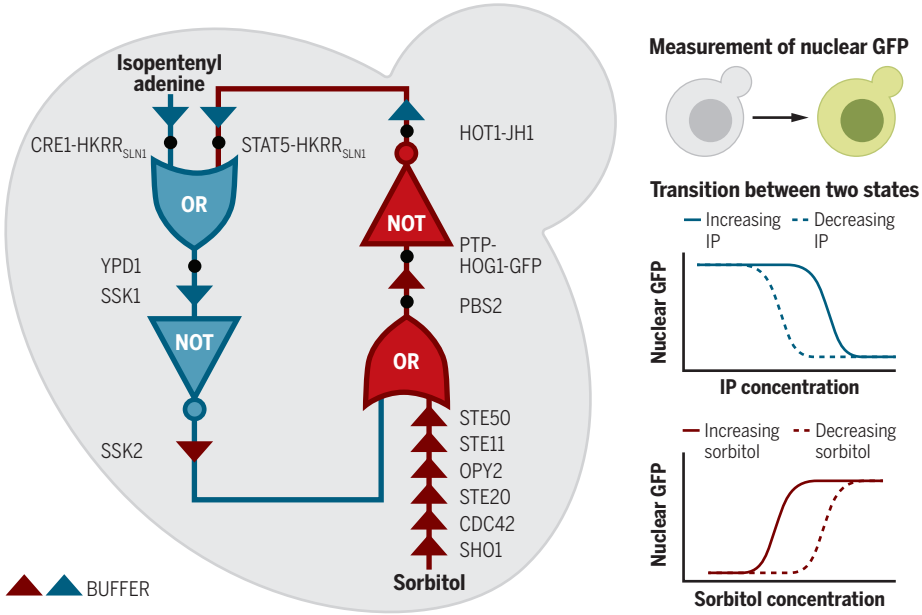

CDC42, cell division control protein 42; CRE1-HKRR$_{SLN1}$, *Arabidopsis thaliana* cytokinin receptor fused to histidine kinase response regulator fused to the intracellular effector domain SLN1; HOG1, high osmolarity glycerol; HOT1-JH1, high osmolarity–induced transcription protein 1 fused to the catalytic domain of Janus kinase JAK 2; OPY2, overproduction-induced pheromone-resistant protein 2; PBS2, polymyxin B resistance protein 2; PTP-HOG1-GFP, PTP domain fused to HOG1 and GFP; GFP, green fluorescent protein; SHO1, high osmolarity signaling protein 1; SSK1, osmolarity two-component system protein 1; SSK2, osmolarity two-component system protein 2; STAT5-HKRR$_{SLN1}$, signal transducer and activator of transcription 5 (STAT5)–histidine kinase response regulator fused to the intracellular effector domains; SLN1 (HKRR$_{SLN1}$) protein; STE11, serine-threonine protein kinase STE11; STE20, serine-threonine protein kinase; STE50, protein Ste50; YPD1, osmotic stress–responsive phosphorelay intermediate sensor protein 1.

Why does the engineered toggle switch have such a sophisticated design of paired OR, NOT, and BUFFER gates? Increasing the number of elements in a circuit enables rapid and robust responses. An amplifier increases the speed of a logic gate, whereas an element with a sigmoidal input-output characteristic, implemented as a BUFFER gate, filters noise and increases robustness to internal and external noise. Synthetic biochemical devices are noisier than electronic circuits because of internal noise in transcription-translation and cell heterogeneity. Future work will assess how speed and robustness of protein logic gates depend on the number and characteristics of individual elements (*13*). This will open possibilities for engineering gate combinations in complex integrative circuits.

Mishra *et al.* also searched the Kyoto Encyclopedia of Genes and Genomes for all known signaling pathways in the yeast *Saccharomyces cerevisiae* and identified several toggled network motifs. Their analysis suggests that biological networks might inherently enable logical operations and computations. This emphasizes the importance of reconstructing causal, directional regulatory networks from "-omics" data; current statistical methods mostly infer correlative nondirectional networks (*14*). When network biology moves from correlation to causation., it will be possible to deconstruct intracellular signaling networks into smaller parts to analyze and, more ambitiously, to reverse-engineer them by creating artificial cells with preprogrammed properties. It may not be long before the precise picture of signaling network abnormalities that cause diseases and the logic of potential treatments are identified from synthetic biology approaches. ■

REFERENCES AND NOTES

1. U. S. Bhalla, R. Iyengar, *Science* **283**, 381 (1999).
2. M. N. McClean *et al.*, *Nat. Genet.* **39**, 409 (2007).
3. N. P. Kaimachnikov, B. N. Kholodenko, *FEBS J.* **276**, 4102 (2009).
4. B. D. MacArthur *et al.*, *Nat. Rev. Mol. Cell Biol.* **10**, 672 (2009).
5. M. Tigges *et al.*, *Nature* **457**, 309 (2009).
6. J. B. Lugagne *et al.*, *Nat. Commun.* **8**, 1671 (2017).
7. D. Mishra *et al.*, *Science* **373**, eaav0780 (2021).
8. S. Chen *et al.*, *Angew. Chem. Int. Ed.* **58**, 18186 (2019).
9. J. E. Toettcher *et al.*, *Cell* **155**, 1422 (2013).
10. A. Bolado-Carrancio *et al.*, *eLife* **9**, e58165 (2020).
11. S. Mochida *et al.*, *Curr. Biol.* **26**, 3361 (2016).
12. G. Yao *et al.*, *Nat. Cell Biol.* **10**, 476 (2008).
13. Z. Chen *et al.*, *Science* **368**, 78 (2020).
14. T. Santra *et al.*, *Curr. Opin. Syst. Biol.* **9**, 11 (2018).

ACKNOWLEDGMENTS

This work was supported by NIH–National Cancer Institute grant R01CA244660 and European Union NanoCommons grant 731032 to B.N.K., Japan Society for the Promotion of Science (JSPS) KAKENHI grants (17H06299, 17H06302, and 18H04031), and Japan Science and Technology Agency (JST)–Mirai Program grant JPMJMI19G7 to M.O.

10.1126/science.abj5028

PLANT SCIENCE

Small RNAs on the move in male germ cells

DNA in plant male meiocytes is methylated by intercellular small interfering RNAs

By **Rebecca A. Mosher**

Plants produce 24-nucleotide (nt) small interfering RNAs (siRNAs) to maintain asymmetric DNA methylation in cis—that is, an siRNA will methylate DNA in the same region from which it is produced (*1*). However, 24-nt siRNAs also direct the methylation of DNA in trans to homologous loci (see the figure) and can move intercellularly to guide methylation in recipient cells (*2*). On page 76 of this issue, Long *et al.* (*3*) describe siRNAs from hundreds of loci that function both intercellularly and at nonallelic sites. Specifically, 24-nt siRNAs move from somatic cells to adjacent male germline cells (meiocytes). This joins a growing list of siRNA movements during plant reproductive development.

Through small RNA directed DNA methylation, the 24-nt RNAs recruit DNA methylation machinery to target loci. Although these siRNAs act in trans, observations of this activity have been limited to specific experimental conditions or rare allelic combinations. Cell-autonomous trans activity of 24-nt siRNAs includes their production from viral RNA, which can trigger DNA methylation of related sequences in the host genome (*4*), or their production from a methylated allele, which can cause the methylation of a related naïve allele (*5*).

By contrast, the siRNAs observed by Long *et al.* are produced from hundreds of locations in the tapetum, a layer of diploid somatic cells that surrounds the developing male germline. The authors demonstrate that these siRNAs move into male meiocytes (cells that eventually differentiate into gametes) and induce DNA methylation at their cis locus as well as

School of Plant Sciences, University of Arizona, Tucson, AZ 85721-0036, USA. Email: rmosher@email.arizona.edu

GRAPHIC: K. FRANKLIN/*SCIENCE*

in trans at protein-coding genes. Tapetal siRNAs also appeared sufficient for asymmetric methylation in sperm cells, indicating that they play a role in establishing the epigenome of the germline. Long *et al.* further show that intercellular methylation is not limited to the cis and trans targets of tapetum-enriched siRNAs but is found at thousands of 24-nt siRNA loci that are not abundantly expressed in the tapetum. This indicates that there is widespread intercellular movement of siRNAs from the tapetum to the germline.

Long *et al.* also show that tapetal siRNAs transcriptionally silence transposons, selfish genetic elements that insert copies of themselves in the genome, causing mutations. Such mutations in germ cells can be passed to the next generation. Thus, movement of siRNAs from tapetum to germline presents a means for somatic cells to protect the next generation from harmful mutations. The ability of these siRNAs to trigger methylation despite mismatches means that transposons will be recognized and silenced even in the face of sequence evolution, whereas the production of siRNAs from diploid somatic cells avoids potential segregation of the siRNA-generating locus away from the transposon during meiosis.

In analyzing siRNA-mediated trans-methylation, Long *et al.* allowed up to three mismatches between the siRNA and the target locus. Although such mismatches are known for 21-nt microRNAs, it was only recently reported that 24-nt siRNAs can target methylation without 100% sequence complementarity (*4*). It is unclear how much complementarity is required for function and whether a specific siRNA-binding protein is associated with trans-methylation. There also may be tissue-specific or chromatin-based limitations to this activity. Long *et al.* observed that trans-methylation does not occur within the tapetum despite high expression of siRNAs in those cells, indicating that trans-methylation is not universal.

Analysis of 24-nt siRNA function at allelic sites revealed that siRNAs can be diluted by acting at multiple locations, falling below a threshold needed to maintain asymmetric methylation (*6*). This suggests that robust trans-methylation might be limited to highly expressed siRNA loci. The tapetal-enriched siRNA loci described by Long *et al.* are expressed 100 to 1000 times more than other 24-nt siRNA loci. This extreme expression requires the Snf2 domain-containing protein CLASSY 3 (CLSY3), which Long *et al.* found to be expressed in the tapetum but not in other cells of the anther. A recent preprint reports that CLSY3 may be required for extreme expression of siRNAs in somatic tissue surrounding the female germline (*7*), suggesting that CLSY3 might be a key determinant of tissue-specific siRNA expression.

Mobile small RNAs

Small RNAs (24 nucleotides) produced in plant somatic (tapetal) cells can guide DNA methylation intracellularly or in adjacent male germ cells (meiocytes). Methylation of both transposons (a source of genome mutations) and of protein-coding genes persists in sperm cells. siRNA, small interfering RNA.

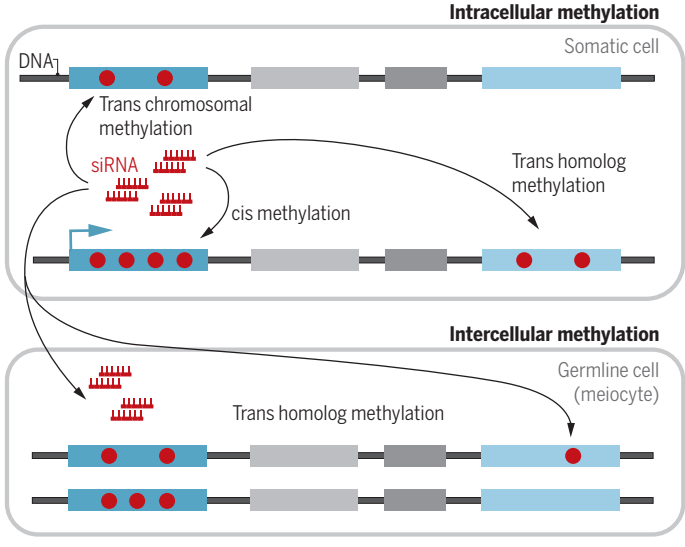

Abundant 24-nt siRNAs produced from maternal somatic cells are also proposed to move into adjacent tissues (*8*). Parallel movement of distinct 24-nt siRNAs into the male and female germlines evokes questions of parental conflict and imprinted gene expression after fertilization (*9*). Consistent with this, loss of 24-nt siRNAs in tetraploid pollen donors overcomes the endosperm failure typically induced by paternal genome excess (*10*). It may be that 24-nt siRNAs balance maternal and paternal influence after fertilization. However, it remains to be determined whether paternal influence is through heritable methylation marks placed in the male germline by tapetal siRNAs or through retention of tapetal siRNAs in sperm cells for delivery during fertilization. The ability of these siRNAs to target methylation despite mismatches with the target locus indicates that paternally derived siRNAs could trans-methylate maternal alleles.

Although the tapetal siRNAs described by Long *et al.* are synthesized differently, they are reminiscent of the 24-nt phased secondary siRNAs (phasiRNAs) present in many plant species. Both classes of siRNA are abundantly expressed in tapetum during meiosis and are proposed to load into meiocytes (*11*). Asymmetric DNA methylation is induced by 24-nt phasiRNAs (*11*), although whether they function in trans at imperfectly complementary regions is not known; 24-nt phasiRNAs are broadly distributed in angiosperms but are not found in Brassicaceae (such as *Arabidopsis*) (*12*), raising the possibility that CLSY3-dependent tapetal siRNAs might substitute for the phasiRNAs that *Arabidopsis* lacks.

Small RNA movement is a key aspect of seed development. During female germline development, 21-nt trans-acting siRNAs move within the developing ovary to restrict germline specification to a single cell (*13*). In gametophytes, 21-nt siRNAs produced in the pollen vegetative nucleus can move in the sperm cells, whereas 24-nt siRNAs from the central cell are proposed to move into the egg cell (*14*). And after fertilization, siRNAs are proposed to move from the endosperm to embryo and from the maternal sporophytic integuments to the endosperm (*8*, *15*). A better understanding of how mobile siRNAs function at trans sites should further illuminate the roles of siRNAs during plant reproduction. ■

REFERENCES AND NOTES

1. J. A. Law, S. E. Jacobsen, *Nat. Rev. Genet.* **11**, 204 (2010).
2. C. W. Melnyk, A. Molnar, D. C. Baulcombe, *EMBO J.* **30**, 3553 (2011).
3. J. Long *et al.*, *Science* **373**, eabh0556 (2021).
4. Y. Fei, T. Nyikó, A. Molnar, *Nucleic Acids Res.* **49**, 1900 (2021).
5. J. B. Hollick, *Curr. Opin. Plant Biol.* **15**, 536 (2012).
6. I. Greaves, M. Groszmann, E. S. Dennis, W. J. Peacock, *Epigenetics* **7**, 800 (2012).
7. M. Zhou *et al.*, *bioRxiv* 10.1101/2021.01.23.427869 (2021).
8. J. W. Grover *et al.*, *Proc. Natl. Acad. Sci. U.S.A.* **117**, 15305 (2020).
9. M. Gehring, *Annu. Rev. Genet.* **47**, 187 (2013).
10. P. R. V. Satyaki, M. Gehring, *Plant Cell* **31**, 1563 (2019).
11. Y. Liu, C. Teng, R. Xia, B. C. Meyers, *Plant Cell* **32**, 3059 (2020).
12. R. Xia *et al.*, *Nat. Commun.* **10**, 627 (2019).
13. Z. Su *et al.*, *Plant Cell* **32**, 2842 (2020).
14. W. Wu, B. Zheng, *New Phytol.* **224**, 86 (2019).
15. C. Lafon-Placette, C. Köhler, *Curr. Opin. Plant Biol.* **17**, 64 (2014).

10.1126/science.abj5020

GRAPHIC: N. CARY/*SCIENCE*

ZEOLITES

New insight from an old concept for zeolites

Two supercage-based large-pore zeolites are potentially useful for industrial applications

By **Dan Xie**

Zeolites are a class of crystalline materials with three-dimensional (3D) framework structures that form uniform micropores. Because the size of the pore windows is comparable to molecular dimensions, they can function as "molecular sieves" by adsorbing molecules that fit inside the pores and excluding larger ones. A small change in the dimension of the pore architecture (channels or cavities in the zeolite) sometimes makes the difference between success and failure in adsorption or catalytic conversion applications. This is why efforts have been made to synthesize zeolites with a variety of different framework structures and compositions. Discovering new zeolites is not trivial, especially for large-pore zeolites with thermal stability and strong acidity under harsh processing conditions. On page 104 of this issue, Lee *et al.* (*1*) report two thermally stable, large-pore aluminosilicate zeolites.

The zeolites, PST-32 and PST-2, were discovered with the "multiple inorganic cation" and the "charge density mismatch" synthetic strategies, respectively. Both zeolites exhibit supercages and wide pore windows comparable to the most used one in the oil industry, zeolite Y. PST-32 and PST-2 are both potential cracking catalysts for hydrocarbon refining applications.

Almost all commercial fluidized catalytic cracking and hydrocracking catalysts are based on zeolite Y, which has the most accessible pore system and as large as ~50% of void space in the structure. Its framework structure, coded as **FAU** (by the Structure Commission of the International Zeolite Association), has a 3D large-pore system with ~7.4 Å of circular pore windows interconnecting to spherical supercages with a volume of ~1.15 nm^3 (see the figure). Even so, zeolite Y has diffusion limitations and access problems for molecules in the higher boiling temperature range. Searching for alternatives, either for tuning cracking product distribution or for a better performance in activity and selectivity, is a topic of interest. Promising results have in fact been reported for a few large-pore zeolites—for instance, ITQ-21 and ITQ-33—that were discovered by the Corma group (*2*, *3*). Now, this racing club has two new members, PST-32 and PST-2. PST-32 has an **SBT** framework structure, and PST-2 is a disordered material having an **SBS/SBT** intergrowth structure. The framework structure codes **SBT** and **SBS** originated from two phosphate-based zeolites, UCSB-10 and UCSB-6, respectively (*4*). The thermal instability UCSB-10 and UCSB-6 impedes any catalytic applications. PST-32 and PST-2 were synthesized as aluminosilicates with slightly higher silicon-to-aluminum ratio (SAR) compared with zeolite Y and demonstrate sufficient thermal stability during catalytic cracking. Both the **SBT** and **SBS** framework structures have a 3D large-pore system. **SBT** contains one type of supercage with a volume of ~1.14 nm^3 that is interconnected by two different pore window sizes (7.8 Å by 7.3 Å and 7.4 Å by 6.4 Å), whereas **SBS** contains two types of supercages (~1.17 nm^3 and ~0.68 nm^3 in volume) interconnected by two different pore window sizes (7.0 Å by 6.9 Å and 6.8 Å by 6.8 Å). These structural features make PST-32 and PST-2 very attractive for catalytic conversion applications.

Apart from the promising structures, PST-32 and PST-2 can be synthesized at relatively low cost. Most industrially relevant zeolites are synthesized by dissolving silica and alumina sources in a basic aqueous solution, where inorganic cations and/or organic molecules help guide zeolite formation and counterbalance the negative charges introduced by aluminum. For catalytic applications, zeolites with higher SAR tend to offer better tolerance to the high temperatures that occur during the catalytic and regeneration cycles. Rather than using inorganic cations alone, synthesizing zeolites is often done with the assistance of organic molecules called organic structure-directing agents (OSDAs). OSDAs have sizes and shapes that correlate well with the pore configuration of the zeolite. Inorganic cations have less size and shape tunability, so are less robust in directing structures with diversified pore configurations. Although a substantial portion of new zeolite discoveries involve designing and screening a large range of OSDAs, the authors focused on a strategy of using multiple inorganic cations along with a relatively simple and inexpensive OSDA to jointly direct crystallization. Although this concept has existed for more than two decades, systematic investigations on the synergistic effect of structure direction were rarely reported. This old strategy, which the authors termed the "multiple inorganic cation" approach, has allowed a number of new zeolites to be discovered (*5*–*7*), and PST-32 appears to be one of the most exciting examples.

This approach may serve as a paradigm for rational synthesis of existing and hypothetical cage-based zeolite structures. However, a better understanding of the exact role of each type of inorganic cations during formation is needed. Moreover, the discovery of PST-32 and PST-2 will likely promote further study of their synthesis, modification, and catalytic performance. This includes both in traditional oil-based cracking processes, but also with biomass conversions to produce renewable chemicals and fuels. Other applications are also possible, such as adsorption, separations, and emerging uses such as drug delivery and gas sensing. ■

Stabilized large-pore zeolites

Two new zeolites called PST-32 (**SBT**-type) and PST-2 (**SBS/SBT**-type intergrowth) have supercage structures, like the commercially used zeolite Y (**FAU**-type). These zeolites can be produced in large amounts and may find uses for various catalytic processes.

Chevron Technical Center, Richmond, CA 94801, USA.
Email: dan.xie@chevron.com

REFERENCES AND NOTES

1. H. Lee *et al.*, *Science* **373**, 104 (2021).
2. A. Corma, M. J. Díaz-Cabañas, J. Martínez-Triguero, F. Rey, J. Rius, *Nature* **418**, 514 (2002).
3. A. Corma, M. J. Díaz-Cabañas, J. L. Jordá, C. Martínez, M. Moliner, *Nature* **443**, 842 (2006).
4. X. Bu, P. Feng, G. D. Stucky, *Science* **278**, 2080 (1997).
5. J. Shin, D. Jo, S. B. Hong, *Acc. Chem. Res.* **52**, 1419 (2019).
6. H. Lee *et al.*, *ACS. Mater. Lett.* **2**, 981 (2020).
7. H. Lee *et al.*, *ACS. Mater. Lett.* **3**, 308 (2021).

10.1126/science.abj1834

GRAPHIC: N. DESAI/*SCIENCE* BASED ON D. XIE

NEURODEVELOPMENT

Astrocytes control the critical period of circuit wiring

Astrocytes regulate the experience-dependent remodeling of brain circuits during development

By **Paulo Kofuji** and **Alfonso Araque**

One of the most extraordinary qualities of the mammalian nervous system is its ability to change with experience and throughout its life span. Mammalian brain plasticity is thought to be mainly mediated by neurons. Increased plasticity during specific windows of time during development called "critical periods" allows neuronal circuitry to be shaped. How this phase ends, however, has not been clear. On page 77 of this issue, Ribot *et al.* (*1*) show that an unsuspected cellular player—astrocytes—control when experience-dependent wiring of brain circuits is permitted in the developing primary visual cortex (V1). This finding points to possible similar roles of astrocytes or other nonneuronal cells in other neural circuits.

The primary visual cortex has long served as a model system to study brain plasticity, since the pioneering work by Hubel and Wiesel in the 1960s, when they showed that the V1 circuit is powerfully shaped by the visual experience during development (*2*). Their seminal studies in kittens revealed that, in response to transient eyelid closure to provoke monocular deprivation (blocking visual stimulation through one eye), the V1 circuits remodel to shift the preference of cortical neurons for the eye that remains open. This results in the so-called ocular dominance (*3*, *4*). Notably, this influence of sensory activity on the organization of neural circuits is restricted to a critical period (*4*), which highlights the importance of early life experiences for the optimal functioning of the brain. Anomalous critical periods are also largely detrimental and associated with various neurodevelopmental disorders (*5*). Hence, how the critical period of ocular dominance plasticity is opened and closed is of fundamental importance for understanding brain development and function.

A new and fruitful development in this area of investigation has been the mouse model (*6*). Ribot *et al.* report that the ocular dominance plasticity in mice is determined by astrocytes. These nonneuronal cells have long been associated with housekeeping functions in the brain, such as regulation of the extracellular ionic environment, reuptake and recycling of neurotransmitters, and structural support (*7*). However, more recently, astrocytes have also been shown to control synapse formation and connectivity (*8*), synaptic transmission and plasticity (*9*), and even animal behavior (*10*). Ribot *et al.* found that grafting immature astrocytes from newborn mice in the V1 of adult mice enhanced the ocular dominance plasticity that occurred after visual stimulation of one eye. The ~200 genes differentially expressed in immature and mature astrocytes include the gene encoding connexin 30 (Cx30). Cx30 is a subunit of a gap junction channel—a specialized intercellular connection between cells. The authors observed that the expression of Cx30 in the V1 peaked approximately when the critical period for ocular dominance plasticity ended. This prompted the authors to assess plasticity in a mouse model genetically engineered to lack Cx30. Although ocular dominance plasticity peaked at about postnatal day 28 (P28) in wild-type mice, it continued to increase in mice lacking Cx30 until P50, indicating impairment in the closure of the critical period.

Electrophysiological recordings of excitatory and inhibitory synaptic transmission in cortical slices revealed that mice lacking Cx30 had reduced inhibitory transmission. Moreover, perineuronal nets were smaller in these animals. Perineuronal nets are a highly organized form of extracellular matrix that contains chondroitin sulfate proteoglycans. They tend to coalesce around inhibitory neurons (*11*) and are thought to contribute to the closure of ocular dominance plasticity (*12*). Altogether, these results indicate that astrocytes control the visual critical period by promoting the maturation of inhibitory circuits through signaling pathways that involve Cx30.

What about a relevant signaling pathway associated with Cx30? Ribot *et al.* discovered that Cx30 is physically associated with the protein-phosphorylating enzyme ROCK2 (Rho-associated coiled-coil–containing protein kinase 2). The expression of the small guanosine triphosphatase (GTPase) RhoA, ROCK2, and the extracellular matrix–degrading enzyme

Astrocytes influence plasticity

During development of the mammalian brain's primary visual cortex, astrocytes regulate the so-called critical period during which plasticity allows the neural network to form. This depends on a signaling pathway controlled by connexin 30.

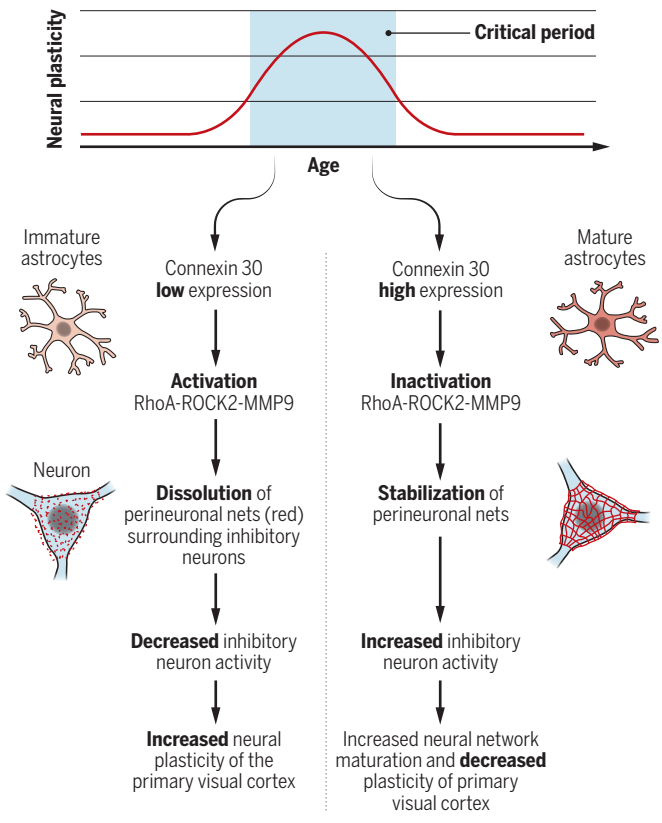

ROCK2, Rho-associated coiled-coil–containing protein kinase 2; MMP9, matrix metalloproteinase 9

GRAPHIC: C. BICKEL/*SCIENCE*

Department of Neuroscience, University of Minnesota, Minneapolis, MN 55455, USA.
Email: araque@umn.edu

matrix metalloproteinase 9 (MMP9) were all increased by either monocular deprivation or the lack of Cx30, indicating a common signaling pathway. The authors therefore propose that astrocytes control the visual critical period by promoting the maturation of inhibitory circuits through signaling pathways that involve Cx30 and inactivation of RhoA and MMP9. This promotes the formation of perineuronal nets, the enhancement of inhibitory transmission, and the closure of ocular dominance plasticity (see the figure).

Cx30 is a member of a large family of proteins that form intercellular channels that enable the direct transfer of ions and molecules between adjacent cells, but whether a Cx30-RhoA-ROCK2 signaling pathway involves ion and molecule permeation into astrocytes remains unknown. Moreover, several human deafness diseases have been associated with Cx30 mutations (*13*). It is unknown whether any changes in critical-period plasticity are found in these patients. Notably, astrocytes in the fruit fly *Drosophila melanogaster* regulate the maturation of the motor circuit and are essential for proper critical-period closure (*14*). In this case, interaction between the cell adhesion proteins neuroligin and neurexin is the likely signaling pathway. Thus, there may be a diversity of molecular and signaling pathways in which astrocytes influence the use-dependent plasticity of neural circuits during development. ■

"...astrocytes control the visual critical period by promoting the maturation of inhibitory circuits..."

REFERENCES AND NOTES

1. J. Ribot *et al.*, *Science* **373**, 77 (2021).
2. D. M. Hubel, T. N. Wiesel, *Brain and Visual Perception: The Story of a 25-Year Collaboration* (Oxford Univ. Press, 2004).
3. D. H. Hubel, T. N. Wiesel, *J. Physiol.* **206**, 419 (1970).
4. J. S. Espinosa, M. P. Stryker, *Neuron* **75**, 230 (2012).
5. J. Li, S. Kim, S. S. Pappas, W. T. Dauer, *JCI Insight* **6**, e142483 (2021).
6. B. M. Hooks, C. Chen, *Neuron* **106**, 21 (2020).
7. B. R. Ransom, H. Kettenmann, *Neuroglia* (Oxford Univ. Press, ed. 3, 2012).
8. N. J. Allen, C. Eroglu, *Neuron* **96**, 697 (2017).
9. L. Sancho, M. Contreras, N. J. Allen, *Neurosci. Res.* **167**, 17 (2021).
10. P. Kofuji, A. Araque, *Annu. Rev. Neurosci*. 10.1146/annurev-neuro-101920-112225 (2021).
11. J. W. Fawcett, T. Oohashi, T. Pizzorusso, *Nat. Rev. Neurosci*. **20**, 451 (2019).
12. T. Pizzorusso *et al.*, *Science* **298**, 1248 (2002).
13. A. D. Martínez, R. Acuña, V. Figueroa, J. Maripillan, B. Nicholson, *Antioxid. Redox Signal*. **11**, 309 (2009).
14. S. D. Ackerman, N. A. Perez-Catalan, M. R. Freeman, C. Q. Doe, *Nature* **592**, 414 (2021).

10.1126/science.abj6745

GENOMICS

Finding genes that control body weight

DNA exome sequencing at scale reveals unknown human biology of adiposity

By **Giles S. H. Yeo** *and* **Stephen O'Rahilly**

Obesity is a common disorder with major adverse effects on morbidity and mortality. Genetic factors play an important role in determining the extent to which people acquire energy and store it as fat, which has implications for the risk of developing obesity. Studies in patients with severe early-onset obesity have identified mutations in >20 genes that have a large effect on body mass index (BMI) (*1*), whereas genome-wide association studies (GWASs) in large populations have identified hundreds of common variants with more-subtle effects (*2*). On page 73 of this issue, Akbari *et al.* (*3*) report rare genetic variants influencing BMI identified through whole-exome sequencing of >600,000 people from the United Kingdom, the United States, and Mexico. The authors identified genes in which rare nonsynonymous variants were associated with either higher or lower BMI, bringing insight to the genetics underlying human adiposity.

When the "first draft" of the human genome was announced in 2003, there was optimism that it would act as a road map that leads to improved treatment of many diseases. GWASs of common variants led to a step change in our understanding of the genetic architecture of many common diseases and traits (*4*). But making the step from variant association to precise causal mechanism has been more challenging. That most polymorphisms associated with disease reside in noncoding regions of the genome makes it difficult to identify the causative gene; and even if one can spot the right gene (recognizing that there may be several), it can be difficult to establish the direction of action and precise mechanism of its effect on phenotype (*5*). Furthermore, many of the genes implicated in disease susceptibility through association with noncoding variation have pleiotropic effects, some of which are exerted during development. These factors reduce the likelihood of beneficial pharmacological manipulation of the products of such genes.

Mutations causing or predisposing an individual to disease by disrupting the protein coding elements of genes (exons) are generally much rarer and, until now, their discovery has relied on studying rare, extreme phenotypes where the prevalence of such variants is much higher. However, such mutations are highly informative because they "self-identify" the causative gene and their impact on function can be established rapidly. Akbari *et al.* demonstrate the power of detecting such variants at scale. Although BMI is an imperfect measure of adiposity (fatness), it correlates well with measures of body fat in large populations. It is a phenotype that is easily measurable and has little day-to-day variability, reflecting a cumulative lifelong imbalance between energy intake and expenditure.

The authors found 16 genes in which rare nonsynonymous variants in exons were associated with BMI at genome-wide levels of significance. Four of these genes, *MC4R* (melanocortin 4 receptor), *PCSK1* (proprotein convertase subtilisin/kexin type 1), *GPR151* (G protein–coupled receptor 151), and *GIPR* (gastric inhibitory polypeptide receptor), have been previously reported. All of these genes are highly expressed in the central nervous system and are known to influence appetite. *GIPR* (*6*) and *GPR151* (*7*) both encode G protein–coupled receptors, and heterozygous loss-of-function (LOF) mutations in these genes are associated with lower BMI in large population studies. *PCSK1* was, together with leptin (*LEP*), one of the first two genes directly implicated in human obesity (*8*). Looking more broadly at the key elements of the signaling pathways that are directly influenced by leptin (which signals satiety), the authors found that heterozygous mutations in *LEP*, *POMC* (proopiomelanocortin), and *PCSK1* were associated with higher BMI (although not all reaching exome-wide statistical significance), whereas heterozygous mutations in *LEPR* (leptin receptor) were not.

LOF mutations in *MC4R* are well established to have a large effect on increasing

Medical Research Council (MRC) Metabolic Diseases Unit, University of Cambridge Metabolic Research Laboratories, Wellcome–MRC Institute of Metabolic Science, Addenbrooke's Hospital, Cambridge, UK.
Email: gshy2@cam.ac.uk; so104@medschl.cam.ac.uk

adiposity—it is the most commonly mutated gene associated with obesity (*9*). Akbari *et al.* present information on the impact of rare variants of *MC4R* on obesity risk, suggesting that the prevalence of *MC4R* haploinsufficiency as a contributor to obesity may be seven times more common in a population in Mexico than in the UK. It is possible that the impact of rare *MC4R* variants, both in terms of the number of people affected and the size of the effect on BMI, may have been somewhat underestimated by the authors, particularly in the UK population. They used very stringent bioinformatic criteria for the categorization of a mutation as likely to be disruptive of its normal biochemical function but did not experimentally establish the functional impact of all variants. They are therefore likely to have excluded a number of variants that impair function and increase BMI. Additionally, the UK Biobank cohort examined in this study is leaner and healthier than the general UK population (*10*). A recent report in an unselected UK birth cohort (*11*) suggests that *MC4R* LOF mutations may have an impact on BMI that is substantially greater than that suggested by Akbari *et al.*, particularly at a younger age.

The other 12 genes identified by Akbari *et al.* have not been previously associated with BMI. Most are highly expressed in the hypothalamus, consistent with evidence that most genes involved in obesity predisposition are associated with parts of the central nervous system that control appetite and energy balance. One of these, *GPR75*, is a G protein–coupled receptor whose natural ligand has been reported to be either the chemokine CCL5 (C-C motif chemokine 5) (*12*) or the eicosanoid 20-hydroxyeicosatetraenoic acid (20-HETE) (*13*). The authors report heterozygous variants predicted to be LOF mutations in *GPR75* in 4 of every 10,000 individuals, with carriers having a 1.9 kg/m^2 lower BMI on average. The authors studied mice in which *Gpr75* had been deleted and found that they gained less weight on a high-fat diet than did wild-type mice. This effect was allele-dose dependent, with heterozygous *Gpr75*$^{-/+}$ mice gaining 25% less and homozygous *Gpr75*$^{-/-}$ mice gaining 44% less weight than wild-type littermates. Although it remains unclear whether the leanness of these animals is due to effects on energy intake, expenditure, or both, this study establishes that GPR75 is involved in the control of energy balance and that inhibiting its signaling might be expected to result in a loss of body weight. Mutations in *CALCR*, the receptor for both calcitonin and amylin, were associated with higher adiposity and obesity risk in humans. This is notable because amylin analogs reduce body weight in rodents and humans through actions on brain-expressed *CALCR* (*14*).

The principles of discovery exemplified in the study of Akbari *et al.* go beyond that of body weight control and obesity. The exome sequencing approach at scale increases our ability to reach deep into the rare allele frequency spectrum for functionally compromised alleles. It bypasses the twin headaches of GWAS: the identification of the causative gene and the determination of direction of causality. In continuous traits such as adiposity or blood pressure, it also allows the detection of protective alleles.

It is likely that human exome sequencing at scale will become an increasingly important entry point for the discovery of mechanistic insights into mammalian biology. Much normal physiology is shared between mammalian species, and the traditional flow of information from discovery of physiological mechanisms in animal models to confirmation in humans will probably become more bidirectional. The power to dissect physiology through tissue-specific and temporally controlled genetic manipulation in animal models will, of course, remain a hugely powerful tool. However, when it comes to disease, pathogenesis tends to be more species-specific. So, if one is interested in finding targets that might be usefully manipulated to treat a human disease, it makes particular sense to focus on the species of interest, that is, *Homo sapiens*. The challenges inherent in going from GWAS "hit" to causative gene, and the relatively slim pickings this approach has so far delivered, have engendered some skepticism regarding the power of human genetics to illuminate biology. The study of Akbari *et al.* clearly demonstrates that when sufficient rare human alleles of functional impact can be detected, and when relevant associated phenotypic information is available, then new, robust, and potentially translatable biological insights can be delivered with high efficiency. ■

There is considerable variation in human body weight, which is strongly influenced by genetic variants that often regulate appetite.

PHOTO: RAWPIXEL.COM/SHUTTERSTOCK

REFERENCES AND NOTES

1. H. Choquet, D. Meyre, *Genome Med.* **2**, 36 (2010).
2. A. E. Locke *et al.*, *Nature* **518**, 197 (2015).
3. P. Akbari *et al.*, *Science* **373**, eabf8683 (2021).
4. Wellcome Trust Case Control Consortium, *Nature* **447**, 661 (2007).
5. M. E. Cannon, K. L. Mohlke, *Am. J. Hum. Genet.* **103**, 637 (2018).
6. V. Turcot *et al.*, *Nat. Genet.* **51**, 1191 (2019).
7. C. A. Emdin *et al.*, *Nat. Commun.* **9**, 1613 (2018).
8. R. L. Leibel, *Nat. Genet.* **16**, 218 (1997).
9. I. S. Farooqi *et al.*, *N. Engl. J. Med.* **348**, 1085 (2003).
10. A. Fry *et al.*, *Am. J. Epidemiol.* **186**, 1026 (2017).
11. K. H. Wade *et al.*, *Nat. Med.* **27**, 1088 (2021).
12. S. Dedoni, L. A. Campbell, B. K. Harvey, V. Avdoshina, I. Mocchetti, *J. Neurochem.* **146**, 526 (2018).
13. V. Garcia *et al.*, *Circ. Res.* **120**, 1776 (2017).
14. W. Cheng *et al.*, *Cell Metab.* **31**, 301 (2020).

10.1126/science.abh3556

BOOKS *et al.*

Pacific Islanders have long been skilled seafarers. Here, a Māori woman welcomes two Hawaiian voyaging canoes to New Zealand.

ANTHROPOLOGY

The peopling of the Pacific

An anthropologist traces the emergence of the rich and varied cultures of the Pacific islands

By **Christopher J. Bae**

The peopling of the Pacific continues to draw intense interest from the public and scientific communities alike. *Voyagers* by anthropologist Nicholas Thomas combines insights gleaned from historical documents, archaeology, geochronology, and ethnographic fieldwork into an eloquent review of this fascinating historical phenomenon.

In the book's introduction, Thomas asks an important question: "What is it to be an Islander"? Those unfamiliar with the region tend to group the Pacific's various peoples together. However, a great deal of physical and cultural diversity exists across the different island communities. Unfortunately, early attempts to acknowledge these variations normalized stereotypes that persist today and have led, in some cases, to systemic racism.

Early European explorers clearly had no idea what to expect when they arrived in the Pacific in the 1500s, reveals Thomas. Many were surprised to find that Pacific Islanders were capable boatbuilders and sailors, able to build sturdy watercraft and navigate large expanses of open ocean by following the stars. Historical records written by Europeans passing through the region during this period indicate that many assumed that Pacific Islanders lived in small, isolated communities. Indigenous communities, however, were often "linked through kinship, ceremony, and exchange networks, as well as through relations of contest and hostility."

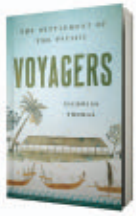

Voyagers: The Settlement of the Pacific
Nicholas Thomas
Basic Books, 2021. 224 pp.

For hundreds of thousands of years, humans had largely lived on the expansive landmasses that made up Earth's continents. To reach the Pacific islands, early peoples would have had to embrace a seafaring lifestyle. "What motivated those who embarked on these voyages constitutes one of the major enigmas of human history," notes Thomas. Climate change, dietary and/or sociopolitical stressors, the inclination to travel for travel's sake, and a series of "accidental voyages" have all been put forth as potential causes, although the last of these has lost favor among experts. Another possible explanation may simply be that "Austronesian cultures seem to have privileged the 'founders' of particular communities."

The spread of the Lapita culture, an ancient people believed to represent a common ancestor of many modern Pacific societies, receives a great deal of attention, and Thomas does a very nice job of synthesizing research conducted across various fields, including groundbreaking work performed by specialists in Pacific archaeology. Together with a plethora of archaeological and linguistic evidence, his own ethnographic observations of Taiwanese villagers, including the fact that many bore "wrist and arm tattoos that were strikingly similar" to those observed in other Polynesian cultures, support the hypothesis that Pacific Islanders likely originated in Taiwan.

Voyagers discusses a number of recent discoveries from the Pacific region, including the *Homo luzonensis* fossils found in Callao Cave on the island of Luzon in the Philippines (*1*) as well as the cave art discovered in Leang Bulu' Sipong Cave in Sulawesi (*2*). The first of these important discoveries is a good example of our growing appreciation for the diversity of hominins once present in the region, and the second reveals that, contrary to prior assumptions, cave art in the Pacific region appears around the same time as—and in some cases even predates—similar findings from Western Europe.

An important point raised throughout the volume is that scholarship on the peopling of the Pacific has been a highly "cross-cultural business from its very beginnings." There have been, for example, many well-known instances in which indigenous Pacific Islander researchers have contributed data that have proven critical to settling academic debates, and Thomas spends a great deal of time detailing the contributions of the well-known Māori scholar Te Rangihiroa. Training Pacific Islanders to investigate questions related to their own origin and diversity will be critical for current and future generations of scholars.

Thomas should be commended for his engaging writing style, which regularly had me looking forward to turning the page. I would not be surprised if, after reading this masterpiece, many readers are compelled to take up voyaging themselves. ■

The reviewer is at the Department of Anthropology, University of Hawai'i at Mānoa, Honolulu, HI 96822, USA. Email: cjbae@hawaii.edu

REFERENCES AND NOTES

1. M. Aubert *et al.*, *Nature* **576**, 442 (2019).
2. A. Brumm *et al.*, *Sci. Adv.* **7**, eabd4648 (2021).

10.1126/science.abi9177

PHOTO: © DAN LIN

HISTORY OF PHYSICS

When Einstein met Curie

Historical documents hint at a fulfilling friendship between the two physicists

By **Graham Farmelo**

Toward the end of his life, when asked which physicist he most respected, Albert Einstein replied "Hendrik Lorentz and Marie Curie." His choice of Dutch theoretical physicist Lorentz was predictable; less obvious was his selection of Polish-born Curie (born Maria Skłodowska). Although undoubtedly one of the great pioneers of radioactivity, she did not work on aspects of physics that usually drew Einstein to express special admiration. Besides, he had occasionally made uncomplimentary private remarks about her, once describing her as "very intelligent" but "as cold as a fish."

Many scholars have mulled over the relationship between Curie and Einstein, despite the paucity of evidence required to establish a rounded view of it. The latest attempt is *The Soul of Genius* by Jeffrey Orens—a former chemical engineer, a historical writer, and, evidently, a serial anecdotalist. The book aims to illuminate the relationship between the two scientists, which first flowered at the inaugural Solvay Conference in late October 1911. At this momentous gathering in Brussels, 18 of Europe's leading physical scientists pondered the failure of classical theories to account for several phenomena and the emergence of a new quantum theory.

Einstein, the meeting's youngest participant, was dazzled by the "sparkling intelligence" of Curie, who was already an internationally famous scientist. She was impressed with him, too, and soon afterward gave him a glowing reference that helped to secure his first professorship in Prague.

On the day after the conference ended, Curie found herself the focus of a scandal in the French press, which published evidence that she—a widow—was having an affair with her unhappily married colleague Paul Langevin. Leaked letters and disobliging reports led to a feeding frenzy in the French press. Even the award of Curie's second Nobel Prize a few weeks later could not lift her spirits. Einstein wrote her to offer his strong support as well as a piece of advice: "If the rabble continues to occupy itself with you, then simply don't read that hogwash."

Previously unpublished documents in the archive of French physicist Léon Brillouin make Orens's description of Curie's torrid experience especially vivid and disturbing. However, the new material sheds less light on her relationship with Einstein than on the vicious treatment meted out in French society at that time to prominent women who did not follow the norms of polite society.

Curie and Einstein did not become closely acquainted until 1922, when they began 9 years of collaboration on projects for League of Nations committees on which they served. Records of the committees make it plain that the two agreed on most matters and that they got along well, although few details remain of their interactions. This is a pity, given the potential conversational fodder offered by the newly discovered quantum mechanics.

Curie and Einstein met for the final time at the Solvay meeting in October 1933, 9 months before she died in a sanatorium in southeast France at the age of 67. In January 1935, the Polish authorities organized a memorial event in her honor, held at the Nicholas Roerich Museum in New York City. Einstein's tribute to her life gives some of the most compelling evidence of the closeness of their friendship and the depth of his admiration for her: "It was my good fortune to be linked with Mme Curie through twenty years of sublime and unclouded friendship. I came to admire her human grandeur to an ever-growing degree. Her strength, her purity of will, her austerity toward herself, her objectivity, her incorruptible judgment—all these were of a kind seldom found joined in a single individual."

Orens devotes surprisingly little space to this testimony, especially as he spends dozens of pages on relatively peripheral matters. In chapter nine, for example, he begins with a lengthy account of the eruption of the Krakatoa volcano, which serves as an introduction to the Swedish chemist Svante Arrhenius, who turned out to be an influential member of the Nobel Prize committee.

This and other detours often make it difficult to follow the development of the human relationship at the heart of Orens's book. Yet, despite its bloat, *The Soul of Genius* is a rewarding read about a relationship that I suspect was more complex than extant documentation suggests. ■

The reviewer is a fellow of Churchill College, University of Cambridge, Cambridge CB3 0DS, UK, and the author of *The Universe Speaks in Numbers* (Basic Books, 2019). Email: graham@grahamfarmelo.com

The Soul of Genius: Marie Curie, Albert Einstein, and the Meeting that Changed the Course of Science
Jeffrey Orens
Pegasus, 2021. 336 pp.

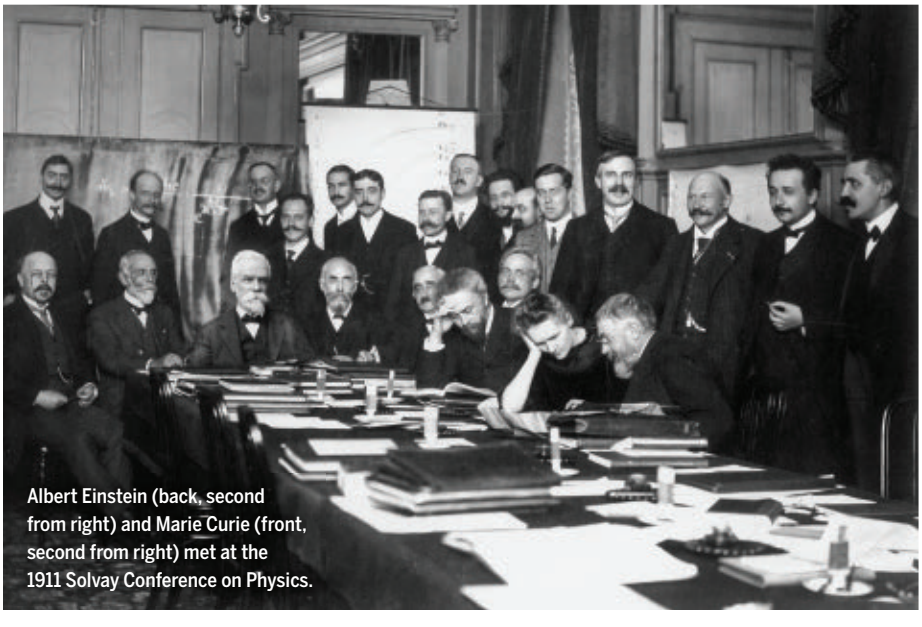

Albert Einstein (back, second from right) and Marie Curie (front, second from right) met at the 1911 Solvay Conference on Physics.

PHOTO: COURTESY THE SOLVAY HERITAGE COLLECTION

10.1126/science.abj1411

NEWS
The plastic eaters p. 36
When plastics are precious p. 40

POLICY FORUM
A binding global agreement to address the life cycle of plastics p. 43

PERSPECTIVES
The myth of historical bio-based plastics p. 47
Achieving a circular bioeconomy for plastics p. 49

REVIEWS
Plastics in the Earth system p. 51
Plastic ingestion as an evolutionary trap: Toward a holistic understanding p. 56
The global threat from plastic pollution p. 61
Toward polymer upcycling—adding value and tackling circularity p. 66

RELATED ITEMS
REPORT p. 107 PODCAST VIDEO

A DEVIL'S BARGAIN

By **Jesse Smith** *and* **Sacha Vignieri**

Plastics have become an essential material of the modern global consumer economy, yet many of the properties that make them useful in so many applications also make them a serious environmental threat. As for much new technology, their development and proliferation occurred with little consideration for their impacts, but now it is impossible to deny their dark side as we confront a rapidly growing plastic pollution problem. In this special issue, we examine a range of topics related to plastics, from their distribution in the environment to their development into an evolutionary trap for animals to ways we can rethink them to create a better future. A series of Reviews discusses how plastics are best understood as novel geomaterials, the evolutionary and ecological dimensions of plastic ingestion by wildlife, the accumulation and effects of plastic pollution in the environment, and how innovations in upcycling and recycling may affect the fate of plastics and drive advances in next-generation materials design. Complementing these Reviews, a Policy Forum and a pair of Perspectives discuss efforts to develop a global agreement to combat plastic pollution, provide an overview of the history of environmental bioplastics and their implications, and offer suggestions for designing plastics for a circular bioeconomy. Finally, a brace of News Features explores how enzymes are being used to aid in plastic recycling efforts and how museums are trying to stop plastics in their exhibits from breaking down. The time for preventing plastic pollution is long past—the time for changing the future of plastics in our world, however, is now.

Michael Funk, Brent Grocholski, Lila Guterman, Marc Lavine, and Brad Wible also contributed to this special issue.

Cumulative global plastics production

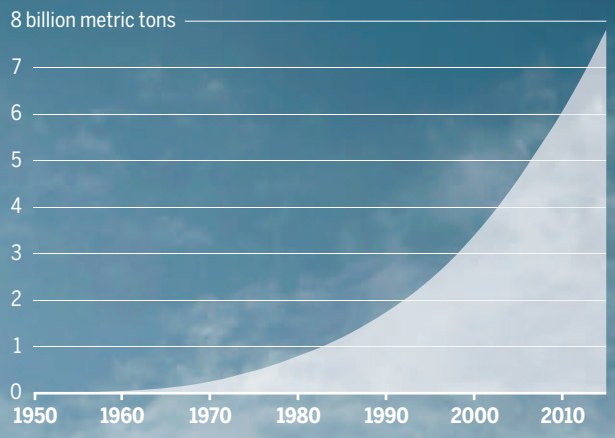

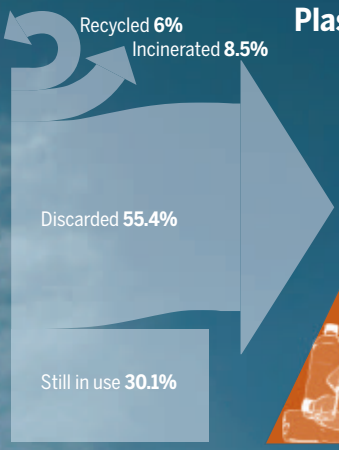

Plastic waste production by sector

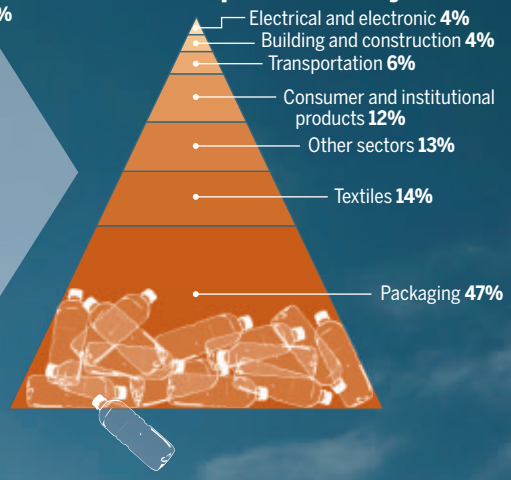

Impacts of plastic waste on marine species

(Species not shown to scale)

By **Sacha Vignieri** *and* **Kelly Franklin**

Seabirds

Plastics have been found in the stomachs of a wide array of species, from the largest albatrosses to the smallest phalaropes, and in birds that feed throughout the water column, from the surface to the depths.

3%

of the global plastic waste is estimated to enter the oceans each year. In 2010, that was around **8 million metric tons**.

Sea turtles

Sea turles often become entangled as hatchlings when they crawl through beach debris on their way to the sea and again as females return to lay eggs. They ingest plastic in many forms, notably as plastic bags, which they may be fooled into thinking are jellyfish.

Seals and sea lions

A variety of, mostly, single-use plastics have been found in the guts of pinnipeds (seals and sea lions). Curious and playful, they often put their heads through loops of plastic, from discarded fishing lines and boat rigging to plastic packing strips.

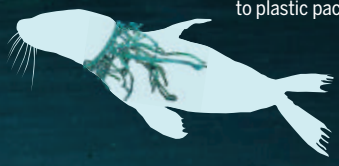

Amphipods

Microplastics have been found in the guts of amphipods across six of the deepest ocean trenches. A new species of amphipod was recently named after the plastics that it had ingested, nearly 7 kilometers deep in the Mariana Trench.

Whales and dolphins

Entanglement threatens all types of whales and dolphins, primarily from discarded or active fishing nets. Large plastic items such as bags and flip-flops have been found in toothed whales. Baleen, or filter-feeding, whales are especially threatened by microplastics.

Corals

Discarded fishing gear and plastic waste physically damage coral reefs, prevent filter feeding, and carry pathogens. Corals also ingest microplastics, and these have been found in corals living across ocean depths, from shallow waters to the deep sea.

PHOTO: NASTCO/ISTOCKPHOTO; GRAPHIC: K. FRANKLIN/*SCIENCE*; DATA SOURCE: HTTPS://OURWORLDINDATA.ORG/PLASTIC-POLLUTION; GEYER *ET AL.*, *SCI. ADV.* **3**, E1700782 (2017); JAMBECK *ET AL.*, *SCIENCE* **347**, 768 (2015)

Plastic trash recovered from an island in the South Pacific Ocean shows decay and bite marks from marine life.

THE PLASTIC EATERS

Bacterial enzymes can digest some plastic waste. Scientists want to harness them for recycling

By **Warren Cornwall**

Muhammad Reza Cordova is searching for treasure amid the water bottles, plastic bags, and plastic foam cups that choke the beaches, reefs, and mangrove forests around Jakarta, Indonesia. In the microbe-rich slime coating some of that trash, he hopes to find organisms to help solve the vexing problem of what to do with the plastic flooding the planet.

Cordova, a marine biologist, collects samples of the slime and brings them back to his lab at Indonesia's Research Center for Oceanography, where he plans to culture the microbes and feed them only plastic to see what thrives. "We are hoping that we find the most effective microbes that can eat or degrade the plastic," he says.

Researchers across the globe are on the same quest. They are looking for plastic-munching microbes in searing hot springs in Yellowstone National Park, remote island beaches in the Pacific Ocean, and a plastic recycling factory in Japan, among other places. Some scientists have already found bacteria that wield enzymes able to break down a common plastic used to make water bottles and clothing.

The scientists think the microbes' enzymes—proteins that speed chemical reactions—might help recycle some kinds of plastic, much of which gets buried in landfills, burned, or washed into rivers and oceans. Although industrial chemicals can break down plastics, using enzymes is potentially a greener approach, requiring less energy, that can also target specific plastics mixed with trash. "Nature is the most amazing recycler because it wastes nothing," says John McGeehan, a structural biologist at the United Kingdom's University of Portsmouth who leads an enzyme-hunting project that Cordova is part of.

A company in France is already building a demonstration factory that will use enzymes to turn plastic trash into raw material for new bottles. Scaling up further means overcoming major challenges, however. Finding enzymes is just a first step. Moving from the laboratory to a recycling factory requires overcoming technical and economic hurdles in an industry with razor-thin profits, and where new plastic can be cheaper than recycling. On top of that, the microbes largely fail to dent some of the most widespread plastics.

"Think about the sheer scale on which we manufacture plastics and the low value of these plastics," says Susannah Scott, a chemical engineer at the University of California, Santa Barbara, who is developing metal-based catalysts, synthesized in the laboratory, to recycle plastic. "It's a tall order to ask biology to do that well."

After 48 hours with an enzyme that breaks down the plastic polyethylene terephthalate, it loses nearly 98% of its mass (right).

PLASTIC IS in many ways a recycler's nightmare. Built to last, plastic encompasses dozens of different molecules, made of long chains of carbon atoms. Those molecules all resist breaking apart, and each has distinct chemical properties that must be tackled differently. Often a single item—a potato chip bag, for example—is a maddening fusion of plastics, confounding the goal of easily extracting pure materials to develop a new product.

A small fraction of plastic is currently recycled, chiefly by sorting out usable types of plastic, melting them, and solidifying them again into pellets to be converted into lower grade plastics such as bags and artificial lumber. In 2014, just 19% of all plastic was being recycled, according to a 2017 study in *Science Advances*. Meanwhile, plastic production is expected to grow 70% by 2050, to almost 600 million tons per year.

The plastic that does go into recycling bins meets a variety of fates. Though some is reused, much is incinerated, buried in landfills, or dumped in the environment. Until recently, more than half the plastic collected in the United States was shipped overseas; of the shipped material, as much as one-quarter was too contaminated to be recycled, according to an estimate in a 2020 *Science Advances* study. In 2018, China stopped accepting most imported plastic waste, and U.S. recyclers reported sending unwanted bales of plastic to landfills. "We can't keep buying more and more plastic, putting it into the blue bin, and feeling like that's OK," says Kara Lavender Law, an oceanographer at the Sea Education Association in Woods Hole, Massachusetts, who has worked to measure global plastic pollution.

Enzymes are an appealing solution. Unlike many industrial chemicals, enzymes work at relatively low temperatures and are choosy about which molecule they interact with—enabling an enzyme to target a single plastic in a stew of polymers. Scientists began hunting for such enzymes in earnest in 2016, after Japanese researchers analyzing mud near a plastic recycling factory found a bacterium with an unusual

PHOTOS: DENNIS SCHROEDER; (OPPOSITE PAGE) MANDY BARKER

Coming full circle

Scientists are engineering enzymes to recycle plastic. These modified versions of natural proteins work at relatively low temperatures, target specific plastics in a mixture, and produce pure monomers that can then form new plastic.

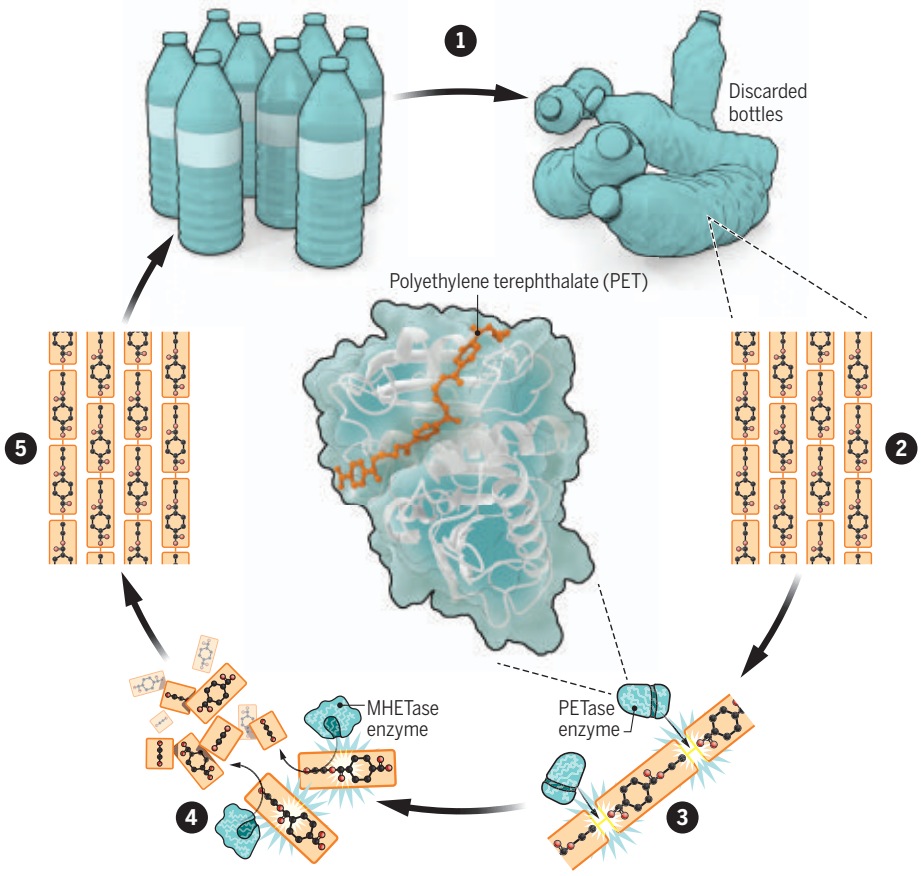

1 A popular target for recycling is PET, a polymer in drink bottles and polyester clothing.

2 PET consists of long strands made from monomers of ethylene glycol and terephthalic acid.

3 Enzymes that digest PET include the bacterial enzyme PETase, which breaks the polymer's oxygen-carbon bonds.

4 The resulting monomers get broken into their constituents by a second enzyme, MHETase.

5 Those products, ethylene glycol and terephthalic acid, can be made into PET again with heat, pressure, and catalysts.

Breaking bonds

PET is held together by bonds between carbon and oxygen, which require less energy to break in a chemical reaction than those formed by links between two carbon atoms. Those bonds, found in many common plastics such as polyethylene and polypropylene, are harder to break.

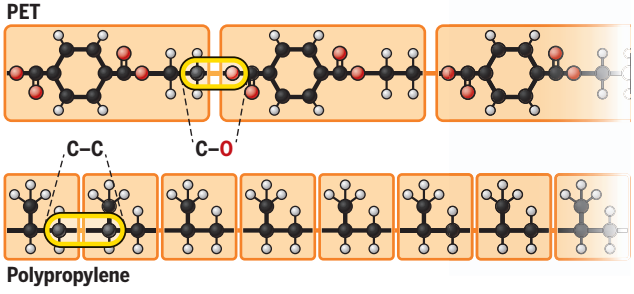

appetite for plastic (*Science*, 11 March 2016, p. 1196). The organism produced two enzymes that together enabled it to feed on polyethylene terephthalate (PET) by breaking it into its building blocks, terephthalic acid and ethylene glycol. PET is found in single-use drink bottles and fibers in polyester clothing, and it makes up about one-fifth of worldwide plastic production. Fabric is challenging to recycle today because it is often mixed with other materials. Although PET bottles are simpler, just 29% of PET bottles in the United States were recycled in 2018.

Before reading about the finding, McGeehan had been studying how organisms use enzymes to break down tough plant fibers. Now, he turned his eye to plastic, setting out to find other enzymes that could target polymers. He went on to recruit enzyme-hunting scientists in some of the world's plastic pollution hot spots, thinking all the plastic trash might have led to the evolution of microbes that attack it. Indonesia is one place he's looking, ranking second after China in one study examining sources of ocean-polluting plastic (*Science*, 13 February 2015, p. 768).

In Indonesia, in addition to collecting bacteria from plastic litter, Cordova plans to delve into the muck at the roots of mangrove trees. Microbes that originally fed on tough mangrove leaves would have had decades to evolve the ability to break down the plastic bags that cling to the roots. He will also suspend small tags of various plastics in Jakarta Bay to see whether any microscopic creatures start to feed on them.

Any promising microbial candidates that Cordova finds will be shipped to McGeehan's lab. His team crystallizes promising enzymes, then uses x-ray crystallography to peer into their structures, deciphering how they bind to polymers and help break their chemical links. The work has already yielded insights about which enzyme shapes hold the most promise. PET-breaking enzymes, for example, have a valley in their surface into which the plastic molecule nestles. There, a distinctive trio of amino acids attacks the molecular bond joining units of the polymer.

Using that information, McGeehan and others are scouring databases of bacterial genomes for DNA sequences that code for similar molecules, signaling potential plastic-cracking enzymes. Researchers in his lab then use computers to model how the proteins might be artificially improved. The goal is to modify the genes that encode the natural enzymes to make them into powerful plastic-busting tools. Already the team has altered the enzyme uncovered by the Japanese researchers to make it more efficient. "We're not looking for superenzymes from nature. That's pretty unlikely," McGeehan says. "We're just looking for enzymes that tickle plastic."

His group isn't the only one on the hunt. A consortium of European and Chinese labs is also working to find and cultivate bacteria whose enzymes break down plastic—and other enzymes that can turn the breakdown products into valuable chemicals. A group of researchers from Germany, France, and Ireland that included members of the consortium recycled PET by using a modified version of an enzyme found in a compost pile that takes apart the waxy layer on leaves. A strain of lab-evolved bacteria then used the raw materials to build two new kinds of plastic.

GRAPHIC: V. ALTOUNIAN/*SCIENCE*

IF THOSE QUESTS succeed, some plastics might be recycled by washing them in enzymes, much as enzyme-based detergents break down food stains in dirty clothes, says Gregg Beckham, a chemical engineer at the U.S. Department of Energy's National Renewable Energy Laboratory (NREL). Beckham heads a $32 million DOE initiative to develop new plastic recycling methods and collaborates with McGeehan on the enzyme search. In late May, NREL scientists gathered to test a scheme in which enzymes would help soldiers turn their plastic trash into building blocks for battlefield essentials.

The vision is "a box … where they could put in plastic and other types of waste, like paper. And out the back of it would come something like food or gun oil," Beckham says of the project, which is sponsored by the Defense Advanced Research Projects Agency (DARPA).

As with many DARPA projects, the research is a long way from practical deployment. Scientists at the NREL lab in Golden, Colorado, cut sheets of PET plastic into small squares. The squares were submerged in a brew of warm water, salt, and a version of the leaf-digesting enzyme found in compost, altered by French researchers to bind more tightly with the plastic and withstand higher temperatures.

When the Colorado researchers returned 24 hours later, 84% of the plastic had dissolved—suggesting the enzyme had broken the plastic down into smaller molecules. Beckham's target is to break down 95% of 5 kilograms of plastic in 1 month, he says. "We'll blow that out of the water."

The French company that developed the enzyme, Carbios, plans to build the world's first enzyme-fueled plastic recycling factory. The endeavor will start with a small demonstration plant in the city of Clermont-Ferrand to test the enzyme's ability to convert plastic trash into raw material for new PET plastic. The company says it will open a full-scale factory in 2024 with a goal of producing the ingredients for 40,000 tons of recycled plastic each year.

SUCH ENZYMES might not break the recycling logjam. They work best on plastic made from carbon atoms joined by an oxygen atom. Such polymers, called polyesters, are also found in plant fibers, which bacteria have had millions of years to evolve to feed on.

By contrast, plastics with bonds linking carbon atoms directly are tougher. Representing more than half of plastics made, they include the polyethylene of ubiquitous grocery bags and the polypropylene that forms a dizzying array of products, as diverse as syrup bottles and car dashboards.

In recent years, scientists have reported organisms that can feed on such plastics, including larvae of wax moths. But Beckham and others doubt the chemical talents of those organisms will translate into practical recycling of polyethylene or polypropylene.

Enzymes can be finicky, failing at the high temperatures needed to coax chemical reactions in many plastics other than PET. Enzymes also tend to work more slowly than industrial chemicals, Scott says, making them inefficient. "You're always coming back to the techno-economic analysis," says George Huber, a chemical engineer at the University of Wisconsin (UW), Madison, who heads a DOE-funded research project on recycling plastic into high-value products. "The economics dominate everything."

That's true for all enzymatic recycling methods. The raw materials—natural gas and oil—that go into most plastic are relatively cheap. Even if a recycled material were cheap enough to compete with a new one, it would have to be integrated into a vast manufacturing infrastructure and meet the exacting demands of companies buying plastics, says William Banholzer, a chemical engineer who was chief technology officer until 2014 at Dow, one of the world's largest plastic manufacturers. "The truth is, recycling still is too expensive and gives crappier products," says Banholzer, now at UW.

Amid a growing public outcry over plastic pollution, major chemical companies are investing in new forms of plastic recycling. But those approaches rely largely on industrial chemicals. In January, two major petrochemical companies, Eastman Chemical Company and SABIC, a subsidiary of the oil and gas giant Saudi Aramco, each announced plans to build factories using chemical treatments to turn plastic trash into materials to help make new plastics.

SABIC's chief technology and sustainability officer, Bob Maughon, says enzyme-boosted reactions move too slowly for plastic recycling. At the moment, "I think enzymatic is not realistic," he says.

But Alain Marty, a biologist and chief technology officer for Carbios, says he is confident his company's enzyme-based approach can chew through PET fast enough to find a place in the market. Although the first factory probably won't compete with the price of unrecycled raw materials, companies will pay a premium for recycled plastic that can be sold to environmentally conscious consumers, he says. "It is another product, and there is a great demand."

Despite Beckham's excitement about enzymes, he says he is agnostic about whether they will win out over other new ways to recycle. The DOE project he oversees is also investigating using heat, light, and electricity to break down plastics. Whatever the method, he just wants to see an increase in the fraction of plastic that goes into his recycling bin and really gets recycled. "My hope," Beckham says, "is that our recycle bins become much, much bigger." ■

Panoply of plastics

The millions of tons (Mt) of plastics produced each year include a vast array of materials tuned for different functions. Recycling processes vary depending on a plastic's identity, so a mix often can't be recycled together. But enzymes may be able to selectively break down a single plastic in a mix.

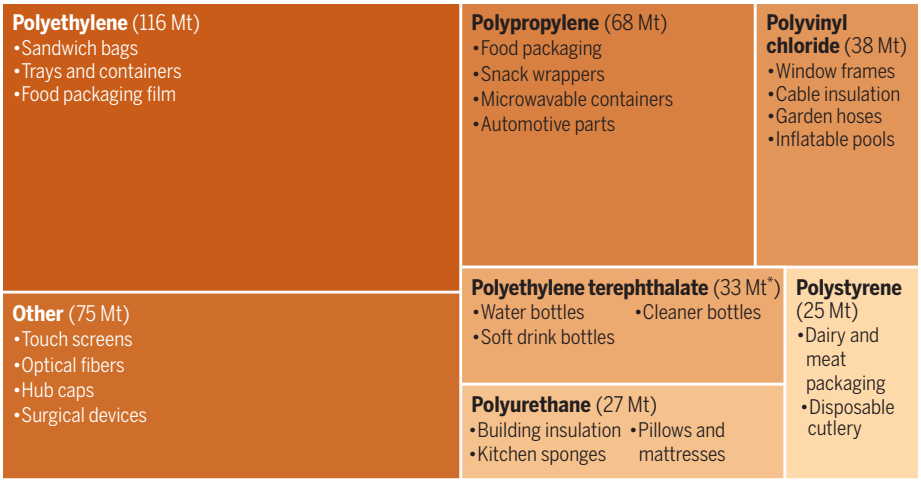

*Total mass does not include that of polyester fibers in clothing.

GRAPHIC: V. ALTOUNIAN/*SCIENCE*

A polyurethane foam "nature carpet" by Italian artist Piero Gilardi.

PHOTO: ALETH LORNE

WHEN PLASTICS ARE PRECIOUS

To prevent museum artifacts from falling apart, conservators experiment with preservation methods

By **Sam Kean**

Leanne Tonkin still remembers the ruined coats. She was doing a fellowship at the Metropolitan Museum of Art's Costume Institute in the mid-2010s when she saw a red mackintosh from the 1960s. The raincoat was so rigid it could stand up on its own, as though inhabited by a ghost. Another mackintosh was hardly recognizable as clothing. "You could make out a button on it, but it was completely melted," she says.

Nothing out of the ordinary had happened to the coats. They didn't get caught in fires or exposed to caustic chemicals. Instead, they were doomed for a simpler reason: They contained inherently unstable plastics.

People often grumble that plastics are too durable. Water bottles, shopping bags, and other trash litter the planet, from Mount Everest to the Mariana Trench, because plastics are ubiquitous and don't break down easily.

But some plastic materials change over time. They crack and frizzle. They "weep" out additives. They melt into sludge. All of which creates huge headaches for institutions, such as museums, trying to preserve culturally important objects.

Until recently, museums only had to worry about traditional materials. "We know how to approach the restoration of paintings, books, and materials like wood, metals, and glass," says Anna Laganà, a research specialist at the Getty Conservation Institute. "But for plastics, our knowledge is still limited." Tonkin, now a doctoral researcher in fashion conservation at Nottingham Trent University, agrees: "We're now scuttling around trying to figure out how to conserve" plastics, she says.

The variety of plastic objects at risk is dizzying: early radios, avant-garde sculptures, celluloid animation stills from Disney films, David Bowie costumes, the first artificial heart. Nearly every museum in the world has plastic items, and even well-cared-for objects can fall apart alarmingly quickly.

Joana Lia Ferreira, an assistant professor of conservation and restoration at the NOVA School of Science and Technology, recalls an exhibit with a lamp that had a black polyurethane foam shade. One day, conservators noticed the shade had started to collapse, so they removed the lamp from the exhibit to save it. But it was too late: The shade began to crumble and soon col-

lapsed completely. "From one week to another," Ferreira says, "it was on the floor."

Museums are doing everything they can to save culturally important items from similar fates. Over the past decade, conservators have developed better tools to identify vulnerable objects. Some conservators have also started to run experiments to shore up preservation practices and arrest decay. Plastics have existed for roughly 150 years at this point, and curators want their plastic treasures to still be recognizable 150 years into the future.

SOME PLASTICS, such as polycarbonate and acrylic, are quite stable. But the long-chain polymer molecules in other plastics can break down when exposed to oxygen or light, among other potential threats. Unfortunately, some of the most "malignant" plastics—cellulose nitrate, cellulose acetate, polyurethane, polyvinyl chloride (PVC)—were common historically, finding use in items as diverse as photography film, billiard balls, and high-end clothing and furniture. The additional ingredients in those plastics, including plasticizers, dyes, and fire retardants, can introduce their own problems. PVC, for instance, forms both sturdy plumbing pipes and supple shower curtains, depending on the additives. And those mixtures can naturally unmix over time, especially when temperatures fluctuate.

One common challenge for conservators is figuring out what materials they're even working with. Techniques such as Raman spectroscopy and pyrolysis–gas chromatography–mass spectrometry can create a molecular "fingerprint" from a sample of material. By looking for a match in a database of spectra posted online by a European-led project called POPART (Preservation of Plastic Artefacts in museum collections), museums can determine what materials they have.

Still, many small museums lack access to fancy lab equipment, which can cost tens of thousands of dollars. So some institutes have developed low-tech approaches based on touching, tapping, and sniffing. Depending on the type, plastics can feel glasslike or waxy. After decay begins, they can also feel sticky as internal plasticizers migrate to the surface. Auditory tests are available, too: Some plastics sound tinny when tapped; others, stolid and dull. And deteriorating plastics can release an astounding array of odors—chlorine, vinegar, pine, burnt hair, used sneakers, mothballs, car tires, sulfur.

Once conservators identify the plastic, they can take steps to preserve it. The general rule is "keep it cold, keep it dark, keep it dry, [and] keep it without oxygen in some cases," says Odile Madden, a senior scientist at the Getty. But the optimal conditions can differ even within the same family of material; it all depends on the specific ingredients and their proportions. Testing new preservation techniques on unique objects is risky, so some conservators have turned to controlled experiments.

After years of light exposure, foam figures on these "nature carpets" were cracking and deteriorating (top). Some of the pieces went back on display after restoration with protective "sunscreen" chemicals (bottom).

PHOTOS: ALETH LORNE

Tonkin, for instance, simulated clothing by adding stitches and metal studs to 20-centimeter squares of PVC fabric (common in modern raincoats). Then, she stored them for months at temperatures ranging from –17.8°C to 21.1°C and humidities between 40% and 50%.

Intuitively, deep-freeze storage might seem the most promising way to preserve

a material. But in the coldest conditions, Tonkin found, PVC molecules crystallized, squeezing out the plasticizers that make the fabric supple. The fabric ended up brittle and pitted with minute holes. Storing plastics at 4.4°C avoided that problem. In addition, Tonkin found that when transferring the material into or out of chilled storage, keeping it at an intermediate temperature of about 15.5°C for 24 hours could help avoid damage from quick temperature changes.

Other conservators have run experiments to artificially age plastics, trying to understand exactly how they break down—and glean clues about how to arrest decay. with an eye toward performing artificial aging tests on them later.

Certain artifacts are especially vulnerable because some pioneers in plastic art didn't always know how to mix ingredients properly, says Thea van Oosten, a polymer chemist who, until retiring a few years ago, worked for decades at the Cultural Heritage Agency of the Netherlands (RCE). "It's like baking a cake: If you don't have exact amounts, it goes wrong," she says. "The object you make is already a time bomb."

And sometimes, it's not the artist's fault. In the 1960s, the Italian artist Piero Gilardi began to create hundreds of bright, colorful foam pieces. Those pieces included small

The results were encouraging. Samples that lacked sunscreen had withered under the barrage of photons: The molecular "struts" shoring up the foam were 42% thinner and notably more brittle than before the lamp treatment. The struts in samples with sunscreen decreased by as little as 12.5%.

Armed with that knowledge, conservators working with RCE infused several Gilardi sculptures, including two nature carpets, with the sunscreen to stabilize them. Van Oosten is proud that several have even gone on display again, albeit sometimes beneath protective cases. Long called the "queen of plastics," in 2012, van Oosten was knighted in the Netherlands

Some polymers go to pieces

Different plastics break down at different rates depending on their compositions and environments. Some plastics are fairly unstable (●), including early plastics from the 19th century and first decades of the 20th century, often found in culturally important plastic objects. Modern plastics (●) are far more stable and can take centuries or longer to decompose.

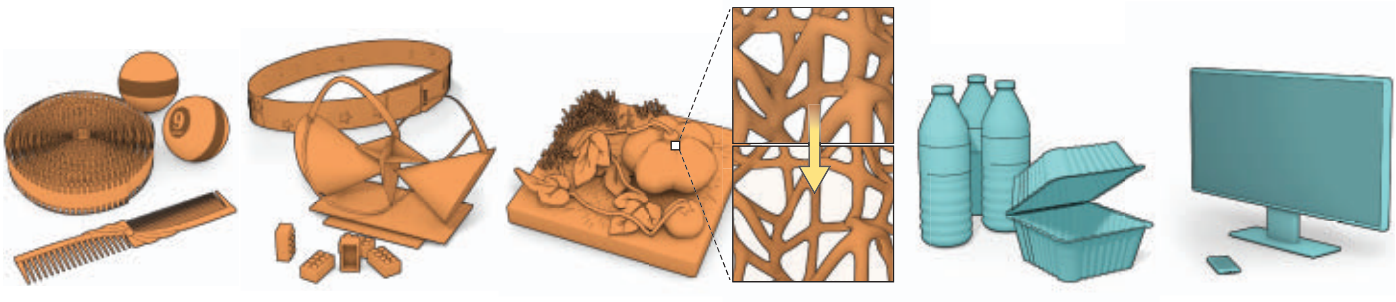

Cellulose nitrate
This plastic, used in early film and consumer goods, can be flammable and dangerous.

Cellulose acetate
This polymer found use in early Legos, sculptures, and fashion items like belts. It can smell of vinegar as it decays.

Polyurethane
Often used in foams, polyurethane has molecular struts that, after 10 to 20 years, can degrade because of light exposure.

Polyethylene terephthalate (PET)
One of the most common plastics in the world, PET is used in water bottles and clamshell food packaging.

Poly(methyl methacrylate)
Also known as acrylic, this often-transparent polymer is common in LCD and smartphone screens.

Xenon arc lamps bombard materials with photons, collapsing years of light exposure into hours. Researchers can use weather chambers to study heat and humidity. Madden has also considered exposing plastics to pollutants to study the effects of dirty air.

Such experiments face a limiting factor: a lack of historically accurate plastics. For safety and stability, today's manufacturers add different ingredients to plastics than in decades past. So the results of experiments on modern polymers might not hold for historic ones.

To skirt that limitation, in 2019 the Getty purchased its own plasticmaking equipment: an extruder and injection-molding system. Staff members then flipped through old issues of magazines such as *Modern Plastics* to find representative recipes. The Getty can now re-create historic plastics with the exact ingredients used originally. Scientists there are already running stress tests on small discs and bars, beds of roses and other items as well as a few dozen "nature carpets"—large rectangles decorated with foam pumpkins, cabbages, and watermelons. He wanted viewers to walk around on the carpets—which meant they had to be durable.

Unfortunately, the polyurethane foam he used is inherently unstable. It's especially vulnerable to light damage, and by the mid-1990s, Gilardi's pumpkins, roses, and other figures were splitting and crumbling. Museums locked some of them away in the dark.

So van Oosten and colleagues at RCE began to study ways to protect polyurethane. First, they took foam samples similar to the nature carpets and infused some with stabilizing and consolidating chemicals that modern manufacturers often use. Van Oosten calls those chemicals "sunscreens" because their goal was to prevent further light damage and rebuild worn polymer fibers. Then the team used xenon lamps to artificially age both treated and untreated samples, and examined them under high-powered microscopes.

for her efforts to preserve plastic objects and spread knowledge to other institutes.

DESPITE SUCH SUCCESS stories, preservation of plastics will likely get harder. Old objects continue to deteriorate. Worse, biodegradable plastics, designed to disintegrate, are increasingly common.

And more is at stake here than individual objects. Ferreira notes that archaeologists first defined the great material ages of human history—Stone Age, Iron Age, and so on—after examining artifacts in museums. We now live in an age of plastic, she says, "and what we decide to collect today, what we decide to preserve … will have a strong impact on how in the future we'll be seen."

Future archaeologists examining the leavings of the 21st century will likely find scads of toxic crud, along with plenty of plastic trash. But if museum preservation efforts succeed, maybe those scholars will also see that plastic items today can be culturally meaningful—and even cherished. ■

GRAPHIC: V. ALTOUNIAN/*SCIENCE*

POLICY FORUM

A binding global agreement to address the life cycle of plastics

To eliminate plastic pollution, a holistic approach is needed

By **Nils Simon[1], Karen Raubenheimer[2], Niko Urho[3], Sebastian Unger[4], David Azoulay[5], Trisia Farrelly[6], Joao Sousa[7], Harro van Asselt[8], Giulia Carlini[5], Christian Sekomo[9], Maro Luisa Schulte[1], Per-Olof Busch[1], Nicole Wienrich[4], Laura Weiand[4]**

Amid the global plastic pollution crisis, a growing number of governments and nongovernmental actors are proposing a new global treaty. In February 2021, at the fifth meeting of the United Nations Environment Assembly (UNEA)—the world's highest-level decision-making body on the environment—many governments spoke in favor of an international agreement to combat plastic pollution. In the past, the international community tended to view the plastics problem from a predominantly ocean-focused and waste-centered perspective. However, plastics are increasingly found in all environmental media, including terrestrial ecosystems and the atmosphere, as well as human matrices, including lungs and placenta. We therefore argue for a new international legally binding agreement that addresses the entire life cycle of plastics, from extraction of raw materials to legacy plastic pollution. Only by taking this approach can efforts match the magnitude and transboundary nature of this escalating problem and its social, environmental, and economic impacts. Targeting the full life cycle of plastics allows for a more equitable distribution of the costs and benefits of relevant actions across the global value chain.

Civil society organizations focusing on biodiversity conservation, health, climate change, and human rights have for years called for a binding global plastics agreement. In 2017, UNEA established the Ad Hoc Open-Ended Expert Group on Marine Litter and Microplastics, a group of international experts who have discussed options to address plastic pollution at a global level, on the basis that maintaining the status quo was not an option (*1*). Support for a legally binding global agreement now comes from at least 79 governments, who endorse the Oceans Day Plastic Pollution Declaration from 1 June 2021. Many civil society organizations, as well as a large coalition of major companies, have for years favored a UN treaty on plastic pollution (*2*). In May 2021, Peru and Rwanda announced they would table a resolution at the upcoming UNEA meeting in February 2022 to establish an intergovernmental negotiating committee to begin developing such an agreement.

The start of negotiations is overdue. In 2019, 368 million metric tons of newly made (or "virgin") plastics were produced. Current solutions will not match the expected growth in plastics production and waste generation, even if massively scaled (*3*). In addition, the further increase in virgin plastics production could, by 2050, consume 10 to 13% of the remaining global carbon budget permissible to keep global warming below a 1.5°C increase from preindustrial levels (*4*). Plastic pollution poses a considerable, even though not yet fully understood, threat to the environment, species, and habitats, as well as to cultural heritage. Its social impacts include harm to human health, in particular among vulnerable communities, and it comes with substantial economic costs affecting especially regions depending on tourism (*5*). Addressing these challenges requires a transformative approach that facilitates measures to reduce production of virgin plastic materials and includes equitable steps toward a safe and circular economy for plastics.

A binding treaty must be ambitious to eliminate the impacts of current amounts of plastic pollution and mitigate impacts of the projected increase in production in a business-as-usual scenario (*6*). An agreement should pursue a vision of zero plastic pollution and no harm to humans and the environment throughout the full life cycle of plastics. To realize this vision, negotiations will need to address the regulatory scope and architecture of the agreement, how it will complement and fill gaps in existing global and regional frameworks, and how the plastics value chain should be transformed, particularly in the "upstream" design and production phases. It is essential to involve all relevant stakeholders in negotiations and get them engaged in implementation efforts, from governments through producers and manufacturers, academia, civil society organizations and consumers, to the informal sector, including waste pickers.

Safe circularity principles

The following principles provide guidance for developing criteria for the circularity of plastics:

Durability
Single-use plastics for which safe and environmentally sound alternatives exist are eliminated; and product design accommodates for safe reusability, repairability, and refillability

Recyclability
Recycling enables cost-effective material recovery with minimum energy loss and multiple recycling rounds without downcycling; and minimum threshold for recycled content agreed

Safety
Use of substances of concern eliminated; and use of primary microplastics eliminated and secondary releases minimized

Transparency
Labelling schemes guide informed choices; definitions are agreed including for "bioplastics" and "biodegradable plastics"; and information is available on the chemical content of products

THE NEED FOR AN INTERNATIONAL AGREEMENT

Based on a review of 20 global and 34 regional binding and voluntary instruments, the UN Environment Programme (UNEP) concluded that the existing fragmented governance landscape is inadequate for addressing marine plastic pollution (*1*). Two major gaps underscore the need for a global agreement.

First, there is a lack of a comprehensive global governance arrangement that addresses all sources of plastic pollution, in particular land-based. Most existing agreements are restricted to marine litter, especially sea-based sources, even though the majority of sources are located on land. For example, the London Convention and Protocol and the International Convention for the Prevention of Pollution from Ships (MARPOL) Annex V prohibits the discharge of garbage from ships into the sea. In addition, a range of nonbinding declarations and action plans

[1]adelphi, Berlin, Germany. [2]University of Wollongong, Wollongong, Australia. [3]University of Massachusetts, Boston, MA, USA. [4]Institute for Advanced Sustainability Studies, Potsdam, Germany. [5]Center for International Environmental Law, Geneva, Switzerland. [6]Massey University, Palmerston North, New Zealand. [7]International Union for the Conservation of Nature, Gland, Switzerland. [8]University of Eastern Finland, Joensuu, Finland. [9]National Industrial and Research Development Agency, Kigali, Rwanda. Email: simon@adelphi.de

aim at reducing marine plastic pollution, e.g., Sustainable Development Goal target 14.1. Regional seas conventions and action plans, regional fisheries management organizations, and other regional instruments focus on coordinated strategies to combat marine litter at sea-basin scale (*11*). Marine litter is also the focus of several UNEA resolutions as well as G7 and G20 Action Plans.

Second, there is no global governance arrangement that addresses the entire life cycle of plastics. Many arrangements cover the waste phase but are weak on the design, production, and use phases (*1*). The gap in addressing the design and production phase is problematic because only 21% of all plastics currently produced are theoretically recyclable, and a mere 15% are actually recycled in practice (*8*). The international trade of plastic waste is regulated under the Basel Convention on the Control of Transboundary Movements of Hazardous Wastes and Their Disposal, which enjoys near-universal participation. Only clean, sorted plastic waste effectively destined for recycling can be freely traded, whereas mixed, contaminated, or hazardous plastic waste requires the prior informed consent of the importing country. Only the Stockholm Convention on Persistent Organic Pollutants regulates the production phase of plastics, but this includes a limited set of prohibited chemicals that may no longer be used as additives. Most additives are therefore not addressed comprehensively under any international agreement, even though more than 1500 have been identified as chemicals of concern in plastics (*9*). Likewise, microplastics are addressed through a patchwork of national and regional initiatives instead of global regulations (*10*, *11*).

These gaps underscore the need for a legally binding global governance arrangement that would effectively and measurably limit and control plastic pollution (*1*, *2*, *12*). The governance failure manifests in various ways, entrenching the entire life cycle of plastics. It starts with the increasing production of virgin nonrenewable materials, and the manufacture of plastic products that are not designed for safe reusability and recyclability and which may be chemically contaminated. At the point of purchase, retailers and consumers are not informed about a product's chemical content and are faced with inconsistent and vague labeling (e.g., compostable, biodegradable, recyclable), leading to suboptimal end-of-life treatments. During use, the release of additives of concern and microplastics may negatively affect the health of consumers (*9*). And the most visible outcome is the rapidly increasing amount of macro- and microplastic waste in the environment.

CORE GOALS OF A PLASTICS AGREEMENT

An international agreement that addresses these governance gaps and effectively combats pollution throughout the plastics life cycle and facilitates a sustainability-focused transformation needs to include three core goals (see the figure).

GOAL 1: Minimize virgin plastics production and consumption

Controlling and minimizing plastic pollution first and foremost requires agreement on a progressively decreasing global production allowance for virgin plastics. Transformative scenarios that outline how plastic pollution can be prevented point toward the need to reduce virgin plastics production as a major contribution (*6*, *8*).

This goal is modeled after the Montreal Protocol, which sets a maximum level for production of ozone-depleting substances and progressively reduces volumes to safe levels (*7*). Similarly, the Paris Agreement sets a measurable goal for limiting the increase in the global average temperature, which can only be achieved by rapidly reducing global greenhouse gas (GHG) emissions. The former caps production by targeting inputs and the latter by focusing on outcomes.

A cap is a powerful instrument that can be tailored to a specific challenge to incentivize action to reduce production and consumption and to find and use more benign alternatives. However, determining the volumes at which production and consumption should be capped will require robust knowledge of current and safe levels of pollution, environmentally sound and cost-effective alternative materials and processes, and a comprehensive tracking system of all materials, processes, and effectiveness of parallel measures undertaken.

An agreed goal to reduce production and consumption of virgin plastic materials would send the clearest signal from governments to producers, consumers, and others along the plastics value chain. It is the key measure needed to reverse worsening trends. It would signal that manufacturers need to enhance their efforts toward sustainability of plastics considerably, that they will need to produce less of it, and that innovation and safety improvements offer substantial new market opportunities. The goal would also prevent GHG emissions by discouraging further investments in expanding plastics production capacities.

Given the urgency of the climate crisis and the need to reach net-zero carbon emissions by 2050, the production and consumption targets should be aligned accordingly: By 2040, the use of virgin plastics should be largely phased out, and most plastic products should be made from recycled content to the extent possible. Exemptions should only be granted for materials like medical supplies for which no safe and nonplastic alternatives exist.

PHOTO: K M ASAD/LIGHTROCKET/GETTY IMAGES

The goal could be reached through a "start and strengthen" approach, first targeting the most problematic types of plastic that are difficult or impossible to recycle and for which alternatives can be easily applied. The agreement will need measures for phasing out or ultimately banning products using plastics (virgin or recycled) unnecessarily—i.e., when safe, affordable, and environmentally benign alternatives exist—and foster the development and use of such alternatives. There are many existing national and regional policy approaches on which to build and expand (*10*). With the Single Use Plastics Directive, the European Union (EU) follows the example of other states, including African and Small Island Developing States, and bans a range of throwaway products. A global plastics agreement should establish international norms to scale up such bans and other appropriate regulations.

Demand for virgin plastics can be further reduced by setting a complementary progressively increasing consumption target for use of recycled content in products, which leads to the second core goal.

GOAL 2: Facilitate safe circularity of plastics

A circularity goal for plastics will incentivize design for recycling, improve recycling rates,

Plastic pollution is a quickly growing problem for human health and the environment. Only by focusing on the entire life cycle of plastics can the challenges be addressed.

and foster the use of recycled content. Safe circularity can be achieved through elimination of hazardous substances. Reuse and refill systems, as well as alternative low-to-no waste delivery systems, also eliminate substantial volumes of plastic pollution and should be prioritized ahead of recycling.

Measures to achieve these goals will help transform the value chain of plastics, bring competitive advantages to producers and retailers, create jobs, and provide health benefits to consumers and ecosystems. The agreement must establish binding technical standards for the design and recyclability of plastics. Hazardous additives, such as phthalates and bisphenols, must be phased out to ensure human safety and minimize impacts on wildlife populations (*9*). Chemical controls required by the agreement should include rules to share information on any potentially harmful additives along the value chain.

Circularity will require a fundamental transformation of the plastics value chain, and though incurring costs, it could benefit all actors in the long term (*13*). In the upstream phases, the agreement must ensure a level playing field for producers and manufacturers through harmonized rules for product safety and sustainability, thus preventing companies from adhering to different standards. In the midstream phases, the agreement should set requirements and a legal basis for information sharing, establishing labeling and certification schemes and detailing harmonized definitions. This will enhance transparency on product contents and sustainability, and it will enable retailers and consumers to make informed choices that will help drive markets toward safe and sustainable products. It will also empower consumer organizations to sue producers and retailers that do not adhere to the strict sustainability and transparency standards.

The general population will also benefit from increased product durability (including reuse, repair, and refill) and safety (less substances of concern in products). In the downstream phases, technical standards on plastic waste enshrined in the agreement will lead to benefits for recyclers, particularly low-income workers, from better-quality and higher residual value, leading to increased investment and job opportunities and improved livelihoods, especially for the informal sector. The legal basis for protecting the rights of the informal sector can be set in the agreement. Once hazardous chemicals are removed from the plastics life cycle, there are potentially substantial economic gains for the recycling industry (*2*, *8*, *13*). Furthermore, the population will be able to enjoy health benefits, including through reduced disposal of plastic waste in suboptimal conditions such as incineration, particularly open burning.

To reach the goal, the agreement must define global criteria for the circularity of plastic products placed on global and domestic markets (see the box). Such harmonized criteria will assist countries in adopting necessary regulatory, voluntary, and market-based measures (*12*). Extended producer responsibility (EPR) schemes should be one of the mechanisms shifting the financial and physical burden of waste management to plastics producers and incentivizing design for circularity from the onset.

Examples for circularity goals include the EU's strategy for plastics in a circular economy, which aims at all plastics packaging used in the EU to become reusable or recyclable in an economically viable way by 2030. The goal of facilitating circularity is closely linked with the global net reduction in consumption of both virgin polymers and chemical additives as per Goal 1. Currently there is a glaring gap between waste management capacities and waste production in many developing countries, but also in developed countries with regards to recycling capacity. Slowing the growth rate of plastic waste, and ultimately reducing total waste, reduces the need to scale waste management to meet the current growing demand. This is a key benefit of fostering transformation of production and consumption patterns, stimulating innovation toward "design for circularity," and promoting systems for reuse, refill, repair, and recycling.

GOAL 3: Eliminate plastic pollution in the environment

This goal aims to safely remove and sustainably dispose of plastics accumulated on land, on waterways, and in oceans. It also aims at preventing those plastics currently in use from ending up in the environment because of their low value at the end of life. Regarding the latter, the agreement should set strict pollution prevention targets, to be implemented at the national and subnational level, and based on analyses of plastic flows.

This goal is designed to complement and scale up instruments already used at the national and regional level. Especially for developing countries, the lack of waste management services will require particular attention. Funding through the plastics agreement should be made available to establish and enhance the use of market-based instruments, including EPR schemes, to subsidize waste management and cleanup. For instance, the EU Single Use Plastics Directive applies EPR schemes to tobacco filters and fishing gear to cover the cost of cleaning up litter.

Engaging in large-scale cleanup measures is a costly undertaking even if an effective

agreement leads to reduced amounts of plastic waste entering the environment. For many nations and cities, it is advantageous to clean up polluted sites, because clogged waterways, drains, and sewers increase the risk of flooding and the spread of diseases. This will also redress reduced tourism revenues from polluted destinations. However, in other areas, there will only be limited economic incentives to clean up. For these areas, additional support measures are required. Such measures could include a fund dedicated to cleanup, requiring contributions from producers, which could fund citizen science audit and cleanup campaigns and repatriate plastics back to producer countries for responsible management.

OPERATIONAL ELEMENTS

To effectively implement the agreement and follow up on its goals, concrete obligations, support measures, institutional arrangements, and mechanisms for strengthening nonstate action and for coordination with existing treaties need to be developed (*12*).

Implementing and tracking progress

A set of binding procedural obligations will help ensure that parties implement and stay on track with the agreement's goals. Countries will still need flexibility in the national pathways; hence, the agreement should include an obligation to develop and implement regularly updated national plastic pollution prevention plans (N4Ps). These must describe how countries endeavor to meet the core goals, based on national circumstances and capacities, and measures. They should contain ambitious and measurable national targets in line with the core goals. The plans must include all relevant measures to be taken by national and subnational governmental actors. They should be well-integrated into existing policies, legislation, and strategies and build on regionally coordinated plans or strategies, where in place. To ensure that the plans help meet the goals, common criteria should be defined for the contents of the plans, such as the setting of targets, determining baselines for various indicators, implementation time frames, and monitoring methodologies used. Moreover, following the model of the Paris Agreement, the agreement should ensure that N4Ps are progressive, reflecting increasing levels of ambition over time.

The plans should also address previously identified main sources of leakage. For this, the preparation of national inventories on the production, consumption, trade, and end-of-life treatment is needed to assess leakage points across the value chain and to enable targeted interventions (*1*). These inventories can also be used for identifying hotspots of accumulation and assessing types of plastics and volumes found there, which can help determine the most cost-effective action.

Another procedural obligation concerns regular reporting by parties on implementation and performance in achieving the core goals. Building on experiences in other agreements, reporting should use a format that requires quantitative and qualitative data that are considered meaningful. A secretariat to the convention will need to be established, which should support reporting (*12*). To ensure that the information provided by governments is comprehensive and to inform future policy-making, a transparent review mechanism for national reports should be included. In addition, countries would need to monitor the presence of plastic pollution in the environment to ensure that the three goals are delivering their intended impacts using harmonized methodologies that are practical, scalable, economically viable, and ecologically representative. Monitoring and assessment should address gaps and create synergies with existing programs at the local, national, and regional level (*11*).

The preparation of a transparent and participatory iterative global review is needed to regularly inform parties of the effectiveness of the agreement. This could be achieved by aggregating data gathered through reporting on performance and monitoring impacts. Lastly, the agreement will also need a transparent compliance mechanism that allows parties to foster mutual implementation of its provisions and create a level playing field. At a minimum, it should help deal with cases of persistent noncompliance, as well as instances in which parties do not comply with their core procedural obligations of submitting regular N4Ps and reporting. More ambitiously, the agreement could explicitly state countries' right to prohibit imports of plastic products from noncompliant parties, because these pose an unacceptable social, environmental, and economic risk.

Supporting mechanisms

Supporting mechanisms are needed to give greater effect to other measures. Funding from both domestic budgets and private sources, coupled with international support, is needed to fund the necessary legislation, infrastructure, technology and capacity building.

To have an impact, the agreement must include mechanisms to support developing countries in the implementation of measures committed to under the agreement, including for enabling activities, such as reporting and the development of N4Ps. This could include a dedicated funding mechanism, which could be managed by an existing body such as the Global Environment Facility (GEF), or be a new fund. Entrusting the GEF would help to avoid proliferation of funding mechanisms and allow for synergies with the Facility's other focal areas, including chemicals and waste and climate change. The problem with the GEF is that it relies on voluntary contributions. The advantage of establishing a new fund is that it could be based on mandatory contributions using the UN scale of assessment that intends to accommodate a country's "capacity to pay," resembling the Multilateral Fund for the Montreal Protocol. Additional voluntary funds could be established, inviting major producers of plastics and plastic products to contribute. Furthermore, a clearing-house mechanism could channel knowledge about existing funds and programs and assist developing countries in accessing them.

Funds should be allocated to spur the use of market-based instruments, helping countries to internalize externalities of plastic

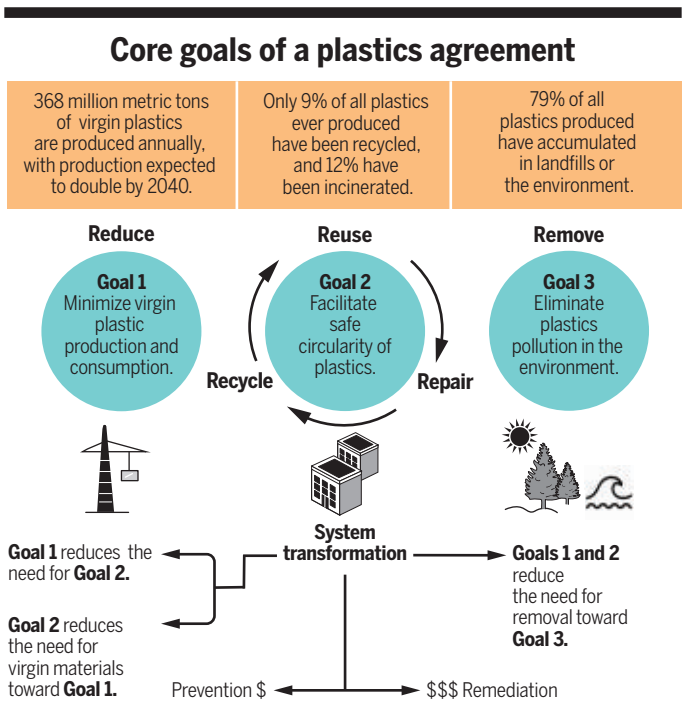

GRAPHIC: H. BISHOP/*SCIENCE*

pollution. Raising funds from plastics producers would align with the "polluter pays" principle and resemble a liability mechanism (*14*). It is important that the agreement ensures equity by helping countries to place the burden on the industry responsible for plastic pollution rather than the consumer. This can be achieved by encouraging the use of market-based instruments that target upstream measures, such as a levy on domestically produced virgin plastics, both generating funds and disincentivizing the excessive use of plastics. Ideally, these are earmarked levies channeled to fulfill the obligations of the agreement including by supporting research, development, and use of benign alternatives.

At the national level, a plastics authority should be designated to ensure the implementation of the agreement. The authority would be responsible for translating the internationally agreed sustainability criteria to the national context.

An evolving and inclusive framework

Not all relevant aspects can be addressed in detail in the agreement itself. A framework for further action will be needed, as well as institutional arrangements to redevelop rules and implementation arrangements. This includes a governing body to convene the contracting parties to adopt decisions, annexes, and protocols where necessary, including technical standards and guidelines on design and production, reuse, recycling, disposal, and retrieval. In addition, subsidiary bodies would be established for areas where scientific and technical support is needed, including defining criteria for the safe circularity of plastics and developing and facilitating use of harmonized methodologies for data collection. A science-policy interface should support the transfer of knowledge between expert communities and policy-makers (*15*).

Lastly, as the agreement is situated in a complex governance landscape, mechanisms would be needed to engage a wide array of societal actors and institutions. Specifically, a stakeholder engagement mechanism to facilitate nonstate and subnational action must support the agreement. This mechanism should include a global commitment platform where nonstate and subnational actors could announce voluntary commitments to be tracked and displayed online, and facilitate the organization of global and regional high-level events, technical dialogues, and other activities. These would allow learning from best-practice examples as well as from failures and to identify opportunities for upscaling ambition and action. A particular challenge will be to include the informal sector in the development and implementation of the agreement—for example, waste pickers as a major component of waste management systems in developing countries. In addition, the agreement would need a coordination mechanism for enhancing cooperation and synergies with existing other multilateral environmental agreements and relevant frameworks.

NEXT STEPS

The decision to launch an intergovernmental negotiating committee lies with the UNEA. The next decision-making meeting (UNEA 5.2) is scheduled for February 2022. A preparatory Ministerial Conference is scheduled for 1 to 2 September 2021 on invitation by Germany, Ghana, Ecuador, and Vietnam.

It will take several years for a new agreement to be negotiated, enter into force, and begin to have an impact. Hence, it is necessary to continuously develop and strengthen action through existing regional and multilateral institutions. Yet governments need to boldly go beyond existing approaches. Although a new agreement will come with costs, it will unlock sizable environmental, social, and economic benefits (*2*, *8*, *13*). ■

REFERENCES AND NOTES

1. U. N. Environment, "Combating marine plastic litter and microplastics" (United Nations Environment Programme, 2017).
2. WWF *et al.*, "The business case for a UN treaty on plastic pollution" (2020).
3. S. B. Borrelle *et al.*, *Science* **369**, 1515 (2020).
4. L. A. Hamilton *et al.*, "Plastic & climate: The hidden costs of a plastic planet" (CIEL, EIP, FracTracker Alliance, GAIA, 5Gyres, #breakfreefromplastic, 2019).
5. N. J. Beaumont *et al.*, *Mar. Pollut. Bull.* **142**, 189 (2019).
6. W. W. Y. Lau *et al.*, *Science* **369**, 1455 (2020).
7. K. Raubenheimer, A. McIlgorm, *Mar. Policy* **81**, 322 (2017).
8. SYSTEMIQ, Pew Charitable Trusts, "Breaking the plastic wave: A comprehensive assessment of pathways towards stopping ocean plastic pollution" (Ellen MacArthur Foundation, 2020).
9. N. Aurisano, R. Weber, P. Fantke, *Curr. Opin. Green Sustain. Chem.* **31**, 100513 (2021).
10. R. Karasik et al., "20 years of government responses to the global plastic pollution problem: The Plastics Policy Inventory" (Nicholas Institute for Environmental Policy Solutions, Duke University, 2020).
11. N. Wienrich *et al.*, "Stronger together: The role of regional instruments in strengthening global governance of marine plastic pollution" (Institute for Advanced Sustainability Studies, Potsdam, 2021).
12. K. Raubenheimer, N. Urho, "Possible elements of a new global agreement to prevent plastic pollution" (Nordic Council of Ministers, 2020).
13. Chemsec, "What goes around: Enabling the circular economy by removing chemical roadblocks" (2021).
14. S. Maljean-Dubois, B. Mayer, *AJIL Unbound* **114**, 206 (2020).
15. P. Busch *et al.*, "Strengthen the global science and knowledge base to reduce marine plastic pollution" (Nordic Council of Ministers, 2021).

ACKNOWLEDGMENTS

The authors thank C. Dixon and T. Gammage (Environmental Investigation Agency), as well as three anonymous reviewers, for helpful comments. The authors declare no competing interests.

10.1126/science.abi9010

PERSPECTIVE

The myth of historical bio-based plastics

Early bio-based plastics, which were neither clean nor green, offer lessons for today

By **Rebecca Altman**

Bioplastics are a broad category of materials encompassing bio-based, biodegradable, or both bio-based and biodegradable plastics. They can be manufactured from diverse sources, including crops (e.g., corn, sugar cane, and, historically, cotton), wood pulp, fungi, and other bio-based feedstocks produced with the help of algae or microbes. Some bio-based plastics, such as polyhydroxyalkanoates (PHAs) and polylactic acid (PLA), are biodegradable under specific environmental conditions. Others, such as bio-polypropylene (bio-PP) and bio–polyethylene terephthalate (bio-PET), are also bio-based but are chemically equivalent to their conventional counterparts and do not biodegrade. Bioplastics can also include materials designed for biodegradation that are derived from fossil fuel–based rather than bio-based sources (*1*). Although bioplastics represent a small and growing segment within the industry, they are not a new idea and have a long history that is often overlooked or misunderstood.

The earliest iterations of industrial-scale molding materials date to the mid-1800s and were sourced from trees (e.g., resins, gums, and latex). Hard rubber and gutta-percha are two early examples. Later bio-based plastics were made using cellulose, including celluloid and viscose rayon (fiber) and cellophane (film). Despite their biological origins, these materials had consequences for human health and the environment, leading to displacement, deforestation, environmental degradation, and workplace hazards.

Popular accounts and even corporate advertisements from this era portray early-generation plastics relieving pressure on natural resources such as tortoise shell or ivory because they could imitate their appearance.

Independent researcher, Providence, RI.
Email: rebecca.altman@gmail.com

For instance, celluloid, a nitrocellulose plastic industrialized in the 1870s, purportedly spared the elephant, especially from the billiard ball industry; however, market data show that celluloid did not decrease ivory demand, which grew in the years after celluloid's introduction. Less well known is how celluloid accelerated the demand for camphor, a tree product used as a solvent and plasticizer. The camphor market intensified as celluloid production expanded toward the end of the 19th century, when the burgeoning photography and cinematography industries required celluloid for film (*2*).

Camphor was distilled from the camphor laurel tree, a species of evergreen especially prevalent in Taiwan, where the imperial regimes of China, Britain, and Japan vied for control over its production. The camphor trade decimated Taiwan's forests and displaced its Indigenous communities—most notably the Atayal peoples, who resisted the commodification of their homelands (*3*).

Likewise, gutta-percha, a rubberlike tree resin harvested across the latter half of the 19th century in the Malay archipelago and throughout Southeast Asia, was used to insulate the growing network of undersea copper telegraphy cables so instrumental in administering the British empire. On average, a single tree would produce less than a pound of gum. In a matter of decades, the region's gutta-bearing trees were harvested to near-extinction (*4*).

Rayon fibers are another 19th-century technology based on chemically regenerated cellulose sourced from cotton, cotton linters (remnants of cotton production), or wood pulp. Multiple rayon processes were developed first in the UK and then elsewhere. In the US, the viscose process (also used to manufacture cellophane) was dominant by the Second World War, the era in which annual global rayon production exceeded 2 billion pounds (*5*).

The pursuit of rayon as a forest product, for example, resulted in clear-cut sections of the Tongass National Forest, a temperate rainforest in southeastern Alaska. After passage of the 1947 Tongass Timber Act, the US Forest Service offered 50-year timber contracts and subsidized the construction of two mills on the unceded lands of the Tlingit, Haida, and Tsimshian peoples. The first mill, built in Ketchikan, went online in 1952. The largest US rayon producer, American Viscose, had a considerable stake in the venture. Major Japanese manufacturers such as Mitsubishi Rayon, Kokoku Rayon, and Teikoku Rayon invested in the second mill built in Sitka.

But deforestation and displacement were not the only consequences. Early bio-based plastics were also as hazardous to harvest as they were to transform into moldable materials, going back to hard rubber (e.g., vulcanite or ebonite). Industrialized in the 1840s after the development of vulcanization, hard rubber was made from caoutchouc (natural latex) extracted from multiple species found in the rainforests of South America and Southeast Asia. These were later husbanded through plantation economies, often violent and exploitative, as exemplified by the rubber plantations overseen by the regime of Belgium's King Leopold II in Congo (*6*). But whether wild or domesticated, harvesting latex was dangerous work.

The hours were equally long in low-wage rubber factories. Poor ventilation exacerbated workers' exposure to a steady stream of toxic feed materials, including naphtha and carbon disulfide. From the outset, vulcanized rubber production caused a range of acute and chronic neurological issues, including mental health effects so severe that in extreme cases, workers were institutionalized. The idiom "to be gassed" originates from early rubber factories (*7*). Despite substantial evidence of its toxicity, carbon disulfide became instrumental to viscose rayon and cellophane production, too. As a result, successive generations of viscose workers into and across the 20th century also experienced neurological as well as cardiovascular effects (*8*).

In the 19th century, rubber trees provided latex for hard rubber, an early molding material, but as with other bio-based plastics, required additional chemical inputs—some toxic, others extracted under colonial regimes.

Occupational hazards extended to other classes of early bio-based plastics as well. Nineteenth-century celluloid factories were notoriously prone to explosion, conflagration, and worker injury (*9*). Pulp mills, such as the Ketchikan mill built in the Tongass, used a noxious sulfite process to convert chipped spruce and hemlock into dissolving pulp. Over its lifetime, the mill racked up hundreds of environmental violations before closing in the 1990s. By then, area health professionals had appealed to state epidemiologists to investigate possible links between mill pollution and conditions prevalent among their patients. Eventually, the mill was subject to both civil and criminal investigations. Further, the environmental legacy of rayon-grade pulp in the Tongass includes dioxins, heavy metals, and polychlorinated biphenyls (PCBs) (*10*).

Natural and semisynthetic plastics were followed by a generation of fossil fuel–derived synthetics. Bakelite, invented in 1907, marked this passage and eventually replaced ivory in pool halls. Bakelite was made from the reaction of coal tar–derived phenol with formaldehyde synthesized via methanol. By the 1920s and early 1930s, a new class of vinyl plastics was also in development. One among several progenitor vinyls was Union Carbide's Vinylite, a copolymer of polyvinyl chloride and polyvinyl acetate, based on mixed feedstocks, notably ethane (a natural gas liquid). Further, Carbide's development of the then-new field of ethylene derivatives, which later capitalized on the hydrocarbon by-products of petroleum production, coupled with the rapid expansion of refinery and plastics manufacturing capacity catalyzed by the Second World War, helped facilitate the industry-wide transition toward the petrochemical-dominant plastics of today (*11*).

But the advent of these fossil fuel feedstocks did not immediately eliminate prior biomass sources. Viscose is one example. Leading into the war, plastics were also an agricultural product, making use of farm waste or farmed products, a field called chemurgy (*12*). Early proponents included George Washington Carver and Henry Ford, who envisioned an integrated forest-farm-factory system. Ford purchased not only a rubber plantation in South America but also large tracts of farmland and timber stands in Michigan's Upper Peninsula, where wood pulp was converted in the chemical distilleries at Iron Mountain into automotive paints and artificial leather.

In general, 20th-century plastics tended to follow available raw materials, both geographically and across time. As nations shifted their energy and industrial systems, plastics manufacturers diversified feed material to make use of systemic by-products or

PHOTO: ANUPAM NATH/AP PHOTO

waste products. One recent example is how some US plastics producers converted from crude oil or naphtha-based feedstocks to ethane, a by-product of natural gas production through hydraulic fracturing.

The transition to renewable energy opens the question of which substrates will be used for future plastics. Understanding plastics' early industrial history is important because these bio-based products established the political-economic relations of modern, conventional plastics and portended problems to come. This history also points to the insufficiency of an ahistorical technological fix, such as swapping in alternative carbon sources, which may not improve plastics' ethics, safety, or sustainability. This is especially true if the same problematic chemistry is used to modify the base plastics' performance characteristics (*13*). For example, even if viscose/rayon is sourced from Forest Stewardship Council (FSC)–certified forests, its production may still rely on carbon disulfide.

To avoid such problems, it is necessary to rethink the premises on which plastics technologies have been developed and produced. Critical adjuncts include reengineering plastics for recovery and reuse, augmenting recycling infrastructure (*14*), and source reduction and dematerialization. This means making fewer plastics by developing alternatives to their short-term, disposable uses, which presumes land access for landfills (i.e., long-term storage of solid waste or ash) (*15*). The challenge for bio-based plastics research is to account for this history and to think critically about the supply chains required by plastics currently in development, including a focus on ethical, sustainable feedstocks; toxics reduction and safer materials; and worker and community health and safety. ■

REFERENCES AND NOTES

1. S. Lambert, M. Wagner, *Chem. Soc. Rev.* **46**, 6855 (2017).
2. R. Friedel, *Pioneer Plastic: The Making and Selling of Celluloid* (Univ. of Wisconsin Press, 1983).
3. T.-A. Roy, *Jpn. Forum* 1794931 (2020).
4. J. Tully, *J. World Hist.* **20**, 559 (2009).
5. Forest Products Laboratory, US Forest Service, "Technical note number 217: The manufacture of rayon" (1949); www.fpl.fs.fed.us/documnts/fpltn/fpltn-217-1949.pdf.
6. A. Hochschild, *King Leopold's Ghost: A Story of Greed, Terror and Heroism in Colonial Africa* (Houghton Mifflin, 1998).
7. J. Tully, *The Devil's Milk: A Social History of Rubber* (Monthly Review Press, 2011).
8. P. Blanc, *Fake Silk: The Lethal History of Viscose Rayon* (Yale Univ. Press, 2016).
9. J. Meikle, *American Plastic: A Cultural History* (Rutgers Univ. Press, 1997).
10. K. Durban, *Tongass: Pulp Politics and the Fight for the Alaska Rain Forest* (Univ. of Oregon Press, ed. 2, 2005).
11. P. Spritz, *Petrochemicals: The Rise of an Industry* (Wiley, 1988).
12. M. R. Finlay, *J. Ind. Ecol.* **7**, 33 (2004).
13. L. Zimmermann, A. Dombrowski, C. Völker, M. Wagner, *Environ. Int.* **145**, 106066 (2020).
14. W. W. Y. Lau *et al.*, *Science* **369**, 1455 (2020).
15. M. Liboiron, *Pollution Is Colonialism* (Duke Univ. Press, 2021).

10.1126/science.abj1003

PERSPECTIVE

Achieving a circular bioeconomy for plastics

Designing plastics for assembly and disassembly is essential to closing the resource loop

By **Sarah Kakadellis**[1] *and* **Gloria Rosetto**[2]

The visual nature of plastic pollution and the scandals of plastic waste exports to developing countries have prompted a shift in how plastics are made, used, and disposed. Plastic waste remains poorly managed, with as much as 12,000 million tonnes projected to have accumulated in landfills or the natural environment by 2050 (*1*). Although mechanical recycling was initially promoted as the solution to rising amounts of postconsumer plastic waste, its failure over the past decades has exposed the severity and scale of the plastic waste management crisis. In light of this, the recovery of plastics through chemical recycling—polymer recycling into their constituting repeat units or monomers (and oligomers)—and the development of bio-based and biodegradable alternatives have gained increasing attention. We consider the technical, chemical, and biological routes to closing the loop and argue for an integrated plastic waste management system rooted in the circular bioeconomy.

Shunning fossil-based plastics has provided a fertile ground for the emergence of alternative materials, loosely referred to as "bioplastics." Despite favorable public opinion, consumer awareness and understanding of the subtleties in the terminology is poor (*2*). The term bioplastics is an umbrella designation that captures a range of polymer chemistries, properties, and application sectors. It encompasses two distinct concepts: the bio-based origin of the raw materials and biodegradability at the end of life. Bio-based sources are necessary for divesting from fossil fuels. However, life-cycle analyses have uncovered complexities in the system, mostly owing to agricultural inputs for bioplastic feedstock production (*3*). Recent approaches using waste or coproducts from the biomass sector as feedstocks offer attractive alternatives.

[1]Centre for Environmental Policy, Imperial College London, London SW7 1NE, UK. [2]Department of Chemistry, University of Oxford, Oxford OX1 3TA, UK.
Email: sarah.kakadellis14@imperial.ac.uk

Some (fully or partly) bio-based plastics, such as bio-polyethylene terephthalate (bio-PET), are chemically identical to their fossil-based counterpart, making them suitable for the current recycling infrastructure. However, biodegradability tends to be perceived as more sustainable over (mechanical) recyclability by consumers (*2*). The biggest advantage of biodegradable plastics may not be their biodegradability per se but their compatibility with food waste, opening new streams for plastic waste management positioned around organics recycling (*3*). Nevertheless, issues associated with separation and contamination in existing mechanical recycling streams and concerns over their complete biodegradability in the current organic waste management infrastructure remain (*4*).

Although biodegradable plastics can return carbon and nutrients to the soil, the energy and resources associated with their production is effectively lost, echoing the linear flow of petrochemical plastics in single-use applications. Maintaining a closed-loop resource flow appears more sustainable. Yet, 67% of plastic waste generated in the UK consists of hard-to-recycle packaging (*6*). Across Europe, only 42% of plastic waste generated is collected for recycling (*5*, *6*). Failing market incentives for plastic recyclate have led to many plastics being exported to Southeast Asia, where they are often disposed of in illegal landfills (*7*).

Thermochemical processes, such as pyrolysis and gasification, have emerged as an alternative recycling strategy for the recovery of plastic waste—notably, hard-to-recycle plastics (*6*). Although they are often referred to as chemical recycling, these processes are not selective for monomer retrieval, producing a wide range of hydrocarbons and carbon dioxide (CO_2). Further separation and transformation steps are required that are energy intensive. By contrast, closed-loop recycling to monomers (CRM) can be seen as ultimate chemical recycling in that it ensures the recovery of a given polymer's building blocks.

The feasibility of CRM is greatly dependent on polymerization-depolymer-

ization thermodynamics (*8*). The most prevalent feature of such polymers is a hydrolyzable functionality in the polymer backbone, such as ester, amide, and carbonate linkages. PET, the most widely mechanically recycled commodity plastic, falls under this category. Polyolefins, such as polyethylene (PE) and polypropylene (PP), pose a challenge for CRM because of their carbon-to-carbon backbone. The introduction of functional groups as break points in a PE chain presents an opportunity to address polyolefin-like polymers with potential for CRM while retaining the desired material properties, as has been demonstrated (*9*). Although challenges remain in this strategy, these technological advances could ensure that monomers are effectively recovered, preventing the issue of downgrading or downcycling, seen with mechanical recycling.

Nevertheless, a sustainable plastics value chain extends beyond monomer recovery. The accumulation of plastic waste points toward a design flaw in the plastics value chain and the need to think systemically about closing the loop of the circular economy. If resources are cheap, the impetus to produce single-use products from virgin materials is high. Suspending trade of low-quality plastic waste from developed to developing countries and introducing taxes on fossil resources can encourage the substitution of raw resources with recycled materials and investment in waste management infrastructure (*7*, *10*).

Although these measures may increase the value of recycled polymers, the quality of recycled materials will remain a substantial challenge, especially for plastic packaging. In the context of a circular economy, the value of durable plastics needs to be recognized, but in conjunction with modularity in polymer and product design. Yet, there seems to be a lack of directionality around plastics-focused policies. If left uncoordinated, the promotion of biodegradable plastics within a bioeconomy framework on one side and of closed-loop recycling from a circular economy perspective on the other may lead to conflicting priorities.

The distinction between biodegradable and recyclable plastics suggests that biological and chemical routes to plastic waste management cannot be merged, perhaps misleadingly so. Most biodegradable plastics are or could be chemically recyclable because they can be fully metabolized by naturally occurring microorganisms. Developing a system in which plastics are designed for both chemical recycling and biodegradation is not only sensible but helps to overcome the artificial dichotomy emerging from current policies (see the figure). Thus, a waste management infrastructure for plastics to be collected and recycled should be prioritized while also fulfilling an end of life in applications for which biodegradability is needed.

Chemical polymer manufacturing and recycling is already technically feasible, cost effective, and scalable. But, development of the chemistry to design out recalcitrant petrochemicals and improve recycling efficiency is still needed. These challenges should be supported with a combined push in both chemistry and biotechnology. More recently, enzymatic hydrolysis of polymers has emerged as a potential bioremediation strategy (*11*). Enzymatic recycling has been demonstrated for PET (*12*, *13*), with the need for other enzymes for metabolizing a greater range of polymers. Obtaining monomers from CO_2 fixation would ultimately decouple production from raw materials (*13*).

The consideration of alternative waste treatment strategies for plastic waste is undoubtedly only part of the bigger issue of a linear economic model. The fallacy of mechanical recycling has already taught us that technology alone will not and cannot solve the plastic pollution crisis. No silver-bullet solution exists for the multifaceted nature of plastic pollution. The answer instead lies in a blend of approaches. Pre- and postconsumer stages need to be more aligned, from a strong regulatory framework and the investment in effective waste collection and management infrastructure to the development of polymer chemistries, life-cycle design, and consumer behavior. Only through committed action and coordination across the value chain will a sustainable future for plastics be secured. ■

Closing the plastics loop

Plastics (polymers) could be designed so that the monomers they are built from can be retrieved. Some plastics can also biodegrade for certain niche applications or when environmental leakage occurs. Monomers may be feedstocks for synthesizing added-value products such as surfactants or new polymers or turned back to their original polymer. Enzymatic or chemical catalysis can prevent property deterioration from this process.

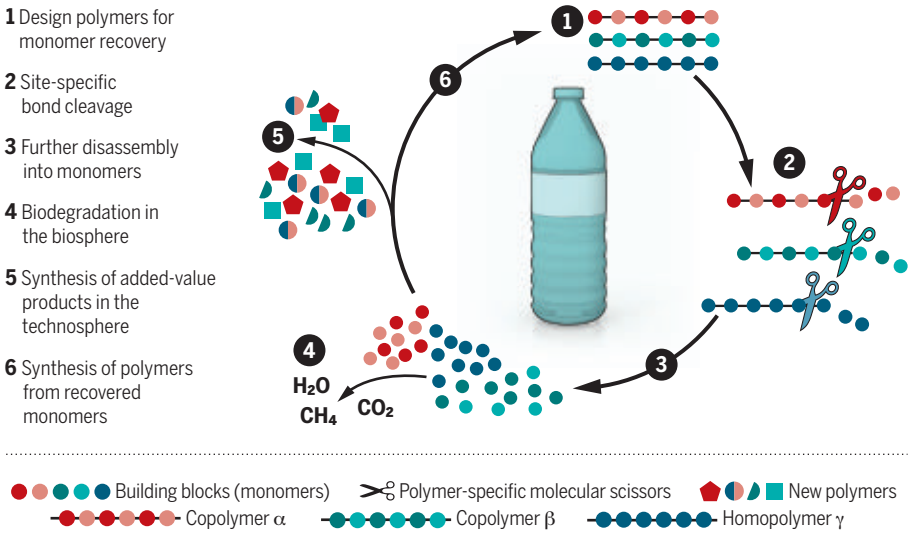

GRAPHIC: N. CARY/*SCIENCE*

REFERENCES AND NOTES

1. R. Geyer *et al.*, *Sci. Adv.* **3**, e1700782 (2017).
2. L. Dilkes-Hoffman, P. Ashworth, B. Laycock, S. Pratt, P. Lant, *Conserv. Recycl.* **151**, 104479 (2019).
3. S. Kakadellis, Z. M. Harris, *J. Clean. Prod.* **274**, 122831 (2020).
4. S. Kakadellis, J. Woods, Z. M. Harris, *Res. Cons. Recycl* **169**, 105529 (2021).
5. C. Partridge, F. Medda, *Res. Cons. Recycl. X* **3**, 100011 (2019).
6. PlasticsEurope, Plastics—The Facts 2019 (2019); www.plasticseurope.org/application/files/9715/7129/9584/FINAL_web_version_Plastics_the_facts2019_14102019.pdf.
7. W. d'Ambrières, *Field Actions Sci. Rep.* **19**, 12 (2019).
8. G. W. Coates, Y. D. Getzler, *Nat. Rev. Mater.* **5**, 501 (2020).
9. M. Häußler, M. Eck, D. Rothauer, S. Mecking, *Nature* **590**, 423 (2021).
10. N. Voulvoulis, R. Kirkman, Shaping the circular economy: Taxing the use of virgin resources (2019); www.veolia.co.uk/sites/g/files/dvc1681/files/document/2019/07/Plastic%20packaging%20tax%20in%20the%20UK%20Whitepaper.pdf.
11. S. Yoshida *et al.*, *Science* **351**, 1196 (2016).
12. V. Tournier *et al.*, *Nature* **580**, 216 (2020).
13. M. Salvador *et al.*, *Genes* **10**, 373 (2019).

ACKNOWLEDGMENTS

The authors acknowledge C. K. Williams, Z. M. Harris, and J. I. Jimenez for providing invaluable insight throughout the revision process. S.K. was supported by a London Interdisciplinary Social Science Doctoral Training Partnership studentship awarded by the Economic and Social Research Council (ES/P000703/1). G.R. was supported by SCG Chemicals.

10.1126/science.abj3476

REVIEW

Plastics in the Earth system

Aron Stubbins[1,2]*, Kara Lavender Law[3], Samuel E. Muñoz[1], Thomas S. Bianchi[4], Lixin Zhu[5]

Plastic contamination of the environment is a global problem whose magnitude justifies the consideration of plastics as emergent geomaterials with chemistries not previously seen in Earth's history. At the elemental level, plastics are predominantly carbon. The comparison of plastic stocks and fluxes to those of carbon reveals that the quantities of plastics present in some ecosystems rival the quantity of natural organic carbon and suggests that geochemists should now consider plastics in their analyses. Acknowledging plastics as geomaterials and adopting geochemical insights and methods can expedite our understanding of plastics in the Earth system. Plastics also can be used as global-scale tracers to advance Earth system science.

Humanity, through its development of novel chemical reactions and the sheer magnitude of its activities, is having an ever-growing impact on Earth's elemental cycles. Through this great acceleration (*1*), we have ushered in a new age in Earth's history: the noosphere or Anthropocene (*2*, *3*). This is an age in which the trajectory of the Earth system is shaped as much by humans as by all other life (*4*) and in which we are increasingly conscious of our role in modifying the global environment and of our potential to influence Earth's future. Plastics, a suite of synthetic polymers, are exempla of this new age. Just as fossils indicate when different life-forms emerged, preserved plastics will provide a geological record of humanity's rise to global prominence (*4*). It has become clear that plastics are an emerging contaminant that may harm organisms and ecosystems not adapted to their presence. Numerous reviews present the potential deleterious effects of plastics (*5*–*9*). Here, instead, we discuss plastics as an emergent carbon-based geomaterial—specifically, a new form of anthropogenic detrital, nonliving OC. We discuss plastic distribution, transport, and eventual loss from the Earth system; how contamination of environmental samples by plastics might affect OC studies; how applying concepts and methods from the geosciences might accelerate our understanding of plastics; and how the study of plastics may advance fundamental biogeochemical knowledge.

[1]Department of Marine and Environmental Sciences and Department of Civil and Environmental Engineering, Northeastern University, Boston, MA 02115, USA. [2]Department of Chemistry and Chemical Biology, Northeastern University, Boston, MA 02115, USA. [3]Sea Education Association, Woods Hole, MA 02543, USA. [4]Department of Geological Sciences, University of Florida, Gainesville, FL 32611, USA. [5]State Key Laboratory of Estuarine and Coastal Research, East China Normal University, Shanghai 200241, China.
*Corresponding author. Email: aron.stubbins@northeastern.edu

The plastic-carbon cycle

Biogeochemistry details the cycling of elements at scales ranging from the organismal to the planetary. Arrow diagrams can detail elemental stocks, sources, fates, and transformations (Fig. 1). The cycling of one specific element, carbon, is of particular biogeochemical and societal significance. Organic carbon (OC) fuels life and forms the elemental backbone of biomolecules. Use of OC stored in fossil fuels drives our economy, provides raw materials for the production of most plastics (*6*), and is warming the planet (*10*). Thus, in concurrence with a growing literature (*11*, *12*), we present plastics as an emergent component of Earth's carbon cycle.

Different polymers have different carbon contents, depending on their elemental composition (Table 1). Furthermore, additives and processing in the environment may modify plastic carbon content. For instance, oxidation adds oxygen and noncarbon mass to plastics (*13*, *14*). Therefore, precise conversion of plastic mass to plastic-carbon (plastic-C) will require knowledge of the contributions that different polymers make to each global stock and flux, plus empirical measurements of polymer carbon content in the environment. The carbon content of materials is usually determined by elemental analysis, but these analyses are rare for environmental plastics. One study reported homogenized microplastics from North Pacific Gyre surface waters to be 83% carbon by mass (*14*), a percentage we adopt here to calculate the carbon content of plastic mass. As plastic production and disposal have presumably increased since the data reviewed in this paper were collected, our estimates of

Fig. 1. The global plastic-carbon cycle circa 2015. Black arrows represent fluxes of plastics between compartments. Blue fluxes represent processes that remove plastics (e.g., incineration to carbon dioxide, or photodegradation to oligomers). References for plastic mass values are shown in parentheses. Plastic-carbon values are calculated as 0.83 times plastic mass (*15*). Question marks indicate plastic-carbon cycle terms without published estimates.

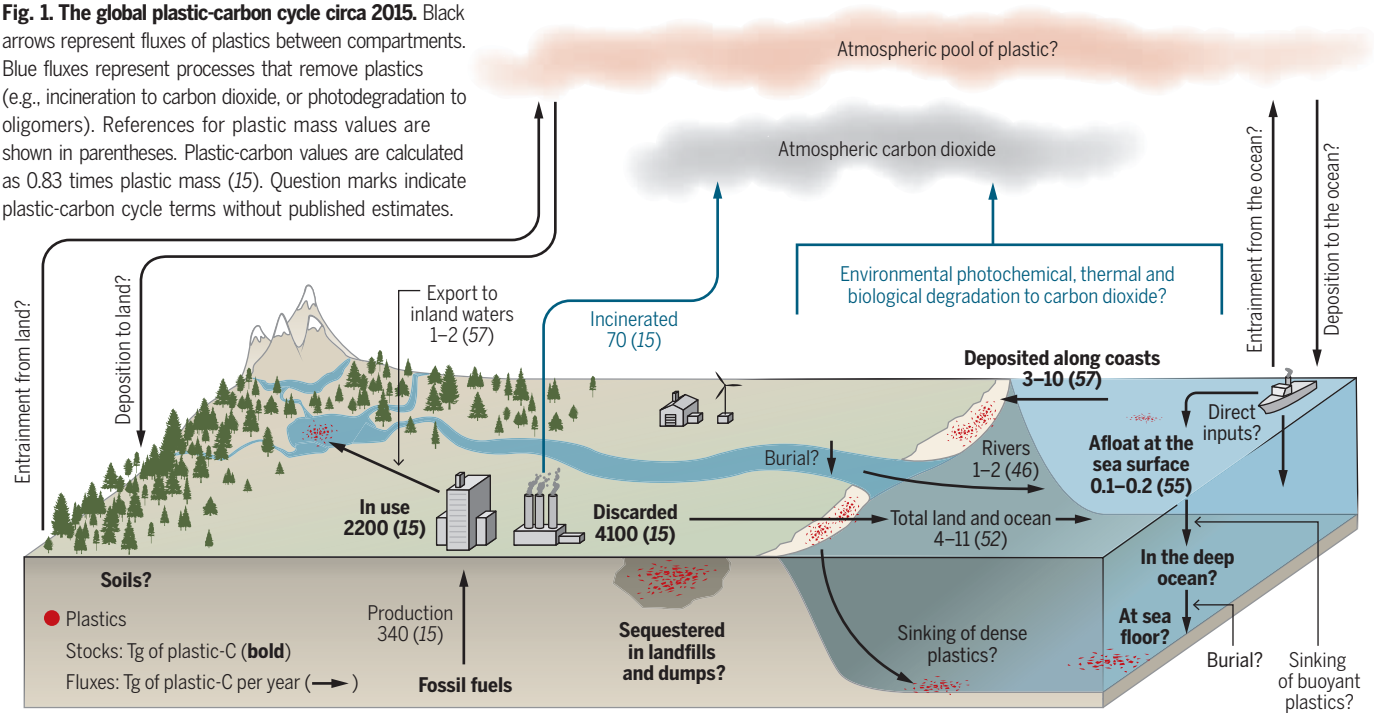

ILLUSTRATION: C. BICKEL/*SCIENCE*

plastic-carbon are likely conservative lower bounds.

From a geochemical perspective, the plastic-carbon cycle (Fig. 1) begins with industrial production of high-molecular-weight polymers and ends when plastics degrade into low-molecular-weight, nonpolymeric compounds, including dissolved and gaseous products (Fig. 2). Large-scale plastics production began around 1950 and has accelerated ever since (Fig. 3). As of 2015, 6.9 Pg of plastic-carbon (Pg-C) had been produced, with 2.2 Pg-C in use, 4.1 Pg-C discarded, and 0.6 Pg-C incinerated (*15*). The 6.3 Pg-C of plastic that has accumulated (production minus incineration) exceeds human (0.06 Pg-C) and total animal (2 Pg-C) biomass (Fig. 3) (*16*) but remains modest compared with global OC pools, such as those for soil OC (1500 to 2400 Pg-C) and oceanic dissolved OC (~700 Pg-C) (*10*). However, plastics have accumulated in mere decades (*15*), whereas OC has accumulated slowly, often over millennia (*10*). Examination of annual plastic-carbon fluxes highlights the relevance of plastics to the current carbon cycle.

Most environmental research focuses on the 0.05 to 0.08 Pg-C $year^{-1}$ of mismanaged plastics dispersed to natural systems (*17*). However, total plastic accumulation includes all in-use and discarded plastics. As of 2015, estimated global plastic production was ~0.34 Pg-C $year^{-1}$ with ~0.07 Pg-C of plastics being incinerated (*15*), the latter of which is equivalent to <1% of anthropogenic CO_2 emissions from fossil fuel burning and cement production (~8 Pg-C $year^{-1}$) (*10*). The difference between production and incineration indicates that plastics accumulated at 0.26 Pg-C $year^{-1}$ in 2015, which is modest compared with global net primary production (~105 Pg-C $year^{-1}$) (*18*). However, OC accumulations in inland waters (~0.2 Pg-C $year^{-1}$) (*10*), deep ocean sediments (~0.2 Pg-C $year^{-1}$) (*10*), forest ecosystems (~0.2 Pg-C $year^{-1}$) (*19*), and coastal systems (in the form of blue carbon; ~0.1 Pg-C $year^{-1}$) (*20*) are studied because of their significance in the carbon cycle, yet each of these is slower than current plastic-carbon accumulation. As the accumulation of plastics will likely accelerate into the future (Fig. 3), plastics will become increasingly prominent carbonaceous geomaterials. To understand plastics distributions and impacts, their transport and reactivity must be defined.

Table 1. Some material properties of the most abundant plastics on Earth.

Polymer	Polyethylene (PE)	Polypropylene (PP)	Polyethylene terephthalate (PET)	Polyvinyl chloride (PVC)	Polystyrene (PS)
Elemental formula	$(C_2H_4)_n$	$(C_3H_6)_n$	$(C_{10}H_8O_4)_n$	$(C_2H_3Cl)_n$	$(C_8H_8)_n$
Backbone structure			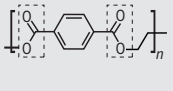		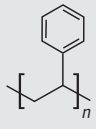
Bond type	C–C	C–C	Hydrolyzable ethylene	C–C	C–C
Carbon content	86%	86%	63%	38%	92%
% Plastics production (2002–2014) (*15*)	36% by mass 40% by C	21% by mass 23% by C	10% by mass 8% by C	12% by mass 6% by C	8% by mass 9% by C
Density (g cm^{-3}) (*24*)	0.92–0.97	0.88–0.91	1.30–1.40	1.35–1.50	1.04–1.50 Foamed: <0.05
Photoreactivity (*24*)	Medium	Medium	Medium	Low	High
Bioreactivity (*34*)	Low	Very low	Medium	Very low	Low
Glass transition temperature (*24*)	–110°C	–20°C	75°C	60°–100°C	90°C
Elongation at break (*24*)	200–900%	150–600%	30–70%	25–80%	1–4%
Limiting oxygen index (*24*)	17–18%	17–18%	23–25%	40–45%	17–18%
Flammability	Burns indefinitely in air	Burns indefinitely in air	Burns for <30 s in air	Burns for <10 s in air	Burns indefinitely in air

Transport and degradation

Natural inorganic sediments, such as quartz clays, silts, and sands (density: ~2.65 g cm^{-3}), are denser than common plastics (Table 1) (*21*). Thus, plastics in soils or sediments may remain near the surface, making them vulnerable to mobilization. Surface chemistry (e.g., hydrophobicity), size, and shape further affect location and movement by influencing plastic aggregation with other soil components (*21*, *22*). Bioturbation, ploughing, and water flow can work plastics into soils (*21*). Deposition in areas with high burial rates can stabilize OC deposits (*23*) and may do likewise for plastics.

Density, size, shape, and processing influence particle transport (Fig. 4). Whereas most natural sediments are denser than fresh water (~1 g cm^{-3}) and seawater (~1.035 g cm^{-3}), plastic densities vary by polymer (Table 1). Pure polyethylene (PE) and polypropylene (PP) are buoyant, but solid polystyrene (PS), polyethylene terephthalate (PET), and polyvinyl chloride (PVC) are denser than water. Polymer density is modified by additives and drastically reduced by foaming (e.g., as in expanded PS) (*24*). Shape is defined by how closely a particle resembles a sphere (sphericity) (*25*) and the smoothness of its edges (roundness) (*26*). Smaller, less spherical, and more angular particles (e.g., fibers, sheets) have higher surface-area-to-volume ratios and should therefore remain in suspension more readily than larger, more spherical, and more rounded particles (e.g., beads, blocks). In air and, for plastics that sink, in water, particles tend to accumulate at the underlying surface with smaller, less spherical, more angular particles being preferentially mixed into the media as flow increases. Conversely, buoyant plastics should accumulate at the water's surface when waters stagnate with smaller, less spherical, more angular particles being preferentially mixed to depth as turbulence increases (Fig. 4). Aggregation and biofouling also modify the effective density, shape, size, and surface chemistry of plastics, with ramifications for transport (*8*). Complicating these relationships further, the degree of aggregation and biofouling is modified by particle density (e.g., as it relates to the environment the particle is in), shape, size, and surface chemistry.

Plastics can be degraded via mechanical, photochemical, thermal, and biochemical mechanisms (*27*). Polymer chemistry is key to determining degradability (Table 1). Additives and the crystal versus amorphous nature of polymers modify their degradability (*24*). Physical properties include elongation at break, which describes the ability of a plastic to resist cracking, and the glass transition temperature, below which plastics become brittle (*24*). PS is prone to mechanical fragmentation (*28*), as it is glassy at environmental temperatures, whereas PE remains nonglassy to –100°C and can be elongated nine times its length before breaking (Table 1).

Mechanical fragmentation reduces particle size and increases surface area.

Photochemistry is cited as the most effective chemical degradation pathway for plastics in the environment (*13*, *27*). To photodegrade, materials must contain or interact with chromophores that absorb photochemically active sunlight. Aromatic compounds are the dominant chromophores in natural waters (*29*). PS contains aromatic chromophores, which may explain its relatively high photodegradability (Table 1). PP and PE are also photoreactive (*14*, *24*), but pure PP and PE contain no chromophoric groups (*27*); instead, their photoreactivity is attributed to chromophoric impurities, including additives, aromatics absorbed from the environment, and oxidized groups incorporated into polymers during thermal processing (*27*). Photodegradation of many organics follows first-order kinetics, with rates slowing with increasing exposure (*29*). By contrast, plastics photodegradation often accelerates, leading to increasingly efficient removal the longer plastics reside in sunlit environments (*14*). The acceleration in rates may arise from the accumulation of photoreactive oxidized groups as plastics photooxidize, plus an increase in surface area-to-volume ratio as plastics photofragment (*13*, *14*).

Thermal oxidation is slow at ambient temperatures (*27*). However, many plastics are flammable upon ignition at atmospheric oxygen concentrations (i.e., they have a limiting oxygen index of <21%) (Table 1) (*24*). Thus, thermal degradation should be rapid during wildfires and biomass burning. Efficient thermal degradation may also occur in geothermal settings, although supply of plastics to these hotspots likely limits realized rates. Both thermal and photodegradation oxidize plastics, reduce polymer molecular weights, produce gaseous products (*30*–*32*), and yield soluble organics (*30*, *33*) that can either promote or inhibit microbial growth (*13*, *14*, *33*).

Plastics are a potential energy source for heterotrophs. To degrade plastics and access this energy, heterotrophs must break the bonds that bind plastics' polymeric chains. Common hydrolytic enzymes can break ester and urethane bonds in PET and polyurethane (*34*). However, plastics with carbon-to-carbon (C–C) bonded chains are more bioresistant (Table 1). Intestinal microbes of some insect larvae, plus some rare, free-living microbes, can degrade C–C bonded PE and PS under laboratory conditions, but it remains unclear whether these rates are ever realized in nature (*34*). The enzymes that degrade C–C bonded plastics remain enigmatic. Enzymes capable of C–C bond cleavage evolved to degrade lignin, a polymeric component of wood, and can slowly degrade PE (*34*). It appears to have taken 125 million years for lignin-degrading enzymes to evolve after lignin emerged in the fossil record (*35*). By contrast, some bacteria have already adapted existing lipases and cutinases to utilize PET (*36*, *37*). However, these PETase genes remain rare in microbial communities (*36*) and target PET's ester bonds. Thus, it is unclear whether PET degradation will become widespread or whether similar evolutionary shortcuts can be found for the biodegradation of other plastics, particularly those with stronger C–C bonds. Furthermore, despite emerging ~400 million years ago (*35*), lignin is still sufficiently resistant to enable trees and houses to stand for centuries and to allow for its accumulation in soils and sediments (*38*). Thus, lignin and plastics will likely resist efficient biodegradation for some time to come.

The transport and degradation pathways of plastics are intimately linked. Photo-, thermo-, and biodegradation oxidize plastics, increasing subsequent photodegradability and biodegradability, and promote fragmentation, altering plastic size distributions with ramifications for transport, distribution, and reactivity. Transport moves plastics between Earth's three physical compartments—land, atmosphere, and water. In each compartment, plastics may have different biogeochemical impacts and be exposed to different environmental conditions, the latter of which impacts plastic degradation and fate. The amount and size distributions of plastics also influence OC studies. For instance, if plastics are analyzed as an unacknowledged fraction of OC, OC concentrations and storage may be overestimated (*12*, *39*). Furthermore, geochemists use radiocarbon to date OC, and plastics are overwhelmingly produced from ancient, radiocarbon-dead fossil fuels. Thus, when occurring in OC samples, plastics will increase the sample's apparent age, influencing perceived OC accumulation and turnover rates.

Plastics on land

Most discarded plastic-C is added to landfills and open dumps (*6*). Just as natural OC in soils, ocean sediments, or fossil fuel stores can remain sequestered until disturbed, plastics should remain sequestered in well-designed

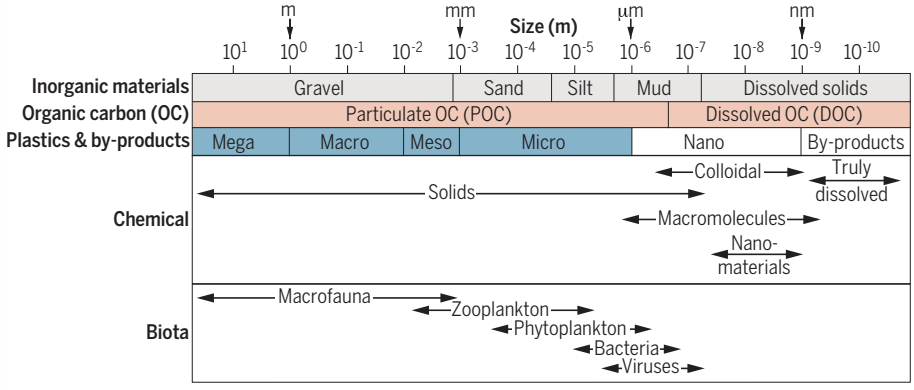

Fig. 2. Size ranges for geomaterials, including plastics. Inorganic materials include gravel, sand, silt, mud, and dissolved solids. Organic carbon is commonly operationally defined as either particulate or dissolved. Plastics are divided into mega-, macro-, meso-, micro-, and nanoplastics, plus the nonplastic by-products of plastic degradation. Commonly applied size distributions for chemical classes and for biota are also included.

Table 2. Potential plastic-carbon contributions to detrital, nonliving organic carbon (OC) concentrations.

Environment	OC	Plastic-C	Units	% Plastic-C*
		Surface soil OC		
Floodplain	8.2 (*42*)	0.004–0.046 (*41*)	g-C kg^{-1}	0.1–0.6
Industrial	8.2 (*42*)	0.25–56 (*43*)	g-C kg^{-1}	3–87
		River particulate OC		
Global export	100–400 (*10*)	1–2 (*47*)	Tg-C $year^{-1}$	0.2–2.0
Amazon, Brazil	5 (*48*)	0.03–0.05 (*47*)	Tg-C $year^{-1}$	0.5–1.0
Brantas, Indonesia	0.015 (*49*)	0.03–0.05 (*47*)	Tg-C $year^{-1}$	64–78
		Ocean subtropical gyre surface water particulate OC		
North Pacific Ocean	26 (*50*)	0.03–34 (*51*)	μg-C $liter^{-1}$	0.1–57

*Assumes OC and plastics are independently quantified fractions of total nonliving OC [i.e., calculated % plastic-C = plastic-C ÷ (OC + plastic-C)].

landfills. However, landfills and dumps are important to study as hotspots of plastic-C accumulation on Earth; as regions of potential plastics erosion and export; to understand the ecological and geomorphologic implications of plastics being a major geomaterial in an ecosystem; and as crucibles forging plastic-degrading life-forms. Plastics enter other soils as mismanaged waste and in sewage-derived fertilizer (*40*). Plastic mass in soils remains poorly constrained and has not been compared with total soil OC within any single sample. In lieu of these data, we compare the scant data on plastic mass in soil to OC measured in similar soils. In Swiss floodplain soils, this gives an estimated plastics contribution of 0.1 to 0.6% (*41*, *42*), whereas plastics may dominate OC stocks in industrially contaminated soils (*43*) (Table 2). Addition of plastic-carbon to soils may lead to overestimates of OC accumulation and radiocarbon ages. Plastics in soils can alter soil aggregation and larger items may alter flow paths, influencing the formation, stability, and hydrology of soils (*22*). The decrease in soil density when adding plastics can promote plant growth, whereas leaching of additives may harm plants (*22*). Thus, changes to carbon loading, soil structure, hydrology, and chemistry in soils amended with plastics will likely alter biogeochemical cycles, including primary production and nutrient cycling (*22*). Whether these effects are significant outside of heavily impacted systems is unclear.

Plastics in the atmosphere

Micro- and nanoplastics (Fig. 2) are found throughout the atmosphere, including in the air we breathe (*44*). Atmospheric studies of ~50- to 5000-μm particles indicate that plastics at the smaller end of this range are most numerous. Deposition is high near urban and industrial sources (*44*), but the low density of plastics compared with natural dust facilitates their long-range transport (*45*). Spatial patterns in the sizes, shapes, and chemistries of deposited plastics and how they covary with atmospheric conditions offer insight into the distribution and sources of plastics in the atmosphere. However, current knowledge is insufficient to allow plastics to be incorporated into atmospheric transport and chemistry models. Such studies are required to understand the atmospheric fate of plastics and how plastics affect air quality and planetary albedo.

Plastics in inland waters

Plastics can enter inland waters as mismanaged waste from land, as direct inputs (e.g., discarded fishing equipment), and through the erosion of soils, landfills, and in-use plastics (e.g., buildings) (*6*). Once entrained, plastics can settle out and accumulate in sediments when water slows (e.g., in reservoirs) (*46*), be degraded in the water column, or be exported to sea (*47*). Empirical data for the mass of plastics exported by rivers remain limited. However, a risk analysis estimated that 1.0 to 2.0 Tg plastic-carbon is carried through rivers to the sea annually (*47*) (Fig. 1). This equates to 0.2 to 2.0% of global riverine fluxes of particulate organic carbon (POC) (*10*) but varies for individual rivers (Table 2). For instance, although the Amazon River is estimated to carry the seventh-largest load of river-borne plastics (*47*), plastics equate to <1% of POC in this massive river (*48*). By contrast, small, urbanized rivers (e.g., the Brantas) may export more plastics than biogenic POC (Table 2) (*47*, *49*). The Brantas drains a catchment >500 times smaller than the Amazon yet exports a greater mass of plastics (*47*). Thus, the contribution of small, urbanized rivers to global plastic export appears oversized compared with their drainage areas. Addition of plastic-C may also alter the fluxes, chemistry, and apparent ages of OC in rivers.

Plastics in the ocean

Sources, stocks, and sinks of plastics are not yet reconciled at sea. Sources include rivers, other coastal inputs, atmospheric deposition, and direct inputs (e.g., jetsam, flotsam, and derelict). A risk analysis suggests that 4.0 to 10.5 Tg of plastic-carbon entered the oceans in 2010 (*50*) (Fig. 1). About 40% of plastics entering the ocean are expected to sink on the basis of polymer type (*51*). Hotspots of sinking plastic accumulation have been identified in coastal and deep ocean sediments (*52*, *53*). However, global estimates of plastics in marine sediments do not exist. The other 60% of plastics entering the oceans should float initially. Floating plastics are usually sampled in the upper 0–10 cm to 0–100 cm of the ocean using tow nets that capture particles larger than ~300 μm (*8*). Estimated standing stocks of surface plastics total 0.07 to 0.20 Tg-C (*54*). According to estimates of inputs and stocks, <10% of buoyant plastics entering the oceans each year are found afloat at sea. This accounting gap may result from overestimated inputs; underestimates of floating plastics (net tows only sample the upper meter of the ocean and mainly collect microplastics); and the loss of floating plastics from surface waters via photodegradation, shoreline deposition, consumption by marine life, and sinking due to aggregation with POC, egestion in fecal pellets, or biofouling (*8*).

In contrast to surface plastic sampling, oceanic POC is usually sampled at depths >1 m by prefiltering to remove zooplankton (>202 μm in size) and then filtering through sub-micrometer filters to collect POC (Fig. 2) (*55*). Acknowledging these differing approaches, we compare plastic and POC concentrations in subtropical gyre surface waters where ocean physics drive the accumulation of plastics (*8*). In the North Pacific Subtropical Gyre, areal surface concentrations of 500- to 5000-μm microplastics sampled from the upper 15 cm of the water column ranged from 0.03 to 34 kg km^{-2} (*51*), which equates to a per-volume carbon concentration of 0.1 to 21.9 μg-C liter^{-1} (average: 4.7 μg-C liter^{-1}). POC concentrations in the upper 5 m of the North Pacific at Station ALOHA average 26 ± 7 μg-C liter^{-1} (*50*). Assuming microplastics and POC were sampled as distinct fractions, microplastic-carbon may make up 0.1 to 57% (average: 15%) of the total particulate nonliving OC in surface waters of the North Pacific Subtropical Gyre (Table 2). The variation in this range illustrates the patchiness of marine debris, while the upper estimate and average highlight the potential significance of plastic-carbon at the ocean's surface. An abundance of plastics at the sea

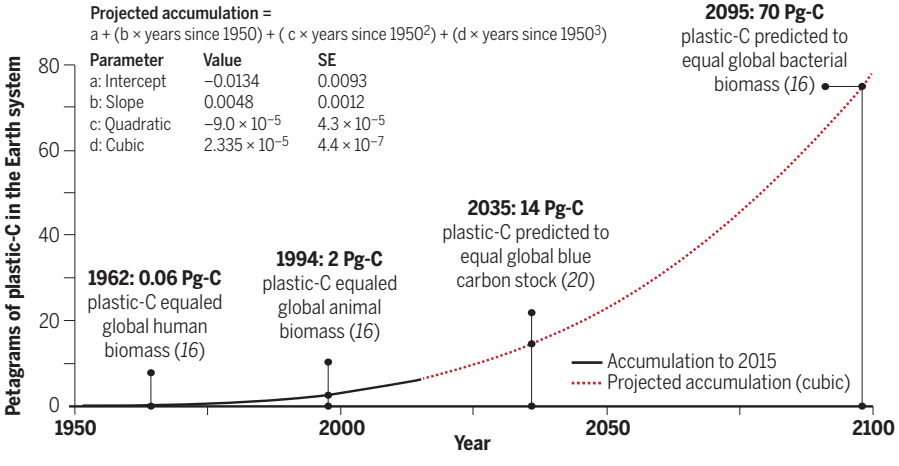

Fig. 3. Accumulation of plastic-carbon in the Earth system. Accumulation of plastic up to 2015 calculated as production minus incineration (*15*). Projected accumulation calculated assuming current trend (cubic growth) for plastic accumulation will continue into the future. The cubic model had the lowest Akaike information criterion of models in JMP. Actual future plastic-carbon accumulation will depend on hard-to-predict socioeconomic factors. Biomass numbers refer to living biomass.

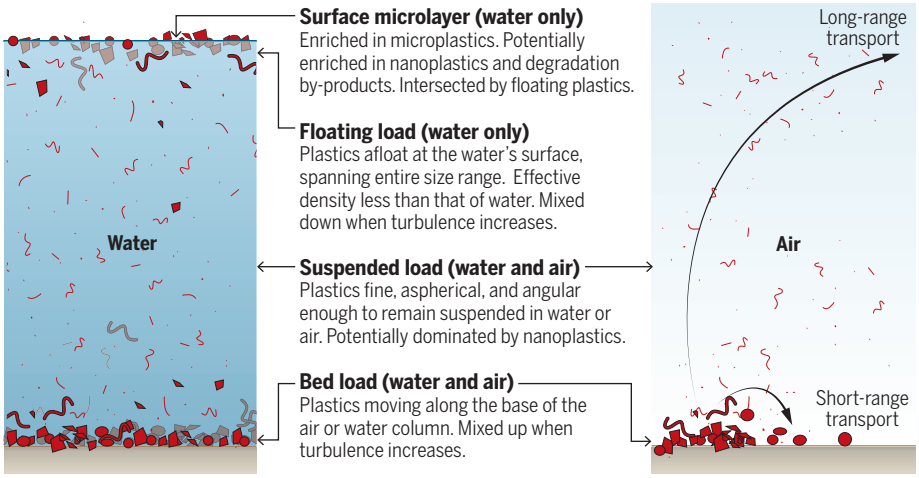

Fig. 4. Distribution of plastics in water and air. In water, four layers are considered: the surface microlayer, the floating load (the most often studied fraction in water), the suspended load (seldom studied in water), and the bed load (somewhat studied in water as deposited materials). Plastics that are less dense than water tend to float and become concentrated in the surface microlayer and floating load, whereas plastics that are denser than water tend to accumulate in the bed load. All plastics are denser than air. Thus, in air, only two layers are considered: the suspended load and the bed load.

surface may affect the ecology and biogeochemical function of a layer that covers two-thirds of the planet's surface, with potential impacts on atmospheric chemistry in the marine boundary layer, surface ocean ecology, and ocean biogeochemistry (*56*).

Accelerated learning

Our estimate of plastic accumulation on Earth assumes that industrial incineration is the only sink (Fig. 3). Environmental degradation also converts plastic-carbon to non-plastic-carbon (e.g., gases and nonpolymeric organics). However, robust estimates of net plastic removal via environmental processes remain unattainable while fundamental information about plastic distribution and reactivity is lacking. Developing this quantitative, mechanistic understanding of the global plastic cycle will require data for the occurrence, flux, and transformation of different polymers in each compartment of the Earth system. To facilitate this, collection and analysis of plastics should be standardized across systems, and studies should report plastic mass along with polymer type and particle size. Improved data for the distribution of plastics must be augmented with quantitative studies of degradation in each environment.

Empirical data on plastic-mass distributions are scarce. Models predict fluxes and distributions for some terms in the global plastic cycle (Fig. 1). Existing knowledge concerning geomaterials can be leveraged to predict gradients of plastics in other systems. By modeling or consulting the geoscience literature first, onerous fieldwork can be designed to test model predictions or focus on hypothesized hotspots of plastic cycling and impact. In this Review, we highlight landfills and dumps, areas of atmospheric and aquatic deposition, urban rivers, and the sea surface as potential sites of major importance for plastic accumulation, transport, degradation, and biogeochemical impact.

In the 1950s, nuclear weapons testing enriched the atmosphere with radiocarbon. This bomb spike obfuscated natural radiocarbon signals, complicating the dating of OC after 1950. However, the bomb spike also represented a new, temporally explicit tracer that helped resolve aspects of ocean circulation and OC cycling. Today, adding explicit analysis of plastics to OC studies would ensure that OC concentrations, ages, and chemistries are correctly interpreted, particularly in plastic-rich systems. However, the temporally resolved emergence of plastics as geomaterials with distinctive physical and chemical characteristics can also be leveraged as a tracer experiment to test our knowledge of particle and carbon cycling in the Earth system. Thus, while the study of the global plastic cycle is critical to understanding the environmental impact of plastics, it also offers an opportunity for geochemical insight to be gained.

REFERENCES AND NOTES

1. W. Steffen, W. Broadgate, L. Deutsch, O. Gaffney, C. Ludwig, *Anthropocene Rev.* **2**, 81–98 (2015).
2. V. I. Vernadsky, *Usp. Sovrem. Biol.* **18**, 113–120 (1944).
3. P. J. Crutzen, E. F. Stoermer, *IGBP Global Change Newsletter* **41**, 17–18 (2000).
4. S. L. Lewis, M. A. Maslin, *Nature* **519**, 171–180 (2015).
5. M. Cole, P. Lindeque, C. Halsband, T. S. Galloway, *Mar. Pollut. Bull.* **62**, 2588–2597 (2011).
6. R. C. Hale, M. E. Seeley, M. J. La Guardia, L. Mai, E. Y. Zeng, *J. Geophys. Res. Oceans* **125**, e2018JC014719 (2020).
7. S. Lambert, M. Wagner, in *Freshwater Microplastics* (Springer, Cham, 2018), pp. 1–23.
8. K. L. Law, *Ann. Rev. Mar. Sci.* **9**, 205–229 (2017).
9. Y. Zhang *et al.*, *Earth Sci. Rev.* **203**, 103118 (2020).
10. P. Ciais *et al.*, in *Climate Change 2013: The Physical Science Basis. Working Group I Contribution to the Fifth Assessment Report of the Intergovernmental Panel on Climate Change*, T. F. Stocker *et al.*, Eds. (Cambridge Univ. Press, 2014), pp. 465–570.
11. J. P. Dees, M. Ateia, D. L. Sanchez, *ACS EST Water* **1**, 214–216 (2021).
12. M. C. Rillig, *Environ. Sci. Technol.* **52**, 6079–6080 (2018).
13. M. Hakkarainen, A.-C. Albertsson, in *Long-Term Properties of Polyolefins*, A.-C. Albertsson, Ed. (Springer, 2004), pp. 177–200.
14. L. Zhu, S. Zhao, T. B. Bittar, A. Stubbins, D. Li, *J. Hazard. Mater.* **383**, 121065 (2020).
15. R. Geyer, J. R. Jambeck, K. L. Law, *Sci. Adv.* **3**, e1700782 (2017).
16. Y. M. Bar-On, R. Phillips, R. Milo, *Proc. Natl. Acad. Sci. U.S.A.* **115**, 6506–6511 (2018).
17. L. Lebreton, A. Andrady, *Palgrave Commun.* **5**, 6 (2019).
18. C. B. Field, M. J. Behrenfeld, J. T. Randerson, P. Falkowski, *Science* **281**, 237–240 (1998).
19. W. H. Schlesinger, E. S. Bernhardt, *Biogeochemistry: An analysis of Global Change* (Elsevier, ed. 3, 2013).
20. D. M. Alongi, *Blue Carbon: Coastal Sequestration for Climate Change Mitigation* (Springer, 2018).
21. K. Waldschläger, S. Lechthaler, G. Stauch, H. Schüttrumpf, *Sci. Total Environ.* **713**, 136584 (2020).
22. M. C. Rillig, A. Lehmann, *Science* **368**, 1430–1431 (2020).
23. N. E. Blair, R. C. Aller, *Ann. Rev. Mar. Sci.* **4**, 401–423 (2012).
24. C. B. Crawford, B. Quinn, *Microplastic Pollutants* (Elsevier, 2017).
25. H. Wadell, *J. Geol.* **43**, 250–280 (1935).
26. R. L. Folk, *Petrology of Sedimentary Rocks* (Hemphill, 1980).
27. B. Gewert, M. M. Plassmann, M. MacLeod, *Environ. Sci. Process. Impacts* **17**, 1513–1521 (2015).
28. Y. K. Song *et al.*, *Environ. Sci. Technol.* **51**, 4368–4376 (2017).
29. K. Mopper, D. J. Kieber, A. Stubbins, in *Biogeochemistry of Marine Dissolved Organic Matter*, D. A. Hansell, C. A. Carlson, Eds. (Academic Press, ed. 2, 2015), pp. 389–450.
30. B. Ranby, J. Lucki, *Pure Appl. Chem.* **52**, 295–303 (1980).
31. S.-J. Royer, S. Ferrón, S. T. Wilson, D. M. Karl, *PLOS ONE* **13**, e0200574 (2018).
32. C. P. Ward, C. J. Armstrong, A. N. Walsh, J. H. Jackson, C. M. Reddy, *Environ. Sci. Technol. Lett.* **6**, 669–674 (2019).
33. B. Eyheraguibel *et al.*, *Chemosphere* **184**, 366–374 (2017).
34. C.-C. Chen, L. Dai, L. Ma, R.-T. Guo, *Nat. Rev. Chem.* **4**, 114–126 (2020).
35. D. Floudas *et al.*, *Science* **336**, 1715–1719 (2012).
36. D. Danso, J. Chow, W. R. Streit, *Appl. Environ. Microbiol.* **85**, e01095-19 (2019).
37. S. Yoshida *et al.*, *Science* **351**, 1196–1199 (2016).
38. M. Thevenot, M.-F. Dignac, C. Rumpel, *Soil Biol. Biochem.* **42**, 1200–1211 (2010).
39. D. Hu, M. Shen, Y. Zhang, G. Zeng, *Sci. Total Environ.* **657**, 108–110 (2019).
40. J.-J. Guo *et al.*, *Environ. Int.* **137**, 105263 (2020).
41. M. Scheurer, M. Bigalke, *Environ. Sci. Technol.* **52**, 3591–3598 (2018).
42. F. Zehetner, G. J. Lair, M. H. Gerzabek, *Global Biogeochem. Cycles* **23**, GB4004 (2009).
43. S. Fuller, A. Gautam, *Environ. Sci. Technol.* **50**, 5774–5780 (2016).
44. G. Chen, Q. Feng, J. Wang, *Sci. Total Environ.* **703**, 135504 (2020).
45. J. Brahney, M. Hallerud, E. Heim, M. Hahnenberger, S. Sukumaran, *Science* **368**, 1257–1260 (2020).
46. L. Watkins, S. McGrattan, P. J. Sullivan, M. T. Walter, *Sci. Total Environ.* **664**, 834–840 (2019).
47. L. C. M. Lebreton *et al.*, *Nat. Commun.* **8**, 15611 (2017).
48. J. I. Hedges, R. G. Keil, R. Benner, *Org. Geochem.* **27**, 195–212 (1997).
49. T. C. Jennerjahn, I. Jänen, C. Propp, S. Adi, S. P. Nugroho, *Estuar. Coast. Shelf Sci.* **130**, 152–160 (2013).
50. J. R. Jambeck *et al.*, *Science* **347**, 768–771 (2015).
51. L. Lebreton *et al.*, *Sci. Rep.* **8**, 4666 (2018).
52. L. Van Cauwenberghe, L. Devriese, F. Galgani, J. Robbens, C. R. Janssen, *Mar. Environ. Res.* **111**, 5–17 (2015).
53. I. A. Kane *et al.*, *Science* **368**, 1140–1145 (2020).
54. E. van Sebille *et al.*, *Environ. Res. Lett.* **10**, 124006 (2015).
55. Data obtained via the Hawaii Ocean Time-series HOT-DOGS application, University of Hawai'i at Mānoa, National Science Foundation Award #1756517 (2020); https://hahana.soest.hawaii.edu/hot/hot-dogs/.
56. L. Galgani, S. A. Loiselle, *Environ. Pollut.* **268**, 115598 (2021).
57. L. Lebreton, M. Egger, B. Slat, *Sci. Rep.* **9**, 12922 (2019).

ACKNOWLEDGMENTS

Funding: A.S. was funded by NSF (CBET 1910621). K.L.L. was funded by NSF (CBET 1911257). L.Z. was funded by the National Key Research and Development Program of China (2016YFC1402205).
Competing interests: None to declare.

10.1126/science.abb0354

ILLUSTRATION: C. BICKEL/*SCIENCE*

REVIEW

Plastic ingestion as an evolutionary trap: Toward a holistic understanding

Robson G. Santos[1]*, Gabriel E. Machovsky-Capuska[2,3], Ryan Andrades[4]

Human activities are changing our environment. Along with climate change and a widespread loss of biodiversity, plastic pollution now plays a predominant role in altering ecosystems globally. Here, we review the occurrence of plastic ingestion by wildlife through evolutionary and ecological lenses and address the fundamental question of why living organisms ingest plastic. We unify evolutionary, ecological, and cognitive approaches under the evolutionary trap theory and identify three main factors that may drive plastic ingestion: (i) the availability of plastics in the environment, (ii) an individual's acceptance threshold, and (iii) the overlap of cues given by natural foods and plastics.

We live in a rapidly changing world, where human activities are altering our biophysical environment and leaving a persistent and substantial footprint on Earth (*1*). The pervasiveness of human-driven impacts has moved key environmental parameters (e.g., CO_2 and CH_4 atmospheric concentrations and soil nitrogen and phosphorus inventories) outside of the ranges found throughout the rest of the Holocene, prompting claims that we are now living in a different geological epoch—the Anthropocene (*1*, *2*). This new epoch is characterized by a range of global phenomena, including changes in Earth's climate (*3*) and a global loss of biodiversity (*4*, *5*). The Anthropocene is also notable for the production of enormous levels of plastic pollution on a scale that will leave identifiable fossil and geochemical records (*1*).

Industrial-scale production of plastic began in earnest in the 1940s (*6*) and scaled up considerably in the 1950s (*7*) during the period known as the great acceleration (*8*), which was characterized by growing pressures on the world's ecosystems. The increasing production and use of plastic were inevitably followed by its accumulation in the natural environment (*7*). Although most of our knowledge on plastic pollution was generated from marine ecosystems, the ubiquity of plastic pollution is now also claimed to be similar across freshwater, terrestrial, and atmospheric systems. Some rivers show concentrations of microplastics that are orders of magnitude higher than those found in marine ecosystems (*9*). Soils store more plastic than ocean basins, and thousands of tons of plastics circulate throughout the atmosphere (*10*, *11*). Although marine ecosystems are generally considered to be sinkholes for plastic (*12*), atmospheric transportation of microplastics and their exchange between soil and bodies of water indicate that oceans are only one component of the global plastic cycle (*11*, *12*).

Plastic is also accumulating in living organisms. Although considerable attention has been given to marine organisms, plastic ingestion is not restricted to these animals, having also been reported in several freshwater species (*13*) and land animals ranging from the Antarctic collembolan (*14*) to African elephants (*15*). Over the last four decades, extensive research has been conducted on the ingestion of plastic in wildlife (*13*, *16*). However, most studies have been limited to quantifying which species are ingesting plastics. After gathering a growing body of evidence showing the ubiquity of plastic pollution and its deleterious effects on living organisms (*17*)—including potential risks to human health (*18*)—we have reached the point where a unifying explanation for plastic ingestion is needed. Here, we directly address this issue by reviewing plastic ingestion through an evolutionary and an ecological lens. Specifically, we link ecology, behavior, and evolution, under the evolutionary trap concept, to provide a unifying framework for understanding why animals ingest plastics.

A widespread problem

The fast pace of plastic-ingestion records can be depicted by the sevenfold increase in the number of marine species ingesting plastics compared with the first comprehensive assessment published in 1997 by Laist (*19*). We have now reached 1288 marine species reported ingesting plastics (Fig. 1). Our Review indicates that 277 terrestrial and freshwater species have also been documented ingesting plastic, which increases the global total to at least 1565 species across environments (Fig. 1 and table S1). Terrestrial and freshwater ecosystems are still understudied (fig. S1) (*10*, *20*, *21*), which may contribute to the disparity in the number of reported species ingesting plastic when compared with marine ecosystems (Fig. 1A). The broad range of taxa known to ingest plastics demonstrates wide contamination across numerous branches of the tree of life—including eight phyla and more than half of the vertebrate orders (Fig. 1B). The sharp rise in the number of studies of plastic ingestion in wildlife is likely related to the increasing load of plastic waste accumulated in the environment combined with the growing interest of scientists and the development of new analytical tools (*22*).

Terrestrial ecosystems

Plastics are manufactured and mainly used and discarded in terrestrial habitats, where their accumulation in the natural environment begins. Although research on plastic pollution in terrestrial habitats is relatively scarce, evidence suggests that it may be potentially interfering with plant-pollinator interactions and soil function by altering the terrestrial geochemistry and biophysical environment (*10*). We find that plastics have been ingested by a diverse group of land animals, including insects, reptiles, birds, and mammals, from the tropics to the temperate and polar regions. Most of the species reported ingesting plastics are often restricted to anthropogenic landscapes, where high volumes of plastic waste can be found (*10*).

Plastic flow is different in terrestrial and aquatic landscapes and is mainly shaped by the properties of the surrounding medium. The greater viscosity and density of water, when compared with those of air, favor plastic dispersion over long distances. However, new evidence has revealed that microplastics can be transported through the atmosphere across thousands of kilometers (*11*) (Fig. 2).

Freshwater ecosystems

Freshwater habitats are among the most rapidly changing and threatened ecosystems on Earth (*23*). Although they serve as an important pathway for the spread of plastics from land to oceans (*24*), the effects of these pollutants on freshwater organisms and ecosystems have been relatively neglected (*25*). Despite the relatively low number of studies, the documented degree of plastic pollution shows that freshwater habitats are highly contaminated (*9*), and documented plastic ingestion in freshwater organisms ranges from insects to mammals, affecting most orders of freshwater vertebrates, including 20% of waterbird and 27% of fish families (Fig. 1C). Plastic ingestion encompasses all food-web levels, from filter feeding and grazing invertebrates to apex predators, and nearly all nodes of river and lake food webs are contaminated by plastics (Fig. 2).

Marine ecosystems

Plastic pollution is widespread in the marine realm, and coastal and ocean ecosystems are still considered the main plastic sink (*12*). The increase of plastics in marine ecosystems was accompanied by a growing number of studies on its ingestion by marine organisms in species distributed from tropical estuaries to cold, deep waters. Data suggest that, for well-studied taxa, plastic consumption seems to be increasing

[1]Laboratório de Biologia Marinha e Conservação, Universidade Federal de Alagoas, Cidade Universitária 57072-900, Maceió, AL, Brazil. [2]Cetacean Ecology Research Group, Massey University, Albany, AKL 0745, New Zealand. [3]The Charles Perkins Centre, The University of Sydney, Sydney, NSW 2006, Australia. [4]Laboratório de Ictiologia, Universidade Federal do Espírito Santo, Goiabeiras 29075-910, Vitória, ES, Brazil.
*Corresponding author. Email: robson.santos@icbs.ufal.br

over time (*26*, *27*). Plastics have also been shown to be ingested by a diverse group of species at the bases of trophic webs, such as planktivorous and herbivorous fish (Fig. 2), which suggests that trophic transfer could result in further plastic distribution across food webs.

Plastic ingestion as an evolutionary trap

Ecosystems are rapidly changing in response to multiple human pressures, creating a great number of low-quality options that mimic cues of high-quality ones, which draw animals into evolutionary traps as they are misled into make maladaptive choices (*28*). In this sense, plastic ingestion can be considered as an evolutionary trap, where the sudden appearance of plastics in the environment created several low-profit options that mimic cues of food items, triggering a maladaptive feeding behavior response (*28*, *29*). The evolutionary trap concept was first evoked to explain plastic ingestion in leatherback turtles (*29*), arguing that transparent plastics were likely to mimic jellyfish, the turtles' main food item. This so-called jellyfish hypothesis has been applied to explain plastic consumption as being a result of a mistaken identity given similarities (e.g., color, size, or shape) with natural prey across a broad range of marine organisms (*30*), although the debris ingested across individuals are often different in their physical characteristics (*31*). More recently, plastic-ingestion studies began to evoke the evolutionary trap concept when referring to the similarities between plastics and food (*32*–*34*). This idea of a close resemblance between plastics and food items is only part of the story, and by using the evolutionary trap framework, we me may be able to disentangle the "plastic ingestion trap."

Two types of evolutionary traps are proposed: (i) the equal-preference trap—a mild trap where a relatively poor option is indistinguishable from a high-quality one—and (ii) the severe trap—in which a lower-fitness choice is preferred over a higher-fitness resource (*28*). Results from laboratory studies have found that plastics are often equally or less-than-equally preferred compared with food items (*32*, *35*, *36*), but selective ingestion of plastics over food is also reported (*37*, *38*). We have little understanding of the relative attractiveness of plastics and how it varies in wildlife; therefore, determining in which trap type plastic ingestion may be classified is a difficult task. In this sense, animals' evolutionary response and plastic availability are key to understanding the trap severity, as these variables will influence the likelihood of plastic ingestion and the accumulation in the organisms.

The unifying framework

Creating a holistic understanding of plastic ingestion is necessary to unify evolutionary, ecological, and cognitive approaches through the perspective of the evolutionary trap theory. To move toward this unifying framework, the use

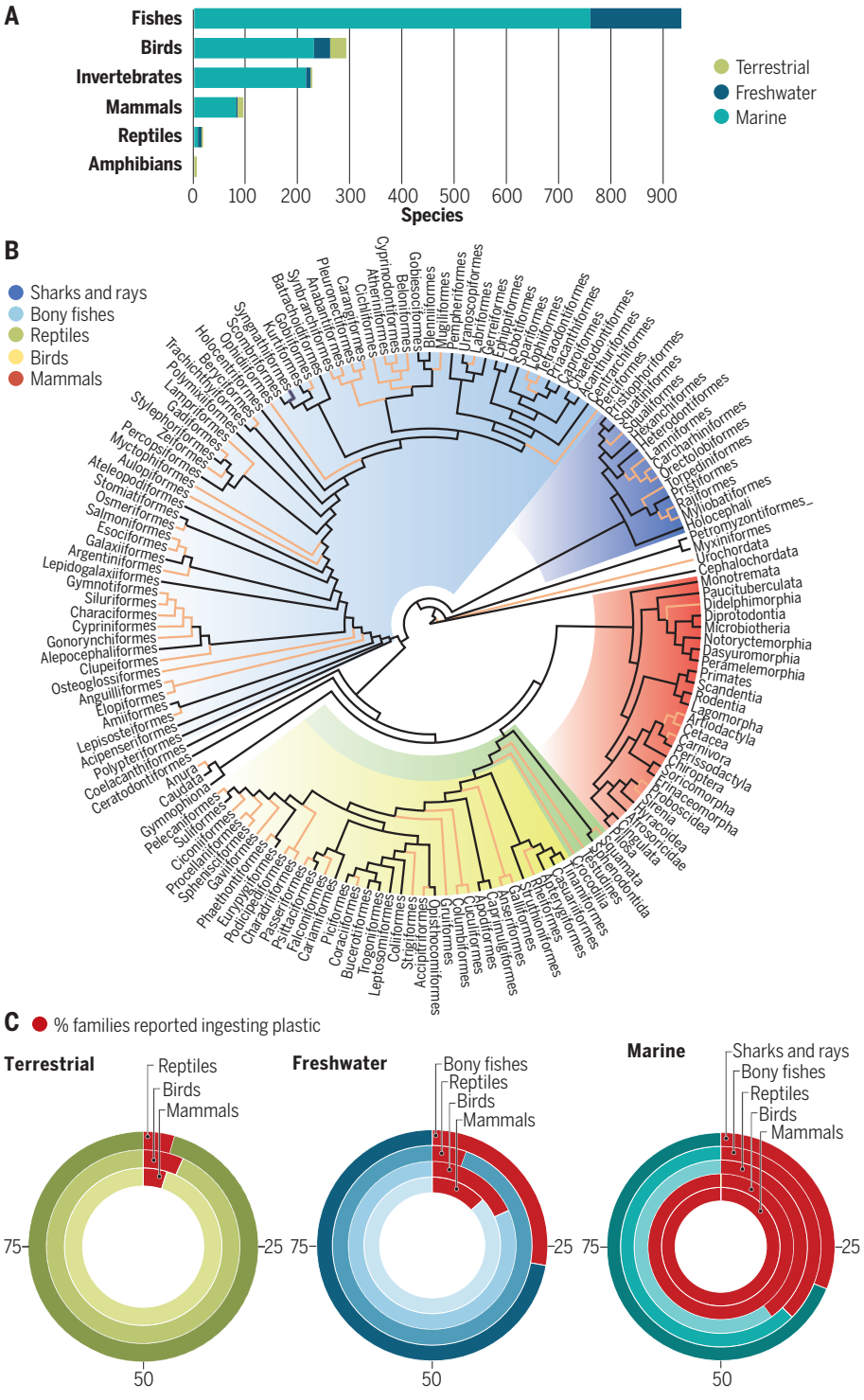

Fig. 1. Global evaluation of plastic ingestion by animals. (**A**) Number of species reported in the literature from 1980 until early 2021 ingesting plastics (macro- and microplastics). Species were classified as either terrestrial, freshwater, or marine (here as estuarine, coastal, and offshore marine seascapes) according to the ecosystem from which the plastic-ingestion record was made. (**B**) Cladogram showing vertebrate orders, with each color representing a different vertebrate group (cartilaginous fishes in dark blue; bony fishes in light blue; reptiles—Lepidosauria + Testudines + Crocodylia—in green; birds in yellow; and mammals in red). Orange branches indicate an account of plastic ingestion for at least one species of the clade. (**C**) Percentage of vertebrate families with plastic ingestion (red bars) reported for at least one species in the terrestrial, freshwater, and marine systems. We classified each family according to living habitat following FishBase (*77*), Vitt and Caldwell (*78*), Rasmussen *et al*. (*79*), Wetlands International (*80*), Croxall *et al*. (*81*), Veron *et al*. (*82*), Burgin *et al*. (*83*), and Feldhamer *et al*. (*84*).

of signal detection theory and its evolutionary application [i.e., acceptance threshold (*39*)] are key to understanding and linking the drivers behind plastic ingestion.

Organisms are faced with the challenge of accurately discriminating between beneficial and detrimental actions at the expense of frequent costly mistakes (*40*). Evolutionary history highlights that species are constantly subjected to a tradeoff between two types of errors: accepting low-profit options or rejecting high-profit ones. Plastic pollution can be seen as the rapid addition of a great variety of low-profit options, challenging the ability of organisms to differentiate food items from detrimental plastic pieces.

The recognition of a profitable food item relies on cues perceived by an individual and its acceptance threshold—the cue level at which it switches from rejecting to accepting an item (*39*, *40*). The acceptance threshold is selected on the basis of the balance between the costs of accepting a poor option and the costs of rejecting a good one. As the ability of an organism to distinguish between sensory stimuli is limited, we should expect some overlap in the distribution of cues between low-profit and high-profit items. Additionally, the acceptance threshold may also be influenced by circumstances, such as risk perception at any given moment (e.g., predation or starvation risk) (*41*).

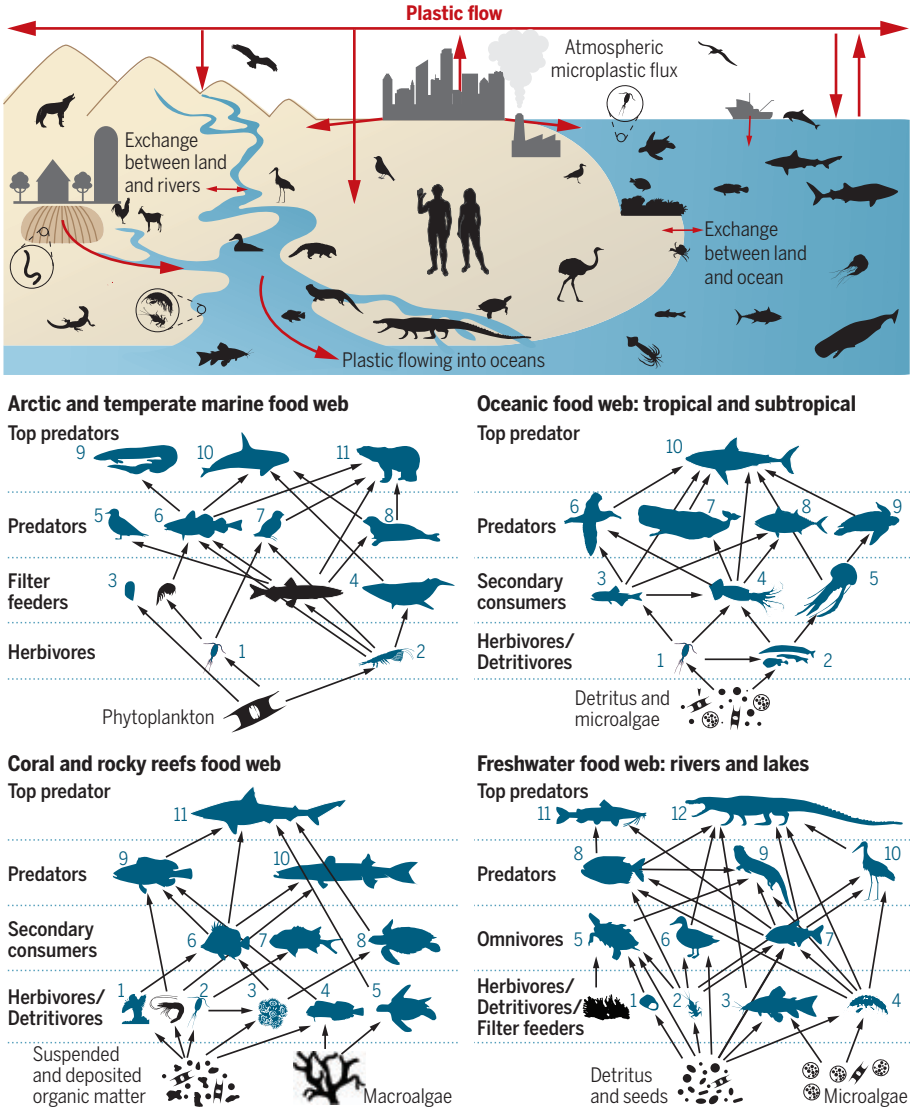

Fig. 2. The pervasiveness of plastic pollution. (**Top**) Plastic flux and accumulation in the environment are shown by red arrows. Plastics are circulating through all Earth systems and have been affecting animals with diverse niches and ecological traits. All depicted animals have a record of plastic ingestion. (**Bottom**) Plastics are ingested (teal silhouettes) by wildlife species distributed across several nodes of aquatic food webs. Arrows denote expected food chain pathways and potential routes for plastics trophic transfer. References used to draw food webs and plastic ingestion are in table S2. Animal silhouettes used are available under a Public Domain 1.0 license at Phylopic (http://phylopic.org), unless otherwise indicated in table S4.

In this context, plastics can be seen as a widespread poor food option. Once encountered, the likelihood of ingestion will be determined by an individual's acceptance threshold and the overlap between plastics and food cues. High cue overlap and/or low acceptance thresholds will increase the chances of an individual accepting a detrimental option (*28*). Interacting with these two drivers is the abundance of plastic "prey" items in the environment. As plastic availability increases, there will be an inevitable increase in the diversity of feeding cues emitted by plastics [i.e., materials, sizes, shapes, and colors (*42*)] and correspondingly higher encounter rates.

The volume and distribution of plastics in the environment combined with the foraging strategies of organisms determine the plastic-encounter rate (i.e., plastic availability), which is an important factor driving their ingestion. In support of this pattern, recent studies have documented a positive relationship between plastic debris abundance and rates of ingestion (*26*, *43*), although this pattern remains to be further explored. The relationship between the increase of plastic in the environment and its ingestion may be of particular importance to filter-feeding animals (*44*).

Acceptance threshold and cues overlap are theoretical parameters from signal detection and acceptance threshold theories (*39*, *40*), but they can be evaluated through some empirical proxies. In the case of plastic ingestion, we proposed that three traits are particularly associated with cues overlap and acceptance thresholds: (i) level of prey resemblance to plastics (physical and chemical), (ii) food selectivity (generalist to specialist), and (iii) nutritional state (e.g., risk of starvation). We suggest that these traits, combined with measures of plastic availability, should become the foundation for risk assessments for plastic ingestion (Fig. 3A). Despite the relatively low number of studies with an appropriate design to test the effects of these traits (n = 43; table S3), our framework is consistent with the current empirical evidence (Fig. 3B).

The dietary generalist-specialist distinction plays an important role in understanding foraging behavior, nutrition, and food selection. In general, specialist species are known for consuming a narrow range of foods and are likely to accept only the most profitable ones (i.e., high acceptance threshold), whereas generalists are known for ingesting a broad range of foods and mostly accepting all encountered prey when foraging (i.e., low acceptance threshold) (*45*). Under similar plastic availability in an environment, we would therefore expect generalist foragers to be more likely to ingest plastics than specialists, which seems to be supported by the literature (*46*–*49*).

The acceptance of a broader range of food items can be also triggered by circumstances, particularly those related to the risk of starvation, such as resource unpredictability (*50*) and the level of hunger (*51*). Starvation can

thus induce poor foraging performance and fluctuations on feeding thresholds, leading to the consumption of less-profitable foods (*52*, *53*). Under these circumstances, an increase in opportunistic feeding behaviors could be expected (*50*). We would thus predict that the risk of plastic ingestion may increase as the risk of starvation increases. Moreover, resource unpredictability is also linked with an increase in generalist (*50*) and opportunistic (*47*) feeding behaviors. Scavenging is a good example of such a behavior—being relatively common among many terrestrial and aquatic species (*54*, *55*)—and has recently been suggested as a possible pathway for plastic ingestion by marine animals (*47*). Additionally, our Review of the existent literature shows that a third of terrestrial species that consumed plastics are obligatory or opportunistic scavengers.

The level of resemblance of plastics to natural food items (i.e., feeding cues overlap) has been thought to influence their ingestion by marine animals (*28*, *30*) and was also implicated in the ingestion of plastics by freshwater (*56*) and terrestrial (*57*) species. This general perception based on the similarities of foods and plastics can likely be related to the limited discriminatory capacity of sensory organs (*58*). Visual cues can both influence plastic detection (*31*) and their ingestion (*59*). Plastics in the environment have different degrees of similarity to natural foods, from a very precise match (*60*) to a vague (e.g., size) (*46*) or no obvious resemblance. The size of food also represents a nonvisual cue, influencing selection, capture success, and handling time (*61*). Animals' body sizes influence the range of plastic sizes ingested; however, more studies are needed to better understand how this applies to the smallest ingestible pieces (*62*). Filter, suspension, and deposit feeders are the most susceptible species to plastic ingestion because of prey size similarity (*44*, *63*). Nonphysical plastic characteristics are no less important, with chemical signatures overlapping those produced by prey also playing a role in plastic ingestion (*32*, *34*, *35*). Misleading infochemical cues emitted by the plastisphere (*34*) are often comparable to chemical signatures produced by natural foods and have been implicated in accounts of plastic ingestion by vertebrates and invertebrates (*34*, *64*).

Nevertheless, prey resemblance is quite difficult to evaluate; even the Eleonora's falcon (*Falco eleonorae*), which has the ability to capture fast-moving prey, has been documented misjudging plastics for natural foods (*57*). Thus, the unfortunate great diversity of plastic characteristics may provide endless nonexclusive possibilities for feeding cues overlap.

The number of studies on plastic ingestion are rising, as are the number of species affected and the knowledge about the impacts on multiple biological and trophic levels. However, only a small fraction of these studies is dedicated to understanding the potential drivers of plastic ingestion. Additionally, most of them are focused on evaluating taxa-specific ecological traits, which commonly lack parallels among species and are usually embedded with multiple potential drivers (e.g., plastic-encounter rate and food selectivity), which undermines their use in a broader risk-assessment evaluation. As a global problem that is spreading at a fast pace throughout diverse ecosystems, a general agreement on how to build a comprehensive risk assessment is needed.

Plastic ingestion can affect animals by a diverse set of mechanisms, such as nutritional dilution, physiological disruption, and impairment of gastrointestinal functions, all of which affect health, growth, and reproductivity output (*17*), which may ultimately lead to demographic effects (*65*). Lethal and chronic physiological health effects on the individual level have been reported in laboratory and field studies (*17*), but potential effects on the populational level are just beginning to emerge (*65*).

We live in a world where the co-occurrence of multiple anthropogenic stressors is the norm, and the risks posed by the plastic ingestion trap need to be examined in this context. Chronic effects of pollutants are hard to estimate at a population level in natural environments, but some studies are present in the literature (*66*). For example, the chronic exposure to organochlorine-persistent pollutants has left worldwide populations of vultures and killer whales (*Orcinus orca*) at the risk of extinction (*67*, *68*). These studies provide unsettling examples of how years of conservation efforts can be severely compromised by diffuse threats. It is possible that some of the threats to wildlife posed by the exposure to plastic pollution are yet to emerge, but useful lessons can be drawn from these examples.

Can the plastic trap be disarmed?

Demographic and eco-evolutionary simulations suggest that evolutionary traps can lead to population declines (*58*, *65*, *69*). Therefore, teasing apart how these traps can be disarmed is important. Three processes, and their interactions, may help to disarm evolutionary traps (*70*): natural selection, learning, and human management. In the first case, the evolution of an adaptive response to plastic pollution requires the appearance and selection of heritable traits related to sensory and cognitive systems that improve the differentiation between plastics and foods. This could potentially take place over multiple lineages across different evolutionary time scales.

Learning, like selection, potentially provides a mechanism for a population to respond to changes in the environment, enabling them to escape from an evolutionary trap (*70*). However, the ability to learn and pass on learned behaviors (cultural transmission) varies among species. To evaluate the feasibility of learning to escape a trap, we consider several factors: (i) animals may have the ability to distinguish cues from plastic and food items and (ii) the plastic ingestion trap offers multiple opportunities to do so, which increases the chances of learning through experience. Studies reporting a negative outcome as a result of plastic ingestion commonly highlight the chronic nature of the deleterious

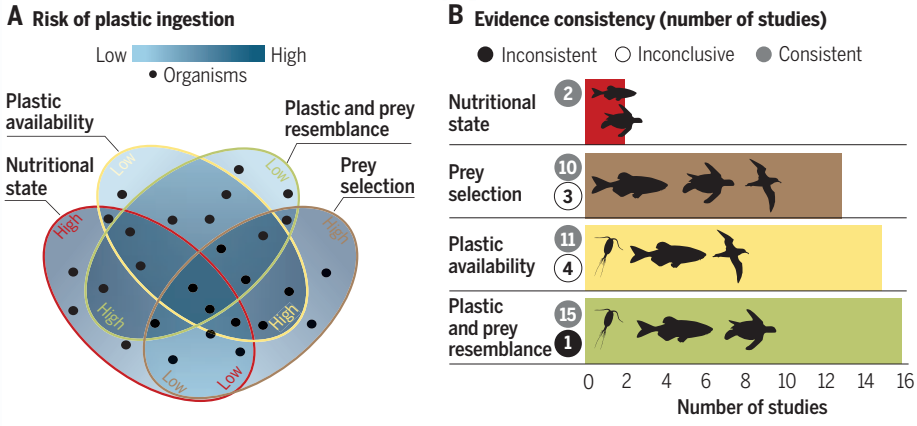

Fig. 3. Plastic ingestion risk assessment and the strength of evidence. (**A**) Diagram showing how the availability of plastics in the environment, the nutritional state of an organism, the prey resemblance with plastics, and prey selection can interact, thereby increasing the risk of plastic ingestion by hypothetical individuals (black dots). (**B**) The number of studies that provide empirical evidence regarding the proposed traits associated with risk of plastic ingestion. Data were collected from a systematic review. Evidence was selected when the study design allowed a credible causal interpretation. Evidence was classified as consistent [statistical results are in accord with the proposed framework (A)], inconclusive (statistical results did not allow a conclusion about causal interpretation), or inconsistent (statistical results contrast with our proposed framework). Depicted organisms indicate the animal groups present in the studies: invertebrates, fishes, reptiles, or birds. Animal silhouettes are available under a Public Domain 1.0 license at Phylopic (http://phylopic.org), unless otherwise indicated in table S4.

effects (*17*, *71*, *72*). This temporal disconnection between the act of ingesting plastics and their negative outcome decreases the possibility for an individual to obtain feedback on the poor payoff of plastic ingestion; therefore, the process of learning through experience is compromised (*70*).

The challenge of relying on natural selection and/or learning highlights the need for human intervention. Two human-mediated actions have been proposed to reduce the risks of animals falling into an evolutionary trap (*28*): (i) decreasing the attractiveness of the low-fitness option and (ii) reducing encounter rates with the trap. Although a reduction in the attractiveness of plastics has been previously proposed (*34*), a wide range of taxa with individual sensory and cognitive systems will prevent a one-size-fits-all solution. Therefore, decreasing plastic production is needed to reduce the encounter rate with the plastic trap.

Conclusions and outlook

The ingestion of plastics has been increasingly reported throughout diverse branches of the tree of life. Much research has reported deleterious effects of plastics in organisms, although research concerning their impacts at the population level is still in its infancy. Models suggest that evolutionary traps can severely affect population viability, and it is therefore imperative that we identify individuals, populations, and species at the greatest risk.

Although several advances in the understanding of plastic-ingestion drivers and effects have been made in the last years (*17*, *31*–*35*, *47*, *65*, *73*, *74*), we suggest that future research focuses on expanding the studies on nutritional and sensory ecology and evaluating animals' behavior within an evolutionary perspective. Studies should be designed to evaluate the relative attractiveness of plastics and their preference related to food under realistic scenarios. The interaction of the plastic-ingestion drivers, as proposed in our framework, should also be integrated in future studies to evaluate the risk of ingestion. Additionally, the threats posed by this evolutionary trap must be considered under the current context of growing pressures on the world's ecosystems, where, combined with the increase in plastic pollution, wildlife populations are exposed to multiple threats and are experiencing the degradation of their habitats (*4*, *5*), which also affects the quality and abundance of their food in relation to plastic debris.

As there are limited options for escaping the plastic evolutionary trap, mitigation efforts should heavily focus on reducing the encounter rates for at-risk populations. We cannot turn back the clock on plastic pollution, but we can adopt measures to minimize the consequences of this ubiquitous trap. Plastic pollution continues to rise, and, even if we were able to scale up the boldest mitigation policies in place today, millions of tons of plastics will still accumulate in the environment each year (*75*, *76*). This scenario calls for international steadfast commitment to transformative change, which must include pre- and postconsumption solutions guided by science, such as substantial decreases in plastic production and use—shifting toward a circular economy—and investments in waste management and recovery around the world (*75*, *76*).

REFERENCES AND NOTES

1. C. N. Waters *et al*., *Science* **351**, aad2622 (2016).
2. S. L. Lewis, M. A. Maslin, *Nature* **519**, 171–180 (2015).
3. PAGES 2k Consortium, *Nat. Geosci.* **6**, 503 (2013).
4. R. Dirzo *et al*., *Science* **345**, 401–406 (2014).
5. G. Ceballos *et al*., *Sci. Adv.* **1**, e1400253 (2015).
6. R. C. Thompson, S. H. Swan, C. J. Moore, F. S. vom Saal, *Phil. Trans. R. Soc. B* **364**, 1973–1976 (2009).
7. R. Geyer, J. R. Jambeck, K. L. Law, *Sci. Adv.* **3**, e1700782 (2017).
8. W. Steffen, J. Grinevald, P. Crutzen, J. McNeill, *Phil. Trans. R. Soc. A* **369**, 842–867 (2011).
9. F. M. Windsor *et al*., *Glob. Change Biol.* **25**, 1207–1221 (2019).
10. A. A. de Souza Machado, W. Kloas, C. Zarfl, S. Hempel, M. C. Rillig, *Glob. Change Biol.* **24**, 1405–1416 (2018).
11. J. Brahney, M. Hallerud, E. Heim, M. Hahnenberger, S. Sukumaran, *Science* **368**, 1257–1260 (2020).
12. C. M. Rochman, T. Hoellein, *Science* **368**, 1184–1185 (2020).
13. A. Cera, G. Cesarini, M. Scalici, *Diversity* **12**, 276 (2020).
14. E. Bergami *et al*., *Biol. Lett.* **16**, 20200093 (2020).
15. J. H. T. Le Breton, *Pachyderm* **60**, 45–54 (2019).
16. S. Kühn, J. A. van Franeker, *Mar. Pollut. Bull.* **151**, 110858 (2020).
17. K. Bucci, M. Tulio, C. M. Rochman, *Ecol. Appl.* **30**, e02044 (2020).
18. S. L. Wright, F. J. Kelly, *Environ. Sci. Technol.* **51**, 6634–6647 (2017).
19. D. W. Laist, in *Marine Debris: Sources, Impacts, and Solutions*, J. M. Coe, D. B. Rogers, Eds. (Springer, 1997), pp. 99–139.
20. A. Malizia, A. C. Monmany-Garzia, *Sci. Total Environ.* **668**, 1025–1029 (2019).
21. A. A. Horton, A. Walton, D. J. Spurgeon, E. Lahive, C. Svendsen, *Sci. Total Environ.* **586**, 127–141 (2017).
22. M. Cole, P. Lindeque, C. Halsband, T. S. Galloway, *Mar. Pollut. Bull.* **62**, 2588–2597 (2011).
23. S. R. Carpenter, E. H. Stanley, M. J. Vander Zanden, *Annu. Rev. Environ. Resour.* **36**, 75–99 (2011).
24. L. C. M. Lebreton *et al*., *Nat. Commun.* **8**, 15611 (2017).
25. M. C. M. Blettler, K. M. Wantzen, *Water Air Soil Pollut.* **230**, 174 (2019).
26. C. Wilcox, E. Van Sebille, B. D. Hardesty, *Proc. Natl. Acad. Sci. U.S.A.* **112**, 11899–11904 (2015).
27. Q. Schuyler, B. D. Hardesty, C. Wilcox, K. Townsend, *Conserv. Biol.* **28**, 129–139 (2014).
28. B. A. Robertson, J. S. Rehage, A. Sih, *Trends Ecol. Evol.* **28**, 552–560 (2013).
29. M. A. Schlaepfer, M. C. Runge, P. W. Sherman, *Trends Ecol. Evol.* **17**, 474–480 (2002).
30. J. G. Derraik, *Mar. Pollut. Bull.* **44**, 842–852 (2002).
31. R. G. Santos, R. Andrades, L. M. Fardim, A. S. Martins, *Environ. Pollut.* **214**, 585–588 (2016).
32. M. S. Savoca, C. W. Tyson, M. McGill, C. J. Slager, *Proc. R. Soc. B.* **284**, 20171000 (2017).
33. M. S. Savoca, A. G. McInturf, E. L. Hazen, *Glob. Change Biol.* **27**, 2188–2199 (2021).
34. M. S. Savoca, M. E. Wohlfeil, S. E. Ebeler, G. A. Nevitt, *Sci. Adv.* **2**, e1600395 (2016).
35. J. B. Pfaller, K. M. Goforth, M. A. Gil, M. S. Savoca, K. J. Lohmann, *Curr. Biol.* **30**, R213–R214 (2020).
36. J. Xu, D. Li, *Environ. Pollut.* **268**, 115648 (2021).
37. E. R. Graham, J. T. Thompson, *J. Exp. Mar. Biol. Ecol.* **368**, 22–29 (2009).
38. R. D. Rotjan *et al*., *Proc. R. Soc. B.* **286**, 20190726 (2019).
39. H. K. Reeve, *Am. Nat.* **133**, 407–435 (1989).
40. H. M. Scharf, A. V. Suarez, H. K. Reeve, M. E. Hauber, *Phil. Trans. R. Soc. B* **375**, 20190475 (2020).
41. E. A. Bernays, W. T. Wcislo, *Q. Rev. Biol.* **69**, 187–204 (1994).
42. M. L. Pedrotti *et al*., *PLOS ONE* **11**, e0161581 (2016).
43. G. V. B. Ferreira, M. Barletta, A. R. A. Lima, *Sci. Total Environ.* **655**, 292–304 (2019).
44. E. S. Germanov, A. D. Marshall, L. Bejder, M. C. Fossi, N. R. Loneragan, *Trends Ecol. Evol.* **33**, 227–232 (2018).
45. R. Heller, *Theor. Popul. Biol.* **17**, 201–214 (1980).
46. P. G. Ryan, *Mar. Environ. Res.* **23**, 175–206 (1987).
47. R. Andrades, R. A. Dos Santos, A. S. Martins, D. Teles, R. G. Santos, *Environ. Pollut.* **248**, 159–165 (2019).
48. F. Gusmão *et al*., *Environ. Pollut.* **216**, 584–590 (2016).
49. C. Not, C. Y. I. Lui, S. Cannicci, *Limnol. Oceanogr.* **5**, 84–91 (2020).
50. S. E. Overington, F. Dubois, L. Lefebvre, *Behav. Ecol.* **19**, 836–841 (2008).
51. E. D. Gribkova, M. Catanho, R. Gillette, *Sci. Rep.* **10**, 9627 (2020).
52. D. M. Perry, *Oecologia* **72**, 360–365 (1987).
53. K. S. Hileman, E. D. Brodie Jr., D. R. Formanowicz Jr., *J. Insect Behav.* **8**, 241–249 (1994).
54. K. McCann, A. Hastings, G. R. Huxel, *Nature* **395**, 794–798 (1998).
55. E. E. Wilson, E. M. Wolkovich, *Trends Ecol. Evol.* **26**, 129–135 (2011).
56. W. Yuan, X. Liu, W. Wang, M. Di, J. Wang, *Ecotoxicol. Environ. Saf.* **170**, 180–187 (2019).
57. R. Steen, C. S. Torjussen, D. W. Jones, T. Tsimpidis, A. Miliou, *Mar. Pollut. Bull.* **106**, 200–201 (2016).
58. B. A. Robertson, A. D. Chalfoun, *Curr. Opin. Behav. Sci.* **12**, 12–17 (2016).
59. N. C. Ory, P. Sobral, J. L. Ferreira, M. Thiel, *Sci. Total Environ.* **586**, 430–437 (2017).
60. Q. Schuyler, B. D. Hardesty, C. Wilcox, K. Townsend, *PLOS ONE* **7**, e40884 (2012).
61. J. E. Ward, S. E. Shumway, *J. Exp. Mar. Biol. Ecol.* **300**, 83–130 (2004).
62. I. B. Jåms, F. M. Windsor, T. Poudevigne-Durance, S. J. Ormerod, I. Durance, *Nat. Commun.* **11**, 1594 (2020).
63. S. L. Wright, R. C. Thompson, T. S. Galloway, *Environ. Pollut.* **178**, 483–492 (2013).
64. A. S. Allen, A. C. Seymour, D. Rittschof, *Mar. Pollut. Bull.* **124**, 198–205 (2017).
65. N. Marn, M. Jusup, S. A. L. M. Kooijman, T. Klanjscek, *Ecol. Lett.* **23**, 1479–1487 (2020).
66. H. R. Köhler, R. Triebskorn, *Science* **341**, 759–765 (2013).
67. P. I. Plaza, E. Martínez-López, S. A. Lambertucci, *Sci. Total Environ.* **687**, 1207–1218 (2019).
68. J. P. Desforges *et al*., *Science* **361**, 1373–1376 (2018).
69. B. A. Robertson, D. T. Blumstein, *Conserv. Sci. Pract.* **1**, e116 (2019).
70. A.L. Greggor, P. C. Trimmer, B. J. Barrett, A. Sih, *Front. Ecol. Evol.* **7**, 408 (2019).
71. R. G. Santos *et al*., *Environ. Pollut.* **265**, 114918 (2020).
72. J. L. Lavers, I. Hutton, A. L. Bond, *Environ. Sci. Technol.* **53**, 9224–9231 (2019).
73. L. Roman, B. D. Hardesty, M. A. Hindell, C. Wilcox, *Environ. Res. Lett.* **15**, 124071 (2020).
74. G. E. Machovsky-Capuska, C. Amiot, P. Denuncio, R. Grainger, D. Raubenheimer, *Sci. Total Environ.* **656**, 789–796 (2019).
75. S. B. Borrelle *et al*., *Science* **369**, 1515–1518 (2020).
76. W. W. Y. Lau *et al*., *Science* **369**, 1455–1461 (2020).
77. R. Froese, D. Pauly, Eds., FishBase (2021); www.fishbase.org.
78. L. J. Vitt, J. P. Caldwell, *Herpetology: An Introductory Biology of Amphibians and Reptiles* (Academic Press, 2013).
79. A. R. Rasmussen, J. C. Murphy, M. Ompi, J. W. Gibbons, P. Uetz, *PLOS ONE* **6**, e27373 (2011).
80. Wetlands International, "Waterbird Population Estimates" (2021); http://wpe.wetlands.org/.
81. J. P. Croxall *et al*., *Bird Conserv. Int.* **22**, 1–34 (2012).
82. G. Veron, B. D. Patterson, R. Reeves, in *Freshwater Animal Diversity Assessment*, E. V. Balian, C. Lévêque, H. Segers, K. Martens, Eds., vol. 198 of *Developments in Hydrobiology* (Springer, 2007), pp. 607–617.
83. C. J. Burgin, J. P. Colella, P. L. Kahn, N. S. Upham, *J. Mammal.* **99**, 1–14 (2018).
84. G. A. Feldhamer, J. F. Merritt, C. Krajewski, J. L. Rachlow, K. M. Stewart, *Mammalogy: Adaptation, Diversity, Ecology* (Johns Hopkins Univ. Press, 2020).

ACKNOWLEDGMENTS

We thank the reviewers, who provided thoughtful and constructive comments. We are grateful for insightful comments from L. M. A. Sousa, R. J. Ladle, and M. E. Hauber, and we thank F. J. Santos for assistance with artwork. **Funding:** The authors received no specific funding for this work. **Author contributions:** R.G.S., R.A., and G.E.M.-C. designed the project. R.G.S. wrote the manuscript. G.E.M.-C. and R.A. contributed to the writing and editing of the manuscript. R.G.S. and R.A. designed the figures. **Competing interests:** The authors declare no competing interests. **Data and materials availability:** All data are available in the manuscript and the supplementary materials.

SUPPLEMENTARY MATERIALS

science.sciencemag.org/content/373/6550/56/suppl/DC1
Fig. S1
Tables S1 to S4
MDAR Reproducibility Checklist

10.1126/science.abh0945

REVIEW

The global threat from plastic pollution

Matthew MacLeod[1]*, Hans Peter H. Arp[2,3]*, Mine B. Tekman[4]*, Annika Jahnke[5,6]*

Plastic pollution accumulating in an area of the environment is considered "poorly reversible" if natural mineralization processes occurring there are slow and engineered remediation solutions are improbable. Should negative outcomes in these areas arise as a consequence of plastic pollution, they will be practically irreversible. Potential impacts from poorly reversible plastic pollution include changes to carbon and nutrient cycles; habitat changes within soils, sediments, and aquatic ecosystems; co-occurring biological impacts on endangered or keystone species; ecotoxicity; and related societal impacts. The rational response to the global threat posed by accumulating and poorly reversible plastic pollution is to rapidly reduce plastic emissions through reductions in consumption of virgin plastic materials, along with internationally coordinated strategies for waste management.

Plastic pollution is found globally from deserts to farms, from mountaintops to the deep ocean, in tropical landfills and in Arctic snow. Reports of plastic debris in the marine environment date back half a century (*1*, *2*), with continuing accumulation on the ocean surface over the past 60 years (*3*).

Emissions of plastic are increasing and will continue to do so even in some of the most optimistic future scenarios of plastic waste reduction (*4*). Estimates of global emissions of plastic waste to rivers, lakes, and the ocean range from 9 to 23 million metric tons per year, with a similar amount emitted into the terrestrial environment, from 13 to 25 million metric tons per year as of 2016 (*4*, *5*). Following business-as-usual scenarios, these estimated 2016 emission rates will be approximately doubled by 2025. Scenarios that include concerted, joint global action—such as implementing the Basel convention to prevent transport of plastic waste to countries with poor management systems, or the European Union target to recycle more plastic as part of the transition to a circular economy—still forecast continuous yearly increases in plastic emissions (*4*, *5*).

Accumulation of plastic in the environment occurs when the rate at which plastic pollution enters an area exceeds the rate of natural removal processes or cleanup actions. Plastic is persistent in the environment, with rates of natural removal on the scale of decades to centuries (*6*). Cleanup actions are not feasible in many areas of the global environment where plastic accumulates, particularly in remote locations. Plastic therefore fits the profile of a "poorly reversible pollutant," both because emissions cannot be curtailed and because it resides in the environment for a long time (*7*). A central concern about poorly reversible pollution is that if it accumulates to levels that exceed effect thresholds, this transgression will trigger negative impacts that themselves cannot be readily reversed because it will not be possible to rapidly reduce pollution levels below the threshold (*8*–*10*).

Here, we identify areas of the global environment that are threatened with impacts from plastic pollution that is both accumulating and poorly reversible. We highlight the complex characteristics of plastic pollution that evolve as it undergoes continuous weathering in the environment, and discuss potential large-scale and poorly reversible effects that could be triggered by continuing accumulation. Our analysis confirms that plastic pollution fits the exposure profile of a planetary boundary threat, which we and others have already asserted (*10*–*13*), and that actions to drastically reduce plastic emissions are the rational policy response.

Environmental exposure to poorly reversible pollution by plastic

Obvious plastic pollution occurs where humans directly litter, such as roadsides, beaches, river banks, and urban estuaries. This type of plastic pollution is, in principle, readily reversible at the local scale because it can be physically removed by cleanups, and because littering can be curtailed through public campaigns and with improved waste collection infrastructure. Similarly, the obvious plastic pollution in and around landfills can, in principle, be reduced with improved site management. However, even at the local scale, plastic pollution becomes poorly reversible when weathering processes cause fragmentation into micro- and nanoplastic particles that are not visible to the human eye. Furthermore, there are several known remote areas of the global environment that are accumulating poorly reversible, weathering plastic pollution. The plastic polluting these remote areas is not per se feasible to remove, and pollution levels would only respond slowly to emission reductions (Fig. 1).

Remote coastlines and the ocean surface—in particular, the five gyres of the North and South Pacific, the North and South Atlantic, and the Indian Ocean—are well-known global accumulation zones for floating plastic debris (*14*) (Fig. 1A). Although a variety of direct, empirical measurements of plastic pollution in ocean gyres have been made, inventories of plastic on the ocean surface largely rely on remote sensing measurements of macroplastic and simulations of plastic debris trajectories because of their huge extent and circulating currents. Less than 0.3 million metric tons of plastic are estimated to be currently circulating on the ocean surface (*14*), which represents a small fraction of the estimated 9 million to 23 million metric tons of plastic that are emitted annually into rivers, lakes, and the ocean (*4*, *5*). The small inventory of plastic floating on the ocean surface relative to annual emissions has sometimes been called "missing plastic," but mass balance modeling of plastic in the ocean surface layer suggests that weathering (including fragmentation) and sinking could rapidly remove initially buoyant plastic from the near-surface ocean to the water column and the deep seafloor (*15*) (Fig. 1, B and C). Thus, the inventory of plastic particles on the ocean surface could be quickly transferred to the water column and deep ocean if emissions were shut off. However, plastic pollution on the surface of the ocean is still poorly reversible because the feasibility of reducing emissions of plastic to the oceans is low at present. Plastic pollution beached on remote coastlines presumably has longer residence times than floating plastic, and thus is even more poorly reversible.

The global ocean reaches several thousand meters of depth in many areas, and its water column is a huge potential reservoir for neutrally buoyant plastic pollution that could have very poor reversibility (Fig. 1B). The mass balance modeling mentioned above estimated that 99.8% of the plastic that entered the ocean since 1950 is located below the surface (*15*). Although most plastic particles are expected to eventually reach the seafloor (*16*), a substantial amount is present in the water column (*16*, *17*). One mechanism for plastic to remain suspended in the water column is through incorporation into biological cycles. Biofilms that form on the surface of plastic excrete sticky polymeric substances that facilitate the formation of heteroaggregates of plastic particles with natural organic matter (*18*). Buoyant polymers with increasing biofilm loads in the photic zone sink and then float upward again when the

[1]Department of Environmental Science, Stockholm University, SE-106 91 Stockholm, Sweden. [2]Department of Environmental Engineering, Norwegian Geotechnical Institute, NO-0806 Oslo, Norway. [3]Department of Chemistry, Norwegian University of Science and Technology (NTNU), NO-7491 Trondheim, Norway. [4]Alfred Wegener Institute, Helmholtz Centre for Polar and Marine Research, Bremerhaven, Germany. [5]Department of Ecological Chemistry, Helmholtz Centre for Environmental Research–UFZ, DE-04107 Leipzig, Germany. [6]Institute for Environmental Research, RWTH Aachen University, DE-52074 Aachen, Germany.
*Corresponding author. Email: matthew.macleod@aces.su.se (M.M.); hans.peter.arp@ngi.no (H.P.H.A.); mine.banu.tekman@awi.de (M.B.T.); annika.jahnke@ufz.de (A.J.)

biofilm decays at greater depths (*19*). The smallest plastic particles, such as those below 10 μm and particularly those that are cylindrical and elongated in shape (such as fibers), will be suspended throughout the water column as a consequence of drag forces and turbulence, leading to very long residence times (*20*). Rates of degradation of neutrally buoyant plastic are expected to be very slow in the deep water column as a result of cold temperatures, quiescent conditions and, in particular, the lack of ultraviolet radiation. Thus, plastic pollution of the water column is likely poorly reversible. Plastic particles with long residence times in the water column are also subject to subsurface lateral advection in the ocean (*16*), which provides a global transport pathway for plastic pollution.

The seafloor is a major accumulation zone for plastic pollution (Fig. 1C), having some of the highest concentrations of microplastic particles in the environment (*16*). A recent study indicated that near-bed thermohaline currents, which supply oxygen and nutrients to deep-sea fauna, also drive plastic deposition into hotspots of seabed biodiversity (*21*). The seafloor is mostly a placid, dark, cold environment that is not conducive to further degradation (*22*). Thus, the persistence of plastic on the seafloor is likely very high, with its residence time determined by time scales for burial in accumulating sediment (*23*).

Terrestrial soils are another accumulation zone for plastic (Fig. 1D). Sources of plastic pollution to urban and rural soils are plastic litter, road runoff (including tire wear particles), and atmospheric deposition of micro- and nanoplastic particles (*24*). Plastic is also deliberately introduced to agricultural soils through plastic mulching with polyethylene films and increasingly also so-called "biodegradable" plastic films, compost, and sludge-derived biosolids that contain plastic residues (*24*, *25*), as well as by the application of polymeric stabilizers against soil erosion (*26*). Current plastic fractions in soils can reach up to 0.1% of soil organic carbon (*24*). On the basis of estimates of sewage sludge inputs alone (*27*), it is likely that the amount of plastic in the world's agricultural soil is larger than on the ocean's surface. Mismanaged plastic mulches are a source of plastic to the surrounding soil (*25*) and can escape to lakes and rivers. Some plastics that are biodegradable in soils, such as those made of polylactic acid, exhibit half-lives in the marine environment similar to that of polyethylene (*6*). Plastic concentrations in soil are expected to increase because of these ongoing emission sources combined with extremely slow degradation rates. It is estimated that less than 1% of the mass of conventional plastic is lost from soils over several years (*24*), despite conversion into smaller plastic particles (*28*). Thus, plastic pollution of soils is poorly reversible.

A Remote ocean surface and coastlines
Ocean gyres are reservoirs for plastic debris and currents can transport plastic to remote and ecologically sensitive coastlines.

B The water column
Neutrally buoyant plastic and plastic aggregates with organic matter accumulate in the water column of the ocean and lakes and can be taken up by organisms.

C The deep sea
Sinking plastic accumulates on the seafloor in conditions ideal for long-term preservation in benthic ecosystems and the sedimentary crust.

D Soils
Plastic applied to cropland as mulch and with contaminated compost accumulates and may be slowly released as weathered microplastic.

E The body
Ingested or inhaled particles can accumulate in body cavities, release fragments and chemicals, and potentially penetrate epithelial layers and tissues.

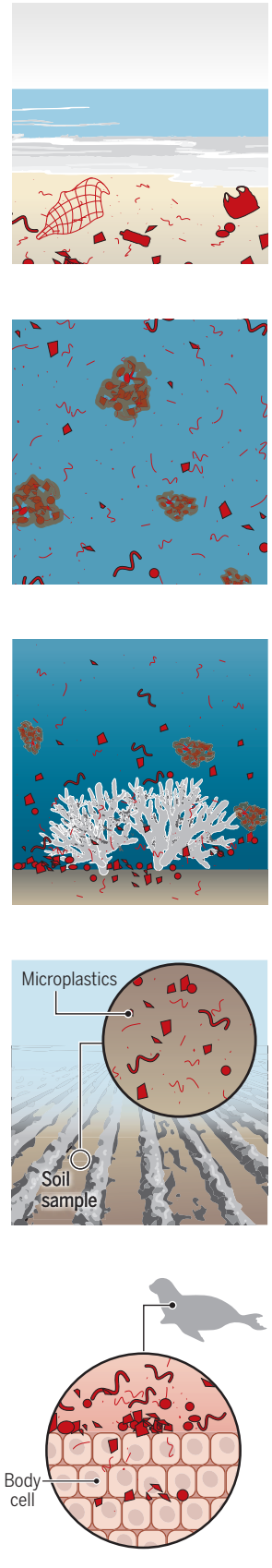

Fig. 1. Locations where poorly reversible plastic pollution accumulates.

ILLUSTRATION: C. BICKEL/*SCIENCE*

Ingestion of plastic particles by diverse biota and humans has been demonstrated in numerous studies (Fig. 1E). Recently, there have been reports that small plastic particles can be taken up from the gastrointestinal tract into tissues [e.g., (*29*)], and small plastic particles have been shown to penetrate biological membranes (*30*, *31*). Current knowledge about absorption, distribution, metabolism, and excretion of plastic by organisms is hampered by limitations of the methods used (*32*) and experimental design (*33*). However, internal tissues and organs of humans and other biota could potentially be another location of accumulating and poorly reversible plastic pollution, in particular for the smallest, nanosized fraction (*34*).

Altered characteristics of poorly reversible plastic pollution due to weathering

Half-lives of plastic in the environment are very long and highly uncertain, and they depend strongly on both the properties of the plastic and environmental conditions (*6*, *35*). Polymer types have been ranked for their tendency to undergo environmental degradation, such as biodegradation rates decreasing in the order polyesters > polyamides (nylon) > polyolefins (e.g., polyethylene), and photodegradation rates decreasing in the order polytetrafluoroethylene > polyesters > polyamides (*36*). In addition to polymer type, degradation rates also depend on properties of the plastic material, such as the surface area/volume ratio and whether antioxidants and other stabilizers were used during formulation and compounding to increase durability. Environmental conditions affecting degradation rates include ultraviolet radiation intensity, temperature, biological activity, and mechanical stress (*10*).

The slow process of plastic weathering begins immediately upon exposure to the environment. The weathering of plastic proceeds along two interconnected and often synergistic tracks (Fig. 2): (i) fragmentation and the release of soluble or volatile components, coinciding with (ii) biofouling and oxidative degradation processes. In the context of the global threat posed by accumulating and poorly reversible plastic pollution, the physical, chemical, and biological weathering processes are important because they affect the ultimate removal and residence time in zones of poorly reversible exposure, as well as the possible impact mechanisms.

Among the first observable indications of environmental weathering of plastic are physicochemical changes in surface properties, including altered surface charge, and cracking and other changes in surface morphology due to increased polymer crystallinity. These changes and the concurrent

biological weathering processes discussed below render the surface more susceptible to fragmentation by mechanical forces (*10*)—for example, during movement across river beds, repeated washing ashore in coastal areas, and freeze-thaw action in soils. The increase in surface area that occurs as plastic fragments into micro- and nanoplastic particles also facilitates the release of chemicals present in the plastic material, including additives, residual unpolymerized monomers and oligomers (*10*), and degradation products of the plastic polymer itself (*37*). Thus, over time, plastic in the environment produces an increasingly diverse lineage of small particles and chemicals that are more mobile and accessible for uptake into wider ranges of biota than the material that originally entered the environment.

Synergistic biological weathering starts even before the fragmentation process is initiated (Fig. 2). Within hours of entering a river, lake, ocean, or likely also soil, an "eco-corona" of organic matter and microorganisms forms around plastic particles, ultimately leading to colonization of the plastic surface that occurs within days (*38*). These so-called biofilms affect the fate of plastic pollution in diverse ways. They can favor colonization by sessile organisms, excrete extracellular enzymes that break down the plastic surface, and form extracellular polymeric substances that facilitate aggregation. Biofilms also lead to the alteration of buoyancy as described above, provide an additional sorption phase for chemicals, and slow down the sorption/desorption kinetics of chemicals. By shielding the particle's surface from ultraviolet radiation and other factors that facilitate weathering, biofilms decrease rates of fragmentation. Uptake of plastic particles coated with biofilm is also enhanced when selective feeders mistake them for food. After ingestion, weathering of plastic may continue because particles can fragment in the digestive system (*39*).

Considering how environmental properties influence plastic weathering (*6*, *10*, *12*, *35*), it is possible to rank how rapidly weathering likely proceeds in the accumulation zones in Fig. 1. The most rapid weathering likely occurs on the ocean surface (Fig. 1A), driven by direct exposure to sunlight, mechanical forces (wind, waves), and temperature variations. Plastic in surface soils (Fig. 1D) also has direct exposure to sunlight and a high concentration of active biological organisms. Weathering rates likely decrease with increasing depth in the water column (Fig. 1, B and C) and in deeper soils and sediments that plastics reach through tilling and bioturbation (Fig. 1D). Degradation of plastic within the body (Fig. 1E) is possibly dependent on the presence of suitable enzymes, their specific location in tissues, and excretion rates within the gastrointestinal tract, but this remains a research frontier.

Potential impacts of global plastic pollution

Conventional ecotoxicological risk assessment (comparing measured or predicted levels in the environment to toxicological effect thresholds derived from standard tests) indicates that plastic currently poses a risk to only a small, although likely increasing, fraction of the global ocean (*40*). However, the limitations of current ecotoxicological risk assessment applied to plastic are numerous [e.g., (*41*)]. The forms of plastic pollution that induce toxic effects, and thus the relevant exposure concentrations, are unknown, although they may already exceed proposed impact thresholds in hotspots (*40*, *42*). Exposure concentrations of small plastic particles are likely underestimated because of the continuous fragmentation of weathering plastic and the scarcity of reliable measurements, especially for nanoplastic. Considered in a broad context, the potential impacts of accumulating and poorly reversible plastic pollution of the global environment are wide-reaching, encompassing both geophysical and biological impacts, and could put added pressure on ecosystems already exposed to multiple stresses (Fig. 3A).

Geophysical impacts

Plastic pollution can influence the global carbon cycle both directly and indirectly. The direct effect is due to the small but non-negligible fraction of the 280 million to 360 million metric tons of fossil carbon converted into plastic per year (*43*) that degrades or is industrially converted (e.g., by incineration or landfilling) to carbon dioxide, methane, and other greenhouse gases. Even if the world completely ceases to use fossil fuels, emissions of greenhouse gases from plastic degradation and waste management will continue for centuries. However, indirect effects of plastic on the carbon cycle through effects on the homeostasis of the marine

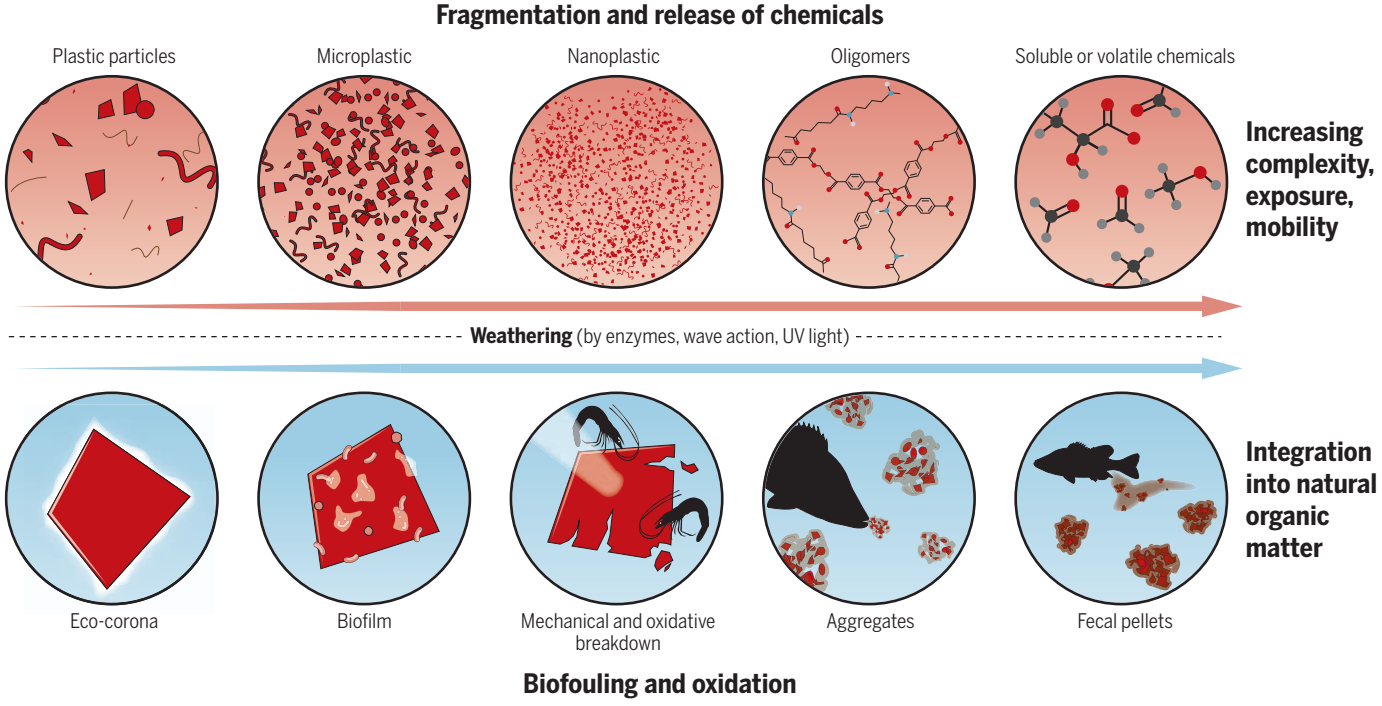

ILLUSTRATION: C. BICKEL/*SCIENCE*

Fig. 2. Weathering processes of poorly reversible plastic pollution in the environment. Weathering proceeds along two co-occurring and synergistic pathways of fragmentation and release of chemicals, and biofouling and oxidation.

carbon pump are potentially larger than the direct effects of greenhouse gas emissions. It was recently estimated that 7.8 million metric tons of plastic carbon per year currently reach the seafloor (*44*). Before settling on the seafloor, as previously described, a large fraction of the plastic will be suspended in the water column as neutrally buoyant particles (*10*, *45*). Accumulating concentrations of suspended plastic particles and heteroaggregates could affect the food sources or the turbidity levels in the habitats of cyanobacteria and phytoplankton communities. Decreasing populations of bacterial communities would lead to reduced carbon sequestration from the atmosphere. The non-sequestered carbon, which would otherwise be contributing to the marine food web, could instead remain in the atmosphere, where it would contribute to global warming (*45*). Meanwhile, the increasing loads of carbon in nonbuoyant plastic will sink, with one estimate indicating that the amount of plastic carbon being buried in seabed sediments could exceed that of natural organic carbon by 2050 in hot-spot regions (*44*).

The mechanisms that affect the marine carbon pump also affect nutrient cycling in diverse ways (*46*). Nitrogen and phosphorus cycling were shown to be affected by biofilms on microplastic in aquatic systems (*47*). Similarly, a microcosm experiment demonstrated that the presence of microplastic altered nitrogen cycling in sediment (*48*). Microplastic incorporated into marine particles may thus affect the delivery of nutrients to deep sea environments (*18*), and Earth system modeling demonstrates that there is a potential for zooplankton grazing on microplastic to accelerate the global decline of oxygen in the ocean (*49*).

Increased loads of plastic can lead to long-term changes in soil properties, such as water-holding capacity, microbial activity and diversity, nutrient availability, and soil structure (*25*). The accumulation of plastic in soils can lead to effects on plant performance and plant diversity (*50*) as well as potentially irreversible soil degradation (*51*). The formation of (micro)plastic hotspots on seabeds could have analogous impacts by changing sediment structure and composition to an extent that sediment fertility and the marine carbon pump are affected. The quantity of global soils and sediments irreversibly affected by accumulating plastic can only increase in the future.

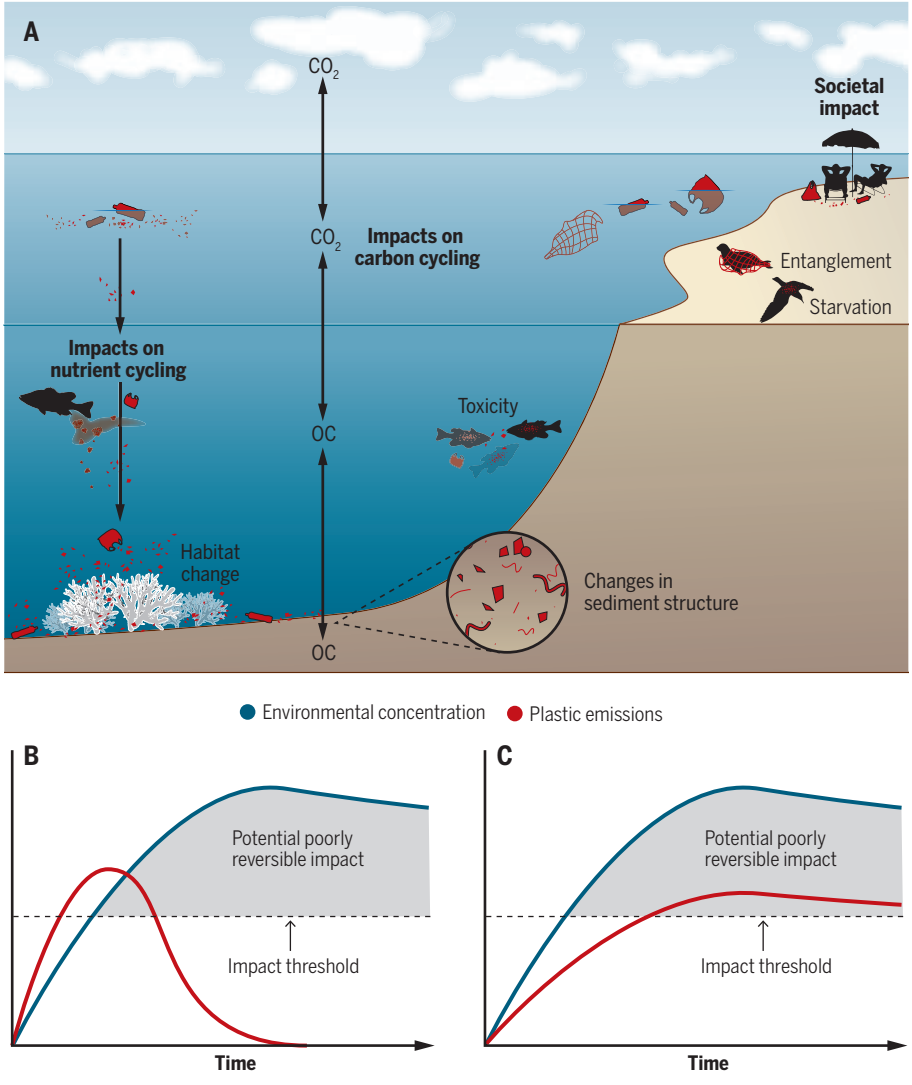

Fig. 3. Diverse potential long-term global impacts of accumulating and poorly reversible plastic pollution. (**A**) Potential impacts include geophysical impacts on carbon cycling, nutrient cycling, soil habitats, and sediment habitats; co-occurring biological impacts on endangered/keystone species and (eco)toxicity; and societal impacts resulting from the public's perception of environmental quality and policy changes. (**B** and **C**) Illustration of how plastic pollution accumulating over an impact threshold can lead to practically irreversible impacts. In (B), plastic pollution has a long residence time in the environment, and therefore concentrations do not respond to emission reductions. In (C), plastic pollution is reversible in the environment (for example, as a result of cleanup actions or degradation), but concentrations remain above the impact threshold because emissions cannot be effectively controlled. CO_2, carbon dioxide; OC, organic carbon.

Biological impacts

Wildlife encounters with macroplastic debris have been widely reported. A recent analysis listed 914 marine megafaunal species (including 226 species of seabirds, 86 species of marine mammals, all species of sea turtles, and 430 species of fishes) affected through entanglement and/or ingestion (*52*). For endangered species, not more than a few encounters are required to threaten population-level consequences. Entanglement and ingestion of plastic jeopardizes 17% of the 693 species on the International Union for Conservation of Nature Red List (*53*). In the northeastern Mediterranean, entanglement of endangered monk seals (*Monachus monachus*, 600 to 700 individuals in total) with fishing gear was identified as the second most frequent cause of mortality after deliberate killing (*54*).

Colonization of plastic surfaces is another type of interaction with organisms. A single tsunami event initiated transoceanic dispersal of nearly 300 living species over 6 years via colonization on rafting debris, indicating the potential for plastic pollution to facilitate species invasions during extreme weather events (*55*). Such complex, system-level impacts of plastic pollution indicate that more effects on species and ecosystems remain to be discovered.

Diverse impacts caused by ingestion of microplastic due to particle and chemical-related toxicity have been reported, including physical injury, changes in physiology, and impaired feeding, growth, reproduction, and oxygen consumption rates (*56*). In sediments, concentrations of macro- and nanoplastics above 0.5% were found to affect macroinvertebrate abundance (*57*). Additives leaching from plastic can also contribute to (eco)toxicological effects. One example is the concern about phthalate esters added to polyethylene mulches that are

ILLUSTRATION: C. BICKEL/*SCIENCE*

taken up in grains destined for consumption by humans and livestock (*58*). Another is the recent discovery that a phototransformation product of a ubiquitous antioxidant used in tire rubber causes acute mortality of coho salmon (*Oncorhynchus kisutch*) after stormwater runoff events (*59*).

Multiple stressors

A less-explored aspect of plastic pollution is how it can act in concert with other geophysical, biological, and chemical stressors to cause impacts. For instance, potential impacts on fisheries from overfishing and climate change could be exacerbated by impacts from plastic on carbon cycling, entanglement, and ingestion as well as toxicity. Aquatic organisms forced into adaptation due to habitat change related to altered temperatures, nutrient supply, and chemical exposure experience plastic as an additional stressor that may contribute to biodiversity loss. Soil biodiversity, as well as the limited supply of fertile soils, could be further reduced through long-term effects of accumulating plastic, which could require wetland destruction and deforestation to obtain new fertile soils. Arid areas of the world, where surface water is in short supply, may find their remaining freshwater ecosystem resources further compromised by plastic pollution, specifically through toxic plastic additives (e.g., phthalate esters, heavy metals, bisphenols, poly- and perfluoroalkyl substances) and small plastic particles that may penetrate through drinking water production systems.

Confronting the global threat from plastic pollution

The public considers plastic pollution to be a serious environmental and public health issue (*60*, *61*) (Fig. 3). Important reasons for this perception are first-hand experiences of visible plastic pollution (*62*) and increasing public concern regarding exposure to plastic-associated chemicals such as bisphenol A (*63*). Public concern about plastic pollution has inspired policy initiatives to address marine microplastic that invoke the precautionary principle because the risks to humans from microplastic have not yet been shown (*60*, *64*), and risks to some ecosystems have only recently been demonstrated [e.g., for coral reefs (*65*)]. Largely missing from this debate, however, is assessment of the potential for delayed toxicological effects due to weathering-related degradation, or additionally nontoxicological impacts on carbon and nutrient cycles, soil and sediment fertility, and biodiversity. These impacts may extend long after emissions cease if they are caused by poorly reversible plastic pollution (Fig. 3, B and C), or exceed a tipping point that causes a regime shift. In the case of possible (eco) toxicity of plastic, the potential for delayed effects has been referred to as a "global toxicity debt" (*28*).

Better understanding and management of the threat posed by plastic pollution in the environment requires research that focuses on environmental processes and fate, including the accumulation of small weathered particles (*41*), associated chemicals, and the formation of biofilms and heteroaggregates with natural organic carbon (*10*). Of particular relevance is a better understanding of these processes within the areas where poorly reversible plastic pollution is currently accumulating (Fig. 1). Discovery-oriented research aimed at identifying currently unknown impacts of weathering plastic on biogeochemical cycling and organism health is also needed.

The rational strategy to confront the potential for poorly reversible global impacts to arise from plastic pollution is to curtail emissions of plastic to the environment as rapidly and comprehensively as possible, following the prescription for transformative change suggested by Borrelle *et al.* (*4*). Precise and focused regulation has been called for to limit production and use of virgin plastic and to foster innovation to more benign yet competitive materials (*66*). Further actions could include expanding the Basel convention to only allow export of plastic waste to countries with better recycling infrastructure than the exporting country, eliminating hazardous chemicals in plastic to increase recycling potential, and developing recycling/reuse targets nationally and globally. Broader societal strategies should include eliminating unnecessary uses of plastic and encouraging behaviors that minimize plastic waste. Emerging inventories of sources of plastic pollution to the environment (*27*) can support these efforts by identifying plastic products and supply chains that should be targeted. The threat that plastic being emitted today could cause global-scale, poorly reversible impacts in the future is compelling motivation to take targeted actions to reduce emissions now.

REFERENCES AND NOTES

1. E. J. Carpenter, S. J. Anderson, G. R. Harvey, H. P. Miklas, B. B. Peck, *Science* **178**, 749–750 (1972).
2. E. J. Carpenter, K. L. Smith Jr., *Science* **175**, 1240–1241 (1972).
3. C. Ostle *et al.*, *Nat. Commun.* **10**, 1622 (2019).
4. S. B. Borrelle *et al.*, *Science* **369**, 1515–1518 (2020).
5. W. W. Y. Lau *et al.*, *Science* **369**, 1455–1461 (2020).
6. A. Chamas *et al.*, *ACS Sustain. Chem. Eng.* **8**, 3494–3511 (2020).
7. P. Harremoës *et al.*, *Late Lessons from Early Warnings: The Precautionary Principle 1896–2000* (Citeseer, 2001).
8. L. M. Persson *et al.*, *Environ. Sci. Technol.* **47**, 12619–12622 (2013).
9. M. MacLeod *et al.*, *Environ. Sci. Technol.* **48**, 11057–11063 (2014).
10. H. P. H. Arp *et al.*, *Environ. Sci. Technol.* **55**, 7246–7255 (2021).
11. T. S. Galloway, C. N. Lewis, *Proc. Natl. Acad. Sci. U.S.A.* **113**, 2331–2333 (2016).
12. A. Jahnke *et al.*, *Environ. Sci. Technol. Lett.* **4**, 85–90 (2017).
13. P. Villarrubia-Gómez, S. E. Cornell, J. Fabres, *Mar. Policy* **96**, 213–220 (2018).
14. E. van Sebille *et al.*, *Environ. Res. Lett.* **15**, 023003 (2020).
15. A. A. Koelmans, M. Kooi, K. L. Law, E. van Sebille, *Environ. Res. Lett.* **12**, 114028 (2017).
16. M. B. Tekman *et al.*, *Environ. Sci. Technol.* **54**, 4079–4090 (2020).
17. C. A. Choy *et al.*, *Sci. Rep.* **9**, 7843 (2019).
18. R. Coyle, G. Hardiman, K. O. Driscoll, *Case Stud. Chem. Environ. Eng.* 100010 (2020).
19. S. Ye, A. L. Andrady, *Mar. Pollut. Bull.* **22**, 608–613 (1991).
20. L. Khatmullina, I. Isachenko, *Mar. Pollut. Bull.* **114**, 871–880 (2017).
21. I. A. Kane *et al.*, *Science* **368**, 1140–1145 (2020).
22. M. B. Tekman, T. Krumpen, M. Bergmann, *Deep Sea Res. I* **120**, 88–99 (2017).
23. J. A. Brandon, W. Jones, M. D. Ohman, *Sci. Adv.* **5**, eaax0587 (2019).
24. M. Bläsing, W. Amelung, *Sci. Total Environ.* **612**, 422–435 (2018).
25. S. Bandopadhyay, L. Martin-Closas, A. M. Pelacho, J. M. DeBruyn, *Front. Microbiol.* **9**, 819 (2018).
26. H. P. H. Arp, H. Knutsen, *Environ. Sci. Technol.* **54**, 3–5 (2020).
27. S. Galafassi, L. Nizzetto, P. Volta, *Sci. Total Environ.* **693**, 133499 (2019).
28. M. C. Rillig, S. W. Kim, T. Y. Kim, W. R. Waldman, *Environ. Sci. Technol.* **55**, 2717–2719 (2021).
29. S. Zeytin *et al.*, *Mar. Pollut. Bull.* **156**, 111210 (2020).
30. A. F. R. M. Ramsperger *et al.*, *Water* **12**, 3216 (2020).
31. A. Ragusa *et al.*, *Environ. Int.* **146**, 106274 (2021).
32. S. Primpke *et al.*, *Appl. Spectrosc.* **74**, 1012–1047 (2020).
33. C. De Sales-Ribeiro, Y. Brito-Casillas, A. Fernandez, M. J. Caballero, *Sci. Rep.* **10**, 12434 (2020).
34. M. Shen *et al.*, *Environ. Pollut.* **252A**, 511–521 (2019).
35. J. Duan *et al.*, *Water Res.* **196**, 117011 (2021).
36. K. Min, J. D. Cuiffi, R. T. Mathers, *Nat. Commun.* **11**, 727 (2020).
37. B. Gewert, M. Plassmann, O. Sandblom, M. MacLeod, *Environ. Sci. Technol. Lett.* **5**, 272–276 (2018).
38. C. D. Rummel, A. Jahnke, E. Gorokhova, D. Kühnel, M. Schmitt-Jansen, *Environ. Sci. Technol. Lett.* **4**, 258–267 (2017).
39. A. L. Dawson *et al.*, *Nat. Commun.* **9**, 1001 (2018).
40. G. Everaert *et al.*, *Environ. Pollut.* **267**, 115499 (2020).
41. L. Wang *et al.*, *J. Hazard. Mater.* **401**, 123415 (2021).
42. E. Besseling, P. Redondo-Hasselerharm, E. M. Foekema, A. A. Koelmans, *Crit. Rev. Environ. Sci. Technol.* **49**, 32–80 (2018).
43. J. P. Dees, M. Ateia, D. L. Sanchez, *ACS ES&T Water* **1**, 214–216 (2020).
44. C. Smeaton, *Limnol. Oceanogr. Lett.* **6**, 113–118 (2021).
45. M. Shen *et al.*, *Mar. Pollut. Bull.* **150**, 110712 (2020).
46. T. J. Mincer, E. R. Zettler, L. A. Amaral-Zettler, in *Hazardous Chemicals Associated with Plastics in the Marine Environment*, H. Takada, H. K. Karapanagioti, Eds. (Springer, 2018), pp. 221–233.
47. X. Chen *et al.*, *Sci. Total Environ.* **719**, 137276 (2020).
48. M. E. Seeley, B. Song, R. Passie, R. C. Hale, *Nat. Commun.* **11**, 2372 (2020).
49. K. Kvale, A. E. F. Prowe, C. T. Chien, A. Landolfi, A. Oschlies, *Nat. Commun.* **12**, 2358 (2021).
50. A. A. de Souza Machado *et al.*, *Environ. Sci. Technol.* **53**, 6044–6052 (2019).
51. Z. Steinmetz *et al.*, *Sci. Total Environ.* **550**, 690–705 (2016).
52. S. Kühn, J. A. van Franeker, *Mar. Pollut. Bull.* **151**, 110858 (2020).
53. S. C. Gall, R. C. Thompson, *Mar. Pollut. Bull.* **92**, 170–179 (2015).
54. A. A. Karamanlidis *et al.*, *Endanger. Species Res.* **5**, 205–213 (2008).
55. J. T. Carlton *et al.*, *Science* **357**, 1402–1406 (2017).
56. N. Prinz, Š. Korez, in *YOUMARES 9—The Oceans: Our Research, Our Future: Proceedings of the 2018 Conference for Young Marine Researchers in Oldenburg, Germany*, S. Jungblut, V. Liebich, M. Bode-Dalby, Eds. (Springer, 2020), pp. 101–120.
57. P. E. Redondo-Hasselerharm, G. Gort, E. T. H. M. Peeters, A. A. Koelmans, *Sci. Adv.* **6**, eaay4054 (2020).
58. M. Shi *et al.*, *Environ. Pollut.* **250**, 1–7 (2019).
59. Z. Tian *et al.*, *Science* **371**, 185–189 (2021).
60. A. I. Catarino, J. Kramm, C. Völker, T. B. Henry, G. Everaert, *Curr. Opin. Green Sustain. Chem.* **29**, 100467 (2021).
61. J. Soares, I. Miguel, C. Venâncio, I. Lopes, M. Oliveira, *J. Hazard. Mater.* **412**, 125227 (2021).
62. B. L. Hartley *et al.*, *Mar. Pollut. Bull.* **133**, 945–955 (2018).
63. T. Jansen, L. Claassen, I. van Kamp, D. R. M. Timmermans, *Food Chem. Toxicol.* **136**, 110959 (2020).
64. T. Wardman, A. A. Koelmans, J. Whyte, S. Pahl, *Environ. Int.* **150**, 106116 (2021).
65. J. B. Lamb *et al.*, *Science* **359**, 460–462 (2018).
66. D. M. Mitrano, W. Wohlleben, *Nat. Commun.* **11**, 5324 (2020).

ACKNOWLEDGMENTS

We thank our colleagues as well as previous and current project partners for stimulating discussions. **Funding:** Supported by the Joint Programming Initiative Healthy and Productive Seas and Oceans (JPI Oceans) project WEATHER-MIC [Swedish Research Council for Environment, Agricultural Sciences and Spatial Planning (FORMAS) grant 942-2015-1866, Research Council of Norway (RCN) grant 257433/E40, German Federal Ministry of Education and Research (BMBF) grant 03F0733A], the BMBF project MICROFATE (grant 03G0268TA), and the RCN project SLUDGEFFECT (grant 302371/E10). M.B.T. was funded by the Helmholtz infrastructure program FRAM (Frontiers in Arctic Marine Research). **Author contributions:** This paper is the product of equal efforts and intellectual contributions by all four authors during conceptual development, writing, revision, and editing. M.B.T. took main responsibility for the literature research and A.J. conceptualized the figures. **Competing interests:** The authors declare no competing interests.

10.1126/science.abg5433

REVIEW

Toward polymer upcycling—adding value and tackling circularity

LaShanda T. J. Korley[1,2,3]*, Thomas H. Epps, III[1,2,3]*, Brett A. Helms[4], Anthony J. Ryan[5]

Plastics have revolutionized modern life, but have created a global waste crisis driven by our reliance and demand for low-cost, disposable materials. New approaches are vital to address challenges related to plastics waste heterogeneity, along with the property reductions induced by mechanical recycling. Chemical recycling and upcycling of polymers may enable circularity through separation strategies, chemistries that promote closed-loop recycling inherent to macromolecular design, and transformative processes that shift the life-cycle landscape. Polymer upcycling schemes may enable lower-energy pathways and minimal environmental impacts compared with traditional mechanical and chemical recycling. The emergence of industrial adoption of recycling and upcycling approaches is encouraging, solidifying the critical role for these strategies in addressing the fate of plastics and driving advances in next-generation materials design.

The rapid rise in global plastics production is largely driven by increasing consumer demands for resilient and lightweight materials, such as in single-use plastics (SUPs), that offer convenience and enhanced functionality. These desires have driven a migration toward multicomponent plastics, particularly in the packaging industry, along with the production of intricate plastic parts facilitated by innovations in manufacturing technology. Complicating this snapshot is the recent surge in SUP usage, including medical packaging, masks, gloves, containers, and utensils, during the ongoing COVID-19 pandemic (*1*, *2*). These pandemic effects may not be long-lasting, but they will certainly influence the plastics waste problem in the immediate future. Unfortunately, because of the increasing demands and complexity associated with plastics production, less than 10% of plastics are recycled world-wide, with less than 1% of plastic being recycled more than once, and only ~12% of plastics are incinerated (*3*). This lack of circularity highlights a serious threat to the environment owing to the escalating prevalence of plastics waste in landfills and aquatic environments. For example, there are over 7.4 billion metric tons of plastic in the Earth system; this number is expected to rise to 40 billion metric tons by 2050, with ~10 million metric tons of that plastic reaching the oceans every year (*4*). The amount flowing into the oceans is dwarfed by the 2.5 billion metric tons of plastics currently in use (*3*); thus, with each passing year, the flux of plastics to surface waters, coastlines, and oceans is amplified—as are the environmental, social, and economic consequences.

Plastics are difficult to recycle from postconsumer waste because of the need for separation prior to reprocessing, and from a raw cost perspective, it is typically cheaper to manufacture new, disposable plastic packaging from virgin feedstocks than to sort and reuse reprocessed material (*5*). This cost differential is exacerbated by the fact that waste disposal infrastructure varies by location, and plastic ends up in the environment through leakages from waste collection, recycling, and disposal systems, or the absence of those systems in general (*3*, *6*).

One major culprit of environmental pollution, SUPs, presents a critical conundrum given the copious volume of plastics waste generated by their use. SUP use has enabled advances in medical technologies and increases in food shelf lives and led to associated reductions in transportation costs and the concomitant lowering in harmful emissions (*7*). Hence, if these materials are banned, there may be substantial and unintended consequences that can have health and socioeconomic impacts across the globe (*4*). In short, one needs to develop and implement policies that minimize SUPs when feasible, while also advancing sustainable reuse and refill, recycling, upcycling, and degradation and composting approaches for cases in which SUPs and other plastics have important economic and performance advantages.

In developing a framework around sustainability, a key challenge is terminology. Recycling typically denotes the reuse of a previously processed or waste material; upgrading refers to the addition of value to an existing chemical or material; upcycling suggests the upgrading and reuse of an existing chemical or material; and circularity implies the act of keeping chemicals and materials in the value chain. However, there is nuance in each of these terms. For instance, the word "recycling" can encompass vastly different processes and outputs depending on the context (*8*–*11*). If one views the recycling processes as a black box, two distinct cases can be considered. First, recycling can describe the separation and deconstruction of a polymer form factor (e.g., bottle, bag, part) through a mechanical approach that usually involves considerable bond breaking of higher-molecular-weight polymer chains. The output is a polymer that normally has reduced toughness, modulus, and other structural characteristics relative to the parent material. Thus, a sizable fraction of virgin (fresh) polymer must typically be added, if the recycled plastic is intended for reuse in its original application (*12*). There are chemical recycling-based dissolution approaches that have potential to address this property degradation issue, but solvent and energy constraints currently limit scalability. Second, recycling can refer to the chemical (pyrolytic or catalytic) or biological (enzymatic) breakdown of plastics into primarily small molecules (*13*–*15*). The depolymerization outputs are commonly used as chemical feedstocks, fuels, and lubricants, but they are rarely reused as precursors to new polymers (*10*), especially in the processing of polyolefin-rich sources (*13*). Although both instances above involve the potential reuse of polymer-derived carbon atoms, a case can be made that neither route is true recycling, in which a plastic material is fully used again for the same application. By contrast, there is a commercially viable route to Nylon-6 made from regenerated caprolactam monomer, exemplified by the Econyl process (*16*), that adds value to chemically recycled (upcycled) carpets and fishing nets through the combination of a "green" marketing opportunity and resilience in materials properties.

There has been substantial focus on the upcycling of polymer waste to increase functionality or add performance (*17*). Although upcycling is a valuable strategy in the polymer sustainability portfolio, a few obstacles should be considered: (i) In many cases, upcycling can be more accurately described as upgrading because the resulting products still need to enter the recycling infrastructure; (ii) the volume of a particular plastics waste stream is typically an order of magnitude or more greater than the market size for the corresponding upgraded materials, hence, a single upgrading approach is likely to oversaturate a valuable market; and (iii) the net costs, energy inputs, and environmental impacts associated with upgrading may be greater than those associated with creating the same product from virgin material (*5*, *18*).

In short, one needs to consider a suite of recycling, upcycling, and complementary routes that minimize energy inputs, cost, and environmental impacts to create a valuable output. Furthermore, many of the current approaches

[1]Center for Plastics Innovation, University of Delaware, Newark, DE 19716, USA. [2]Center for Research in Soft matter and Polymers, and Department of Chemical and Biomolecular Engineering, University of Delaware, Newark, DE 19716, USA. [3]Department of Materials Science and Engineering, University of Delaware, Newark, DE 19716, USA. [4]The Molecular Foundry, Materials Sciences Division, and Chemical Sciences Division, Lawrence Berkeley National Laboratory, 1 Cyclotron Road, Berkeley, CA 94720, USA. [5]Grantham Centre for Sustainable Futures and the Department of Chemistry, The University of Sheffield, Brookhill, Sheffield S3 7HF, UK.
*Corresponding author. Email: lkorley@udel.edu (L.T.J.K.); thepps@udel.edu (T.H.E.)

do not necessarily result in closed-loop processes (e.g., processes in which polymers or polymer by-products are not released into the environment) and instead, "kick the can" several years down the road. Even for those that are approaching closed loop, eliminating losses remains a challenge, particularly for polyolefins, and interactions among polymers, catalysts, and additives in both homogeneous and mixed-waste chemical recycling are major contributors to process inefficiencies.

Highlighting the complexity of plastics waste

The low rate of recycling is exacerbated by increasingly mixed-waste streams that can include polymers of heterogeneous compositions sourced from various petroleum- and bio-based feedstocks (*9*, *19*, *20*). Although the complexity can stem from multilayered and additive manufactured constructs and mixed-waste streams, the compositional heterogeneity of a single-polymer waste stream should not be overlooked. For example, such a stream may contain functional additives (e.g., foaming agents, stabilizers, flame retardants, antistatic agents, plasticizers), colorants (e.g., pigments, dyes), and fillers (e.g., glass or carbon fibers, silica, calcium carbonate) (*21*). Thus, even a relatively simple, "single-component" waste product may harbor agents that kill enzymes and microbes, poison catalysts, migrate into water and soil upon mechanical processing, release harmful by-products at high temperatures, and hamper demixing efforts (*19*, *20*). Hence, it is prudent to consider not only the type(s) of polymer, i.e., high-density polyethylene (HDPE) and low-density PE (LDPE), but also the other components that comprise the material formulation. The continued development of plastics derived either fully or partially from bio-based sources adds further complexity to the recycling or upcycling landscape (*22*, *23*). It is worth noting that two classes of bio-based polymers can be featured—one, in which a bio-based feedstock is used to generate a monomer, and hence a polymer, that is chemically identical to the petroleum-derived analog, and another, in which a bio-based feedstock is employed to produce a monomer, and hence a polymer, with similar functional performance but with a chemically distinct structure [e.g., usually increased heteroatom (oxygen) content]. The first case has no mechanistic impact on the recycling or upcycling process, whereas the second case can introduce considerable materials heterogeneity to the waste stream. Thus, even though the ultimate potential for biosourcing or biodegradation can be advantageous (e.g., increased opportunities for composting or anaerobic digestion, reduced necessity to clean food residue from waste plastics), the gradual inclusion of bioplastics in mixed-waste streams can lead to a constant compositional evolution that complicates established waste treatment approaches (*11*).

The above scientific topics also intersect with policy considerations, such as differences in recycling mandates by region. Although most waste volume comes from plastics packaging in developed countries (*6*), the recycling policies (e.g., multistream versus single-stream or commingled waste collection) may vary widely across national, state, and municipal levels. Single-stream collection has led to increased consumer adoption of recycling initiatives and higher recycling rates (*24*), but this recycling policy has a direct impact on the material and energy inputs (e.g., separation requirements, multicomponent streams, impurities) that affect recyling and upcycling strategies. Thus, the interplay of consumer habits and waste management policies highlights the global effort required to tackle plastics waste pollution. Powered by technoeconomic and life-cycle analyses, valuable opportunities exist to coordinate regulatory frameworks, industrial incentives (*11*), and plastics waste infrastructure to maximize efforts toward the valorization of plastics waste.

Circularity and upcycling through synthetic innovations

For plastics and other classes of polymers to positively contribute as renewable resources to the economy, a shift toward circularity is needed. Circularity in polymer life cycles is a challenge of thermodynamics, both in the sense that no process is 100% efficient, and every process is irreversible. Furthermore, circularity in polymer recycling cannot be achieved with mechanical recycling alone owing to the chemical heterogeneity of waste streams and property deterioration; thus, chemical approaches must continue to emerge. Chemical recycling offers the conceptual ability to remove additives efficiently, and recover and refine monomers and polymers for remanufacturing; however, it is somewhat difficult to design complete pathways in a manner that requires a lower energy input than the synthesis of the polymers from virgin, small-molecule sources.

For chemical recycling by depolymerization, innovations in both catalysts and processes often go hand-in-hand. These innovations have enabled circularity opportunities for poly(ethylene terephthalate) (PET) via catalytic solvolysis (*25*) (e.g., methanolysis—Loop Industries, Indorama, and others; glycolysis—IBM and Axens) and enzymatic hydrolysis (Carbios) (*26*); note that PET is one of the easiest polymers to either mechanically or chemically/enzymatically recycle. Similarly, HPDE can be deconstructed catalytically by pyrolysis to naphtha, which reenters the manufacturing cycle for ethylene monomer and PE resin (BASF, Sabic, Plastic Energy, and others). Pyrolysis also is an effective strategy for the depolymerization of polystyrene (PS) to styrene monomer (Ineos Styrolution, Agilyx, and others), and in the special case of Nylon-6, chemical circularity has been achieved using ring-closing depolymerization (BASF, Aquafil, and others) (*27*). These thermally driven, chemical recycling processes remain energy intensive, often are intolerant to common polymer additives or impurities, give broad product distributions, and have relatively low yields of higher-value products, all of which hamper scalability. Additionally, given the intensity of the thermal processes required, current approaches are projected to generate large amounts of greenhouse gas (GHG) emissions.

For chemical recycling by dissolution–precipitation, advances have instead focused on identifying solvents for specific polymers that are nonsolvents for other polymers in mixed-plastic waste streams, as well as finding sorbents that can dissociate polymers from additives. Notably, the dissolved and precipitated polymer must be dried before repelletization for remanufacturing, which can be energy intensive. Currently, dissolution–precipitation has gained industrial traction for the recycling of isotactic polypropylene (iPP) and PS as practiced by PureCycle and Polystyvert, respectively. Selective dissolution–precipitation also has been shown to be effective in the deconstruction of multilayer films, e.g., comprising PE and PET and a soluble tie layer between them (*28*). However, there are open questions as to whether similar processes can be broadly applied to other commodity or specialty polymers. It is also unclear whether dissolution–precipitation processes are lower in life-cycle energy or GHG intensity than competing thermal depolymerization approaches. Specifically, whereas chemical recycling to monomer consumes energy by breaking chemical bonds and through refinement of chemical and monomer feedstocks, dissolution–precipitation methods require energy for evaporation and solvent recovery. A comparative study of the life-cycle impacts for depolymerization versus dissolution–precipitation processes would clarify the benefits and trade-offs of each route in pursuit of meeting global sustainability goals.

There are a growing number of new polymer chemistries (Fig. 1) for which circularity in chemical recycling is a part of the macromolecular design (*9*, *29*, *30*). The incorporation of bonds or implementation of catalysts to tailor the energetics of addition–elimination reactions underlying solvolysis or hydrolysis of condensation polymers, similar to the characteristics of PET, has emerged as a powerful strategy for deconstructing polymer chains to linear monomers. Such processes have facilitated the closed-loop chemical recycling of linear and networked conventional polyesters, polycarbonates, and polyimines, as well as new polymers based on polydiketoenamines (*7*). Notably, polydiketoenamines hydrolyze at ambient temperature in mixed-waste streams, and life-cycle assessments

have shown that the GHG and energy intensities associated with monomer recovery and refinement are lower than those for the primary production of commodity polymer resins (*31*). Similarly, and analogous to caprolactam recovery from Nylon-6, exerting kinetic control over ring-chain equilibria has been leveraged for efficient recycling of emerging classes of polymers, such as polydisulfides and polycycloolefins, from cyclic monomers (*32*). These recent demonstrations highlight how one can depolymerize polymers by inverting the thermodynamic stability of the monomer relative to the polymer as dictated by the temperature, monomer structure, polymer chain tacticity, chemical environment, and, in some cases, the catalyst. However, an added complexity arises when several monomers are combined in a copolymer to tailor properties for a specific end use. Upon depolymerization, a mixture of monomers is obtained, and refining this mixture requires processes that effectively manage the materials entropy along with the chemical entropy associated with making and breaking bonds to achieve a more sustainable life cycle (*33*).

Athough recycle-by-design concepts are still in their nascency, the market remains uncertain, if not skeptical, regarding the prospects of introducing new polymers to make products more sustainable. This position is warranted; it has taken decades to tailor commodity polymers and additives to yield manufacturable formulations that perform well in their desired end uses. Also uncertain is whether recycle-by-design concepts can advance in stride with a transition to more sustainable, bio-based feedstocks for the chemicals needed for resin production, addressing the growing market pull for bio-based circular plastics. In this regard, pairing polymer design for circularity with performance-advantaged bio-monomers may turn the traditional cost–benefit analysis of biochemicals in resin production on its head, toward disruptive and more sustainable innovations and solutions. It may be possible to use artificial intelligence and machine learning approaches to accelerate advances in polymer research and development, such as the identification of new atom- and energy-efficient strategies that hasten a transition to circular manufacturing.

Adding value beyond chemical recycling strategies

Another approach to upcycling or upgrading polymer waste is focused on innovative transformations that impart precise functionality and tailored material properties. The C–H bond has been heralded as a strategic target for property expansion of commodity polymers, such as PS, PP, polycarbonate, and poly(ethylene glycol), with chemoselectivity that facilitates upgrading of plastics waste, improves compatibilization, enables spatial patterning, and promotes the development of copolymers otherwise inaccessible through traditional synthetic methods (*34*). This suite of material diversification pathways builds upon recent advances in photoredox catalysis, radical-mediated techniques, and C–H activation (*14*, *34*, *35*). A key advantage of this upgrading strategy is that small amounts of functionalization lead to pronounced modification of material properties (e.g., adhesion, surface tension) without polymer chain degradation, generating functional materials without the synthetic complexity (e.g., monomer reactivity considerations) associated with copolymerization (*34*). These approaches also are readily applied to aromatic polymers. In the case of PS, upgrading via C–H activation to generate sulfonated polymers for electronic materials applications (*34*, *36*) may be particularly advantageous given the substantial gulf between PS's widespread usage in the food industry as packaging, containers, and utensils and its low rates of recycling because of sorting constraints and limited reuse (*12*, *37*, *38*). Moving forward in the context of life-cycle management and circularity, critical questions emerge: (i) Are these functionalization methods suitably tolerant to mixed waste or contaminated waste streams? (ii) What opportunities exist to install latent functionality to target both property tuning and closed-loop recycling? (iii) Are these upgraded materials now even more challenging to recycle and/or separate with conventional strategies? (iv) Is the market size for the differentiated upgraded materials commensurate with the supply of recycled precursor? and (v) Will polymers designed for easier recycling and upcycling generate hazardous by-products owing to their breakdown mechanisms, or will they have unintended failure mechanisms that affect their useful lifetime? Implementation of these upgrading and upcycling strategies in the current paradigm of the plastics waste dilemma will require strong academic–industry–municipality partnerships, with a systems-level focus to maximize innovation impacts from application and materials management perspectives.

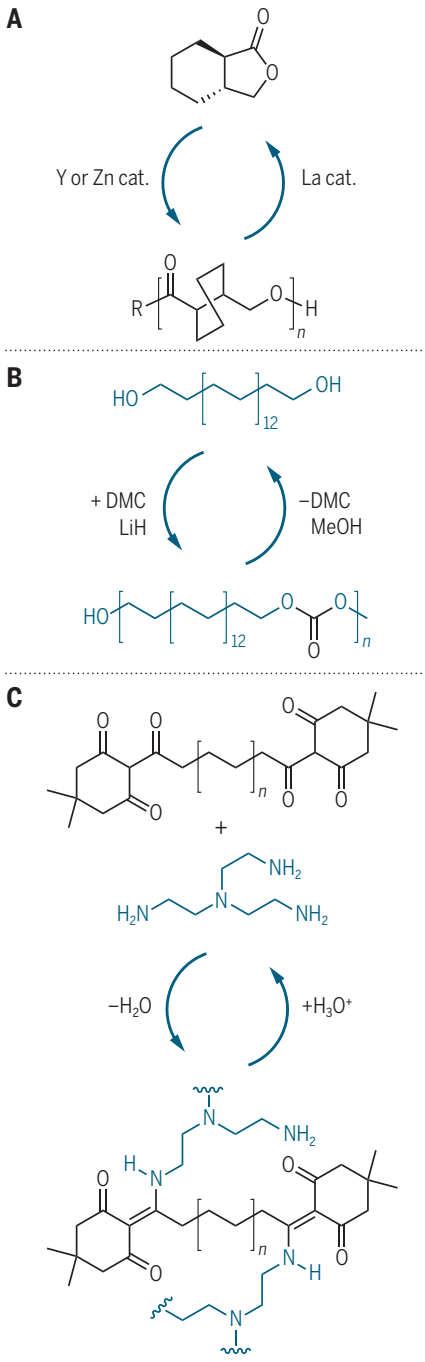

Fig. 1. Circularity in novel polymers. (**A**) Catalytic ring-opening polymerization and catalytic ring-closing depolymerization of a bicyclic lactone monomer (*29*). (**B**) Polymerization and solvolysis of a polyethylene-like polycarbonate using dimethyl carbonate (DMC) (*30*). (**C**) Polymerization and hydrolysis of a polydiketoenamine resin (*7*).

Striving for global equity

China's import ban on plastic waste in 2018 left much of the developed world with few options (*39*). The United States, Germany, the United Kingdom, and Japan initially redirected their waste shipments to Vietnam, Thailand, and Malaysia, where officials responded with their own restrictions to limit imports. Indonesia has emerged as the next epicenter for waste disposal, and the environmental impacts to crops, marine life, and air quality are growing. With global trade restrictions in place, however, more countries, provinces, and municipalities will be left to decide what to do with the growing piles of waste at home. Poor communities appear increasingly at risk to bear the brunt of the burden, and the toxic legacy of plastic waste in these communities likely will affect select regions for many years to come.

Much in the same way that the aluminum and glass industries have worked with communities to contribute to the development of recycling infrastructure for those materials, it may be time to do a similar exercise for

plastics. The European Union has been more forthcoming in this regard (*40*), where SUPs bans and extended producer responsibility regulations are in place, stimulating innovations and upgrades to materials recovery facilities, along with nucleating partnerships for managing logistics and accountability. In the United States, however, various headwinds have so far been able to stymie most legislative efforts at municipal, state, and national levels, despite general commitments to improving the sustainability of materials and products. There is growing sentiment to tax virgin resin or provide other economic incentives to level the playing field and spur increased incorporation of recyclates in resin production (*41*). For example, the United Kingdom has just introduced a new tax (*42*) that applies to plastic packaging produced in, or imported into, the United Kingdom that does not contain at least 30% recycled plastic, which is driving innovation and changes in practice. If such measures succeed in increasing recycling rates and lowering the volume of waste that is landfilled or incinerated in under resourced communities, a more equitable outcome may be within reach. Jobs creation tied to plastics recycling also could provide substantial economic benefits, factoring into the sustainability equation (*43*).

Building a more sustainable future

The plastics waste dilemma is a global challenge that requires urgent intervention (*11*, *44*) and a concerted effort that links partners across industrial, academic, financial, and government sectors buttressed by large investments in sustainability. Solutions must balance an appreciation for how advances in plastics technology have enhanced the human condition with necessary circularity considerations and life-cycle management strategies toward a sustainable ecosystem. Many current approaches tend to focus on singular aspects (e.g., waste management, process design, manufacturing strategies, catalytic innovations, or synthetic pathways) of the recycling and upcycling value proposition. Polymer upcycling will certainly be a critical piece of the solution, but it is not the silver bullet to address the entire plastics dilemma. It needs to be part of a plastics circular economy that embraces the varied forms of a reduce, reuse, and recycle philosophy. To achieve a more sustainable future, integration of not only technological considerations but also equity analysis, consumer behavior, geographical demands, policy reform, life-cycle assessment, infrastructure alignment, and supply chain partnerships is vital (*43*). Only by adopting a systems-based, multidisciplinary strategy can we implement effective and long-lasting solutions to the staggering amount of plastics waste and minimize the impacts of current and next-generation plastics.

REFERENCES AND NOTES

1. A. L. Patrício Silva *et al*., *Chem. Eng. J.* **405**, 126683 (2021).
2. E. G. Xu, Z. J. Ren, *Front. Environ. Sci. Eng.* **15**, 125 (2021).
3. R. Geyer, J. R. Jambeck, K. L. Law, *Sci. Adv.* **3**, e1700782 (2017).
4. J. R. Jambeck *et al*., *Science* **347**, 768–771 (2015).
5. S. A. Miller, *Environ. Sci. Technol.* **54**, 14143–14151 (2020).
6. D. G. Bucknall, *Philos. Trans. A Math. Phys. Eng. Sci.* **378**, 20190268 (2020).
7. P. R. Christensen, A. M. Scheuermann, K. E. Loeffler, B. A. Helms, *Nat. Chem.* **11**, 442–448 (2019).
8. J. M. Garcia, M. L. Robertson, *Science* **358**, 870–872 (2017).
9. J. Hopewell, R. Dvorak, E. Kosior, *Philos. Trans. R. Soc. Lond. B Biol. Sci.* **364**, 2115–2126 (2009).
10. H. Sardon, A. P. Dove, *Science* **360**, 380–381 (2018).
11. *Nature* **590**, 363–364 (2021).
12. Z. O. G. Schyns, M. P. Shaver, *Macromol. Rapid Commun.* **42**, e2000415 (2021).
13. A. Tennakoon *et al*., *Nat. Catal.* **3**, 893–901 (2020).
14. I. Vollmer *et al*., *Angew. Chem. Int. Ed.* **59**, 15402–15423 (2020).
15. J. C. Worch, A. P. Dove, *ACS Macro Lett.* **9**, 1494–1506 (2020).
16. Econyl, www.econyl.com/the-process/ (accessed 28 May 2021).
17. Basic Energy Sciences Roundtable on Chemical Upcycling of Polymers, https://science.osti.gov/-/media/bes/pdf/reports/2020/Chemical_Upcycling_Polymers.pdf?la=en&hash=3140F5851DD78F7D45A3B7BEF1AAC5BAA03ECD30 (accessed 18 March 2021).
18. S. Billiet, S. R. Trenor, *ACS Macro Lett.* **9**, 1376–1390 (2020).
19. A. Valavanidis, "Technological Challenges in Plastic Recycling. Can technological innnovation tackle the problem of plastic waste?" http://chem-tox-ecotox.org/ScientificReviews (2018).
20. Y.-B. Zhao, X.-D. Lv, H.-G. Ni, *Chemosphere* **209**, 707–720 (2018).
21. J. N. Hahladakis, C. A. Velis, R. Weber, E. Iacovidou, P. Purnell, *J. Hazard. Mater.* **344**, 179–199 (2018).
22. R. M. O'Dea, J. A. Willie, T. H. Epps III, *ACS Macro Lett.* **9**, 476–493 (2020).
23. Y. Zhu, C. Romain, C. K. Williams, *Nature* **540**, 354–362 (2016).
24. C. Lakhan, *Resources* **4**, 384–397 (2015).
25. C. Jehanno, M. M. Pérez-Madrigal, J. Demarteau, H. Sardon, A. P. Dove, *Polym. Chem.* **10**, 172–186 (2019).
26. V. Tournier *et al*., *Nature* **580**, 216–219 (2020).
27. T. F. Corbin, E. A. Davis, J. A. Dellinger, Reclaiming epsilon-caprolactam from Nylon 6 carpet. US 5,169,870 (1992).
28. T. W. Walker *et al*., *Sci. Adv.* **6**, eaba7599 (2020).
29. J.-B. Zhu, E. M. Watson, J. Tang, E. Y. X. Chen, *Science* **360**, 398–403 (2018).
30. M. Häußler, M. Eck, D. Rothauer, S. Mecking, *Nature* **590**, 423–427 (2021).
31. N. Vora *et al*., *Sci. Adv.* **7**, eabf0187 (2021).
32. G. W. Coates, Y. D. Y. L. Getzler, *Nat. Rev. Mater.* **5**, 501–516 (2020).
33. K. Kümmerer, J. H. Clark, V. G. Zuin, *Science* **367**, 369–370 (2020).
34. J. B. Williamson, S. E. Lewis, R. R. Johnson 3rd, I. M. Manning, F. A. Leibfarth, *Angew. Chem. Int. Ed.* **58**, 8654–8668 (2019).
35. L. Chen *et al*., *Chem* **7**, 137–145 (2021).
36. K. Wang *et al*., *ACS Appl. Mater. Interfaces* **9**, 5348–5357 (2017).
37. B. Tajeddin, B. Ahmadi, F. Sohrab, H. A. Chenarbon, in *Food Packaging and Preservation,* A. M. Grumezescu, A. M. Holban, Eds. (Academic Press, 2018), pp. 457-499.
38. J. M. García, *Chem* **1**, 813–815 (2016).
39. A. L. Brooks, S. Wang, J. R. Jambeck, *Sci. Adv.* **4**, eaat0131 (2018).
40. E. De Tandt *et al*., *Waste Manag.* **119**, 315–329 (2021).
41. Plastics Tax - A Consulting Document. https://assets.publishing.service.gov.uk/government/uploads/system/uploads/attachment_data/file/871559/Plastic_Packaging_Tax_-_Consultation.pdf (accessed 24 March 2021).
42. Plastic packaging tax, www.gov.uk/government/publications/introduction-of-plastic-packaging-tax/plastic-packaging-tax (accessed 27 March 2021.
43. A. Cecchin, R. Salomone, P. Deutz, A. Raggi, L. Cutaia, *Circ. Econ. Sust.* 10.1007/s43615-021-00021-4 (2021).
44. United Nations Environment Assembly of the United Nations Environment Programme. 3/7. https://wedocs.unep.org/bitstream/handle/20.500.11822/22773/K1800210%20-%20UNEP-EA-3-RES-7%20-%20Advance.pdf?sequence=15&isAllowed=y (accessed 24 March 2021).

ACKNOWLEDGMENTS

L.T.J.K. and T.H.E. acknowledge the US Department of Energy, Energy Frontier Research Center program (DOE DE-SC0021166; Center for Plastics Innovation), and the National Science Foundation, Growing Convergence Research program (NSF GCR CMMI—1934887), for financial and administrative support during the writing of this manuscript. B.A.H. acknowledges support from the EERE Office of Strategic Programs and Advanced Manufacturing Office under US Department of Energy contract no. DE-AC02-05CH11231. A.J.R. acknowledges support from the Grantham Foundation for the Protection of the Environment and the UKRI Smart Sustainable Plastic Packaging project, Many Happy Returns - Enabling Reusable Packaging Systems (NE/V010638/1).The views expressed in this perspective do not necessarily represent the views of the US DOE or the US government.

10.1126/science.abg4503

RESEARCH

IN *SCIENCE* JOURNALS

Edited by **Michael Funk**

Artificially colored photograph of a laser soliton microcomb chip

APPLIED OPTICS

Chip-based frequency combs

The realization of optical frequency combs, light sources with precisely spaced frequencies across a broad spectrum of wavelengths, in dielectric microresonators has affected a range of applications from imaging and ranging to precision time keeping and metrology. Xiang *et al.* demonstrate that the entire system, the laser-pumping system and the comb-generating microresonators, can be combined into an integrated silicon-based platform. Compatibility with foundry fabrication methods will enable this innovation to have a major impact on coherent communications, optical interconnects, and low-noise microwave generation. —ISO

Science, abh2076, this issue p. 99

SPATIAL GENETICS

Localizing gene expression

Single-cell RNA sequencing can provide information about cellular relationships based on shared transcriptomes, but most methods lose spatial information. Those methods that do retain spatial information can be limited to a specific set of genes and/or a small area. Srivatsan *et al*. introduce sci-Space, a spatial transcriptomic method that uses a grid of barcoded oligos on a slide that can be transferred to nuclei of an overlaid frozen tissue section to obtain both the spatial origin and the transcriptome of thousands of single cells per slide. The researchers used sci-Space to create a spatial atlas of mouse E14 sagittal sections, revealing spatially expressed genes across cell types. This application illustrates how sci-Space complements existing approaches in spatial genomics. —LMZ

Science, abb9536, this issue p. 111

NEUROIMMUNOLOGY

Encephalitis protection

Viral encephalitis is caused by infection of the central nervous system (CNS) by neurotropic viruses and can result in long-term neurological complications or death. Ghita *et al.* studied the role of the innate immune signaling adapter myeloid differentiation primary response gene 88 (MyD88) in a vesicular stomatitis virus (VSV) murine model of CNS infection. They observed that MyD88 was required for the recruitment of leukocytes to the CNS, especially $CD8^+$ T cells, and was critical for protection against death. MyD88 signaling in neurons was needed for chemokine production and leukocyte recruitment to the CNS. Together, these findings provide insight into the innate immune mechanisms involved in protection against viral encephalitis. —CNF

Sci. Immunol. **6**, eabc9165 (2021).

APPLIED PHYSICS

Direct optical polymer patterning

As a platform for electronic devices, polymeric materials offer the advantages of intrinsic flexibility and stretchability relative to hard material devices. However, unlike materials such as silicon, there are few tools for large-scale patterning of monolithic devices. Zheng *et al*. developed an optical lithography technique for the high-throughput fabrication of transistor circuitry on stretchable substrates. In this method, ultraviolet light is used to control the local solubility of the polymer, which makes it possible to fabricate

IMAGE: XIANG *ET AL.*

transistors on the micrometer scale. These devices can be made with high yield and excellent uniformity without compromising their electronic and mechanical characteristics. —MSL

Science, abh3551, this issue p. 88

MESOSCOPIC PHYSICS

A Majorana look-alike

Most experimental claims of Majorana bound states, unusual quasiparticles that may become the cornerstone of topological quantum computing, rest on the observation of a persistent zero bias peak (ZBP) in tunneling spectra. In semiconductor–superconductor heterostructures, this feature may also be caused by the topologically trivial Andreev bound states. Valentini *et al*. provide comprehensive evidence that the ZBPs observed in their experiments with semiconductor nanowires fully coated with a superconducting shell are indeed of this topologically trivial origin, in contrast to the interpretation of similar earlier experiments. The researchers identify the length of the tunnel junction in their devices as a crucial experimental parameter. —JS

Science, abf1513, this issue p. 82

ENZYME STRUCTURE

How to feed an enzyme ethane

When released from ocean floor seeps, small hydrocarbons are rapidly consumed by microorganisms. Methane is highly abundant and is both produced and consumed by microbes through well understood biochemical pathways. Less well understood is how ethane, also a major natural component of gaseous hydrocarbons, is metabolized. To understand how microbes take advantage of this energy and carbon source, Hahn *et al*. solved the x-ray crystal structures of an enzyme they call ethyl coenzyme-M reductase, which converts ethane into the thioether ethyl-coenzyme M as the entry point for catabolism. They found an expanded active site and, using a xenon gas derivatization experiment, a distinctive tunnel through the protein that is proposed to permit access of the gaseous substrate. —MAF

Science, abg1765, this issue p. 118

NEURODEVELOPMENT

How astrocytes close a critical period

During the visual critical period, brain circuits are rewired to adjust to sensory input. Closure of the critical period stabilizes the circuits. Looking at development in the mouse visual cortex, Ribot *et al*. found that astrocytes increase their expression of the gap junction channel subunit connexin 30, which in turn inhibits expression of a matrix-degrading enzyme (see the Perspective by Kofuji and Araque). As the matrix stabilizes, inhibitory interneurons mature, and the unusual flexibility of the critical period comes to an end. —PJH

Science, abf5273, this issue p. 77; see also abj6745, p. 29

CANCER

Control ALT to delete tumors

A cell's telomeres progressively shorten with each mitotic division, which eventually halts proliferation. Robinson *et al*. uncovered a mechanism that supports a type of telomere maintenance called alternative lengthening of telomeres (ALT) (see the Focus by Churikov and Géli). In cancer cell lines that maintain telomere length through ALT, the telomere-binding protein RAP1 was modified, dissociated from telomeres, and localized to the cytoplasm, where it promoted ALT-associated gene expression. This work reveals potential therapeutic opportunities to halt the growth of some tumors. —LKF

Sci. Signal. **14**, eabe9613, eabj1166 (2021)

IN OTHER JOURNALS

Edited by **Caroline Ash** *and* **Jesse Smith**

Studies in mice show that short-wavelength violet light is protective against myopia.

NEURODEVELOPMENT

Of mice, light, and eyeball length

The incidence of myopia continues to increase, fueling hypotheses that link society's increasingly indoor lifestyle to nearsightedness. Indeed, violet light, with the shortest wavelengths of visible light (360 to 400 nm), protects against the development of myopia in the mouse, chicken, and human. Jiang *et al.* have found a link with circadian rhythm, showing that violet light delivered to mice (which are nocturnal) in the evening is protective against induced myopia. The protective effect depends on neuropsin, which is required for photoentrainment of mouse retinal circadian clocks. Neuropsin is expressed in retinal ganglion cells, which support the development of the vascular choroid layer that nourishes the retina. A robust choroid normalizes eyeball shape. The authors hypothesize that equivalent timing of violet light exposure for humans might be dawn. Maybe the early bird gets the worm because it can actually see it? —PJH

Proc. Natl. Acad. Sci. U.S.A. **118**, e2018840118 (2021).

ELECTROCHEMISTRY

On the Volmer reaction mechanism

Proton-coupled electron transfer reactions at an electrochemical interface, such as electrosorption of a solvated proton (the Volmer reaction), are the key elementary steps in many electrocatalytic processes. Their characterization is challenging mainly because of the presence of an electric double layer (EDL). Using operando vibrational spectroscopy accompanied by

PHOTO: *PROC. NATL. ACAD. SCI. U.S.A.* **118**, E2018840118 (2021)

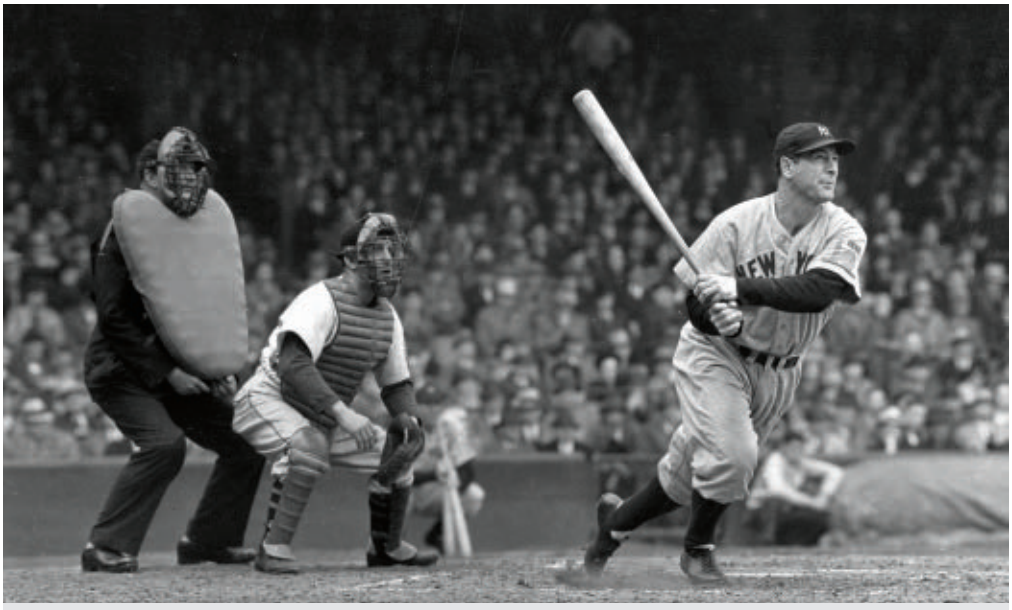

HUMAN GENOMICS

Exercise and genes linked to ALS

Amyotrophic lateral sclerosis (ALS) is a degenerative motor neuron disease with a genetic and environmental interaction. Lou Gehrig was a renowned professional American baseball player whose career was cut short by ALS, which has now also become known as Lou Gehrig's disease. Using Mendelian randomization (MR), which can help to identify genetic factors linked to phenotype, Julian *et al.* looked for genetic differences between individuals within the UK Biobank correlated with their activity level, including strenuous activity. From this, they identified genetic variants associated with ALS risk in individuals who regularly performed strenuous exercise. Of the validated ALS risk genes, 52% showed differential gene expression during exercise in individuals with such variants. Strenuous exercise is a highly heterogenous environmental factor, and more study is needed to determine how it becomes a risk factor for ALS. —LMZ *EBioMedicine* **68**, 103397 (2021).

Lou Gehrig, a renowned professional American baseball player, lent his name to a career-shortening degenerative motor neuron disease associated with strenuous exercise.

theoretical analysis, Sarkar *et al.* identified the main stages of the Volmer reaction corresponding to proton discharge from tertiary ammonium with a benzonitrile vibrational tag to a silver electrode surface, and revealed the role of the EDL in this process. They anticipate that their mechanistic insights are general and may be useful in the rational design of materials for electrochemical energy storage and conversion. —YS

J. Am. Chem. Soc. **143**, 8381 (2021).

SIGNAL TRANSDUCTION

T cell receptor dynamics

T cells are thought to integrate information from multiple encounters with antigen-presenting cells to become activated. To explore how the dynamics of T cell receptor signaling influence such a process, Harris *et al.* developed an optically controlled chimeric antigen receptor (CAR) that allowed signaling to be abruptly terminated by light pulses onto cultured cells. Signals were rapidly damped and effectively lost within 15 minutes after signal termination. This appeared to limit the window within which stimulatory signals were integrated. Nevertheless, it was possible to augment CAR-T cell activation with properly timed pulsatile stimulation of the receptors. —LBR

Mol. Syst. Biol. **17**, e10091 (2021).

CHROMATIN

Measure for nuclear measure

DNA is packaged in the nucleus in basic structural units called nucleosomes, each consisting of a segment of DNA wound around eight histone proteins. Nucleosomes are evenly spaced along the DNA unless they are interrupted by other structural landmarks such as transcription factors. What determines the spacing and phasing distances of nucleosomes is unknown, but the answer seems to lie with a group of proteins called chromatin remodelers, which are known to assemble, slide, and dismantle the histone part of nucleosomes. Oberbeckmann *et al.* show that some chromatin remodelers also contain a ruler element. Using this built-in ruler, these remodelers sense and process information in the nucleosome environment and then adjust nucleosome sliding direction bias, thus determining the spacing and phasing of nucleosomes. —DJ

Nat. Commun. **12**, 3232 (2021).

INNOVATION POLICY

Taxes on income can tax innovation

Government-funded research, which is fueled by tax revenue, drives innovation, but higher rates of taxation can suppress invention. Akcigit *et al*. show that in the United States from 1940 to 2000, personal and corporate income taxes limited the number of patents at the state level, and inventors were less likely to locate in states with higher taxes. Higher corporate tax rates lowered the share of patenting by firms compared with individuals. Higher personal income tax rates lowered the likelihood of inventors having any patent and of producing patents that were highly cited or that produced high value for their firm. —BW

Q. J. Econ. 10.1093/qje/qjab022 (2021).

GEOLOGY

Better bathymetry

Knowing the depth and evolutionary history of ocean basins is vital for understanding Earth's surface. Basin structure is controlled in large part by the topmost layer of the planet, the lithosphere. Korenaga *et al.* constructed a new reference model for the ocean lithosphere. The model incorporates accurate physical properties of crust and mantle rock, along with a variety of dynamic processes. One underappreciated way that seafloor topography is modified is through the long-term cooling of Earth. This reference model should be useful for a wide number of geophysical applications. —BG

J. Geophys. Res. Solid Earth 10.1029/2020JB021528 (2021).

PHOTO: TRANSCENDENTAL GRAPHICS/GETTY IMAGES

ALSO IN *SCIENCE* JOURNALS

Edited by **Michael Funk**

HUMAN GENOMICS

How genes affect human obesity

Obesity is linked to many human diseases, including diabetes, cancer, and heart disease. There is thus great interest in understanding how genes predispose individuals to, or protect individuals from, obesity. Akbari *et al*. sequenced more than 600,000 exomes from the United Kingdom, the United States, and Mexico and identified 16 rare coding variants (see the Perspective by Yeo and O'Rahilly). Some of the alleles associated with body mass index (BMI) were brain-expressed G protein–coupled receptors. One variant allele was found in Mexican populations at low frequency and was associated with lower BMI. Deletion of this gene in mice resulted in a resistance to weight gain, suggesting that this gene provides an avenue of study for the prevention or treatment of obesity. —LMZ

Science, abf8683, this issue p. 73; see also abh3556, p. 30

IMMUNOMETABOLISM

Macrophages: key mediators of fat storage

Recent work has suggested that macrophages may regulate adiposity, but the mechanisms underlying this process remain unresolved. Cox *et al*. report that a macrophage-derived growth factor, Pvf3, and its receptor on fat body cells are needed for lipid storage in fruit fly larvae (see the Perspective by O'Brien and Domingos). The mouse Pvf3 ortholog, PDGFcc, was similarly required to store fat in newborn and adult mice. When PDGFcc was blocked or deleted, food intake and absorption were normal, but mice increased their energy expenditure partly due to enhanced brown adipose tissue thermogenesis. PDGFcc was produced exclusively by fat-resident macrophages rather than by those mediating inflammation and insulin resistance. This work may inform future treatments for lipodystrophy, cachexia, and obesity. —STS

Science, abe9383, this issue p. 74; see also abj5072, p. 24

SYNTHETIC BIOLOGY

Building synthetic protein–based switches

Synthetic circuits can potentially help to control complex biological processes, but systems based on regulating gene expression respond to stimuli at the minute to the hour time scale. Working in yeast cells, Mishra *et al*. report synthetic regulatory circuits based on protein phosphorylation reactions that respond to inputs within seconds (see the Perspective by Kholodenko and Okada). Multicomponent logic gates allowed ultrasensitive and stable switching between states. After validating their effective synthetic circuit, the authors searched known yeast protein interaction networks for similar regulatory motifs and found previously unrecognized circuits that function as native toggle switches in yeast. —LBR

Science, aav0780, this issue p. 75; see also abj5028, p. 25

PLANT SCIENCE

Germline defense against transposons

Genomes of germ cells present an existential vulnerability to organisms because germ cell mutations will propagate to future generations. Transposable elements are one source of such mutations. In the small flowering plant *Arabidopsis*, Long *et al*. found that genome methylation in the male germline is directed by small interfering RNAs (siRNAs) imperfectly transcribed from transposons (see the Perspective by Mosher). These germline siRNAs silence germline transposons and establish inherited methylation patterns in sperm, thus maintaining the integrity of the plant genome across generations. —PJH

Science, abh0556, this issue p. 76; see also abj5020, p. 26

ZEOLITES

Stabilizing large pores

Zeolites with very large cages, such as zeolite Y, are rare but extremely useful in processing the large hydrocarbons in petroleum. Lee *et al*. report a route for preparing thermally stable forms of the large-cage phosphate-based molecular sieves UCSB-6 and UCSB-10 (see the Perspective by Xie). They used mainly sodium and cesium ions as inorganic structure-directing agents, along with an organic molecule, in their charge-density mismatch approach. These zeolites were used as diesel-cracking catalysts at 600°C. —PDS

Science, abi7208, this issue p. 104; see also abj1834, p. 28

SPECTROSCOPY

Single-molecule nanospectroscopy

Microscopic understanding and molecular-level control of individual electronic quantum states of a single molecule are a long-standing challenge in spectroscopy. Imada *et al*. found that a narrow-line tunable laser combined with a scanning tunneling microscope was able to generate photoluminescence spectra of the electronic and vibrational states of single molecules with micro–electron volt energy resolution and submolecular spatial resolution. The authors also discovered a way to tune the energy levels through a linear Stark effect and plasmon-exciton coupling in the tunneling junction. The proposed technique paves the way to efficient exploitation of energy conversion dynamics in electronic excited states, which constitutes the bedrock principle of such systems as LEDs, photovoltaics, and photosynthetic cells. —YS

Science, abg8790, this issue p. 95

PLASTIC POLLUTION

No missing sink

Estimates of the flux of microplastics from rivers, in the context of the mass of plastic that has been observed in the ocean, have made it appear that a large, unidentified sink of plastics must exist there. Weiss *et al*. show that there may not be a missing sink after all. By reformulating how mass fluxes are calculated from observations of particle numbers, they demonstrate that those mass fluxes were overestimated by two to three orders of magnitude. This explains why the residence time of plastics in the ocean seemed so puzzlingly short and implies that ocean plastics may persist and degrade over longer periods than previously thought. —HJS

Science, abe0290, this issue p. 107

CANCER

SOXing it to glioblastoma

Glioma stem cells promote the progression and therapeutic resistance of glioblastoma, a lethal brain tumor. Stemness of these cells is maintained by the transcription factor SOX2. Fang *et al*. identified DNA-dependent protein kinase (DNA-PK) as being crucial for SOX2 stability and for the maintenance of glioma stem cells. The DNA-PK catalytic subunit phosphorylated SOX2, preventing its ubiquitination and promoting stemness. Inhibition of DNA-PK with the inhibitor NU7441 led to tumor regression, prolonged survival of tumor-bearing mice, and sensitized glioblastoma xenografts to radiotherapy. DNA-PK may thus have potential as a therapeutic target for treating glioblastoma. —DLH

Sci. Transl. Med. **13**, eabc7275 (2021)

VIROLOGY

Mechanism of membrane insertion

Human papilloma viruses (HPVs), which are the source of up to 5% of human cancers, use a specialized cellular protein–trafficking complex called retromer to enter the cell from endosomes and transit to the nucleus. Xie *et al*. previously found that cell-penetrating peptides facilitated movement of part of the capsid protein of the virus into the endosomal membranes. Now, they have isolated multiple "traptamers" that inhibit HPV entry, each at different steps in the entry process. This discovery permitted an elucidation of the sequential steps required for viral entry. —PLY

Sci. Adv. 10.1126/sciadv.abh4276 (2021).

RESEARCH ARTICLE SUMMARY

HUMAN GENOMICS

Sequencing of 640,000 exomes identifies *GPR75* variants associated with protection from obesity

Parsa Akbari†, Ankit Gilani†, Olukayode Sosina†, Jack A. Kosmicki, Lori Khrimian, Yi-Ya Fang, Trikaldarshi Persaud, Victor Garcia, Dylan Sun, Alexander Li, Joelle Mbatchou, Adam E. Locke, Christian Benner, Niek Verweij, Nan Lin, Sakib Hossain, Kevin Agostinucci, Jonathan V. Pascale, Ercument Dirice, Michael Dunn, Regeneron Genetics Center, DiscovEHR Collaboration, William E. Kraus, Svati H. Shah, Yii-Der I. Chen, Jerome I. Rotter, Daniel J. Rader, Olle Melander, Christopher D. Still, Tooraj Mirshahi, David J. Carey, Jaime Berumen-Campos, Pablo Kuri-Morales, Jesus Alegre-Díaz, Jason M. Torres, Jonathan R. Emberson, Rory Collins, Suganthi Balasubramanian, Alicia Hawes, Marcus Jones, Brian Zambrowicz, Andrew J. Murphy, Charles Paulding, Giovanni Coppola, John D. Overton, Jeffrey G. Reid, Alan R. Shuldiner, Michael Cantor, Hyun M. Kang, Goncalo R. Abecasis, Katia Karalis, Aris N. Economides, Jonathan Marchini, George D. Yancopoulos, Mark W. Sleeman, Judith Altarejos, Giusy Della Gatta, Roberto Tapia-Conyer‡, Michal L. Schwartzman‡, Aris Baras‡*, Manuel A. R. Ferreira‡, Luca A. Lotta‡*

INTRODUCTION: Obesity accounts for a substantial and growing burden of disease globally. Body adiposity is highly heritable, and human genetic studies can lead to biological and therapeutic insights.

RATIONALE: Whole-exome sequencing of hundreds of thousands of individuals is complementary to approaches used to date in obesity genetics and has the potential to identify rare protein-coding variants with large phenotypic impact. We sequenced the exomes of 645,626 individuals from the UK, the US, and Mexico and estimated associations of rare coding variants with body mass index (BMI), a measure of overall adiposity used to define obesity in clinical practice. We complemented exome sequencing with fine-mapping of common alleles, polygenic score analysis, and in vitro and in vivo modeling work.

RESULTS: We identified 16 genes for which the burden of rare nonsynonymous variants was associated with BMI at exome-wide statistical significance (inverse-variance weighted meta-analysis $P < 3.6 \times 10^{-7}$), including associations at five brain-expressed G protein–coupled receptors (*CALCR*, *MC4R*, *GIPR*, *GPR151*, and *GPR75*). We observed an overrepresentation of genes highly expressed in the hypothalamus, a key center for the neuroendocrine regulation of energy balance. Protein-truncating variants in *GPR75* were found in ~4/10,000 sequenced people and were associated with 1.8 kg/m^2 lower BMI, 5.3 kg lower bodyweight, and 54% lower odds of obesity in heterozygous carriers. Knock out of *Gpr75* in mice resulted in resistance to weight gain in a high-fat diet model, which was allele-dose dependent (25% and 44% lower weight gain, respectively, for heterozygous *Gpr75*$^{-/+}$ mice and knockout *Gpr75*$^{-/-}$ mice compared with wild type) and accompanied by improved glycemic control and insulin sensitivity. Protein-truncating variants in *CALCR* were associated with higher BMI and obesity risk, whereas protein-truncating variants in *GIPR* and two missense alleles [Arg^{190}→Gln (Arg190Gln), Glu288Gly], which we show result in loss of function in vitro, were associated with lower adiposity. Among monogenic obesity genes in the leptin-melanocortin pathway, heterozygous predicted loss-of-function variants in *LEP*, *POMC*, *PCSK1*, and *MC4R* (but not *LEPR*) were associated with higher BMI. Rare protein-truncating variants in *UBR2*, *ANO4*, and *PCSK1* were associated with more than twofold higher odds of obesity in heterozygous carriers, similar to predicted-deleterious nonsynonymous variants in *MC4R*, which are considered the most common cause of monogenic obesity. Polygenic predisposition due to >2 million common genetic variants influenced the penetrance of obesity in rare variant carriers in an additive fashion.

CONCLUSION: These results suggest that inhibition of GPR75 may be a therapeutic strategy for obesity and illustrate the power of massive-scale exome sequencing for the identification of large-effect coding variant associations and drug targets for complex traits. ■

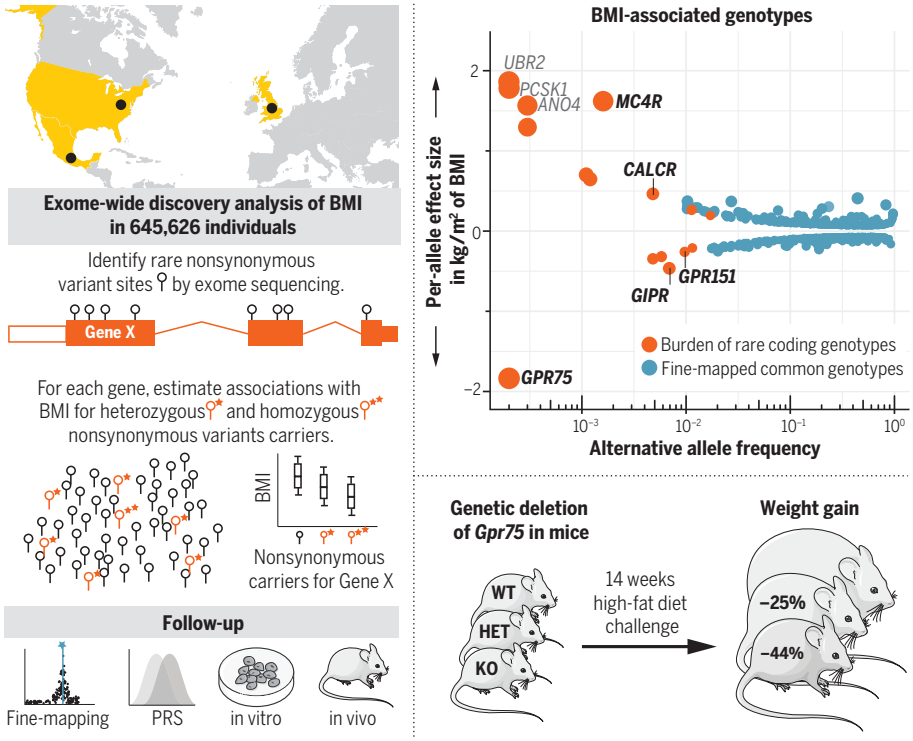

Exome sequencing–based discovery of BMI-associated genes. (Left) Design for the discovery gene-burden analysis, with a depiction of follow-up analyses along the bottom. (Top right) Relationship between allele frequency and effect-size estimates for BMI-associated genotypes. (Bottom right) Weight gain for *Gpr75*$^{+/+}$ (wild type, WT), *Gpr75*$^{-/+}$ (heterozygous, HET), and *Gpr75*$^{-/-}$ (knockout, KO) mice during a high-fat diet challenge. PRS, polygenic risk score.

The list of author affiliations is available in the full article online.
*Corresponding author. Email: luca.lotta@regeneron.com (L.A.L.); aris.baras@regeneron.com (A.B.)
†These authors contributed equally to this work.
‡These authors contributed equally to this work.
Cite this article as P. Akbari *et al.*, *Science* 373, eabf8683 (2021). DOI: 10.1126/science.abf8683

READ THE FULL ARTICLE AT
https://doi.org/10.1126/science.abf8683

RESEARCH ARTICLE

HUMAN GENOMICS

Sequencing of 640,000 exomes identifies *GPR75* variants associated with protection from obesity

Parsa Akbari[1]†, Ankit Gilani[2]†, Olukayode Sosina[1]†, Jack A. Kosmicki[1], Lori Khrimian[3], Yi-Ya Fang[3], Trikaldarshi Persaud[1], Victor Garcia[2], Dylan Sun[1], Alexander Li[1], Joelle Mbatchou[1], Adam E. Locke[1], Christian Benner[1], Niek Verweij[1], Nan Lin[1], Sakib Hossain[2], Kevin Agostinucci[2], Jonathan V. Pascale[2], Ercument Dirice[2], Michael Dunn[3], Regeneron Genetics Center‡, DiscovEHR Collaboration‡, William E. Kraus[4,5], Svati H. Shah[6,7], Yii-Der I. Chen[8], Jerome I. Rotter[8], Daniel J. Rader[9], Olle Melander[10,11], Christopher D. Still[12], Tooraj Mirshahi[12], David J. Carey[12], Jaime Berumen-Campos[13], Pablo Kuri-Morales[13], Jesus Alegre-Díaz[13], Jason M. Torres[14], Jonathan R. Emberson[14], Rory Collins[14], Suganthi Balasubramanian[1], Alicia Hawes[1], Marcus Jones[1], Brian Zambrowicz[3], Andrew J. Murphy[3], Charles Paulding[1], Giovanni Coppola[1], John D. Overton[1], Jeffrey G. Reid[1], Alan R. Shuldiner[1], Michael Cantor[1], Hyun M. Kang[1], Goncalo R. Abecasis[1], Katia Karalis[1], Aris N. Economides[1,3], Jonathan Marchini[1], George D. Yancopoulos[3], Mark W. Sleeman[3], Judith Altarejos[3], Giusy Della Gatta[1], Roberto Tapia-Conyer[13]§, Michal L. Schwartzman[2]§, Aris Baras[1]§*, Manuel A. R. Ferreira[1]§, Luca A. Lotta[1]§*

Large-scale human exome sequencing can identify rare protein-coding variants with a large impact on complex traits such as body adiposity. We sequenced the exomes of 645,626 individuals from the United Kingdom, the United States, and Mexico and estimated associations of rare coding variants with body mass index (BMI). We identified 16 genes with an exome-wide significant association with BMI, including those encoding five brain-expressed G protein–coupled receptors (*CALCR*, *MC4R*, *GIPR*, *GPR151*, and *GPR75*). Protein-truncating variants in *GPR75* were observed in ~4/10,000 sequenced individuals and were associated with 1.8 kilograms per square meter lower BMI and 54% lower odds of obesity in the heterozygous state. Knock out of *Gpr75* in mice resulted in resistance to weight gain and improved glycemic control in a high-fat diet model. Inhibition of GPR75 may provide a therapeutic strategy for obesity.

Obesity and its health complications account for a substantial and growing burden of global disease. Understanding the genetic and molecular underpinnings of body adiposity can be a pathway to the development of safe and effective therapeutic strategies. Body fat is a highly heritable trait, and genetic studies have revealed biological pathways that regulate energy balance. Studies in mouse models (*1*–*3*) and human forms of extreme, early-onset obesity (*4*–*10*) have uncovered the influence of the leptin-melanocortin system on appetite regulation. Additionally, genome-wide association studies (GWASs) of body mass index (BMI) have highlighted the polygenic contribution to the inherited basis of adiposity, identifying thousands of common genetic variants, each with small effect size, and reaffirming the broad influence of the central nervous system on body mass regulation (*11*–*15*).

Studies of rare protein-coding variants have helped translate genetic associations into biological and therapeutic insights (*4*, *6*–*10*, *16*–*24*). Analyses of coding variation in human obesity have focused on (i) candidate gene or exome sequencing in pedigrees or case collections with extreme phenotypes or (ii) array-genotyping of cataloged variant sites in large cohorts. Whole-exome sequencing of hundreds of thousands of individuals from population or health system–based studies is a complementary approach that may identify large-effect coding variants influencing the propensity to become obese or protection against obesity (*25*–*28*). Here, we report a multiethnic exome-sequencing association study for BMI in more than 640,000 individuals across three distinct cohorts and regions of the world (the United Kingdom, the United States, and Mexico).

Exome-wide gene-burden association of rare coding alleles with body mass index

We performed high-coverage whole-exome sequencing in 645,626 individuals (*29*), including 428,719 individuals of European ancestry from the UK Biobank cohort (UKB; table S1) (*30*), 121,061 individuals of European ancestry from the MyCode Community Health Initiative cohort from the US-based Geisinger Health System (GHS; table S1) (*31*), and 95,846 individuals of admixed American ancestry from the Mexico City Prospective Study (MCPS; table S1) (*32*).

In an exome-wide meta-analysis across these three cohorts, there were 16 genes for which the burden of rare nonsynonymous genetic variants was associated with BMI at the exome-wide level of statistical significance [inverse-variance weighted (IVW) meta-analysis $P < 3.6 \times 10^{-7}$, a Bonferroni correction for 20,000 genes, and seven variant selection models (*29*); Table 1 and fig. S1]. These associations were conditionally-independent of BMI-associated common variants identified by fine-mapping genome-wide association signals (*29*) and were consistent across the constituent datasets of the meta-analysis (table S2).

Among the 16 genes, our analysis identified two for which rare mutations are known to cause monogenic obesity [*MC4R* (melanocortin 4 receptor) (*8*, *9*) and *PCSK1* (proprotein convertase subtilisin/kexin type 1) (*6*)] and two genes where rare coding variants have been associated with BMI [*GPR151* (G protein–coupled receptor 151) (*33*) and *GIPR* (gastric inhibitory polypeptide receptor) (*16*)]. For the other 12 genes, our study provides genetic evidence linking rare coding variation to BMI and obesity-related phenotypes. Five of the 16 genes encode G protein–coupled receptors (GPCRs; the largest class of drug targets in the human genome) (*34*) expressed in the brain and central nervous system [*GPR75* (G protein–coupled receptor 75), *CALCR* (calcitonin receptor), *GIPR*, *GPR151*, and *MC4R*]. A tissue expression analysis for BMI-associated genes in our results revealed an overrepresentation of genes that are highly and specifically expressed in the hypothalamus, a key center for the neuroendocrine regulation of energy balance (fig. S2).

[1]Regeneron Genetics Center, Regeneron Pharmaceuticals Inc., Tarrytown, NY 10591, USA. [2]Department of Pharmacology and Medicine, New York Medical College School of Medicine, Valhalla, NY 10595, USA. [3]Regeneron Pharmaceuticals Inc., Tarrytown, NY 10591, USA. [4]Division of Cardiology, Duke University Medical Center, Durham, NC 27710, USA. [5]Duke Center for Living, Duke University Medical Center, Durham, NC 27705, USA. [6]Department of Medicine, Duke University Medical Center, Durham, NC 27710, USA. [7]Duke Molecular Physiology Institute, Duke University Medical Center, Durham, NC 27701, USA. [8]Institute for Translational Genomics and Population Sciences, The Lundquist Institute for Biomedical Innovation, and Department of Pediatrics, Harbor-UCLA Medical Center, Torrance, CA 90502, USA. [9]Department of Genetics, Perelman School of Medicine, University of Pennsylvania, PA 19104, USA. [10]Department of Clinical Sciences Malmö, Lund University, 221 00 Malmö, Sweden. [11]Department of Emergency and Internal Medicine, Skåne University Hospital, 214 28, Malmö, Sweden. [12]Geisinger Obesity Institute, Geisinger Health System, Danville, PA 17882, USA. [13]Faculty of Medicine, National Autonomous University of Mexico, Copilco Universidad, Coyoacán, 4360 Ciudad de México, Mexico. [14]Nuffield Department of Population Health, University of Oxford, Oxford OX3 7LF, England, UK.

*Corresponding author. Email: luca.lotta@regeneron.com (L.A.L.); aris.baras@regeneron.com (A.B.)

†These authors contributed equally to this work. ‡A complete list of investigators contributing to the Regeneron Genetics Center and DiscovEHR Collaboration is provided at the end of this paper. §These authors contributed equally to this work.

Table 1. Associations with body mass index in the exome-wide gene-burden analysis. The table reports genes for which the gene burden of rare nonsynonymous variants was associated with body mass index at the exome-wide level of statistical significance ($P < 3.6 \times 10^{-7}$). Analyses were performed in 645,626 participants from the UKB, GHS, and MCPS studies. Genomic coordinates reflect chromosome and physical position in base pairs according to Genome Reference Consortium Human Build 38. Abbreviations: CI, confidence interval; SD, standard deviation; BMI, body mass index; AAF, alternative allele frequency; RR, reference-reference genotype; RA, reference-alternative heterozygous genotype; AA, alternative-alternative homozygous genotype; pLOF, predicted loss of function; missense (1/5), missense variant predicted to be deleterious by at least 1 out of 5 in silico prediction algorithms; missense (5/5), missense variant predicted to be deleterious by 5 out of 5 in silico prediction algorithms.

Gene	Genomic coordinates	Genetic exposure, variant type; frequency cutoff in %	Beta (95% CI) per allele in SD units of BMI	*P*	AAF (fraction of 1)	Genotype counts (RR|RA|AA genotypes)	Beta (95% CI) per allele in kg/m^2 units of BMI	Beta (95% CI) per allele in kg of body weight	Beta (95% CI) per allele in lb of body weight
UHMK1	1: 162497250	pLOF plus missense (5/5); AAF < 1%	−0.06 (−0.09, −0.04)	4.9×10^{-8}	0.0048	639,499|6,117|10	−0.3 (−0.5, −0.2)	−1.0 (−1.4, −0.6)	−2.2 (−3.0, −1.4)
GPR75	2: 53853133	pLOF; AAF < 1%	−0.34 (−0.46, −0.22)	2.6×10^{-8}	0.0002	645,398|228|0	−1.8 (−2.5, −1.2)	−5.3 (−7.1, −3.4)	−11.6 (−15.7, −7.5)
ROBO1	3: 78598912	pLOF; AAF < 1%	0.24 (0.15, 0.32)	5.6×10^{-8}	0.0003	645,182|444|0	1.3 (0.8, 1.7)	3.7 (2.4, 5.0)	8.1 (5.2, 11.1)
KIAA1109	4: 122170647	pLOF; AAF < 1%	0.13 (0.09 0.18)	5.1×10^{-8}	0.0011	644,238|1,388|0	0.7 (0.5, 1.0)	2.1 (1.3, 2.9)	4.6 (3.0, 6.3)
PCSK1	5: 96393000	pLOF; AAF < 1%	0.33 (0.21, 0.44)	1.0×10^{-8}	0.0002	645,368|258|0	1.8 (1.2, 2.4)	5.1 (3.3, 6.8)	11.2 (7.4, 15.0)
GPR151	5: 146514853	pLOF plus missense (5/5); AAF < 1%	−0.05 (−0.06, −0.03)	5.7×10^{-9}	0.0097	633,209|12,372|45	−0.3 (−0.4, −0.2)	−0.7 (−1.0, −0.5)	−1.7 (−2.2, −1.1)
SPARC	5: 151663570	pLOF plus missense (1/5); AAF < 1%	0.05 (0.03, 0.06)	1.2×10^{-10}	0.0113	631,094|14,494|38	0.3 (0.2, 0.4)	0.8 (0.5, 1.0)	1.7 (1.2, 2.2)
UBR2	6: 42564319	pLOF; AAF < 1%	0.34 (0.23, 0.45)	2.4×10^{-9}	0.0002	645,363|263|0	1.8 (1.2, 2.4)	5.2 (3.5, 7.0)	11.5 (7.8, 15.3)
CALCR	7: 93426355	pLOF plus missense (1/5); AAF < 0.1%	0.09 (0.06, 0.11)	1.4×10^{-13}	0.0048	639,416|6,208|2	0.5 (0.3, 0.6)	1.3 (1.0, 1.7)	3.0 (2.2, 3.8)
PDE3B	11: 14644075	pLOF; AAF < 1%	0.12 (0.08 0.17)	1.7×10^{-7}	0.0012	644,074|1,552|0	0.7 (0.4, 0.9)	1.9 (1.2, 2.6)	4.2 (2.6, 5.7)
ANO4	12: 100901785	pLOF; AAF < 1%	0.29 (0.19, 0.38)	1.1×10^{-9}	0.0003	645,248|378|0	1.6 (1.1, 2.1)	4.5 (3.0, 5.9)	9.9 (6.7, 13.0)
KIAA0586	14: 58427628	pLOF plus missense (5/5); AAF < 1%	−0.04 (−0.05, −0.02)	3.1×10^{-7}	0.0115	630,769|14,844|13	−0.2 (−0.3, −0.1)	−0.6 (−0.8, −0.4)	−1.3 (−1.8, −0.8)
MC4R	18: 60371350	pLOF plus missense (5/5); AAF < 1%	0.30 (0.26, 0.34)	4.0×10^{-48}	0.0016	643,589|2,036|1	1.6 (1.4, 1.8)	4.6 (4.0, 5.3)	10.2 (8.8, 11.6)
DPP9	19: 4676563	pLOF plus missense (5/5); AAF < 1%	−0.06 (−0.08, −0.04)	2.0×10^{-8}	0.0058	638,141|7,469|16	−0.3 (−0.4, −0.2)	−0.9 (−1.3, −0.6)	−2.0 (−2.8, −1.3)
ANKRD27	19: 32598144	pLOF plus missense (1/5); AAF < 1%	0.04 (0.02, 0.05)	5.9×10^{-9}	0.0171	623,572|22,016|38	0.2 (0.1, 0.3)	0.6 (0.4, 0.8)	1.3 (0.8, 1.7)
GIPR	19: 45669520	pLOF plus missense (1/5); AAF < 1%	−0.09 (−0.11, −0.07)	9.3×10^{-19}	0.0069	636,680|8,937|9	−0.5 (−0.6, −0.4)	−1.3 (−1.6, −1.0)	−3.0 (−3.6, −2.3)

Protein-truncating *GPR75* variants associated with leanness and protection against obesity in humans

We explored in depth the association for rare predicted loss-of-function (pLOF) variants in the *GPR75* gene, as this gene encodes a GPCR highly expressed in the brain across species, and this association was the largest effect-size association with lower BMI in our exome-wide analysis. Predicted loss-of-function variants in *GPR75* were observed in ~4 out of every 10,000 sequenced people, with similar frequency across populations (table S2), and carrier status was associated with 0.34 standard deviations lower BMI, corresponding to 1.8 kg/m^2 lower BMI or about 5.3 kg, or 12 lb, lower body weight (Table 1 and Fig. 1A).

The association with lower BMI was directionally consistent and statistically significant in each of the constituent cohorts of our discovery meta-analysis (table S2) as well as within age and sex subgroups (table S3). We further corroborated the association of *GPR75* pLOF variants with lower BMI in a combined analysis including an additional 91,328 individuals not included in the discovery set [per-allele beta in standard deviation (SD) units of BMI in the meta-analysis of discovery and additional cohorts, −0.34; 95% confidence interval (CI), −0.45, −0.22; $P = 6.9 \times 10^{-9}$] (Fig. 1B). This strong association with lower BMI was accompanied by a corresponding association with protection against obesity. Heterozygous carriers of *GPR75* pLOF variants had 54% lower odds of obesity compared with noncarriers in a meta-analysis of the UKB, GHS, and MCPS cohorts [table S4; per-allele odds ratio (OR), 0.46; 95% CI, 0.31, 0.67; $P = 6.9 \times 10^{-5}$], and their distribution across BMI categories was drastically shifted toward lower BMI categories (Fig. 2). None of 228 heterozygous carriers of *GPR75* pLOF variants were underweight

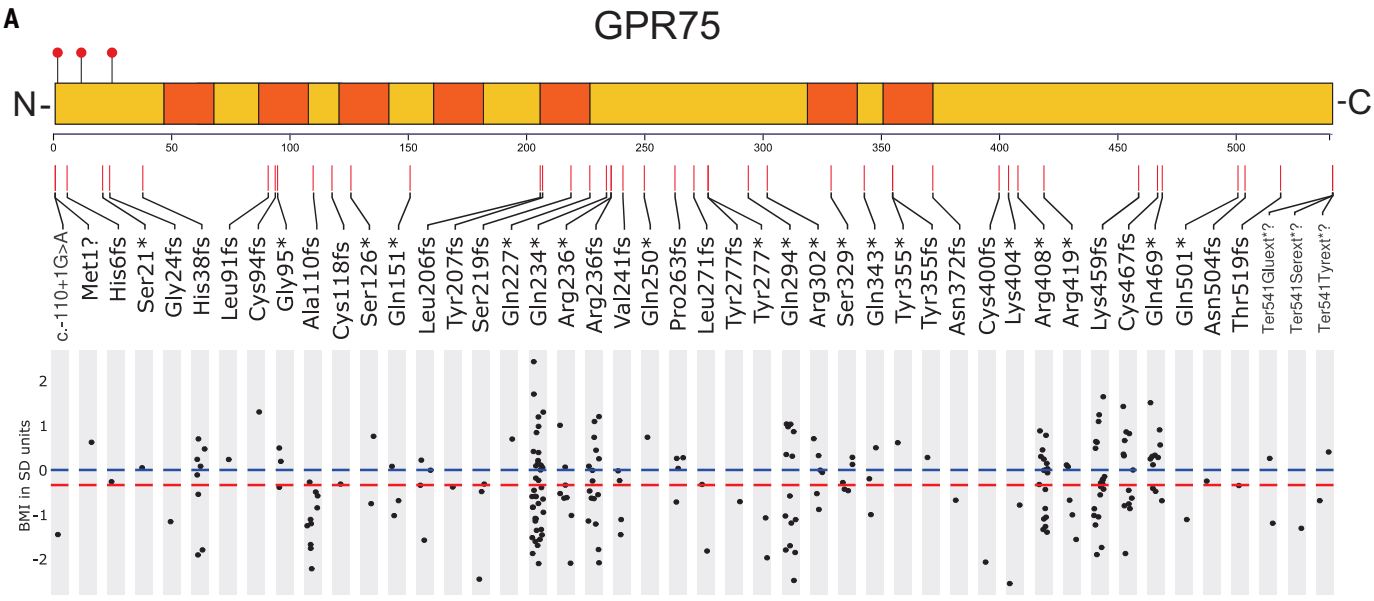

B

Study	Beta (95% CI) in SDs of BMI	Genotypes (RR|RA|AA)	p-value	Beta (95% CI) in kg/m² of BMI	Beta (95% CI) in kg of body weight
Discovery Cohorts					
MCPS	-0.48 (-0.82, -0.13)	95,816|30|0	7.1E-03	-2.6 (-4.4, -0.7)	-7.4 (-12.8, -2)
GHS_EUR	-0.27 (-0.52, -0.02)	121,010|51|0	3.6E-02	-1.4 (-2.8, -0.1)	-4.2 (-8, -0.3)
UKB_EUR	-0.34 (-0.49, -0.19)	428,572|147|0	6.6E-06	-1.8 (-2.6, -1)	-5.3 (-7.6, -3)
Subgroup meta-analysis results	-0.34 (-0.46, -0.22)	645,398|228|0	2.6E-08	-1.8 (-2.5, -1.2)	-5.3 (-7.1, -3.4)
Additional Cohorts					
DHS_AMR	-1.85 (-3.81, 0.10)	699|1|0	6.4E-02	-10 (-20.6, 0.6)	-28.9 (-59.5, 1.6)
SINAI_EAS	1.01 (-0.87, 2.90)	745|1|0	2.7E-01	5.5 (-4.7, 15.7)	15.8 (-13.7, 45.3)
DHS_EUR	-1.56 (-3.52, 0.40)	1,387|1|0	1.2E-01	-8.4 (-19, 2.2)	-24.4 (-54.9, 6.2)
DUKE_AFR	-1.66 (-3.62, 0.30)	1,637|1|0	9.7E-02	-9 (-19.5, 1.6)	-25.9 (-56.5, 4.7)
DUKE_EUR	-0.60 (-2.56, 1.36)	6,532|1|0	5.5E-01	-3.3 (-13.8, 7.3)	-9.4 (-40, 21.2)
TAICHI_EAS	0.10 (-1.86, 2.06)	11,222|1|0	9.2E-01	0.6 (-10, 11.1)	1.6 (-29, 32.1)
PMBB_EUR	-2.09 (-4.05, -0.14)	7,518|1|0	3.7E-02	-11.3 (-21.9, -0.7)	-32.7 (-63.3, -2.1)
SINAI_EUR	-0.04 (-1.37, 1.30)	9,135|2|0	9.7E-01	-0.2 (-7.4, 7)	-0.6 (-21.4, 20.2)
SINAI_AFR	-0.26 (-1.62, 1.10)	11,258|2|0	7.0E-01	-1.4 (-8.8, 6)	-4.1 (-25.3, 17.2)
UKB_EAS	-0.59 (-1.68, 0.51)	2,200|3|0	2.9E-01	-3.2 (-9.1, 2.7)	-9.2 (-26.2, 7.9)
UKB_SAS	-0.11 (-1.08, 0.87)	10,114|4|0	8.3E-01	-0.6 (-5.8, 4.7)	-1.7 (-16.9, 13.5)
MALMO_EUR	0.33 (-0.53, 1.19)	28,858|5|0	4.5E-01	1.8 (-2.8, 6.5)	5.2 (-8.2, 18.6)
Subgroup meta-analysis results	-0.33 (-0.73, 0.07)	91,305|23|0	1.1E-01	-1.8 (-3.9, 0.4)	-5.1 (-11.4, 1.2)
Overall meta-analysis results **Between subgroups p-heterogeneity = 0.96**	-0.34 (-0.45, -0.22)	736,703|251|0	6.9E-09	-1.8 (-2.4, -1.2)	-5.3 (-7, -3.5)

Fig. 1. Protein-truncating variants in *GPR75* associated with lower body mass index in humans. (**A**) Linear model of the GPR75 protein and its domains (top; intra- and extracellular domains in yellow, transmembrane domains in orange), the distribution on the GPR75 protein of 46 pLOF variants found by exome sequencing (middle), and the distribution of BMI in standardized units among heterozygous carriers of each variant (bottom). In the bottom subpanel, horizontal blue bars show the mean BMI in noncarriers, while horizontal red bars show the overall covariates-adjusted mean BMI in carriers of any pLOF genetic variant in *GPR75*. (**B**) Meta-analysis of the association with BMI of pLOF variants in *GPR75* in discovery and additional cohorts. Abbreviations: CI, confidence interval; RR, reference-reference genotype; RA, reference-alternative heterozygous genotype; AA, alternative-alternative homozygous genotype; DHS, Dallas Heart Study; SINAI, Mount Sinai BioMe cohort; DUKE, Duke Catheterization Genetics cohort; TAICHI, Taiwanese Chinese persons from the Taiwan Metabochip Consortium; PMBB, University of Pennsylvania Medicine BioBank; MALMO, Malmö Diet and Cancer Study; AFR, African ancestry; AMR, American ancestry; EAS, East Asian ancestry; EUR, European ancestry; SAS, South Asian ancestry. MCPS included individuals of admixed American ancestry.

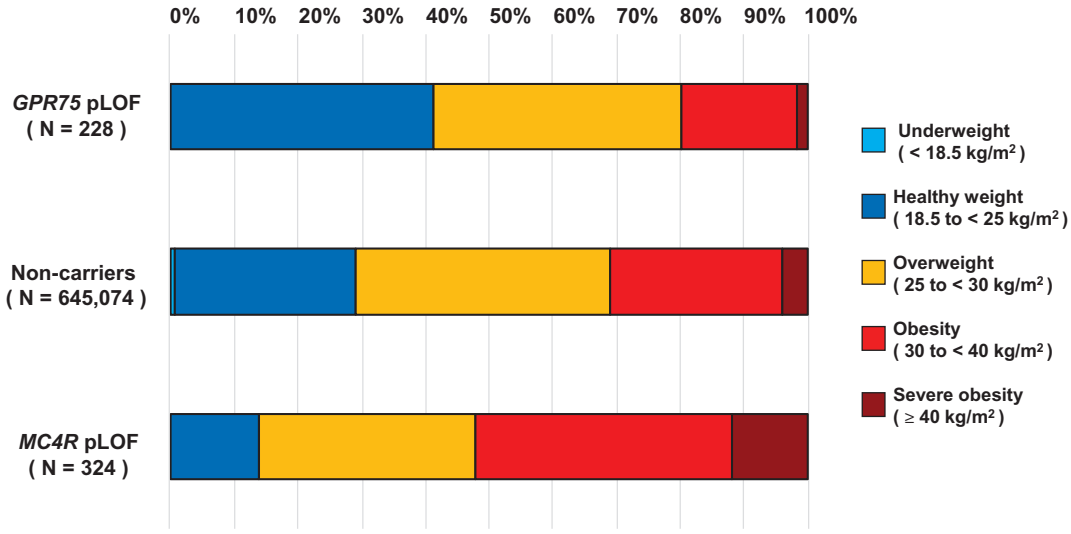

Fig. 2. Distribution in body mass index categories for carriers and noncarriers of predicted loss-of-function variants in *GPR75* or *MC4R*. Distribution of heterozygous carriers of pLOF genetic variants in *GPR75* (top), noncarriers (middle), and heterozygous carriers of pLOF genetic variants in *MC4R* (bottom) in body mass index categories according to the World Health Organization's classification in the UKB, GHS, and MCPS cohorts.

(Fig. 2). In the UKB cohort, *GPR75* pLOF carriers were more likely than noncarriers to self-report a thinner-than-average comparative body size at age 10 (table S5).

We examined the genomic context of the BMI association for pLOF variants in *GPR75*. The first and smallest exon of *GPR75*, containing untranslated sequence, is included in both *GPR75* and in a putative *GPR75-ASB3* readthrough gene with the nearby ankyrin repeat and SOCS box containing 3 (*ASB3*) (fig. S3). The second and final *GPR75* exon (containing the entire translated region of *GPR75*) is not shared with any other gene or transcript (fig. S3). We conducted a number of analyses to ensure that the association of pLOF variants could be firmly attributed to the *GPR75* gene. First, 45 of the 46 pLOF variants in *GPR75* that contributed to the association with lower BMI were located in exon 2 (table S6), which is exclusive to the *GPR75* gene (fig. S3). Accordingly, the burden genotypes for pLOF variants in *GPR75* had no linkage disequilibrium [LD; squared Pearson correlation coefficient (R^2) < 0.0001] with the burden genotype for pLOF variants affecting the *GPR75-ASB3* readthrough gene or the *ASB3* gene. Second, we estimated the association with BMI of the burden of rare coding variants in *ASB3* or in the *GPR75-ASB3* readthrough gene in our large exome sequencing meta-analysis. There was no association with BMI for the burden of rare nonsynonymous variants in *ASB3* or *GPR75-ASB3* across multiple statistical models with different variant annotation and allele frequency inclusion criteria (table S7), nor was there an association for pLOF variants in either *ASB3* or *GPR75-ASB3* (table S7). Finally, we estimated the association with BMI for the burden of rare pLOF variants in *GPR75* conditional upon *ASB3* and *GPR75-ASB3* genotypes. The association of *GPR75* pLOF variants with lower BMI was unaffected by adjusting for *ASB3* and *GPR75-ASB3* genotypes (table S8). Therefore, the association with lower BMI for rare pLOF variants in *GPR75* can be confidently attributed to the *GPR75* gene.

We also explored whether there were common variant associations in the locus. In the 1-Mb window surrounding *GPR75* (500 kb to either side of the gene), there were 26 common variants associated with BMI at the genome-wide level of statistical significance (IVW meta-analysis, $P < 5 \times 10^{-8}$) in our GWAS of imputed common variants in Europeans (table S9 and fig. S4), whereas there were no genome-wide significant associations in admixed Americans (fig. S4). These 26 variants all fine-mapped to a signal led by rs59428052 (G-allele frequency, 14.7%; posterior probability of causal association, 30.4%; per-allele beta in SD units of BMI, −0.015; 95% CI, −0.020 to −0.010; $P = 1.3 \times 10^{-9}$), which is an intergenic variant nearest to *ASB3* and ~200 kb downstream of *GPR75*. The rs59428052 variant did not colocalize with any expression quantitative trait locus (eQTL) signal nor were any of the additional 25 variants at the locus in LD ($R^2 > 0.8$) with any sentinel eQTLs in Genotype-Tissue Expression (GTEx) Portal v8 (table S9). Two of the 26 variants were in LD with a missense variant in *ASB3* and *GPR75-ASB3* (rs36020289), which does not affect the *GPR75* transcript (table S9).

We performed a formal conditional analysis adjusting for the 26 common variants associated with BMI in the region and identified that the association with lower BMI for pLOF variants in *GPR75* remains unchanged (table S8). Therefore, the association with lower BMI for rare pLOF variants in *GPR75* is conditionally independent of any of the 26 common variants associated with BMI at the locus in Europeans.

In summary, our human genetic analysis at the locus indicates that: (i) rare pLOF variants in *GPR75* are associated with lower BMI with a large effect association, (ii) the pLOF association is attributed to *GPR75* and not to other nearby transcripts, (iii) the signal is independent of BMI-associated common variants in the region, and (iv) the small-effect intergenic common variant signal found in that region by GWAS fine-mapping in Europeans has no apparent link with *GPR75*.

The association with lower BMI for pLOF variants in *GPR75* was due to multiple independent rare pLOF variants predicted to truncate GPR75 at different locations (Fig. 1A and table S6). Because of their rarity, none of the 46 rare pLOF variants found by exome sequencing in our analysis were well ascertained by array-genotyping or imputation (table S6). Leave-one-out analyses showed that the burden signal was robust to the exclusion of one pLOF variant at a time (table S10). Out of 46 rare pLOF variants in *GPR75*, five (Ala110fs, Ser219fs, Gln234*, Cys400fs, and Lys404*) were individually associated with lower BMI at a nominal level of statistical significance (IVW meta-analysis $P < 0.05$; table S11), whereas none were associated with higher BMI. When excluding all five of these variant sites from analysis, the remaining set of pLOF variants was still associated with lower BMI (table S10).

We expressed in vitro the two most frequent (minor allele count ≥ 10) among the pLOF variants individually associated with BMI and show that they result in cellular retention of a truncated receptor likely leading to a complete loss of function (Fig. 3). We predict that the loss of a functional copy (i.e., haploinsufficiency) or production of a truncated protein that disrupts receptor multimers (i.e., dominant negative effects) may explain the association of GPR75 truncation with lower BMI. We hypothesized that in the case of haploinsufficiency, the earlier N-terminal truncation of GPR75 would result in greater phenotypic impact than a C-terminal truncation within

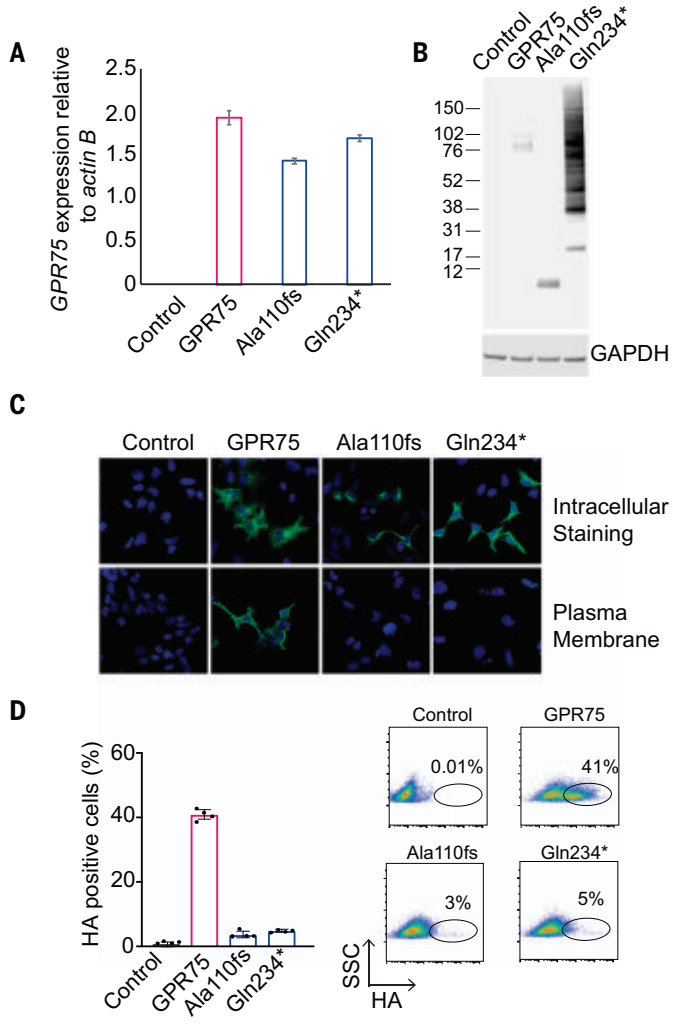

Fig. 3. In vitro expression studies of two predicted loss-of-function genetic variants in *GPR75*. (**A**) Results of quantitative reverse transcription polymerase chain reaction experiments which measured *GPR75* mRNA levels. Expression of *GPR75* was calculated relative to the beta-actin gene. Values represent the mean and standard deviation of three technical replicates representative of one of three biological replicate experiments performed for each condition. (**B**) Western blotting analysis of GPR75 protein levels. GPR75 Ala110fs and Gln234* protein products correspond to the predicted molecular weight of 14 and 25 kDa, respectively. The results are representative of three biological replicates. (**C**) Immunofluorescence staining experiments describing the cellular localization of GPR75. The top images show intracellular staining achieved by membrane permeabilization, while the bottom images show plasma membrane localization (nonpermeabilized cellular membrane). (**D**) Flow cytometry analysis of the cell surface expression of GPR75. Identified cell populations are presented in percent (%) of live HA-TAG GPR75 positive cells. Values represent the mean of four biological replicates per condition and their standard deviation. All experiments were performed in HEK293 cells that were transfected with green fluorescent protein control plasmids (Control), *GPR75* wild type (GPR75), *GPR75*-Ala110fs, or *GPR75*-Gln234* plasmids. Abbreviations: GAPDH, glyceraldehyde-3-phosphate dehydrogenase; SSC, side scatter; HA, hemagglutinin tag.

the last intracellular domain. Genetic variants resulting in truncation of GPR75 before the final intracellular domain were associated with a −2.1 kg/m^2 lower BMI (IVW meta-analysis, $P = 4.1 \times 10^{-7}$) as compared with a −1.4 kg/m^2 lower BMI (IVW meta-analysis, $P = 0.012$) for variants resulting in truncation within the final domain (table S12). This difference was even more pronounced for truncations within the last 100 amino acids of the final C-terminal domain (table S12).

Body composition analysis with bioimpedance in the UKB cohort showed that the association with lower BMI was driven by an association with lower overall body fat mass and lower body fat percentage (fig. S5). In an agnostic phenome-wide analysis of *GPR75* pLOF variants (*29*), we did not observe statistically significant associations with common diagnoses or measured continuous traits after correction for the number of statistical tests performed (2173 phenotypes tested; Bonferroni-corrected P value threshold, $P < 2.3 \times 10^{-5}$), reflecting the rarity of these variants and the stringent multiple test correction.

A detailed analysis of metabolic traits revealed a nominally-significant association (IVW meta-analysis $P < 0.05$) with higher high-density lipoprotein cholesterol, which is consistent with a favorable metabolic profile (table S13). Carriers of pLOF in *GPR75* had lower odds of type 2 diabetes than did noncarriers (63,492 cases and 549,961 controls; per-allele OR, 0.92; 95% CI, 0.59, 1.45; $P = 0.73$; table S13), but the difference was not statistically significant. We interrogated exome sequencing association statistics from up to 20,791 type 2 diabetes cases and 24,440 controls included in the Type 2 Diabetes (T2D) Knowledge Portal (https://t2d.hugeamp.org/; accessed 8 January 2021) and similarly observed numerically lower odds of type 2 diabetes in carriers of *GPR75* pLOF variants (OR for type 2 diabetes, 0.52; 95% CI, 0.14 to 1.97; $P = 0.30$; alternative allele frequency, 0.03%). Owing to the rarity of pLOF variants in *GPR75* and given the genetic relationship between BMI and type 2 diabetes, we estimate that millions of people would need to be sequenced to detect an association at $P < 0.05$ (table S13). An analysis for HbA1c, a continuous biomarker of glycemic levels, led to similar results (table S13).

Gpr75 deletion confers resistance to high-fat diet–induced obesity in mice

In a mouse model of high-fat diet (HFD)–induced obesity, experimental deletion of *Gpr75* protected against weight gain and its associated abnormalities in glucose and insulin metabolism (Fig. 4). When placed on HFD for 14 weeks, *Gpr75*$^{+/+}$ mice approximately doubled their weight. Body weight changed from an average (standard deviation) of 20.9 (2.1) to 43.3 (6.5) grams (body weight change, +22.4 g). In contrast, mice with a genetic deletion of *Gpr75* gained less weight in an allele-dose–dependent fashion (body weight change +16.9 g, difference in weight change compared with wild type −5.5 g or −25% for *Gpr75*$^{+/-}$ mice; body weight change +12.6 g, difference in weight change compared with wild type −9.8 g or −44% for the *Gpr75*$^{-/-}$ mice; Fig. 4A). Increases in fasting blood glucose seen with HFD in *Gpr75*$^{+/+}$ mice were reduced in an allele-dose–dependent manner in *Gpr75*$^{-/+}$ and *Gpr75*$^{-/-}$ mice (Fig. 4B). Mice with a genetic deletion in *Gpr75* were also resistant to HFD-induced impairments in glucose tolerance and insulin sensitivity (Fig. 4, C and D). At the end of 14 weeks of HFD, plasma leptin levels were lower in *Gpr75*$^{-/-}$ and *Gpr75*$^{+/-}$ mice compared with wild-type mice (fig. S6), whereas adiponectin levels were higher, resulting in a 2- and 10-fold lower leptin-to-adiponectin ratio in *Gpr75*$^{+/-}$ and *Gpr75*$^{-/-}$ mice compared with wild type (fig. S6).

Genomic insights at other BMI-associated GPCRs and known monogenic obesity genes from exome sequencing

Gene-burden associations at other GPCRs illustrate the complementarity of large-scale exome sequencing analyses to common variants GWAS in identifying effector genes, establishing directionality of association (i.e., whether LOF in a gene is associated with higher or lower BMI levels), and identifying variants whose functional follow-up can provide biological insights.

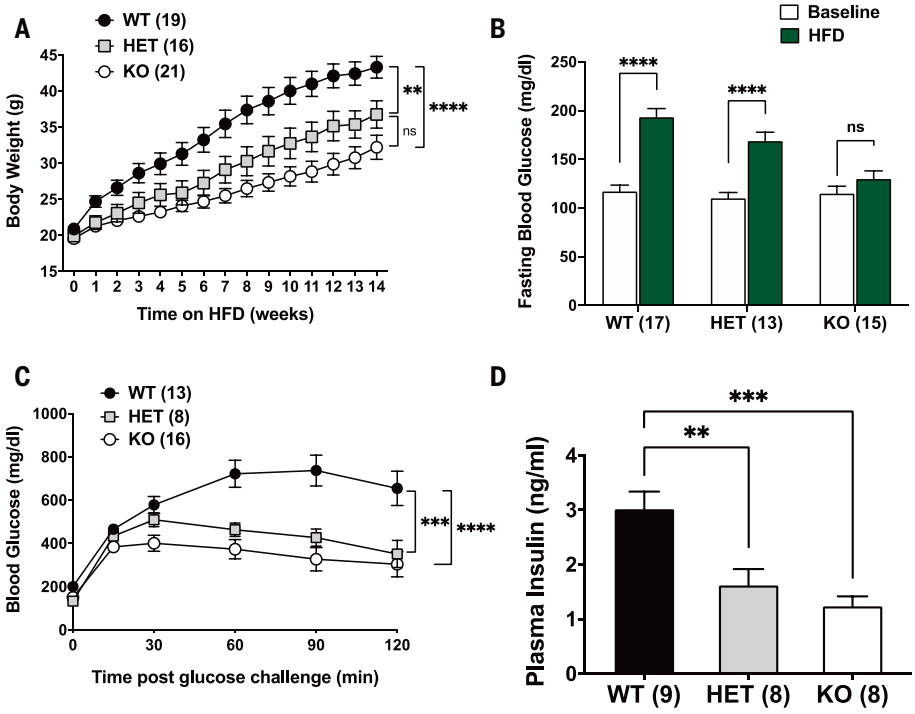

Fig. 4. Weight gain during high-fat diet and metabolic phenotype in mice with a genetic deletion of *Gpr75*. (**A**) Weekly body weight gain during a 14-week high-fat diet (HFD) challenge. (**B**) Changes in fasting blood glucose before and after the high-fat diet challenge. (**C**) Results of a glucose tolerance test at the end of the 14-week high-fat diet challenge. (**D**) Plasma insulin at the end of the 14-week high-fat diet challenge. Each panel shows results in $Gpr75^{+/+}$ (WT), $Gpr75^{+/-}$ (HET), and $Gpr75^{-/-}$ (KO) mice. Number of mice included in each group and analysis is shown in parentheses. Results are presented as mean ± standard error. Abbreviations: ns, not statistically significant; $^{**}P < 0.01$, $^{***}P < 0.001$, $^{****}P < 0.0001$ by two-way analysis of variance with Tukey's multiple comparisons test.

In our GWAS fine-mapping analysis, we identified four distinct signals in the 1-Mb region around the *CALCR* gene (table S14). Although these common variant associations point to *CALCR* as a possible effector gene, they do not on their own inform whether reduced CALCR function would be associated with higher or lower BMI. In the exome analysis, we identified a significant association for the burden of rare [alternative allele frequency (AAF) of <0.1%] pLOF and predicted-deleterious missense variants in *CALCR* with 0.09 SDs (~0.5 kg/m^2) higher BMI and 20% higher odds of obesity (OR, 1.20; 95% CI, 1.12, 1.29; $P = 8.9 \times 10^{-7}$; Table 1 and table S4). In addition, the burden of *CALCR* pLOF genetic variants alone (i.e., excluding missense variants) was associated with higher BMI (table S15), indicating that loss of function in *CALCR* is associated with higher adiposity and obesity risk in humans.

At *GIPR*, a known BMI locus (*16*), we identified an exome-wide significant association with lower BMI for the burden of pLOF and predicted deleterious missense variants (Table 1). This association remained statistically significant, albeit attenuated, after accounting for Arg^{190}→Gln (Arg190Gln) or Glu288Gly (table S15), two rare missense variants with uncertain functional consequences previously associated with lower BMI (*16*).

In our exome sequencing meta-analysis, rare protein-truncating variants in *GIPR* were associated with lower BMI, with a similar effect size to that of Arg190Gln or Glu288Gly (Fig. 5A and table S15), suggesting that these missense variants may result in a loss of function. We tested this hypothesis in cell-based expression experiments, showing that both Arg190Gln-GIPR and Glu288Gly-GIPR result in a near-complete loss of function with respect to Gs and Gq signaling when agonized with recombinant glucose-dependent insulinotropic polypeptide (Fig. 5, B and C, and fig. S7) as compared with wild type. These results indicate that heterozygous loss of function in *GIPR* results in lower BMI and obesity risk in humans.

Using exome sequencing, we confirmed the association of pLOF and deleterious missense variants in *MC4R* with higher BMI (Table 1) and that of gain-of-function variants in *MC4R* (Val103Ile and Ile251Leu) with lower BMI (table S15). In cell-based experiments, we also show that the Val103Ile variant is resistant to the agouti-related peptide–mediated inhibition of MC4R signaling and confirm the signaling preference toward β-arrestin pathway of this gain-of-function variant (*17*) (fig. S8).

In the MCPS cohort, we identified an *MC4R* signal that was fine-mapped to a single likely-causal missense variant (Ile269Asn, 18:60371544:A:T in table S14). This variant was previously associated with childhood and adult obesity in Mexico (*35*) and experimentally shown to result in a complete LOF of both cyclic adenosine monophosphate signaling and β-arrestin recruitment (*17*). The variant is extremely rare in non-Latino ancestries, but the allele frequency was 1% in admixed American individuals from the MCPS cohort. Heterozygous *MC4R* deficiency is considered the most common monogenic form of human obesity (prevalence in cases of severe early-onset obesity, ~6%) (*36*). In obese individuals of European ancestry from the UKB cohort, the prevalence of pLOF or rare (AAF < 1%) deleterious missense variants in *MC4R* was 0.4%, indicating that MC4R deficiency is a rare genetic contributor to general obesity in that population. In obese admixed American participants from the MCPS cohort, the prevalence of MC4R deficiency due to the Ile269Asn variant was ~3%. Therefore, the prevalence of heterozygous *MC4R* deficiency in general obesity is more than sevenfold greater in admixed Americans from Mexico than in Europeans from the UK.

Homozygous *MC4R* deficiency has been described in only a handful of cases of severe early-onset obesity (*36*), but the penetrance of obesity in this condition is unknown. In the MCPS cohort, there were 17 homozygous carriers of Ile269Asn, 12 of whom were obese and 5 overweight. These data suggest that homozygous *MC4R* deficiency might be incompatible with the maintenance of a healthy weight in adulthood.

Our exome-wide study also identified additional large effect-size associations with higher BMI and obesity risk for rare coding variants in other genes, including associations with more than twofold higher odds of obesity for protein-truncating variants in *PCSK1* (in a heterozygous state), *UBR2* (ubiquitin protein ligase E3 component n-recognin 2), and *ANO4* (anoctamin 4) (Table 1 and table S4). These associations were similar in effect size to those for rare (AAF < 1%) pLOF or deleterious missense variants in *MC4R*, but the frequency of these genotypes was lower than that of *MC4R* pLOF or deleterious missense alleles (Table 1). Hence, these rare mutations occur in only a small number of people in the general population. However, they may have a large impact on obesity risk in those small groups of carriers.

We used our large exome-sequencing dataset to investigate the association with BMI of heterozygous pLOF variants in five leptin-melanocortin pathway genes where pLOF variants have been previously linked to monogenic obesity {*LEP* [leptin deficiency, Mendelian

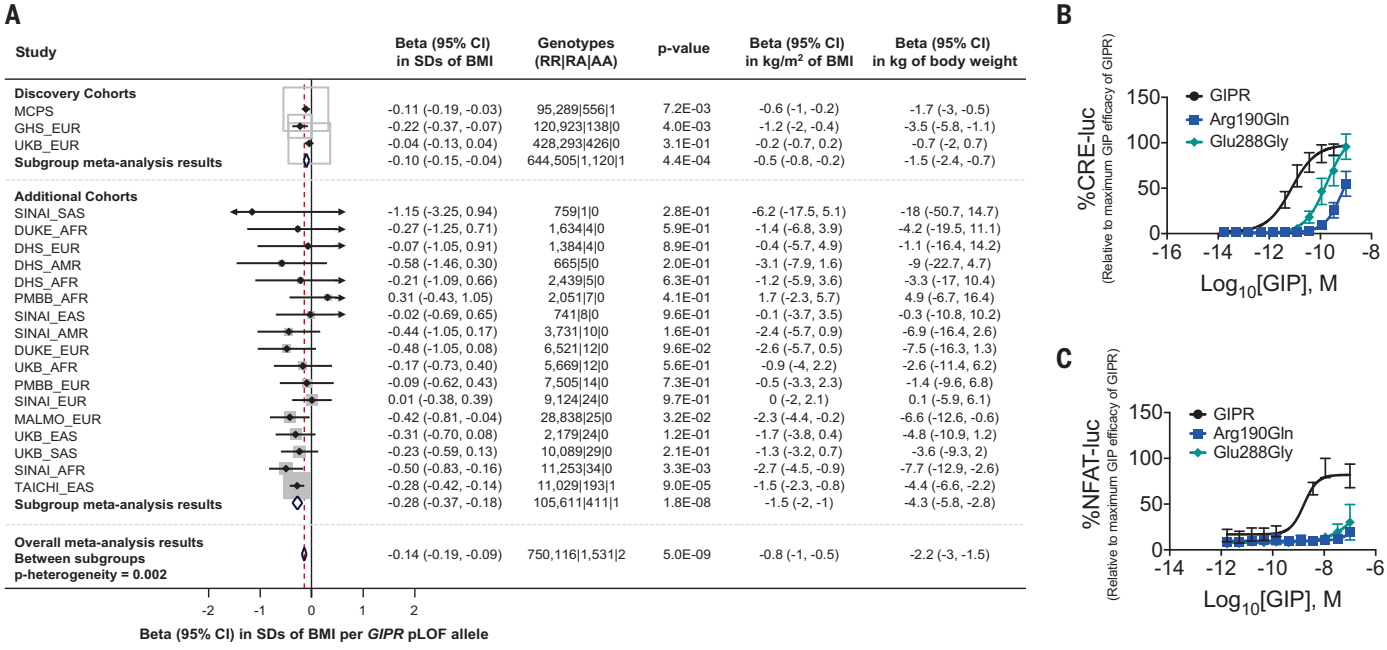

Fig. 5. Association of protein-truncating genetic variants in *GIPR* with lower body mass index. (**A**) Association with BMI for pLOF genetic variants in *GIPR* across both discovery and additional cohorts. Abbreviations: CI, confidence interval; RR, reference-reference genotype; RA, reference-alternative heterozygous genotype; AA, alternative-alternative homozygous genotype; DHS, Dallas Heart Study; SINAI, Mount Sinai BioMe cohort; DUKE, Duke Catheterization Genetics cohort; TAICHI, Taiwanese Chinese persons from the Taiwan Metabochip Consortium; PMBB, University of Pennsylvania Medicine BioBank; MALMO, Malmö Diet and Cancer Study; AFR, African ancestry; AMR, American ancestry; EAS, East Asian ancestry; EUR, European ancestry; SAS, South Asian ancestry. (**B**) In vitro expression results using the CRE-reporter assay for the Arg190Gln and Glu288Gly missense variants in *GIPR*, which were associated with lower BMI. (**C**) In vitro expression results using the nuclear factor of activated T cells (NFAT)–dependent assay for the variants. Both missense variants showed lower glucose-dependent insulinotropic polypeptide (GIP)–induced Gs signaling and lower GIP-induced Gq signaling than wild type.

Inheritance in Man (MIM): 614962], *LEPR* [leptin receptor deficiency, MIM: 614963], *POMC* [proopiomelanocortin deficiency, MIM: 609734], *PCSK1* [proprotein convertase 1/3 deficiency, MIM: 600955], and *MC4R* [melanocortin 4 receptor deficiency, MIM: 618406]}. Of these, only *MC4R* deficiency is considered to have autosomal dominant inheritance, while all other deficiencies are considered to be autosomal recessive. Heterozygous carrier status for pLOF variants in *LEP*, *POMC*, *PCSK1*, or *MC4R* was associated with higher BMI (IVW meta-analysis $P < 0.05$; table S16), whereas heterozygous carrier status for pLOF variants in *LEPR* was not associated with BMI, suggesting a pure autosomal recessive inheritance for leptin receptor deficiency.

Rare single-variant exome-wide analysis reveals additional signals at the *SOS2* and *SRRM2* genes

In addition to the gene-burden association analyses, we also conducted single-variant association analyses, looking for rare nonsynonymous alleles individually associated with BMI (IVW meta-analysis $P < 5 \times 10^{-8}$) conditional on GWAS fine-mapped common variants (*29*). We identified seven such variants, including five occurring in genes identified in the primary gene-burden analysis [*GPR151*, *SPARC* (secreted protein acidic and cysteine rich), *MC4R*, *GIPR*, and *ANKRD27* (ankyrin repeat domain 27); table S17) and two variants in genes not identified in other analyses [Arg2033Pro in *SRRM2* (serine/arginine repetitive matrix 2) and Pro191Arg in *SOS2* (SOS Ras/Rho guanine nucleotide exchange factor 2); table S17]. The missense variant in *SOS2* was associated with 0.05 SDs (0.27 kg/m^2) lower BMI per allele. Notably, mutations in *SOS2* are associated with autosomal dominant forms of Noonan syndrome (MIM: 616559), a condition that has been associated with a lower prevalence of being overweight (*37*).

Combined use of common variant GWAS fine-mapping and exome-sequencing gene-burden associations to prioritize likely effector genes for BMI

Fine-mapping of GWAS associations in the discovery cohorts of our analysis identified 1905 independent signals led by sentinel common variants (*29*) (AAF > 1%; table S18), which had a median 95% credible set size of 36 likely-causal variants (interquartile range, 12 to 119). We used MANTRA (Meta-Analysis of Transethnic Association) studies (*38*), a Bayesian transethnic meta-analysis approach, to estimate associations of fine-mapped signals across ancestries and observed strong evidence of association across datasets (median $\log_{10}$ Bayes factor, 7.0; interquartile range, 4.9 to 10.4; table S18).

Of the 1905 signals, 13 (0.7%) fine-mapped to a single nonsynonymous sentinel variant with >95% posterior probability of causal association (12 missense variants and 1 splice site variant in 12 genes; table S19). These included a gene identified in our gene-burden analysis (*MC4R*) and an additional 11 genes. We investigated whether there were associations for the burden of rare (AAF < 1%) pLOF or pLOF plus predicted deleterious (5/5 in silico prediction algorithms) missense variants in these genes prioritized by GWAS fine-mapping. We found evidence of association (IVW meta-analysis $P < 0.05$) for 4 of these 11 genes (36%; table S19). These common and rare variants association pairs included the His48Arg missense variant and the burden of rare pLOF or predicted deleterious missense variants in *ADH1B*, encoding the key ethanol metabolism enzyme alcohol dehydrogenase 1B. His48Arg is known to associate with higher BMI via increased alcohol consumption (*39*), and our rare variant analysis corroborates the causal nature of that association and the importance of alcohol consumption in weight regulation.

We used exome sequencing results to investigate whether there were associations for rare

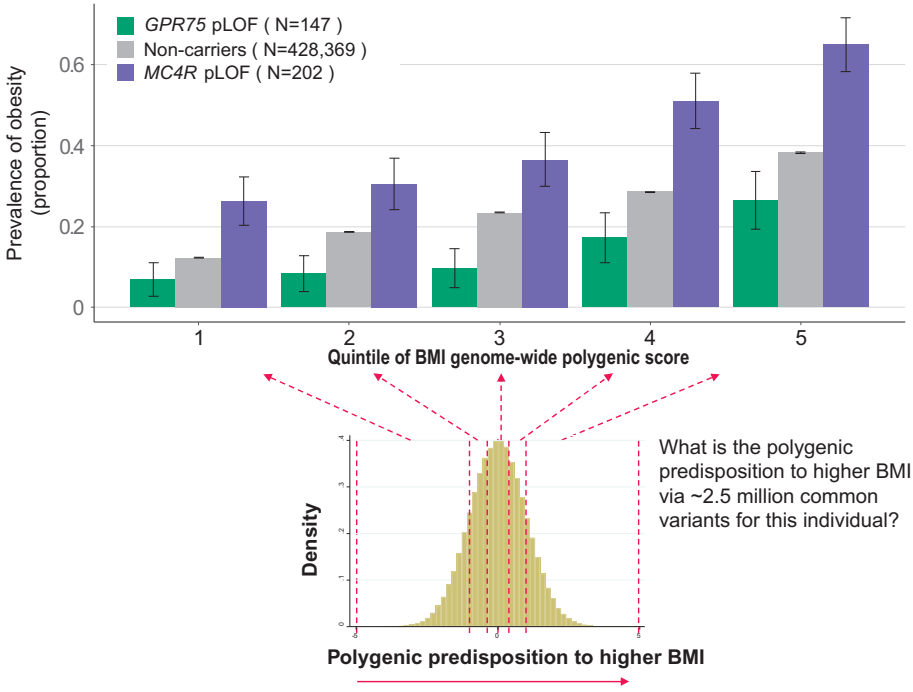

Fig. 6. Interplay of a genome-wide polygenic score for higher body mass index with rare genetic mutations in *GPR75* and *MC4R*. This figure shows the prevalence of obesity (defined as BMI ≥ 30 kg/m^2) in heterozygous carriers of pLOF variants in *GPR75*, noncarriers, or heterozygous carriers of pLOF variants in *MC4R* within quintiles of a genome-wide polygenic score for higher BMI. *P* values for interaction between the polygenic score and rare pLOF variants on body mass index were 0.09 and 0.85 for *GPR75* and *MC4R*, respectively. Error bars represent 95% confidence intervals.

nonsynonymous variants in genes at the *FTO* locus, where common variants have been associated with BMI in early GWASs (*11*, *12*) and where experimental studies have suggested the distant *IRX3* and *IRX5* as likely effector genes (*40*). We did not observe an association with BMI for rare coding variants in *FTO*, *IRX3*, or *IRX5* (table S20). Because pLOF variants in these genes were rare (AAF ≤ 0.02%; table S20), this analysis can only exclude large-effect associations with BMI for heterozygous pLOF variants in those genes. The strongest associations for the burden of rare coding variants in the region was for rare (AAF < 1%) pLOF or predicted deleterious (5/5 in silico prediction algorithms) missense variants in the *CHD9* gene (table S20).

At 10 of the 16 1-Mb regions around the genes identified in our exome-wide gene-burden analysis, there were common variant (sentinel AAF > 1%) signals identified by GWAS fine-mapping, while at the remaining six regions there were no nearby fine-mapped common sentinel variants (table S14). At the 10 loci with common variant signals, we used physical proximity, common nonsynonymous variants, and eQTL colocalization in either European or all-ancestry GTEx v8 datasets to identify likely effector genes for the common variant associations (*29*) (tables S14 and S21). At 6 of the 10 regions, the gene identified in the exome-wide analysis was also one of the genes that were prioritized by common variants associations (table S14). However, at four of those six loci, other genes were also prioritized, resulting in an uncertain effector gene attribution on the basis of common variants alone. In these four loci, gene-burden associations for the gene identified in the exome analysis had an average of 19 orders of magnitude stronger statistical association than any of the other possible effector genes prioritized by common variants [average difference in −log10(p), 19.3; range, 6.3 to 46.6; table S14], suggesting that gene-burden analyses may considerably help to prioritize effector genes at some GWAS-associated loci. At the remaining loci, common variant associations prioritized different genes than the ones identified in the exome-wide analysis (table S14). These results suggest that, at those loci, common variant associations act via different genes than the ones found by exome sequencing or that the gene prioritization from common variant associations did not identify the correct effector gene for those common variant signals.

Polygenic burden influences the penetrance of obesity in carriers of high-impact rare coding alleles

Both common and rare alleles contribute to the risk of general obesity, but their interplay in shaping obesity risk has been understudied because of the lack of datasets with both common and rare variant ascertainment. Here, we generated a genome-wide polygenic score capturing genetic predisposition to higher BMI due to more than 2.5 million common alleles (*29*) and studied its interplay with rare, large effect-size coding variants in shaping risk for obesity in the population-based UKB cohort. This analysis suggests that polygenic burden influences the penetrance of obesity and the level of BMI in carriers of *GPR75* (large-effect protective association) or *MC4R* (large-effect risk-increasing association) pLOF variants in a linearly additive manner (Fig. 6 and fig. S9). The penetrance of obesity in individuals carrying protein-truncating variants in *MC4R* varied from less than 30% to more than 60% in people at the bottom versus top quintile for the distribution of the polygenic score (Fig. 6). There was a nearly 60% absolute difference in the prevalence of obesity between extremes of genetic predisposition, that is, *GPR75* pLOF carriers in the bottom quintile of polygenic burden and *MC4R* pLOF carriers in the top quintile (Fig. 6).

Discussion

By conducting a large exome-sequencing study on the influences of rare coding variation on body adiposity, we made a number of observations that advance our understanding of the genes and pathways involved in propensity for and resistance to obesity in humans. We discovered an association for rare protein-truncating genetic variants in *GPR75* with lower adiposity and substantial protection against obesity. We validated this human genetic association in a high-fat diet model of obesity in mice, where genetic ablation of *Gpr75* was associated with resistance to weight gain, greater insulin sensitivity, and improved glycemic control. In our analysis, the association for pLOF variants in *GPR75* showed the largest effect-size genetic association with lower adiposity and protection against obesity at the genome-wide level. The estimated effect size for this association appears to be three to four times larger than the largest effect-size associations for common genetic variants at the *FTO* locus (*11*, *13*) or for low-frequency gain-of-function variants in *MC4R* (*17*). The observation of a consistent association across cohorts from different regions of the world and with different study design as well as multiple ancestries highlights the generalizability of this association in people with various genetic backgrounds and environmental exposures.

Human genetics validation is a predictor of the likely success of drug development programs (*41*, *42*) where the identification of naturally occurring protective alleles has catalyzed the translation from genetic association to therapeutic drug development in a growing number

of examples (17–22, 43–45). Therefore, our findings suggest that GPR75 inhibition could be a therapeutic approach for obesity.

The expression of *GPR75* in the hypothalamic nuclei and other brain regions, protection against weight gain for *Gpr75* knockout mice under high-fat diet challenge, and previous evidence of the role of brain GPCRs in energy balance regulation suggest that this receptor may be implicated in the brain-mediated regulation of energy balance, providing an important direction for future mechanistic research. It will also be important to clarify whether 20-hydroxyeicosatetraenoic acid (20-HETE), an eicosanoid metabolite of arachidonic acid, or C-C motif chemokine ligand 5 (CCL5), a chemokine, which have been previously proposed as putative ligands for GPR75 (46, 47) or other yet-undiscovered ligands are responsible for the link between GPR75 loss of function and body weight regulation.

In addition to *GPR75*, our agnostic exome-wide analysis identified four other GPCRs expressed in the brain and previously implicated in energy balance regulation. This highlights once again the importance of neurological pathways in obesity risk in humans first shown in family studies of extreme obesity and more recently in genome-wide association analyses of common variants. GIPR is expressed in adipose, brain, bone, and other metabolically-active tissues where it acts as the receptor for glucose-dependent insulinotropic polypeptide, an incretin hormone involved in the regulation of insulin secretion, gastric emptying, and other metabolic processes (48). CALCR is the receptor of calcitonin and amylin, a peptide hormone secreted by pancreatic beta cells, which has been shown to promote satiety, delayed gastric emptying, and weight control in patients with type 2 diabetes (49–51). Ablation of *Calcr*-expressing neurons in the nucleus tractus solitarius has been recently implicated in the disruption of a leptin-independent pathway of appetite regulation in murine models (52). *GPR151* encodes a habenular receptor involved in addictive behavior and differential food-intake response to nicotine (53). The association effect size for pLOF and predicted deleterious missense variants in our analysis as well as the previously reported association for the Arg95* allele (33) is tiny (−0.3 kg/m^2 per allele), suggesting that it may be secondary to other behavioral or neurological phenotypes possibly related to addiction. In addition to these GPCRs, our exome-wide analysis revealed associations with body adiposity for rare coding variants in several other genes. Although in this study we primarily focused on the associations in *GPR75* and other GPCRs owing to their more immediate translational potential, the identification of these additional associations in our large study provides an initial foundation for understanding the role of these genes in the regulation of body fat and obesity risk.

Our study illustrates the power and versatility of massive-scale exome sequencing in population- or health system–based cohort studies as a genetic discovery approach complementary to common variant GWASs and pedigree-based studies. We show the utility of this approach in (i) discovering large-effect protective or risk-increasing associations for genes and individual rare coding variants, (ii) identifying functional variants that can be studied in vitro for biological insight, (iii) prioritizing effector genes for common variant signals identified by fine-mapping, and (iv) understanding the impact of rare variants on complex traits such as obesity across populations and their interplay with common variation in shaping disease risk or resistance. The results from this exome-sequencing analysis in more than 640,000 people suggest that inhibition of GPR75 may be a therapeutic strategy for obesity and illustrate the power of massive-scale exome sequencing for the identification of large-effect coding variant associations and drug targets for complex traits.

Methods summary

Detailed materials and methods are provided in the supplementary materials (29). Briefly, we performed high-coverage whole-exome sequencing in 645,626 individuals, including 428,719 individuals of European ancestry from the UK Biobank cohort, 121,061 individuals of European ancestry from the MyCode Community Health Initiative cohort from the US-based Geisinger Health System, and 95,846 individuals of admixed American ancestry from the Mexico City Prospective Study. The outcome measure was BMI, calculated as weight in kilograms divided by the square of standing height in meters. We estimated associations with BMI for the burden of rare nonsynonymous variants in each sequenced gene by fitting mixed-effects regression models accounting for population stratification and relatedness using BOLT-LMM v2.3.4 (54) or REGENIE v1.0 (55). Results across studies were pooled by inverse-variance weighted meta-analysis. Consistent with previous literature (27, 28), for our primary gene-burden association analysis, we considered a threshold of exome-wide statistical significance of $P < 3.6 \times 10^{-7}$, a Bonferroni correction for 20,000 genes, and seven variant selection models. In parallel, to leverage evidence from common variants, we performed genome-wide association studies of imputed common alleles in the same discovery dataset used for our exome sequencing analysis. We leveraged fine-mapping of common alleles, formal conditional analyses, physical proximity mapping, linkage disequilibrium with common nonsynonymous alleles, eQTL colocalization, and polygenic score analysis to highlight the complementarity of evidence from exome sequencing and GWASs of common variants. To illustrate the translational value of exome sequencing–identified rare coding associations, we performed targeted in vitro and in vivo experiments. We performed in vitro expression studies for the functional characterization of naturally-occurring variants in *GPR75*, *MC4R*, and *GIPR*. We also developed genetically engineered knockout *Gpr75*$^{-/-}$ mouse strains using the VelociGene technology (56, 57) and studied the weight gain, glycemic, and insulinemic phenotypes of knockout*Gpr75*$^{-/-}$, heterozygous *Gpr75*$^{-/+}$, and wild-type *Gpr75*$^{+/+}$ mice in a high-fat diet model.

REFERENCES AND NOTES

1. Y. Zhang *et al*., Positional cloning of the mouse obese gene and its human homologue. *Nature* **372**, 425–432 (1994). doi: 10.1038/372425a0; pmid: 7984236
2. W. Fan, B. A. Boston, R. A. Kesterson, V. J. Hruby, R. D. Cone, Role of melanocortinergic neurons in feeding and the agouti obesity syndrome. *Nature* **385**, 165–168 (1997). doi: 10.1038/385165a0; pmid: 8990120
3. D. Huszar *et al*., Targeted disruption of the melanocortin-4 receptor results in obesity in mice. *Cell* **88**, 131–141 (1997). doi: 10.1016/S0092-8674(00)81865-6; pmid: 9019399
4. C. T. Montague *et al*., Congenital leptin deficiency is associated with severe early-onset obesity in humans. *Nature* **387**, 903–908 (1997). doi: 10.1038/43185; pmid: 9202122
5. S. O'Rahilly *et al*., Brief report: Impaired processing of prohormones associated with abnormalities of glucose homeostasis and adrenal function. *N. Engl. J. Med.* **333**, 1386–1390 (1995). doi: 10.1056/NEJM199511233332104; pmid: 7477119
6. R. S. Jackson *et al*., Obesity and impaired prohormone processing associated with mutations in the human prohormone convertase 1 gene. *Nat. Genet.* **16**, 303–306 (1997). doi: 10.1038/ng0797-303; pmid: 9207799
7. K. Clément *et al*., A mutation in the human leptin receptor gene causes obesity and pituitary dysfunction. *Nature* **392**, 398–401 (1998). doi: 10.1038/32911; pmid: 9537324
8. G. S. Yeo *et al*., A frameshift mutation in *MC4R* associated with dominantly inherited human obesity. *Nat. Genet.* **20**, 111–112 (1998). doi: 10.1038/2404; pmid: 9771698
9. C. Vaisse, K. Clement, B. Guy-Grand, P. Froguel, A frameshift mutation in human MC4R is associated with a dominant form of obesity. *Nat. Genet.* **20**, 113–114 (1998). doi: 10.1038/2407; pmid: 9771699
10. H. Krude *et al*., Severe early-onset obesity, adrenal insufficiency and red hair pigmentation caused by POMC mutations in humans. *Nat. Genet.* **19**, 155–157 (1998). doi: 10.1038/509; pmid: 9620771
11. T. M. Frayling *et al*., A common variant in the *FTO* gene is associated with body mass index and predisposes to childhood and adult obesity. *Science* **316**, 889–894 (2007). doi: 10.1126/science.1141634; pmid: 17434869
12. R. J. Loos *et al*., Common variants near *MC4R* are associated with fat mass, weight and risk of obesity. *Nat. Genet.* **40**, 768–775 (2008). doi: 10.1038/ng.140; pmid: 18454148
13. A. E. Locke *et al*., Genetic studies of body mass index yield new insights for obesity biology. *Nature* **518**, 197–206 (2015). doi: 10.1038/nature14177; pmid: 25673413
14. L. Yengo *et al*., Meta-analysis of genome-wide association studies for height and body mass index in ~700000 individuals of European ancestry. *Hum. Mol. Genet.* **27**, 3641–3649 (2018). doi: 10.1093/hmg/ddy271; pmid: 30124842
15. A. V. Khera *et al*., Polygenic prediction of weight and obesity trajectories from birth to adulthood. *Cell* **177**, 587–596.e9 (2019). doi: 10.1016/j.cell.2019.03.028; pmid: 31002795
16. V. Turcot *et al*., Protein-altering variants associated with body mass index implicate pathways that control energy intake and expenditure in obesity. *Nat. Genet.* **50**, 26–41 (2018). doi: 10.1038/s41588-017-0011-x; pmid: 29273807
17. L. A. Lotta *et al*., Human gain-of-function *MC4R* variants show signaling bias and protect against obesity. *Cell* **177**, 597–607.e9 (2019). doi: 10.1016/j.cell.2019.03.044; pmid: 31002796

18. K. Musunuru *et al*., Exome sequencing, *ANGPTL3* mutations, and familial combined hypolipidemia. *N. Engl. J. Med.* **363**, 2220–2227 (2010). doi: 10.1056/NEJMoa1002926; pmid: 20942659
19. F. E. Dewey *et al*., Genetic and pharmacologic inactivation of ANGPTL3 and cardiovascular disease. *N. Engl. J. Med.* **377**, 211–221 (2017). doi: 10.1056/NEJMoa1612790; pmid: 28538136
20. N. S. Abul-Husn *et al*., A protein-truncating *HSD17B13* variant and protection from chronic liver disease. *N. Engl. J. Med.* **378**, 1096–1106 (2018). doi: 10.1056/NEJMoa1712191; pmid: 29562163
21. A. B. Jørgensen, R. Frikke-Schmidt, B. G. Nordestgaard, A. Tybjærg-Hansen, Loss-of-function mutations in *APOC3* and risk of ischemic vascular disease. *N. Engl. J. Med.* **371**, 32–41 (2014). doi: 10.1056/NEJMoa1308027; pmid: 24941082
22. J. Crosby *et al*., Loss-of-function mutations in *APOC3*, triglycerides, and coronary disease. *N. Engl. J. Med.* **371**, 22–31 (2014). doi: 10.1056/NEJMoa1307095; pmid: 24941081
23. J. Flannick *et al*., Loss-of-function mutations in *SLC30A8* protect against type 2 diabetes. *Nat. Genet.* **46**, 357–363 (2014). doi: 10.1038/ng.2915; pmid: 24584071
24. G. Marenne *et al*., Exome sequencing identifies genes and gene sets contributing to severe childhood obesity, linking *PHIP* variants to repressed *POMC* transcription. *Cell Metab.* **31**, 1107–1119.e12 (2020). doi: 10.1016/j.cmet.2020.05.007; pmid: 32492392
25. F. E. Dewey *et al*., Distribution and clinical impact of functional variants in 50,726 whole-exome sequences from the DiscovEHR study. *Science* **354**, aaf6814 (2016). doi: 10.1126/science.aaf6814; pmid: 28008009
26. C. V. Van Hout *et al*., Exome sequencing and characterization of 49,960 individuals in the UK Biobank. *Nature* **586**, 749–756 (2020). doi: 10.1038/s41586-020-2853-0; pmid: 33087929
27. J. Flannick *et al*., Exome sequencing of 20,791 cases of type 2 diabetes and 24,440 controls. *Nature* **570**, 71–76 (2019). doi: 10.1038/s41586-019-1231-2; pmid: 31118516
28. R. Do *et al*., Exome sequencing identifies rare *LDLR* and *APOA5* alleles conferring risk for myocardial infarction. *Nature* **518**, 102–106 (2015). doi: 10.1038/nature13917; pmid: 25487149
29. Materials and methods are available as supplementary materials.
30. C. Sudlow *et al*., UK Biobank: An open access resource for identifying the causes of a wide range of complex diseases of middle and old age. *PLOS Med.* **12**, e1001779 (2015). doi: 10.1371/journal.pmed.1001779; pmid: 25826379
31. D. J. Carey *et al*., The Geisinger MyCode community health initiative: An electronic health record-linked biobank for precision medicine research. *Genet. Med.* **18**, 906–913 (2016). doi: 10.1038/gim.2015.187; pmid: 26866580
32. R. Tapia-Conyer *et al*., Cohort profile: The Mexico City Prospective Study. *Int. J. Epidemiol.* **35**, 243–249 (2006). doi: 10.1093/ije/dyl042; pmid: 16556648
33. C. A. Emdin *et al*., Analysis of predicted loss-of-function variants in UK Biobank identifies variants protective for disease. *Nat. Commun.* **9**, 1613 (2018). doi: 10.1038/s41467-018-03911-8; pmid: 29691411
34. A. S. Hauser, M. M. Attwood, M. Rask-Andersen, H. B. Schiöth, D. E. Gloriam, Trends in GPCR drug discovery: New agents, targets and indications. *Nat. Rev. Drug Discov.* **16**, 829–842 (2017). doi: 10.1038/nrd.2017.178; pmid: 29075003
35. M. Vázquez-Moreno *et al*., The melanocortin 4 receptor p.Ile269Asn mutation is associated with childhood and adult obesity in Mexicans. *J. Clin. Endocrinol. Metab.* **105**, e1468–e1477 (2020). doi: 10.1210/clinem/dgz276; pmid: 31841602
36. I. S. Farooqi *et al*., Clinical spectrum of obesity and mutations in the melanocortin 4 receptor gene. *N. Engl. J. Med.* **348**, 1085–1095 (2003). doi: 10.1056/NEJMoa022050; pmid: 12646665
37. G. Binder *et al*., Health and quality of life in adults with Noonan syndrome. *J. Pediatr.* **161**, 501–505.e1 (2012). doi: 10.1016/j.jpeds.2012.02.043; pmid: 22494877
38. A. P. Morris, Transethnic meta-analysis of genomewide association studies. *Genet. Epidemiol.* **35**, 809–822 (2011). doi: 10.1002/gepi.20630; pmid: 22125221
39. M. V. Holmes *et al*., Association between alcohol and cardiovascular disease: Mendelian randomisation analysis based on individual participant data. *BMJ* **349**, g4164 (2014). doi: 10.1136/bmj.g4164; pmid: 25011450
40. M. Claussnitzer *et al*., FTO obesity variant circuitry and adipocyte browning in humans. *N. Engl. J. Med.* **373**, 895–907 (2015). doi: 10.1056/NEJMoa1502214; pmid: 26287746
41. D. Cook *et al*., Lessons learned from the fate of AstraZeneca's drug pipeline: A five-dimensional framework. *Nat. Rev. Drug Discov.* **13**, 419–431 (2014). doi: 10.1038/nrd4309; pmid: 24833294
42. M. R. Nelson *et al*., The support of human genetic evidence for approved drug indications. *Nat. Genet.* **47**, 856–860 (2015). doi: 10.1038/ng.3314; pmid: 26121088
43. N. O. Stitziel *et al*., ANGPTL3 deficiency and protection against coronary artery disease. *J. Am. Coll. Cardiol.* **69**, 2054–2063 (2017). doi: 10.1016/j.jacc.2017.02.030; pmid: 28385496
44. T. I. Pollin *et al*., A null mutation in human *APOC3* confers a favorable plasma lipid profile and apparent cardioprotection. *Science* **322**, 1702–1705 (2008). doi: 10.1126/science.1161524; pmid: 19074352
45. J. C. Cohen, E. Boerwinkle, T. H. Mosley Jr., H. H. Hobbs, Sequence variations in *PCSK9*, low LDL, and protection against coronary heart disease. *N. Engl. J. Med.* **354**, 1264–1272 (2006). doi: 10.1056/NEJMoa054013; pmid: 16554528
46. V. Garcia *et al*., 20-HETE signals through G-protein–coupled receptor GPR75 (G_q) to affect vascular function and trigger hypertension. *Circ. Res.* **120**, 1776–1788 (2017). doi: 10.1161/CIRCRESAHA.116.310525; pmid: 28325781
47. S. Dedoni, L. A. Campbell, B. K. Harvey, V. Avdoshina, I. Mocchetti, The orphan G-protein-coupled receptor 75 signaling is activated by the chemokine CCL5. *J. Neurochem.* **146**, 526–539 (2018). doi: 10.1111/jnc.14463; pmid: 29772059
48. J. J. Holst, M. M. Rosenkilde, Recent advances of GIP and future horizons. *Peptides* **125**, 170230 (2020). doi: 10.1016/j.peptides.2019.170230; pmid: 31838219
49. P. A. Hollander *et al*., Pramlintide as an adjunct to insulin therapy improves long-term glycemic and weight control in patients with type 2 diabetes: A 1-year randomized controlled trial. *Diabetes Care* **26**, 784–790 (2003). doi: 10.2337/diacare.26.3.784; pmid: 12610038
50. P. Hollander *et al*., Effect of pramlintide on weight in overweight and obese insulin-treated type 2 diabetes patients. *Obes. Res.* **12**, 661–668 (2004). doi: 10.1038/oby.2004.76; pmid: 15090634
51. O. Schmitz, B. Brock, J. Rungby, Amylin agonists: A novel approach in the treatment of diabetes. *Diabetes* **53** (suppl. 3), S233–S238 (2004). doi: 10.2337/diabetes.53.suppl_3.S233; pmid: 15561917
52. W. Cheng *et al*.., Calcitonin receptor neurons in the mouse nucleus tractus solitarius control energy balance via the non-aversive suppression of feeding. *Cell Metab.* **31**, 301–312.e5 (2020). doi: 10.1016/j.cmet.2019.12.012; pmid: 31955990
53. B. Antolin-Fontes *et al*., The habenular G-protein–coupled receptor 151 regulates synaptic plasticity and nicotine intake. *Proc. Natl. Acad. Sci. U.S.A.* **117**, 5502–5509 (2020). doi: 10.1073/pnas.1916132117; pmid: 32098843
54. P. R. Loh, G. Kichaev, S. Gazal, A. P. Schoech, A. L. Price, Mixed-model association for biobank-scale datasets. *Nat. Genet.* **50**, 906–908 (2018). doi: 10.1038/s41588-018-0144-6; pmid: 29892013
55. J. Mbatchou *et al*., Computationally efficient whole-genome regression for quantitative and binary traits. *Nat. Genet.* 10.1038/s41588-021-00870-7 (2021). doi: 10.1038/s41588-021-00870-7; pmid: 34017140
56. D. M. Valenzuela *et al*., High-throughput engineering of the mouse genome coupled with high-resolution expression analysis. *Nat. Biotechnol.* **21**, 652–659 (2003). doi: 10.1038/nbt822; pmid: 12730667
57. W. T. Poueymirou *et al*., F0 generation mice fully derived from gene-targeted embryonic stem cells allowing immediate phenotypic analyses. *Nat. Biotechnol.* **25**, 91–99 (2007). doi: 10.1038/nbt1263; pmid: 17187059

ACKNOWLEDGMENTS

The authors thank J. C. Cohen, University of Texas Southwestern, Dallas (USA). **Funding:** This research received funding from Regeneron Pharmaceuticals. New York Medical College investigators received funding from the National Institutes of Health grants HL034300 (M.L.S.) and HL139793 (M.L.S.) and the diversity supplement HL139793-1S (V.G.). The Mexico City Prospective Study is funded by a core grant from the UK Medical Research Council to the MRC Population Health Research Unit at the University of Oxford and has previously received funding from the Mexican Health Ministry, the Mexican National Council of Science and Technology, the Wellcome Trust, the British Heart Foundation, Cancer Research UK, and the Nuffield Department of Population Health at the University of Oxford. Y.I.C. and J.I.R. were supported by the National Center for Advancing Translational Sciences, CTSI grant UL1TR001881, and the National Institute of Diabetes and Digestive and Kidney Disease Diabetes Research Center (DRC) grant DK063491 to the Southern California Diabetes Endocrinology Research Center. **Author contributions:** All authors contributed to the collection of data, interpretation of results, critical review of the manuscript for important intellectual content, and final approval of submission of the manuscript for publication. Project conceptualization: A.B., M.A.R.F., and L.A.L. Development or application of methods: P.A., A.G., O.S., J.A.K., L.K., Y.-Y.F., T.P., V.G., D.S., A.Li, J.Mb., A.E.L., C.B., N.V., N.L., S.H., K.A., J.V.P., E.D., M.D., S.B., A.H., M.J., B.Z., A.J.M., C.P., G.C., J.D.O., J.G.R., A.R.S., M.C., H.M.K., G.R.A., K.K., A.N.E., J.Ma., G.D.Y., M.W.S., J.A., G.D.G., M.L.S., A.B., M.A.R.F., and L.A.L. Paper drafting: P.A., O.S., and L.A.L. Data analysis: P.A., O.S., J.A.K., D.S., A.Li, J.Mb., A.E.L., C.B., N.V., N.L., S.B., A.H., H.M.K., G.R.A., J.Ma., M.A.R.F., and L.A.L. In vitro experiments design, analysis, and interpretation: L.K., Y.-Y.F., T.P., M.W.S., J.A., and G.D.G. Design, analysis, interpretation of mouse models and experiments: A.G., V.G., S.H., K.A., J.V.P., E.D., M.D., and M.L.S. Design, data and biological sample collection and organization, securing funding, implementation and coordination for the Mexico City Prospective Study; J.B.-C., P.K.-M., J.A., J.M.T., J.R.E., R.C., and R.T.-C. Design, data and biological sample collection and organization, securing funding, implementation and coordination for the Geisinger Health System study: C.D.S., T.M., and D.J.C. Design, data and biological sample collection and organization, securing funding, implementation and coordination for the Malmö Diet and Cancer study: O.M. Design, data and biological sample collection and organization, securing funding, implementation and coordination for the Taiwan metabochip consortium: Y.I.C. and J.I.R. Design, data and biological sample collection and organization, securing funding, implementation and coordination for the University of Pennsylvania Penn Medicine BioBank: D.J.R. Design, data and biological sample collection and organization, securing funding, implementation and coordination for the Duke Catheterization Genetics cohort: W.E.K. and S.H.S. **Competing interests:** Regeneron authors receive salary from and own options and/or stock of the company. J.R.E. reports grant funding from Boehringer Ingelheim to the University of Oxford for the EMPA-KIDNEY trial of empagliflozin in patients with chronic kidney disease (clinical trials registration number NCT03594110). R.C. has obtained grants to the University of Oxford for the independent design, conduct, analysis, and reporting of randomized trials of lipid modifying therapies from Merck & Co. and from Medco/Novartis. In addition, R.C. received a research prize from Pfizer. This work has been described in one or more pending provisional patent applications. R.C. is an inventor on a patent application, for which he has waived personal royalties in favor of the Nuffield Department of Public Health, held/submitted by University of Oxford that covers a statin-related myopathy genetic test. Emma Link, Rory Collins, Sarah Parish, and Mark Lathrop are inventors on patent application EP2857525A1 held/submitted by Oxford University Innovation Ltd. that covers the method of determining the susceptibility to statin-induced myopathy. M.A.R.F. and L.A.L. are inventors on a provisional patent application (no. 63/019,589) submitted by RGC relating to PCSK1 genetics. P.A., O.S., A.B., M.A.R.F., and L.A.L. are inventors on a provisional patent application (no. 63/042,327) submitted by RGC relating to GPR75 genetics. P.A., O.S., A.B., M.A.R.F., and L.A.L. are inventors on a provisional patent application (no. 63/066,182) submitted by RGC relating to CALCR genetics. G.D.Y. is the chief scientific officer and member of the board of directors at Regeneron Pharmaceuticals. A.J.M. is an executive officer of Regeneron Pharmaceuticals. **Data and materials availability:** The data supporting the findings of this manuscript are reported in the main text, in the figures, or in the supplementary materials and are tabulated in Table 1 and tables S1 to S21. UKB individual-level genotypic and phenotypic data are available to approved investigators via the UK Biobank study (www.ukbiobank.ac.uk/). Additional information about registration for access to the data are available at www.ukbiobank.ac.uk/register-apply/. Data access for approved applications requires a data transfer agreement between the researcher's institution and UK Biobank, the terms of which are available on the UK Biobank website (www.ukbiobank.ac.uk/media/ezrderzw/applicant-mta.pdf). GHS individual-level data are available to qualified academic noncommercial researchers through the portal at https://regeneron.envisionpharma.com/vt_regeneron/ under a data access agreement. MCPS individual-level data are available to qualified noncommercial researchers by emailing mcps-access@ndph.ox.ac.uk. The data access policy is outlined at www.ctsu.ox.ac.uk/files/mcps-data-access-policy-v2-1-english.pdf. Summary association statistics for GHS and MCPS are available as online supplemental files or at https://rgc-community.regeneron.com subject to a license. eQTL summary statistics were downloaded from the GTEx portal (https://gtexportal.org/). T2D Knowledge Portal summary statistics for associations with type 2 diabetes were accessed via the web portal (https://t2d.hugeamp.org/).

Regeneron Genetics Center
Goncalo Abecasis[1], Aris Baras[1], Michael Cantor[1], Giovanni Coppola[1], Andrew Deubler[1], Aris Economides[1], Katia Karalis[1], Luca A. Lotta[1], John D. Overton[1], Jeffrey G. Reid[1], Alan R. Shuldiner[1], Nilanjana Banerjee[1], Dadong Li[1], Deepika Sharma[1], Xiaodong Bai[1], Suganthi Balasubramanian[1], Andrew Blumenfeld[1], Gisu Eom[1], Lukas Habegger[1], Alicia Hawes[1], Shareef Khalid[1], Evan K. Maxwell[1], William Salerno[1], Jeffrey C. Staples[1], Josh Backman[1], Mathew Barber[1], Christian Benner[1], Shan Chen[1], Amy Damask[1], Lee Dobbyn[1], Manuel A. R. Ferreira[1], Arkopravo Ghosh[1], Lauren Gurski[1], Eric Jorgenson[1], Bindu Kalesan[1], Jack A. Kosmicki[1], Hyun Min Kang[1], Alexander Li[1], Nan Lin[1], Daren Liu[1], Adam E. Locke[1], Jonathan Marchini[1], Anthony Marcketta[1], Joelle Mbatchou[1], Arden Moscati[1], Colm O'Dushlaine[1], Charles Paulding[1], Jonathan Ross[1], Eli Stahl[1], Dylan Sun[1], Cristopher Van Hout[1], Kyoko Watanabe[1], Bin Ye[1], Andrey Ziyatdinov[1], Marcus B. Jones[1], Michelle G. LeBlanc[1], Jason A. Mighty[1], Lyndon J. Mitnaul[1], Ariane Ayer[1], Kavita Praveen[1]

DiscovEHR Collaboration
Lance J. Adams[2], Jackie Blank[2], Dale Bodian[2], Derek Boris[2], Adam Buchanan[2], David J. Carey[2], Ryan D. Colonie[2], F. Daniel Davis[2], Dustin N. Hartzel[2], Melissa Kelly[2], H. Lester Kirchner[2], Joseph B. Leader[2], David H. Ledbetter[2], J. Neil Manus[2], Christa L. Martin[2], Michelle Meyer[2], Tooraj Mirshahi[2], Matthew Oetjens[2], Thomas Nate Person[2], Christopher D. Still[2], Natasha Strande[2], Amy Sturm[2], Jen Wagner[2], Marc Williams[2]

[1]Regeneron Genetics Center, Regeneron Pharmaceuticals Inc., Tarrytown, NY 10591, USA. [2]Geisinger Health System, Danville, PA 17882, USA.

SUPPLEMENTARY MATERIALS

science.sciencemag.org/content/373/6550/eabf8683/suppl/DC1
Materials and Methods
Figs. S1 to S9
Tables S1 to S21
References (*58*–*79*)
MDAR Reproducibility Checklist

8 December 2020; accepted 17 May 2021
10.1126/science.abf8683

Pushing the Boundaries of Knowledge

As AAAS's first multidisciplinary, open access journal, *Science Advances* publishes research that reflects the selectivity of high impact, innovative research you expect from the *Science* family of journals, published in an open access format to serve a vast and growing global audience. Check out the latest findings or learn how to submit your research: **ScienceAdvances.org**

Science Advances
AAAS

GOLD OPEN ACCESS, DIGITAL, AND FREE TO ALL READERS

RESEARCH ARTICLE SUMMARY

IMMUNOMETABOLISM

Diet-regulated production of PDGFcc by macrophages controls energy storage

Nehemiah Cox†, Lucile Crozet†, Inge R. Holtman, Pierre-Louis Loyher, Tomi Lazarov, Jessica B. White, Elvira Mass, E. Richard Stanley, Olivier Elemento, Christopher K. Glass, Frederic Geissmann*

INTRODUCTION: To accommodate daily and seasonal variation in caloric intake, metazoans have evolved specialized tissues dedicated to dynamic storage and release of energy. Excessive or impaired energy storage in these adipose tissues results in obesity, lipodystrophy, or cachexia, and impairs organismal homeostasis. Adipose tissues consist of fat-storing adipocytes, supporting stromal cells, and immune cells. Adipocytes dynamically accumulate or release lipids in late embryos and during the postnatal period. Stromal cells include tissue macrophages, which are tightly associated with adipocytes across the animal kingdom from *Drosophila* to humans. Landmark studies have demonstrated that in the obese state, monocyte-derived macrophages are recruited into tissues via C-C chemokine receptor type 2 (CCR2) and produce cytokines such as tumor necrosis factor (TNF) that cause systemic inflammation, ectopic lipid storage, and insulin resistance. However, neither CCR2 nor monocytes appear to regulate fat mass or adiposity on their own. Recent observations in several models suggest that macrophages may also control adiposity, although their actual function and the underlying cellular and molecular mechanisms remain poorly understood.

RATIONALE: Macrophages are phagocytes that can eliminate unfit cells, microorganisms, and metabolic waste, and produce a large range of bioactive molecules and growth factors. In addition to monocyte-derived macrophages—which are the short-lived progeny of hematopoietic stem cells in vertebrates—most animals possess long-lived tissue macrophages. In mice, these cells originate from early mesodermal erythromyeloid progenitors, which invade the embryo proper soon after gastrulation and represent a foundational cell type within most organ anlagen. Resident macrophages serve tissue-specific purposes. For example, osteoclasts are critical for the development and remodeling of bones, whereas microglia in the central nervous system support neuronal circuit development, Kupffer cells scavenge blood particles and dying red blood cells in the liver, and alveolar macrophages uptake surfactant and remove airborne pollutants and microbes from the airways. We therefore hypothesized that resident macrophages associated with fat-storing cells may also support their function. In this study, we took advantage of the presence of equivalent cell types and orthologous genes in *Drosophila* and mice to identify a conserved molecular mechanism that mediates the control of adiposity and energy storage in metazoans by macrophages.

RESULTS: Using a combination of genetic and pharmacological approaches, we found that resident macrophage deficiency prevents storage of lipids in adipocytes from wild-type and *Ccr2*$^{-/-}$ mice fed a high-fat diet, as well as hyperphagic leptin receptor–deficient mice. Moreover, we observed that macrophage deficiency impairs lipid storage in newborn mice and *Drosophila* larvae. Thus, we carried out a genetic screen in *Drosophila* and discovered that the macrophage-derived PDGF/VEGF-family growth factor Pvf3 and its receptor on fat-body cells are required for lipid storage in *Drosophila* larvae. We next identified the mouse Pvf3 ortholog PDGFcc, which controls lipid storage in mouse adipocytes. PDGFcc was produced by fat-resident macrophages in a diet-regulated manner and acted on subcutaneous and visceral white adipocytes in an adipose tissue–autonomous manner to control lipid storage in newborn and adult mice. PDGFcc blockade or deficiency did not affect food intake and absorption but resulted in increased energy expenditure at the organismal level, in part via increased thermogenesis in brown adipose tissue. This function of fat-resident macrophages was distinct from that of CCR2-dependent monocyte-derived macrophages, which mediate systemic inflammation and insulin resistance in obese mice and do not produce PDGFcc.

CONCLUSION: Our data identify an evolutionarily conserved function of adipose tissue–resident macrophages that couples energy intake with fat storage in adipocytes through the production of PDGFcc and independently from inflammation promoted by CCR2-dependent macrophages. By promoting energy storage over expenditure in neonates and adults, the production of PDGFcc by resident macrophages appears to regulate or buffer the systemic availability of lipids for metabolic purposes. These findings may be conducive to the design of pharmacological interventions in obesity, lipodystrophy, and cachexia. ■

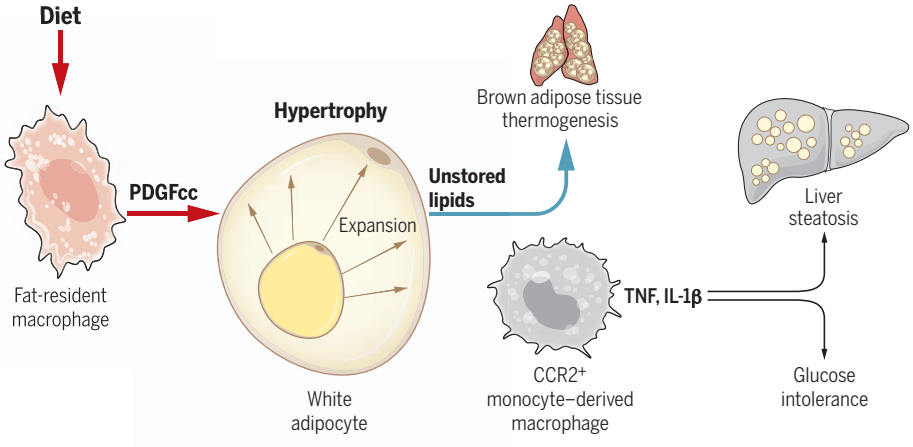

Parsimony diagram for the control of adiposity by macrophages. Fat-resident macrophages produce PDGFcc in response to diet, which increases lipid storage by white adipocytes (red arrows). PDGFcc blockade, in contrast, results in reduced lipid storage by adipocytes, and lipids not stored are redirected toward increased thermogenesis in brown adipose tissue (blue arrow). On the other hand, monocyte-derived macrophages recruited to hypertrophic adipocytes produce TNF and interleukin (IL)–1β, which mediate hepatosteatosis and insulin resistance (black arrows).

The list of author affiliations is available in the full article online.
*Corresponding author. Email: geissmaf@mskcc.org
†These authors contributed equally to this work.
Cite this article as N. Cox *et al.*, *Science* **373**, eabe9383 (2021). DOI: 10.1126/science.abe9383

READ THE FULL ARTICLE AT
https://doi.org/10.1126/science.abe9383

RESEARCH ARTICLE

IMMUNOMETABOLISM

Diet-regulated production of PDGFcc by macrophages controls energy storage

Nehemiah Cox[1]†, Lucile Crozet[1,2]†, Inge R. Holtman[3], Pierre-Louis Loyher[1], Tomi Lazarov[1,2], Jessica B. White[2], Elvira Mass[1,4], E. Richard Stanley[5], Olivier Elemento[6,7], Christopher K. Glass[3], Frederic Geissmann[1,2]*

The mechanisms by which macrophages regulate energy storage remain poorly understood. We identify in a genetic screen a platelet-derived growth factor (PDGF)/vascular endothelial growth factor (VEGF)–family ortholog, Pvf3, that is produced by macrophages and is required for lipid storage in fat-body cells of *Drosophila* larvae. Genetic and pharmacological experiments indicate that the mouse Pvf3 ortholog PDGFcc, produced by adipose tissue–resident macrophages, controls lipid storage in adipocytes in a leptin receptor– and C-C chemokine receptor type 2–independent manner. PDGFcc production is regulated by diet and acts in a paracrine manner to control lipid storage in adipose tissues of newborn and adult mice. At the organismal level upon PDGFcc blockade, excess lipids are redirected toward thermogenesis in brown fat. These data identify a macrophage-dependent mechanism, conducive to the design of pharmacological interventions, that controls energy storage in metazoans.

Daily and seasonal variation in caloric intake results in cycles of energy storage and expenditure (*1*). To accommodate these cycles, metazoans have evolved specialized fat-storing tissues dedicated to dynamic storage of energy without the common lipotoxicity associated with fat accumulation in other cells (*1*, *2*). These adipose tissues consist of lipid-storing adipocytes, stromal cells, and immune cells. Landmark studies have firmly established that recruitment of monocytes into adipose and peripheral tissues of obese animals promotes inflammation, ectopic fat deposition in the liver, and insulin resistance, and that these occur via the production of inflammatory cytokines such as tumor necrosis factor (TNF) by monocyte-derived macrophages (*3*–*15*). Genetic or pharmacological inhibition of the C-C chemokine receptor type 2 (CCR2)–dependent recruitment of bone marrow–derived monocytes into tissues prevents or alleviates metabolic syndrome in obese animals (*9*, *12*, *13*, *16*–*18*). Thus, CCR2-dependent macrophages are a therapeutic target in metabolic diseases associated with obesity.

[1]Immunology Program, Sloan Kettering Institute, Memorial Sloan Kettering Cancer Center, New York, NY 10065, USA. [2]Weill Cornell Graduate School of Medical Sciences, New York, NY 10065, USA. [3]Department of Cellular and Molecular Medicine, University of California, San Diego, CA, USA. [4]Developmental Biology of the Immune System, LIMES Institute, University of Bonn, 53115 Bonn, Germany. [5]Department of Developmental and Molecular Biology, Albert Einstein College of Medicine, Bronx, NY 10461, USA. [6]Department of Physiology and Biophysics, Institute for Computational Biomedicine, Weill Cornell Medicine, New York, NY 10065, USA. [7]Caryl and Israel Englander Institute for Precision Medicine, Weill Cornell Medicine, New York, NY 10065, USA.
*Corresponding author. Email: geissmaf@mskcc.org
†These authors contributed equally to this work.

CCR2 blockade or deficiency, however, does not prevent weight gain, but only its inflammatory and metabolic complications. Recent studies in models of macrophage-deficient animals suggest that macrophages may also regulate mouse weight and adiposity (*19*–*24*). For example, solute carrier family 6 member 2 (*Slc6a2*) deficiency (*23*), which reduces clearance of sympathetic norepinephrine by neuron-associated macrophages in the adipose tissue, leads to sustained weight loss in obese mice. *Trib1*$^{-/-}$ (Tribbles homolog 1–deficient) mice, which lack pro-adipogenic TRIB1-dependent macrophages (*19*), are also lean and develop metabolic syndrome akin to lipodystrophy (*19*). Colony-stimulating factor 1 receptor (CSF1R) blockade, which depletes all macrophages, keeps mice lean under a high-fat diet and protects them against metabolic syndrome, in part possibly because of the role of microglia in regulating leptin sensitivity in the mediobasal hypothalamus (*21*, *22*). Finally, *Trem2*$^{-/-}$ (triggering receptor expressed on myeloid cells 2–deficient) mice (*24*) develop worse obesity and metabolic syndrome due to a global control of a lipid-associated macrophage program by TREM2 (*24*). Although the systemic effects of CSF1R blockade and germline deletion of *Csf1r*, *Ccr2*, *Trib1*, *Slc6a2*, or *Trem2* combined with the developmental and functional heterogeneity of macrophages may confound the analysis of macrophage functions in these models (*4*, *19*, *24*–*40*), these data nonetheless suggest that macrophages are involved, directly or indirectly, in the regulation of energy storage. Here, we attempted to identify a molecular mechanism that mediates the direct control of adiposity and energy storage by macrophages.

CSF1R-dependent control of lipid storage in newborn, hyperphagic, and high-fat diet–fed adult mice

Six-week-old adult wild-type C57Bl/6J and *Ccr2*$^{-/-}$ mice fed a high-fat diet (45% kcal from fat, 4.73 kcal/g) and treated with the CSF1R tyrosine kinase inhibitor PLX5622 (PLX) for 8 weeks stayed lean, with fat pads half the weight of controls (Fig. 1A and fig. S1), whereas untreated wild-type and *Ccr2*$^{-/-}$ mice became obese (*9*) (Fig. 1A and fig. S2). White adipocytes from PLX-treated mice did not increase their BODIPY^{+} lipid content, thus lacking the hypertrophy normally induced by a high-fat diet (Fig. 1, B and C). Mice treated with a blocking anti-CSF1R antibody [AFS98 (*41*)] presented with a similar phenotype (Fig. 1A and fig. S1, C to L), indicating that an off-target effect of the kinase inhibitor was unlikely. PLX treatment also reduced obesity and adipocyte hypertrophy in hyperphagic leptin receptor–deficient mice (*Lepr*$^{-/-}$, *db/db*) fed a control diet (10% kcal from fat, 3.85 kcal/g) (Fig. 1, A and B, and fig. S1, M and N). Thus, CSF1R blockade prevents fat storage and adipocyte hypertrophy in high-fat diet–fed and hyperphagic mice, in a manner independent of CCR2 and at least partially independent of LEPR.

The initial hypertrophy of adipocytes, which allows for fat storage during the first month of life, was abolished by global genetic deletion of *Csf1r* in *Csf1r*^{Cre}*; Csf1r*$^{f/f}$ mice (Fig. 2A and fig. S3). Similarly, genetic deletion of *Csf1r* or *Spi1* in resident macrophages (*42*) (in *Tnfrsf11a*^{Cre}*; Csf1r*$^{f/f}$ mice and *Tnfrsf11a*^{Cre}*; Spi1*$^{f/f}$ mice) resulted in mice with small fat pads, corresponding to small perilipin (PLIN1)$^{+}$ adipocytes with little BODIPY^{+} lipid content (Fig. 2A and fig. S4). By contrast, adipose tissue weight and morphology of adipocytes were normal in young *Ccr2*$^{-/-}$ mice (*43*) (fig. S2, A, B, and D), as well as in mice carrying a *Csf1r* deletion in the *Flt3* (fms-like tyrosine kinase 3)–expressing hematopoietic stem cell lineage (*42*, *44*) (fig. S2, A, B, and E). Thus, in addition to limiting adipocyte hypertrophy in adult hyperphagic and high-fat diet–fed mice, *Csf1r* deficiency in the CCR2-independent resident macrophage lineage may also prevent the initial hypertrophy of adipocytes in newborn mice. The adipocyte phenotype of genetic mutant animals, however, may be compounded by the effects of global macrophage deficiency during development.

Macrophage-dependent control of lipid storage in *Drosophila* larvae

We hypothesized that these adipocyte phenotypes may be attributable to a macrophage defect. Because fat-storing cells and macrophages are conserved across the animal kingdom, we generated macrophage-less *Drosophila* larvae by inducing apoptosis in hemocytes (*Drosophila* macrophages) using either *Srp*^{Hemo}*-gal4* > *uas-reaper* or *Hml-gal4* > *uas-reaper* lines (*45*–*47*)

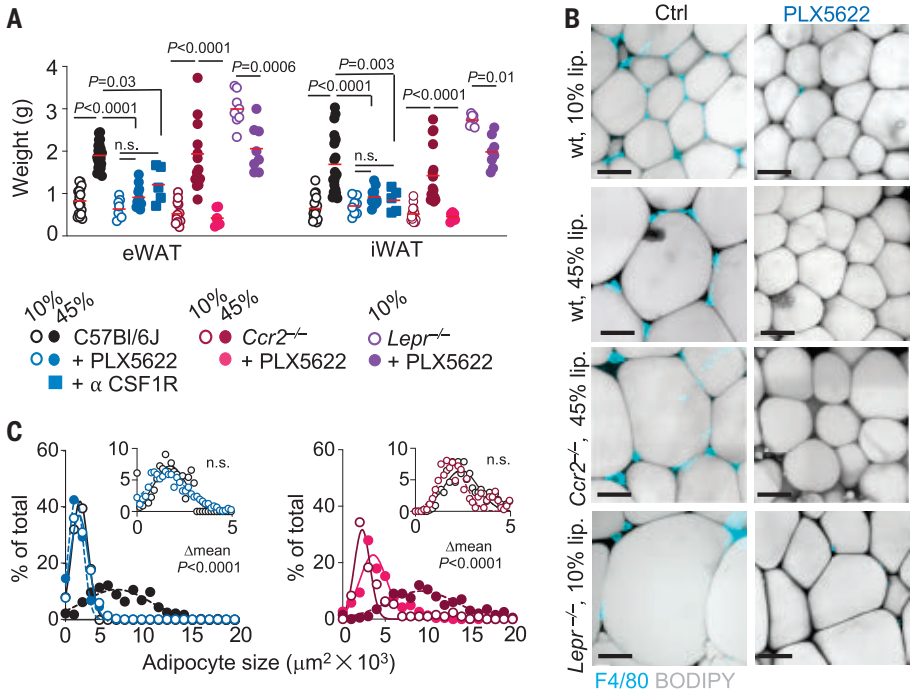

Fig. 1. CCR2-independent macrophages control lipid storage in adipocytes. (**A**) Weight of epididymal (eWAT) and inguinal (iWAT) fat pads from 14-week-old C57Bl/6J and *Ccr2*$^{-/-}$ mice and 12-week-old *Lepr*$^{-/-}$ mice subjected to the indicated treatments for 8 weeks (n = 12 to 20 mice per experimental group from four independent experiments for C57Bl/6J mice; n = 8 to 16 mice per experimental group from three independent experiments for *Ccr2*$^{-/-}$ and *Lepr*$^{-/-}$ mice). Dots represent individual mice; n.s., not significant. (**B**) Representative fluorescent whole-mount images of iWAT from mice in (A). Scale bars, 40 μm. (**C**) Adipocyte size in iWAT of mice from (A) (n = 10 C57Bl/6J mice and n = 6 *Ccr2*$^{-/-}$ mice per experimental group from two or three independent experiments). See also figs. S1 and S2. Dots represent percent of adipocytes per size interval. P values in (A) and (C) were obtained using one-way ANOVA with Sidak's correction. Red lines indicate mean values.

(Fig. 2, B to E, and fig. S5). In both cases, we observed reduced buoyancy (*48*) in hemocyte-deficient wandering third-stage larvae (L3), corresponding to a ~60% reduction in triglyceride content and fat-body cell size as compared to control larvae (Fig. 2, C to E). Genetic labeling of *Drosophila* hemocytes with *Hml-gal4 > uas-GFP* or *Srp*^{Hemo}*-mCherry* (*49*) reporters also confirmed a close association between hemocytes and fat-body cells labeled with *c564-gal4 > uas-GFP*$^{+}$ (*46*) in L3 larvae (Fig. 2B). Thus, a genetic screen for macrophage-derived factors may reveal a potentially conserved mechanism by which *Drosophila* and mouse macrophages control lipid storage and adipocyte hypertrophy.

Macrophage-derived PDGF-family growth factor Pvf3 controls lipid storage in *Drosophila* fat-body cells

Drosophila larvae represent a highly tractable model for screening the role of conserved families of growth factors and cytokines produced by macrophages (*50*–*52*). Among these, hemocyte-specific RNA interference (RNAi) of the platelet-derived growth factor (PDGF)/vascular endothelial growth factor (VEGF)–family ortholog *Pvf3* (PDGF- and VEGF-related factor 3; *Srp*^{Hemo}*-gal4 > uas-pvf3-IR*) decreased triglyceride content (Fig. 3A) and fat-body cell size by >50% (Fig. 3, B and C, and fig. S5C). Hemocyte-specific RNAi of the closely related *Pvf1* presented with a milder phenotype (Fig. 3, A and B, and fig. S5C). To confirm the role of *Pvf3* and to control for off-target effects of the RNAi constructs, we analyzed *Pvf3* mutant flies (*Pvf3*^{EY09531}; Fig. 3, D to F). L3 *Pvf3*^{EY09531} larvae had reduced buoyancy (Fig. 3D), a >50% reduction in triglyceride content (Fig. 3E), and small fat-body cells relative to controls (Fig. 3F). By contrast, the genetic rescue of *Pvf3* expression in *Pvf3*^{EY09531} larvae (*Pvf3*^{EY09531}*; He-gal4 > uas-Pvf3*) restored triglyceride content and fat-body cell size (Fig. 3, E and F). In addition, because all *Drosophila* PDGF-family orthologs share the same receptor—PDGF/VEGF receptor (Pvr) (*50*, *53*), which is expressed by fat-body cells (*54*)—we generated fat-body–specific *Pvr* RNAi (*c564-gal4 > uas-Pvr-IR*), which yielded L3 larvae with reduced triglyceride content and small fat-body cells (Fig. 3, G and H). These data strongly suggest that *Drosophila* hemocytes control fat-body cell size and triglyceride storage via production of the PDGF/VEGF-family growth factor Pvf3 by hemocytes, likely acting on Pvr on fat-body cells.

Macrophage-derived PDGFcc controls lipid storage in newborn and adult mice

Among mouse *Pvf3* orthologs, data from the ImmGen Consortium (*55*) indicated that platelet-derived growth factor C (*Pdgfc*) is the most abundantly expressed PDGF/VEGF-family member in mouse fat-associated macrophages (Fig. 4A). *Pdgfc* expression was up-regulated in the fat tissue of high-fat diet–fed wild-type and *Ccr2*$^{-/-}$ mice as well as control diet–fed hyperphagic *Lepr*$^{-/-}$ (*db/db*) mice in a CSF1R-dependent manner (Fig. 4B). Additionally, *Pdgfc* expression was severely decreased in fat pads from 4-week-old *Csf1r*^{Cre}*; Csf1r*$^{f/f}$ mice (Fig. 4C). Hypothesizing that PDGFcc produced by macrophages may be the growth factor involved in adipocyte hypertrophy in mice, we generated *Csf1r*^{Cre}*; Pdgfc*$^{f/f}$ mice (Fig. 4, D to F, and fig. S6, A to E). Adipocytes developed normally in *Csf1r*^{Cre}*; Pdgfc*$^{f/f}$ mice, as assessed by *Plin1* and *Ucp1* expression (fig. S6E), but white adipose tissue weight was decreased by 35% in 4-week-old *Csf1r*^{Cre}*; Pdgfc*$^{f/f}$ mice (Fig. 4D). Adipocyte size and lipid content were also reduced (Fig. 4E). In contrast to *Csf1r*$^{-/-}$ mice (fig. S3A), *Csf1r*^{Cre}*; Pdgfc*$^{f/f}$ mice had teeth and were not runted (Fig. 4F and fig. S6A), which implied that macrophage functions were otherwise largely intact. Furthermore, this suggested that the adipocyte phenotype was not compounded by a failure to thrive, as is the case in mice with global *Csf1r* deficiency (fig. S3, A to D). To test the hypothesis that PDGFcc also controls lipid storage in adult mice, we treated 6-week-old C57Bl/6J mice with PDGFcc-neutralizing antibodies (AF1447) for 6 weeks (Fig. 4, G to I, and fig. S6, F to K). Mice treated with anti-PDGFcc antibodies and fed a high-fat diet remained lean (Fig. 4G), with lower fat mass and smaller adipocytes than controls (Fig. 4, H and I). Thus, the production of PDGFcc by macrophages appears to control lipid storage in the adipocytes of newborn mice. Additionally, PDGFcc blockade in adult mice prevents adipocyte hypertrophy in response to a high-fat diet.

Pdgfc expression by resident macrophages is increased in response to high-fat diet

Flow cytometry, RNA-seq, and quantitative polymerase chain reaction (qPCR) analyses revealed the presence of three main *Csf1r*-dependent F4/80^{+} myeloid subsets—TIM4^{+}F4/80^{+} macrophages and two populations of small TIM4^{-}F4/80^{+} cells (where TIM4 denotes large T cell immunoglobulin and mucin domain–containing 4)—within visceral and subcutaneous white adipose tissue (Fig. 5A and figs. S7 and S8). *Pdgfc* was preferentially expressed and induced by a high-fat diet in white adipose tissue TIM4^{+}F4/80^{+} macrophages but not in liver

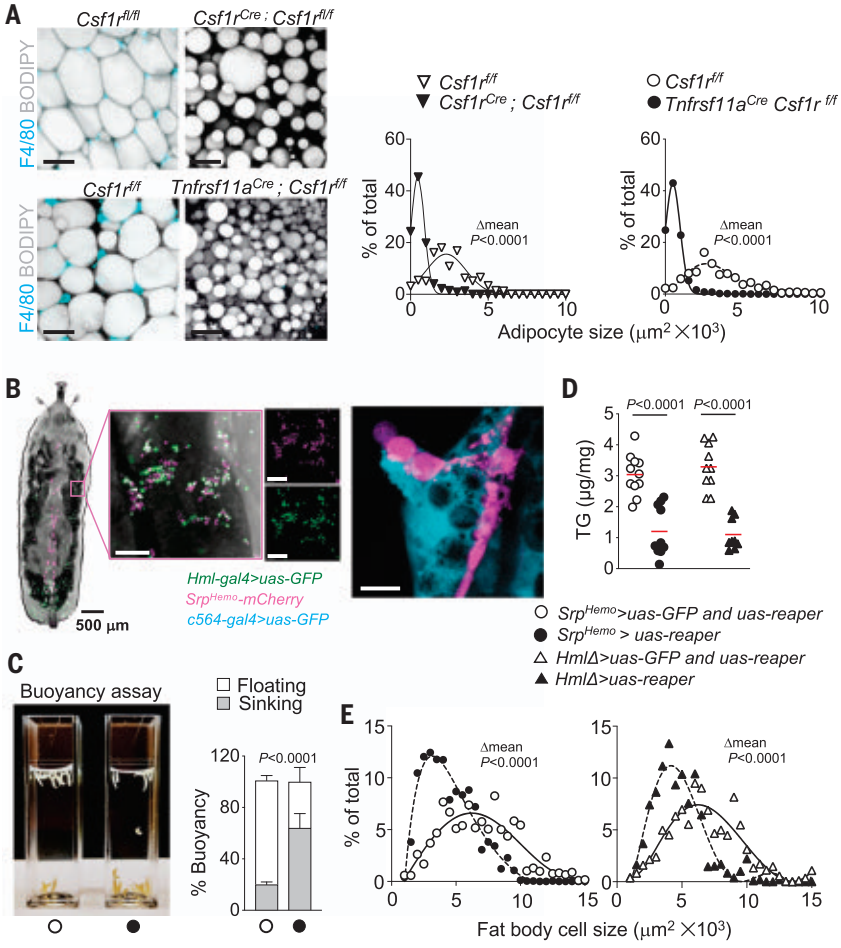

Fig. 2. Macrophages control lipid storage in adipocytes of newborn mice and fat-body cells of *Drosophila* larvae. (**A**) Representative fluorescent whole-mount images (left) and adipocyte size (right) for iWAT from 4-week-old mice (n = 6 per genotype obtained from three to six litters). Scale bars, 40 μm. See also figs. S3 and S4. (**B**) Representative fluorescent images of L3 larvae depicting the expression of hemocyte-specific drivers Hemolectin (Hml) and Serpent (Srp) and fat-body–specific driver c564. Scale bars, 500 μm (whole larvae), 80 μm (larvae insets), 10 μm (far right). (**C**) Buoyancy (mean ± SD) in wandering L3 larvae (n = 6 experimental groups per genotype from three crosses). (**D**) Triglyceride level (TG) normalized to total protein in L3 larvae (n = 10 or 11 experimental groups per genotype from four crosses). (**E**) BODIPY$^+$ fat-body cell size in wandering L3 larvae (n = 6 to 9 experimental groups per genotype from three to four crosses). Dots in (A) and (E) represent percent of adipocytes per size interval. Dots in (D) represent individual experimental groups. P values in (A), (C), and (E) were obtained using Student's t test. P values in (D) were obtained using one-way ANOVA with Sidak's correction. Red lines indicate mean values.

Kupffer cells or brown adipose tissue (iBAT) TIM4$^+$ macrophages (Fig. 5, B and C). By contrast, the production of *Tnf* and *interleukin (Il)1b* was restricted to small TIM4$^-$F4/80$^+$ cells, monocytes, and Kupffer cells (Fig. 5C). White adipose tissue TIM4$^+$ macrophages were present in *Ccr2*$^{-/-}$ and *Flt3*^{Cre}*; Csfr1r*$^{f/f}$ mice but were absent in *Tnfrsf11a*^{Cre}*; Csfr1r*$^{f/f}$ mice (Fig. 5D and figs. S2C and S4K), whereas TIM4$^-$F4/80$^+$ monocyte/macrophages were absent or reduced in *Ccr2*$^{-/-}$ and *Flt3*^{Cre}*; Csfr1r*$^{f/f}$ mice (Fig. 5D and fig. S2C). Lineage-mapping analysis of *Csf1r*$^+$ erythromyeloid progenitors labeled at embryonic day 8.5 showed postnatal labeling of large adipose tissue TIM4$^+$F4/80$^+$ macrophages, but not of small TIM4$^-$F4/80$^+$ cells (Fig. 5E and fig. S7D). Parabiosis experiments showed that TIM4$^+$F4/80$^+$ cells do not exchange between parabionts, in contrast to TIM4$^-$F4/80$^+$ cells and monocytes (Fig. 5F). Thus, *Pdgfc* is preferentially expressed in embryo-derived white adipose tissue–resident macrophages. Finally, immunofluorescence analysis confirmed that PDGFcc was undetectable in the fat pads of *Tnfrsf11a*^{Cre}*; Csfr1r*$^{f/f}$ mice (Fig. 5G). Global transcriptional analysis (RNA-seq) further showed that TIM4$^+$ and TIM4$^-$ cells cluster by population rather than diet in multidimensional scaling and hierarchical clustering of differentially expressed genes (fig. S8 and data S1). Stable transcriptional signatures associated with TIM4$^+$-resident macrophages primarily included homeostatic processes (clusters 1 and 7), whereas TIM4$^-$ monocytes/macrophages highly expressed genes associated with innate immune response and cell proliferation (clusters 2 and 5) (fig. S8, A to E). Thus, TIM4$^+$F4/80$^+$ white adipose tissue–resident macrophages are the main PDGFcc-producing cells in mouse fat pads and respond to a high-fat diet by increasing *Pdgfc* expression, in contrast to TIM4$^-$F4/80$^+$ *Ccr2*-dependent cells, which respond to a high-fat diet by expressing *Tnf* and *Il1b*.

PDGFcc blockade results in increased energy expenditure and hepatic storage

To further investigate the consequence of PDGFcc blockade and the mechanisms that underlie leanness at the organismal level, we performed metabolic studies in high-fat diet–fed mice. Food intake and fecal caloric density in anti-PDGFcc–treated mice were comparable to controls (Fig. 6, A and B, and fig. S6H), indicating that PDGFcc blockade did not affect food intake or intestinal absorption, as observed similarly for mice treated with CSFR1 inhibitor (PLX) (fig. S1, H to J). In addition, PDGFcc blockade did not protect mice against high-fat diet–induced hepatosteatosis (Fig. 6C), inflammation, or insulin resistance (fig. S6, I to K). This was in sharp contrast to *Ccr2*$^{-/-}$ mice and PLX-treated mice, which lack CCR2-dependent inflammatory monocytes/macrophages and are protected against hepatosteatosis, inflammation, and insulin resistance (fig. S1, D to G, and fig. S2, I to L). Thus, PDGFcc blockade decreases adiposity without limiting food intake, intestinal absorption, or the metabolic syndrome, the latter being promoted by a different cell type (i.e., CCR2-dependent monocytes/macrophages).

Six weeks of treatment with anti-PDGFcc under a high-fat diet resulted in a 20% increase in ectopic storage of triglycerides in the liver relative to controls (Fig. 6C), although this was not observed in developing *Csf1r*^{Cre}*; Pdgfc*$^{f/f}$ mice (Fig. 6D); this finding suggested that ectopic lipid storage may not be the cause for reduced lipid storage in adipocytes. Indeed, although thermogenesis-associated transcripts (*56*, *57*) were not altered in the white adipose tissue (Fig. 6, E to G), they were induced in the brown adipose tissue by a high-fat diet and further increased by PDGFcc blockade and CSFR1 inhibition (Fig. 6, E and F). Thermogenic transcripts were also induced in the brown adipose tissue from *Csf1r*^{Cre}*; Pdgfc*$^{f/f}$ mice as well as *Csf1r*^{Cre}*; Csf1r*$^{f/f}$ and *Tnfrsf11a*^{Cre}*; Csf1r*$^{f/f}$ mice (Fig. 6G). Accordingly, PDGFcc blockade

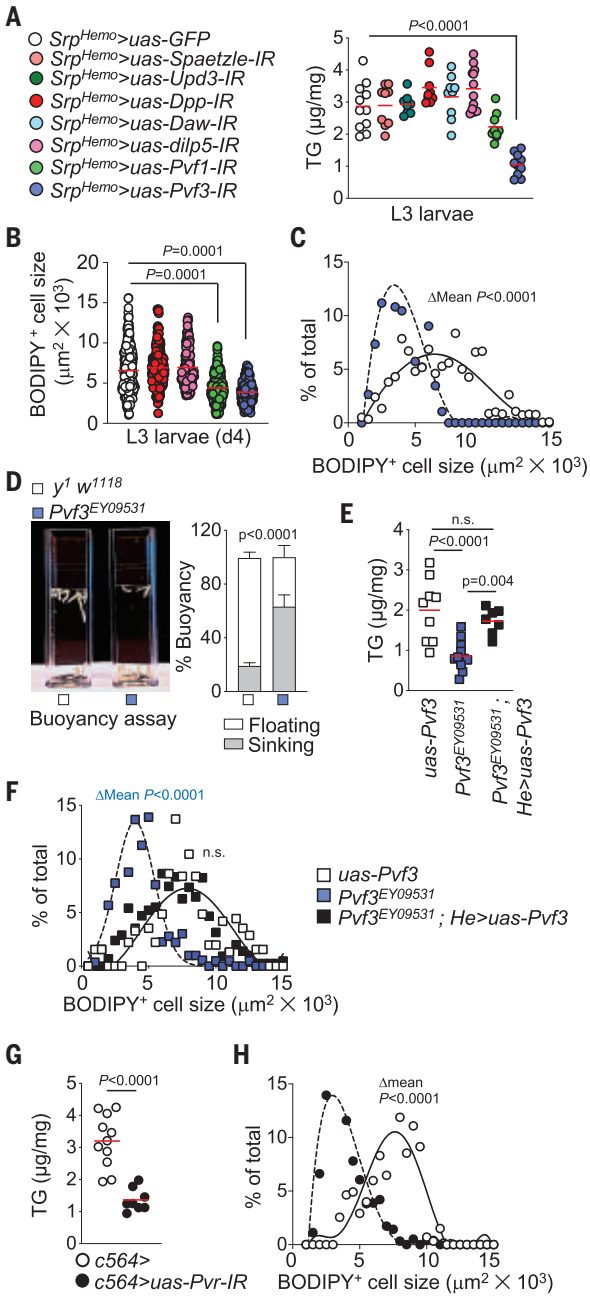

Fig. 3. Hemocyte-derived PDGF-family growth factor Pvf3 controls lipid storage in *Drosophila* fat-body cells. (**A**) Triglyceride level (TG) normalized to total protein in wandering L3 larvae from flies with hemocyte-specific RNAi for the indicated genes and Srp^{Hemo} > *uas-GFP* control (n = 8 to 12 experimental groups per genotype from four crosses). (**B**) BODIPY$^+$ fat-body cell size in L3 larvae (n = 4 to 7 experimental groups per genotype from three to six crosses). (**C**) BODIPY$^+$ fat-body cell size distribution in L3 larvae (n = 3 experimental groups per genotype from three crosses). (**D**) Buoyancy (mean ± SD) in wandering L3 larvae from $Pvf3^{EY09531}$ and control L3 larvae (n = 6 experimental groups per genotype from three crosses). (**E**) TG normalized to total protein in *uas-Pvf3* (control), $Pvf3^{EY09531}$ (mutant), *and* $Pvf3^{EY09531}$*; He > uas-Pvf3* (rescue) L3 larvae (n = 7 to 12 experimental groups per genotype from four crosses). (**F**) BODIPY$^+$ fat-body cell size distribution in L3 larvae from (E) (n = 5 experimental groups per genotype from three crosses). (**G**) TG level normalized to total protein in L3 larvae from flies with fat-body–specific RNAi of *Pvr* and controls (n = 8 to 11 experimental groups per genotype from four crosses). (**H**) BODIPY$^+$ fat-body cell size distribution in L3 larvae from (G) (n = 4 experimental groups per genotype from four crosses). Dots in (A), (E), and (G) represent individual experimental groups. Dots in (B) represent individual fat-body cells. Dots in (C), (F), and (H) represent percent of fat-body cells per size interval. P values in (A) and (B) were obtained with one-way ANOVA with Dunnett's correction for multiple group comparison with a single control group. P values in (E) and (F) were obtained using one-way ANOVA with Sidak's correction. P values in (C), (D), (G), and (H) were obtained using Student's t test. Red lines indicate mean values.

raised surface body temperature in the interscapular area (Fig. 6, H and I) and increased total energy expenditure (Fig. 6, J and K). Thus, reduced lipid storage in white adipocytes is associated with increased energy expenditure at the organismal level, at least in part in the form of thermogenesis by the brown adipose tissue, and with redistribution of excess lipids to the liver in conditions of high-fat diet. We therefore reasoned that PDGFcc may act either locally by promoting storage by adipocytes in a paracrine manner, and/or systemically by limiting expenditure/thermogenesis and lipid redistribution.

PDGFcc is required and sufficient for adipocyte hypertrophy in fat-pad explants

We next performed loss-of-function and rescue experiments in murine isolated fat-pad explants. Wild-type neonatal (P4) murine epididymal fat-pad (eWAT) anlagen contain PDGFRα$^+$ cells, capillaries, and macrophages but lack PLIN1$^+$, BODIPY$^+$, or LipidTox$^+$ adipocytes (fig. S9A). Upon ex vivo culturing, these eWAT explants develop PLIN1$^+$ BODIPY$^+$ adipocytes (*58*) (Fig. 7A and fig. S9B). We found that treatment of wild-type anlagen explants with PDGFcc neutralizing antibodies (AF1447) resulted in the development of small PLIN1$^+$ cells with little BODIPY$^+$ content as compared to anlagen treated with control goat immunoglobulin G (IgG) (Fig. 7, A to C, and fig. S9C). Similarly, anlagen from $Tnfrsf11a^{Cre}$; $Csf1r^{f/f}$ mice also gave rise to small PLIN1$^+$ cells that contain little to no lipids, as evidenced by scant BODIPY staining relative to control littermates (Fig. 7, D to F, and fig. S9D). Addition of recombinant PDGFcc to $Tnfrsf11a^{Cre}$; $Csf1r^{f/f}$ fat-pad anlagen, however, rescued BODIPY staining and size of adipocytes to near wild-type levels (Fig. 7, D to F). These data demonstrate that PDGFcc produced by macrophages is required and sufficient for lipid storage ex vivo in isolated fat-pad explants. PDGFcc appears to promote lipid storage at least in part via a paracrine effect on white adipocytes within fat pads. Thus, increased energy expenditure in vivo is likely to be secondary to the increased systemic availability of lipids that are not stored, although our data do not exclude the possibility that PDGFcc may also act systemically—for example, on brown adipocytes to alter thermogenesis.

PDGFcc controls expression of negative regulators of lipid synthesis and storage

PDGF-receptor signaling in mammals is complex and supports many cellular functions (*59*–*61*). To gain an initial insight into the molecular mechanisms that link PDGFcc to adipocyte hypertrophy, we performed an transcriptional analysis of iWAT from wild-type mice treated with PDGFcc-neutralizing antibodies or goat IgG for 2 weeks, a time point before marked changes in fat mass are observed. An unbiased analysis of hallmark pathways in iWAT using a pre-ranked gene set enrichment analysis (GSEA) identified adipogenesis as the pathway most differentially regulated by PDGFcc blockade after accounting for dietary effects (Fig. 8A). By contrast, the hallmark fatty acid metabolism pathway, which includes genes involved in lipid uptake, lipid oxidation, and lipid mobilization, was not significantly enriched after anti-PDGFcc treatment (data S2). Similarly, hallmark pathways for glycolysis, MTORC1 signaling, or TGFb signaling were not differentially regulated by anti-PDGFcc treatment after accounting for diet effects (Fig. 8A and data S2). An additional GSEA of genes involved in lipid synthesis and storage identified a subset of genes whose expression was up-regulated by PDGFcc blockade regardless of diet, which included several negative regulators of lipid synthesis and storage such as *Insig1* (*62*), *Ppara* (*63*), and *Idh2* (*64*) (Fig. 8B), all of which are associated with obesity. Together these data

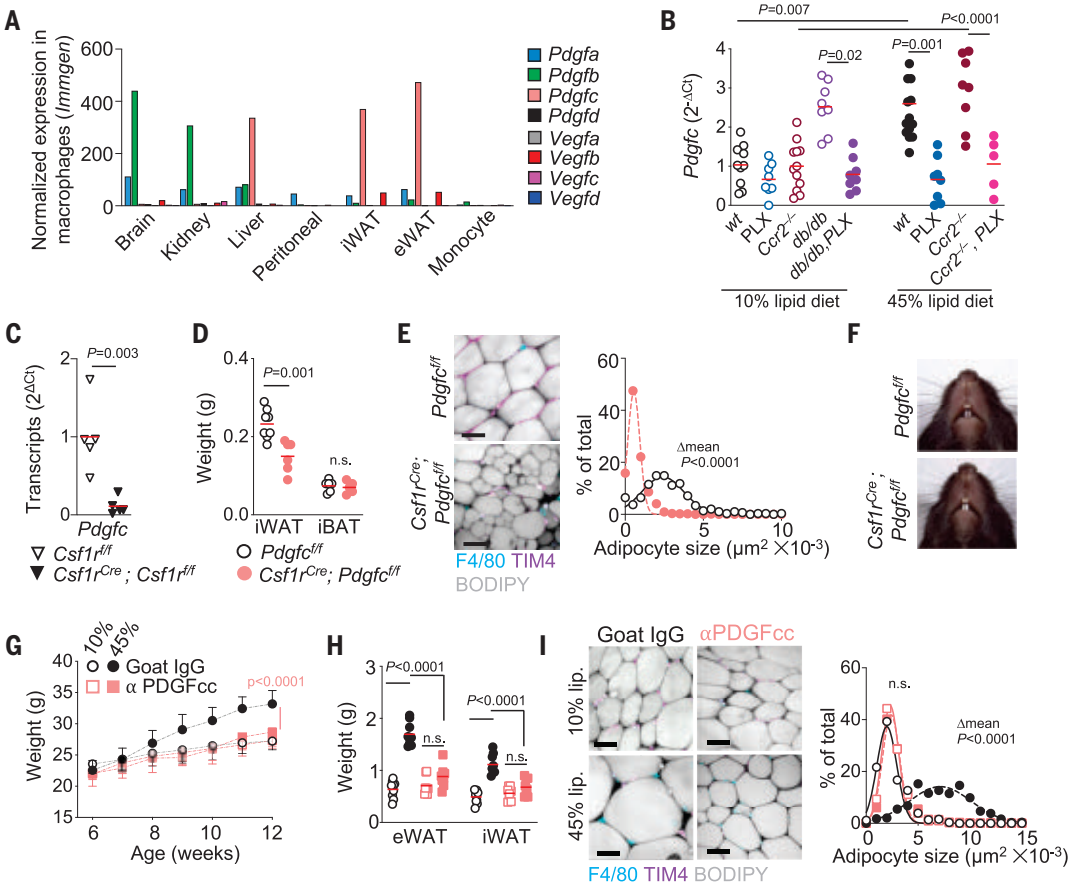

Fig. 4. Macrophage-derived PDGFcc is required for adipocyte hypertrophy in mice. (**A**) Expression of *Pdgf/Vegf* family genes in murine macrophages. Data were obtained from the Immgen database and the expression values were normalized by DESeq2. (**B**) *Pdgfc* expression normalized to *Gapdh* ($2^{-\Delta Ct}$) in iWAT of mice from Fig. 1A (n = 8 to 15 per experimental group from two or three independent experiments). (**C**) *Pdgfc* expression, normalized to *Gapdh* ($2^{-\Delta Ct}$), in iWAT of 4-week-old mutant mice and littermate controls (n = 5 mice per genotype from three independent litters). (**D**) Weight of iWAT and iBAT from 4-week-old *Csf1r*^{Cre}; *Pdgfc*$^{f/f}$ mice and littermate controls (n = 4 to 7 mice per genotype from four litters). (**E**) Representative whole-mount images and adipocyte sizes of iWAT from 4-week-old mice (n = 5 mice per genotype from four independent litters). Scale bars, 40 μm. (**F**) Representative photographs of teeth from 4-week-old mice (n = 4 to 7 mice per genotype from four litters). (**G**) Weight (mean ± SD) of C57Bl/6J mice treated with anti-PDGFcc antibodies or goat IgG for 6 weeks (n = 9 mice per experimental group from two independent experiments). (**H**) Weight of eWAT and iWAT from 12-week-old C57Bl/6J mice in (G). (**I**) Whole-mount images and adipocyte sizes for iWAT from mice in (G). Scale bars, 40 μm. Dots in (B), (C), (D), and (H) represent individual mice. Dots in (E) and (I) represent percent of adipocytes per size interval. P values in (B), (D), (H), and (I) were obtained using one-way ANOVA with Sidak's correction. P values in (C) and (E) were obtained using Student's t test. P values in (G) were obtained using two-way ANOVA. All red lines indicate mean values.

suggest that PDGFcc—rather than lipid uptake, lipid mobilization, lipid oxidation, or extracellular matrix remodeling—regulates lipid synthesis and storage.

Insig1 restricts SREBP-mediated lipogenesis in mature adipocytes and blocks lipid storage (*62*), and *Insig1* deficiency causes obesity in mice fed a control diet (*65*). We thus investigated the regulation of *Insig1* by qPCR in white adipose tissue of wild-type, *Ccr2*$^{-/-}$, and *Lepr*$^{-/-}$ mice treated with PLX or PDGFcc blocking antibodies (Fig. 8C). These experiments indicated that *Insig1* expression is strongly up-regulated in vivo by PLX treatment and by PDGFcc blockade in all experimental models (Fig. 8C). Additionally, a qPCR of isolated fat-pad explants from *Tnfrsf11a*^{Cre}; *Csf1r*$^{f/f}$ mice and control littermates (Fig. 8D), as well as wild-type mice treated with PDGFcc neutralizing antibodies or goat IgG (Fig. 8E), indicated that *Insig1* expression is up-regulated by macrophage deficiency and PDGFcc blockade in an adipose tissue–autonomous manner. This analysis is consistent with the hypothesis that PDGFcc controls lipid synthesis and storage in white adipocytes.

Discussion

Our observations indicate that PDGF-family growth factors (PDGFcc and Pvf3) produced by resident macrophages in response to dietary changes mediate the storage of lipids in the adipocytes of hyperphagic mice, adult mice fed a lipid-rich diet, developing mice, and *Drosophila* larvae. According to our data, the lean phenotypes observed in the absence of macrophages or PDGFcc are unlikely to be attributable to decreased food intake, increased leptin signaling, intestinal malabsorption, or white adipose tissue browning. Rather, our findings indicate that the diet-regulated production of PDGFcc by macrophages is dispensable for adipocyte differentiation but controls their lipid content in a paracrine manner. Excess lipids that are not stored in the absence of PDGFcc appear to be redirected for thermogenesis or ectopic storage. This function of adipose tissue–resident macrophages appears to be evolutionarily conserved in *Drosophila* and mice. *Drosophila* do not have fibroblasts or endothelial cells, and *Pvr* silencing in fat-body cells phenocopies *Pvf3* silencing in hemocytes, which suggests that the interaction between macrophages and fat cells may be a direct one, at least in flies. Nonetheless, we acknowledge that PDGF-receptor signaling in mammals is complex and supports many cellular functions (*59*–*61*). Whether macrophages directly signal to adipocytes in mice, and which member(s) of the PDGF/VEGF-receptor family might mediate the effect of PDGFcc on mouse adipocytes, are both unknown. An initial transcriptional analysis of white adipose tissue suggests that PDGFcc controls the expression of negative regulators of lipid synthesis and storage, including *Insig1*, but more detailed studies are warranted. Overall, our data suggest that resident macrophages and specialized fat-storing cells constitute a functional unit in metazoans, whereby macrophages sense the organism's nutritional state and, when intake is high, signal to adipocytes for increased lipid storage through regulated paracrine production of PDGF-family growth factors.

Macrophage developmental heterogeneity frequently underlies specialized functions associated with distinct macrophage cell types.

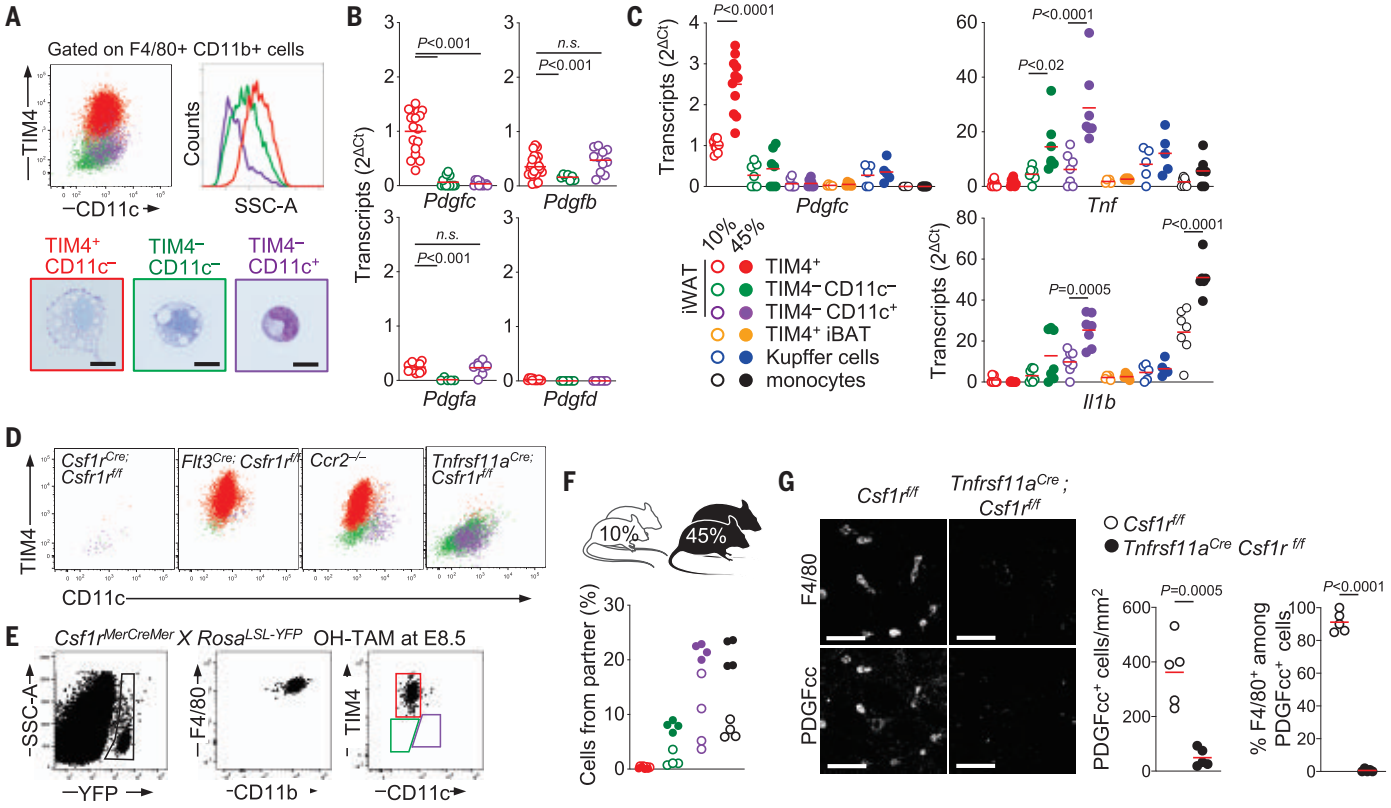

Fig. 5. Diet regulates PDGFcc production by adipose tissue-resident macrophages. (**A**) Representative tSNE flow plot (top) and May-Grunwald Giemsa staining (bottom) of macrophage subsets from iWAT of C57Bl/6J mice (n = 30 from 10 independent experiments; see fig. S7). Scale bars, 10 μm. (**B**) *Pdgfa*, *Pdgfb*, *Pdgfc*, and *Pdgfd* expression, normalized to *Gapdh* and *Actb*, in iWAT macrophages from 4-week-old C57Bl/6J mice (n = 10 to 30 samples from 30 mice). (**C**) *Pdgfc*, *Tnf*, and *Il1b* expression, normalized to *Gapdh* and *ActinB*, in indicated cells isolated from C57Bl/6J mice in Fig. 1A (n = 5 to 7 sorted macrophage samples and n = 9 blood monocyte samples per indicated treatment). (**D**) Representative tSNE flow plot of macrophage subsets from iWAT of 4-week-old mutant mice and control littermates (n = 4 to 9 per genotype obtained from at least three independent litters). (**E**) Flow cytometry analysis of YFP$^+$ embryo-derived macrophages in iWAT from 4-week-old *Csf1r*^{MeriCreMer}; *Rosa*$^{LSL\text{-}YFP}$ mice pulse-labeled at embryonic day 8.5 with 4-hydroxy tamoxifen (OH-TAM) (n = 10 from eight independent litters). (**F**) Flow cytometry analysis of blood monocytes and iWAT macrophages from CD45.1-CD45.2 female parabiotic pairs maintained for 8 weeks on 10% or 45% fat diet (n = 8 mice). (**G**) Fluorescent whole-mount images and quantification of PDGFcc$^+$F4/80$^+$ cells from iWAT of 4-week-old mice (n = 5 per genotype from four independent litters). Scale bars, 40 μm. Dots in (B), (C), (F), and (G) represent values from individual mice. P values in (B) and (C) were obtained using one-way ANOVA with Sidak's correction. P values in (G) were obtained using Student's t test. Red lines indicate mean values.

In the present study, our data clearly show that CCR2-independent TIM4$^+$-resident macrophages are required and sufficient for lipid storage but not sufficient to promote diet-associated inflammation or insulin resistance. By contrast, TIM4$^-$ CCR2-dependent monocytes/macrophages promote inflammation and metabolic syndrome (*9*, *12*–*18*) but are neither required nor sufficient for fat storage in white adipose tissue. Therefore, our data do not support a model where obesity, inflammation, and insulin resistance in mice would all be controlled by the reprogramming of resident macrophages from a homeostatic into a pro-inflammatory role in the setting of metabolic stress. Instead, our data strongly suggest that distinct developmental subsets (i.e., resident macrophages and recruited hematopoietic stem cell–derived monocytes/macrophages) perform distinct functions in the adipose tissue "niche" and are targeted independently by CCR2 and PDGFcc blockade.

This work identifies a mechanism that controls adiposity (i.e., the expansion of fat stores) in metazoans in the context of a cellular and molecular "dissection" of macrophage functions. This may help to explain and predict the effect of genetic variants and pharmacological interventions on lipid storage.

Materials and methods

Mice, diets, and treatments

All experiments on mice were carried out in accordance with our animal license issued by the Institutional Review Board (IACUC 15-04-006) from MSKCC. All mice were maintained under Specific pathogen-free (SPF) conditions. C57Bl/6J male mice were purchased from Jackson Laboratories. *Rosa26*$^{LSL\text{-}Tomato}$ (stock no. 007908), *Rosa26*$^{LSL\text{-}YFP}$ (stock no. 006148), *Rosa26*^{mTmG} (stock no. 007576), and *Lepr*$^{-/-}$*(db/db)* (stock no. 000697) mice were purchased from Jackson Laboratories and bred in-house. *Csf1r*^{Cre}, *Csf1r*^{MeriCreMer}, and *Csf1r*$^{f/f}$ mice were obtained from J. W. Pollard (University of Edinburgh). *Cx3cr1*$^{GFP/+}$ mice were obtained from D. Littman (NYU Skirball Institute). *Flt3*^{Cre} mice were obtained from T. Boehm (Max Planck Institute). *Tnfrsf11a*^{Cre} mice were obtained from Y. Kobayashi (Matsumoto Dental University) (*25*–*27*, *66*). *Ccr2*$^{-/-}$ mice were obtained from I. F. Charro (UCSF). *Pdgfc*$^{f/f}$ mice were purchased from the International Knockout Mouse Consortium. *Csf1r*$^{-/-}$ mice (*67*) were backcrossed to FVB/NJ for more than 10 generations.

Six-week-old C57Bl/6J mice and *Ccr2*$^{-/-}$ mice as well as littermate controls were fed ad libitum an irradiated rodent diet containing 45% kcal from lipids (Research Diets Inc., reference D12451i), 10% kcal from lipids (Research Diets Inc., reference D12450hi), 45% kcal from lipids impregnated with 1200 mg of PLX5622 (Plexxikon) per kilogram of food, or 10% kcal

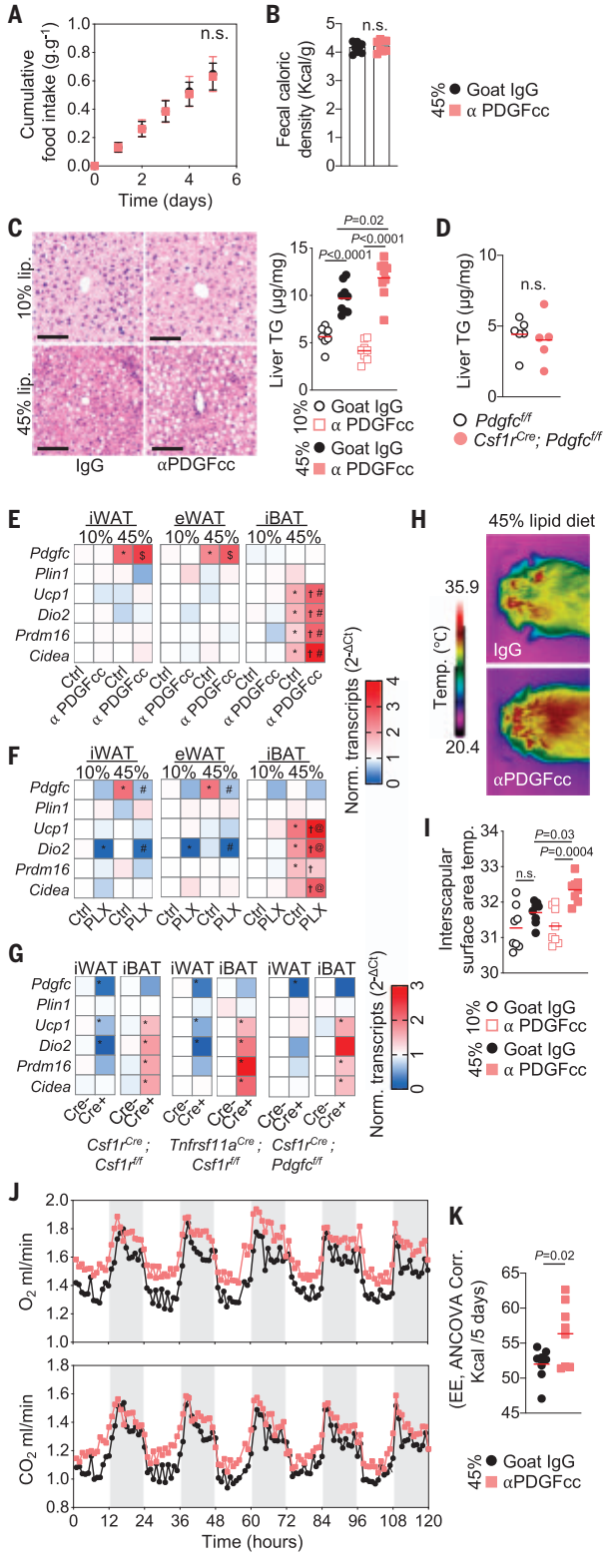

Fig. 6. PDGFcc controls adipocyte hypertrophy and thermogenesis in mice. (**A** and **B**) Cumulative food intake (mean ± SD) (A) and fecal caloric density (B) in 8-week-old C57Bl/6J mice subjected to the indicated treatments for 2 weeks (n = 8 mice per experimental group from one experiment). (**C**) Representative H&E staining (left) and TG content per milligram of tissue (right) of livers from 12-week-old C57Bl/6J mice subjected to the indicated treatments for 6 weeks (n = 8 mice per group from two independent experiments). Scale bars, 100 μm. (**D**) TG content per milligram of tissue from 4-week-old mutant and control littermate mice (n = 5 to 6 mice per genotype from three litters). (**E**) Heatmap of gene expression ($2^{-\Delta Ct}$ relative to *Gapdh*) in iWAT, eWAT, and iBAT of mice in (C). The color scale is normalized to the mean expression value of each transcript in fat tissues of mice fed a control diet (10% lipid) and treated with control goat IgG (n = 5 to 10 mice per experimental group from two independent experiments). *P < 0.01 as compared to control diet–fed mice injected with goat IgG controls, †P < 0.01 as compared to control diet–fed mice injected with PDGFcc neutralizing antibodies, #P < 0.001 as compared to high-fat diet–fed (45% lipid) mice injected with goat IgG controls. (**F**) Heatmap representation as in (E) from iWAT, eWAT, and iBAT of mice in Fig. 1A (n = 5 to 10 mice per experimental group from two independent experiments). The color scale is normalized to transcripts in fat pads from control diet–fed mice treated with vehicle control. *P < 0.01 as compared to control diet–fed mice, †P < 0.01 as compared to control diet–fed mice and treated with PLX, @P < 0.01 as compared to high-fat diet–fed mice. (**G**) Heatmap representation as in (E) from iWAT and iBAT of 4-week-old mutant and control littermate mice (n = 5 to 12 mice per genotype from three to six litters). The color scale is normalized to expression in fat pads of Cre-negative controls. *P < 0.01 as compared to Cre-negative littermate controls. (**H** and **I**) Representative infrared images (H) and interscapular area body temperature (I) in wild-type mice from (A). (**J** and **K**) Analysis of oxygen uptake (VO_2) and carbon dioxide (VCO_2) kinetics (J) and covariance-corrected cumulative energy expenditure (EE, ANCOVA corrected) (K) of wild-type mice from (A). Dots in (B), (C), (D), (I), and (K) represent values from individual mice. Dots in (J) represent mean values over time. P values in (A), (B), (D), (G), and (K) were obtained using Student's t test. P values in (C), (E), (F), and (I) were obtained using one-way ANOVA with Sidak's correction. All red lines indicate mean values.

from lipids impregnated with 1200 mg of PLX5622 per kilogram of food for 8 weeks. Mice were weighed three times per week and then the values were averaged for the week. Four-week-old *Lepr*$^{-/-}$*(db/db)* mice were fed ad libitum a rodent irradiated diet containing 10% kcal from lipids (Research Diets Inc., reference D12450hi) for 8 weeks.

Six-week-old C57Bl/6J mice were fed a diet containing 45% kcal from lipids or 10% kcal from lipids and injected intraperitoneally for 6 weeks with CSF1R (clone AFS98, BioXcell) blocking antibodies at 50 mg/kg in 100 μl of PBS or PDGFcc (AF1447 R&D Systems) neutralizing antibodies at 50 μg per mouse in 100 μl of PBS. Antibodies were administrated three times per week.

Tnfrsf11a^{Cre}*; Csf1r*$^{f/f}$, *Tnfrsf11a*^{Cre}*; Spi1*$^{f/f}$, and *Csf1r*^{Cre}*; Csf1r*$^{f/f}$ mice are osteopetrotic and as such lack teeth. To prevent confounding systemic effects due to nutritional intake problems, the *Tnfrsf11a*^{Cre}*; Csf1r*$^{f/f}$, *Tnfrsf11a*^{Cre}*; Spi1*$^{f/f}$, *Csf1r*^{Cre}*; Csf1r*$^{f/f}$, and control littermates were fed a nutritionally fortified water gel. The nutritional gels were replaced every 12 hours.

For tissue collection, mice were euthanized by overdose of anesthetic, with intraperitoneal injection of ketamine (50 mg/kg), xylazine (10 mg/kg), and acepromazine (1.7 mg/kg). Once the withdrawal reflexes were abolished, intracardiac puncture was performed for blood collection, with an EDTA (100 mM, Sigma)–coated syringe (26G needle, 1-ml syringe, BD). The heart was then perfused with 10 ml of phosphate-buffered saline (PBS) at room temperature. The tissues were then collected and analyzed as described below.

Parabiosis and fate mapping

For parabiosis experiments, 6-week-old congenic CD45.1 and CD45.2 mice were surgically joined (*68*). Skin was incised from elbow to knee, forelimbs and hindlimbs were joined with nylon suture, then skin incisions were sutured with stainless steel clips. The mice were fed a sulfatrim diet for 2 weeks after the surgery and before starting 10% lipid diet or 45% lipid diet for 8 weeks. Chimerism in TIM4$^+$ and TIM4$^-$ macrophage populations, as well as in liver Kupffer cells and blood lymphocytes and monocytes, was assessed by flow cytometry.

Fate-mapping experiments in *Csf1r*^{MeriCreMer} mice were performed as described (*27*). In brief, *Csf1r*^{MeriCreMer} females were crossed to *Rosa26*$^{LSL\text{-}tomato}$ *or Rosa26*$^{LSL\text{-}YFP}$ males and injected intraperitoneally at 8.5 days post coitum with 4-hydroxytamoxifen (75 mg/kg body weight; Sigma) plus progesterone (37.5 mg/kg body weight; Sigma) to counteract possible abortion induction. tdTOMATO or yellow fluorescent protein (YFP) expression was then assessed in adult progeny by flow cytometry.

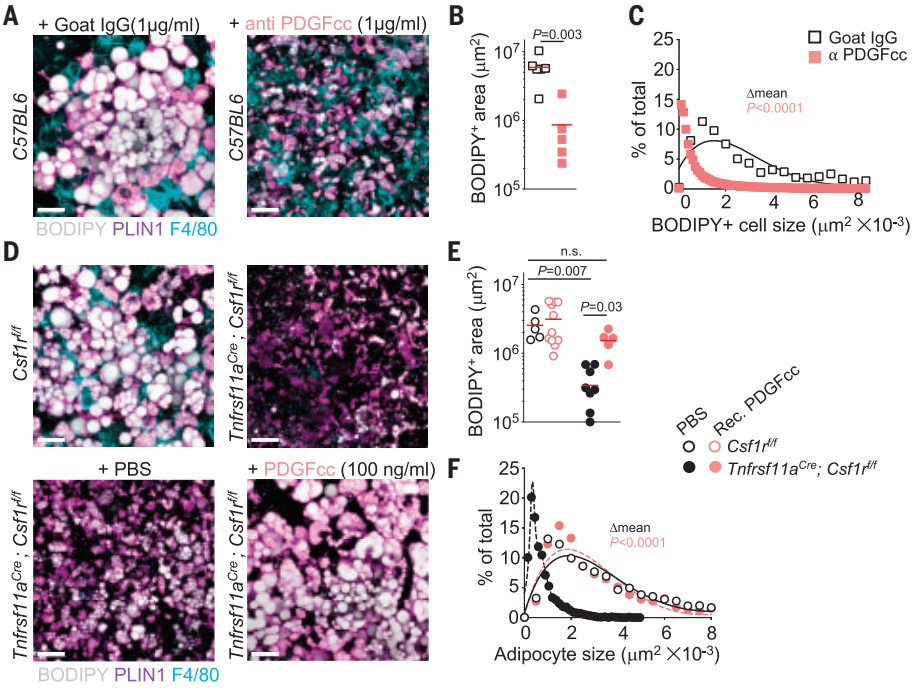

Fig. 7. PDGFcc is both required and sufficient for adipocyte hypertrophy in isolated fat explants. (**A** to **C**) Representative whole-mount images (A), BODIPY$^+$ area (B), and adipocyte size (C) in eWAT explants stained for PLIN1, F4/80, and BODIPY (n = 5 per experimental group obtained from two independent experiments). (**D**) Representative whole-mount images of eWAT explants from mutant mice and littermate *Csf1r*$^{f/f}$ controls (n = 10 to 15 explants from five litters). (**E** and **F**) BODIPY$^+$ areas (E) and adipocyte sizes (F) in explants from mutant mice and littermate controls (n = 5 to 11 explants obtained from five litters). All scale bars, 20 µm. Dots in (B) and (E) represent individual explants. Dots in (C) and (F) represent percent of adipocytes per size interval. P values in (B) and (C) were obtained using Student's t test. P values in (E) and (F) were obtained using one-way ANOVA with Sidak's correction. Red lines indicate mean values.

Glucose and insulin tolerance test

Glucose and insulin tolerance testing was performed as described (*69*). In brief, for the glucose tolerance test, the mice were fasted for 4 hours before experiment but received water ad libitum. Weight and glycemia were measured, and mice were injected intraperitoneally with 2 g of glucose (Thermo Scientific) per kilogram of body weight. After the glucose injection, glycemia was measured every 30 min for 2 hours. For the insulin tolerance test, the mice were fasted for 4 hours before experiment but received water ad libitum. Weight and glycemia were measured, and the mice were injected with 0.25 U of insulin (Sigma) per kilogram of body weight. After the glucose injection, glycemia was measured every 30 min for 2 hours. To measure glycemia, the tails were pricked with a 27G needle and a drop of blood was placed on a glucometer (ACCU-CHECK AVIVA, Roche).

Metabolic analysis of mice

Seven-week-old C57Bl/6J mice fed a diet containing 45% kcal from lipids or 10% kcal from lipids for 1 week and treated with anti-PDGFcc or goat IgG as described above were individually housed in a temperature-controlled Promethion Metabolic Screening System (Sable Systems International). Food intake was acquired gravimetrically and ambulatory activity was acquired using a laser matrix. Mice were acclimated to this environment on a 12-hour light-dark cycle for 48 hours before the indicated length of the recording period (24 to 120 hours) began. Fecal bomb calorimetry was performed on feces collected during the last day of the metabolic cage recording period. The collected samples were then dehydrated in an oven at 60°C for 48 hours and combusted in technical duplicates with a Parr 6725 Semimicro Calorimeter to determine gross caloric intake.

Infrared imaging of mice

Infrared images were taken on the last day of metabolic analysis using a FLIR T430sc infrared camera. These images were converted into RAW files and then analyzed in AMIDE (*70*). A box was then drawn over the interscapular region (70 × 30 pixels). The 10% top warmest pixels were measured for the quantification of heat dissipated from the interscapular region.

Liver triglyceride measurement

To measure triglycerides, 100 mg of mouse liver was homogenized in 100 µl of PBS + 0.05% Tween 20. Triglyceride was then measured using the free glycerol reagent (Sigma F6428) as described in the manufacturer's protocol and normalized to milligram of tissue analyzed.

Cell suspension preparation for flow cytometry and flow cytometry analysis

For the blood, red blood cells were lysed twice in ACK lysis buffer. Adipose tissue was collected in PBS, incubated for 20 min at 37°C in collagenase II at 2 mg/ml (Sigma) in PBS supplemented with 0.25% bovine serum albumin (BSA) (Thermo Scientific) and 5 mM $CaCl_2$ (Sigma) under agitation, before mechanical disruption with a 10-ml pipette. Cell suspensions were centrifuged for 10 min at 500*g* (*71*). Liver, brain, and kidney samples were digested for 30 min at 37°C in PBS containing collagenase D (1 mg/ml; Roche), DNase I (100 U/ml; Sigma), dispase (2.4 mg/ml; Invitrogen), and 3% fetal calf serum (FCS, Invitrogen). Once processed, all samples were resuspended in FACS buffer (PBS, 0.5% BSA, and 2 mM EDTA) containing anti-mouse CD16/32 (FcRIII/II, Biolegend 101302) and anti-mouse CD16.2 (Biolegend 149502) for 10 min and stained with antibody mixes for 30 min on ice. Table S1 lists the antibodies used. After two washes with FACS buffer, samples were incubated with 2 µM Hoechst 33342 (Thermo Scientific) just prior to analysis on a LSR Fortessa X-20 (BD Biosciences) or sorting on an ARIA III (BD Biosciences). The number of cells per gram of tissue was determined using a cell counter (GUAVA easyCyte HT).

Flow cytometry data were analyzed with Flow Jo 9.9. For tSNE analysis of the adipose tissue stromal vascular fraction, FCS files of different conditions or genotypes were concatenated. tSNE algorithm, from Flow Jo 9.9, was used on singlets (determined by FSC-A, SSC-A gate, live cells and FSC-W, FSC-A) with 1000 iterations, perplexity at 20, and Theta at 0.5. All channels with antibody staining were considered as well as FSC-A and SSC-A. Expression of the markers by each cluster was determined after the separation of the concatenated samples.

Preparation of libraries for RNA sequencing from FACS-sorted macrophages and blood monocytes

To optimize cell viability, decrease cell activation, and improve library quality, a low-input RNA sequencing strategy was adopted. Libraries were prepared on 200 cells, reducing the sorting time, and 2 mM flavopiridol (Sigma) was added during the sample preparation to inhibit transcription.

Blood was processed as described above. For adipose tissue, the enzymatic digestion was performed with collagenase II (4 mg/ml), resuspended in 0.25% BSA and 5 mM $CaCl_2$, and supplemented with 2 µM flavopiridol for 30 min at room temperature under agitation. The rest of the procedure was performed as

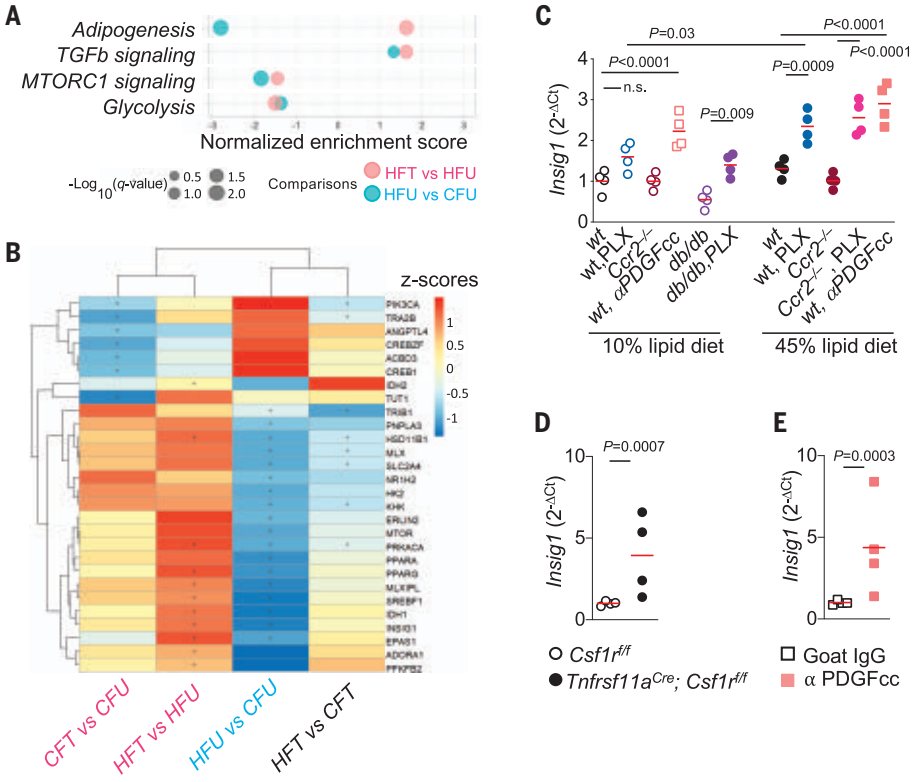

Fig. 8. PDGFcc blockade regulates genes involved in lipid storage. (**A**) Hallmark pathway analysis of RNA-seq dataset obtained from whole iWAT of 8-week-old mice treated with anti-PDGFcc antibodies or goat IgG for 2 weeks (n = 4 mice per experimental group from one experiment), representing a selection of hallmark pathways significantly affected (FDR < 0.05) in untreated high-fat diet–fed mice (HFU) as compared to untreated control fat–fed mice (CFU) and in anti-PDGFcc antibody–treated high-fat diet–fed mice (HFT) as compared to untreated high-fat diet–fed mice (HFU). (**B**) Heatmap depicting row-based $\log_2$(fold change) z-scores are shown for leading-edge genes from the custom lipogenesis/lipid storage gene set (See materials and methods) in anti-PDGFcc antibody–treated control fat–fed mice (CFT) as compared to untreated control fat–fed mice (CFU), HFT as compared to HFU, HFU as compared to CFU, and HFT as compared to CFT. Crosses denote leading-edge genes. (**C**) *Insig1* expression normalized to *Perilipin* ($2^{-\Delta Ct}$) in iWAT of mice in Fig. 1A (n = 4 mice per experimental group from two experiments). (**D** and **E**) *Insig1* expression ($2^{-\Delta Ct}$ relative to *Perilipin*) in eWAT explants in Fig. 7 (n = 4 explants per experimental condition from two independent experiments). Dots in (C) and (D) represent individual mice/explants. q values were obtained via Benjamini-Hochberg multiple hypothesis correction. P values in (C) were obtained using one-way ANOVA with Sidak's correction. P values in (D) and (E) were obtained using Student's t test. Red lines indicate mean values.

described above. Two hundred cells from each sample were directly sorted in a 96-well plate (Biorad) in 4 µl of H_2O containing 0.2% Triton X-100 (Sigma) and RNase inhibitor (0.8 U/ml; Clontech). RNA was extracted with RNeasy mini kit (Qiagen), following manufacturer instructions, and was quantified with ribogreen quantification (Thermo Scientific). Agilent Bioanalyzer was used for quality control. For each sample, 400 pg of the sample was amplified for 14 cycles with SMART-seq V4 (Clontech) ultralow-input RNA kit for sequencing. Illumina HiSeq libraries were prepared with 10 ng of amplified cDNA, using eight cycles of PCR with Kapa library preparation chemistry kit (Kapa Biosystems). Barcoded samples were run on a HiSeq 2500 1T in a 50 bp/50 bp paired-end run using TrueSeq SBS Kit V3 (Illumina). An average of 33 million reads were generated per sample, with an average of 57% mRNA bases.

Fastq read files were aligned with STAR (v020201) (*72*) to mm10 reference genome and quantified with HOMER (v4.9) (*73*), then subsequently analyzed in R with Bioconductor package limma (v3.28.21) and voom (*74*–*77*). For the cell type analysis between groups, differential gene expression was performed with FDR-corrected P < 0.05 and absolute log(fold change) > 1 of any group and the mean expression. K-means clustering was applied with 20 clusters, and highly correlating clusters with Spearman rank correlation higher than 0.9 were subsequently combined, resulting in eight clusters. Clusters were reordered according to number of genes. Functional enrichment was performed using Metascape (*78*). For the effects of food intake, linear model contrasts were set up for each cell type for pairwise comparisons of the 10% lipid diet, 45% lipid diet, and 45% → 10% lipid diet. Explained variance for all expressed genes in the RNA-seq data was calculated using the Variance Partition Bioconductor package (*79*).

Preparation of libraries for RNA sequencing and analysis of whole adipose tissue

Anti-PDGFcc (AF1447 R&D Systems) antibody was administered to 6-week-old C57BL6/J mice intraperitoneally at 50 mg per kg in 100 µl of PBS. Mice were injected every 2 days; after 2 weeks of treatment, inguinal white adipose tissues were collected into TRIzol. RNA was extracted with RNeasy Lipid Tissue Mini Kit (Qiagen) following manufacturer's instructions. Messenger RNA was enriched from the total RNA samples using poly-A selection, and libraries were prepared using the TruSeq Stranded mRNA prep kit (Illumina). Libraries were then sequenced using the NovaSeq6000 platform (Illumina).

The resulting fastq files were preprocessed using fastp (v0.20.1) to remove low-quality reads and to trim poly-G and poly-X tails. Reads were mapped to a reference genome (*Mus musculus*: Ensembl/GRCm38) using STAR (v2.7.0e) with two-pass mode enabled to improve novel splice junction discovery (*80*, *81*). Read mapping was determined using featureCounts in the Subread package (v1.6.2) (*82*). Differential gene expression analysis was performed in R with Bioconductor package limma (v3.42.2) and voom (*83*).

To determine which pathways were differentially regulated as a result of PDGFcc blockade, we carried out a pre-ranked gene set enrichment analysis (GSEA) using the R package fgsea (v1.12.0) with default parameters and 1000 permutations (*84*). The ranking metric used was $-\log_{10}(P \text{ value}) \times \text{sign}(\log_2 \text{ fold change})$. Gene sets were obtained from the Molecular Signatures Database (MSigDB), and results from the hallmark pathway gene sets are shown (*85*). To better characterize changes in genes associated with lipid storage in adipocytes, we performed an additional GSEA using a custom gene set that included the GeneRIF "lipogenesis" gene set, which includes genes pertaining to lipid synthesis and storage (*86*).

qRT-PCR analysis of sorted macrophages and adipose tissue samples

For qRT-PCR, 10,000 cells were sorted in 300 µl of RNA lysis buffer (Macherey-Nagel, Nucleospin TriPrep), after preparation of the samples as described for RNA sequencing. RNA extraction was performed following manufacturer's instructions (Macherey-Nagel, Nucleospin

TriPrep). RNA concentration was measured with a NanoDrop 2000. cDNA was prepared with QuantiTect Reverse Transcription Kit (Qiagen) as per manufacturer's instructions. qRT-PCR were performed with 1 ng of cDNA.

For qRT-PCR of eWAT and iWAT, tissue samples were weighed and snap-frozen in liquid nitrogen. RNA was extracted from 20 mg of tissue using the RNAeasy Lipid Tissue Mini Kit (Qiagen) per manufacturer's instructions. cDNA was prepared with Quantitect Reverse transcription kit (Qiagen) and 5 ng of cDNA was used to perform qRT-PCR analysis.

qRT-PCR was performed on a Quant Studio 6 Flex using TaqMan Fast Advance Mastermix, and with TaqMan probes for *ActinB* (Mm02619580_g1), *Gapdh* (Mm99999915_g1), *Tnf* (Mm00443258_m1), *Il1b* (Mm00434228_m1), *Pdgfa* (Mm01205760_m1), *Pdgfb* (Mm00440677_m1), *Pdgfc* (Mm00480205_m1), *Pdgfd* (Mm00546829_m1), *Bmp2* (Mm01340178_m1), *Pparg* (Mm00440940_m1), *Perilipin* (Mm00558672_m1), *Ucp1* (Mm01244861_m1), *Dio2* (Mm00515664_m1), *Prdm16* (Mm00712556_m1), and *Cidea* (Mm00432554_m1).

Whole-mount imaging of adipose tissue

For whole-mount immunofluorescence imaging, after anesthesia and blood collection by cardiac puncture, the mice were perfused with 10 ml of PBS at room temperature. Approximately 3-mm^3 pieces of the fat tissue were incubated in 4% paraformaldehyde (PFA) (Electron Microscopy) diluted in PBS for 30 min at room temperature with agitation. Fixed samples were then rinsed with PBS, stained with directly conjugated antibodies for 30 min, and washed three times with PBS before mounting on cavity slides (Sigma) with Fluoromount G (eBioscience). Table 2 lists the antibodies used. Approximately 50-μm-thick *z*-stack and tile scans were acquired with a LSM880 Zeiss inverted confocal microscope with a 40×/1.3 N.A. objective (oil). Image analysis was performed using Imaris (Bitplane) software. At least 100 adipocytes per fat pad were measured.

May-Grunwald Giemsa staining of sorted macrophages

Analysis of macrophages was performed on May-Grunwald Giemsa staining of sorted cells from each population. For each sample, 1000 to 2000 cells were sorted directly in fetal bovine serum (FBS) (Invitrogen) and centrifuged for 10 min at 800*g* with low acceleration onto Superfrost slides (Thermo Scientific). After air-drying for at least 30 min, the slides were fixed in methanol, air-dried for at least 30 min, stained with May-Grunwald (Sigma) solution for 5 min followed by Giemsa (Sigma) solution 14% for 15 min, and rinsed with Sorenson buffer pH 6.8. After air drying, the slides were mounted with Entellan (Merck). Pictures were taken using Axio Lab.A1 Zeiss microscope with N-Achroplan and Axiocam 105 using a 100×/01.25 N.A. objective.

Adipose tissue and liver histology

For perilipin staining, samples were collected in 4% methanol-free PFA, fixed for 1 day at 4°C, and embedded in paraffin. Slides (5 μm) were cut with a Leica RM2265 microtome, dewaxed with xylene, and then rehydrated with ethanol bath of decreasing concentrations. Antigen retrieval was performed with pH 6 citrate solution (Cell Signaling). After endogenous peroxidase was quenched for 10 min with 3% H_2O_2 solution (Sigma), the samples were blocked with a Tris-buffered saline solution (Sigma) containing 0.3% Tween 20 (Sigma), 5% BSA, and 5% normal goat serum (Sigma). Slides were incubated overnight at 4°C with anti-mouse perilipin antibody (1/200, clone D1D8, Cell Signaling). The slides were then washed three times with PBS and incubated for 1 hour at room temperature with horseradish peroxidase–coupled goat anti-rabbit antibody (1/200, Catalog #7074, Cell Signaling). The staining was developed with peroxidase substrate kit (Vector, SK4805) and slides were counterstained with hematoxylin (0.25%, Sigma). Slides were finally dehydrated in ethanol and mounted in Entellan (Merck).

Paraffin sections from the white adipose tissue and the liver were stained with hematoxylin and eosin (H&E). Images were captured with different objectives (N-Achroplan 2.5×/0.07 N.A., N-Achroplan 10×/0.25 N.A., N-Achroplan 20×/0.45 N.A., N-Achroplan 63×/0.85 N.A.) on an Axio Lab.A1 Zeiss with Axiocam 105. Crown-like structures were quantified on the sections of H&E-stained slides. For each sample, three to five regions were analyzed. Crown-like structures were defined as microscopic foci of dying adipocytes surrounded by macrophages as visualized by H&E staining.

Epididymal adipose tissue explants

Epididymal adipose tissue of 4-day-old mice were dissected and incubated in RPMI with 10% heat-deactivated FBS at 37°C for 10 days (*58*). Fresh medium was added to the explants on day 5. At the termination of the experiment, the explants were fixed in 4% PFA for 30 min at room temperature with agitation and then rinsed in PBS and permeabilized for 15 min in PBS + 0.03% Triton. Subsequently, the explants were blocked with 2% BSA and stained with directly conjugated antibodies. For the in vitro rescue experiments, epididymal fat pads of $Tnfrsf11a^{Cre}$; $Csf1r^{fl/fl}$ mice and littermates were supplemented with recombinant mouse PDGFcc (100 ng/ml; R&D Systems) three times on days 0, 3, and 6. Fluorescent whole-mount images were acquired with a LSM880 Zeiss inverted confocal microscope with a 40×/1.3 N.A. objective (oil) and analyzed using Imaris (Bitplane) image analysis software.

Drosophila lines and crosses

Flies (table S3) were raised at 25°C in a 12-hour light-dark cycle and maintained on food containing 10% weight/volume Brewer's yeast, 8% fructose, 2% polenta, and 0.8% agar. Adult flies in vials were allowed to lay eggs for 2 hours, whereupon the adults were removed, and eggs were allowed to develop until the wandering larval stage.

Triglyceride measurement, buoyancy assay, and fat-body cell size in Drosophila

To measure triglycerides, 10 wandering third-stage larvae (L3) were homogenized in 100 μl of PBS + 0.05% Tween 20 with a pestle on ice. Triglyceride was then measured using the free glycerol reagent (Sigma; F6428) as described (*87*) and normalized to the protein content.

To measure larval buoyancy, 20 L3 larvae were placed in a 30% sucrose solution that was then gradually diluted to an 8% sucrose solution in PBS. Subsequently, the larvae were left to equilibrate for 30 min, at which point the position of the larvae in the solution was recorded.

To measure fat-body cell size, fat-body from the anterior half of 10 to 20 L3 larvae per cross were dissected out and then fixed in 4% PFA for 30 min at room temperature. The fixed tissues were stained with BODIPY for 30 min and washed and imaged on a LSM880 Zeiss inverted confocal microscope with a 40×/1.3 N.A. objective (oil). The sizes of at least 100 fat-body cells were measured using Imaris (Bitplane) image analysis software for each replicate.

qPCR on sorted Drosophila hemocytes and whole larvae

Ten thousand hemocytes were sorted into 300 μl of TRIzol LS (Life Technologies). RNA extraction was performed following manufacturer's instructions (Direct-zol RNA microPrep, Zymo Research). RNA concentration was measured with a NanoDrop 2000. cDNA preparation was performed with Quantitect Reverse transcription kit (Qiagen) as per manufacturer's instructions. qRT-PCR was done with 10 ng of cDNA.

For qRT-PCRs performed on whole larvae, 5 to 10 larvae were homogenized in TRIzol with a pestle on ice. RNA extraction and cDNA preparation was as described above. The qRT-PCR was performed on 10 ng of cDNA. qRT-PCR was performed on a Quant Studio 6 Flex using TaqMan Fast Advance Mastermix and TaqMan probes for Gapdh2 (Dm01843776_s1), *dilp2* (Dm01822534_g1), *dilp4* (Dm01801938_g1), *dilp5* (Dm01798339_g1), *dilp6* (Dm01829746_g1), *Pvf1* (Dm01813949_m1), *Pvf3* (Dm01814376_m1), and *dpp* (Dm01842959_m1).

Statistical tests

Data are represented as individual values per mouse, unless otherwise stated. The *n* value

represents biological replicates. Statistical significance was calculated using the GraphPad Prism software using unpaired *t* tests when comparing two groups. One-way or two-way analyses of variance (ANOVA) were used to compare more than two groups, as indicated in the figures. For RNA sequencing, R software was used, as described above.

Data availability

RNA-seq data from FACS-sorted iWAT macrophages are available from GEO under reference number GSE106084, and RNA-seq data from whole iWAT are available from GEO under reference number GSE169226. Other datasets that support the findings of this study are available from the corresponding author.

REFERENCES AND NOTES

1. E. D. Rosen, B. M. Spiegelman, Adipocytes as regulators of energy balance and glucose homeostasis. *Nature* **444**, 847–853 (2006). doi: 10.1038/nature05483; pmid: 17167472
2. A. Wise, Adipocyte number and size in hypothalamic obesity induced in weanling mice by gold thioglucose and bipiperidyl mustard. *Nutr. Metab.* **19**, 291–298 (1975). doi: 10.1159/000175676; pmid: 822374
3. J. Hirsch, B. Batchelor, Adipose tissue cellularity in human obesity. *Clin. Endocrinol. Metab.* **5**, 299–311 (1976). doi: 10.1016/S0300-595X(76)80023-0; pmid: 1085232
4. T. McLaughlin, S. E. Ackerman, L. Shen, E. Engleman, Role of innate and adaptive immunity in obesity-associated metabolic disease. *J. Clin. Invest.* **127**, 5–13 (2017). doi: 10.1172/JCI88876; pmid: 28045397
5. G. S. Hotamisligil, P. Arner, J. F. Caro, R. L. Atkinson, B. M. Spiegelman, Increased adipose tissue expression of tumor necrosis factor-alpha in human obesity and insulin resistance. *J. Clin. Invest.* **95**, 2409–2415 (1995). doi: 10.1172/JCI117936; pmid: 7738205
6. G. S. Hotamisligil, N. S. Shargill, B. M. Spiegelman, Adipose expression of tumor necrosis factor–α: Direct role in obesity-linked insulin resistance. *Science* **259**, 87–91 (1993). doi: 10.1126/science.7678183; pmid: 7678183
7. S. P. Weisberg *et al*.., Obesity is associated with macrophage accumulation in adipose tissue. *J. Clin. Invest.* **112**, 1796–1808 (2003). doi: 10.1172/JCI200319246; pmid: 14679176
8. H. Xu *et al*., Chronic inflammation in fat plays a crucial role in the development of obesity-related insulin resistance. *J. Clin. Invest.* **112**, 1821–1830 (2003). doi: 10.1172/JCI200319451; pmid: 14679177
9. S. P. Weisberg *et al*.., CCR2 modulates inflammatory and metabolic effects of high-fat feeding. *J. Clin. Invest.* **116**, 115–124 (2006). doi: 10.1172/JCI24335; pmid: 16341265
10. T. Suganami, Y. Ogawa, Adipose tissue macrophages: Their role in adipose tissue remodeling. *J. Leukoc. Biol.* **88**, 33–39 (2010). doi: 10.1189/jlb.0210072; pmid: 20360405
11. P. Pekala, M. Kawakami, W. Vine, M. D. Lane, A. Cerami, Studies of insulin resistance in adipocytes induced by macrophage mediator. *J. Exp. Med.* **157**, 1360–1365 (1983). doi: 10.1084/jem.157.4.1360; pmid: 6833952
12. J. Kim *et al*., Silencing CCR2 in Macrophages Alleviates Adipose Tissue Inflammation and the Associated Metabolic Syndrome in Dietary Obese Mice. *Mol. Ther. Nucleic Acids* **5**, e280 (2016). doi: 10.1038/mtna.2015.51; pmid: 26812653
13. A. E. Obstfeld *et al*.., C-C chemokine receptor 2 (CCR2) regulates the hepatic recruitment of myeloid cells that promote obesity-induced hepatic steatosis. *Diabetes* **59**, 916–925 (2010). doi: 10.2337/db09-1403; pmid: 20103702
14. H. Kanda *et al*., MCP-1 contributes to macrophage infiltration into adipose tissue, insulin resistance, and hepatic steatosis in obesity. *J. Clin. Invest.* **116**, 1494–1505 (2006). doi: 10.1172/JCI26498; pmid: 16691291
15. N. Kamei *et al*., Overexpression of monocyte chemoattractant protein-1 in adipose tissues causes macrophage recruitment and insulin resistance. *J. Biol. Chem.* **281**, 26602–26614 (2006). doi: 10.1074/jbc.M601284200; pmid: 16809344
16. T. J. Sullivan *et al*., Experimental evidence for the use of CCR2 antagonists in the treatment of type 2 diabetes. *Metabolism* **62**, 1623–1632 (2013). doi: 10.1016/j.metabol.2013.06.008; pmid: 23953944
17. A. Ito *et al*., Role of CC chemokine receptor 2 in bone marrow cells in the recruitment of macrophages into obese adipose tissue. *J. Biol. Chem.* **283**, 35715–35723 (2008). doi: 10.1074/jbc.M804220200; pmid: 18977759
18. R. Parker *et al*., CC chemokine receptor 2 promotes recruitment of myeloid cells associated with insulin resistance in nonalcoholic fatty liver disease. *Am. J. Physiol. Gastrointest. Liver Physiol.* **314**, G483–G493 (2018). doi: 10.1152/ajpgi.00213.2017; pmid: 29420066
19. T. Satoh *et al*., Critical role of Trib1 in differentiation of tissue-resident M2-like macrophages. *Nature* **495**, 524–528 (2013). doi: 10.1038/nature11930; pmid: 23515163
20. C. Pridans *et al*., Pleiotropic Impacts of Macrophage and Microglial Deficiency on Development in Rats with Targeted Mutation of the *Csf1r* Locus. *J. Immunol.* **201**, 2683–2699 (2018). doi: 10.4049/jimmunol.1701783; pmid: 30249809
21. M. Valdearcos *et al*., Microglia dictate the impact of saturated fat consumption on hypothalamic inflammation and neuronal function. *Cell Rep.* **9**, 2124–2138 (2014). doi: 10.1016/j.celrep.2014.11.018; pmid: 25497089
22. M. Valdearcos *et al*., Microglial Inflammatory Signaling Orchestrates the Hypothalamic Immune Response to Dietary Excess and Mediates Obesity Susceptibility. *Cell Metab.* **26**, 185–197.e3 (2017). doi: 10.1016/j.cmet.2017.05.015; pmid: 28683286
23. R. M. Pirzgalska *et al*., Sympathetic neuron-associated macrophages contribute to obesity by importing and metabolizing norepinephrine. *Nat. Med.* **23**, 1309–1318 (2017). doi: 10.1038/nm.4422; pmid: 29035364
24. D. A. Jaitin *et al*., Lipid-Associated Macrophages Control Metabolic Homeostasis in a Trem2-Dependent Manner. *Cell* **178**, 686–698.e14 (2019). doi: 10.1016/j.cell.2019.05.054; pmid: 31257031
25. C. Schulz *et al*., A lineage of myeloid cells independent of Myb and hematopoietic stem cells. *Science* **336**, 86–90 (2012). doi: 10.1126/science.1219179; pmid: 22442384
26. E. Gomez Perdiguero *et al*., Tissue-resident macrophages originate from yolk-sac-derived erythro-myeloid progenitors. *Nature* **518**, 547–551 (2015). doi: 10.1038/nature13989; pmid: 25470051
27. E. Mass *et al*., Specification of tissue-resident macrophages during organogenesis. *Science* **353**, aaf4238 (2016). doi: 10.1126/science.aaf4238; pmid: 27492475
28. S. F. Hassnain Waqas *et al*., Adipose tissue macrophages develop from bone marrow-independent progenitors in *Xenopus laevis* and mouse. *J. Leukoc. Biol.* **102**, 845–855 (2017). doi: 10.1189/jlb.1A0317-082RR; pmid: 28642277
29. M. Zeyda *et al*., Newly identified adipose tissue macrophage populations in obesity with distinct chemokine and chemokine receptor expression. *Int. J. Obes.* **34**, 1684–1694 (2010). doi: 10.1038/ijo.2010.103; pmid: 20514049
30. H. M. Silva *et al*., Vasculature-associated fat macrophages readily adapt to inflammatory and metabolic challenges. *J. Exp. Med.* **216**, 786–806 (2019). doi: 10.1084/jem.20181049; pmid: 30862706
31. B. R. Coats *et al*., Metabolically Activated Adipose Tissue Macrophages Perform Detrimental and Beneficial Functions during Diet-Induced Obesity. *Cell Rep.* **20**, 3149–3161 (2017). doi: 10.1016/j.celrep.2017.08.096; pmid: 28954231
32. M. Kratz *et al*., Metabolic dysfunction drives a mechanistically distinct proinflammatory phenotype in adipose tissue macrophages. *Cell Metab.* **20**, 614–625 (2014). doi: 10.1016/j.cmet.2014.08.010; pmid: 25242226
33. H. Debels *et al*., Macrophages play a key role in angiogenesis and adipogenesis in a mouse tissue engineering model. *Tissue Eng. A* **19**, 2615–2625 (2013). doi: 10.1089/ten.tea.2013.0071; pmid: 23844978
34. S. Wei *et al*., Modulation of CSF-1-regulated post-natal development with anti-CSF-1 antibody. *Immunobiology* **210**, 109–119 (2005). doi: 10.1016/j.imbio.2005.05.005; pmid: 16164017
35. Y. H. Lee, A. P. Petkova, J. G. Granneman, Identification of an adipogenic niche for adipose tissue remodeling and restoration. *Cell Metab.* **18**, 355–367 (2013). doi: 10.1016/j.cmet.2013.08.003; pmid: 24011071
36. I. Wernstedt Asterholm *et al*., Adipocyte inflammation is essential for healthy adipose tissue expansion and remodeling. *Cell Metab.* **20**, 103–118 (2014). doi: 10.1016/j.cmet.2014.05.005; pmid: 24930973
37. C. Pang *et al*., Macrophage infiltration into adipose tissue may promote angiogenesis for adipose tissue remodeling in obesity. *Am. J. Physiol. Endocrinol. Metab.* **295**, E313–E322 (2008). doi: 10.1152/ajpendo.90296.2008; pmid: 18492768
38. C. N. Lumeng, S. M. Deyoung, J. L. Bodzin, A. R. Saltiel, Increased inflammatory properties of adipose tissue macrophages recruited during diet-induced obesity. *Diabetes* **56**, 16–23 (2007). doi: 10.2337/db06-1076; pmid: 17192460
39. M. T. Nguyen *et al*., A subpopulation of macrophages infiltrates hypertrophic adipose tissue and is activated by free fatty acids via Toll-like receptors 2 and 4 and JNK-dependent pathways. *J. Biol. Chem.* **282**, 35279–35292 (2007). doi: 10.1074/jbc.M706762200; pmid: 17916553
40. Y. Wolf *et al*., Brown-adipose-tissue macrophages control tissue innervation and homeostatic energy expenditure. *Nat. Immunol.* **18**, 665–674 (2017). doi: 10.1038/ni.3746; pmid: 28459435
41. T. Sudo *et al*., Functional hierarchy of c-kit and c-fms in intramarrow production of CFU-M. *Oncogene* **11**, 2469–2476 (1995). pmid: 8545103
42. C. E. Jacome-Galarza *et al*., Developmental origin, functional maintenance and genetic rescue of osteoclasts. *Nature* **568**, 541–545 (2019). doi: 10.1038/s41586-019-1105-7; pmid: 30971820
43. L. Boring *et al*., Impaired monocyte migration and reduced type 1 (Th1) cytokine responses in C-C chemokine receptor 2 knockout mice. *J. Clin. Invest.* **100**, 2552–2561 (1997). doi: 10.1172/JCI119798; pmid: 9366570
44. J. L. Christensen, I. L. Weissman, Flk-2 is a marker in hematopoietic stem cell differentiation: A simple method to isolate long-term stem cells. *Proc. Natl. Acad. Sci. U.S.A.* **98**, 14541–14546 (2001). doi: 10.1073/pnas.261562798; pmid: 11724967
45. K. J. Woodcock *et al*., Macrophage-derived upd3 cytokine causes impaired glucose homeostasis and reduced lifespan in Drosophila fed a lipid-rich diet. *Immunity* **42**, 133–144 (2015). doi: 10.1016/j.immuni.2014.12.023; pmid: 25601202
46. A. Franz, W. Wood, P. Martin, Fat Body Cells Are Motile and Actively Migrate to Wounds to Drive Repair and Prevent Infection. *Dev. Cell* **44**, 460–470.e3 (2018). doi: 10.1016/j.devcel.2018.01.026; pmid: 29486196
47. K. Brückner *et al*., The PDGF/VEGF receptor controls blood cell survival in Drosophila. *Dev. Cell* **7**, 73–84 (2004). doi: 10.1016/j.devcel.2004.06.007; pmid: 15239955
48. T. Reis, M. R. Van Gilst, I. K. Hariharan, A buoyancy-based screen of Drosophila larvae for fat-storage mutants reveals a role for Sir2 in coupling fat storage to nutrient availability. *PLOS Genet.* **6**, e1001206 (2010). doi: 10.1371/journal.pgen.1001206; pmid: 21085633
49. A. Gyoergy *et al*., Tools Allowing Independent Visualization and Genetic Manipulation of *Drosophila melanogaster* Macrophages and Surrounding Tissues. *G3* **8**, 845–857 (2018). doi: 10.1534/g3.117.300452; pmid: 29321168
50. R. V. Hoch, P. Soriano, Roles of PDGF in animal development. *Development* **130**, 4769–4784 (2003). doi: 10.1242/dev.00721; pmid: 12952899
51. R. I. Clark, K. J. Woodcock, F. Geissmann, C. Trouillet, M. S. Dionne, Multiple TGF-β superfamily signals modulate the adult Drosophila immune response. *Curr. Biol.* **21**, 1672–1677 (2011). doi: 10.1016/j.cub.2011.08.048; pmid: 21962711
52. W. Brogiolo *et al*., An evolutionarily conserved function of the Drosophila insulin receptor and insulin-like peptides in growth control. *Curr. Biol.* **11**, 213–221 (2001). doi: 10.1016/S0960-9822(01)00068-9; pmid: 11250149
53. H. Zheng *et al*., Premature remodeling of fat body and fat mobilization triggered by platelet-derived growth factor/VEGF receptor in *Drosophila*. *FASEB J.* **31**, 1964–1975 (2017). doi: 10.1096/fj.201601127R; pmid: 28126734
54. D. P. Leader, S. A. Krause, A. Pandit, S. A. Davies, J. A. T. Dow, FlyAtlas 2: A new version of the Drosophila melanogaster expression atlas with RNA-Seq, miRNA-Seq and sex-specific data. *Nucleic Acids Res.* **46**, D809–D815 (2018). doi: 10.1093/nar/gkx976; pmid: 29069479
55. T. S. Heng *et al*., The Immunological Genome Project: Networks of gene expression in immune cells. *Nat. Immunol.* **9**, 1091–1094 (2008). doi: 10.1038/ni1008-1091; pmid: 18800157
56. S. Enerbäck *et al*., Mice lacking mitochondrial uncoupling protein are cold-sensitive but not obese. *Nature* **387**, 90–94 (1997). doi: 10.1038/387090a0; pmid: 9139827
57. L. A. de Jesus *et al*., The type 2 iodothyronine deiodinase is essential for adaptive thermogenesis in brown adipose tissue. *J. Clin. Invest.* **108**, 1379–1385 (2001). doi: 10.1172/JCI200113803; pmid: 11696583
58. J. Han *et al*., The spatiotemporal development of adipose tissue. *Development* **138**, 5027–5037 (2011). doi: 10.1242/dev.067686; pmid: 22028034
59. Y. Onogi *et al*., PDGFRβ Regulates Adipose Tissue Expansion and Glucose Metabolism via Vascular Remodeling in Diet-

Induced Obesity. *Diabetes* **66**, 1008–1021 (2017). doi: 10.2337/db16-0881; pmid: 28122789
60. Z. Gao, A. C. Daquinag, F. Su, B. Snyder, M. G. Kolonin, PDGFRα/PDGFRβ signaling balance modulates progenitor cell differentiation into white and beige adipocytes. *Development* **145**, dev155861 (2018). pmid: 29158445
61. C. Sun, W. L. Berry, L. E. Olson, PDGFRα controls the balance of stromal and adipogenic cells during adipose tissue organogenesis. *Development* **144**, 83–94 (2017). doi: 10.1242/dev.135962; pmid: 28049691
62. J. Li, K. Takaishi, W. Cook, S. K. McCorkle, R. H. Unger, Insig-1 "brakes" lipogenesis in adipocytes and inhibits differentiation of preadipocytes. *Proc. Natl. Acad. Sci. U.S.A.* **100**, 9476–9481 (2003). doi: 10.1073/pnas.1133426100; pmid: 12869692
63. P. Costet *et al*., Peroxisome proliferator-activated receptor alpha-isoform deficiency leads to progressive dyslipidemia with sexually dimorphic obesity and steatosis. *J. Biol. Chem.* **273**, 29577–29585 (1998). doi: 10.1074/jbc.273.45.29577; pmid: 9792666
64. J. H. Lee *et al*., Isocitrate dehydrogenase 2 protects mice from high-fat diet-induced metabolic stress by limiting oxidative damage to the mitochondria from brown adipose tissue. *Exp. Mol. Med.* **52**, 238–252 (2020). doi: 10.1038/s12276-020-0379-z; pmid: 32015410
65. S. Carobbio *et al*., Adaptive changes of the Insig1/SREBP1/SCD1 set point help adipose tissue to cope with increased storage demands of obesity. *Diabetes* **62**, 3697–3708 (2013). doi: 10.2337/db12-1748; pmid: 23919961
66. K. Maeda *et al*., Wnt5a-Ror2 signaling between osteoblast-lineage cells and osteoclast precursors enhances osteoclastogenesis. *Nat. Med.* **18**, 405–412 (2012). doi: 10.1038/nm.2653; pmid: 22344299
67. X. M. Dai *et al*., Targeted disruption of the mouse colony-stimulating factor 1 receptor gene results in osteopetrosis, mononuclear phagocyte deficiency, increased primitive progenitor cell frequencies, and reproductive defects. *Blood* **99**, 111–120 (2002). doi: 10.1182/blood.V99.1.111; pmid: 11756160
68. G. Gasteiger, X. Fan, S. Dikiy, S. Y. Lee, A. Y. Rudensky, Tissue residency of innate lymphoid cells in lymphoid and nonlymphoid organs. *Science* **350**, 981–985 (2015). doi: 10.1126/science.aac9593
69. J. E. Ayala *et al*., Standard operating procedures for describing and performing metabolic tests of glucose homeostasis in mice. *Dis. Model. Mech.* **3**, 525–534 (2010). doi: 10.1242/dmm.006239; pmid: 20713647
70. A. M. Loening, S. S. Gambhir, AMIDE: A free software tool for multimodality medical image analysis. *Mol. Imaging* **2**, 131–137 (2003). doi: 10.1162/153535003322556877; pmid: 14649056
71. J. S. Orr, A. J. Kennedy, A. H. Hasty, Isolation of adipose tissue immune cells. *J. Vis. Exp.* e50707 (2013). pmid: 23728515
72. A. Dobin *et al*., STAR: Ultrafast universal RNA-seq aligner. *Bioinformatics* **29**, 15–21 (2013). doi: 10.1093/bioinformatics/bts635; pmid: 23104886
73. S. Heinz *et al*., Simple combinations of lineage-determining transcription factors prime cis-regulatory elements required for macrophage and B cell identities. *Mol. Cell* **38**, 576–589 (2010). doi: 10.1016/j.molcel.2010.05.004; pmid: 20513432
74. M. D. Robinson, D. J. McCarthy, G. K. Smyth, edgeR: A Bioconductor package for differential expression analysis of digital gene expression data. *Bioinformatics* **26**, 139–140 (2010). doi: 10.1093/bioinformatics/btp616; pmid: 19910308
75. C. W. Law, Y. Chen, W. Shi, G. K. Smyth, voom: Precision weights unlock linear model analysis tools for RNA-seq read counts. *Genome Biol.* **15**, R29 (2014). doi: 10.1186/gb-2014-15-2-r29; pmid: 24485249
76. M. E. Ritchie *et al*., A comparison of background correction methods for two-colour microarrays. *Bioinformatics* **23**, 2700–2707 (2007). doi: 10.1093/bioinformatics/btm412; pmid: 17720982
77. M. E. Ritchie *et al*., Empirical array quality weights in the analysis of microarray data. *BMC Bioinformatics* **7**, 261 (2006). doi: 10.1186/1471-2105-7-261; pmid: 16712727
78. S. Tripathi *et al*., Meta- and Orthogonal Integration of Influenza "OMICs" Data Defines a Role for UBR4 in Virus Budding. *Cell Host Microbe* **18**, 723–735 (2015). doi: 10.1016/j.chom.2015.11.002; pmid: 26651948
79. G. E. Hoffman, E. E. Schadt, variancePartition: Interpreting drivers of variation in complex gene expression studies. *BMC Bioinformatics* **17**, 483 (2016). doi: 10.1186/s12859-016-1323-z; pmid: 27884101
80. A. D. Yates *et al*., Ensembl 2020. *Nucleic Acids Res.* **48**, D682–D688 (2020). pmid: 31691826
81. S. Chen, Y. Zhou, Y. Chen, J. Gu, fastp: An ultra-fast all-in-one FASTQ preprocessor. *Bioinformatics* **34**, i884–i890 (2018). doi: 10.1093/bioinformatics/bty560; pmid: 30423086
82. Y. Liao, G. K. Smyth, W. Shi, featureCounts: An efficient general purpose program for assigning sequence reads to genomic features. *Bioinformatics* **30**, 923–930 (2014). doi: 10.1093/bioinformatics/btt656; pmid: 24227677
83. M. E. Ritchie *et al*., limma powers differential expression analyses for RNA-sequencing and microarray studies. *Nucleic Acids Res.* **43**, e47 (2015). doi: 10.1093/nar/gkv007; pmid: 25605792
84. V. S. G. Korotkevich, A. Sergushichev, Fast gene set enrichment analysis. bioRxiv 060012 [preprint]. 22 October 2019.
85. A. Liberzon *et al*., The Molecular Signatures Database (MSigDB) hallmark gene set collection. *Cell Syst.* **1**, 417–425 (2015). doi: 10.1016/j.cels.2015.12.004; pmid: 26771021
86. J. A. Mitchell *et al*., Gene indexing: Characterization and analysis of NLM's GeneRIFs. *AMIA Annu. Symp. Proc.* **2003**, 460–464 (2003). pmid: 14728215
87. J. M. Tennessen, W. E. Barry, J. Cox, C. S. Thummel, Methods for studying metabolism in Drosophila. *Methods* **68**, 105–115 (2014). doi: 10.1016/j.ymeth.2014.02.034; pmid: 24631891

ACKNOWLEDGMENTS

This study is dedicated to the memory of Lucile Crozet. We thank J. Frampton, J. Pollard, and T. Boehm for providing mouse strains; H. Ketchum for technical assistance; the molecular cytology core at MSKCC for their help; and all members of the Geissmann lab for helpful suggestions. **Funding:** Supported by NIH/NCI grant P30CA008748 to MSKCC; NIH/NIAID grant 1R01AI130345, NIH/NHLBI grant R01HL138090, a Ludwig Institute for Cancer Research basic immunology grant, and Cycle for Survival grants (F.G.); the Leducq Transatlantic Network of Excellence program (C.K.G. and F.G.); NIH/NCI grant F32CA225036 (N.C.); and an Alan and Sandra Gerry Metastasis and Tumor Ecosystems Center fellowship (P.-L.L.). **Author contributions:** N.C., L.C., and F.G. and designed the study, analyzed data, and wrote the manuscript; L.C., N.C., and P.-L.L. performed and analyzed experiments in mice; N.C. performed *Drosophila* experiments; E.M. contributed to the generation of *Tnfrsf11a*^{Cre}; *Csf1r*$^{f/f}$ mice; T.L. helped with the analysis of flow cytometry data; I.R.H., C.K.G., and J.B.W. analyzed RNA-seq experiments and helped prepare the manuscript; and E.R.S. and O.E. provided intellectual input. **Competing interests:** F.G. and N.C. are co-inventors on a patent relating to the use of PDGFcc, CSF1R, and CCR2 inhibitors in obesity. J.B.W. is a compensated consultant for SpringWorks Therapeutics. **Data and materials availability:** All materials are available from F.G. under a material transfer agreement with MSKCC. All data are available in the main text or the supplementary materials.

SUPPLEMENTARY MATERIALS

science.sciencemag.org/content/373/6550/eabe9383/suppl/DC1
Figs. S1 to S9
Tables S1 to S3
Data S1 and S2
MDAR Reproducibility Checklist

23 September 2020; accepted 13 May 2021
10.1126/science.abe9383

RESEARCH ARTICLE SUMMARY

SYNTHETIC BIOLOGY

An engineered protein-phosphorylation toggle network with implications for endogenous network discovery

Deepak Mishra, Tristan Bepler, Brian Teague, Bonnie Berger, Jim Broach, Ron Weiss*

INTRODUCTION: Synthetic biology applies engineering methodologies to biology to build new functions into living cells. Through the assembly and characterization of engineered genetic modules, synthetic biologists have created cells with "prosthetic networks" implementing a variety of behaviors. To date, many of these efforts have focused on regulating gene expression at the transcriptional and translational levels. Because of the time required by cells to transcribe and translate regulatory proteins, synthetic networks based on these types of regulatory modalities operate on time scales of minutes to hours, which is too slow for various real-time sense-and-respond systems.

RATIONALE: By comparison, certain natural cellular processes such as signal transduction and metabolism use reversible protein-protein interaction networks to operate at much faster speeds. Among the various sophisticated behaviors that these networks encode is bistability, that is, exhibiting two distinct stable states and an ability to switch between them. Fast bistable switches are found in a range of important biological processes from cellular cycle progression to innate immune cell activation and memory formation. For protein synthetic biology, engineering bistable switches and, more generally, fast feedback control, represents a foundational tool with great utility. Although synthetic biologists have successfully implemented toggle switch networks using transcriptional and translational regulation, engineering analogous synthetic protein networks capable of switching state in seconds has not yet been achieved.

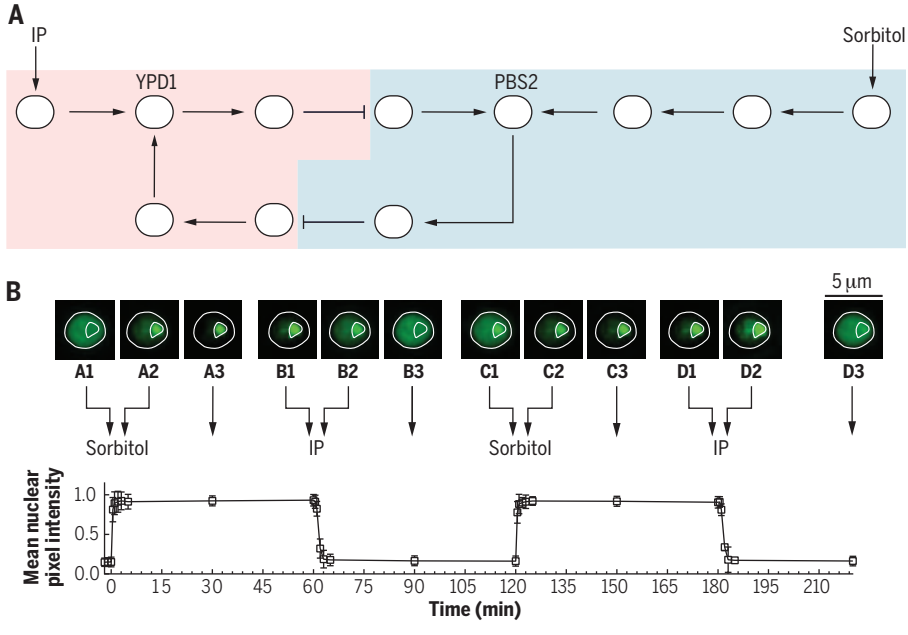

Network schematic and characterization of the engineered bistable toggle switch network comprising exogenous chimeric fusion proteins and endogenous proteins from the high-osmolarity MAPK pathway. (**A**) The network implements cross-repression, with each network node representing a protein phosphorylation interaction with either positive or negative regulation. If isopentenyl adenine (IP) is transiently introduced, then the YPD1 branch is set high and the PBS2 branch is set low (red shading). If sorbitol is transiently introduced, then the PBS2 branch is set high and the YPD1 branch is set low (blue shading). (**B**) The network has a fluorescent localized green fluorescent protein that is in the cytoplasm when YPD1 is set high and in the nucleus when PBS2 is set low. A trace of mean nuclear fluorescence intensity for $n = 100$ individual cells when exposed to alternating 30-s pulses of sorbitol and IP inducers with a 59.5-min pause between pulses is plotted. Insets at the time points indicated by arrows are representative individual toggle cell micrographs showing GFP localization (cytoplasm or nuclear).

RESULTS: We built a bistable toggle switch in *Saccharomyces cerevisiae* with a regulatory network based solely on reversible protein-protein phosphorylation interactions. The network encodes positive feedback regulation through two branches arranged such that they repress each other (mutual cross-repression) and two distinct inputs to switch between the two possible states of the system. The engineered network is built from 11 phospho-in and phospho-out signal transduction elements comprising exogenous chimeric fusion proteins and endogenous proteins from the high-osmolarity mitogen-activated protein kinase (MAPK) pathway.

The resulting toggle network responds to extracellular inputs within seconds and exhibits long-term bistability across cell divisions. The toggle network also demonstrates ultrasensitivity, because cells encoding the toggle network respond to very-low-input signal concentrations that do not elicit observable responses in similar networks lacking feedback regulation. To highlight how protein networks may be advantageous in interfacing with certain natural processes in the cell, we rewired our toggle to control abrogation of cell budding through nuclear localization of a cytoskeletal protein.

Our engineered toggle network's topology and size are distinct from existing synthetic toggles and well-studied endogenous bistable networks. This motivated us to develop a computational framework for searching endogenous systems for network connectivity similar to our engineered toggle that may also exhibit bistability. A search for toggle networks in endogenous pathways within *S. cerevisiae* from two to nine nodes in length yielded 109,401 toggle network candidates. Pruning this list to 186 candidates that could be readily experimentally tested, we discovered five previously unreported protein-protein interaction networks that were observed to exhibit bistability.

CONCLUSION: This work demonstrates an engineered fast, bistable toggle network composed solely of reversible protein-phosphorylation interactions and a framework for identifying bistable toggle networks embedded within natural settings. Future synthetic protein-protein networks similar to ours will enable biological engineers to create fast sensing and processing systems for regulating cellular processes that operate in real time. In turn, the design and implementation of these protein networks will enable the discovery of new embedded endogenous networks with prescribed behaviors. ■

The list of author affiliations is available in the full article online.
*Corresponding author. Email: rweiss@mit.edu
Cite this article as D. Mishra *et al.*, *Science* **372**, eaav0780 (2021). DOI: 10.1126/science.aav0780

READ THE FULL ARTICLE AT
https://doi.org/10.1126/science.aav0780

RESEARCH ARTICLE

SYNTHETIC BIOLOGY

An engineered protein-phosphorylation toggle network with implications for endogenous network discovery

Deepak Mishra[1,2,3], Tristan Bepler[3,4,5], Brian Teague[6], Bonnie Berger[3,4,7], Jim Broach[8], Ron Weiss[1,2,3,4,9]*

Synthetic biological networks comprising fast, reversible reactions could enable engineering of new cellular behaviors that are not possible with slower regulation. Here, we created a bistable toggle switch in *Saccharomyces cerevisiae* using a cross-repression topology comprising 11 protein-protein phosphorylation elements. The toggle is ultrasensitive, can be induced to switch states in seconds, and exhibits long-term bistability. Motivated by our toggle's architecture and size, we developed a computational framework to search endogenous protein pathways for other large and similar bistable networks. Our framework helped us to identify and experimentally verify five formerly unreported endogenous networks that exhibit bistability. Building synthetic protein-protein networks will enable bioengineers to design fast sensing and processing systems, allow sophisticated regulation of cellular processes, and aid discovery of endogenous networks with particular functions.

Synthetic biology applies engineering methodologies to build new functions into living cells. Many efforts to date have focused on regulating gene expression at the transcriptional and translational levels. Synthetic biologists have adapted natural DNA- and RNA-binding proteins and created de novo designs to engineer transcriptional and translational circuits within cells. These networks are capable of dynamic behaviors that implement cascades, switches, oscillators, Boolean logic, and analog logic (*1*–*7*). Such synthetic networks that are based on regulating gene expression respond to changes in inputs on time scales that range from minutes to hours because of the time required by the cell to transcribe and translate regulatory proteins. For certain applications such as guiding developmental processes, these time scales are sufficient.

By contrast, many natural biological systems need to operate in real time and respond to stimuli in seconds or less. Cellular processes such as signal transduction, metabolism, and cell division use protein interaction networks to rapidly detect extra- and intracellular inputs, process information, and actuate outputs (*8*–*12*). One important behavior encoded within these networks is bistability, that is, exhibiting two distinct stable states and an ability to switch between them. Bistability is widespread in biology, found in a range of processes from cellular cycle progression to innate immune cell activation and memory formation (*13*–*15*). Such natural switches often rely on phosphorylation and can be switched between two states by applying two different transient inputs [e.g., the cyclin-dependent kinase 1:cyclin B (Cdk1:CycB) complex for mitotic M phase entry (*16*)]. Analogous to their important role in natural contexts, engineering protein interaction–based bistable toggle switches, and more generally feedback control, is essential for protein synthetic biology. Such advances would allow us to implement systems exhibiting memory, hysteresis, and dynamical properties that are otherwise not possible (*17*).

Creation of synthetic protein networks that implement specific functions, e.g., toggle switches or other feedback-regulated systems, remains challenging (*18*). This is largely because of the difficulty in engineering protein-protein regulatory interactions, an effort inherently more complex than forging transcription and translational connections (*1*, *19*). Modalities for engineering protein interactions include allosteric, cooperative, and multimeric binding in addition to posttranslational modifications (*12*). Foundational strategies have emerged within protein synthetic biology to use these modalities. Binding interactions have been engineered by repurposing natural orthogonal protein domains, de novo protein design, and irreversible viral protease tags (*20*–*24*). Networks with these interactions have implemented signaling cascades that regulate transcription (*25*–*28*), hybrid protein and transcriptional networks incorporating feedback (*29*, *30*), and Boolean logic gates (*20*, *22*, *31*). However, the speed of certain state transitions in these engineered networks is governed by transcriptional and translational processes, resulting in operational time scales on the order of minutes or slower. Engineered networks that rely only on reversible posttranslational modifications of proteins would operate much faster. We therefore decided to design and construct a protein phosphorylation–based bistable toggle network. Our toggle serves as an important building block for protein synthetic biology, providing for fast memory and demonstrating reversible protein-protein–based feedback regulation.

Engineering a protein-protein toggle network

A successfully demonstrated topology for building bistable transcriptional toggle switches in synthetic biology uses positive feedback regulation with two nodes that cross-repress each other and several different approaches to support small molecule–based state switching (*5*, *6*, *32*, *33*). Our implementation of an analogous protein-protein interaction network is also based on cross-repression. To simplify the engineering effort, we allowed either positive or negative regulatory interactions between any two proteins but not both. A mutual cross-repression network that satisfies this constraint and uses two different inputs to switch between its two states is shown in Fig. 1A. The network consists of two cross-repressing branches of node pairs (A_1/A_2 and B_1/B_2). In this topology, two cascades (A and B) are arranged such that they repress one another, and each cascade has a separate external input (I_1 and I_2). In the absence of inputs, two stable states are possible: one in which A_1 activates A_2 and A_2 represses B_1 (A high and B low), and one in which B_1 activates B_2 and B_2 represses A_1 (A low and B high). Introducing input I_2 transiently will switch from the A high state to the B high state. Similarly, I_1 will switch the toggle back from the B high state to the A high state.

An alternate representation of the cross-repression network in Fig. 1A is a Boolean logic diagram comprising two OR and two NOT gates (Fig. 1B). This network representation is commonly used in synthetic biology and occasionally in systems and computational biology (*34*). Such logical device abstractions aid in the understanding, design, and study of regulatory network structure and function (*35*, *36*). The relationships depicted by A_2 regulating B_1, as well as B_2 regulating A_1, each implement a NOT logic gate. For a NOT gate, a low input yields a high output and a high input yields a low input. Thus, when branch A is high, branch B is repressed and kept low and vice versa. The networks

[1]Department of Biological Engineering, Massachusetts Institute of Technology, Cambridge, MA, USA. [2]Synthetic Biology Center, Massachusetts Institute of Technology, Cambridge, MA, USA. [3]Computer Science and Artificial Intelligence Laboratory, Massachusetts Institute of Technology, Cambridge, MA, USA. [4]Computational and Systems Biology Graduate Program, Massachusetts Institute of Technology, Cambridge, MA, USA. [5]Simons Machine Learning Center, New York Structural Biology Center, New York, NY, USA. [6]Department of Biology, University of Wisconsin, Stout, WI, USA. [7]Department of Mathematics, Massachusetts Institute of Technology, Cambridge, MA, USA. [8]Department of Biochemistry and Molecular Biology, Penn State College of Medicine, Hershey, PA, USA. [9]Department of Electrical Engineering and Computer Science, Massachusetts Institute of Technology, Cambridge, MA, USA.
*Corresponding author. Email: rweiss@mit.edu

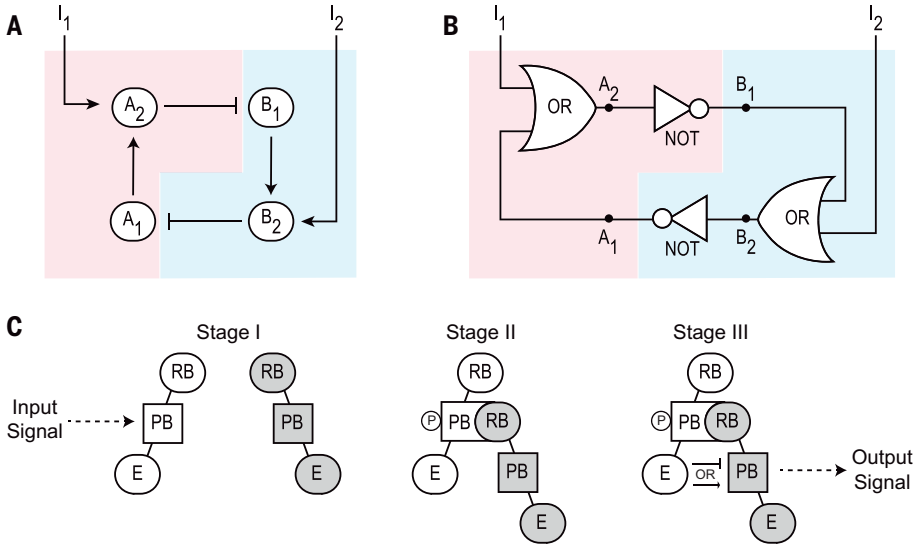

Fig. 1. Cross-repression phosphorylation-based toggle switch schematics and PRIME. (**A**) Four-node network consisting of two cross-repressing node pairs (A_1/A_2 and B_1/B_2) that implement a bistable toggle. Each pair of nodes constitutes a branch such that either branch A is high and branch B is low (state 1) or vice versa (state 2). Applying input I_1 or I_2 can set branch A or branch B high, respectively, enabling switching between states. (**B**) Alternative representation of a bistable cross-repression toggle shown in (A) using two pairs of connected OR and NOT gates. Each pair of OR and NOT gates constitutes a branch, and only one branch A or B can be high at a time because of their respective NOT gates acting on the other. Switching is enabled by applying a high input to the OR gate on the low branch. (**C**) Each chimeric protein fusion consists of three domains, a ready-binder (RB), a phospho-binder (PB), and an effector (E). The ready-binder needs no conditional regulation to bind. The phospho-binder is affected by the upstream protein's effector and only when activated can bind a downstream protein's ready-binder. The upstream effector acts upon the phospho-binder of the downstream protein only upon colocalization enabled by binding between the upstream protein's phospho-binder and the downstream protein's ready-binder. When the upstream effector is a kinase, input signal and output signal match. When the upstream effector is a phosphatase, input signal and output signal are inverted.

relationship depicted by I_1 and A_1 co-regulating A_2 as well as I_2 and B_1 co-regulating B_2 implements a two-input OR logic gate. For a two-input OR gate, if either or both inputs are high, the output is high. The Boolean logic diagram in Fig. 1B provides another perspective to Fig. 1A of how applying high-input I_1 or I_2 sets branch A or B high, respectively, enabling switching.

To achieve the abstract network topology depicted in Fig. 1, A and B, we used a combination of endogenous and exogenous proteins to obtain the overall desired positive feedback cross-repression connectivity. The endogenous elements of our implementation are based on the high-osmolarity glycerol (HOG) mitogen-activated protein kinase (MAPK) pathway of *S. cerevisiae* (*37*–*39*) (fig. S1A). In wild-type cells, extracellular osmolarity sensing occurs by two independent transmembrane osmosensors, SLN1 and SHO1, detecting turgor pressure and osmolarity changes, respectively. A complete description of the native HOG1-signaling pathway can be found in supplementary note 1.1. SLN1 and SHO1 form a natural OR gate converging on MAPKK PBS2 that ultimately results in phosphorylation, activation, and nuclear translocation of its MAPK, HOG1 (*40*, *41*). SLN1 and SHO1 differ in sensing mechanisms because SHO1 signaling comprises only activating nodes, whereas SLN1's signaling includes a natural NOT gate upstream of PBS2. Fig. S1B shows the mapping of the SLN1/SHO1 → PBS2 → HOG1 reactions to the network depicted in Fig. 1B. Three protein phosphorylation cascades ranging in size between two and three elements are used to connect the inputs to the NOT and OR gates. Each of the phosphorylation interactions in these cascades transmits a signal without change and can be referred to as BUFFER logic gates (fig. S1B) (*42*).

Design and construction of engineered OR and NOT gates

We then added synthetic elements that, when combined with the endogenous HOG1 pathway, implement the abstract toggle network depicted in Fig. 1. To create synthetic OR and NOT gates, chimeric protein fusions were constructed such that phosphorylation of an upstream protein results in binding the downstream protein and modulating its phosphorylation state (Fig. 1C). Specifically, both upstream and downstream chimeric proteins comprise three domains: a ready-binder, a phospho-binder, and an effector. These protein domains implement phospho-in and phospho-out gates, in which the input and output are the phosphorylation states of the phospho-binder of the upstream and downstream proteins, respectively. Protein colocalization is driven by interactions between phospho-binder of the upstream protein and the ready-binder of the downstream protein. The phospho-binder needs to be phosphorylated to bind, whereas the ready-binder is always capable of binding; therefore, it is the phosphorylation state of the upstream protein that determines whether binding occurs. Upon binding, the phosphorylation state of the downstream protein's phospho-binder is determined by the effector domain of the upstream protein. We call this mechanism of forging a functional connection between an upstream and a downstream protein phosphorylation-required interaction and mediated effect (PRIME). PRIME may provide a scalable platform for creating additional logic gates (supplementary note 1.2).

We used the PRIME mechanism to engineer a two-input OR gate. The upstream proteins are two chimeras formed by fusing *Arabidopsis thaliana* CRE1 (*43*, *44*) or *Mus musculus* STAT5 (*11*) each to intramolecular histidine kinase response regulator domains from endogenous SLN1 (denoted $HKRR_{SLN1}$) to create CRE1-$HKRR_{SLN1}$ and STAT5-$HKRR_{SLN1}$ (fig. S2) (*41*, *45*–*47*). For clarity, we designate the chimeric proteins in all our systems by hyphenation of their major constituent domains. After upstream activation of either phospho-binder domain of CRE1-$HKRR_{SLN1}$ or STAT5-$HKRR_{SLN1}$, the chimeric protein homodimerizes through the ready-binder domain. In turn, either of the dimer's effector domains leads to phosphorylation of YPD1, and thus OR logic is implemented (Fig. 2A). Complete mapping and dynamics of the ready-binder, phospho-binder, and effector domains of CRE1-$HKRR_{SLN1}$ and STAT5-$HKRR_{SLN1}$ are described in fig. S2.

To engineer a functional OR gate, we first generated several variants of each input chimeric fusion protein. We then tested them by controlling each variant with a synthetic hybrid transcriptional-translational network. The network allowed us to regulate experimental inputs to an individual protein variant and measurement of output phospho-YPD1 levels through downstream transcriptional activation of green fluorescent protein (GFP) expression (supplementary note 1.3 and fig. S3). We chose the best chimeric fusion protein that maximized the fold-change increase between high and low input and constructed a new hybrid transcriptional-translational genetic circuit to test the full OR logic gate. We controlled one of the inputs to the OR gate by introducing external isopentenyl adenine (IP) to regulate

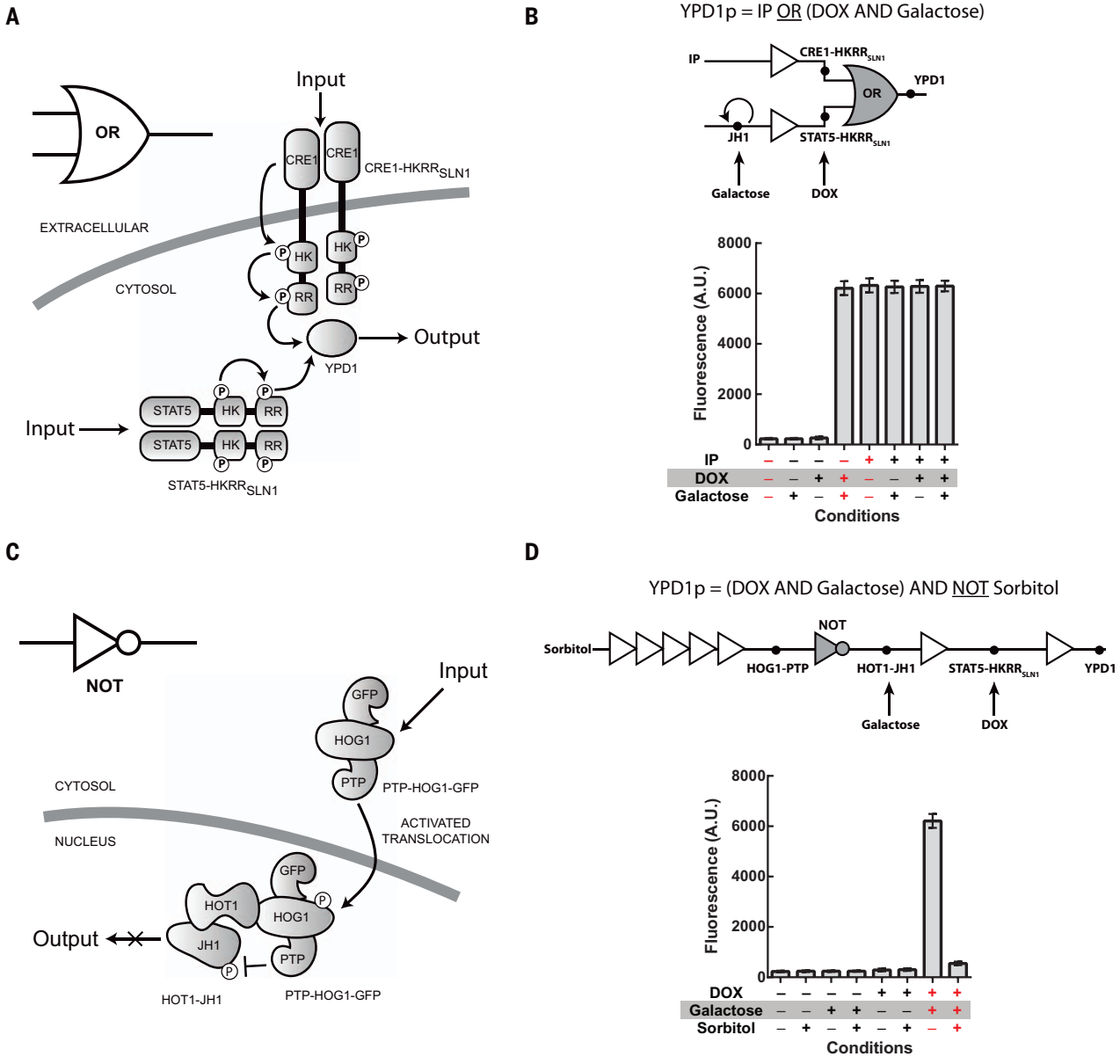

Fig. 2. Development of engineered OR and NOT logic gates. (**A**) Schematic of a protein phosphorylation OR gate formed by PRIME with a kinase effector domain (fig. S2). The concentrations of phospho-STAT5-HKRR$_{SLN1}$ and phospho-CRE1-HKRR$_{SLN1}$ serve as input signals, and the concentration of phospho-YPD1 is the output signal. If either input is high, output signal is high. (**B**) The OR gate is embedded within a larger transcriptional (vertical arrows) and/or translational (gates) network for testing (fig. S4). The OR gate is evaluated by modulating three small-molecule inputs (IP, DOX, and galactose) and monitoring the subsequent phospho-YPD1 state through GFP expression from $P_{TR\text{-}SSRE}$. The three input cases showing OR functionality (no activation and activation of either CRE1 vs STAT5 branches) are denoted in red, and the fold change between no inputs and either DOX and galactose or just IP were 26.8× and 27.3×, respectively. (**C**) Schematic of a protein-phosphorylation NOT gate formed by PRIME with a phosphatase effector domain (fig. S5). Concentration of phospho-PTP-HOG1-GFP is the input signal, and concentration of phospho-HOT1-JH1 is the output signal. If input is high, phospho-PTP-HOG1-GFP translocates into the nucleus and binds HOT1-JH1. Colocalization of the proteins allows the PTP effector to regulate the phospho-binder domain of HOT1-JH1. (**D**) The NOT gate is embedded within a larger network (fig. S7). The gate is evaluated by modulating three small-molecule inputs (DOX, galactose, and sorbitol) and monitoring subsequent phospho-YPD1 state through GFP expression from $P_{TR\text{-}SSRE}$. The two input cases showing NOT functionality are denoted in red and represent a 14.6-fold change. In (B) and (D), *S. cerevisiae* cells were in W303A with ΔHog1ΔHot1ΔFus3ΔKss1ΔSln1::*At*Cre1-HKRR background with the respective circuit integrated into the *HO* locus and dosage of inducer as noted in methods. Resulting fluorescence was measured at 240 min by batched flow cytometry for a population of 30,000 cells and the population mean is reported. Error bars indicate SD from $n = 3$ biological population replicates.

the CRE1-HKRR$_{SLN1}$ phosphorylation state. The other inputs were galactose and doxycycline (DOX) to enable indirect control of STAT5-HKRR$_{SLN1}$ phosphorylation (fig. S4). By administering IP alone or DOX and galactose combined, we were able to induce activation of CRE1-HKRR$_{SLN1}$ and STAT5-HKRR$_{SLN1}$, respectively. Measurement of GFP expression confirmed successful OR logic implementation (Fig. 2B).

We next engineered a NOT gate using the PRIME mechanism by building two additional chimeric proteins. The upstream protein is PTP-HOG1-GFP, a fusion between yeast HOG1, a protein tyrosine phosphate (PTP) domain

from *M. musculus* SHP-1, and GFP (*48*). The downstream protein is HOT1-JH1, a fusion between yeast HOT1 and elements from *M. musculus* transcription factor JAK2 (*11*, *49*) (fig. S5). Without input to the phospho-binder of PTP-HOG1-GFP, the protein remains cytosolic. Within the nucleus, HOT1-JH1's phospho-binder autophosphorylates, and its effector domain can act on downstream proteins. Administering extracellular sorbitol leads to activation of the phospho-binder domain of PTP-HOG1-GFP. Activated PTP-HOG1-GFP translocates into the nucleus, where its phospho-binder can bind the ready-binder of HOT1-JH1. This allows the upstream PTP effector domain to dephosphorylate the phospho-binder domain within JH1, preventing HOT1-JH1 from acting downstream. In this manner, NOT logic is implemented (Fig. 2C). Complete mapping and dynamics of the ready-binder, phospho-binder, and effector domains of PTP-HOG1-GFP and HOT1-JH1 are described in fig. S5.

To engineer a functional NOT gate, we first generated several variants of HOT1-JH1 and PTP-HOG1 and tested them independently for functionality (supplementary note 1.4 and fig. S6). We then inserted the best-performing variant in terms of fold-change activation into a genetic circuit to test the full NOT gate connected to the STAT5-HKRR$_{SLN1}$ input of the engineered OR gate. We controlled activation of PTP-HOG1 by administering external sorbitol and measured output phospho-YPD1 levels in an identical manner as the OR gate network to verify NOT operation (fig. S7 and Fig. 2D). Next, we fused GFP (*50*) to PTP-HOG1, creating PTP-HOG1-GFP to measure its nuclear localization directly, and confirmed that the OR logic was maintained.

Building and characterizing the protein toggle switch

The combination of our engineered OR and NOT gates (Fig. 2) with the endogenous high-osmolarity pathway (fig. S1) creates the topology of a two-input bistable cross-repression toggle switch (Fig. 3A). The complete toggle phosphorylation network consists of two cross-repressing branches, the first of which is HOT1-JH1 → STAT5-HKRR$_{SLN1}$ → YPD1 → SSK1 and the second is SSK2 → PBS2 → PTP-HOG1-GFP (Fig. 3B). Toggle bistability is maintained by two opposing NOT gate inversion operations in which either PTP-HOG1-GFP inhibits HOT1-JH1 (Fig. 3, A and B, red shading) or SSK1 inhibits SSK2 (Fig. 3, A and B, blue shading) (*51*, *52*). Thus, either the YPD1 branch or the PBS2 branch is phosphorylated and inactivates the other branch, resulting in one of the two distinct stable states. Transient administration of one of two small-molecule inputs, IP or sorbitol, propagates a phosphorylation signal into one of the two OR gates and can subsequently switch toggle state. Regardless of the current state of the toggle, administering IP sets the YPD1 branch high, administering sorbitol sets the PBS2 branch high, and the branch state is maintained by the cross-repressing NOT gates after removal of inputs. Additional details on individual protein phosphorylation, switching, and additional host optimization for the toggle network are provided in supplementary note 1.5.

To guide the creation of a functional toggle switch, we developed and analyzed a mathematical model of the network (supplementary note 1.6). We performed computational simulations and analysis varying all network parameters to identify the most important factors for bistability. The analyses revealed that absolute and relative gene expression rates of HOT1-JH1, STAT5-HKRR$_{SLN1}$, and PTP-HOG1-GFP are critical for toggle bistability (figs. 8 to 10 and supplementary notes 1.6.4 to 1.6.5). We experimentally built and assessed a toggle library with varied expressions of these proteins and chose the toggle network variant with the highest fold difference between the two bistable states at steady state as measured by fluorescence. We refer to this particular optimized bistable network as the toggle network going forward. In cases where we perturb the toggle's connectivity, we refer to the resulting network as a defective toggle and indicate in parentheses the particular difference compared with the toggle network.

To verify the toggle's switching operation and stability, we immobilized the genetically engineered cells in microfluidic devices and quantified PTP-HOG1-GFP nuclear localization using fluorescence microscopy. We applied alternating 30-s inducer pulses separated by 60 min of no inducer and observed that sorbitol pulses led to sustained PTP-HOG1-GFP nuclear localization and IP pulses led to sustained cytoplasmic PTP-HOG1-GFP (Fig. 3C). This confirmed that the network had two distinct states that could be switched by administering molecular inputs.

To verify that the toggle network and its protein connections were responsible for our observed switching and maintenance of the two states, we created nine defective toggles that each disrupted a single protein-protein interaction while avoiding synthetic lethal phenotypes (table S1). Specifically, each defective toggle switch had a protein-protein interaction removed through either removal of a phospho-binder or effector domain within a chimeric protein or through point mutations that render phospho-binder or effector domains a null substrate or kinase, respectively. As expected, these defective toggle networks did not have two distinct states or switch after administering IP or sorbitol for any of them, indicating that the other toggle proteins by themselves do not support bistability (figs. S11 and S12). We also compared behavior of our toggle network with wild-type cells to ensure that differences in osmotic stress response (e.g., cell cycle arrest) were not responsible for the observed bistability (supplementary note 1.7 and fig. S13). Our experimental results confirmed that the switching behavior observed in Fig. 3C was indeed a direct result of our toggle network and was not from cell cycle arrest, perfect adaptation, or other regulation within the wild-type osmolarity pathway.

Next, we determined what input conditions to the toggle network were sufficient to switch between states. First, we administered constant input at fixed concentrations and measured the proportion of cells harboring the toggle that switched states (fig. S14). We administered transient pulses of inducer of varying durations at constant concentration measured to be sufficient to switch the entire cell population. For 30-s inducer pulses at saturation, we observed that PTP-HOG1-GFP nuclear localization stabilized by 2 min, remained constant over 240 min, and was maintained across cell division (Fig. 4A and fig. S15). In the case of the two control networks, defective toggles such that cross-repression was removed through genetic knockouts in the HOT1-JH1 → STAT5-HKRR$_{SLN1}$ → YPD1→ SSK1 branch, the input pulses were sensed but did not result in sustained state changes (fig. S16). We performed additional fine-grained dynamic experiments on the toggle by varying both the concentration and the duration of transient inducer input pulses and then measuring the percentage of toggle cells that switched successfully (Fig. 4B). The results indicated that both IP and sorbitol switching of the toggle followed a quasilinear, flux-dependent relationship (concentration multiplied by time).

Inspired by ultrasensitivity analysis of endogenous transcriptional toggles (*10*, *53*, *54*), we investigated the ability of our phosphorylation toggle to detect weak transient inputs. We measured single-cell trajectories of both a functional toggle and an open loop network, a defective toggle in Δ*Ssk1*Δ*Ssk2*Δ*Ssk22* background solely for osmolarity detection, after administration of 2-s input pulses of varying inducer concentration (Fig. 4C). For the defective toggle, a readily observable response required sorbitol concentrations of at least 300 μM (Fig. 4C and fig. S17), consistent with other studies of the yeast osmolarity pathway (*37*, *55*). For the toggle network, however, at concentrations as low as 30 μM, ~2% of the cells reproducibly transitioned from the off to the on state (Fig. 4D). As such, a population of toggle cells exhibited ultrasensitivity and were able to sense input concentrations an order of magnitude lower than concentrations detectable by the defective toggle network. To better understand our toggle network's ultrasensitivity, we developed a schematic (fig. S18 and supplementary note 1.6.6) and used additional computational analysis. A closed-form

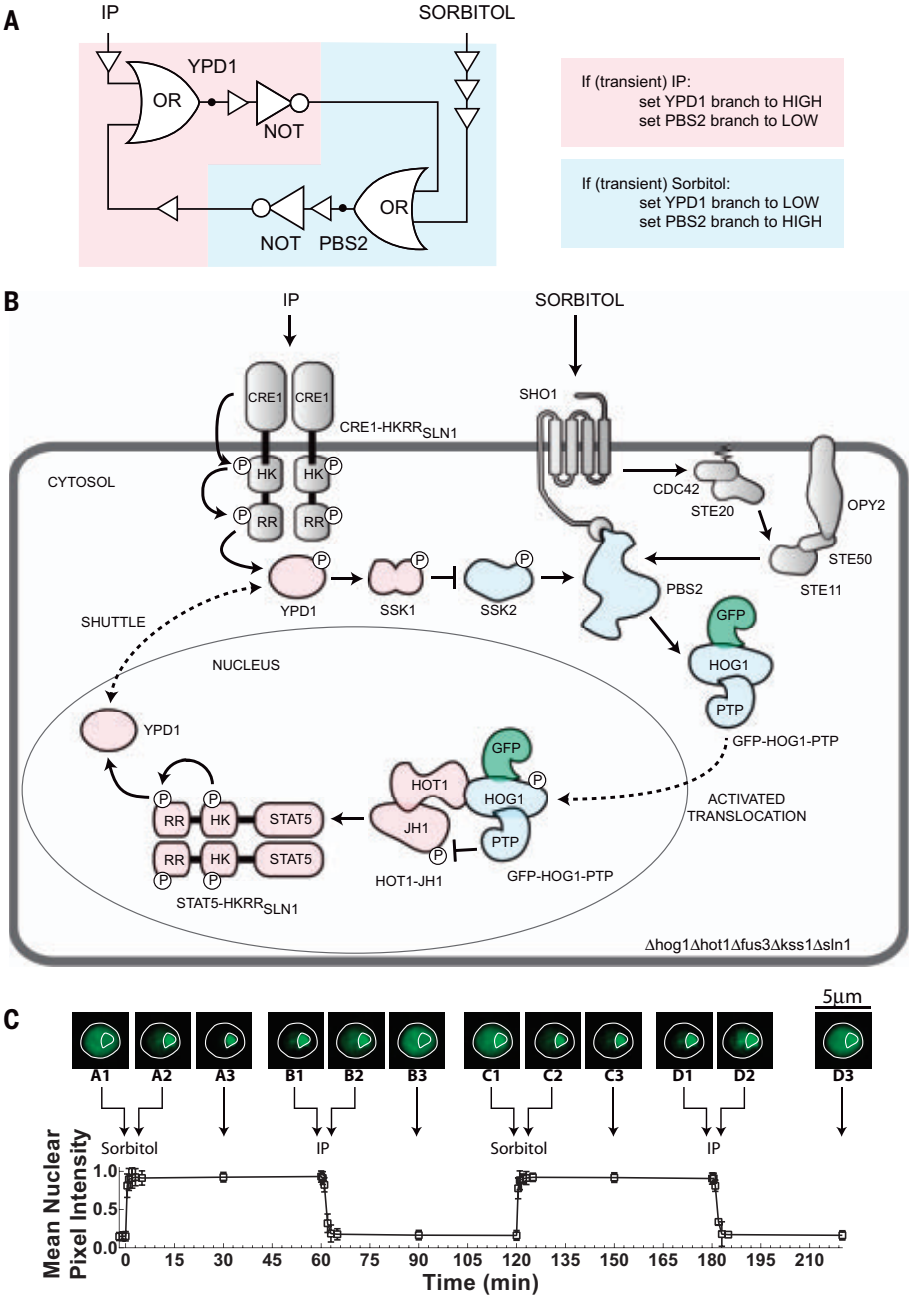

Fig. 3. Design and characterization of engineered protein toggle switch. (**A**) (Left) Logic circuit diagram of our cross-repression toggle switch implementation comprising OR, NOT, and BUFFER gates and the two inputs, IP and sorbitol. (Right) Pseudocode for the two-input toggle network consisting of YPD1 and PBS2 branch responsive to IP input and sorbitol input, respectively. (**B**) Mapping the toggle to a biological implementation comprising protein-protein interactions using the designed OR and NOT phospho-in and phospho-out gates described in Fig. 2 in conjunction with the endogenous high-osmolarity MAPK pathway. A more detailed description of toggle elements and state switching is provided in supplementary note 1.5. Blue shading corresponds to PBS2 high, stable state 1, and red shading corresponds to YPD1 high, stable state 2. All proteins are expressed constitutively by either their native promoters in the case of endogenous elements or by carefully selected constitutive promoters in the case of exogenous elements. For simplicity in signaling pathways and unless specifically noted in genotypes, SSK2 in the text refers to SSK2 and SSK22, the latter being a redundant homolog of the former due to a genomic duplication event. (**C**) Representative trace of an individual toggle cell's PTP-HOG1-GFP fluorescence when exposed to alternating 30-s pulses of each inducer with a 59.5-min pause between pulses. The cell membrane is identified from bright-field images and is denoted by an outer boundary line; the nucleus is identified from expression of HTB-azurite and is denoted by the inner boundary line. A trace of mean nuclear fluorescence intensity for n = 100 individual cells is depicted, with error bars indicating SD. In (C) and data referenced to be from the full toggle, the network is integrated into yeast strain W303A with ΔHog1ΔHot1ΔFus3ΔKss1ΔSln1::AtCre1–HKRRΔHtb1::Htb1–azurite background. All cells were grown in the liquid log phase before being immobilized within a microfluidic device and exposed to inducer concentrations as noted.

analytical solution for use in bifurcation analysis of our toggle model would have required many simplifying assumptions that remove biological relevance. Instead, we used numerical methods and ran stochastic simulations of single toggle cells to generate dynamic trajectories given an input signal (fig. S19 and supplementary note 1.6.7). This allowed us to create a probability-based model of attractor states for a community of toggle-integrated cells that can predict ultrasensitive responses for even very weak transient input pulses (fig. S20).

To illustrate how systems composed of engineered protein-protein interactions can directly modulate cellular behavior, we created a toggle switch network to regulate yeast budding. In the endogenous process for bud emergence, BEM2, a rho GTPase–activating protein, localizes to the sites of polarized growth and is critical for proper cellular division. By knocking out endogenous BEM2 and replacing the GFP domain of PTP-HOG1-GFP with BEM2 to create PTP-HOG1-BEM2, we directly connected the toggle network to actuate BEM2 localization and regulate cell budding (Fig. 5A). In the corresponding experiments, we first set the toggle network to be in the YPD1 high state by administering IP. Upon administration of a short transient sorbitol input stimulus of 30 s, the translocation of PTP-HOG1-BEM2 to the nucleus from the cytosol abrogated the multihour yeast-budding process and led to the elongation of individual cells. Applying IP stimuli to cells with nuclear-localized BEM2 fusion attenuated bud arrest and allowed the formation of daughter cells (Fig. 5, B and C). Thus, control of our toggle network through external stimuli allowed direct modulation of an endogenous protein network and cell phenotype.

Synthetic biology–inspired network discovery

Although our engineered toggle network uses cross-repression, its network topology is distinct

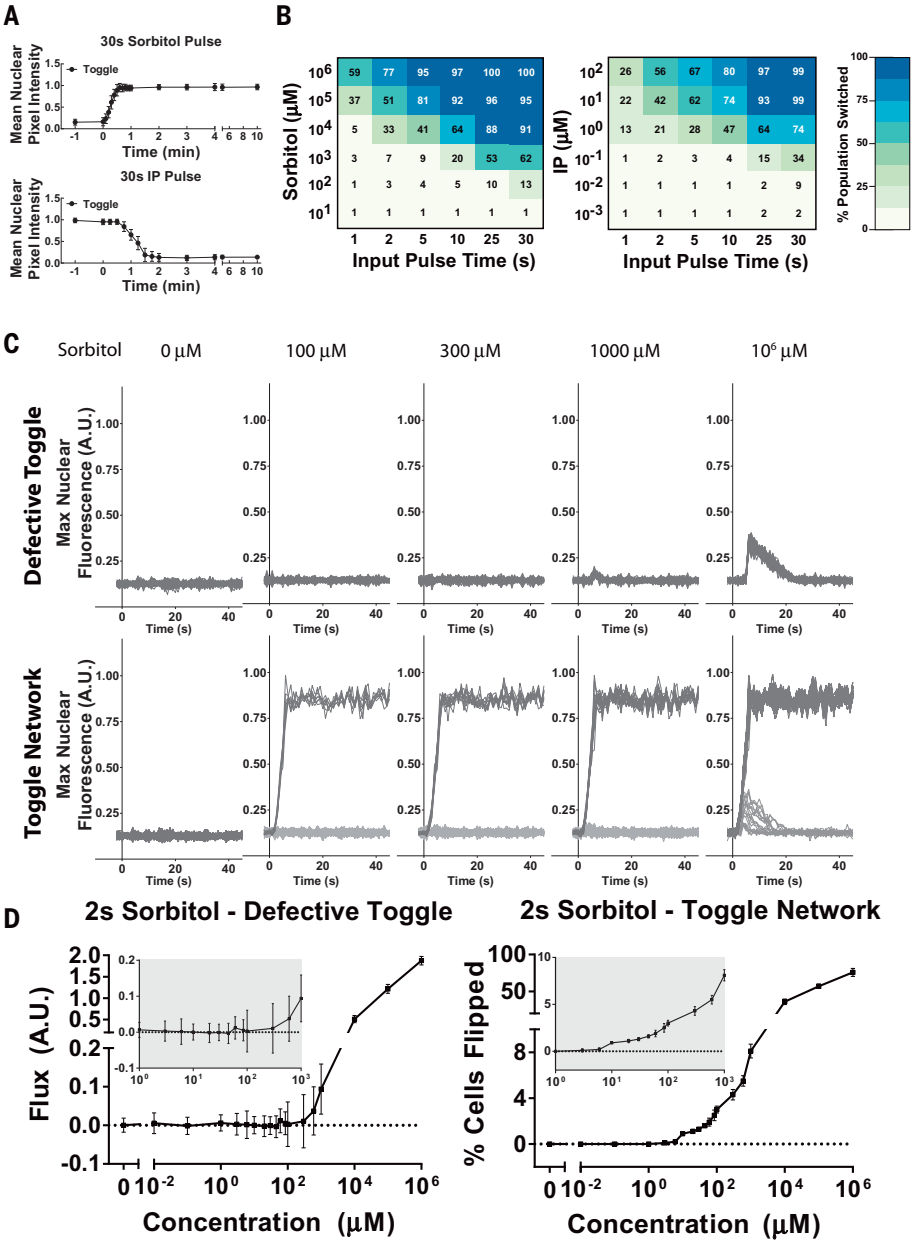

Fig. 4. Steady-state and dynamic response to inputs. (**A**) Cells previously grown in the presence of sorbitol (top) or IP (bottom) in liquid culture before wash-out of inducers, immobilization, and subsequent application of 30-s saturating pulse of the opposite inducer (10^6 μM sorbitol and 10^2 μM IP) for the full toggle network. Average mean is plotted, and error bars indicate SD for n = 100 cells. (**B**) Modulation of IP and sorbitol concentration and pulse duration for toggle cells and the resulting percentage of cells that switched states from low to high (left; sorbitol) or high to low (right; IP) measured through nuclear fluorescence. Plotted number is from analysis of n = 100 individual cells for each experiment, measured at t = 600 s. (**C**) Single-cell trajectories of nuclear fluorescence resulting from PTP-HOG1-GFP translocation after a 2.0-s pulse of increasing sorbitol concentrations. The defective toggle (ΔSsk1ΔSsk2ΔSsk22) is shown in the top panel and the toggle network in the bottom panel. For 2.0-s/1.0 μM sorbitol induction, a subpopulation of the toggle cells (9.7%) returned back to the low state after input. (**D**) Summary statistics of all cell trajectories as a function of increasing sorbitol input pulses for the defective toggle (ΔSsk1ΔSsk2ΔSsk22) (left panel) and toggle network (right panel). Flux is calculated as area under a single-cell trajectory and reported for n = 100 single defective toggle cells. Percentage of cells flipped is calculated per population of 332 toggle network cells and reported for n = 3 populations. Cells are from the full toggle as in Fig. 3 except as noted for defective toggles. All cells were grown in the liquid log phase before being immobilized within a microfluidic device and exposed to inducer concentrations as noted. The minimum microfluidic device mixing time is 0.5 s (*55*). A comparison of the fold changes collected through transcriptional control in Fig. 2 and microscopy in all other figures is presented in fig. S25.

from existing synthetic transcriptional toggles and known endogenous bistable networks. This motivated us to search endogenous systems for encoded network connectivity similar to our engineered toggle that may also exhibit bistability. We started by defining a high-level narrative description of a toggle switch, that is, a network that switches between two stable states. On the basis of this informal description, we formulated a structural specification of a particular network family encoding cross-repression that can implement toggle switch function: any nonredundant directed loop of n connected protein nodes, an even number m inhibitory edges, and n-m activating edges (*56*). We created custom code that takes a large network as input and finds all subnetworks up to a given size that satisfy this structural specification. Pruning of the results can then be used to reduce the number of candidate networks to be tested experimentally. We call this method biological function encoded by connected edges (BioFENCE), an algorithm for searching endogenous networks for specific function, in this case, bistability (Fig. 6A and supplementary note 1.9).

We ran a query to find potentially bistable subnetworks within a directed graph comprising 216 unique nodes, 124 inhibitory edges, and 408 activating edges. Restricting the search to a maximum network size of up to n = 9 nodes yielded 109,401 candidate networks that satisfied our topological requirements (Fig. 6B) (*57*, *58*). We pruned these toggle candidates in an automated manner into a set of 186 networks that could be readily tested experimentally. The pruning criteria included the degree of network orthogonality, availability of at least two specific small-molecule kinase inhibitors (SMKIs) to nodes within opposing network branches, and knowledge of potential transcriptional readouts of opposing branches (supplementary note 1.9.1). After running the search, we computationally examined networks for any variation in gene ontology categories between candidate nodes versus input nodes but did not observe any additional enrichment from the sieve process (supplementary note 1.9.2). For the resulting final 186 candidates, we first experimentally administered a single SMKI pulse that would

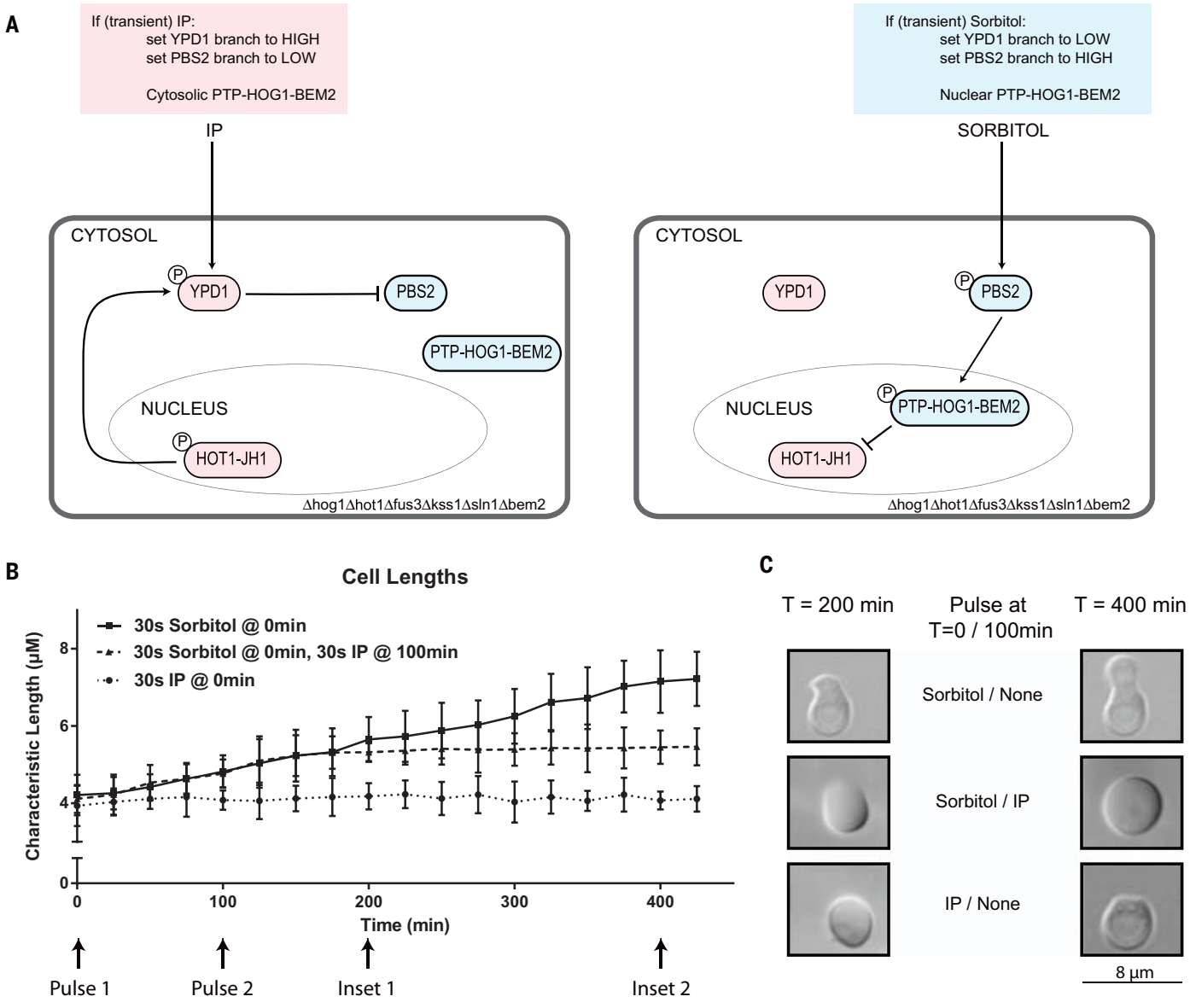

Fig. 5. Toggle network to control yeast budding. (**A**) PTP-HOG1-BEM2 replaces the PTP-HOG1-GFP fusion protein within the full toggle. When PTP-HOG1-BEM2 is inactive (i.e., YPD1 branch is high), yeast cells are able to bud and proliferate naturally, whereas when PTP-HOG1-BEM2 is active (i.e., PBS2 branch is high), the localization of BEM2 to the nucleus prevents budding. (**B**) Digitally measured characteristic lengths of toggle cells with PTP-HOG1-BEM2 fusion in lieu of PTP-HOG1-GFP fusion after initially in a high YPD1 state being exposed to two inducer pulses at 0 and 100 min, respectively. Data reported are for n = 100 cells, with error bars indicating SD. (C) Representative bright-field images of toggle cells from time points indicated by arrows in (B). The circuit is integrated into yeast strain W303A with a ΔHog1ΔHot1ΔFus3ΔKss1ΔSln1::AtCre1–HKRRΔBem2 background.

act upon one branch of each network and measured a transcriptional readout by quantitative polymerase chain reaction (qPCR) of both network branches. For those network candidates that showed experimental promise, we administered two different SMKI pulses serially such that each SMKI would act upon a single but opposing network branch. We measured transcriptional readouts by qPCR of each network branch and looked for networks that exhibited paired, inverse switches in gene expression (fig. S21). We observed paired switching in five networks and chose to analyze these networks further with more fine-grained time course experiments (fig. 6, C and D and table S2).

Of the five experimentally measured toggle candidates, two shared a connected edge, MAD2 activating CDC27, but differed in overall topology. For these two networks, we performed additional experimental studies in a yeast strain with a W303A-RNAi background (*59*), administering small interfering RNA and SMKI pulses to further study their interconnection and independence (figs. S22 and S23). When decoupled, both candidates functioned as independent toggles but did exhibit paired switching behavior (supplementary note 1.9.3 and fig. S24). The five networks identified by BioFENCE were experimentally observed to encode toggle behavior. It is possible that our observations resulted from other overlapping unidentified toggle networks that were modulated effectively by the two SMKIs, or perhaps the relevant regulation is not based purely on protein-protein interactions. Furthermore, the candidates that did not exhibit a paired transcriptional readout switching from administering SMKIs may nonetheless act as toggles

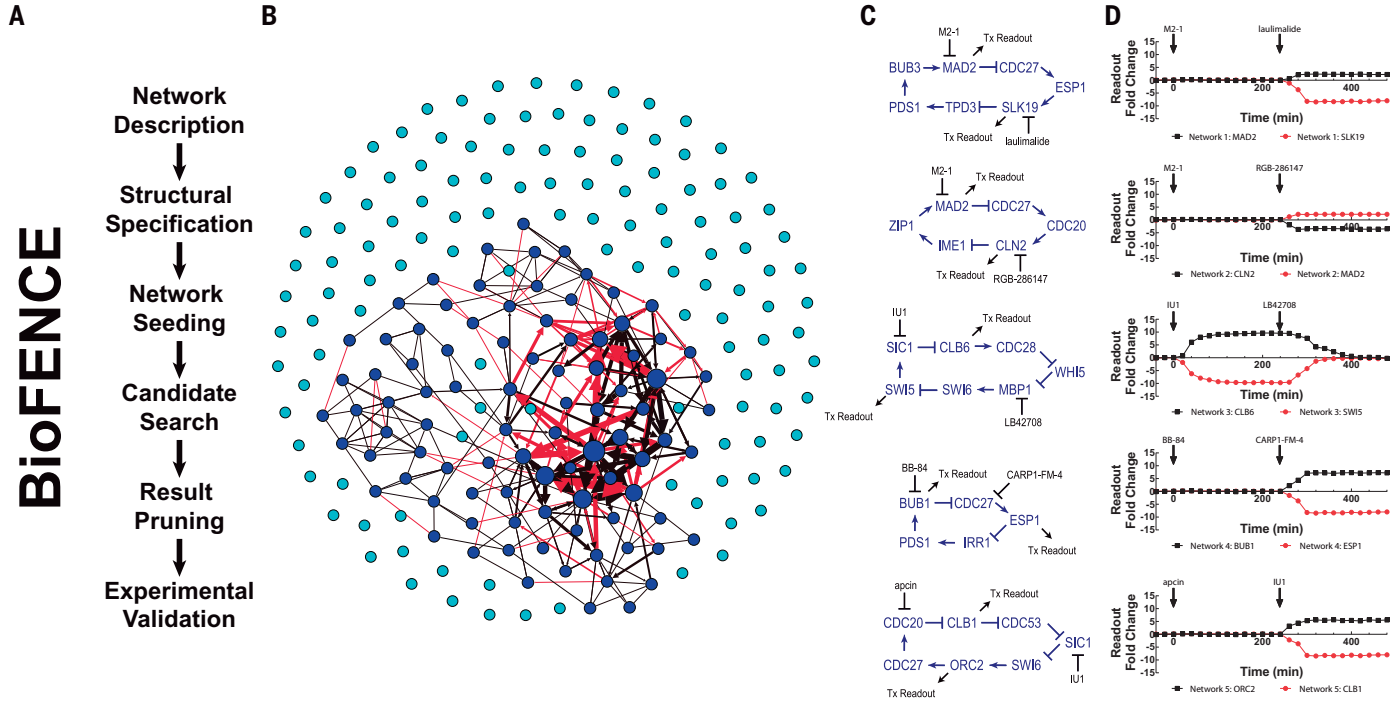

Fig. 6. BioFENCE discovery of endogenous toggle networks. (**A**) Overview of steps in BioFENCE as described in main text. (**B**) Directed graph of all *S. cerevisiae* protein-protein interactions contained within the KEGG database drawn using the Fruchterman-Reingold algorithm (*80*). Although initial seeding of the 216-protein-node graph had 408 activating interactions (black) and 124 inhibitory interactions (red), only those edges that appeared in any possible toggle candidate are shaded. For the 109,401 possible toggle networks, nodes that appeared in any toggle candidate are shown in dark blue, and nodes that appear in none are shown in light blue. The size of the node and the thickness of the edges are scaled to correspond to the frequency of occurrences in the candidate set. (**C**) Five endogenous toggle networks (blue text) that were identified by BioFENCE and passed screening for qPCR changes in downstream measured gene expression as a result of small-molecule kinase or phosphatase inhibitors (labeled in black). (**D**) Time-course fold change results obtained from qPCR on five BioFENCE-discovered toggle candidates. Results obtained from qPCR readouts for two 5-min pulses administered 240 min apart. All qPCR results were normalized using GAPDH control probe sets. All cells are *S. cerevisiae* W303A, and data points represent the mean of $n = 3$ biological triplicates independently prepared for cDNA before qPCR.

under different conditions (e.g., growth, environmental, other SMKIs, etc.).

Discussion

We combined the HOG1-MAPK cascade from *S. cerevisiae* alongside synthetic NOT and OR gates built using the PRIME mechanism into an engineered endogenous-exogenous network composed solely of fast, reversible phospho-in and phospho-out interactions. The resulting protein phosphorylation network exhibited bistability and ultrasensitive small-molecule sensing, with the toggle state controlling different actuation mechanisms (e.g., fluorescent readout through nuclear localization or abrogating cellular division). We envision that populations of cells harboring our toggle could enable the construction of highly sensitive environmental sensor arrays that detect and help to precisely map spatiotemporal changes in input chemical conditions. Future enhancements of our engineered protein toggle include the use of other protein sensors [e.g., humanized G protein–coupled receptors or engineered receptors connected to PBS2 (*60*–*62*)], coupling to organelle specific processes, and multiplexing protein sensors within a cell population. Another direction is creating an ingestible micro-bioelectronic device for delivery into the gut, with the toggle network controlling alternative luminescent outputs. Fast detection coupled with wireless electronic communication and monitoring would enable quick sensing and intervention to inadvertent consumption of food allergens, internal bleeding, or other medically relevant conditions within the gut environment (*63*, *64*).

The creation and optimization of our engineered toggle network highlighted two observations. First, synthetic network designs often aim to create architectures that are easy to understand, manipulate, or are based on elegant solutions (i.e., in terms of modularity and a minimal number of elements). By contrast, we achieved the desired topology by leveraging known endogenous pathways and used the PRIME mechanism to create specific connections, in some cases requiring several additional protein nodes. As a result, our approach yields engineered networks similar in complexity and size to natural regulatory networks. For example, M-G_1 or G_2-M bistable cell cycle checkpoints do not use the "shortest path" to implement a particular function (*10*). Nevertheless, regardless of the length of path used, synthetic and natural networks share criteria in forging new connections such as protein and domain orthogonality to existing pathways, input-output signal matching, and signal sensitivity. Our second observation is that graded changes in protein levels within our engineered toggle network had a substantial impact on behavior. Our engineered toggle's bistability was especially dependent on the balance between three key protein expression levels. The range of expression levels analyzed for each of these proteins spanned less than an order of magnitude but nonetheless had pronounced effects on performance. By contrast, knockouts and knockdowns for loss of function are often used to disrupt and observe network behavior within endogenous systems. Using similar precise manipulation within endogenous pathways may offer greater ability to decipher cellular behaviors (*65*).

Examination of natural systems through BioFENCE identified encoded networks similar to our engineered toggle switch that may

also exhibit bistability. Stemming from our analysis of yeast protein phosphorylation interactions, we identified five endogenous networks that demonstrated bistable behavior. We anticipate that BioFENCE can be applied across organisms to uncover other sophisticated regulatory programs, to interrogate networks that comprise other regulatory modalities, and to detect misregulation within complex disease states. Extending BioFENCE to model interactions beyond phosphorylation may enable queries of epigenetics or multicellular immune interactions (e.g., cytokine networks) and provide insight into how complex phenotypes are embedded within these other biological processes.

Protein interaction circuits may be advantageous compared with transcriptional and translational regulation in cases where quick responses are essential (real-time biosensors, etc.), nontranscriptional regulation is required [i.e., postmitotic cells, red blood cells (*66*)], or direct coupling to protein processes is necessary [e.g., cytoskeletal rearrangement (*8*, *18*, *67*)]. More recently, protein-protein proteolytic interactions have been produced for facile creation of regulatory devices, and these devices could readily interface with *phospho-in* and *phospho-out* regulatory devices (*20*, *22*, *24*). We envision that, analogous to transcriptional circuit development, in which design rules for interfacing with mixed modalities were and are continuously being developed (*4*, *68*–*70*), a similar renaissance in protein synthetic biology will follow.

Materials and Methods

Reagents

Nucleic acid manipulation

AccuPrime Pfx SuperMix from Life Technologies (Carlsbad, CA) and oligonucleotides manufactured by Integrated DNA Technologies (Coralville, IA) were used for all PCR amplification. BP Clonase II Enzyme Mix and LR Clonase II Plus Enzyme Mix from Life Technologies were used for all BP and LR reactions, respectively. Taq ligase, NAD^+, dNTPs, and Phusion Polymerase from New England Biolabs (Ipswich, MA) and T5 Exonuclease from Epicentre Biotechnologies (Madison, WI) were used for Gibson assembly reactions (*71*). All other restriction enzymes were obtained from New England Biolabs. All buffer components were obtained from Sigma-Aldrich (St. Louis, MO).

Bacteria

All plasmid construction used *E. coli* strain *E. cloni 10G* (Lucigen) made chemically competent by kit (Zymo Research, San Diego, CA) and were transformed by the suggested Z-comp heat-shock procedure. Bacterial cultures were grown in Luria-Bertani medium (Miller, BD Biosciences) and supplemented with kanamycin, ampicillin, or chloramphenicol (Sigma-Aldrich) as appropriate.

Yeast

All strains were prepared using standard transformation procedures (*72*) in a yeast strain with W303 background, YSC1058 (ThermoFisher Scientific, Waltham, MA). 5-Fluoro-orotic acid was obtained from Zymo Research, phleomycin from Invivogen, and G418 from Stratagene. All Synthetic Defined-URA (SD-URA) dropout media contained dextrose and was formulated by Sunrise Science (San Diego, CA). Single-stranded DNA was obtained from Life Technologies and all other chemical components from Sigma-Aldrich.

DNA circuit construction

The hierarchical assembly protocol outlined in Guye *et al.* was followed using yeast-specific components (*73*) as described below.

Plasmid DNA constructs for promoter ENTR vectors

All promoter ENTR vectors were verified by sequencing using standard M13F(-21) and M13R primers.• pENTR L4-pTEF-R1 was prepared by PCR amplification of pTEF from pYM-N183 (*74*) (EUROSCARF accession no. P30274), digesting the resulting fragment by XhoI, EcoRI and ligation using T4 DNA Ligase into a XhoI, EcoRI linearized pDONR-L4-R1 vector backbone.• pENTR L4-pTR-SSRE-R1 was prepared by PCR amplification of pTR-SSRE from p413-TR-SSRE-GFP (*43*) (GenBank DQ232596), digesting the resulting fragment by XhoI, EcoRI and ligation using T4 DNA Ligase into a XhoI, EcoRI linearized pDONR-L4-R1 vector backbone.• pENTR L4-pTET-R1 was prepared by PCR amplification of pTET from pCM185 (*75*) (EUROSCARF accession no. P30322), digesting the resulting fragment by XhoI, EcoRI and ligation using T4 DNA Ligase into a XhoI, EcoRI linearized pDONR-L4-R1 vector backbone.• pENTR L4-pGALS-R1 was prepared by PCR amplification of pTET from pCM185 (*75*) (EUROSCARF Accession No. P30322), digesting the resulting fragment by XhoI, EcoRI and ligation using T4 DNA Ligase into a XhoI, EcoRI linearized pDONR-L4-R1 vector backbone.• pENTR L4-pREV1-R1 was prepared by synthesis from the promoter sequence given in pAH005 (*76*) prepended and appended with flanking BsaI sites followed by a one-step digestion and ligation using T4 DNA Ligase and BsaI into a pGGDONR-L4-R1 vector backbone.• pENTR L4-pRNR2-R1 was prepared by synthesis from the promoter sequence given in pSL030 (*76*) prepended and appended with flanking BsaI sites followed by a one-step digestion and ligation using T4 DNA Ligase and BsaI into a pGGDONR-L4-R1 vector backbone.• pENTR L4-pRPR18B-R1 was prepared by synthesis from the promoter sequence given in pAH007 (*76*) prepended and appended with flanking BsaI sites followed by a one-step digestion and ligation using T4 DNA Ligase and BsaI into a pGGDONR-L4-R1 vector backbone.• pENTR L4-pHOT1-R1 was prepared by synthesis from the 750-bp genomic sequence immediately upstream of the HOT1 CDS in the yeast genome prepended and appended with flanking BsaI sites followed by a one-step digestion and ligation using T4 DNA Ligase and BsaI into a pGGDONR-L4-R1 vector backbone.• pENTR L4-pHOG1-R1 was prepared by synthesis from the 750-bp genomic sequence immediately upstream of the HOG1 CDS in the yeast genome prepended and appended with flanking BsaI sites followed by a one-step digestion and ligation using T4 DNA Ligase and BsaI into a pGGDONR-L4-R1 vector backbone.

Plasmid DNA constructs for gene ENTR vectors

• pENTR L1-rtTA-L2 was prepared by PCR amplification of rtTA from pCM252 (*75*) (EUROSCARF accession no. P30340) to produce flanking attB sites and a subsequent BP reaction using pDONR221 (Life Technologies); sequenced using standard M13F(-21) and M13R.• pENTR L1-JAK2-L2 was prepared by PCR amplification of JAK2 from mouse genomic DNA to produce flanking attB sites and a subsequent BP reaction using pDONR221; sequenced using standard M13F(-21) and M13R.• pENTR L1-JH1-L2 was prepared by PCR amplification of JH1 from pENTR L1-JAK2-L2 to produce flanking attB sites and a subsequent BP reaction using pDONR221; sequenced using standard M13F(-21) and M13R.• pENTR L1-eGFP-L2 was prepared by PCR amplification of eGFP from p413-SSRE-GFP (*43*) (GenBank DQ232595) to produce flanking attB sites and a subsequent BP reaction using pDONR221; sequenced using standard M13F (-21) and M13R.• pENTR L1-STAT5-HKRR-L2 was prepared by PCR amplification of previously constructed STAT5-HKRR (gift from Ming-Tan Chen) to produce flanking attB sites and a subsequent BP reaction using pDONR221; sequenced using standard M13F (-21) and M13R.• pENTR L1-kanMX-L2 was prepared by PCR amplification of kanMX from pYM-N183 (*74*) (EUROSCARF accession no. P30274) to produce flanking attB sites and a subsequent BP reaction using pDONR221; sequenced using standard M13F(-21) and M13R.• pENTR L1-blank-L2 was prepared from a BP reaction between TS019 and pDONR221; sequenced using standard M13F (-21) and M13R.• pENTR L1-YPD1-L2 was obtained from the Dana-Farber/Harvard Cancer Center Plasmid Repository (HIP Clone ID 201048); sequenced using M13(-21)F and M13R.• pENTR L1-JH1-HOT1 Library-L2 were prepared from a BP reaction between synthesized

dsDNA gBlocks (IDT) and pDONR221; sequenced using standard M13F(-21) and M13R.• pENTR L1-STAT5-HKRR Library-L2 were prepared from a BP reaction between synthesized dsDNA gBlocks (IDT) and pDONR221; sequenced using standard M13F(-21) and M13R.• pENTR L1-SSK1-L2 was obtained from the Dana-Farber/Harvard Cancer Center Plasmid Repository (HIP Clone ID 013092); sequenced using M13(-21)F and M13R.• pENTR L1-SSK2-L2 was obtained from the Dana-Farber/Harvard Cancer Center Plasmid Repository (HIP Clone ID 025160); sequenced using M13(-21)F and M13R.• pENTR L1-AtCRE1-HKRR-L2 was prepared from a BP reaction between synthesized dsDNA gBlocks (IDT) and pDONR221; sequenced using standard M13F(-21) and M13R.• pENTR L1-PTP-HOG1 Library-L2 were prepared from a BP reaction between synthesized dsDNA gBlocks (IDT) and pDONR221; sequenced using standard M13F(-21) and M13R.

DNA constructs for the OR, NOT, and toggle network

Destination vectors with flanking position sequences [attR4 – Gateway cassette – attR2 – yeast terminator] were used for all LR reactions. Table S4 summarizes LR reactions performed using a low-volume–modified Gateway reaction protocol (*77*). All plasmids were sequence verified. Single transcriptional units were combined using Gibson assembly into a PacI linearized carrier vector containing a [HO-L homology region – Seq1 – PacI – SeqX – HO-R homology region] cassette. The final circular plasmids were verified by sequencing. The toggle network is named pTS-Final and the BEM2 variant pTS-BEM2.

Yeast strains

We integrated all exogenous transcriptional units as a single copy with kanMX selection into the growth-neutral HO locus (*78*). All transformations used the standard LiAc protocol (*72*). A summary of all yeast strains is provided in table S5.

Yeast strains with gene deletions

All knock-out strains were prepared by Cre-lox genetic disruption as previously described (*79*).

YTS001 (W303A in ΔHOG1ΔHOT1ΔFUS3 ΔKSS1ΔSLN1::AtCRE1 ΔHTB1::HTB1-Azurite background)

1. Intermediate W303 in ΔHOG1 background: loxP flanked K. lactis URA3 was amplified by PCR from pUG72 (*79*) (EUROSCARF accession no. P30117) and then transformed into W303 yeast before selection. Clones were verified for successful integration by colony PCR before after standard transformation of the Cre containing plasmid, pSH65 (*79*) (EUROSCARF accession no. P30122), followed by selection/counterselection protocols and colony PCR verification.

2. Intermediate W303 in ΔHOG1ΔHOT1 background: loxP flanked K. lactis URA3 was amplified by PCR from pUG72 and then that product was amplified further by TSk005, TSk006. This PCR fragment was transformed into the W303 strain with ΔHOG1 background described above. Subsequent steps proceeded as described in HOG1 deletion.

3. Intermediate W303 in ΔHOG1ΔHOT1ΔFUS3 background: loxP flanked K. lactis URA3 was amplified by PCR from pUG72 and this PCR fragment was transformed into the W303 strain with ΔHOG1ΔHOT1 background described above. Subsequent steps proceeded as described in HOG1 deletion.

4. Intermediate W303 in ΔHOG1ΔHOT1 ΔFUS3ΔKSS1 background: loxP flanked K. lactis URA3 was amplified by PCR from pUG72 and then that PCR fragment was transformed into the W303 strain with ΔHOG1ΔHOT1ΔFUS3 background described above. Subsequent steps proceeded as described in HOG1 deletion.

5. Intermediate W303 in ΔHOG1ΔHOT1 ΔFUS3ΔKSS1ΔSLN1::AtCRE1 background: As described in (21), an AtCRE1 insertion cassette for the SLN1 locus was PCR amplified and transformed into the W303 strain with ΔHOG1 ΔHOT1ΔFUS3ΔKSS1 background described above. Subsequent steps proceeded as described in HOG1 deletion.

6. Intermediate W303 in ΔHOG1ΔHOT1 ΔFUS3ΔKSS1ΔSLN1::AtCRE1 ΔHTB1::HTB1-Azurite background: HTB1-Azurite was amplified by PCR and then that PCR fragment was transformed into the W303 strain described above. Strains were screened by flow cytometry to identify blue fluorescent signatures.

YTS002 (W303A in ΔHOG1ΔHOT1ΔFUS3 ΔKSS1ΔSLN1::AtCRE1 ΔHTB1::HTB1-Azurite ΔSSK2ΔSSK22ΔSSK1 background)

1. Intermediate W303A in ΔHOG1ΔHOT1 ΔFUS3ΔKSS1ΔSLN1::AtCRE1 ΔHTB1::HTB1-Azurite ΔSSK2 back- ground loxP flanked K. lactis URA3 was amplified by PCR from pUG72 and this PCR fragment was transformed into the YTS001 strain described above. Subsequent steps proceeded as described in HOG1 deletion.

2. Intermediate W303A in ΔHOG1ΔHOT1 ΔFUS3ΔKSS1ΔSLN1::AtCRE1 ΔHTB1::HTB1-Azurite ΔSSK2ΔSSK22 background loxP flanked K. lactis URA3 was amplified by PCR from pUG72 and this PCR fragment was transformed into the YTS001 strain described above. Subsequent steps proceeded as described in HOG1 deletion.

3. Intermediate W303A in ΔHOG1ΔHOT1 ΔFUS3ΔKSS1ΔSLN1::AtCRE1 ΔHTB1::HTB1-Azurite ΔSSK2ΔSSK22ΔSSK1 background loxP flanked K. lactis URA3 was amplified by PCR from pUG72 and this PCR fragment was transformed into the YTS001 strain described above. Subsequent steps proceeded as described in HOG1 deletion.

YTS003 (W303A in ΔHOG1ΔHOT1ΔFUS3 ΔKSS1ΔSLN1::AtCRE1 ΔHTB1::HTB1-Azurite ΔBEM2 background)

loxP flanked K. lactis URA3 was amplified by PCR from pUG72 and this PCR fragment was transformed into the W303A strain with ΔHOG1ΔHOT1ΔFUS3ΔKSS1ΔSLN1::AtCRE1 ΔHTB1::HTB1-Azurite background described above. Subsequent steps proceeded as described in HOG1 deletion.

Yeast strains with integrated circuits

All circuit strains were prepared in the following manner. First, the individual circuits (listed above) were linearized with I-SceI and purified by the Qiagen PCR Cleanup Kit before subsequent LiAc transformation into strain YTS001 (with the exception of Endogenous OR and NOT testing circuits and the BEM2 circuit, which used YTS002 and YTS003, respectively), and selection on YPAD solid media supplemented with G418. Clones were verified for successful integration into the HO locus by colony PCR.

Methods

Yeast strains harboring toggle circuits were grown in SD complete liquid media supplemented with G418 for 16 hours and combined with equal parts glycerol to form cell stocks. For all experiments, these cell stocks were used to inoculate 4-ml liquid cultures and grown under full selection for 12 hours at 30°C on a rotary shaker at 280 rpm. These "starter cultures" were diluted to OD_{660} = 0.10 and grown under selection for 4 additional hours at 30°C with 280 rpm rotary shaking before being collected by centrifugation and resuspended in fresh selection media. OD_{660} was obtained using a NanoDrop 2000c (NanoDrop, Wilmington, DE) and calibrated to cell density counts through a hemocytometer calibration curve. All experiments were performed with resuspensions at OD_{660} = 0.10. For those using the microfluidic chamber, immobilization was performed as previously described (*55*).

Flow cytometry

GFP intensities were analyzed by flow cytometry using a BD-FACS LSRFortessa cell analyzer (BD Biosciences) equipped with 488-nm laser – 505 LP – 530/15 EM with PMT of 360V, a 405-nm laser – 460 LP – 450/50 EM with PMT of 425V, and 561-nm laser – 586/15 EM with PMT of 350V. Measurements were calibrated using Rainbow Calibration Particles (Spherotech RCP-30-5A) to normalize data between different experimental runs. For each sample, 30,000 events were collected, and their median fluorescence is reported. Mean measurements for samples were calculated using the Cytoflow tool, available at https://github.com/bpteague/cytoflow.

Microscopy

Nuclear localization studies were analyzed by microscopy using yeast strains immobilized on a #1 coverslip bonded to a microfluidic device for extracellular environmental control and imaged using a Zeiss Axiovert 200M epifluorescent microscope (Zeiss) equipped with a 1344 × 1024 pixel Axiocam MR CCD camera (Zeiss) and a Zeiss 63× oil-immersion objective. False coloring was performed by capturing images with the appropriate filter sets (Zeiss Filter 38 GFP: EX BP 470/40, BS FT 495, EM BP 525/50, Zeiss Filter 34 BFP EX BP 390/22, BS FT 420, EM BP 460/50). Measurements used same exposure settings and pixel intensities and were normalized between experiments to a fluorescent slide standard. For each sample, entire fields of view were collected.

Segmentation was performed as follows:

1. Bright-field images were used to establish cell boundaries. To minimize computational complexity, only individual cells were considered (omitting clusters from the start). If a cell boundary disappeared within the course of the experiment (i.e., a cell was washed away by channel flow), then that cell was omitted from analysis. Except during the longer cell division experiments, any cell that divided during experiments was also removed from the analysis to minimize segmentation artifacts.

2. For each cell that met criterion 1 based on bright-field imaging, we used thresholding of the blue channel (Htb1-Azurite) to establish the nuclear boundary, which was then used for Hog1-GFP quantification.

3. For Hog1-GFP quantification:

a. If time series data used >15-s spacing, then blue channel, green channel, and bright-field images were captured for each time point and GFP/azurite–thresholded colocalization pixels were computed.

b. If time series data used <15-s spacing, then a green channel image was captured at the specified frequency, whereas bright-field and blue channel data were taken initially and at the end of capture. If either the bright-field or blue channel overlay segmented centroid moved by >15% of characteristic length between initial and end images, the cell was removed from analysis because colocalization could not be inferred. Because of the delay in switching reflectors on the motorized turret between GFP and azurite filters, simultaneous green, blue, and bright-field capture for time series with <15-s frequency was not possible.

c. All Hog1-GFP experiments were performed to balance CCD camera exposure time and the lowest power excitation setting to minimize photobleaching. Maximum exposure times were for the single-cell traces with 47 captures in 1-s intervals.

Thus, for all experiments, the same set of cells were used for an entire trace, and those cells that were computationally hard to segment, washed out, or moved substantially during an experiment were not considered. Comparison with other segmentation methods is provided in supplementary note 1.10.

REFERENCES AND NOTES

1. B. C. Stanton *et al*., Genomic mining of prokaryotic repressors for orthogonal logic gates. *Nat. Chem. Biol.* **10**, 99–105 (2014). doi: 10.1038/nchembio.1411; pmid: 24316737
2. S. Hooshangi, R. Weiss, The effect of negative feedback on noise propagation in transcriptional gene networks. *Chaos* **16**, 026108 (2006). doi: 10.1063/1.2208927; pmid: 16822040
3. M. B. Elowitz, S. Leibler, A synthetic oscillatory network of transcriptional regulators. *Nature* **403**, 335–338 (2000). doi: 10.1038/35002125; pmid: 10659856
4. T. S. Moon, C. Lou, A. Tamsir, B. C. Stanton, C. A. Voigt, Genetic programs constructed from layered logic gates in single cells. *Nature* **491**, 249–253 (2012). doi: 10.1038/nature11516; pmid: 23041931
5. L. B. Andrews, A. A. K. Nielsen, C. A. Voigt, Cellular checkpoint control using programmable sequential logic. *Science* **361**, eaap8987 (2018). doi: 10.1126/science.aap8987; pmid: 30237327
6. T. S. Gardner, C. R. Cantor, J. J. Collins, Construction of a genetic toggle switch in Escherichia coli. *Nature* **403**, 339–342 (2000). doi: 10.1038/35002131; pmid: 10659857
7. J. J. Lohmueller, T. Z. Armel, P. A. Silver, A tunable zinc finger-based framework for Boolean logic computation in mammalian cells. *Nucleic Acids Res.* **40**, 5180–5187 (2012). doi: 10.1093/nar/gks142; pmid: 22323524
8. M. C. Good, J. G. Zalatan, W. A. Lim, Scaffold proteins: Hubs for controlling the flow of cellular information. *Science* **332**, 680–686 (2011). doi: 10.1126/science.1198701; pmid: 21551057
9. S. Palani, C. A. Sarkar, Synthetic conversion of a graded receptor signal into a tunable, reversible switch. *Mol. Syst. Biol.* **7**, 480 (2011). doi: 10.1038/msb.2011.13; pmid: 21451590
10. J. E. Ferrell Jr.., S. H. Ha, Ultrasensitivity part III: Cascades, bistable switches, and oscillators. *Trends Biochem. Sci.* **39**, 612–618 (2014). doi: 10.1016/j.tibs.2014.10.002; pmid: 25456048
11. D. S. Aaronson, C. M. Horvath, A road map for those who don't know JAK-STAT. *Science* **296**, 1653–1655 (2002). doi: 10.1126/science.1071545; pmid: 12040185
12. B. N. Kholodenko, J. F. Hancock, W. Kolch, Signalling ballet in space and time. *Nat. Rev. Mol. Cell Biol.* **11**, 414–426 (2010). doi: 10.1038/nrm2901; pmid: 20495582
13. V. P. Zhdanov, A neuron model including gene expression: Bistability, long-term memory, etc. *Neural Process. Lett.* **39**, 285–296 (2014). doi: 10.1007/s11063-013-9304-y
14. S. Kadelka, B. P. Boribong, L. Li, S. M. Ciupe, Modeling the bistable dynamics of the innate immune system. *Bull. Math. Biol.* **81**, 256–276 (2019). doi: 10.1007/s11538-018-0527-y; pmid: 30387078
15. J. J. Tyson, R. Albert, A. Goldbeter, P. Ruoff, J. Sible, Biological switches and clocks. *J. R. Soc. Interface* **5** (Suppl 1), S1–S8 (2008). doi: 10.1098/rsif.2008.0179.focus; pmid: 18522926
16. S. Mochida, S. Rata, H. Hino, T. Nagai, B. Novák, Two bistable switches govern M phase entry. *Curr. Biol.* **26**, 3361–3367 (2016). doi: 10.1016/j.cub.2016.10.022; pmid: 27889260
17. D. Del Vecchio, A. J. Dy, Y. Qian, Control theory meets synthetic biology. *J. R. Soc. Interface* **13**, 20160380 (2016). doi: 10.1098/rsif.2016.0380; pmid: 27440256
18. R. Grünberg, L. Serrano, Strategies for protein synthetic biology. *Nucleic Acids Res.* **38**, 2663–2675 (2010). doi: 10.1093/nar/gkq139; pmid: 20385577
19. T. Cermak *et al*., Efficient design and assembly of custom TALEN and other TAL effector-based constructs for DNA targeting. *Nucleic Acids Res.* **39**, e82 (2011). doi: 10.1093/nar/gkr218; pmid: 21493687
20. X. J. Gao, L. S. Chong, M. S. Kim, M. B. Elowitz, Programmable protein circuits in living cells. *Science* **361**, 1252–1258 (2018). doi: 10.1126/science.aat5062; pmid: 30237357
21. J. E. Dueber, B. J. Yeh, K. Chak, W. A. Lim, Reprogramming control of an allosteric signaling switch through modular recombination. *Science* **301**, 1904–1908 (2003). doi: 10.1126/science.1085945; pmid: 14512628
22. T. Fink *et al*., Design of fast proteolysis-based signaling and logic circuits in mammalian cells. *Nat. Chem. Biol.* **15**, 115–122 (2019). doi: 10.1038/s41589-018-0181-6; pmid: 30531965
23. K. E. Thompson, C. J. Bashor, W. A. Lim, A. E. Keating, SYNZIP protein interaction toolbox: In vitro and in vivo specifications of heterospecific coiled-coil interaction domains. *ACS Synth. Biol.* **1**, 118–129 (2012). doi: 10.1021/sb200015u; pmid: 22558529
24. F. Cella, L. Wroblewska, R. Weiss, V. Siciliano, Engineering protein-protein devices for multilayered regulation of mRNA translation using orthogonal proteases in mammalian cells. *Nat. Commun.* **9**, 4392 (2018). doi: 10.1038/s41467-018-06825-7; pmid: 30349044
25. S. G. Peisajovich, J. E. Garbarino, P. Wei, W. A. Lim, Rapid diversification of cell signaling phenotypes by modular domain recombination. *Science* **328**, 368–372 (2010). doi: 10.1126/science.1182376; pmid: 20395511
26. W. R. Whitaker, S. A. Davis, A. P. Arkin, J. E. Dueber, Engineering robust control of two-component system phosphotransfer using modular scaffolds. *Proc. Natl. Acad. Sci. U.S.A.* **109**, 18090–18095 (2012). doi: 10.1073/pnas.1209230109; pmid: 23071327
27. B. Groves, A. Khakhar, C. M. Nadel, R. G. Gardner, G. Seelig, Rewiring MAP kinases in Saccharomyces cerevisiae to regulate novel targets through ubiquitination. *eLife* **5**, e15200 (2016). doi: 10.7554/eLife.15200; pmid: 27525484
28. A. J. Smith, F. Thomas, D. Shoemark, D. N. Woolfson, N. J. Savery, Guiding biomolecular interactions in cells using de novo protein-protein interfaces. *ACS Synth. Biol.* **8**, 1284–1293 (2019). doi: 10.1021/acssynbio.8b00501; pmid: 31059644
29. S.-H. Park, A. Zarrinpar, W. A. Lim, Rewiring MAP kinase pathways using alternative scaffold assembly mechanisms. *Science* **299**, 1061–1064 (2003). doi: 10.1126/science.1076979; pmid: 12511654
30. C. J. Bashor, N. C. Helman, S. Yan, W. A. Lim, Using engineered scaffold interactions to reshape MAP kinase pathway signaling dynamics. *Science* **319**, 1539–1543 (2008). doi: 10.1126/science.1151153; pmid: 18339942
31. Z. Chen *et al*., De novo design of protein logic gates. *Science* **368**, 78–84 (2020). doi: 10.1126/science.aay2790; pmid: 32241946
32. T. Lebar *et al*., A bistable genetic switch based on designable DNA-binding domains. *Nat. Commun.* **5**, 5007 (2014). doi: 10.1038/ncomms6007; pmid: 25264186
33. B. P. Kramer *et al*., An engineered epigenetic transgene switch in mammalian cells. *Nat. Biotechnol.* **22**, 867–870 (2004). doi: 10.1038/nbt980; pmid: 15184906
34. U. Alon, Network motifs: Theory and experimental approaches. *Nat. Rev. Genet.* **8**, 450–461 (2007). doi: 10.1038/nrg2102; pmid: 17510665
35. S. A. Kauffman, Metabolic stability and epigenesis in randomly constructed genetic nets. *J. Theor. Biol.* **22**, 437–467 (1969). doi: 10.1016/0022-5193(69)90015-0; pmid: 5803332
36. J. D. Schwab, S. D. Kühlwein, N. Ikonomi, M. Kühl, H. A. Kestler, Concepts in Boolean network modeling: What do they all mean? *Comput. Struct. Biotechnol. J.* **18**, 571–582 (2020). doi: 10.1016/j.csbj.2020.03.001; pmid: 32257043
37. J. T. Mettetal, D. Muzzey, C. Gómez-Uribe, A. van Oudenaarden, The frequency dependence of osmo-adaptation in *Saccharomyces cerevisiae*. *Science* **319**, 482–484 (2008). doi: 10.1126/science.1151582; pmid: 18218902
38. D. Muzzey, C. A. Gómez-Uribe, J. T. Mettetal, A. van Oudenaarden, A systems-level analysis of perfect adaptation in yeast osmoregulation. *Cell* **138**, 160–171 (2009). doi: 10.1016/j.cell.2009.04.047; pmid: 19596242
39. H. Saito, F. Posas, Response to hyperosmotic stress. *Genetics* **192**, 289–318 (2012). doi: 10.1534/genetics.112.140863; pmid: 23028184
40. J. L. Brewster, M. C. Gustin, Hog1: 20 years of discovery and impact. *Sci. Signal.* **7**, re7 (2014). doi: 10.1126/scisignal.2005458; pmid: 25227612
41. I. M. Ota, A. Varshavsky, A yeast protein similar to bacterial two-component regulators. *Science* **262**, 566–569 (1993). doi: 10.1126/science.8211183; pmid: 8211183
42. R. Katz, G. Borriello, *Contemporary Logic Design* (Pearson, ed. 2, 2004).
43. M.-T. Chen, R. Weiss, Artificial cell-cell communication in yeast *Saccharomyces cerevisiae* using signaling elements from *Arabidopsis thaliana*. *Nat. Biotechnol.* **23**, 1551–1555 (2005). doi: 10.1038/nbt1162; pmid: 16299520
44. V. Reiser, D. C. Raitt, H. Saito, Yeast osmosensor Sln1 and plant cytokinin receptor Cre1 respond to changes in turgor pressure. *J. Cell Biol.* **161**, 1035–1040 (2003). doi: 10.1083/jcb.200301099; pmid: 12821642
45. F. Janiak-Spens, P. F. Cook, A. H. West, Kinetic analysis of YPD1-dependent phosphotransfer reactions in the yeast

osmoregulatory phosphorelay system. *Biochemistry* **44**, 377–386 (2005). doi: 10.1021/bi048433s; pmid: 15628880
46. J. P. Dexter, P. Xu, J. Gunawardena, M. N. McClean, Robust network structure of the Sln1-Ypd1-Ssk1 three-component phospho-relay prevents unintended activation of the HOG MAPK pathway in Saccharomyces cerevisiae. *BMC Syst. Biol.* **9**, 17 (2015). doi: 10.1186/s12918-015-0158-y; pmid: 25888817
47. D. B. Ostrander, J. A. Gorman, The extracellular domain of the Saccharomyces cerevisiae Sln1p membrane osmolarity sensor is necessary for kinase activity. *J. Bacteriol.* **181**, 2527–2534 (1999). doi: 10.1128/JB.181.8.2527-2534.1999; pmid: 10198019
48. A. W. Poole, M. L. Jones, A SHPing tale: Perspectives on the regulation of SHP-1 and SHP-2 tyrosine phosphatases by the C-terminal tail. *Cell. Signal.* **17**, 1323–1332 (2005). doi: 10.1016/j.cellsig.2005.05.016; pmid: 16084691
49. F. Barahmand-Pour, A. Meinke, B. Groner, T. Decker, Jak2-Stat5 interactions analyzed in yeast. *J. Biol. Chem.* **273**, 12567–12575 (1998). doi: 10.1074/jbc.273.20.12567; pmid: 9575217
50. J. R. Houser *et al*., An improved short-lived fluorescent protein transcriptional reporter for Saccharomyces cerevisiae. *Yeast* **29**, 519–530 (2012). doi: 10.1002/yea.2932; pmid: 23172645
51. T. Horie, K. Tatebayashi, R. Yamada, H. Saito, Phosphorylated Ssk1 prevents unphosphorylated Ssk1 from activating the Ssk2 mitogen-activated protein kinase kinase kinase in the yeast high-osmolarity glycerol osmoregulatory pathway. *Mol. Cell. Biol.* **28**, 5172–5183 (2008). doi: 10.1128/MCB.00589-08; pmid: 18573873
52. F. Posas, H. Saito, Activation of the yeast SSK2 MAP kinase kinase kinase by the SSK1 two-component response regulator. *EMBO J.* **17**, 1385–1394 (1998). doi: 10.1093/emboj/17.5.1385; pmid: 9482735
53. M.-A. Félix, M. Barkoulas, Pervasive robustness in biological systems. *Nat. Rev. Genet.* **16**, 483–496 (2015). doi: 10.1038/nrg3949; pmid: 26184598
54. S. Srinivasan *et al*., A BMP-FGF morphogen toggle switch drives the ultrasensitive expression of multiple genes in the developing forebrain. *PLOS Comput. Biol.* **10**, e1003463 (2014). doi: 10.1371/journal.pcbi.1003463; pmid: 24550718
55. P. Hersen, M. N. McClean, L. Mahadevan, S. Ramanathan, Signal processing by the HOG MAP kinase pathway. *Proc. Natl. Acad. Sci. U.S.A.* **105**, 7165–7170 (2008). doi: 10.1073/pnas.0710770105; pmid: 18480263
56. D. Del Vecchio, R. Murray, *Biomolecular Feedback Systems* (Princeton Univ. Press, ed. 1, 2014).
57. M. Kanehisa, S. Goto, KEGG: Kyoto encyclopedia of genes and genomes. *Nucleic Acids Res.* **28**, 27–30 (2000). doi: 10.1093/nar/28.1.27; pmid: 10592173
58. M. Kanehisa, Y. Sato, M. Kawashima, M. Furumichi, M. Tanabe, KEGG as a reference resource for gene and protein annotation. *Nucleic Acids Res.* **44** (D1), D457–D462 (2016). doi: 10.1093/nar/gkv1070; pmid: 26476454
59. I. A. Drinnenberg *et al*., RNAi in budding yeast. *Science* **326**, 544–550 (2009). doi: 10.1126/science.1176945; pmid: 19745116
60. S. J. Dowell, A. J. Brown, "Yeast assays for G protein-coupled receptors," in *G Protein-Coupled Receptors in Drug Discovery*, W. R. Leifert, Ed. (Humana, 2009), pp. 213–229.
61. N. M. Daringer, R. M. Dudek, K. A. Schwarz, J. N. Leonard, Modular extracellular sensor architecture for engineering mammalian cell-based devices. *ACS Synth. Biol.* **3**, 892–902 (2014). doi: 10.1021/sb400128g; pmid: 24611683
62. A. Mazé, Y. Benenson, Artificial signaling in mammalian cells enabled by prokaryotic two-component system. *Nat. Chem. Biol.* **16**, 179–187 (2020). doi: 10.1038/s41589-019-0429-9; pmid: 31844302
63. M. Mimee *et al*., An ingestible bacterial-electronic system to monitor gastrointestinal health. *Science* **360**, 915–918 (2018). doi: 10.1126/science.aas9315; pmid: 29798884
64. Q. H. Sam, M. W. Chang, L. Y. A. Chai, The Fungal Mycobiome and Its Interaction with Gut Bacteria in the Host. *Int. J. Mol. Sci.* **18**, 330 (2017). doi: 10.3390/ijms18020330; pmid: 28165395
65. M. Elowitz, W. A. Lim, Build life to understand it. *Nature* **468**, 889–890 (2010). doi: 10.1038/468889a; pmid: 21164460
66. N. Pishesha *et al*., Engineered erythrocytes covalently linked to antigenic peptides can protect against autoimmune disease. *Proc. Natl. Acad. Sci. U.S.A.* **114**, 3157–3162 (2017). doi: 10.1073/pnas.1701746114; pmid: 28270614
67. W. A. Lim, C. M. Lee, C. Tang, Design principles of regulatory networks: Searching for the molecular algorithms of the cell. *Mol. Cell* **49**, 202–212 (2013). doi: 10.1016/j.molcel.2012.12.020; pmid: 23352241
68. D. Mishra, P. M. P. M. Rivera, A. Lin, D. Del Vecchio, R. Weiss, A load driver device for engineering modularity in biological networks. *Nat. Biotechnol.* **32**, 1268–1275 (2014). doi: 10.1038/nbt.3044; pmid: 25419739
69. C. Lou, B. Stanton, Y.-J. Chen, B. Munsky, C. A. Voigt, Ribozyme-based insulator parts buffer synthetic circuits from genetic context. *Nat. Biotechnol.* **30**, 1137–1142 (2012). doi: 10.1038/nbt.2401; pmid: 23034349
70. C. J. Bashor *et al*., Complex signal processing in synthetic gene circuits using cooperative regulatory assemblies. *Science* **364**, 593–597 (2019). doi: 10.1126/science.aau8287; pmid: 31000590
71. T. M. J. Fruchterman, E. M. Reingold, Graph drawing by force-directed placement. *Softw. Pract. Exper.* **21**, 1129–1164 (1991). doi: 10.1002/spe.4380211102
72. D. G. Gibson *et al*., Enzymatic assembly of DNA molecules up to several hundred kilobases. *Nat. Methods* **6**, 343–345 (2009). doi: 10.1038/nmeth.1318; pmid: 19363495
73. D. Gietz, A. St Jean, R. A. Woods, R. H. Schiestl, Improved method for high efficiency transformation of intact yeast cells. *Nucleic Acids Res.* **20**, 1425 (1992). doi: 10.1093/nar/20.6.1425; pmid: 1561104
74. P. Guye, Y. Li, L. Wroblewska, X. Duportet, R. Weiss, Rapid, modular and reliable construction of complex mammalian gene circuits. *Nucleic Acids Res.* **41**, e156 (2013). doi: 10.1093/nar/gkt605; pmid: 23847100
75. C. Janke *et al*., A versatile toolbox for PCR-based tagging of yeast genes: New fluorescent proteins, more markers and promoter substitution cassettes. *Yeast* **21**, 947–962 (2004). doi: 10.1002/yea.1142; pmid: 15334558
76. E. Garí, L. Piedrafita, M. Aldea, E. Herrero, A set of vectors with a tetracycline-regulatable promoter system for modulated gene expression in *Saccharomyces cerevisiae*. *Yeast* **13**, 837–848 (1997). doi: 10.1002/(SICI)1097-0061(199707)13:9<837::AID-YEA145>3.0.CO;2-T; pmid: 9234672
77. M. E. Lee, A. Aswani, A. S. Han, C. J. Tomlin, J. E. Dueber, Expression-level optimization of a multi-enzyme pathway in the absence of a high-throughput assay. *Nucleic Acids Res.* **41**, 10668–10678 (2013). doi: 10.1093/nar/gkt809; pmid: 24038353
78. S. Alberti, A. D. Gitler, S. Lindquist, A suite of Gateway cloning vectors for high-throughput genetic analysis in *Saccharomyces cerevisiae*. *Yeast* **24**, 913–919 (2007). doi: 10.1002/yea.1502; pmid: 17583893
79. W. P. Voth, J. D. Richards, J. M. Shaw, D. J. Stillman, Yeast vectors for integration at the HO locus. *Nucleic Acids Res.* **29**, E59-9 (2001). doi: 10.1093/nar/29.12.e59; pmid: 11410682
80. U. Gueldener, J. Heinisch, G. J. Koehler, D. Voss, J. H. Hegemann, A second set of loxP marker cassettes for Cre-mediated multiple gene knockouts in budding yeast. *Nucleic Acids Res.* **30**, e23 (2002). doi: 10.1093/nar/30.6.e23; pmid: 11884642

ACKNOWLEDGMENTS

We thank members of the Weiss laboratories for discussions, M.-T. Chen for plasmids containing STAT5-HKRR and JAK2, the Synthetic Biology Center at MIT's cytometry facility, and the Microsystems Technology Laboratories at MIT Research Laboratory of Electronics. **Funding:** D.M. was supported by a Siebel Scholars Award, Eni-MIT Energy Research Fellowship, and a Graduate Research Fellowship Program through grant DGE-1122374 from the National Science Foundation. This research was supported by the Institute for Collaborative Biotechnologies through grant W911NF-09-D-0001 from the U.S. Army Research Office, SynBERC through grant SA5284-11210 from the National Science Foundation, and the Center for Integrated Synthetic Biology through center grant P50 GM098792 from the National Institutes of Health. The content of the information does not necessarily reflect the position or the policy of the government, and no official endorsement should be inferred. **Author contributions:** D.M., J.B., and R.W. designed the project. D.M. and R.W. designed the experiments and analyzed the data. D.M. performed the experiments and developed BioFENCE. T.B. and B.B. constructed mathematical models and performed parameter estimation. D.M., B.T., and R.W. wrote the manuscript. **Competing interests:** The authors declare no competing interests. **Data and materials availability:** All data needed to evaluate the conclusions in this study are provided in the main text or the supplementary materials.

SUPPLEMENTARY MATERIALS

science.sciencemag.org/content/373/6550/eaav0780/suppl/DC1
Figs. S1 to S25
Tables S1 to S6
Supplementary Notes
References (*81*–*88*)
Code for BioFENCE
MDAR Reproducibility Checklist

17 August 2018; accepted 29 April 2021
10.1126/science.aav0780

RESEARCH ARTICLE SUMMARY

PLANT SCIENCE

Nurse cell–derived small RNAs define paternal epigenetic inheritance in *Arabidopsis*

Jincheng Long†, James Walker†, Wenjing She†, Billy Aldridge, Hongbo Gao, Samuel Deans, Martin Vickers, Xiaoqi Feng*

INTRODUCTION: Epigenetic modifications to chromatin, such as the methylation of DNA cytosines, carry regulatory information across the generations in plants and animals. Epigenetic marks are inherited through germlines, which can undergo epigenetic reprogramming that affects germline function. Mammalian germlines undergo genome-wide demethylation and remethylation, which resets epigenetic marks and restores cellular pluripotency. Germlines of flowering plants differentiate later than those of mammals and undergo distinct DNA methylation reprogramming. Global methylation level changes have been observed in plant germ cells, as well as local de novo methylation that regulates germline gene expression. However, the reprogramming mechanism remains unclear, which limits the understanding of tissue-specific and transgenerational epigenetic inheritance in plants.

RATIONALE: De novo methylation of genes in the *Arabidopsis* male germline is catalyzed by the small RNA-directed DNA methylation pathway (RdDM). RdDM uses 24-nucleotide (nt) small interfering RNAs (siRNAs) transcribed from a source locus, typically a transposon, to guide methyltransferases to methylate the cognate region. RdDM is ubiquitous among cells and normally methylates transposons. We investigated how RdDM targets genes in the germline, how such reprogramming is limited to the germline, and how the hundreds of target genes are selected.

RESULTS: We show that in *Arabidopsis*, germline-specific methylation at hundreds of genes is established by 24-nt siRNAs transcribed from hypermethylated transposons with imperfect sequence homology. CRISPR deletion of siRNA source transposons abolishes DNA methylation at corresponding genes in male meiocytes, demonstrating the ability of these siRNAs to target methylation in trans with mismatches. Furthermore, we found that meiocytes are quiescent in 24-nt siRNA biogenesis, and the gene targeting siRNAs are produced in tapetal nurse cells and transported into meiocytes. The siRNA profile of tapetal cells resembles that of meiocytes, suggesting bulk siRNA movement through the cytoplasmic channels (known as plasmodesmata) that connect these cells during early meiosis. Although gene-targeting siRNAs accumulate to levels in the tapetum comparable with those in meiocytes, the target genes are not methylated in the tapetum, showing that meiocytes can use imperfectly matching siRNAs to target DNA methylation.

We also show that the biogenesis of gene-targeting siRNAs in the tapetum is driven by a putative chromatin remodeler, CLASSY3 (CLSY3). CLSY3 is absent in vegetative tissues but enriched in female and male organs. In male organs, CLSY3 is specifically expressed in tapetal cells. The *clsy3* mutation eliminates de novo methylation at genes in male meiocytes as well as sperm, revealing the role of tapetal siRNAs in driving methylation reprogramming throughout the male germline. This conclusion was reinforced with experiments with a genetic mosaic system that restricted siRNA biogenesis to the tapetum. In the mosaic lines, tapetal siRNAs restore methylation in the male germline at genes specifically methylated in the germline and at transposons targeted by RdDM in all tissues. This shows that tapetal siRNAs shape the full spectrum of RNA-directed DNA methylation throughout the male germline, from meiocytes to sperm.

As tapetal siRNAs induce methylation at transposons in the male germline, we investigated whether these siRNAs serve to silence germline transposons in addition to their gene regulatory function. We found that tapetal siRNAs methylate and prevent the expression of a Gypsy retrotransposon (*GPI*) that is specifically active in reproductive cells, demonstrating that tapetal siRNAs ensure germline genome integrity by suppressing transposons.

CONCLUSION: Our work reveals the role of tapetum-derived 24-nt siRNAs in determining the paternal methylome. Tapetal siRNAs drive de novo methylation at genes in the germline and safeguard genome integrity by silencing transposons. The ability of meiocytes to use mismatched 24-nt siRNAs to induce methylation allows RdDM to target sequences similar to those of transposons that produce siRNAs in the tapetum. This should facilitate recognition and silencing of new transposons, indicating that meiosis is a key stage for genome surveillance and allows RdDM to specifically regulate germline gene expression. The broad targeting competence of tapetal siRNAs resembles that of metazoan gonad-expressed Piwi-interacting RNAs (piRNAs), suggesting convergent evolution of specialized small RNA pathways to control transposons and genes in plant and animal germlines. ■

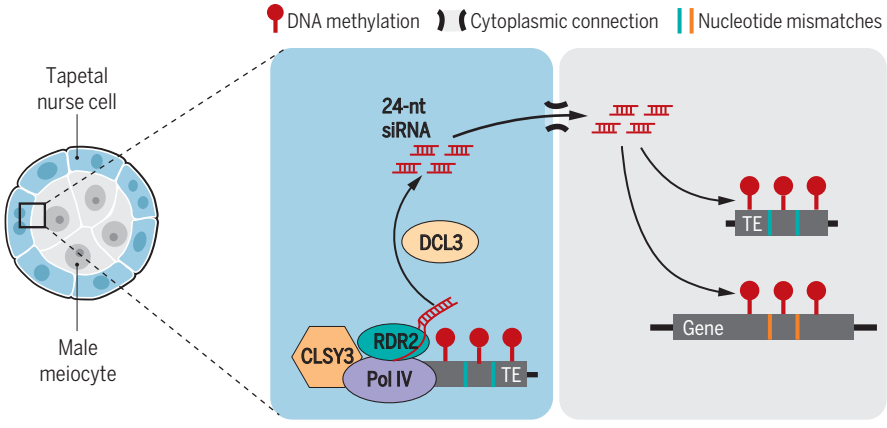

Tapetal siRNAs shape germline DNA methylation. RNA polymerase IV (Pol IV) transcripts are processed by RNA-dependent RNA polymerase 2 (RDR2) and Dicer-Like 3 (DCL3) into 24-nt siRNAs. Tapetal siRNAs are transcribed from transposons, enabled by CLSY3 expression. Tapetal siRNAs move to meiocytes and induce methylation at corresponding transposons and genes with similar sequences. This genic methylation is germline-specific, indicating that the siRNA-targeted de novo methylation pathway is hypersensitive in meiocytes. TE, transposable element.

Department of Cell and Developmental Biology, John Innes Centre, Norwich NR4 7UH, UK.
*Corresponding author. Email: xiaoqi.feng@jic.ac.uk
†These authors contributed equally to this work.
Cite this article as J. Long *et al.*, *Science* 373, eabh0556 (2021). DOI: 10.1126/science.abh0556

READ THE FULL ARTICLE AT
https://doi.org/10.1126/science.abh0556

CREDIT: ADAPTED BY N. CARY/*SCIENCE*

RESEARCH ARTICLE

PLANT SCIENCE

Nurse cell–derived small RNAs define paternal epigenetic inheritance in *Arabidopsis*

Jincheng Long†, James Walker†, Wenjing She†, Billy Aldridge, Hongbo Gao‡, Samuel Deans, Martin Vickers, Xiaoqi Feng*

The plant male germline undergoes DNA methylation reprogramming, which methylates genes de novo and thereby alters gene expression and regulates meiosis. Here, we reveal the molecular mechanism underlying this reprogramming. We demonstrate that genic methylation in the male germline, from meiocytes to sperm, is established by 24-nucleotide small interfering RNAs (siRNAs) transcribed from transposons with imperfect sequence homology. These siRNAs are synthesized by meiocyte nurse cells (tapetum) through activity of CLSY3, a chromatin remodeler absent in other anther cells. Tapetal siRNAs govern germline methylation throughout the genome, including the inherited methylation patterns in sperm. Tapetum-derived siRNAs also silence germline transposons, safeguarding genome integrity. Our results reveal that tapetal siRNAs are sufficient to reconstitute germline methylation patterns and drive functional methylation reprogramming throughout the male germline.

Methylation of the fifth carbon of cytosine carries essential regulatory functions in eukaryotic genomes, including transcriptional regulation of genes and transposable elements (TEs) (*1*–*3*). DNA methylation patterns are faithfully replicated during cell division, thus allowing methylation to have homeostatic functions during development (*1*, *2*). However, animal and plant germlines undergo DNA methylation reprogramming (*4*–*6*). In mammals, impaired reprogramming is associated with misregulation of genes and TEs and arrests male meiosis (*7*). In plants, DNA methylation reprogramming occurs during gametogenesis, when global methylation levels change (*8*–*11*) and thousands of loci are actively demethylated in gamete companion cells (*9*, *10*). DNA methylation reprogramming in the *Arabidopsis thaliana* male germline also involves de novo methylation at hundreds of genes, which regulates gene expression and meiosis (*6*). This germline-specific methylation is catalyzed by the small RNA-directed DNA methylation pathway (RdDM) (*6*), which generally methylates TEs (*12*). How RdDM targets genes specifically in the male germline and how particular genes are selected for methylation are unknown.

24-nucelotide siRNA pattern in meiocytes

In RdDM, 24-nucleotide (nt) small interfering RNAs (siRNAs), which are produced from transcripts synthesized by RNA polymerase IV (Pol IV; a plant-specific derivative of Pol II) and RNA-dependent RNA polymerase 2 (RDR2), guide methyltransferases DRM1 and -2 to target loci through association with a homologous transcript generated by Pol V (another plant-specific derivative of Pol II) (*12*). To understand how specific loci are methylated by RdDM exclusively in the male germline, we sequenced siRNAs from isolated *Arabidopsis* male meiocytes (prophase I, mostly pachytene stage) (Fig. 1A). In somatic tissues such as leaves, roots, and seedlings, 24-nt siRNAs associate with methylated RdDM loci (~10,000 loci, predominantly TEs) (Fig. 1, B and C, and fig. S1A) (*6*). In relation to somatic tissues, nearly all (98%) of these canonical RdDM loci have substantially fewer 24-nt siRNAs in meiocytes (Fig. 1, B and C, and fig. S1, A and B), and CHH methylation at these loci is reduced (Fig. 1, B and D). However, when normalized to 21-nt microRNAs, the levels of 24-nt siRNAs at canonical RdDM loci are similar in meiocytes and soma (fig. S1C). The vast relative difference in 24-nt siRNA abundance occurs because male meiocyte 24-nt siRNAs are concentrated [$\log_2$(RPKM+1) > 7] in 854 clusters, most of which (80%) do not overlap canonical RdDM loci. These clusters have higher levels of siRNAs and DNA methylation in meiocytes as compared with that in somatic tissues (Fig. 1, B to D, and fig. S1, A and D) and overlap the 724 loci we previously identified as hypermethylated in the male germline (fig. S1E) (*6*).

Consistent with RdDM targeting, the majority (93%, 797) of meiocyte siRNA clusters have significantly reduced CHH methylation in *drm1 drm2* double-mutant (simplified as *drm*) or *rdr2* mutant plants (Fig. 1, B and D, and table S1) and, like canonical RdDM loci (*13*), overlap mostly noncoding regions (fig. S1F). These 797 siRNA clusters span 588 kb (0.4% of the genome) but comprise 94% of the clustered 24-nt siRNAs, mostly (70%) overlapping TEs (TEs make up 18% of the genome) (fig. S1G and table S2). Altogether, our results demonstrate that male meiocytes have a distinctive RdDM-associated siRNA profile, with the majority of 24-nt siRNAs targeting a small number of hypermethylated loci (we will refer to these 797 loci as HyperTEs) (table S2).

TE-derived siRNAs methylate genes with mismatches

We found few 24-nt siRNAs in meiocytes associated with genes hypermethylated in the male germline (MetGenes) (Fig. 1, B and C, and fig. S1, A and G), even though MetGenes are targeted by RdDM (*6*). A comparison revealed that MetGenes and HyperTEs share similar sequences, leading us to hypothesize that MetGenes may be targeted by siRNAs produced from HyperTEs. Supporting this hypothesis, we found that 24-nt siRNAs generated from HyperTEs can be aligned to MetGenes if up to three mismatches are allowed (Fig. 1, B and E, and table S3). The association of siRNAs with MetGenes is not caused by random mapping of mismatched siRNAs because neither all genes nor random control loci associate with mismatched siRNAs (Fig. 1E). Furthermore, we found that for 89% of HyperTE-associated siRNAs that map to MetGenes, MetGenes are the best hits in the genome aside from the source HyperTEs. These analyses suggest that siRNAs produced from HyperTEs cause methylation at MetGenes with similar sequences.

To test the causal relationship between HyperTE-associated siRNAs and the methylation at MetGenes, we created two independent CRISPR/Cas9 lines with deletions of a HyperTE (HyperTE224, *AT2TE15980*) (Fig. 1F and fig. S2A). We observed abolishment of methylation at the predicted target MetGene (MetGene186, *AT3G04230*) (Fig. 1F and table S3) in meiocytes isolated from both deletion lines (Fig. 1G), whereas overall methylation did not change (fig. S2B). We applied this experimental strategy to another HyperTE (HyperTE315, *AT2TE72995*), siRNAs from which are predicted to target two MetGenes (MetGene24, *AT1G15520*, and MetGene86, *AT1G56410*) (fig. S2C and table S3). Consistently, we observed complete loss of methylation at both target MetGenes in meiocytes of the HyperTE315-deletion lines (Fig. 1H and fig. S2, B and D). These results demonstrate that methylation at MetGenes is induced in trans by siRNAs derived from HyperTEs.

Meiocytes and tapetum share siRNA profiles

In RdDM, Pol IV and Pol V preferentially associate with methylated DNA, making RdDM a self-reinforcing pathway, in which methylation promotes the generation of methylation-inducing

Department of Cell and Developmental Biology, John Innes Centre, Norwich NR4 7UH, UK.
***Corresponding author. Email: xiaoqi.feng@jic.ac.uk**
†These authors contributed equally to this work. ‡Present address: Joint Center for Single Cell Biology, School of Agriculture and Biology, Shanghai Jiao Tong University, Shanghai 200240, China.

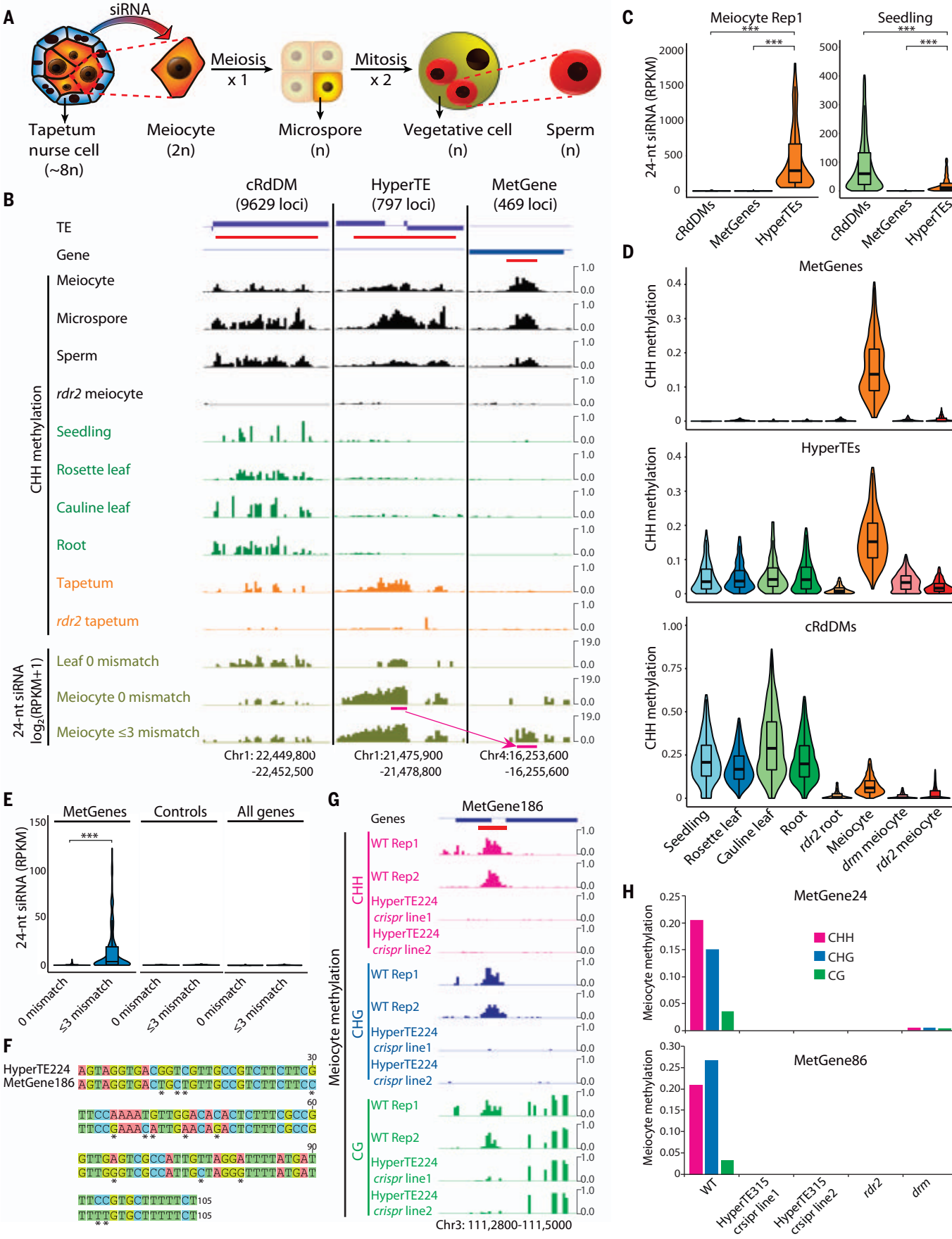
A
siRNA
Meiosis x 1
Mitosis x 2
Tapetum nurse cell (~8n)
Meiocyte (2n)
Microspore (n)
Vegetative cell (n)
Sperm (n)
B
cRdDM (9629 loci)
HyperTE (797 loci)
MetGene (469 loci)
TE
Gene
Meiocyte
Microspore
Sperm
rdr2 meiocyte
Seedling
Rosette leaf
Cauline leaf
Root
Tapetum
rdr2 tapetum
CHH methylation
Leaf 0 mismatch
Meiocyte 0 mismatch
Meiocyte ≤3 mismatch
24-nt siRNA log2(RPKM+1)
Chr1: 22,449,800 -22,452,500
Chr1:21,475,900 -21,478,800
Chr4:16,253,600 -16,255,600
C
Meiocyte Rep1
Seedling
24-nt siRNA (RPKM)
cRdDMs
MetGenes
HyperTEs
D
MetGenes
HyperTEs
cRdDMs
CHH methylation
Seedling
Rosette leaf
Cauline leaf
Root
rdr2 root
Meiocyte
drm meiocyte
rdr2 meiocyte
E
MetGenes
Controls
All genes
24-nt siRNA (RPKM)
0 mismatch
≤3 mismatch
F
HyperTE224 AGTAGGTGACGGTCGTTGCCGTCTTCTTCG
MetGene186 AGTAGGTGACTGCTGTTGCCGTCTTCTTCC
TTCCAAAATGTTGGACACACTCTTTCGCCG
TTCCGAAACATTGAACAGACTCTTTCGCCG
GTTGAGTCGCCATTGTTAGGATTTTATGAT
GTTGGGTCGCCATTGCTAGGGTTTTATGAT
TTCCGTGCTTTTTCT
TTTTGTGCTTTTTCT
G
MetGene186
Genes
Meiocyte methylation
CHH
CHG
CG
WT Rep1
WT Rep2
HyperTE224 crispr line1
HyperTE224 crispr line2
Chr3: 111,2800-111,5000
H
MetGene24
MetGene86
Meiocyte methylation
CHH
CHG
CG
WT
HyperTE315 crsipr line1
HyperTE315 crsipr line2
rdr2
drm

Fig. 1. HyperTE-derived siRNAs drive MetGene methylation in male meiocytes. (**A**) A schematic of male germline development in *Arabidopsis*. (**B**) CHH methylation and 24-nt siRNA abundance (mapped with 0 or ≤3 mismatches) at a canonical RdDM locus (cRdDM), a HyperTE, and a MetGene across tissues and cells as indicated. Each locus is underlined in red. siRNAs that target the MetGene with mismatches originate from the HyperTE, with both source and sink regions underlined in magenta. (**C** and **D**) Levels of (C) 24-nt siRNAs and (D) CHH methylation at cRdDMs, HyperTEs, and MetGenes in male meiocytes and indicated somatic tissues. (**E**) Abundance of meiocyte 24-nt siRNAs mapped with 0 or ≤3 mismatches to MetGenes, a control set of random loci of similar sizes, and all genes. (**F**) DNA sequence alignment between HyperTE224 and MetGene186, with mismatches indicated with asterisks. (**G**) DNA methylation at MetGene186 (underlined in red) in meiocytes from wild-type (WT) and two independent HyperTE224 deletion lines. (**H**) DNA methylation levels at MetGene24 and -86 in meiocytes from indicated genotypes. ***$P < 2.2 \times 10^{-16}$, Kolmogorov-Smirnov test. In (C) and (E), Rep, biological replicate; RPKM, reads per kilobase per million.

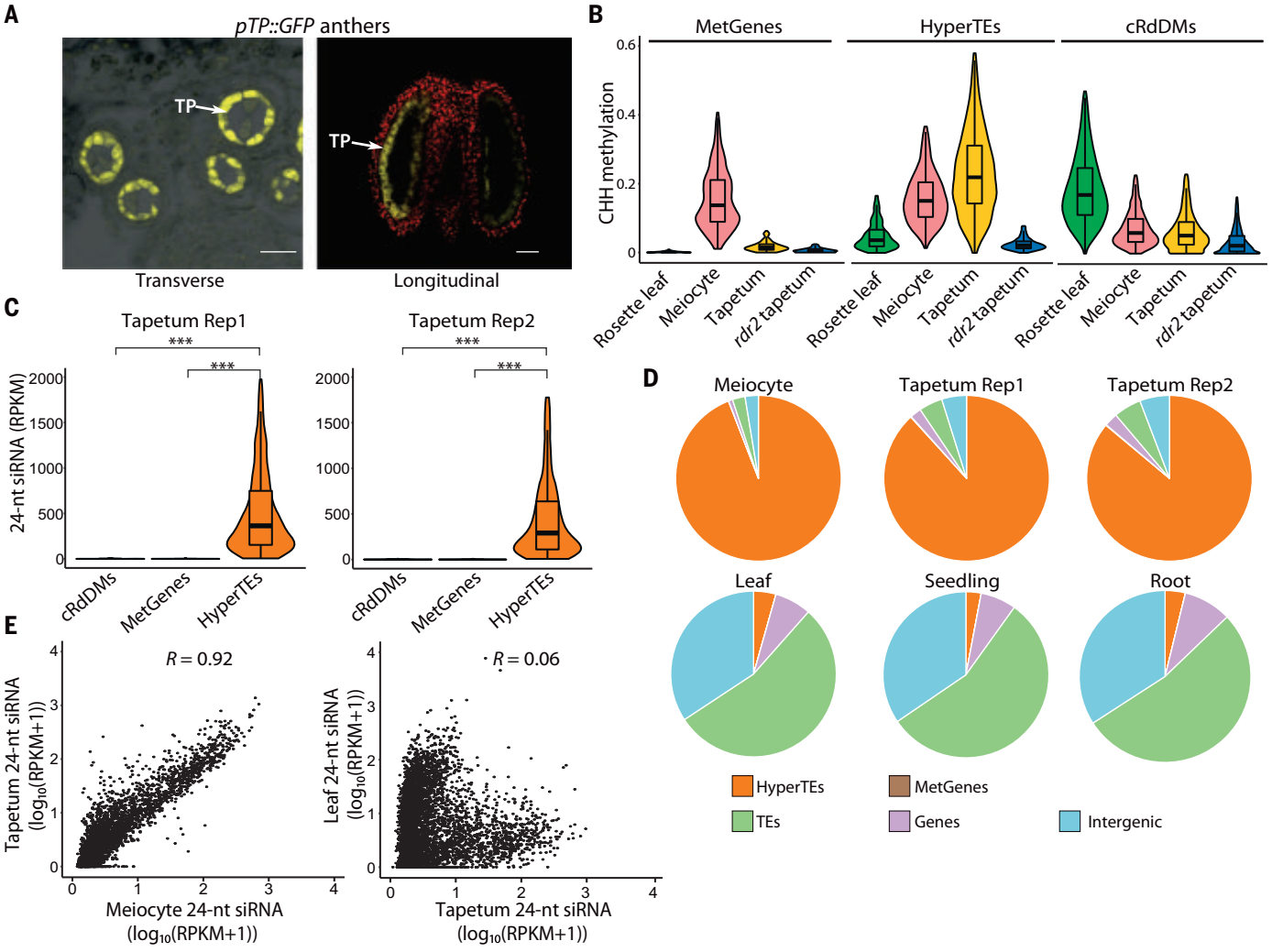

Fig. 2. Tapetal nurse cells have a similar 24-nt siRNA profile to meiocytes. (**A**) Images of *pTP::GFP* anthers. TP, tapetum; yellow, GFP fluorescence; red, autofluorescence. Scale bars, 25 μm. (**B**) CHH methylation at MetGenes, HyperTEs, and cRdDMs in the leaf, meiocyte, and tapetum. (**C**) 24-nt siRNA levels at cRdDMs, MetGenes, and HyperTEs in the tapetum. Rep, biological replicate. *** $P < 2.2 \times 10^{-16}$, Kolmogorov-Smirnov test. (**D**) Proportions of 24-nt siRNAs associated with different features in the meiocyte, tapetum, and somatic tissues. (**E**) Correlations (Pearson's *R*) between 24-nt siRNA abundance in the indicated cells and tissues at meiocyte (left; *n* = 3712) or tapetum (right; *n* = 5841) siRNA clusters.

siRNA (*14*, *15*). Therefore, regardless of the initial guiding siRNA, Pol V–mediated DNA methylation attracts the Pol IV pathway in situ to generate perfectly matching siRNAs (*12*, *14*). The observation that few perfectly matching siRNAs are associated with MetGenes (Fig. 1, B, C, and E) suggests that the Pol IV pathway is quiescent in meiocytes, with MetGene-inducing siRNAs generated from HyperTEs in other cells.

Male meiocytes are enclosed by a layer of tapetal nurse cells (Fig. 1A) (*16*). The meiocytes and tapetal cells are connected by cytoplasmic channels called plasmodesmata (*17*, *18*), which are regarded as the most likely route for intercellular siRNA movement in plants (*19*–*21*). Furthermore, 24-nt siRNAs have been proposed to accumulate in maize tapetum during early meiosis (*22*), exactly the stage when plasmodesmata connect meiocytes and tapetal cells. Therefore, siRNAs that induce methylation at

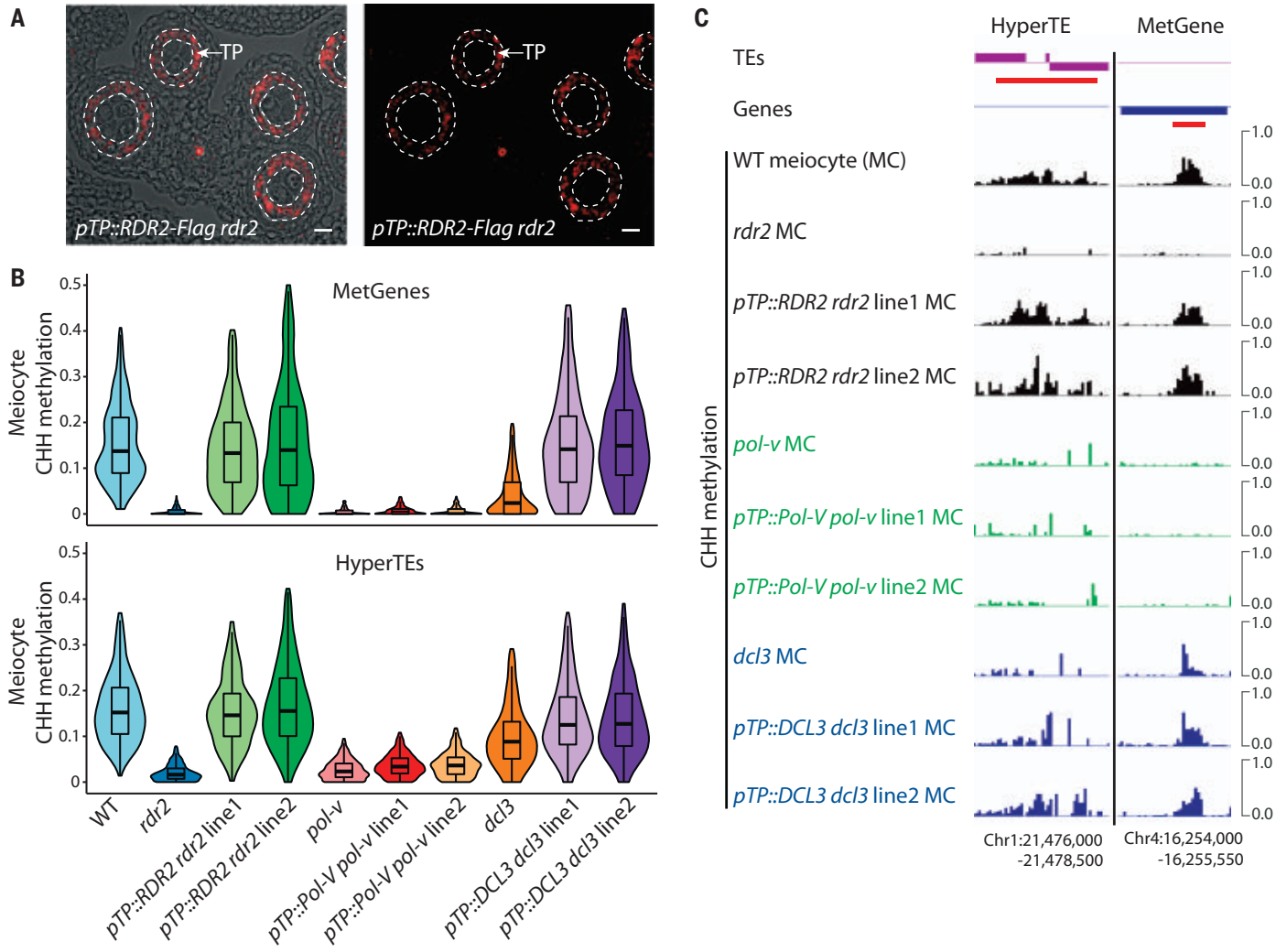

Fig. 3. siRNAs that drive methylation in meiocytes are produced by tapetal cells. (**A**) Immunostaining of a *pTP::RDR2-Flag rdr2* anther. Anti-Flag signal (red) is observed specifically in the tapetum (TP, outlined in white). Scale bars, 10 μm. (**B** and **C**) CHH methylation at MetGenes and HyperTEs [(B); examples shown in (C), underlined in red] in the meiocytes from WT, RdDM mutants, and their corresponding mosaic lines (two independent transgenic lines for each).

MetGenes may be generated by HyperTEs in the tapetum and transported into meiocytes. To test this hypothesis, we developed a method to isolate tapetal cells. We generated *Arabidopsis* transgenic plants carrying green fluorescent protein (GFP) driven by a tapetum-specific promoter (*pA9*, simplified as *pTP*) (Fig. 2A) (*23*, *24*) and isolated GFP-positive tapetal cells by means of fluorescence-activated cell sorting (FACS) (fig. S3A). The isolated tapetal cells are of high purity, evaluated through fluorescence microscopy (>95% purity) and RNA-sequencing (RNA-seq), which shows enrichment of tapetum-specific genes and depletion of somatic and meiotic genes (table S4).

DNA methylation analysis of tapetal cells revealed that HyperTEs are hypermethylated in the tapetum in comparison with somatic tissues, at levels even higher than in meiocytes (Figs. 1B and 2B). As in meiocytes (Fig. 1, B and D), HyperTE methylation in the tapetum requires RDR2 (Figs. 1B and 2B). Tapetal cells also show enrichment of 24-nt siRNAs at HyperTEs (Fig. 2, C and D, and fig. S3B), similar to that in meiocytes (Fig. 1C). As in meiocytes (Fig. 1C), siRNA levels at canonical RdDM loci are relatively low but similar in absolute terms to somatic cells (Fig. 2C and fig. S1C), and DNA methylation at these loci is low (Figs. 1B and 2B). Genome-wide, 24-nt siRNAs in identified siRNA clusters strongly correlate between tapetal cells and meiocytes (Fig. 2E). As in meiocytes (Fig. 1C), few siRNAs match MetGenes perfectly in tapetal cells (Fig. 2C). The resemblance between siRNA profiles suggests en masse siRNA movement from tapetum to meiocytes, which is consistent with knowledge of intercellular siRNA transport through plasmodesmata (*25*). In contrast to meiocytes, MetGenes are not methylated in tapetal cells (Figs. 1B and 2B). This is consistent with tapetum having an active Pol IV pathway because RdDM-mediated methylation should not exist in the absence of perfectly matching siRNAs in such cells. Our results also imply that unlike in meiocytes, the tapetal Pol V pathway is unable to induce DNA methylation with mismatched siRNAs.

Tapetal siRNAs drive meiocyte methylation reprogramming

To test whether tapetum-derived siRNAs work in trans to induce methylation in meiocytes, we created a genetic mosaic system with 24-nt siRNA biogenesis confined to the tapetum. We expressed RDR2 (fused with a Flag tag) in the *rdr2* null mutant background using the tapetum-specific *pA9* promoter (simplified as *pTP::RDR2 rdr2*) (Fig. 3A). Immunolocalization with anti-Flag antibodies in anther cross sections confirmed the specific induction of RDR2 in the tapetum in two independent mosaic lines (Fig. 3A). In the meiocytes isolated

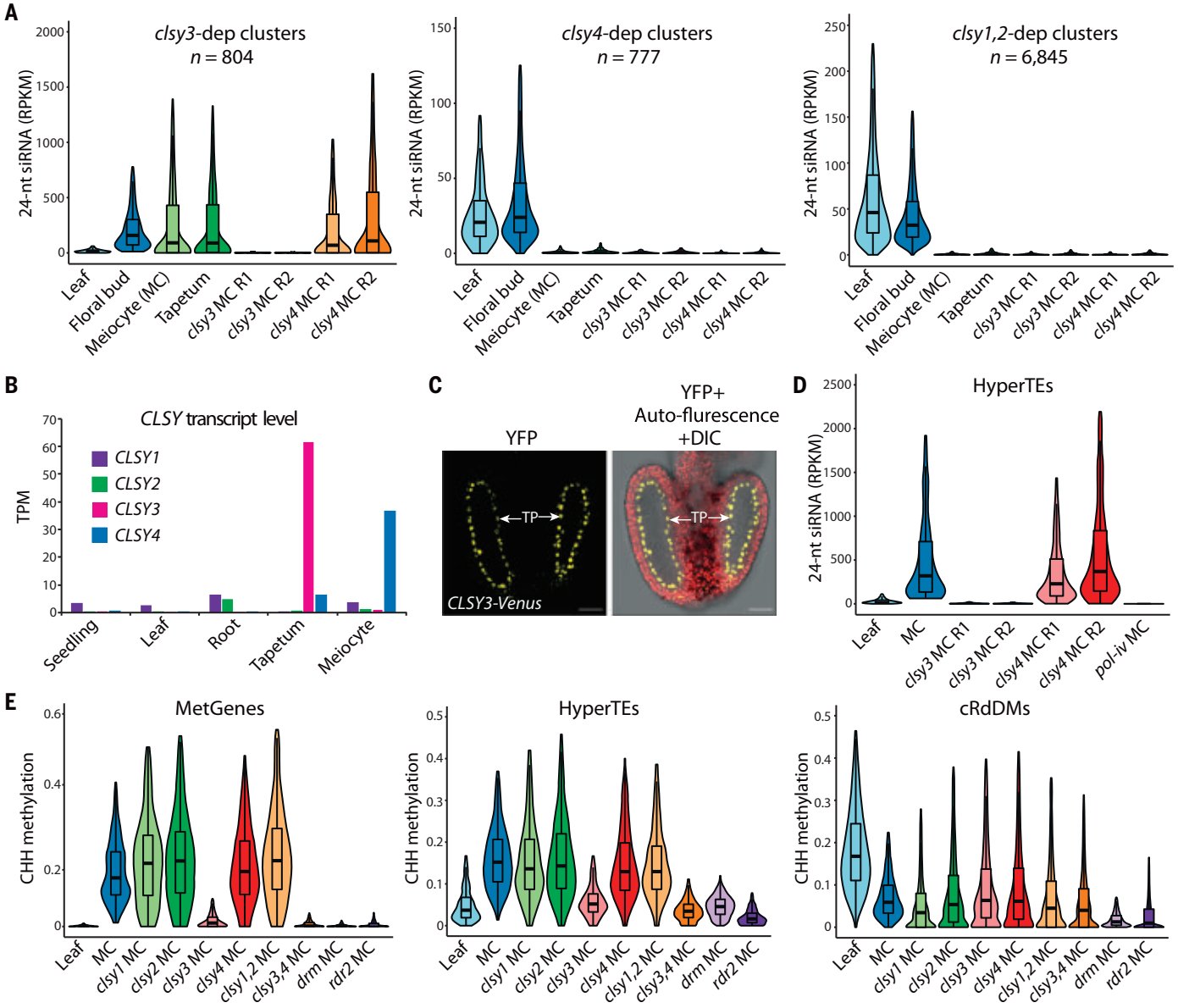

Fig. 4. CLSY3 is required for HyperTE siRNAs. (**A**) 24-nt siRNA abundance at *clsy3*-, *clsy4*-, and *clsy1,2*–dependent (dep) clusters in indicated tissues and cells. (**B**) Abundance of *CLSY* transcripts across tissues and cells. TPM, transcripts per million. (**C**) CLSY3-Venus localization in the tapetum (TP). Scale bars, 25 μm. (**D**) 24-nt siRNA levels at HyperTEs in the leaf and meiocytes (MC) from indicated genotypes. (**E**) CHH methylation at MetGenes, HyperTEs, and cRdDMs in the leaf and MC across genotypes. In (A), (D), and (E), MC, meiocyte; R, biological replicate.

from both lines, methylation at MetGenes and HyperTEs was increased to levels comparable with that of wild type (Fig. 3, B and C, and fig. S4, A and B). As a control, we generated a *pTP::POL-V pol-v* mosaic line. Because Pol V mediates DNA methylation rather than siRNA biogenesis, it must work in cis. Consistently, meiocytes from two independent lines show no methylation at MetGenes (Fig. 3, B and C; fig. S4C shows that Pol V protein is correctly expressed). These results demonstrate that activity of the Pol IV pathway in the tapetum is sufficient to methylate MetGenes and HyperTEs in meiocytes.

RDR2 produces double-stranded RNA (dsRNA) precursors, which are converted to 24-nt siRNAs by DCL3 (*12*). Because the dsRNA precursors have been shown to move between cells (*19*, *20*), we sought to understand whether these molecules or siRNAs are the primary signals that move from the tapetum to meiocytes. We therefore generated two independent mosaic lines with DCL3 confined to the tapetum (*pTP::DCL3 dcl3*) (fig. S4C shows that DCL3 is correctly expressed). Meiocytes from both lines show wild-type methylation at MetGenes and HyperTEs, whereas *dcl3* mutants have reduced methylation at both sets of loci in meiocytes (Fig. 3, B and C). This indicates that tapetal 24-nt siRNAs are sufficient to trigger methylation at MetGenes and HyperTEs in meiocytes. Furthermore, *DCL3* expression is 9.4 times greater in tapetal cells than in meiocytes (fig. S4D), suggesting that most 24-nt siRNA dicing occurs in the tapetum. These results suggest that 24-nt siRNAs are the predominant non–cell-autonomous signal that originates in the tapetum and drives methylation in meiocytes.

HyperTEs produce siRNAs through CLSY3

We next investigated how the distinctive siRNA profile in the tapetum is generated (Fig. 2, C

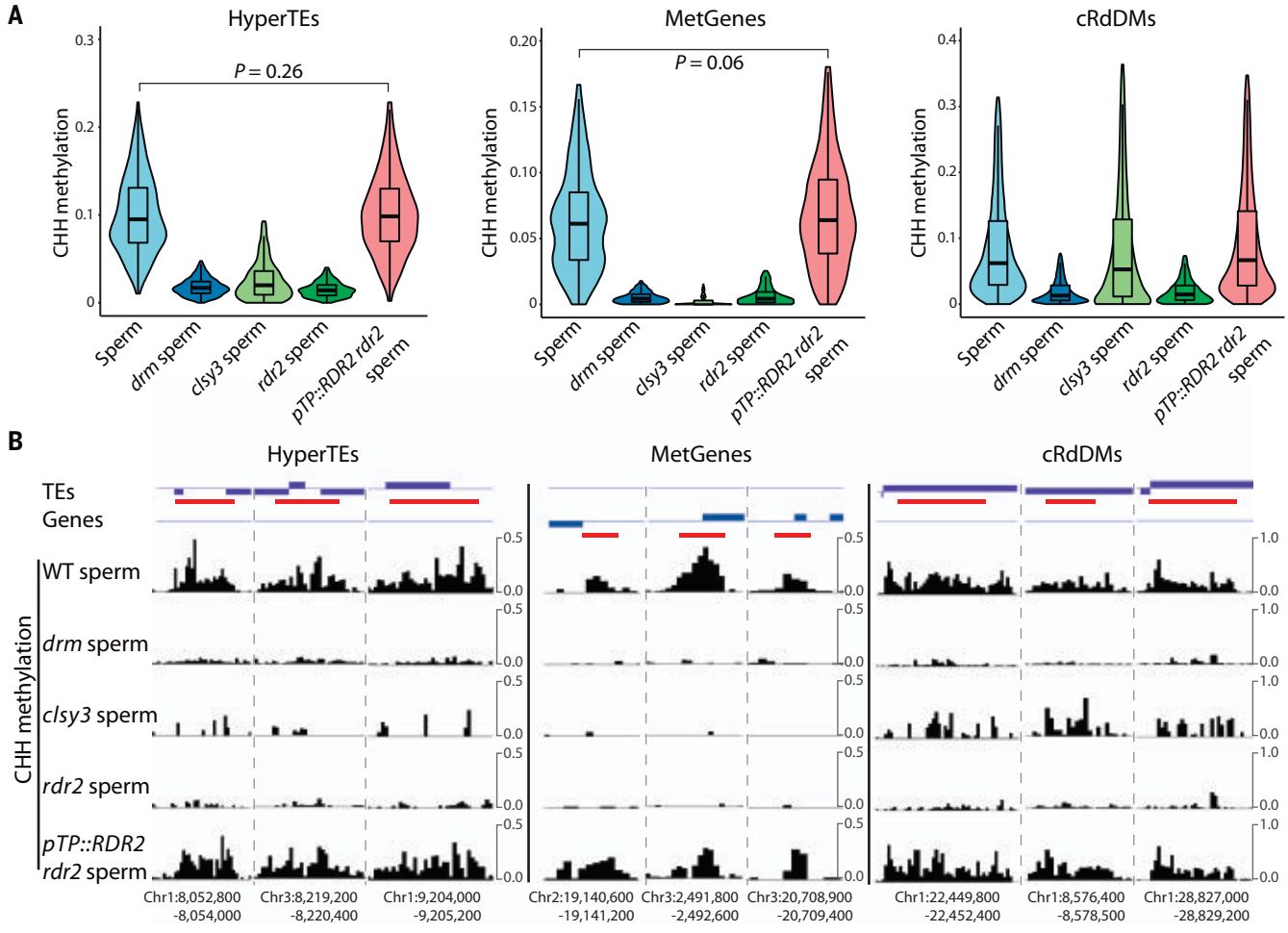

Fig. 5. Tapetal siRNAs determine the sperm DNA methylome. (**A** and **B**) CHH methylation at HyperTEs, MetGenes, and cRdDMs [(A); examples are displayed in (B), underlined in red] in sperm cells from wild-type and indicated genotypes. *P* values, Kolmogorov-Smirnov test.

and D). Four putative chromatin remodelers, CLASSY1 to -4 (CLSYs), recruit Pol IV to produce siRNAs at largely discrete sets of loci (*26*). Therefore, we evaluated the relationship of the *clsy1/2/3/4*–dependent siRNA clusters identified in floral buds (*26*) with HyperTEs. We found a proportion of HyperTEs (66%; 524 out of 797) overlap *clsy3*-dependent siRNA clusters (804 loci), whereas only 1 to 8% of HyperTEs overlap *clsy1*-, *clsy2*- or *clsy4*-dependent clusters (fig. S5A). Consistently, in both tapetal cells and meiocytes, relatively few 24-nt siRNAs are associated with *clsy1*-, *clsy2*-, or *clsy4*-dependent clusters, whereas *clsy3*-dependent clusters are enriched in siRNAs (Fig. 4A). By contrast, in leaves most siRNAs are associated with *clsy1*-, *clsy2*-, and *clsy4*-dependent clusters (Fig. 4A).

We next examined the transcription of *CLSY*s in the tapetum, meiocytes, and somatic tissues. We found that *CLSY1* and *-2* are the predominant homologs in somatic tissues, whereas *CLSY3* is the most highly expressed *CLSY* in the tapetum (Fig. 4B). To validate this result and examine the expression pattern of CLSY3, we generated a *CLSY3-Venus* fusion line (*pCLSY3::Venus-CLSY3*). Confocal microscopy showed that CLSY3 is undetectable in seedlings and leaves but enriched in carpels and anthers (Fig. 4C and fig. S5B). In the anther, CLSY3 is specifically expressed in tapetal cells and absent from all other cell types, including meiocytes (Fig. 4C). On the basis of these results, CLSY3 is likely responsible for the distinctive siRNA profile in tapetal and meiocyte cells. CLSY3 is also enriched in ovules (fig. S5B), where accumulation of 24-nt siRNAs from ~200 loci was recently observed in *Brassica* (*27*), suggesting a similar methylation reprogramming phenomenon on the female side. CLSY3 activity also likely contributes to the high siRNA abundance in the floral bud (Fig. 4A), a mixture of cells and tissues that express different CLSY proteins.

To test our hypothesis that tapetal CLSY3 drives the production of HyperTE-associated siRNAs, we isolated meiocytes from the *clsy3* mutant and performed siRNA sequencing. We also examined *clsy4* meiocytes because *CLSY3* and *-4* were reported to be partially redundant (*26*) and *CLSY4* transcripts are detected in the tapetum (Fig. 4B). We found that 24-nt siRNAs at HyperTEs are lost in *clsy3* mutant meiocytes, similarly to *pol iv* mutant meiocytes, whereas *clsy4* meiocytes are unaffected (Fig. 4D). Consistently, we found loss of methylation at HyperTEs and MetGenes in *clsy3* meiocytes, whereas *clsy1*, *-2*, or *-4* mutant meiocytes and *clsy1;2* double-mutant meiocytes have wild-type levels of methylation (Fig. 4E). These results establish that CLSY3 is required for the production of HyperTE-associated siRNAs in the tapetum and the consequent methylation of HyperTEs and MetGenes. Given that in anthers CLSY3 is absent from meiocytes and only expressed in the tapetum (Fig. 4C), these results further demonstrate that siRNA biogenesis is suppressed in meiocytes and that meiocyte siRNAs are derived from the tapetum.

Tapetal siRNAs shape sperm DNA methylation

Because the methylation at MetGenes persists throughout male germline development to gametogenesis (Fig. 1B) (*6*), we wondered whether tapetum-derived siRNAs can drive

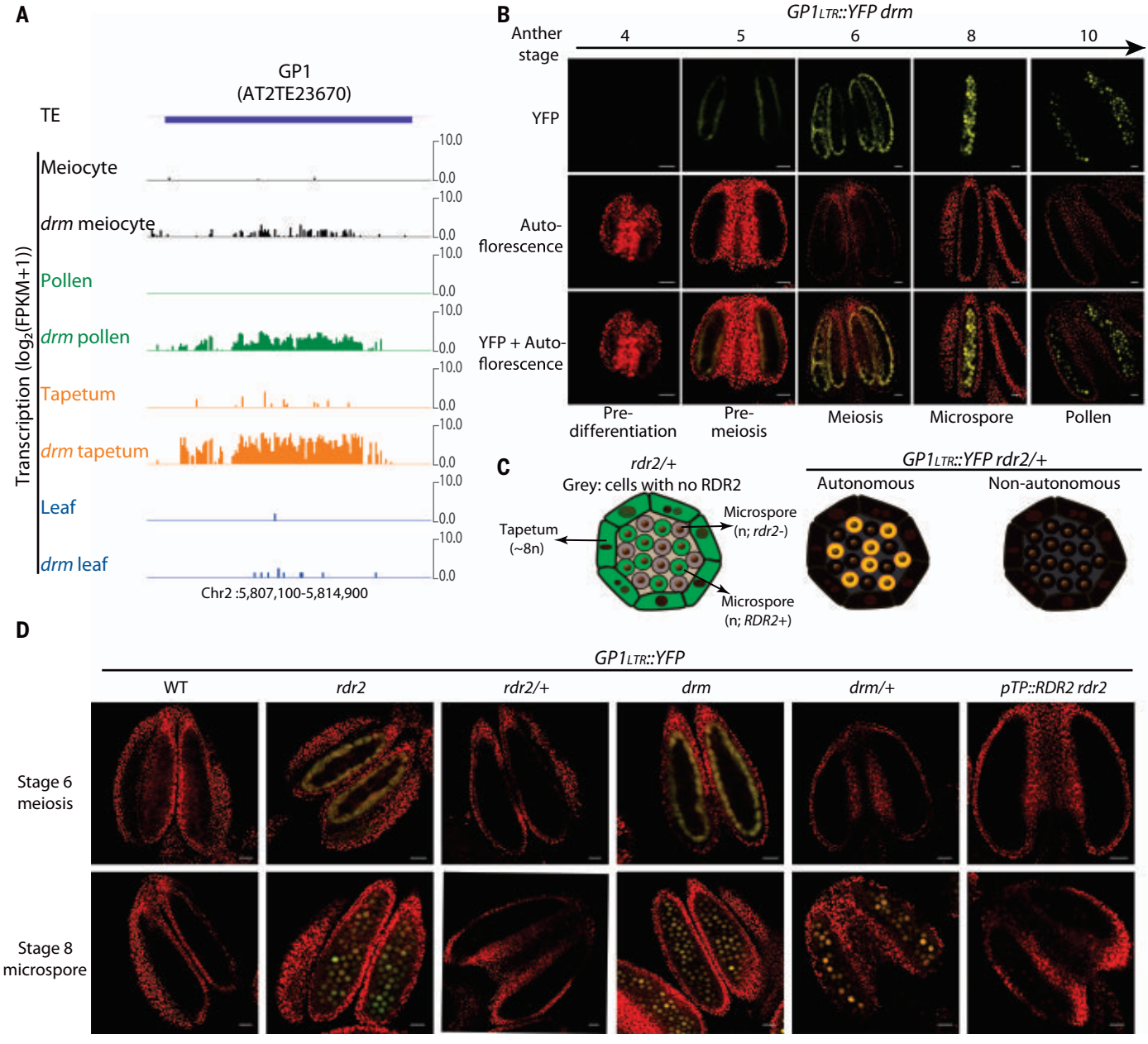

Fig. 6. Tapetal siRNAs silence the *GP1* transposon in the germline. (**A**) *GP1* transcription in indicated cells and tissues. FPKM, fragments per kilobase per million. (**B**) Confocal images of $GP1_{LTR}$*::YFP drm* anthers during development. (**C**) Schematics illustrating (left) RDR2 functionality in *rdr2/+* heterozygous mutant anther and the expected outcome if *GP1*-silencing siRNA is (middle) cell autonomous or (right) nonautonomous. (**D**) $GP1_{LTR}$*::YFP* anthers in indicated genetic backgrounds at (top) stage 6 and (bottom) stage 8. In (B) and (D), Yellow, YFP; red, auto-fluorescence. Scale bars, (B) 20 μm and (D) 25 μm.

methylation throughout the germline. To test this, we analyzed DNA methylation in sperm isolated from the *clsy3* mutant. DNA methylation at MetGenes and HyperTEs is reduced in *clsy3* mutant sperm to levels resembling those of *drm* mutant sperm (Fig. 5, A and B, and fig. S6). By contrast, methylation at canonical RdDM loci is not affected by the *clsy3* mutation (Fig. 5, A and B, and fig. S6).

To confirm the competence of tapetal siRNAs to shape sperm methylation, we examined sperm from the *pTP::RDR2 rdr2* mosaic line. DNA methylation at MetGenes and HyperTEs is restored to wild-type levels in *pTP::RDR2 rdr2* sperm (including CG, CHG, and CHH methylation) (Fig. 5, A and B, and fig. S6). Furthermore, methylation at canonical RdDM loci is also restored (Fig. 5, A and B, and fig. S6), which is in line with soma-like absolute levels of 24-nt siRNA at canonical RdDM loci in the tapetum (fig. S1C). These results demonstrate that tapetal siRNAs drive DNA methylation reprogramming in the male germline all the way to the gametes.

Tapetal siRNAs silence germline transposons

MetGene methylation was shown to regulate gene expression and male meiosis (*6*). Besides MetGenes, our results demonstrate that tapetal siRNAs also induce methylation at TEs in the male germline (Figs. 3B, 4D, and 5A). Therefore, we investigated whether siRNAs serve to silence germline TEs in addition to their gene regulatory function. To address this question, we performed RNA-seq of tapetal cells and pollen from wild type and the *drm* mutant. Analysis of these data in combination with

analogous data from meiocytes and leaves (*6*) identified retrotransposons from a Gypsy family (*GP1*) that are specifically activated in RdDM-defective germline cells (Fig. 6A). *GP1* transcription is not activated in *drm* mutant leaves but strongly activated in the tapetum and pollen (and slightly in meiocytes) (Fig. 6A). We observed loss of methylation in RdDM (*drm* and *rdr2*) mutants at the long terminal repeats (LTRs) in the tapetum and meiocytes (fig. S7A), indicating that *GP1* is directly suppressed by RdDM.

To further examine *GP1* activity during germline development, we generated a yellow fluorescent protein (YFP) reporter line driven by *GP1*'s LTR sequence ($GP1_{LTR}$::*YFP*) and crossed it to *rdr2* and *drm* mutants. Consistent with the RNA-seq data, YFP signal was undetectable in wild type and specifically observed in the anthers of *rdr2* and *drm* mutants (Fig. 6, B to D). In both mutants, *GP1* activity can be first observed in the tapetum at a stage before meiosis (Fig. 6B). Subsequently, YFP signal is strongest in the tapetum at the onset of meiosis and in microspores (and to a lesser extent pollen) after meiosis (Fig. 6, B to D). These observations confirm that *GP1* is specifically activated in the germline and tapetum when RdDM is compromised. Although DNA methylation of the *GP1* LTRs requires RdDM in the soma, tapetum, and germline (fig. S7A), loss of RdDM does not activate *GP1* in somatic tissues (Fig. 6A). This suggests that *GP1* targets expression in reproductive cells, possibly by exploiting transcription factors specific to these cell types.

To confirm that tapetum is the origin of *GP1*-silencing siRNAs, we first took advantage of microspores being haploid meiotic products in which genetic segregation has occurred (Figs. 1A and 6C). In a mutant carrying a recessive heterozygous *rdr2* mutation, the diploid tapetal cells (of *rdr2*/+ genotype) are able to produce siRNAs, whereas half of the haploid microspores (the ones of *rdr2* genotype) are not (Fig. 6C). We did not detect *GP1* activity in any anther tissue, including the tapetum and microspores, of $GP1_{LTR}$::*YFP rdr2*/+ plants (Fig. 6D), confirming that *GP1*-silencing siRNAs are produced in diploid somatic cells. By contrast, half (50.7%, n = 1391) of the microspores from $GP1_{LTR}$::*YFP drm*/+ plants exhibit YFP signal (Fig. 6D), which is consistent with the cis action of DRM methyltransferases.

To validate the silencing of *GP1* by tapetal siRNAs, we crossed the *GP1* YFP reporter into the *pTP::RDR2 rdr2* genetic background that limits siRNA production to the tapetum. No *GP1* activity was observed in $GP1_{LTR}$::*YFP pTP::RDR2 rdr2* anthers (Fig. 6D), demonstrating the competence of tapetal siRNAs to silence *GP1* in the male germline. *GP1* is a canonical RdDM locus (fig. S7, A and B), further demonstrating that tapetal siRNA production and germline activity are not confined to HyperTEs (fig. S8).

Discussion

Our study demonstrates that DNA methylation reprogramming in the male germline is driven by tapetum-derived siRNAs. Although quiescent in 24-nt siRNA biogenesis, male meiocytes can use imperfectly matching siRNAs to target DNA methylation, suggesting that the Pol V branch of RdDM is hypersensitive in meiocytes (fig. S8). Thus, meiosis appears to be a key stage for genome surveillance, during which RdDM targets genes and TEs with sequences sufficiently similar to those of TEs that produce siRNAs in the tapetum (such as *GP1*) (fig. S8). Methylation of genes allows transcriptional regulation by RdDM in the germline (*6*), which has the potential to improve fitness and hence be selected during evolution at specific loci.

Tapetal siRNAs can induce DNA methylation not only in meiocytes but throughout the male germline (Fig. 5A). Furthermore, tapetal siRNAs are competent to restore not only sperm MetGene methylation but also the full spectrum of sperm RdDM (Fig. 5A and figs. S6 and S8). The central role of tapetal siRNAs in determining the paternally inherited DNA methylome illustrates the reprogramming potential of nurse cells. This theme has also emerged in studies of animal germlines (*28*), indicating convergent functional evolution between plant and animal germline epigenetic reprogramming systems.

Materials and methods summary

Arabidopsis male meiocytes, tapetal cells, and sperm nuclei were isolated by means of microdissection or FACS to produce siRNA, RNA, and bisulfite sequencing libraries. Sequencing data was processed by use of the following software: Bowtie, Bismark, Kallisto, Shortstack, Cutadapt, TrimGalore, and MarkDuplicates. HyperTEs were identified by requiring higher levels of 24-nt siRNA as compared with 25-nt siRNA in wild-type meiocytes as well as requiring a loss of meiotic CHH methylation in *drm2* or *rdr2* mutant meiocytes. Canonical RdDM loci and MetGenes were previously reported (*6*). HyperTE CRISPR deletion lines were created by using guide RNAs listed in table S5. Immunolocalization of *pA9::RDR2-Flag rdr2* anthers was examined with a Zeiss DM6000 microscope. Expression of *pA9::Pol-V-3×Flag* and *pA9::DCL3-3×Flag* was confirmed by means of inflorescence immunoblot assay. *CLSY3-Venus* and $GP1_{LTR}$::*YFP* lines were examined by using a Leica SP5 confocal microscope.

REFERENCES AND NOTES

1. Z. D. Smith, A. Meissner, DNA methylation: Roles in mammalian development. *Nat. Rev. Genet.* **14**, 204–220 (2013). doi: 10.1038/nrg3354; pmid: 23400093
2. H. Zhang, Z. Lang, J. K. Zhu, Dynamics and function of DNA methylation in plants. *Nat. Rev. Mol. Cell Biol.* **19**, 489–506 (2018). doi: 10.1038/s41580-018-0016-z; pmid: 29784956
3. A. Zemach, D. Zilberman, Evolution of eukaryotic DNA methylation and the pursuit of safer sex. *Curr. Biol.* **20**, R780–R785 (2010). doi: 10.1016/j.cub.2010.07.007; pmid: 20833323
4. G. Wang, C. Köhler, Epigenetic processes in flowering plant reproduction. *J. Exp. Bot.* **68**, 797–807 (2017). pmid: 28062591
5. S. Seisenberger *et al*., Reprogramming DNA methylation in the mammalian life cycle: Building and breaking epigenetic barriers. *Philos. Trans. R Soc. Lond. B Biol. Sci.* **368**, 20110330 (2013). doi: 10.1098/rstb.2011.0330; pmid: 23166394
6. J. Walker *et al*., Sexual-lineage-specific DNA methylation regulates meiosis in *Arabidopsis*. *Nat. Genet.* **50**, 130–137 (2018). doi: 10.1038/s41588-017-0008-5; pmid: 29255257
7. M. V. C. Greenberg, D. Bourc'his, The diverse roles of DNA methylation in mammalian development and disease. *Nat. Rev. Mol. Cell Biol.* **20**, 590–607 (2019). doi: 10.1038/s41580-019-0159-6; pmid: 31399642
8. M. W. Schmid *et al*., Extensive epigenetic reprogramming during the life cycle of *Marchantia polymorpha*. *Genome Biol.* **19**, 9 (2018). doi: 10.1186/s13059-017-1383-z; pmid: 29368664
9. C. A. Ibarra *et al*., Active DNA demethylation in plant companion cells reinforces transposon methylation in gametes. *Science* **337**, 1360–1364 (2012). doi: 10.1126/science.1224839; pmid: 22984074
10. J. P. Calarco *et al*., Reprogramming of DNA methylation in pollen guides epigenetic inheritance via small RNA. *Cell* **151**, 194–205 (2012). doi: 10.1016/j.cell.2012.09.001; pmid: 23000270
11. P. H. Hsieh *et al*., Arabidopsis male sexual lineage exhibits more robust maintenance of CG methylation than somatic tissues. *Proc. Natl. Acad. Sci. U.S.A.* **113**, 15132–15137 (2016). doi: 10.1073/pnas.1619074114; pmid: 27956643
12. M. A. Matzke, R. A. Mosher, RNA-directed DNA methylation: An epigenetic pathway of increasing complexity. *Nat. Rev. Genet.* **15**, 394–408 (2014). doi: 10.1038/nrg3683; pmid: 24805120
13. T. K. To *et al*., RNA interference-independent reprogramming of DNA methylation in Arabidopsis. *Nat. Plants* **6**, 1455–1467 (2020). doi: 10.1038/s41477-020-00810-z; pmid: 33257860
14. J. M. Wendte, C. S. Pikaard, The RNAs of RNA-directed DNA methylation. *Biochim. Biophys. Acta. Gene Regul. Mech.* **1860**, 140–148 (2017). doi: 10.1016/j.bbagrm.2016.08.004; pmid: 27521981
15. H. Y. Kuo, E. L. Jacobsen, Y. Long, X. Chen, J. Zhai, Characteristics and processing of Pol IV-dependent transcripts in *Arabidopsis*. *J. Genet. Genomics* **44**, 3–6 (2017). doi: 10.1016/j.jgg.2016.10.009; pmid: 28089091
16. X. Feng, D. Zilberman, H. Dickinson, A conversation across generations: Soma-germ cell crosstalk in plants. *Dev. Cell* **24**, 215–225 (2013). doi: 10.1016/j.devcel.2013.01.014; pmid: 23410937
17. E. A. Mamun, L. C. Cantrill, R. L. Overall, B. G. Sutton, Cellular organisation and differentiation of organelles in pre-meiotic rice anthers. *Cell Biol. Int.* **29**, 792–802 (2005). doi: 10.1016/j.cellbi.2005.05.009; pmid: 16085434
18. R. Sager, J. Y. Lee, Plasmodesmata in integrated cell signalling: Insights from development and environmental signals and stresses. *J. Exp. Bot.* **65**, 6337–6358 (2014). doi: 10.1093/jxb/eru365; pmid: 25262225
19. C. W. Melnyk, A. Molnar, D. C. Baulcombe, Intercellular and systemic movement of RNA silencing signals. *EMBO J.* **30**, 3553–3563 (2011). doi: 10.1038/emboj.2011.274; pmid: 21878996
20. D. E. Pyott, A. Molnar, Going mobile: Non-cell-autonomous small RNAs shape the genetic landscape of plants. *Plant Biotechnol. J.* **13**, 306–318 (2015). doi: 10.1111/pbi.12353; pmid: 25756494
21. L. Liu, X. Chen, Intercellular and systemic trafficking of RNAs in plants. *Nat. Plants* **4**, 869–878 (2018). doi: 10.1038/s41477-018-0288-5; pmid: 30390090
22. J. Zhai *et al*., Spatiotemporally dynamic, cell-type-dependent premeiotic and meiotic phasiRNAs in maize anthers. *Proc. Natl. Acad. Sci. U.S.A.* **112**, 3146–3151 (2015). doi: 10.1073/pnas.1418918112; pmid: 25713378
23. X. Feng, H. G. Dickinson, Tapetal cell fate, lineage and proliferation in the *Arabidopsis* anther. *Development* **137**, 2409–2416 (2010). doi: 10.1242/dev.049320; pmid: 20570940
24. W. Paul, R. Hodge, S. Smartt, J. Draper, R. Scott, The isolation and characterisation of the tapetum-specific *Arabidopsis*

thaliana A9 gene. *Plant Mol. Biol.* **19**, 611–622 (1992). doi: 10.1007/BF00026787; pmid: 1627774
25. C. Faulkner, Plasmodesmata and the symplast. *Curr. Biol.* **28**, R1374–R1378 (2018). doi: 10.1016/j.cub.2018.11.004; pmid: 30562524
26. M. Zhou, A. M. S. Palanca, J. A. Law, Locus-specific control of the de novo DNA methylation pathway in *Arabidopsis* by the CLASSY family. *Nat. Genet.* **50**, 865–873 (2018). doi: 10.1038/s41588-018-0115-y; pmid: 29736015
27. J. W. Grover *et al.*, Abundant expression of maternal siRNAs is a conserved feature of seed development. *Proc. Natl. Acad. Sci. U.S.A.* **117**, 15305–15315 (2020). doi: 10.1073/pnas.2001332117; pmid: 32541052
28. K. F. Tóth, D. Pezic, E. Stuwe, A. Webster, The piRNA pathway guards the germline genome against transposable elements. *Adv. Exp. Med. Biol.* **886**, 51–77 (2016). doi: 10.1007/978-94-017-7417-8_4; pmid: 26659487

ACKNOWLEDGMENTS

We thank the John Innes Centre Bioimaging Facility (S. Lopez, E. Wegel, and K. Findlay) for their assistance with microscopy and the Norwich BioScience Institute Partnership Computing Infrastructure for Science Group for high-performance computing resources. **Funding:** This work was funded by a European Research Council Starting Grant ("SexMeth" 804981; J.L., J.W., and X.F.), a Sainsbury Charitable Foundation studentship (J.W.), two Biotechnology and Biological Sciences Research Council (BBSRC) grants (BBS0096201 and BBP0135111; W.S., M.V., and X.F.), two John Innes Foundation studentships (B.A. and S.D.), and a BBSRC David Phillips Fellowship (BBL0250431; H.G. and X.F.). **Author contributions:** J.L., J.W., and X.F. designed the study and wrote the manuscript; J.L., W.S., B.A., H.G., and S.D. performed the experiments; and J.L., J.W., B.A., H.G., S.D., M.V., and X.F. analyzed the data. **Competing interests:** The authors declare no competing interests. **Data and material availability:** All sequencing data have been deposited in the Gene Expression Omnibus (GEO) under accession no. GSE161625. Accession nos. of published datasets used in this study are listed in table S6. Published software used in this study include Bowtie v1.2.2 (https://doi.org/10.1002/0471250953.bi1107s32), Bismark v0.22.2 (https://doi.org/10.1093/bioinformatics/btr167), Kallisto v0.43.0 (https://doi.org/10.1038/nbt0816-888d), Shortstack v3.8.5 (https://doi.org/10.1534/g3.116.030452), and Cutadapt v1.15 (https://doi.org/10.1089/cmb.2017.0096). TrimGalore v0.4.1 and MarkDuplicates v1.141 are available from https://github.com/FelixKrueger/TrimGalore and https://github.com/broadinstitute/picard, respectively. All remaining data are in the main paper or the supplementary materials.

SUPPLEMENTARY MATERIALS

science.sciencemag.org/content/373/6550/eabh0556/suppl/DC1
Materials and Methods
Figs. S1 to S8
Tables S1 to S6
References (*29*–*56*)
MDAR Reproducibility Checklist

12 February 2021; accepted 10 May 2021
10.1126/science.abh0556

ScienceSignaling.org

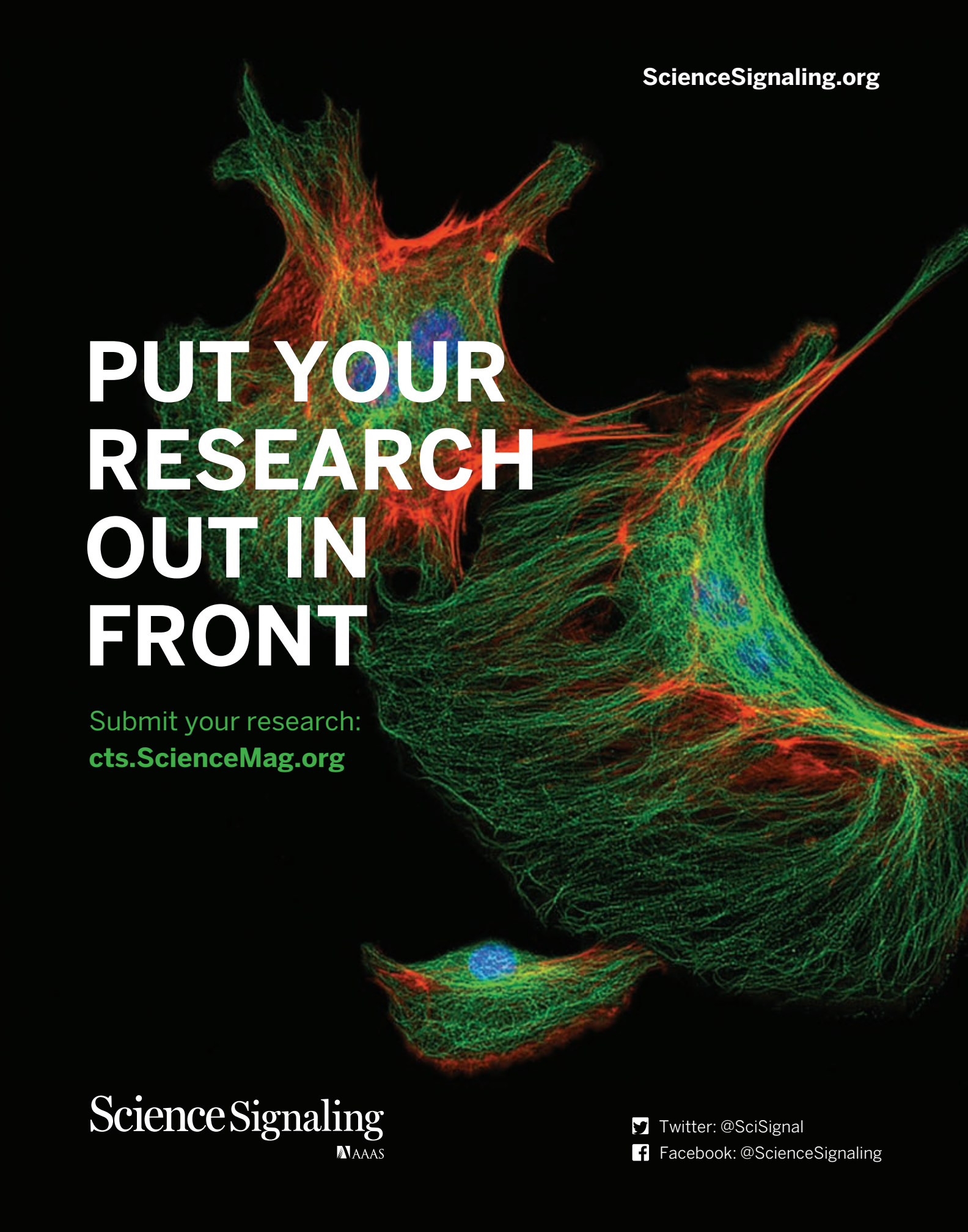

PUT YOUR RESEARCH OUT IN FRONT

Submit your research:
cts.ScienceMag.org

Science Signaling
AAAS

Twitter: @SciSignal
Facebook: @ScienceSignaling

RESEARCH ARTICLES

NEURODEVELOPMENT

Astrocytes close the mouse critical period for visual plasticity

Jérôme Ribot[1]†, Rachel Breton[1,2,3]†, Charles-Félix Calvo[1], Julien Moulard[1,4], Pascal Ezan[1], Jonathan Zapata[1], Kevin Samama[1], Matthieu Moreau[5], Alexis-Pierre Bemelmans[6], Valentin Sabatet[7], Florent Dingli[7], Damarys Loew[7], Chantal Milleret[1], Pierre Billuart[5], Glenn Dallérac[1]‡§, Nathalie Rouach[1]*§

Brain postnatal development is characterized by critical periods of experience-dependent remodeling of neuronal circuits. Failure to end these periods results in neurodevelopmental disorders. The cellular processes defining critical-period timing remain unclear. Here, we show that in the mouse visual cortex, astrocytes control critical-period closure. We uncover the underlying pathway, which involves astrocytic regulation of the extracellular matrix, allowing interneuron maturation. Unconventional astrocyte connexin signaling hinders expression of extracellular matrix–degrading enzyme matrix metalloproteinase 9 (MMP9) through RhoA–guanosine triphosphatase activation. Thus, astrocytes not only influence the activity of single synapses but also are key elements in the experience-dependent wiring of brain circuits.

During the first weeks of mouse life, massive synaptogenesis is followed by the shaping of synaptic circuits (*1*). Astrocyte processes, as structural and signaling partners of individual synapses, regulate neurotransmission and plasticity (*2*, *3*). Astrocytes are also implicated in the tuning and synchronization of neuronal network activities and influence cognitive functions such as memory formation (*4*). However, whether astrocytes take part in the wiring of the neuronal circuitry that occurs during critical periods of mouse postnatal development remains to be investigated. In the visual cortex, experience shapes synaptic circuits during a period of enhanced plasticity that follows eye opening (*5*, *6*). Introducing immature astrocytes in adult cats reopens a period of high plasticity, reminiscent of the critical period (*7*). However, whether and how the maturation of astrocytes actually controls critical-period closure remain unclear.

Immature astrocytes favor plasticity

We first investigated the ability of immature astrocytes to promote visual cortex plasticity in adult mice. To this end, we cultured and labeled, using lentivirus PGK-GFP (phosphoglycerate kinase–green fluorescent protein), immature astrocytes from the cortex of P1 to P3 (postnatal day 1 to 3) mice—which we characterized using immunolabeling (fig. S1)—and implanted them 10 days later in the primary visual cortex (V1) of adult mice (P100), in which the critical period is closed (Fig. 1A). Two weeks after the graft, we tested mice for ocular dominance (OD) plasticity—a form of plasticity typical of the critical period, where changes in visual inputs alter the natural dominance of the contralateral eye. To do so, we assessed visual cortex activity using optical imaging of intrinsic signals after 4 days of monocular deprivation (MD) (Fig. 1A). We found that mice engrafted with immature astrocytes displayed a high level of plasticity, unlike control mice subjected to MD with injection of culture medium or noninjected mice (Fig. 1B). Whereas in the wild-type (WT) mature visual cortex this plasticity is the result of an increase in the nondeprived eye response, in engrafted mice, it resulted from a reduction of the deprived eye response, which is typical of immature systems (*8*) (fig. S2). These data indicate that immature astrocytes reopen OD plasticity in adult mice.

To identify how immature astrocytes allow OD plasticity, we then investigated the molecular determinants of astrocyte maturation. Comparing gene expression of immature (P7) versus mature (P30) astrocytes using the transcriptome database for astrocytes during development (*9*) revealed ~200 genes that were differentially expressed with a fold-change >5 (table S1). Gene ontology analysis of enriched astrocyte gene groups identified a functional switch during maturation from cell division to cell communication, with the cell junction genes being the most represented (table S2 and fig. S3). Among these genes, *Gjb6*, encoding the astrocyte gap-junction channel subunit connexin 30 (Cx30), displayed one of the highest increases in expression (fold-change = 9; $P = 0.0274$; table S1). Accordingly, Cx30 regulates the structural maturation of hippocampal astrocytes during postnatal development (*10*). Together, these data led us to investigate the role of Cx30 in the astrocytic control of the critical period. To do so, we first assessed the regional and temporal expression of Cx30 in the mouse V1. Using immunohistochemistry, we found that Cx30 is enriched in layer 4 (Fig. 1C), the main V1 input layer, identified by wisteria floribunda agglutinin (WFA)—a marker of perineuronal nets important for the time course of the critical period (*11*). This enrichment correlates with a high density of astrocytes labeled in the Aldh1l1-GFP mice (Fig. 1C). Moreover, the Cx30 protein level in V1 increased from P10 to P50, as shown by Western blot (Fig. 1D), reaching its maximum when the critical period ends, which suggests that it may contribute to its closure. If so, reopening a phase of high plasticity should be associated with a down-regulation of Cx30. As a period of dark exposure (DE) can reinstate visual cortex plasticity during adulthood after closure of the critical period (*12*, *13*), we placed WT adult mice (P50) in the dark for 4 days and quantified V1 Cx30 levels. We found that this manipulation reduced Cx30 protein levels (~−70%) (Fig. 1E). We also found that 4 days of DE induced V1 plasticity, as indicated by the change in OD index (Fig. 1F). Thus, the drop in Cx30 expression correlated with plasticity induction.

Astrocytic Cx30 closes the critical period

We then investigated whether Cx30 inhibits OD plasticity. To do so, we first generated a knockdown mouse line for astrocytic Cx30 (KD), where Cx30 expression is decreased in V1 astrocytes by ~80% (fig. S4). In these mice, electroretinograms were unaltered, suggesting normal retinal functions (fig. S5). We found that OD plasticity peaked at P28 in WT

[1]Center for Interdisciplinary Research in Biology, Collège de France, CNRS UMR 7241, INSERM U1050, Labex Memolife, PSL Research University, Paris, France. [2]Doctoral School N°568, Paris Saclay University, PSL Research University, Le Kremlin Bicetre, France. [3]Université Paris-Saclay, CNRS, Institut des neurosciences Paris-Saclay, Gif-sur-Yvette, France. [4]Doctoral School N°158, Sorbonne University, Paris, France. [5]Université de Paris, Institute of Psychiatry and Neuroscience of Paris (IPNP), INSERM U1266, Genetic and Development of Cerebral Cortex Laboratory, GHU Paris Psychiatrie et Neurosciences, Hôpital Saint Anne, Paris, France. [6]Commissariat à l'Energie Atomique et aux Energies Alternatives (CEA), Département de la Recherche Fondamentale, Institut de biologie François Jacob, MIRCen, and CNRS UMR 9199, Université Paris-Saclay, Neurodegenerative Diseases Laboratory, Fontenay-aux-Roses, France. [7]Institut Curie, PSL Research University, Mass Spectrometry and Proteomics Laboratory, Paris, France.
***Corresponding author. Email: nathalie.rouach@college-de-france.fr**
†These authors contributed equally to this work.
‡Present address: Université Paris-Saclay, CNRS, Institut des neurosciences Paris-Saclay, Gif-sur-Yvette, France.
§These authors contributed equally to this work.

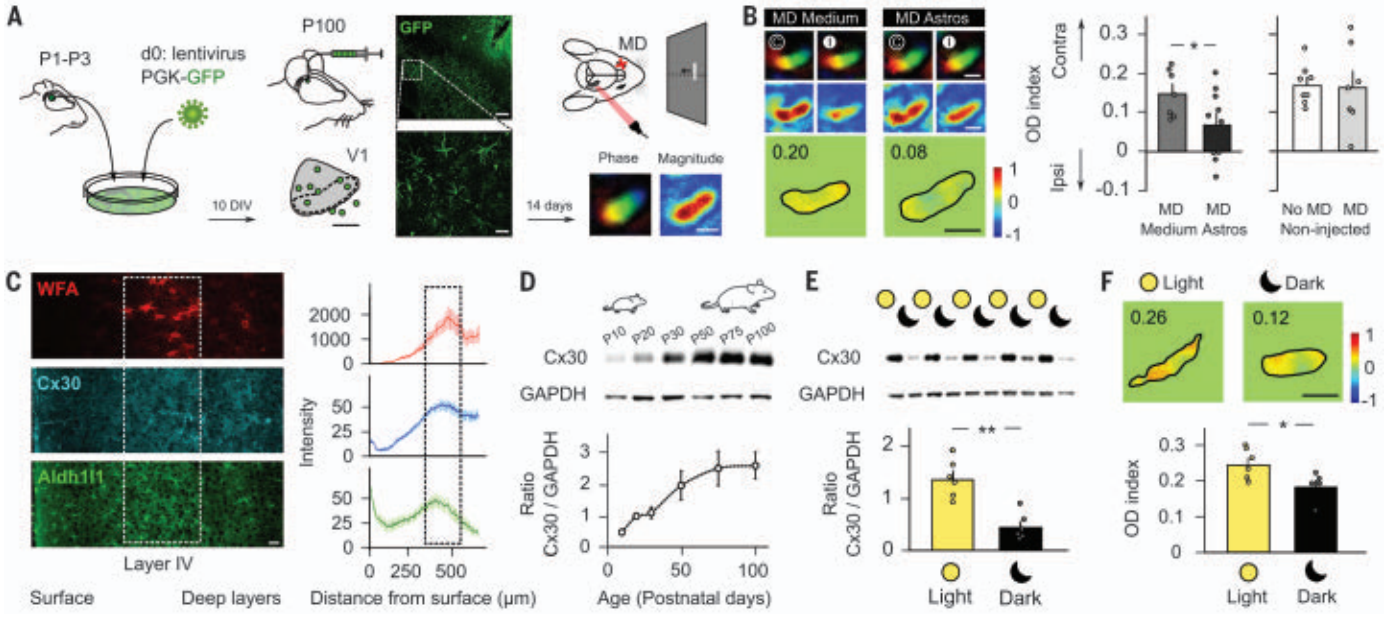

Fig. 1. Immature astrocytes favor cortical plasticity. (**A**) Immature astrocytes from P1 to P3 mice were transduced with PGK-GFP lentivirus, cultured for 10 days in vitro (DIV), and injected in the right V1 area of adult mice (P100), as shown on the schematic (green circles), where the dashed line represents the binocular zone. Scale bar, 1 mm. Confocal images of GFP-expressing astrocytes integrated in the mouse visual cortex 14 days after the injection are shown. Scale bars, 200 μm (top) and 20 μm (bottom). Intrinsic optical imaging was then conducted 14 days after the graft to record phase and magnitude retinotopic maps for each eye stimulation after 4 days of MD of the contralateral (left) eye. Scale bar, 1 mm. (**B**) These maps are shown in top panels for animals injected with control medium (medium MD; $n = 7$) or immature astrocytes (astro MD; $n = 10$). Contralateral (C) and ipsilateral (I) visual stimulations are indicated with a white (nondeprived eye) or black (deprived eye) circle. Bottom panels show the normalized OD map with average value inset. Mice injected with immature astrocytes showed a marked increase in OD plasticity compared with control mice injected with culture medium [$P = 0.043$, degree of freedom (DF) = 15, two-tailed t test], whereas no effect was observed in noninjected mice (no MD, $n = 8$; MD, $n = 7$; $P = 0.899$, DF = 13, two-tailed t test). (**C**) Representative immunostaining for WFA (top), Cx30 (middle), and Aldh1l1 (bottom) in V1 of P50 mouse (left panels) and corresponding quantification of spatial distributions across V1 layers (right panels; $n = 3$ mice). Scale bar, 50 μm. (**D** and **E**) Western blot analysis reveals changes in Cx30 levels in the visual cortex during development (D) [$n = 6$ per age; $P = 0.0001$, Kruskal-Wallis (KW) = 22.31)] and after 4 days of DE (E) ($n = 6$ per group; $P = 0.0022$, $U = 0$, Mann-Whitney test). GAPDH, glyceraldehyde 3-phosphate dehydrogenase. (**F**) Intrinsic optical imaging for light ($n = 6$) and dark ($n = 5$) exposed animals showing that DE decreased OD index ($P = 0.035$, DF = 9, two-tailed t test). Scale bar, 1 mm.

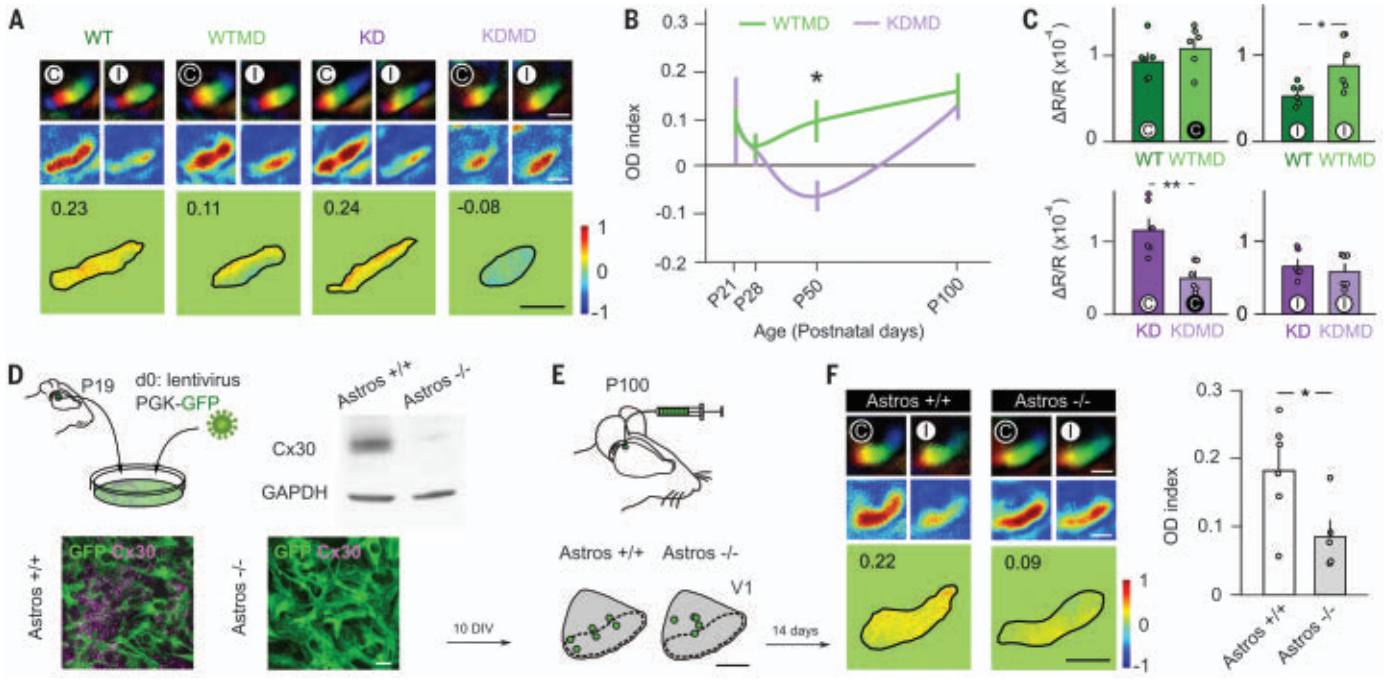

Fig. 2. Astrocytic Cx30 closes the critical period. (**A**) Functional maps in P50 WT and KD mice in control and MD conditions (WTMD and KDMD). Scale bar, 1 mm. (**B**) Developmental profile of OD index after MD in WT (P21, $n = 6$; P28, $n = 7$; P50, $n = 6$; and P100, $n = 7$) and KD mice (P21, $n = 3$; P28,

n = 8; P50, *n* = 6; and P100, *n* = 11), indicating a protracted and enhanced plasticity at P50 in KD mice [*P* = 0.0232, DF = 46, two-way analysis of variance (ANOVA) followed by Sidak post hoc test]. (**C**) Changes in response magnitude after MD in P50 mice results from an increased response to the nondeprived (white circle) eye (ipsilateral, I) stimulation in WT mice (*n* = 6 for WT and WTMD; *P* = 0.0411, *U* = 5, Mann Whitney test) and from a decreased response to the deprived (black circle) eye (contralateral, C) stimulation in KD mice (*n* = 6 for KD and KDMD; *P* = 0.0022, *U* = 0, Mann-Whitney test). (**D**) Mature astrocytes expressing or not expressing Cx30 were isolated from P19 WT (Astros +/+) or Cx30 constitutive knockout mice (Astros −/−), respectively, and were then transduced with PGK-GFP lentiviruses and cultured for 10 DIV. Western blots and immunostaining show expression of Cx30 in Astros +/+ but not in Astros −/−. Scale bar, 50 μm. (**E**) The cultured astrocytes were injected in adult mice (P100), as shown on the schematics (green circles). Scale bar, 1 mm. (**F**) Functional maps assessed 14 days after the graft show that OD plasticity after 4 days of MD is enhanced in mice injected with Astros −/− (*n* = 5) compared with mice injected with Astros +/+ (*n* = 6; *P* = 0.038, DF = 9, two-tailed *t* test). Scale bar, 1 mm.

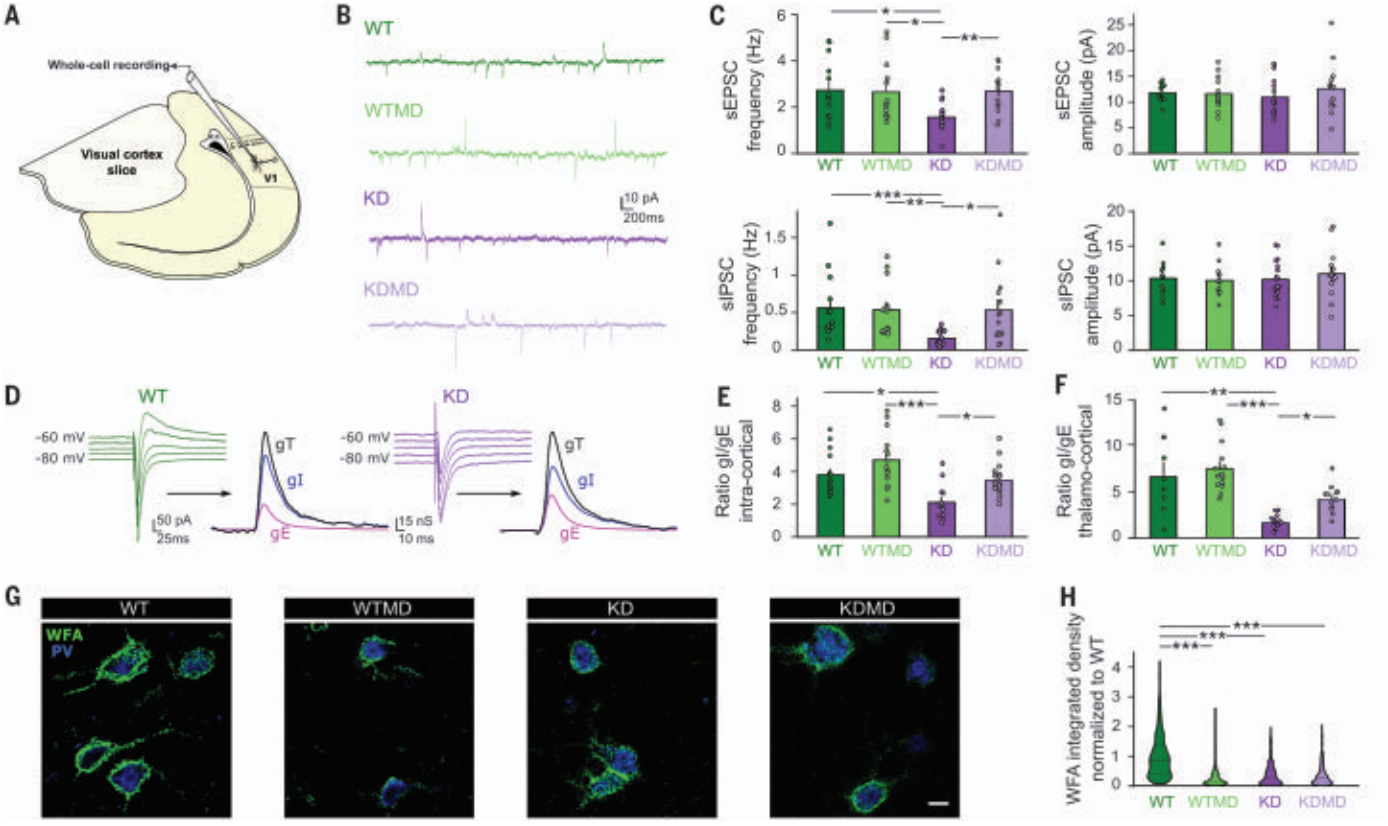

Fig. 3. Astrocytic Cx30 promotes the maturation of inhibitory circuits. (**A**) Schematic diagram depicting the brain slice from which V1 pyramidal neurons from layer 4 were recorded. (**B**) Example traces of sEPSCs (inward) and sIPSCs (outward). (**C**) Frequency, but not amplitude, of both sEPSCs and sIPSCs was decreased in KD (*n* = 17 cells; *P* = 0.0307 for sEPSCs and *P* = 0.009 for sIPSCs) compared with WT mice (*n* = 13 cells). MD induced no plasticity in WT mice (WTMD: *n* = 13 cells; *P* > 0.9999 for sEPSCs, *P* > 0.9999 for sIPSCs), whereas it potentiated both the sEPSCs and sIPSCs in KD mice (KDMD: *n* = 14 cells; *P* = 0.0084 for sEPSCs and *P* = 0.0227 for sIPSCs, Dunn's post hoc test after Kruskal-Wallis, KW = 13.61 for sEPSCs and KW = 20.04 for sIPSCs). (**D**) Example of evoked composite responses at increasing holding potentials allowing decomposition of the total conductance (gT) into excitatory (gE) and inhibitory (gI) conductances in WT and KD mice. (**E**) I/E ratio after intracortical stimulation was reduced in KD mice (*n* = 12 cells; *P* = 0.0143) compared with WT mice (*n* = 16 cells). MD induced no change in WT mice (WTMD: *n* = 14 cells; *P* = 0.78), whereas it increased the I/E ratio in KD mice (KDMD: *n* = 16 cells; *P* = 0.0498, Dunn's post hoc test after Kruskal-Wallis, KW = 19.53). (**F**) I/E ratio after thalamocortical stimulation was reduced in KD mice (*n* = 14 cells; *P* = 0.0029) compared with WT (*n* = 8 cells). MD induced no change in WT mice (WTMD: *n* = 14 cells; *P* > 0.9999), whereas it increased the I/E ratio in KD mice (KDMD: *n* = 12 cells; *P* = 0.0462, Dunn's post hoc test after Kruskal-Wallis, KW = 29.79). (**G** and **H**) WFA immunostaining (G) and violin plot (H) showing smaller PNN around PV interneurons in KD (*n* = 177 cells from 16 mice; *P* < 0.0001), WTMD (*n* = 171 cells from six mice; *P* < 0.0001), and KDMD mice (*n* = 238 cells from six mice; *P* < 0.0001) compared with WT mice (*n* = 295 cells from 19 mice) (Kruskal-Wallis, KW = 247.9, followed by Dunn's multiple comparisons post hoc).

mice. By contrast, this plasticity continued to increase in KD mice until P50, which indicates an impairment in the closure of the critical period (Fig. 2, A and B). Whereas in WT mice this plasticity was the result of an increase in the nondeprived eye response, in KD mice, it resulted from a reduction of the deprived eye response (Fig. 2C), which typically reflects changes occurring in mature and immature systems, respectively (*8*). These data thus indicate that Cx30 is required for proper maturation of the visual cortex. To further test whether the expression of Cx30 in mature astrocytes inhibits OD plasticity, we engrafted mature astocytes expressing or not expressing

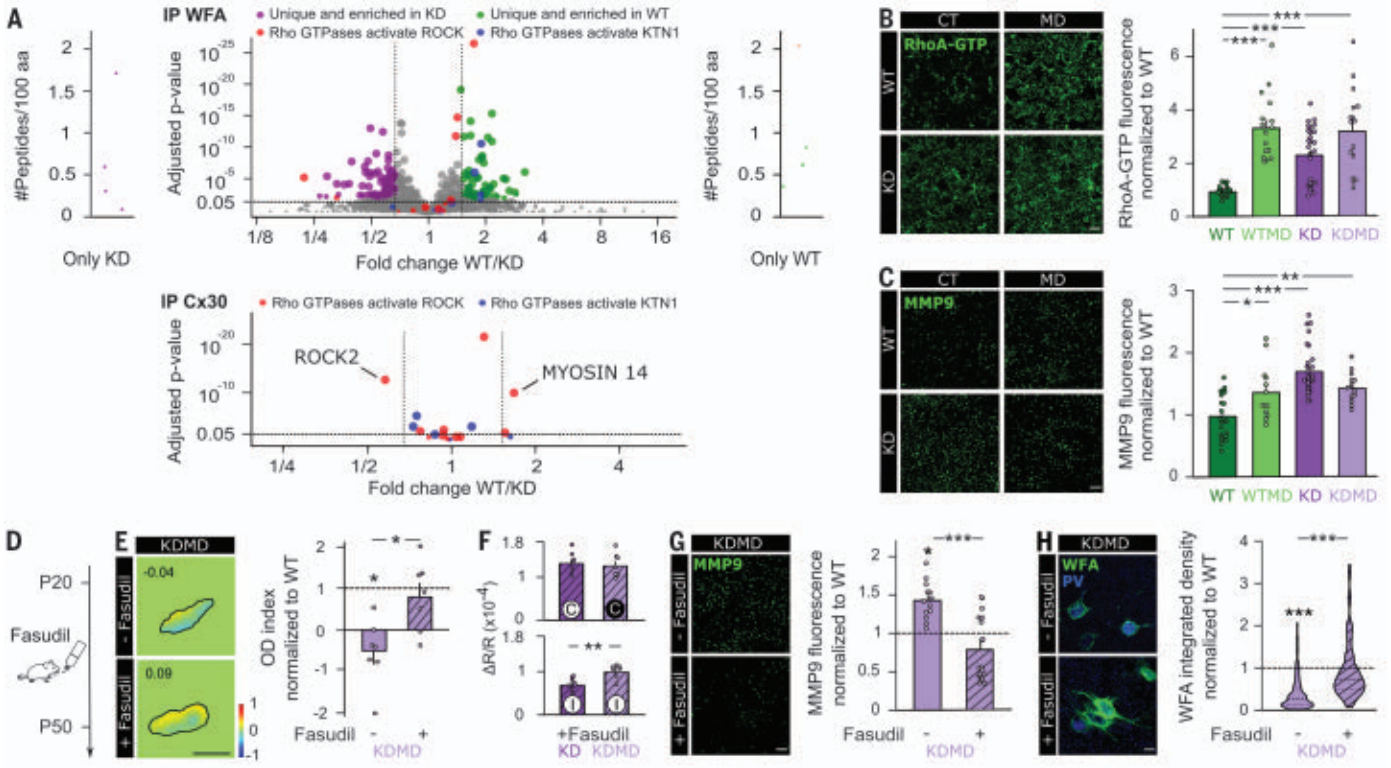

Fig. 4. Astrocytic Cx30 down-regulates the RhoA-MMP9 pathway involved in OD plasticity. (**A**) Identification of WFA and Cx30 binding partners by quantitative label-free mass spectrometry analysis. (Top) Volcano plot representing the 2096 quantified proteins enriched with biotinylated WFA lectin in KD and WT mice (n = 3). Proteins from the enriched pathways Rho-GTPase activate KTN1 (blue) and Rho-GTPase activate ROCK (red) are highlighted. (Bottom) Volcano plot analysis representing interactors of Cx30 from the Rho-GTPase activate KTN1 (blue) and Rho-GTPase activate ROCK (red) pathways. The fold-change in WT (n = 5) versus KD mice (n = 4) is shown with selected proteins (Rock2 and Myosin 14). Dashed vertical and horizontal lines show absolute fold-change of 1.5 and adjusted P value of ratio significance of 0.05, respectively. aa, amino acid. (**B**) Immunostaining for RhoA-GTP showed a marked increase in KD (n = 27; P = 0.0003), KDMD (n = 16; P < 0.0001), and WTMD mice (n = 16; P < 0.0001) compared with WT mice (n = 22) (fields of view from three mice per group) (Kruskal-Wallis, KW = 41.23, followed by Dunn's post hoc test). Scale bar, 10 μm. (**C**) Immunostaining for MMP9 shows a marked increase in KD mice (n = 28; P < 0.0001, DF = 71), KDMD (n = 13; P = 0.0059, DF = 71), and WTMD mice (n = 12; P = 0.0322, DF = 71) compared with WT mice (n = 22) [one-way ANOVA F(3.71) = 15.07 followed by Tukey's post hoc test]. Scale bar, 4 μm. (**D**) Diagram depicting the protocol for experimental treatment with fasudil. (**E** to **H**) Fasudil in KD mice after MD fully rescued WT OD plasticity (E), adult pattern of visual cortex responses to eye stimulation (F), MMP9 levels (G), and PNN extent (H). Contralateral (C) and ipsilateral (I) visual stimulations are indicated with a white (nondeprived eye) or black (deprived eye) circle. Scale bars, 1 mm (E), 4 μm (G), and 10 μm (H). Statistics for (E) OD index: KDMD, n = 6 mice; KDMD + fasudil, n = 7 mice; WTMD, n = 6 mice. P = 0.0343 between KDMD and KDMD + fasudil; P = 0.0215 between WTMD and KDMD; and P = 0.9357 between KDMD + fasudil and WTMD; ANOVA [F(2,16) = 5.534] followed by Tukey's post hoc test. (F) Signal amplitude of visual cortex responses: KD + fasudil, n = 7 mice; KDMD + fasudil, n = 7 mice. Contralateral eye (top): P = 0.7104, U = 21, Mann-Whitney test; ipsilateral eye (bottom): P = 0.0041, U = 3, Mann-Whitney test. (G) MMP9 levels: KDMD, n = 13; KDMD + fasudil, n = 18; WT, n = 22 from three mice (n represents the number of fields of view). P = 0.0001 between KDMD and KDMD + fasudil; P = 0.0124 between WT and KDMD; P = 0.349 between KDMD + fasudil and WT; Kruskal-Wallis (KW = 17.25) followed by Dunn's post hoc test. (H) PNN levels: KDMD, n = 238 PV cells from six mice; KDMD + fasudil, n = 105 PV cells from three mice; WT, n = 295 PV cells from 19 mice. P < 0.0001 between KDMD and KDMD + fasudil; P < 0.0001 between WT and KDMD; P > 0.9999 between WT and KDMD + fasudil; Kruskal-Wallis (KW = 164.7) followed by Dunn's post hoc test.

Cx30. To do so, we isolated astrocytes from P19 WT or constitutive Cx30 knockout mice, then cultured them for 10 days (fig. S6 and Fig. 2, D and E). We found that only the graft of mature astrocytes lacking Cx30 reopened OD plasticity in adult mice (Fig. 2F). Altogether, these data indicate that astrocytic Cx30 controls the timing of the critical-period closure.

Astrocytic Cx30 promotes maturation of inhibitory circuits

The temporal course of the visual cortex critical period is determined by the maturation of local inhibitory circuits controlling the excitation-inhibition (E/I) balance (*14*–*16*). To get insights on the physiological processes by which Cx30 closes the critical period, we measured changes in excitatory and inhibitory synaptic transmission after MD in pyramidal neurons from layer 4 of the visual cortex of WT and KD adult mice (P50) (Fig. 3A). The frequency, but not the amplitude, of both spontaneous excitatory and inhibitory postsynaptic currents (sEPSCs and sIPSCs) was reduced in KD mice compared with WT mice (Fig. 3, B and C), with sIPSCs being significantly more reduced than sEPSCs in KD mice (sIPSCs: −71.42 ± 3.91%; sEPSCs: −42.42 ± 4.89%; n = 17 cells; P = 0.0002, U = 35, Mann-Whitney test). These effects were not a result of changes in pyramidal cell membrane properties (table S5). Furthermore, to ensure that these effects were resulting from synaptic changes per se, we recorded miniature post-synaptic currents (mPSCs) and found that mIPSCs were also more affected than mEPSCs in KD mice (mIPSCs: −61.30 ± 8.35%; mEPSCs: −39.02 ± 4.54%; n = 16 cells; P = 0.01108, U = 61, Mann-Whitney test; fig. S7). Additionally, MD induced an increase in the frequency of

sEPSCs and sIPSCs in KD mice, whereas it had no effect in WT mice, which indicates that experience-dependent plasticity of both excitatory and inhibitory synapses occurs in KD but not in WT adult mice. As excitation and inhibition influence each other through homeostatic processes (*17*), we then assessed whether the E/I balance was affected by analyzing the dynamic conductances of composite synaptic responses evoked by intracortical or thalamocortical stimulation. In both cases, we found the inhibition-excitation (I/E) ratio to be reduced in KD mice (Fig. 3, D to F), which indicates that inhibition is predominantly affected by Cx30 down-regulation. Further, as found for the sEPSC versus sIPSC data, the I/E ratio increased when plasticity was induced through MD. Together, these data suggest that experience-dependent maturation of inhibitory circuits ending the critical period requires astrocytic Cx30. To investigate this possibility, we assessed the maturity of PV interneurons, which settles visual cortex inhibition, by determining the abundance of their perineuronal nets (PNN) of extracellular matrix (ECM) proteins (*11*). We found PNN to be significantly smaller in KD mice (Fig. 3, G and H), which suggests that these cells were immature. Additionally, whereas MD also decreased PNN in WT mice, it had no further effect in KD mice, which is indicative of an occlusion. Together, these data indicate that the increased expression of Cx30 through development during the critical period is required for the timely maturation of visual cortex inhibition.

RhoA-MMP9 pathway down-regulation mediates Cx30 effect

We then sought to identify the molecular pathway through which Cx30 modulates PNN extent and maturation of PV interneurons. To this end, we performed coimmunoprecipitation experiments with biotinylated WFA lectin followed by quantitative proteomics of pulled-down proteins in the visual cortex of WT and KD mice (P50) using label-free mass spectrometry. Reactome pathway analysis of enriched or unique proteins in WT compared with KD samples indicated an enrichment of proteins associated with the Rho–guanosine triphosphatases (GTPases)–KTN1 pathway (table S3 and Fig. 4A, upper panel). Conversely, analysis of proteins unique and enriched in KD compared with WT samples revealed enrichment of the Rho-GTPases–ROCK pathway (table S3 and Fig. 4A). Besides, mass spectrometry analysis of Cx30 coimmunoprecipitates indicated interactions with Rho-GTPases signaling pathways, among which the Rho-associated protein kinase ROCK2 was significantly enriched in KD compared with WT mice (table S4 and Fig. 4A, lower panel). These results suggest a role of the Rho family of GTPases in the PNN differences between WT and KD mice. RhoA, one family member of the Rho-GTPases, plays a role in cell remodeling (*18*) through the activation of ROCKs, and its interactions with different connexins have been described in other cell types (*19*, *20*). We thus investigated the expression of RhoA–GTP (guanosine triphosphate), the active form of RhoA, using immunohistochemistry in layer 4 of the visual cortex, and we found an increase in KD mice (Fig. 4B). Additionally, whereas MD also increased RhoA-GTP in WT mice, it had no further effect in KD mice, which is indicative of an occlusion.

As the RhoA-ROCK pathway can modulate the expression of the ECM-degrading enzyme matrix metalloproteinase 9 (MMP9) (*21*, *22*), we next tested whether this signaling is involved in the Cx30 regulation of PNNs and PV interneuron maturation. To do so, we assessed MMP9 expression in layer 4 of the visual cortex and found that MMP9 levels were increased in KD mice compared with WT mice (Fig. 4C). In addition, akin to RhoA-GTP, whereas MD increased MMP9 levels in WT mice, it had no additional effect in KD mice (Fig. 4C). This suggests that activation of the RhoA-ROCK pathway leads to the degradation of PNNs through MMP9, which promotes OD plasticity. We tested this hypothesis by inhibiting the ROCK signaling pathway in vivo with fasudil (Fig. 4D). Fasudil not only functionally rescued OD plasticity in KD mice to WT levels (Fig. 4E) by restoring the WT adult pattern of visual cortex responses after MD (Fig. 4F), it also fully rescued both MMP9 levels and PNN extent in KD MD mice (Fig. 4, G and H). These data therefore indicate that astrocytic Cx30 regulates OD plasticity through the RhoA-ROCK signaling pathway controlling MMP9 levels and PV cell maturation.

In all, we demonstrate that astrocytes regulate experience-dependent plasticity in the mouse visual cortex during the critical period. We show that astrocytes achieve this through a developmental increase in Cx30 expression, which inhibits expression of MMP9 through the RhoA-ROCK pathway, thereby hindering maturation of local inhibitory neuronal circuits. Thus, astrocytes coordinate the shaping of synaptic circuits that trigger critical-period closure. Beyond its role in regulating the visual critical period, the signaling pathway identified here may also be involved in the structural synaptic plasticity associated with cognitive functions, because Cx30 regulates the structure and efficacy of the tripartite synapse in the hippocampus (*23*). The regulation of MMP9 levels that we describe occurs by means of signaling through Cx30, which regulates the wiring of brain circuits. Because extended critical periods are associated with neurodevelopmental defects resulting in sensorimotor or psychiatric disorders (*24*, *25*), our results may provide a basis for the development of strategies to reinduce a period of enhanced plasticity in adults to favor rehabilitation after brain damage or developmental malfunction.

REFERENCES AND NOTES

1. C. A. Doll, K. Broadie, *Front. Cell. Neurosci.* **8**, 30 (2014).
2. G. Dallérac, J. Zapata, N. Rouach, *Nat. Rev. Neurosci.* **19**, 729–743 (2018).
3. T. Papouin, J. Dunphy, M. Tolman, J. C. Foley, P. G. Haydon, *Phil. Trans. R. Soc. B* **372**, 20160154 (2017).
4. L. E. Clarke, B. A. Barres, *Nat. Rev. Neurosci.* **14**, 311–321 (2013).
5. D. H. Hubel, T. N. Wiesel, *J. Physiol.* **206**, 419–436 (1970).
6. K. Lehmann, S. Löwel, *PLOS ONE* **3**, e3120 (2008).
7. C. M. Müller, J. Best, *Nature* **342**, 427–430 (1989).
8. S. B. Hofer, T. D. Mrsic-Flogel, T. Bonhoeffer, M. Hübener, *Curr. Opin. Neurobiol.* **16**, 451–459 (2006).
9. J. D. Cahoy *et al*., *J. Neurosci.* **28**, 264–278 (2008).
10. G. Ghézali *et al*., *Development* **145**, dev155275 (2018).
11. T. Pizzorusso *et al*., *Science* **298**, 1248–1251 (2002).
12. I. Erchova, A. Vasalauskaite, V. Longo, F. Sengpiel, *Phil. Trans. R. Soc. B* **372**, 20160159 (2017).
13. H. Y. He, B. Ray, K. Dennis, E. M. Quinlan, *Nat. Neurosci.* **10**, 1134–1136 (2007).
14. G. Di Cristo *et al*., *Nat. Neurosci.* **10**, 1569–1577 (2007).
15. T. K. Hensch *et al*., *Science* **282**, 1504–1508 (1998).
16. D. Tropea *et al*., *Nat. Neurosci.* **9**, 660–668 (2006).
17. G. G. Turrigiano, S. B. Nelson, *Nat. Rev. Neurosci.* **5**, 97–107 (2004).
18. C. Gonzalez-Billault *et al*., *Cytoskeleton* **69**, 464–485 (2012).
19. H. J. Kim *et al*., *Int. J. Mol. Sci.* **21**, 1255 (2020).
20. A. Mendoza-Naranjo *et al*., *PLOS ONE* **7**, e37374 (2012).
21. K. J. Jeong *et al*., *Oncogene* **31**, 4279–4289 (2012).
22. L. Tong, V. Tergaonkar, *Biosci. Rep.* **34**, e00115 (2014).
23. U. Pannasch *et al*., *Nat. Neurosci.* **17**, 549–558 (2014).
24. J. J. LeBlanc, M. Fagiolini, *Neural Plast.* **2011**, 921680 (2011).
25. R. M. Meredith, *Neurosci. Biobehav. Rev.* **50**, 180–188 (2015).

ACKNOWLEDGMENTS

The authors thank N. Dufour, C. Joséphine, MIRCen's viral vector facility, G. Sadoc for his help with Elphy, the animal and imaging facilities of College de France, as well as M. Roux from the mouse clinical institute for technical assistance. **Funding:** This work was supported by grants from the European Research Council (consolidator grant no. 683154), European Union's Horizon 2020 research and innovation program (Marie Sklodowska-Curie Innovative Training Networks, grant no. 722053, EU-GliaPhD), and UNADEV-Aviesan to N.R.; from Région Ile-de-France and Fondation pour la Recherche Médicale to D.L.; from College de France to G.D.; from Fyssen Fondation to J.Z.; and from French Research Ministry (Biosigne Doctoral school) to R.B. **Author contributions:** Conceptualization: N.R., G.D., J.R., and C.M.; Data curation: G.D., J.R., R.B., D.L., and N.R.; Formal analysis: G.D., J.R., R.B., P.B., J.Z., V.S., D,L., M.M., and N.R.; Funding acquisition: N.R. and G.D.; Investigation: J.R., R.B., G.D., C.-F.C., F.D., P.E., K.S., J. Z., and N.R.; Methodology: J.R., G.D., and J.M.; Resources: D.L. and A.-P.B.; Supervision: N.R. and G.D.; Project administration: N.R.; Validation: J.R., G.D., and N.R.; Visualization: J.R., R.B., G.D., and N.R.; Writing original draft: G.D. and N.R.; Writing – review and editing: all authors. **Competing interests:** The authors declare no competing interests. **Data and materials availability:** All data are available in the manuscript or the supplementary materials. Reasonable requests for materials sharing will be fulfilled upon completion of a material transfer agreement.

SUPPLEMENTARY MATERIALS

science.sciencemag.org/content/373/6550/77/suppl/DC1
Materials and Methods
Figs. S1 to S8
Tables S1 to S5
References (*26*–*49*)
MDAR Reproducibility Checklist

1 November 2020; accepted 13 May 2021
10.1126/science.abf5273

MESOSCOPIC PHYSICS

Nontopological zero-bias peaks in full-shell nanowires induced by flux-tunable Andreev states

Marco Valentini[1]*, Fernando Peñaranda[2], Andrea Hofmann[1]†, Matthias Brauns[1]‡, Robert Hauschild[1], Peter Krogstrup[3], Pablo San-Jose[2], Elsa Prada[2,4], Ramón Aguado[2]*, Georgios Katsaros[1]*

A semiconducting nanowire fully wrapped by a superconducting shell has been proposed as a platform for obtaining Majorana modes at small magnetic fields. In this study, we demonstrate that the appearance of subgap states in such structures is actually governed by the junction region in tunneling spectroscopy measurements and not the full-shell nanowire itself. Short tunneling regions never show subgap states, whereas longer junctions always do. This can be understood in terms of quantum dots forming in the junction and hosting Andreev levels in the Yu-Shiba-Rusinov regime. The intricate magnetic field dependence of the Andreev levels, through both the Zeeman and Little-Parks effects, may result in robust zero-bias peaks—features that could be easily misinterpreted as originating from Majorana zero modes but are unrelated to topological superconductivity.

The superconducting Bardeen-Cooper-Schrieffer (BCS) density of states (DOS) is characterized by a gap Δ around the Fermi energy that prevents quasiparticle excitations at energies below it. However, in systems with spatially inhomogeneous pairing potentials, such as weak links between two superconductors (SCs), the DOS contains states inside the gap known generically as Andreev bound states (ABSs) (*1*). Such ABSs have been observed in, e.g., carbon nanotubes (*2*, *3*), superconducting atomic point contacts (*4*), graphene (*5*), and hybrid semiconducting-superconducting systems based on nanowires (NWs) (*6*–*15*). ABSs are notable in their own right, as Andreev qubits (*16*, *17*), and for the rich physics they offer; however, the intense research activity of the past few years in the hybrid NW platform has arguably been motivated by the prediction that a topological SC state with Majorana zero modes (MZMs) can be engineered out of them (*18*, *19*) [see also (*20*–*22*) for recent reviews]. Despite the fact that several experiments in such platforms have reported on signatures compatible with MZMs (*23*–*28*), the Majorana interpretation has been challenged because zero-energy ABSs, in the absence of an underlying topological state, can mimic MZMs (*22*, *29*–*38*).

[1]Institute of Science and Technology Austria, Am Campus 1, 3400 Klosterneuburg, Austria. [2]Instituto de Ciencia de Materiales de Madrid (ICMM), Consejo Superior de Investigaciones Científicas (CSIC), Sor Juana Inés de la Cruz 3, 28049 Madrid, Spain. [3]Microsoft Quantum Materials Lab and Center for Quantum Devices, Niels Bohr Institute, University of Copenhagen, Kanalvej 7, 2800 Kongens Lyngby, Denmark. [4]Departamento de Física de la Materia Condensada, Condensed Matter Physics Center (IFIMAC) and Instituto Nicolás Cabrera, Universidad Autónoma de Madrid, E-28049 Madrid, Spain.
***Corresponding author. Email: marco.valentini@ist.ac.at (M.V.); raguado@icmm.csic.es (R.A.); georgios.katsaros@ist.ac.at (G.K.)**
†Present address: Swiss Re Insurance Company Ltd, Mythenquai 50/60, 8002 Zürich, Switzerland. ‡Present address: XARION Laser Acoustics GmbH, Ghegastrasse 3, 1030 Vienna, Austria.

Recently, it has been argued that full-shell NWs (*39*) threaded by a magnetic flux $\phi = AB$, with A the cross section of the NW and B an external axial magnetic field, are an alternative platform for realizing topological superconductivity (*40*). The full-shell geometry has the great advantage that a topological phase can be induced at known and relatively low magnetic fields, typically when ϕ is close to one flux quantum $\phi_0 = h/2e$ [the precise range depends on the geometry of the full-shell NW (*41*); here, h is the Planck's constant and e is the electron's charge]. As shown by experiments (*40*, *42*, *43*), InAs/Al full-shell NWs exhibit flux tunability of the superconducting gap, including its complete destruction and reemergence, owing to the Little-Parks (LP) effect (*44*, *45*). The LP effect is accompanied by zero-bias peaks (ZBPs) in tunneling conductance, which appear in reentrant superconducting regions around $\phi \sim \phi_0$ and have been interpreted as MZMs (*40*). In this study, we use similar InAs/Al full-shell NWs and perform tunneling spectroscopy measurements to investigate the role of the tunneling junction (green region of length X in Fig. 1A) on the subgap spectra. Details on the measured NWs can be found in the supplementary materials and methods (*46*). We use three experimental knobs, the magnetic flux, the junction length X, and the global backgate voltage. Data from more than 40 devices demonstrate that for $X \lesssim 100$ nm, the bare InAs NW acts as a tunnel barrier, whereas for $X \gtrsim 150$ nm, a quantum dot (QD) is formed in the tunnel junction region. Data for 100 nm $\lesssim X \lesssim 150$ nm show that, in this range, a QD may or may not form; we therefore do not work in this tunnel junction length regime. The main text discusses data from five devices, which we refer to as A, B, C, D, and E. Data from eight more devices are presented in the supplementary materials (*46*). All measurements have been performed in a dilution refrigerator with a base temperature of 20 mK.

Short-junction devices

We initially focus on the short-junction devices for which the bare InAs NW plays the role of a tunnel barrier (Fig. 1B). Figure 1C displays the measured differential conductance at zero magnetic field of device A with a short tunnel junction of $X \approx 40$ nm. With increasingly negative V_{bg}, the tunneling conductance at source-drain voltages V below the superconducting gap Δ decreases and reveals a hard gap of size $\Delta \approx 200$ μeV. The line trace shown in Fig. 1E confirms the absence of subgap states and a hard gap with a subgap conductance suppressed by a factor of ~300 relative to the above-gap conductance. Similar tunneling spectroscopy data have been observed for all devices with a junction length $X < 100$ nm (fig. S6). The hardness of the gap and the absence of subgap features make the short-junction devices the best candidates for an unambiguous detection of MZM signatures.

We now discuss transport spectroscopy data as a function of an external parallel magnetic field B. Figure 1D shows the dI/dV evolution (I, current; V, voltage) as a function of B at a fixed value of V_{bg} for device A. The modulation of Δ with B is the result of the destructive LP effect (*42*, *47*, *48*), with regions where the gap is completely suppressed and subsequently regenerated (hereafter, we label the regions with finite gaps as zeroth lobe, first lobe, and so on). Theory predicts the observation of a ZBP in the first lobe, owing to the formation of MZMs (*40*, *41*). Notwithstanding these predictions, none of the nine short-junction devices reported here (Fig. 1 and fig. S6) exhibit a ZBP (or any other subgap state) as the magnetic field increases. Instead, a hard gap slightly smaller than at zero field is observed in the first lobe (Fig. 1F). Possible explanations for the absence of ZBPs in the first lobe include the NWs always being topologically trivial, owing to the renormalization of the semiconductor properties caused by strong coupling to the SC (*49*, *50*), or lack of proper tuning into a topological phase (*41*, *51*, *52*). The described short-junction results seemingly contradict a recent experimental report on MZMs in similar NWs (*40*). However, the lithographic length of the shown tunnel junction in (*40*) seems to be larger than 100 nm and falls into what we call the long-junction regime. In the next section, we discuss how, in this regime, we observe ZBPs of nontopological origin, owing to QD physics.

Long-junction devices

Figure 2A shows a micrograph of device B with $X \approx 240$ nm, for which a QD is formed in the tunnel junction as sketched in Fig. 2B. In this QD-SC system, two ground states (GSs) are accessible: a spin doublet, $|D\rangle$, with spin ½, and a spin singlet, $|S\rangle$, with spin 0. Whether the GS is a doublet or a singlet is determined

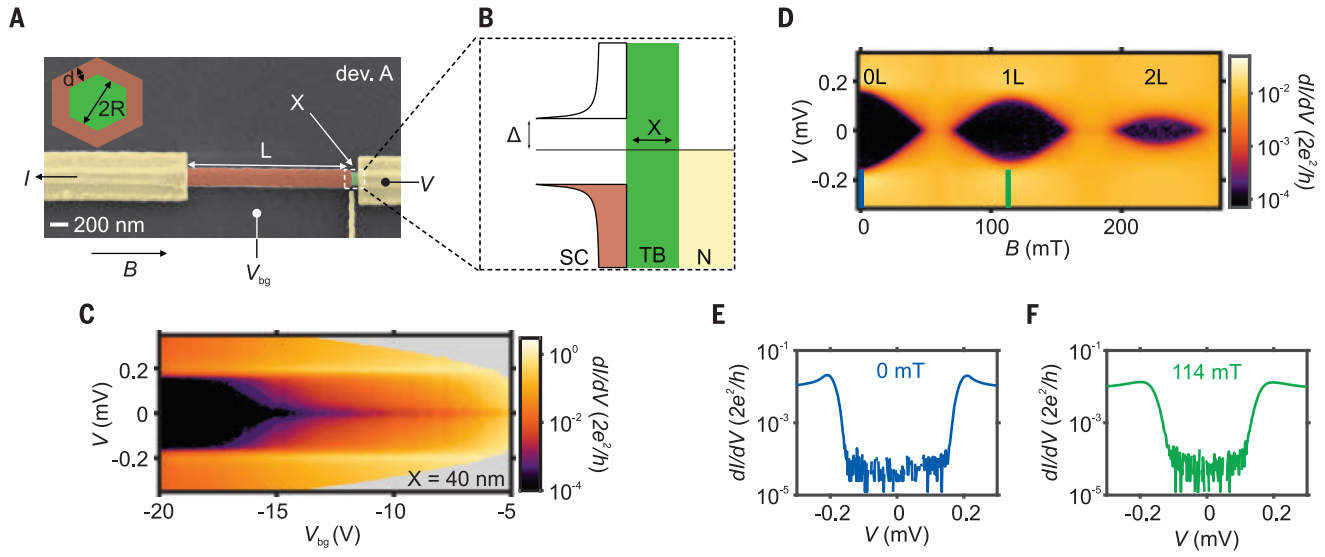

Fig. 1. Tunneling spectroscopy of a short-junction device. (**A**) False-color scanning electron micrograph of device A. A tunnel junction of length $X \approx 40$ nm created in the bare InAs NW (green) is formed between the normal contact (yellow) and the proximitized full-shell NW (red) of length L. It can be tuned by the overall backgate V_{bg} (sidegate is grounded). The electrochemical potential μ inside the full shell cannot be gated because of the Al screening; hence, V_{bg} affects only the tunnel region. A magnetic field B is applied parallel to the NW. The inset shows the hexagonal NW cross section with a semiconducting core radius $R \approx 55$ nm and a shell thickness $d \approx 30$ nm. (**B**) Sketch of a superconductor (SC)–tunnel barrier (TB)–normal metal (N) junction. Our measurements show that no QD is formed in the bare InAs NW for $X \lesssim 100$ nm. (**C**) Differential conductance dI/dV plotted on a logarithmic scale as a function of source-drain bias voltage V and V_{bg}, which tunes the tunnel barrier transparency. (**D**) dI/dV as a function of V and B for device A at $V_{bg} = -17$ V. LP oscillations are observed, where superconducting lobes (denoted 0L, 1L, and 2L) are separated by regions in which superconductivity is completely suppressed. From the shape of the lobes, one can extract the NW dimensions ($R \approx 64$ nm and $d \approx 24$ nm, in good agreement with the nominal values mentioned above) and the coherence length ($\xi \approx 160$ nm), as shown in fig. S5. (**E** and **F**) Linecuts taken from (D) at the center of 0L and 1L, respectively. In both cases, the gap is hard.

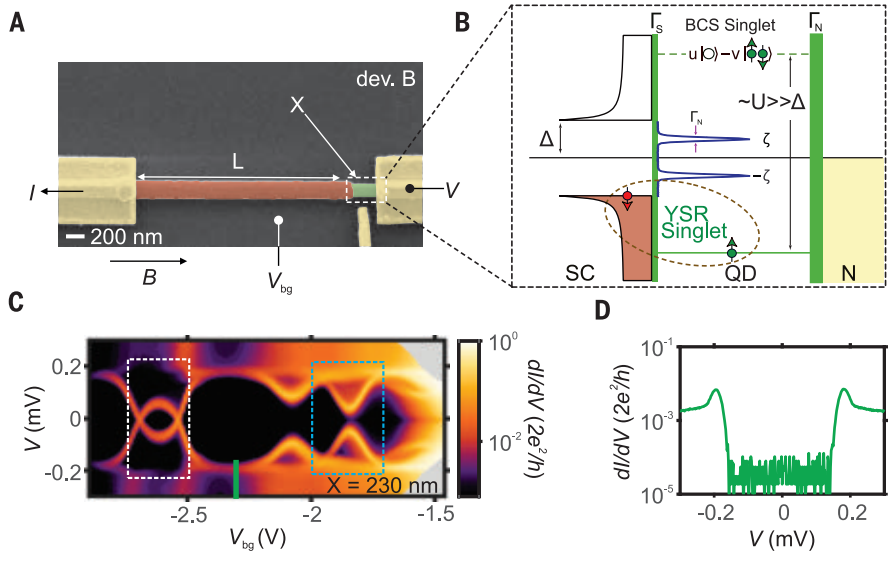

Fig. 2. Tunneling spectroscopy of a long-junction device. (**A**) False-color scanning electron micrograph of device B. The tunnel region of length $X \approx 240$ nm accommodates a QD with charging energy $U \approx 2.5$ meV, as measured from the stability diagram taken at a magnetic field that suppresses superconductivity. (**B**) Sketch of a superconductor (SC)–quantum dot (QD)–normal metal (N) junction, showing all of the physical energy scales involved in this problem—namely, U, the superconducting gap Δ, and the tunnel rates $\Gamma_S/\hbar$ and $\Gamma_N/\hbar$ into the SC and the metal ($\Gamma_{S,N}$ have energy units). For the devices indicated here, $U \gg \Delta$ and the first excited state over the doublet GS at odd occupation is a Kondo-like singlet between the unpaired spin in the QD and the quasiparticles in the SC (YSR singlet). This excitation creates subgap states inside Δ at energies $\pm\zeta$. Another possible excitation is the BCS-like singlet superposition of even charge states in the QD, which, however, is much higher in energy (order ~U). (**C**) dI/dV plotted on a logarithmic scale as a function of V and V_{bg}. White and blue dashed boxes indicate a doublet and a singlet GS region, respectively. (**D**) Linecut extracted from (C) at $V_{bg} = -2.3$ V. Although this device supports ABSs, a hard gap can be observed for certain gate-voltage values.

by the interplay between the Andreev processes at the SC-QD interface and Coulomb blockade (CB), with charging energy U in the QD. CB enforces a one-by-one electron filling, making it possible to have odd electron occupations with a doublet GS (*53*–*56*). The coupling to the SC, Γ_S, on the other hand, favors a singlet GS. Its physical nature depends on the ratio Δ/U. In the large Δ/U limit, the coupling to the SC mainly induces local superconducting correlations in the QD that lead to Bogoliubov-type singlets, which are superpositions of the empty $|0\rangle$ and doubly occupied $|\uparrow\downarrow\rangle$ states in the QD. In the opposite, small Δ/U limit, the unpaired spin in the QD couples to the quasiparticles in the SC (Fig. 2B), with an exchange interaction $J \sim 2\Gamma_S/U$. This exchange interaction creates so-called Yu-Shiba-Rusinov (YSR) singlets, the superconducting counterpart of Kondo singlets (*57*–*60*). For small $J \ll 1$, the GS is a doublet and the YSR singlets occur as discrete

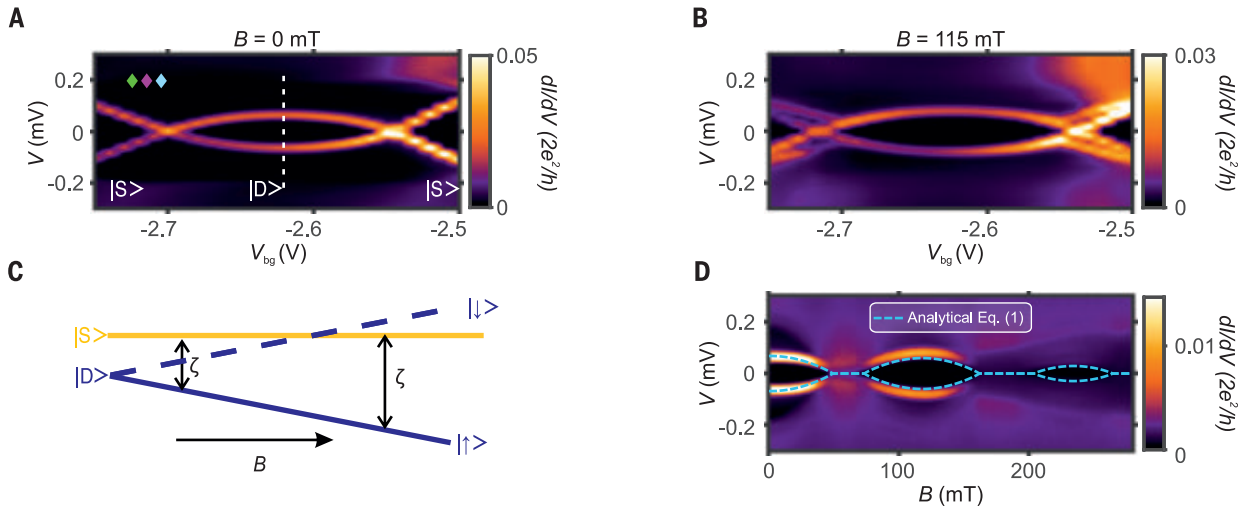

Fig. 3. ABSs in the LP regime with a doublet GS. (**A**) Plot showing a zoomed-in view of the region denoted by the white box in Fig. 2C for device B. From V_{bg} = −2.70 to −2.55 V, the QD is in a doublet GS. Colored diamonds correspond to images in Fig. 4E. (**B**) Same as (A) but for B = 115 mT, at the center of the first lobe; see (D). (**C**) Schematics showing the evolution of the ABSs with a doublet GS when a magnetic field B is switched on. (**D**) dI/dV as a function of V and B for V_{bg} = −2.62 V, at the center of the doublet GS [white dashed line in (A)]. The blue dashed curve corresponds to the analytical level positions given in Eq. 1, showing that these ABSs are of the YSR type [where we use U = 2.5 meV (see Fig. 2 caption), and $\Gamma_S = 0.8\text{meV} = 0.34U$ is inferred from the position of the ABSs at B = 0]. Linecuts taken at different magnetic fields, as well as the Kondo effect observed in the destructive regimes, are discussed in (*46*).

ABS excitations near the edge of the SC gap. A larger J, however, moves these excitations to subgap energies and, eventually, may induce zero-energy crossings when $J \approx 1$, signaling a quantum phase transition (QPT) in which the YSR singlet becomes the new GS. Because our experiments are always in the large U limit (even for the largest gap at $\phi = 0$, we always have $U \gg \Delta$), the YSR regime (*7*–*10*, *56*, *61*, *62*) is the relevant one [for a full theoretical discussion of all physical regimes, see (*46*)]. Transitions between the GS and the first excited state of the system—i.e., between a doublet and a singlet state or vice versa—manifest in transport spectroscopy as a subgap resonance at voltage $V = \zeta$ [and its electron-hole symmetric partner at $V = -\zeta$ (ζ, energy difference between excited state and GS)]. Furthermore, changes in the parity of the GS of the system appear as points in parameter space (here, V_{bg} or B) where ζ changes sign (signaled by the crossing of ABSs at zero energy) (*7*–*10*).

Figure 2C displays the measured differential conductance of the long-junction device B at zero magnetic field. As explained above, a symmetric pair of conductance peaks appears at $|V| < \Delta$. V_{bg} can tune the position of these subgap states that move up and down in energy and can even induce zero-energy crossings that form a characteristic eye-shaped loop (white dashed rectangle), which is the superconducting analog of an odd-occupation CB valley. In the middle of this valley, the system behaves as a spin-½ impurity, which induces YSR physics. Far from the odd valleys, V_{bg} tunes the ABSs to higher energies (green vertical line) where they merge and disappear into the continuum of states. In this region, the line trace in Fig. 2D again reveals a hard gap, with a subgap conductance suppressed by a factor of ~90 relative to the above-gap conductance.

Magnetic field evolution of ABSs in the YSR limit

Next, we consider a doublet GS, occurring in a V_{bg} region between −2.70 and −2.55 V (white box in Fig. 2C). Figure 3A displays a zoomed-in view of this region, illustrating that the gap is clean, apart from a single pair of ABSs at energies $\pm\zeta$. At finite magnetic fields, $|\zeta|$ slightly increases in the doublet region compared with its value at zero field (Fig. 3B). The increasing energy results from the decreasing doublet GS energy, owing to the Zeeman effect. The spin-polarized doublet states change their energy with B by the Zeeman energy $\pm V_Z = \pm g\mu_B B/2$ (with g and μ_B being the g-factor and the Bohr's magneton, respectively), whereas the excited singlet energy remains unaffected (Fig. 3C). Notably, because the GS is spin-polarized, there is only one allowed excitation (vertical arrows in Fig. 3C). This excitation results in a pair of ABSs inside the LP lobes (as opposed to the short junction discussed in Fig. 1). This is illustrated in Fig. 3D, where we show the full magnetic field evolution for fixed V_{bg} = −2.62 V (dashed line in Fig. 3A). This B-field evolution strongly deviates from the linear increase expected for a standard Zeeman effect and stays nearly constant within the zeroth lobe. Because we fix V_{bg} in the middle of the loop (middle of the CB valley), charge fluctuations are substantially suppressed in this configuration, and the system should essentially behave as a spin-½ coupled to a SC. Indeed, by modeling the system as a CB QD coupled to a SC lead (the so-called superconducting Anderson model), we can write an analytic expression for the ABSs in this large-U limit of the form (*46*)

$$\zeta = \pm\Delta(\phi)\frac{1-\left(\frac{2\Gamma_S}{U+V_Z}\right)^2}{1+\left(\frac{2\Gamma_S}{U+V_Z}\right)^2} \qquad (1)$$

where the QD level position is fixed to $\epsilon_0 = -U/2$ to describe the spinful odd CB valley. This equation is the expression for YSR bound states (*60*) written in the language of our system and including the external magnetic flux [through both the LP modulation of the superconducting gap $\Delta(\phi)$ and the Zeeman effect V_Z in the QD]. The dashed blue curves in Fig. 3D are calculated with this analytical expression [where the charging energy U is extracted from the experimental stability diagram in the normal state, $\Delta(\phi)$ is fitted to the experimental LP gap evolution, and the remaining free parameter Γ_S is fixed by the experimental position of the ABS at zero magnetic field]. The good agreement between Eq. 1 and the experiment demonstrates that, indeed, our ABSs are YSR singlets [for comparison, the excitations to the BCS-like singlet $|S\rangle = |0\rangle - |\uparrow\downarrow\rangle$ would occur at a much higher energy, of order $\zeta \approx \pm(U - \Gamma_S)/2 = 0.85$ meV $\gg \Delta$].

Magnetic field evolution of ABSs with a singlet GS: Deep-in-gap limit

We can tune the device to a singlet GS region by making the backgate voltage less negative

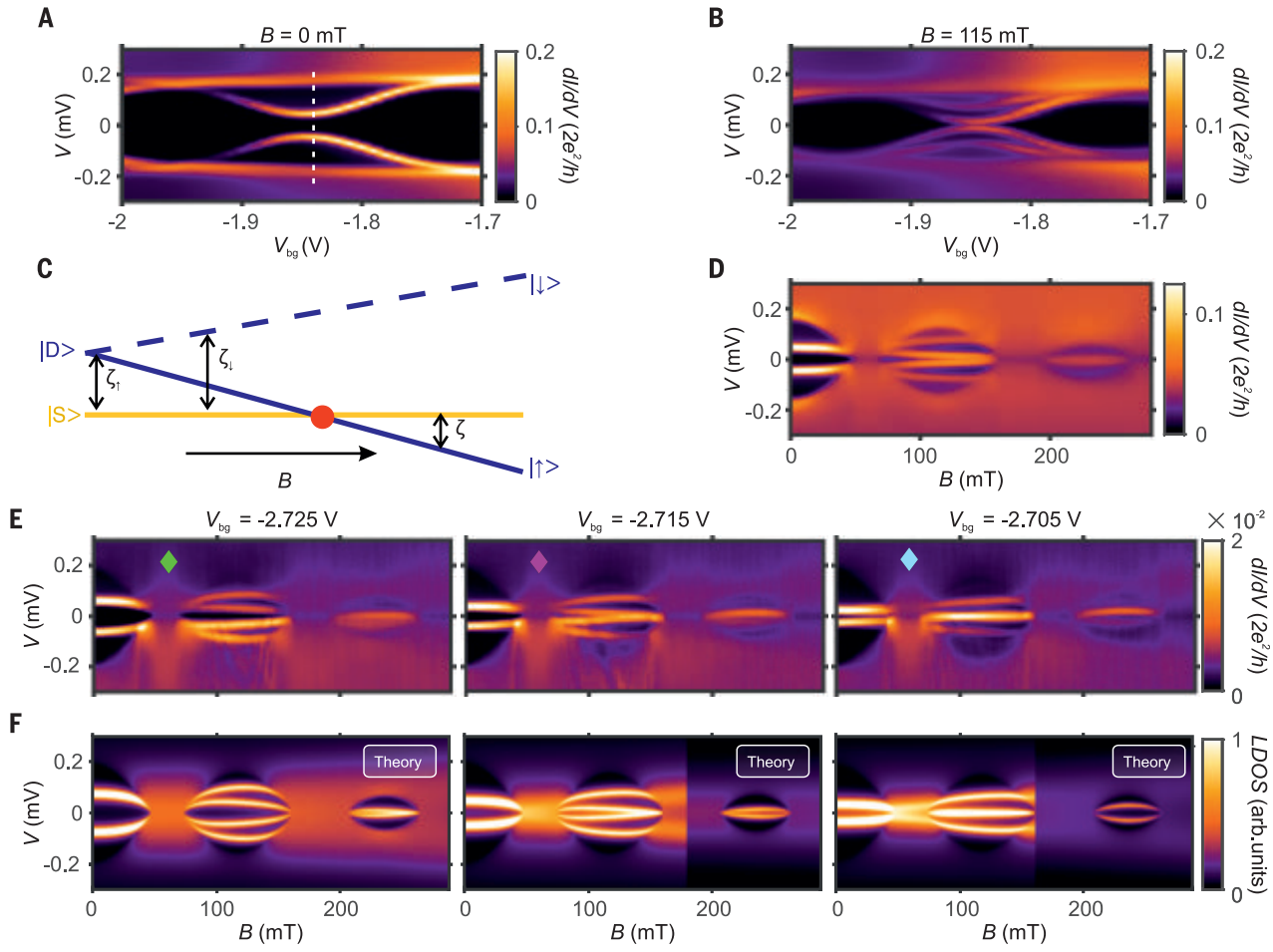

Fig. 4. ABSs in the LP regime with a singlet GS. (**A**) Plot showing a zoomed-in view of the region denoted by the blue dashed box in Fig. 2C around a singlet GS for device B. (**B**) Same as (A) but at finite magnetic field B = 115 mT. The ABSs split, and the splitting depends on V_{bg}. (**C**) Schematics of the ABS behavior with a singlet GS when a magnetic field B is switched on. (**D**) dI/dV as a function of V and B for V_{bg} = −1.84 V [dashed white line in (A)]. A ZBP starts at the end of the 1L and persists throughout all of the 2L, thus extending for more than 100 mT. (**E**) dI/dV plotted on a logarithmic scale as a function of V and B for V_{bg} = −2.725, −2.715, and −2.705 V (left to right); see colored diamonds in Fig. 3A. By changing the ABS position at zero field, it is possible to create a situation in which the ABSs form a ZBP throughout the 1L. (**F**) Numerical simulation of the LDOS versus V and B in a QD-SC system, with the SC in the destructive LP regime and the QD in a singlet GS, for three different gate configurations (parameters in table S1). The QD-SC system is modeled as a superconducting Anderson model, with finite level broadening induced by Γ_N to qualitatively match the experimental dI/dV peak widths.

(see Fig. 2C around V_{bg} = −1.84 V; blue dashed rectangle). The excitations from this singlet GS are doublet-like and hence split under a Zeeman field (*8*), as opposed to the previous case. Figure 4A presents a detailed zoomed-in view of device B in this gate region. Figure 4B shows the same scan but for B = 115 mT (corresponding to the center of the first LP lobe). Because two spin-polarized excitations from the singlet GS are possible (*8*), two pairs of ABSs are observed: one near the gap center and one closer to the gap edge (denoted as $\zeta_\uparrow$ and $\zeta_\downarrow$ in Fig. 4C). The B-field evolution at V_{bg} = −1.84 V (dashed line in Fig. 4A) is displayed in Fig. 4D. In the zeroth lobe, the pair of ABSs neither splits nor moves. By contrast, the ABSs show a clear Zeeman splitting in the first lobe. For increasing magnetic fields, the lowest ABS excitation moves toward zero energy at the end of the first lobe, forming a ZBP. This zero-energy crossing signals a QPT to a spin-polarized doublet GS. The ZBP persists throughout the second lobe, as revealed in Fig. 4D. Our theoretical analysis of this regime supports this interpretation and explains the absence of a clear Zeeman splitting in the zeroth lobe (fig. S3).

We now examine B-field–driven ZBPs in a different parameter regime. We consider the evolution of in-gap ABSs far from the gap edge at B = 0 but close to a singlet-doublet transition enabled by varying V_{bg} (see the three colored diamonds in Fig. 3A). Our results are presented in Fig. 4E. The three subpanels show the evolution in magnetic field of the same pair of ABSs but at slightly different backgate values (fig. S11). As the backgate moves closer to the singlet-doublet zero-energy crossing, the ABS energy decreases. For increasing magnetic fields, this B = 0 energy influences the particular B value at which the excitation reaches zero energy (compare the panels in Fig. 4E from left to right). This gate dependence makes it possible to tune the value of B at which the ZBP emerges. For V_{bg} = −2.705 V (blue diamond), the ZBP appears at the beginning of the first lobe and persists throughout its full extent. The three panels of Fig. 4F show numerical simulations of the local density of states (LDOS) in this regime, whose overall agreement with the tunneling dI/dV spectroscopy is excellent [for technical details on the relation between the two quantities, see (*46*)]. This showcases how ABSs may produce a strong ZBP that persists across a large range of magnetic fields (*8*) as a result of their finite linewidth and the repulsion from the field-modulated gap edge. After the formation of the ZBP, the GS changes from singlet to doublet when the field is increased.

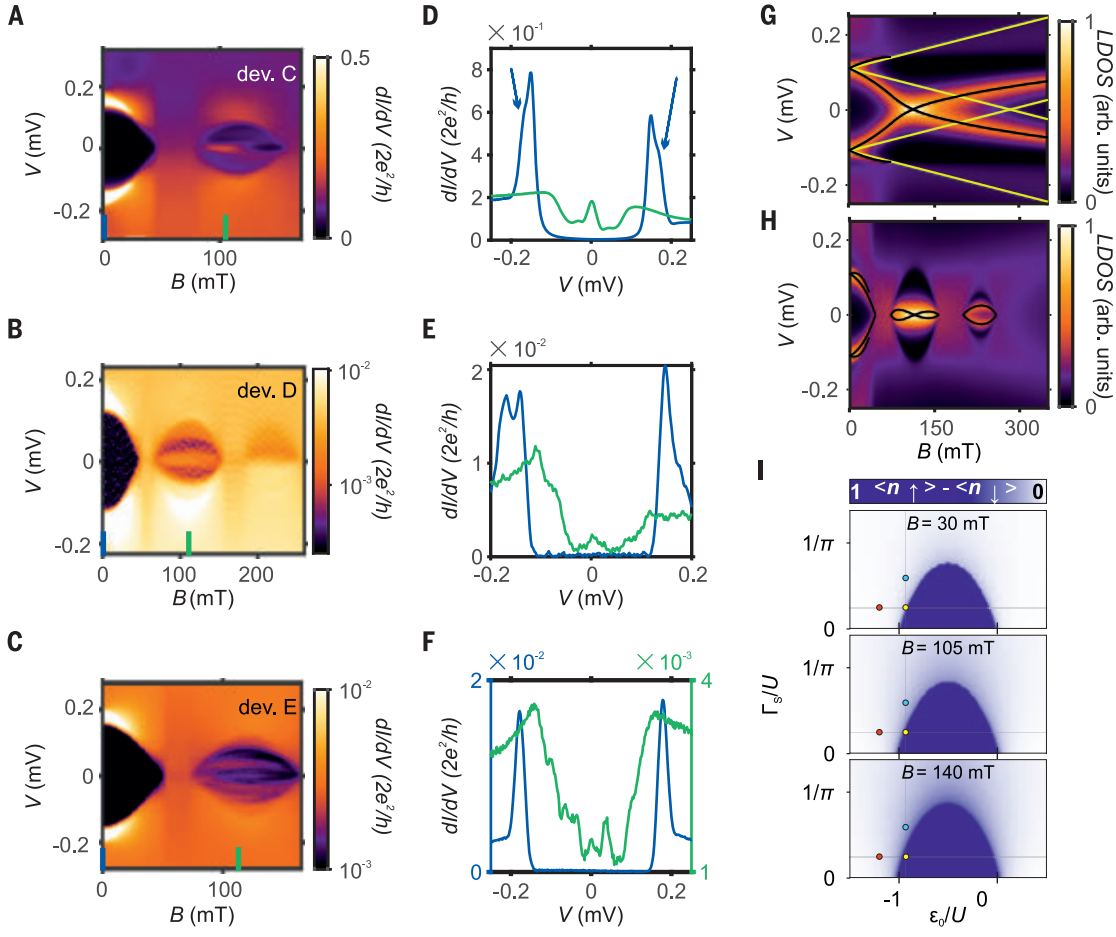

Fig. 5. ZBPs arising from ABSs "hidden" in the superconducting gap edge. (**A** to **C**) *dI/dV* for three different devices as a function of *V* and *B* for V_{bg} = −1.84, −1.27, and −1.89 V, respectively. For (B) and (C), a logarithmic scale has been used. ABSs close to the gap edge at zero field, where the GS is in the singlet state, converge to a ZBP in the 1L. (**D** to **F**) *dI/dV* versus *V* traces extracted from (A) to (C), at *B* = 0 mT (blue) and at the middle of the 1L at *B* = 102, 112, and 123 mT (green), respectively, showing a ZBP. (**G** and **H**) Numerical simulation of the LDOS as a function of *V* and *B* for parameters corresponding to device D. In (G), there is a constant pairing equal to Δ, whereas a destructive LP modulation of the BCS gap is considered in (H). The evolution with *B* of the Green's function poles of a superconducting Anderson model are shown in black. For comparison, we also show in (G) the evolution of the ABS with increasing *B*, assuming that only Zeeman splitting is relevant (yellow lines). The observation of the nonlinear *B* evolution of the ABSs strongly depends on the individual parameters of the device—namely Γ_S, *U*, and their position at *B* = 0. (**I**) Phase diagram of the dot-level spin-polarized occupations $\langle n_\uparrow \rangle - \langle n_\downarrow \rangle$ versus Γ_S/U and ϵ_0/U for three different magnetic fields: *B* = 30, 105, and 140 mT [for the model parameters, see (*46*)]. ϵ_0 is the dot-level energy at zero field. The yellow circle corresponds to the specific configuration in the phase diagram that leads to (H). The singlet-doublet transition line (between white and blue regions) as a function of *B* exhibits a strong dependence on Γ_S/U. As the magnetic field increases, a singlet phase (top) becomes a doublet phase (bottom), across a parity crossing located at *B* = 105 mT (center). The red and blue circles denote similar experimental configurations, but with slightly different gating and coupling to the SC, that never cross the singlet-doublet transition line for the magnetic fields shown.

This spin-polarized YSR doublet again follows Eq. 1 (*46*).

Magnetic field evolution of ABSs with a singlet GS: Near-gap-edge limit

Finally, we turn our attention to devices that show ZBPs without an apparent subgap structure in the zeroth lobe. In Fig. 5, we present data from devices C, D, and E, with tunnel junction lengths of $X \approx 290$, 200, and 300 nm, respectively. Figure 5, A to C, depicts the magnetic field dependence of the respective tunneling spectra, with a ZBP emerging in the first lobe after the first LP closing. Notably, and as opposed to our previous results, no obvious signatures of ABSs can be inferred from the spectra of the zeroth lobe. Taken together, all of these spectroscopic features could be interpreted as originating from MZMs. However, as we argue now, these spectra can also be understood in terms of the magnetic field evolution of ABSs. We note that the *dI/dV* linecuts reveal a sizable bias asymmetry. This breakdown of *dI/dV* particle-hole symmetry can be attributed to the bias dependence of the tunnel barrier transparencies (*63*), an effect that does not enter the LDOS, which is symmetric by construction (Figs. 4E and 5, G and H).

As mentioned, the ZBPs in Fig. 5, A to C, are not preceded by Zeeman-split ABSs, a finding that is seemingly at odds with our previous singlet-doublet transition picture. Moreover, the naive estimation that magnetic field–mediated zero-energy crossings should occur near $V_Z \approx \Delta$ because $|\zeta(B=0)| \sim \Delta$ does not explain the data, which show ZBPs at much smaller Zeeman energies.

To clarify this, we again use our generalized superconducting Anderson model, but now in a different regime where $|\zeta(B=0)| \sim \Delta$ and with a singlet GS close enough in parameter space to the singlet-doublet boundary. Even in the constant pairing case, i.e., neglecting the LP modulation of Δ, the magnetic field evolution of the ABSs strongly differs from that corresponding to a purely Zeeman-driven regime. This is a consequence of the nonzero coupling Γ_S to the SC. Figure 5G illustrates this fact (compare black and yellow curves).

This can be understood from the analytical expression that governs zero-energy parity crossings

$$\tilde{V}_Z = \pm\sqrt{\tilde{\epsilon}^2 + \tilde{\Gamma}_S^2} \qquad (2)$$

where $\tilde{V}_Z \equiv V_Z + \frac{U}{2}(\langle n_\uparrow \rangle - \langle n_\downarrow \rangle)$, $\tilde{\epsilon} \equiv \epsilon_0 + \frac{U}{2}(\langle n_\uparrow \rangle + \langle n_\downarrow \rangle)$, and $\tilde{\Gamma}_S \equiv \Gamma_S + U\langle d_\uparrow d_\downarrow \rangle$. Here $\langle n_\sigma \rangle = \langle d_\sigma^\dagger d_\sigma \rangle$ and $\langle d_\uparrow d_\downarrow \rangle$ are the QD spin-polarized occupations and the anomalous average, respectively. $\tilde{V}_Z$, $\tilde{\epsilon}$, and $\tilde{\Gamma}_S$ can be physically interpreted, respectively, as an exchange field, a level shift, and an effective coupling that are renormalized owing to correlations [for a full derivation, see (*46*, *56*)]. Note that, for large *U*, the finite spin polarization $\langle n_\uparrow \rangle \neq \langle n_\downarrow \rangle$ induced at the singlet-doublet crossing explains the deviation from the pure Zeeman regime governed by V_Z. The same happens for large Γ_S.

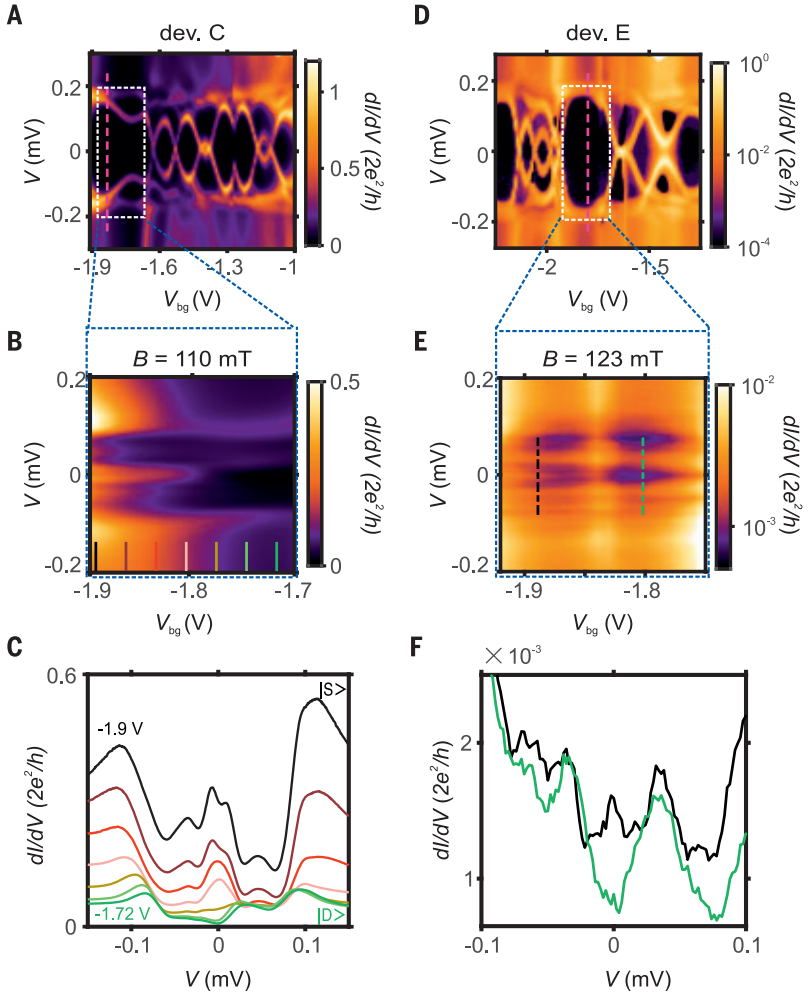

Fig. 6. Gate-voltage dependence of ZBPs. (**A** and **D**) *dI/dV* as a function of *V* and V_{bg} = −1.84*V* in the absence of magnetic field for devices C and E, respectively. The dashed pink lines indicate where the magnetic field scans shown in Fig. 5, A and C, were taken. (**B** and **E**) Zoomed-in views of (A) and (D), but taken at the center of the 1L—i.e., at *B* = 110 and 123 mT, respectively. For (D) and (E), a logarithmic scale has been used. (**C**) Line traces extracted from (B), ranging from V_{bg} = −1.9 V (black) to V_{bg} = −1.72 V (dark green) and shifted by $0.25\frac{e^2}{h}$ with respect to each other. At V_{bg} = −1.8*V*, the ABSs cross zero bias, and the GS becomes a doublet. (**F**) Linecuts extracted from (E) at V_{bg} = −1.89 V (black) and V_{bg} = −1.8 V (dark green). A ZBP is present at V_{bg} = −1.89 V but disappears for higher gate voltages.

It is also notable that the criterion for parity crossings of YSR states in Eq. 2 is essentially the same as the criterion for topological superconductivity in a proximitized NW by just substituting the renormalized QD parameters by the equivalent ones in a NW—i.e., the external Zeeman field, the chemical potential, and the induced superconducting pairing: $\tilde{V}_Z \rightarrow V_Z^{NW}, \tilde{\epsilon} \rightarrow \mu^{NW}$, and $\Gamma_S \rightarrow \Delta^{NW}$ (*18*, *19*). This is yet another example that emphasizes the difficulty of making a clear distinction between parity crossings in QDs and MZMs in NWs. The LP modulation of the gap adds further complexity to the problem [because the ratio $\Delta(B)/U$ evolves with magnetic field], which results in a singlet-doublet transition in the first lobe at *B* = 105 mT (black curves in Fig. 5H) with little resemblance to the original Zeeman-split lines (yellow lines in Fig. 5G). Together with the tunneling broadening Γ_N, this can result in a robust zero-bias anomaly in the LDOS across the first LP lobe (Fig. 5H). Our theoretical analysis shows that the observed ZBPs are actually the result of a magnetic field evolution (the full phase diagrams at three different *B* fields are shown in Fig. 5I).

Indeed, by further investigating the gate-voltage dependence of the observed ZBPs, it can be demonstrated that they do not originate from MZMs. We discuss here the behavior of devices C and E; that of device D is further presented in (*46*). We first focus on the subgap spectrum for a large range of gate voltages at zero magnetic field. Figure 6, A and D, demonstrates that the gap is populated by ABSs. In addition, by measuring the conductance in the middle of the first lobe and sweeping the backgate voltage, one can observe that the ZBP exists only for a certain gate-voltage range (Fig. 6, B and E). This is further highlighted in Fig. 6, C and F. For device C, the gate range over which the ZBP persists can exceed 100 mV. However, as can be seen in Fig. 6C, the ZBP is actually the result of two ABSs merging together and splitting again for voltages around −1.8 V.

Conclusions

In summary, tunneling spectroscopy measurements on hybrid full-shell InAs/Al NWs have shown that, for short-junction devices with $X \lesssim 100$ nm, no ABSs or other subgap states are observed. For long junctions, a rich spectral structure arises in the LP lobes and destructive regimes. When the GS is odd, we demonstrate that the subgap excitations of the system are YSR singlets. In the metallic state within the destructive LP regions, these YSR singlets fully develop a Kondo effect, confirming our interpretation in terms of QDs. When the gap reopens, subgap YSR singlets reemerge. Conversely, when the GS is a singlet, the flux may induce a QPT to a spin-polarized odd GS. This zero-energy fermionic parity crossing leads to a ZBP. Depending on gate conditions, this ZBP can persist for an extended magnetic field range in the first LP lobe around $\phi \sim \phi_0$. When the ABS energy at zero magnetic field is close to the superconducting gap, such robust ZBPs could be mistaken for topological MZMs. The reported measurements demonstrate that, in this system, it is experimentally possible to distinguish ABSs, and their physical character, from MZMs. The competition of various physical phenomena in the same device can produce different QPTs, giving rise to ZBPs in transport spectroscopy in completely different QD parameter regimes. In the future, the reproducible fabrication of devices in which the tunnel junction does not host a QD will allow a controlled and systematic characterization of truly topological ZBPs. This is a critical step to start unveiling and exploiting the exotic physics governing topological superconductivity.

REFERENCES AND NOTES

1. J. A. Sauls, *Philos. Trans. R. Soc. A* **376**, 20180140 (2018).
2. J. Pillet *et al.*, *Nat. Phys.* **6**, 965–969 (2010).
3. A. Eichler *et al.*, *Phys. Rev. Lett.* **99**, 126602 (2007).
4. L. Bretheau, C. O. Girit, H. Pothier, D. Esteve, C. Urbina, *Nature* **499**, 312–315 (2013).
5. T. Dirks *et al.*, *Nat. Phys.* **7**, 386–390 (2011).
6. E. J. H. Lee *et al.*, *Phys. Rev. Lett.* **109**, 186802 (2012).
7. W. Chang, V. E. Manucharyan, T. S. Jespersen, J. Nygård, C. M. Marcus, *Phys. Rev. Lett.* **110**, 217005 (2013).
8. E. J. H. Lee *et al.*, *Nat. Nanotechnol.* **9**, 79–84 (2014).
9. A. Jellinggaard, K. Grove-Rasmussen, M. H. Madsen, J. Nygård, *Phys. Rev. B* **94**, 064520 (2016).
10. E. J. H. Lee *et al.*, *Phys. Rev. B* **95**, 180502 (2017).
11. K. Grove-Rasmussen *et al.*, *Nat. Commun.* **9**, 2376 (2018).
12. Z. Su *et al.*, *Phys. Rev. Lett.* **121**, 127705 (2018).
13. C. Jünger *et al.*, *Commun. Phys.* **2**, 76 (2019).
14. C. Jünger *et al.*, *Phys. Rev. Lett.* **125**, 017701 (2020).

15. Z. Su *et al*., *Phys. Rev. B* **101**, 235315 (2020).
16. C. Janvier *et al*., *Science* **349**, 1199–1202 (2015).
17. M. Hays *et al*., *Nat. Phys.* **16**, 1103–1107 (2020).
18. R. M. Lutchyn, J. D. Sau, S. Das Sarma, *Phys. Rev. Lett.* **105**, 077001 (2010).
19. Y. Oreg, G. Refael, F. von Oppen, *Phys. Rev. Lett.* **105**, 177002 (2010).
20. R. Aguado, *Riv. Nuovo Cim.* **40**, 523–593 (2017).
21. R. M. Lutchyn *et al*., *Nat. Rev. Mater.* **3**, 52–68 (2018).
22. E. Prada *et al*., *Nat. Rev. Phys.* **2**, 575–594 (2020).
23. V. Mourik *et al*., *Science* **336**, 1003–1007 (2012).
24. S. M. Albrecht *et al*., *Nature* **531**, 206–209 (2016).
25. M. T. Deng *et al*., *Science* **354**, 1557–1562 (2016).
26. F. Nichele *et al*., *Phys. Rev. Lett.* **119**, 136803 (2017).
27. H. Zhang *et al*., *Nat. Commun.* **8**, 16025 (2017).
28. Ö. Gül *et al*., *Nat. Nanotechnol.* **13**, 192–197 (2018).
29. E. Prada, P. San-Jose, R. Aguado, *Phys. Rev. B* **86**, 180503 (2012).
30. G. Kells, D. Meidan, P. W. Brouwer, *Phys. Rev. B* **86**, 100503 (2012).
31. C.-X. Liu, J. D. Sau, T. D. Stanescu, S. Das Sarma, *Phys. Rev. B* **96**, 075161 (2017).
32. C. Moore, T. D. Stanescu, S. Tewari, *Phys. Rev. B* **97**, 165302 (2018).
33. C. Reeg, O. Dmytruk, D. Chevallier, D. Loss, J. Klinovaja, *Phys. Rev. B* **98**, 245407 (2018).
34. J. Chen *et al*., *Phys. Rev. Lett.* **123**, 107703 (2019).
35. A. Vuik, B. Nijholt, A. R. Akhmerov, M. Wimmer, *SciPost Phys.* **7**, 061 (2019).
36. J. Avila, F. Peñaranda, E. Prada, P. San-Jose, R. Aguado, *Commun. Phys.* **2**, 133 (2019).
37. H. Pan, S. Das Sarma, *Phys. Rev. Res.* **2**, 013377 (2020).
38. J. Cayao, E. Prada, P. San-Jose, R. Aguado, *Phys. Rev. B* **91**, 024514 (2015).
39. W. Chang *et al*., *Nat. Nanotechnol.* **10**, 232–236 (2015).
40. S. Vaitiekėnas *et al*., *Science* **367**, eaav3392 (2020).
41. F. Peñaranda, R. Aguado, P. San-Jose, E. Prada, *Phys. Rev. Res.* **2**, 023171 (2020).
42. S. Vaitiekėnas, P. Krogstrup, C. M. Marcus, *Phys. Rev. B* **101**, 060507 (2020).
43. D. Sabonis *et al*., *Phys. Rev. Lett.* **125**, 156804 (2020).
44. G. Schwiete, Y. Oreg, *Phys. Rev. B* **82**, 214514 (2010).
45. N. Shah, A. Lopatin, *Phys. Rev. B* **76**, 094511 (2007).
46. See supplementary materials.
47. W. A. Little, R. D. Parks, *Phys. Rev. Lett.* **9**, 9–12 (1962).
48. Y. Liu *et al*., *Science* **294**, 2332–2334 (2001).
49. C. Reeg, D. Loss, J. Klinovaja, *Phys. Rev. B* **97**, 165425 (2018).
50. A. E. G. Mikkelsen, P. Kotetes, P. Krogstrup, K. Flensberg, *Phys. Rev. X* **8**, 031040 (2018).
51. B. D. Woods, S. Das Sarma, T. D. Stanescu, *Phys. Rev. B* **99**, 161118 (2019).
52. A. A. Kopasov, A. S. Mel'nikov, *Phys. Rev. B* **101**, 054515 (2020).
53. E. Vecino, A. Martín-Rodero, A. Levy Yeyati, *Phys. Rev. B* **68**, 035105 (2003).
54. T. Meng, S. Florens, P. Simon, *Phys. Rev. B* **79**, 224521 (2009).
55. R. S. Deacon *et al*., *Phys. Rev. Lett.* **104**, 076805 (2010).
56. R. Z. Žitko, J. S. Lim, R. López, R. Aguado, *Phys. Rev. B* **91**, 045441 (2015).
57. L. Yu, *Acta Phys. Sin.* **21**, 75 (1965).
58. H. Shiba, *Prog. Theor. Phys.* **40**, 435–451 (1968).
59. A. Rusinov, *Sov. Phys. JETP* **9**, 85–87 (1969).
60. A. V. Balatsky, I. Vekhter, J.-X. Zhu, *Rev. Mod. Phys.* **78**, 373–433 (2006).
61. V. Koerting, B. M. Andersen, K. Flensberg, J. Paaske, *Phys. Rev. B* **82**, 245108 (2010).
62. G. Kiršanskas, M. Goldstein, K. Flensberg, L. I. Glazman, J. Paaske, *Phys. Rev. B* **92**, 235422 (2015).
63. A. Melo, C.-X. Liu, P. Rożek, T. Ö. Rosdahl, M. Wimmer, *SciPost Phys.* **10**, 037 (2021).
64. M. Valentini, Research data for: Non-topological zero bias peaks in full-shell nanowires induced by flux tunable Andreev states, IST Austria Research Explorer (2021); https://doi.org/10.15479/AT:ISTA:9389.
65. F. Peñaranda, Simulation code for: Non-topological zero bias peaks in full-shell nanowires induced by flux tunable Andreev states, Zenodo (2021); https://doi.org/10.5281/zenodo.4768060.

ACKNOWLEDGMENTS

The authors thank A. Higginbotham, E. J. H. Lee, and F. R. Martins for helpful discussions. **Funding:** This research was supported by the Scientific Service Units of IST Austria through resources provided by the MIBA Machine Shop and the nanofabrication facility; the NOMIS Foundation and Microsoft; the European Union's Horizon 2020 research and innovation program under the Marie Skłodowska-Curie grant agreement 844511; the FETOPEN grant agreement 828948; the European Research Commission through grant agreement HEMs-DAM 716655; the Spanish Ministry of Science and Innovation through grants PGC2018-097018-B-I00, PCI2018-093026, FIS2016-80434-P (AEI/FEDER, EU), RYC-2011-09345 (Ramón y Cajal Programme), and the María de Maeztu Programme for Units of Excellence in R&D (CEX2018-000805-M); and the CSIC Research Platform on Quantum Technologies PTI-001. **Author contributions:** M.V. and G.K. designed the experiment. M.V. fabricated the devices, performed the measurements, and analyzed the data under the supervision of G.K. M.B. and R.H. contributed to the device fabrication. P.K. developed the NW materials. M.V., G.K., A.H., F.P., P.S.-J., E.P., and R.A. discussed the data and contributed to their interpretation. F.P. performed the numerical simulations, with input from P.S.-J., E.P., and R.A. The analytics and interpretation of the YSR limit were developed by R.A. All authors contributed to the writing of the manuscript. **Competing interests:** The authors declare no competing interests. **Data and materials availability:** All experimental data included in this work and related to this work but not explicitly shown in the paper are available via the IST Austria repository (*64*). Data and plot scripts from the theoretical analysis can be found online (*65*).

SUPPLEMENTARY MATERIALS

science.sciencemag.org/content/373/6550/82/suppl/DC1
Supplementary Text
Additional Experimental Data
Figs. S1 to S14
Tables S1 and S2
References (*66*–*83*)

7 October 2020; accepted 21 May 2021
10.1126/science.abf1513

REPORTS

APPLIED PHYSICS

Monolithic optical microlithography of high-density elastic circuits

Yu-Qing Zheng[1]†, Yuxin Liu[2]†, Donglai Zhong[1]†, Shayla Nikzad[1], Shuhan Liu[1], Zhiao Yu[1,3], Deyu Liu[1], Hung-Chin Wu[1], Chenxin Zhu[1], Jinxing Li[1], Helen Tran[1], Jeffrey B.-H. Tok[1], Zhenan Bao[1]*

Polymeric electronic materials have enabled soft and stretchable electronics. However, the lack of a universal micro/nanofabrication method for skin-like and elastic circuits results in low device density and limited parallel signal recording and processing ability relative to silicon-based devices. We present a monolithic optical microlithographic process that directly micropatterns a set of elastic electronic materials by sequential ultraviolet light–triggered solubility modulation. We fabricated transistors with channel lengths of 2 micrometers at a density of 42,000 transistors per square centimeter. We fabricated elastic circuits including an XOR gate and a half adder, both of which are essential components for an arithmetic logic unit. Our process offers a route to realize wafer-level fabrication of complex, high-density, and multilayered elastic circuits with performance rivaling that of their rigid counterparts.

Skin-like and elastic electronics that conform to biological tissue and accommodate body movements are ideal for on-skin sensors (*1*–*3*), body area networks (*4*, *5*), and implantable bioelectronics (*6*, *7*). Relative to conventional rigid electronics, such as silicon-based devices, elastic electronics are currently limited with respect to parallel signal recording and processing because of low device density. Therefore, bio-integrated electronics typically adopt a hybrid approach of integrating rigid and stretchable parts (*8*–*10*), but this hybrid approach results in localized stress at rigid-soft interfaces and mismatch in mechanical properties when in contact with biological systems. To construct fully elastic sensing systems, rigid chips in direct contact with biological systems should be replaced by elastic ones. The main limitation to making dense circuits is the lack of scalable patterning methods for polymeric electronic materials, especially for micro/nanopatterning soft and elastic electronic materials into complex, high-density, multilayered functional devices and circuits (*11*–*13*).

A staple technique in the silicon-based semiconductor industry, photolithography, has successfully enabled shrinking of the channel length of silicon transistors down to the nanometer scale, thus allowing highly integrated circuit fabrication. Unfortunately, conventional photolithography does not accommodate micro/nanofabrication of polymeric electronic materials (e.g., semiconductors and conductors) because the photoresists used in photolithography lack chemical orthogonality with active polymeric electronic materials (*14*, *15*). Although solution processing of polymeric materials allows ease of fabrication at low production cost (such as screen or inkjet printing), these

[1]Department of Chemical Engineering, Stanford University, Stanford, CA 94305, USA. [2]Department of Bioengineering, Stanford University, Stanford, CA 94305, USA. [3]Department of Chemistry, Stanford University, Stanford, CA 94305, USA.
***Corresponding author. Email: zbao@stanford.edu**
†These authors contributed equally to this work.

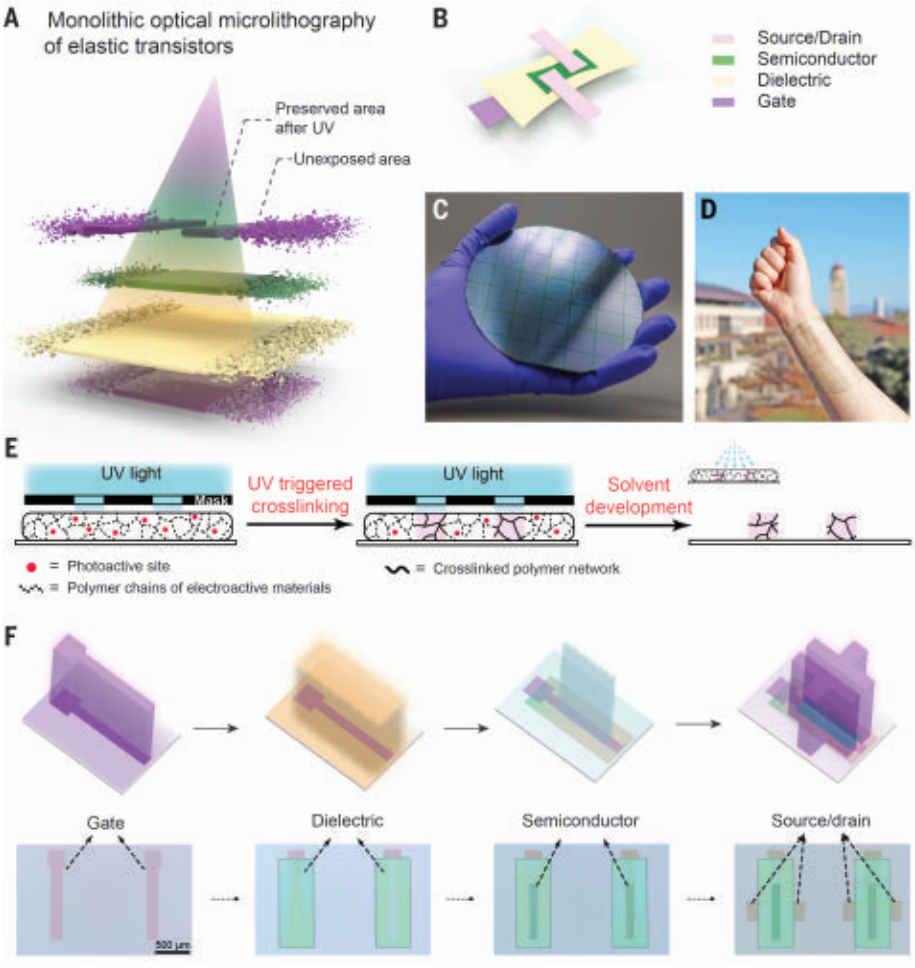

Fig. 1. Monolithic optical microlithography for high-density elastic circuits. (**A**) Schematic illustration of monolithic optical microlithography. Elastic electronic materials are directly patterned sequentially by a series of UV light–triggered solubility modulation processes. The UV-exposed area has substantially reduced solubility and thus is preserved after the solvent development process. (**B**) Device configuration of elastic transistors with bottom gate and top contact. (**C**) Photograph of a 4-inch wafer-scale elastic circuit array fabricated by monolithic optical microlithography. (**D**) Photograph showing appearance of elastic circuit array released from a supportive wafer and attached to a human forearm. (**E**) General mechanism of the PhotoAssist strategy for direct optical lithography of elastic electronic materials based on UV-triggered crosslinking. (**F**) Monolithic optical microlithography process for sequential patterning of each layer in an elastic transistor (top) and optical image for each step (bottom).

are low-density patterning techniques with spatial resolution of hundreds of micrometers (*16*–*18*).

To address these limitations, we describe a monolithic optical microlithographic process (termed PhotoAssist) for high-density production of elastic circuits. This process involves direct optical lithography on polymeric electronic materials (Fig. 1, A to D). We took advantage of both the post-functionalization property of polymeric materials and the benefits of traditional photolithography, including high spatial resolution and low cost per patterned element. PhotoAssist directly patterns multiple electroactive materials via a sequence of ultraviolet (UV) light exposures without the need for photoresist and stripping processes. Specifically, we used an efficient light-triggered carbene insertion reaction as a general crosslinking method for semiconducting polymers and insulating polymers (Fig. 1E). In addition, we introduced UV-sensitive polyethylene glycol dimethacrylate (PEGDMA) to realize double network–mediated direct optical lithography of a chemically unmodified conducting polymer. All our polymer-based transparent elastic electronics were fabricated through only four steps of direct optical microlithography, without the need for additional protection, etching, transfer, or lamination processes (Fig. 1F). The crosslinking-based patterning strategy enabled robust immobilization of each layer and chemical resistance, thus enabling layer-by-layer sequential deposition at wafer scale.

Typical conducting polymers such as poly (3,4-ethylenedioxythiophene) polystyrene sulfonate (PEDOT:PSS) have limited reaction sites for direct covalent crosslinking. Therefore, we used a "double network" physical crosslinking strategy for direct optical lithography to pattern PEDOT:PSS with high spatial resolution. We hypothesized that solubility modulation of PEDOT:PSS can be realized through embedding of a physical crosslinked conductive network into a covalently crosslinkable PEGDMA network. We observed that the strong interaction between PEDOT and PEG linker resulted in a microstructure transition of PEDOT:PSS from a core-shell structure into more extended chains, thus forming the first conductive network (Fig. 2A). After UV light (365 nm) initiation, the dimethyl acrylate (DMA)–modified PEG undergoes a rapid radical polymerization to form the second network. The strong intermolecular interaction between the two networks enabled the UV-exposed regions to be resistant to subsequent water development, whereas the UV-unexposed regions remained water-soluble.

We observed that the photopatternability is highly dependent on the PEGDMA/PEDOT weight ratio, which needs to be in the range 1.10:1 to 1.58:1 (Fig. 2B and supplementary text). Films with insufficient PEGDMA (<1.10:1 versus PEDOT) did not become insoluble against developer, whereas excessive PEGDMA (>1.58:1 versus PEDOT) led to undesirable physical crosslinking before UV exposure. With the addition of more PEG linkers, the PEDOT π-π stacking distance gradually decreased and larger crystallites were formed as a result of the stronger interchain coupling between PEDOT molecules (Fig. 2, C and D, and figs. S2 and S3). Atomic force microscopy images confirmed that when 1.10:1 PEGDMA/PEDOT was added to PEDOT:PSS, the morphology of PEDOT:PSS changed from a featureless film (fig. S4) to interconnected PEDOT fibers. Such microstructure change confirms that a physically crosslinked PEDOT network with denser

packing can be retained within a secondary chemically crosslinked PEG network formed under UV, endowing the system with UV-modulated solubility (fig. S5). By mixing 1.15:1 PEGDMA/PEDOT and 5% weight ratio of water-soluble initiator versus PEGDMA, we achieved a negative PEDOT:PSS pattern after UV light (365 nm) exposure and subsequent development with water. High-resolution PEDOT:PSS patterns with feature sizes down to 2 μm, which include fine lines (line width = 2 μm) and narrow gaps between lines (gap width = 2 μm) (Fig. 2, E and F, and figs. S6 and S7), were demonstrated.

Addition of PEGDMA also substantially increased the PEDOT:PSS conductivity; the PEDOT formed closer stacking and a more interconnected nanofiber network, and the insulating PSS shell was reduced (Fig. 2G). The conductivity was enhanced from 12.0 ± 3.1 S/m for the original PEDOT:PSS to 3.15 ± 0.68 kS/m for PEDOT:PSS with 1.29:1 PEGDMA/PEDOT. We also observed that methanol treatment further improved the conductivity to 52.5 ± 1.69 kS/m.

Direct optical lithography of both semiconducting and insulating polymers was accomplished by chemical crosslinking via UV-triggered reactions (Fig. 3A). To prevent degradation of the semiconducting polymer charge transport properties, the light-triggered crosslinking reaction needs to be specific to the nonconjugated side chains without breaking the conjugation in the backbone. Inspired by photoaffinity labeling in biological applications (*19*, *20*), we introduced a double-end functionalized trifluoromethyl-substituted diazirine crosslinker (branched-diazirine crosslinker) into the semiconducting polymer films (Fig. 3A). Carbene species formed by rapid photolysis can undergo a clean reaction specific to nonconjugated bonds on side chains of conjugated polymers, leading to increased molecular weight and therefore UV-induced solubility modulation (*21*, *22*). A branched alkyl chain was selected as the linker to reduce crosslinker crystallization and to improve miscibility with semiconducting polymers for efficient photo-crosslinking and greater film deformability (*23*). Carbene generation and reaction could be achieved during UV radiation (365 nm) with a dose of 720 mJ cm^{-2} (figs. S11 and S12). Unchanged positions and integrals of ^{1}H peaks corresponding to thiophene groups (8.9, 7.7, and 7.3 ppm) in nuclear magnetic resonance spectra suggest that carbene does not react with the π-conjugated core (fig. S13). Instead, the main photo-crosslinking products are from insertion of carbene into nonconjugated C-H bonds, as evidenced by the disappearance of CH_2 (symmetric stretching υ_s = 2854 cm^{-1}; asymmetric stretching υ_{as} = 2926 cm^{-1}) and CH_3 (υ_{as} = 2957 cm^{-1}) in Fourier-transform infrared spectroscopy (Fig. 3C). Therefore, the photoreactions of the branched-diazirine crosslinker are deemed "electronically clean" and are compatible with semiconducting polymer applications. Moreover, activation and decomposition of the branched-diazirine crosslinker occurred at 120°C and >350°C, respectively (figs. S14 and S15), providing a wide processing window for subsequent thermal annealing steps.

Photo-crosslinking efficiency varies with polymer molecular weight (Fig. 3B). Polymers with higher molecular weight and therefore lower initial solubility require a lower crosslinker concentration to achieve full insolubility against the developing solvent. As a representative semiconducting polymer, diketopyrrolopyrrole (DPP)–based conjugated polymer, poly(tetrathienoacene-diketopyrrolopyrrole) (PTDPPTFT4), is used here as a model compound for photo-crosslinking efficiency measurement. We observed that when the molecular weight of the DPP polymer was equal to or higher than 49,000, less than 10 wt% of branched-diazirine crosslinker was needed to realize 99% film retention. Semiconducting polymers containing patterns with feature sizes down to 4 μm were successfully obtained using the carbene-mediated direct optical lithography process (Fig. 3D and fig. S16). The resolution can be further improved by lowering the molecular weight distribution. The branched-diazirine crosslinker was shown to be effective as a general crosslinker that can be used to pattern all common alkylated conjugated polymers, including poly(3-hexylthiophene) (P3HT),

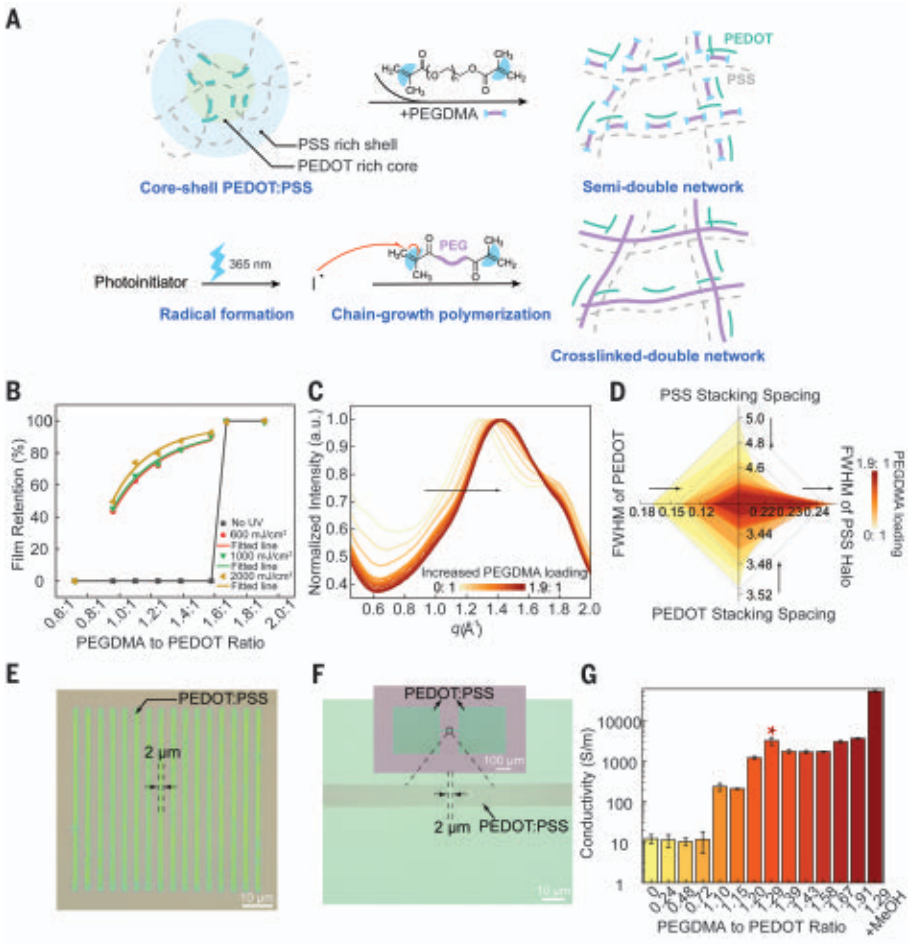

Fig. 2. Double network–mediated direct optical lithography of conductive polymers. (**A**) Mechanism of direct optical lithography of PEDOT:PSS by selective crosslinking of PEGDMA to form a double network that is insoluble in water. (**B**) Gel curves of PEDOT:PSS with different amounts of PEGDMA under different doses of UV exposure. (**C**) Polarization-corrected meridian line cuts from 2D grazing incidence x-ray diffraction (GIXD) for films spin-cast from PEDOT:PSS solutions mixed with different amounts of PEGDMA versus PEDOT. (**D**) Radar chart displaying PSS π-π stacking distance, PEDOT π-π stacking distance, full width at half maximum (FWHM) of PSS scattering halo, and FWHM of PEDOT scattering halo determined from GIXD of UV-exposed PEDOT:PSS/PEGDMA films. (**E**) Optical image of a representative PEDOT:PSS fine line pattern with 2-μm resolution by direct optical lithography. (**F**) Optical image of a PEDOT:PSS pattern with a 2-μm gap by direct optical lithography. (**G**) Dependence of UV-exposed PEDOT:PSS/PEGDMA film conductivity on proportion of PEGDMA. Error bars denote SD. The sample marked as 1.29+MeOH is with 1.29:1 weight ratio of PEGDMA versus PEDOT and is treated with methanol after crosslinking.

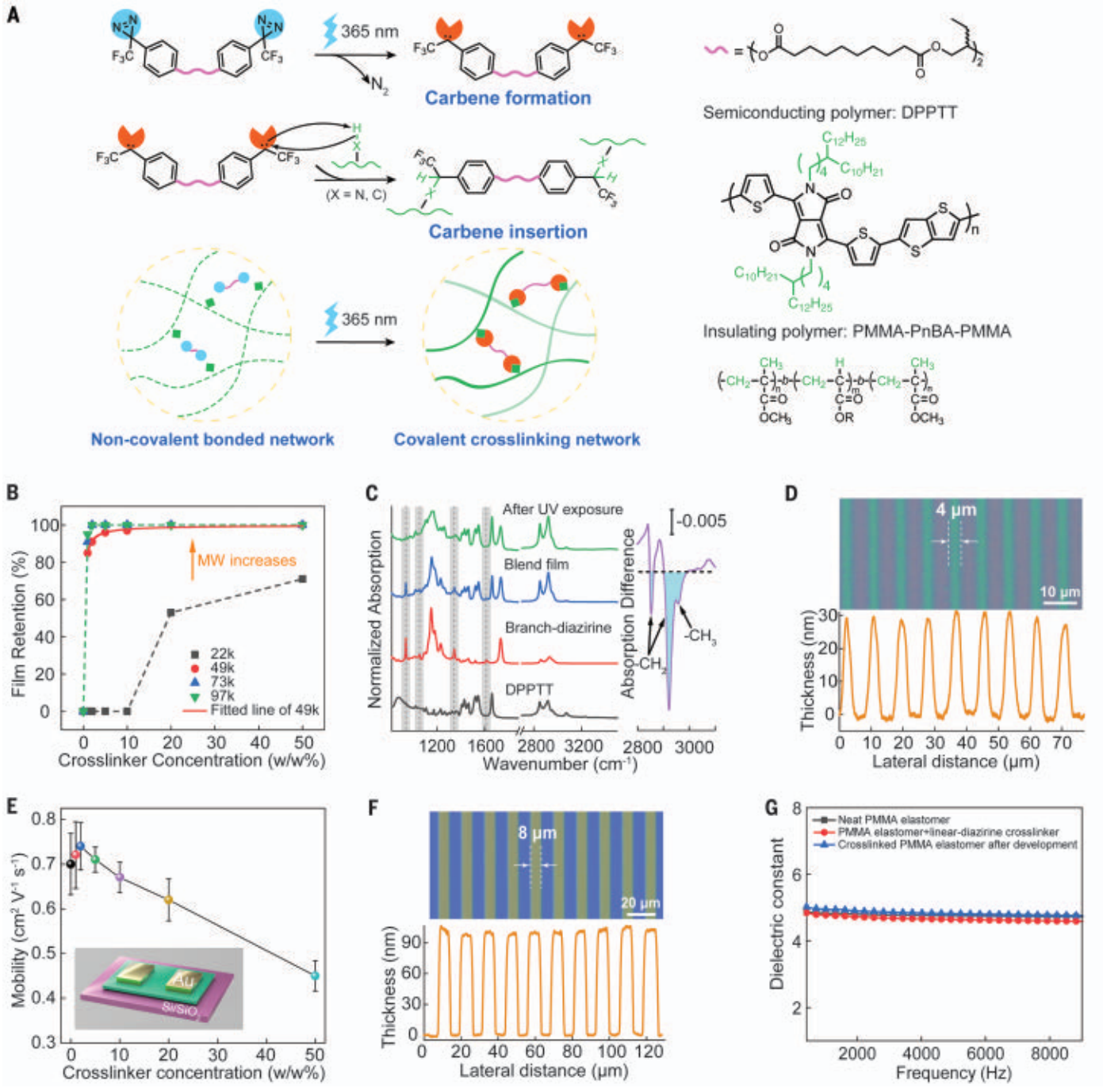

Fig. 3. Carbene-mediated direct optical lithography of semiconducting and insulating polymers. (**A**) Mechanism of direct optical lithography for semiconducting and dielectric polymers based on UV-triggered carbene insertion crosslinking. (**B**) Gel curves of representative semiconducting DPP polymer with different molecular weights mixed with different amounts of branched-diazirine crosslinker (0, 1, 2, 5, 10, 20, and 50 wt% versus DPP polymer) under different doses of UV exposure. Film retention percentage is the ratio of crosslinked film thickness before developing versus after developing. (**C**) Left: Fourier-transform infrared spectrum of neat DPPTT, neat branched-diazirine crosslinker, DPPTT with 20 wt% of branched-diazirine crosslinker blend, and UV-crosslinked blend. Right: Photoreaction spectra obtained as the difference before and after UV exposure, showing branched-diazirine reaction with -CH_2 and -CH_3 groups. (**D**) Top: Optical image of DPPTT fine line pattern with 4-μm resolution by direct optical lithography. Bottom: Height profile of DPPTT polymer pattern obtained from PhotoAssist. (**E**) Average mobility of crosslinked polymer films containing different amounts of branched-diazirine crosslinker. Error bars denote SD. Inset: Schematic of OFET device fabricated on OTS-modified SiO_2/Si. (**F**) Top: Optical image of PMMA-PnBA-PMMA elastomer pattern with 8-μm resolution by direct optical lithography. Bottom: Height profile of PMMA-PnBA-PMMA pattern obtained from PhotoAssist. (**G**) Dielectric constant values as a function of frequency for neat PMMA-PnBA-PMMA elastomer, crosslinked PMMA-PnBA-PMMA elastomer mixed with 10 wt% of linear diazirine crosslinker, and crosslinked film after methyl ethyl ketone development.

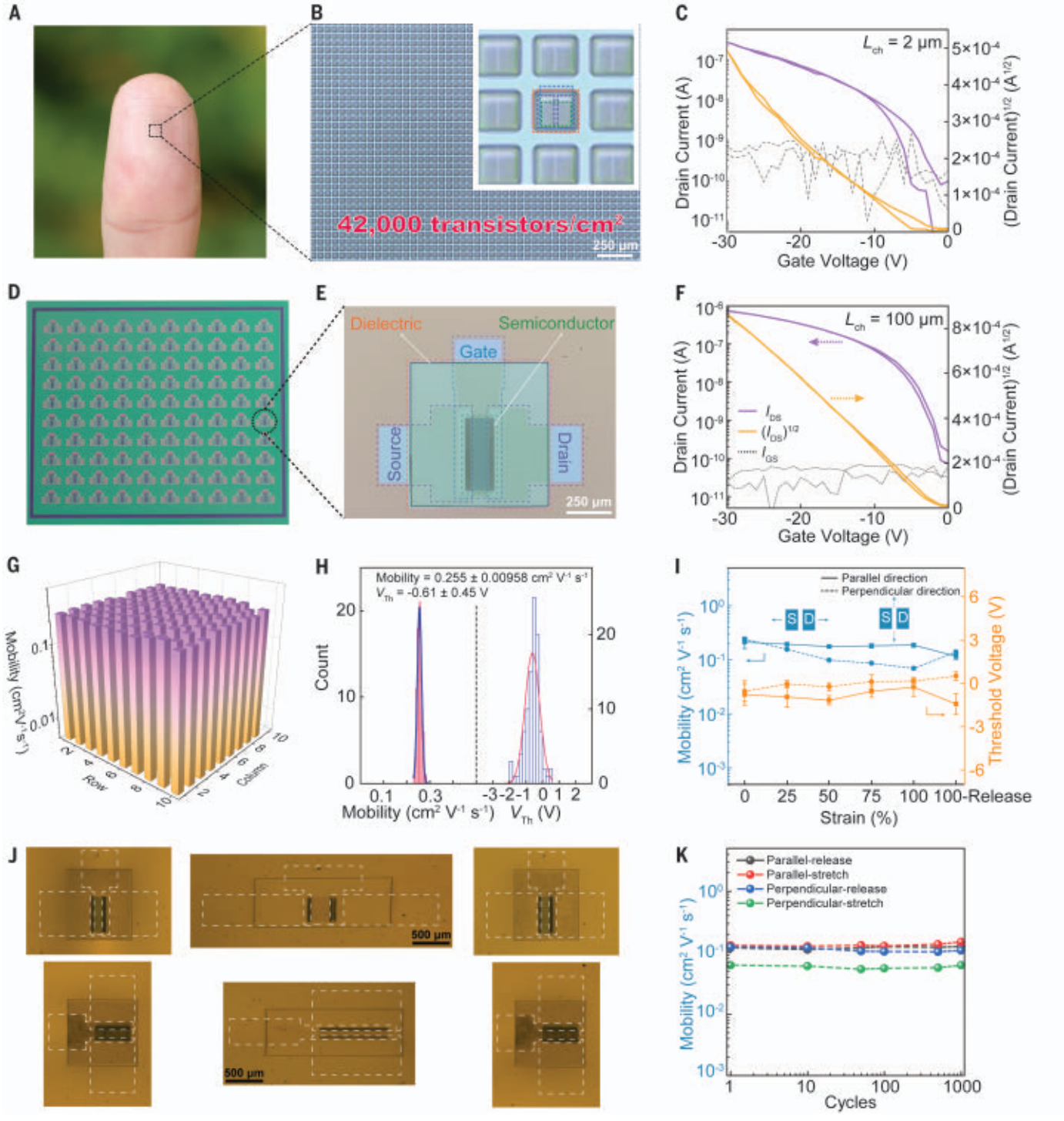

Fig. 4. High-density, highly uniform elastic transistor array fabricated by monolithic optical microlithography. (**A**) An elastic transistor array containing 10,000 transistors attached seamlessly onto the finger. (**B**) Microscope image of the transistor array. Inset: Zoomed-in microscope image of the transistor array (blue dashed line, contour of gate layer; orange dashed line, contour of dielectric layer; green dashed line, contour of semiconductor layer; purple dashed line, contour of source/drain layer). (**C**) Representative transfer curve of a transistor with channel length L_{ch} = 2 μm. (**D**) Photograph of a 10×10 transistor array. (**E**) Microscope image of one transistor from the array with L_{ch} = 100 μm. (**F**) Representative transfer curve of a transistor with L_{ch} = 100 μm. (**G**) Mobility distribution in the 10×10 transistor array. (**H**) Statistical distribution histograms of mobilities (left) and threshold voltage (right) for 98 working devices out of 100 fabricated devices. (**I**) Change of mobility and threshold voltage during stretching up to 100% strain along directions parallel and perpendicular to the charge transport direction. Error bars denote SD. (**J**) Microscope image of a transistor stretched from its original size to 100% strain, then released back to its original size (top, stretched parallel to the charge transport direction; bottom, stretched perpendicular to the charge transport direction). (**K**) Change of mobility under 50% strain and release states during 1000 stretching cycles parallel and perpendicular to the charge transport direction.

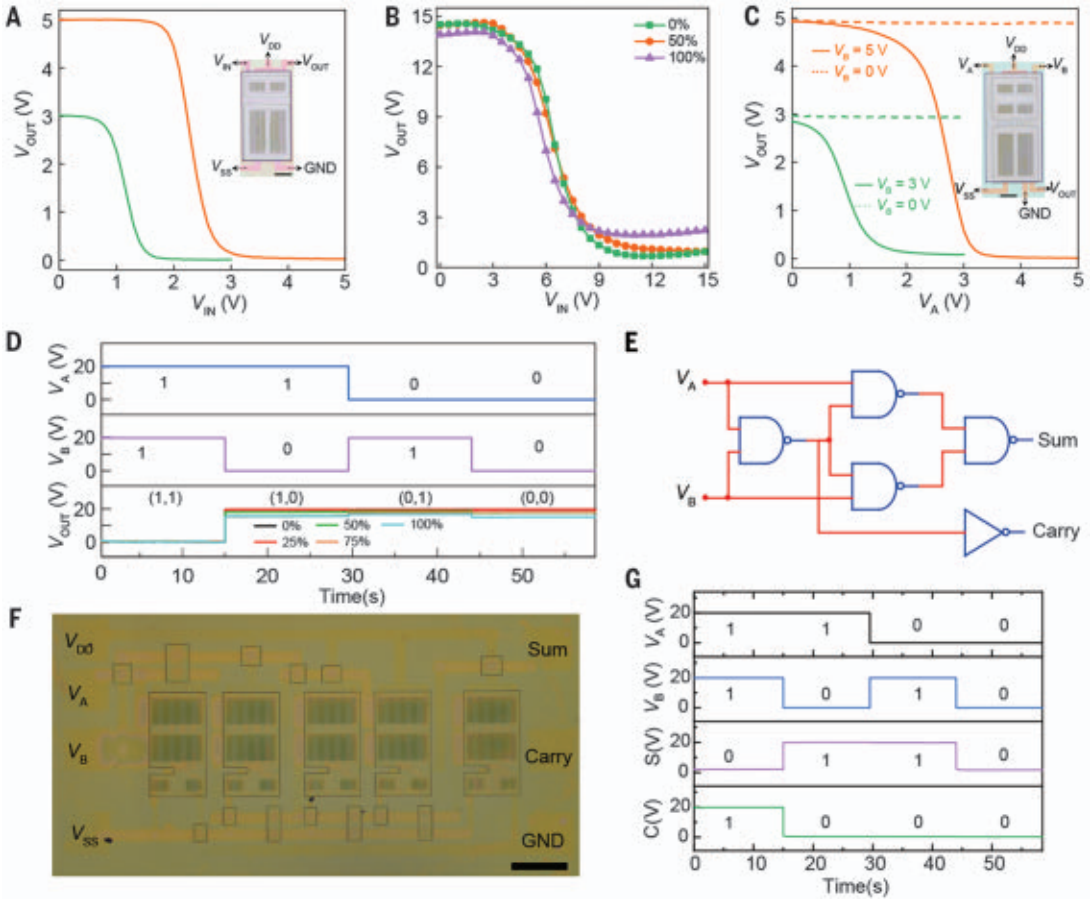

Fig. 5. Elastic functional circuits. (**A**) Transfer characteristics of pseudo-D 10-μm inverter. Inset: Optical image of the inverter. Scale bar, 100 μm. (**B**) Transfer characteristics of pseudo-E 50-μm inverter under strain. (**C**) Transfer characteristics of pseudo-D 10-μm NAND gate. Inset: Optical image of the NAND. Scale bar, 100 μm. (**D**) Output characteristics of pseudo-E 50-μm NAND gate under strain. (**E**) Circuit diagram of a half adder. (**F**) Photograph of a half adder consisting of 30 transistors. Scale bar, 500 μm. (**G**) Output characteristics of the half adder.

isoindigo-bithiophene semiconducting polymers with carbosilane side chains (PII2T-C6), and an n-type naphthalenediimide (NDI)–based polymer, P(NDI2TOD) (fig. S17).

A crosslinker amount less than 10 wt% is sufficient for achieving good patterning with moderate conjugated polymer molecular weight while maintaining charge transport almost unchanged from that of unpatterned films. Higher crosslinker content led to a decrease in mobility (Fig. 3E and table S1). The polymer aggregation behavior, crystalline domain size, and π-π stacking distances were hardly changed even with as high as 50 wt% of crosslinker versus DPP polymer (figs. S18 to S21 and supplementary text). This result indicates that the branched-diazirine crosslinker selectively interacted with the alkyl chains of the conjugated polymers as a consequence of the chemical structure similarity between the crosslinker and alkyl chains, rather than by interrupting π-stacking between conjugated backbones. Therefore, the decrease in mobility with a large amount of crosslinker may be simply due to the dilution of the semiconducting fraction in the mixture, or to variation in backbone packing orientation (fig. S22).

The carrier mobility of the semiconducting polymer remained unaffected throughout the multiple PhotoAssist steps, including UV exposure and development (fig. S23 and table S2), thanks to the well-preserved conjugated backbone structure and the crystalline microstructures of the conjugated polymers (figs. S24 to S27 and supplementary text). Solvent (chloroform) development showed only a slight decrease in mobility, with average mobility of 0.62 $cm^2 V^{-1} s^{-1}$, indicating good retention of the crosslinked films under solvent development; this is consistent with the gel curve results.

Dielectric polymers can also be directly patterned into different shapes with resolution down to 8 μm by adding 10 wt% of branched-diazirine crosslinker into the system (Fig. 3F and fig. S28). Dielectric properties of poly(methyl methacrylate)–poly(*n*-butyl acrylate)–poly(methyl methacrylate) (PMMA-PnBA-PMMA) and polystyrene-*block*-poly(ethylene-*ran*-butylene)-*block*-polystyrene (SEBS) elastomers showed negligible dependence on UV crosslinking and solvent development steps during the PhotoAssist fabrication processes (Fig. 3G and fig. S29).

Our PhotoAssist methodology is a direct optical lithography applicable to a variety of stretchable electronic materials. Its crosslinking-based mechanism allows the obtained polymer patterns to be resistant against solvents during subsequent processing. Furthermore, electronic properties of all materials remained unaffected, or even improved, after the patterning steps. These properties make PhotoAssist a viable strategy for monolithic manufacturing of high-density elastic electronics. The fabrication process for an elastic transistor array is illustrated in Fig. 1E. The process starts with a sacrificial layer (e.g., dextran) coated onto a Si substrate for eventual device release later. Next, a layer of stretchable elastomer, PMMA-PnBA-PMMA, is deposited, serving as the supporting substrate. The PMMA-PnBA-PMMA elastomer is crosslinked with 10 wt% of branched-diazirine crosslinkers to facilitate subsequent direct deposition of electronic polymer materials without chemical erosion. Next, bottom-gate and top-contact transistors are constructed by consecutive deposition and patterning of a stretchable gate layer (PEDOT:PSS/PEGDMA), a stretchable dielectric layer (PMMA-PnBA-PMMA/branched diazirine), a stretchable semiconductor layer [thieno[3,2-b]thiophene-diketopyrrolopyrrole (DPPTT)/branched diazirine], and a stretchable source/drain layer (PEDOT:PSS/PEGDMA) by direct optical lithography (Fig. 1E and fig. S30). Finally, the fabricated device is released from the supporting Si wafer as a free-standing stretchable electronic device (fig. S31).

We have successfully fabricated an all-polymer elastic transistor array containing 10,000 transistors within a 0.238-cm^2 substrate (Fig. 4, A and B), enabling a device density of ~42,000 transistors/cm^2, more than 100 times the density reported by (*11*), which had involved shadow masking and etching processes. The transistor was designed to have a channel length L_{ch} of 2 μm and channel width W_{ch} of 40 μm. A representative transfer curve of the device indicates typical p-type characteristics, with an on/off ratio of 10^4 and a low off-state current of 0.5 nA (Fig. 4C). Transistors with different channel lengths were fabricated using the PhotoAssist process, and their mobility values showed a dependence on channel length. We observed the highest value of 0.27 $cm^2 V^{-1} s^{-1}$ in a transistor with L_{ch} = 100 μm (figs. S32 and S33). With a decrease in channel length from 100 μm to 5 μm, the increased ratio of contact resistance over channel resistance may result in an underestimation of the charge carrier mobility (fig. S34), which is a common phenomenon for organic semiconductor–based transistors. Therefore, performance for short-L_{ch} elastic transistors can potentially be improved by interfacial modification to achieve better contacts between PEDOT:PSS and semiconducting polymers.

Construction of integrated circuits requires that the elastic transistors be fabricated in a uniform manner and with high yield (*24*). We therefore measured the transfer characteristics of 100 transistors (W_{ch} = 400 μm, L_{ch} = 100 μm) from two different batches of the 10×10 array (Fig. 4, D and E, and figs. S35 and S36). All the transistors showed ideal p-type transfer characteristics with small hysteresis and average saturation mobility of 0.255 $cm^2 V^{-1} s^{-1}$, as extracted from a near-ideal, quadratic current dependence on gate-source voltage (Fig. 4F). In addition, a high device yield of 98.5% and narrow distribution of mobilities with a standard deviation of only 3.76% were achieved (Fig. 4G). The threshold voltage (V_{th}) exhibited a distribution of –0.61 ± 0.45 V (Fig. 4H), a deviation of only 1.5% of the operating gate-source voltage window (–30 V). Minimum variability between transistors is critical for designing complex integrated circuits based on the device modeling and circuit simulation.

The 10×10 transistor array was subjected to 100% strain both parallel and perpendicular to the charge transport direction without any observable cracks or delamination (Fig. 4J), confirming the robust mechanical properties of each layer. The electrical performance of the transistors, including carrier mobilities, threshold voltages, and on-currents, remained stable at <100% applied strain along the charge transport direction, with mobility maintained at 88% of its original value and threshold voltage close to 0 V (Fig. 4I). When the transistors were stretched perpendicular to the charge transport direction, the on-current remained unaffected, with only a slight decrease in mobility (Fig. 4I and fig. S37), which may be due to strain-induced polymer chain alignment (*25*, *26*). Mobility changes in the transistors after being released from parallel stretching may be due to the changes in interface contacts from mechanical mismatches between different layers. The elastic transistors were observed to sustain up to 1000 repeated stretching cycles under 50% mechanical deformation in both directions with negligible changes in mobility (Fig. 4K).

We proceeded to fabricate both inverters and NAND gates, which constitute the basic functional units in elastic digital integrated circuits for on-skin signal processing and computing. Both pseudo-D and pseudo-E inverters with channel lengths ranging from 10 to 100 μm were demonstrated (Fig. 5A and figs. S38 and S39). PhotoAssist allowed fabrication of elastic inverters with channel lengths of 10 μm, which is more than an order of magnitude improvement in spatial resolution relative to previous reports (fig. S40). With its high uniformity and close-to-zero transistor threshold voltage, the pseudo-D 10-μm inverter can be powered by an input voltage of 3 V (Fig. 5A). By varying the input voltage from 0 to 3 V, the output voltage changes from ~3 V to GND. Pseudo-E 50-μm inverters operated normally with logic output states of 1 and 0 under logic input states of 0 and 1, even while being stretched up to 100% strain (Fig. 5B). The excellent uniformity and high yield of the transistors allowed us to build an accurate device model for circuit simulation and optimization to allow the realization of large-scale pseudo–complementary circuits. Simulations based on transistor performance accurately predicted the voltage transfer curves of pseudo-E 50-μm NAND gates (fig. S41). NAND gates consisting of six transistors demonstrated well-defined high- and low-output logic levels as logic "1" and "0" with a low operation voltage down to 3 V (Fig. 5C and fig. S42). Even under 100% strain along the channel length direction, the NAND gate retained the correct output logic (Fig. 5D). More complicated logic circuits—a XOR gate [24 elastic transistors (fig. S43)] and a half adder [30 elastic transistors (Fig. 5E)]—were fabricated (Fig. 5F) and exhibited rail-to-rail outputs (Fig. 5G and fig. S44), indicating that all the elastic transistors worked collectively.

Our PhotoAssist strategy enables direct optical lithography of elastic polymeric electronic materials with micrometer-scale resolution, high yield, and excellent uniformity without compromising their electronic and mechanical characteristics. This work constitutes an increase in elastic-transistor density by more than two orders of magnitude relative to the previously reported highest density (*11*). The general strategy of direct optical patterning of electroactive materials can be extended to both direct laser- and electron beam–writing approaches to further increase the spatial resolution. Additional materials such as biosensing polymers and organic light-emitting materials can also be integrated to construct complex electronic devices.

REFERENCES AND NOTES

1. A. Chortos, J. Liu, Z. Bao, *Nat. Mater.* **15**, 937–950 (2016).
2. Y. Dai, H. Hu, M. Wang, J. Xu, S. Wang, *Nat. Electron.* **4**, 17–29 (2021).
3. S. Lee *et al.*, *Science* **370**, 966–970 (2020).
4. S. Sundaram *et al.*, *Nature* **569**, 698–702 (2019).
5. T. Araki *et al.*, *Adv. Mater.* **32**, e1902684 (2020).
6. J. A. Rogers, T. Someya, Y. Huang, *Science* **327**, 1603–1607 (2010).
7. M. Magliulo *et al.*, *J. Mater. Chem. C* **3**, 12347–12363 (2015).
8. Z. Huang *et al.*, *Nat. Electron.* **1**, 473–480 (2018).
9. A. D. Valentine *et al.*, *Adv. Mater.* **29**, 1703817 (2017).
10. S. Xu *et al.*, *Science* **344**, 70–74 (2014).
11. S. Wang *et al.*, *Nature* **555**, 83–88 (2018).
12. A. Chortos *et al.*, *Adv. Mater.* **28**, 4441–4448 (2016).
13. J. Liang *et al.*, *Nat. Commun.* **6**, 7647 (2015).
14. J. F. Chang, M. C. Gwinner, M. Caironi, T. Sakanoue, H. Sirringhaus, *Adv. Funct. Mater.* **20**, 2825–2832 (2010).
15. P. E. Malinowski *et al.*, *Org. Electron.* **15**, 2355–2359 (2014).
16. F. Molina-Lopez *et al.*, *Nat. Commun.* **10**, 2676 (2019).
17. M. Singh, H. M. Haverinen, P. Dhagat, G. E. Jabbour, *Adv. Mater.* **22**, 673–685 (2010).
18. S. Chung *et al.*, *Adv. Mater.* **25**, 4773–4777 (2013).
19. J. Brunner, H. Senn, F. M. Richards, *J. Biol. Chem.* **255**, 3313–3318 (1980).
20. J. Das, *Chem. Rev.* **111**, 4405–4417 (2011).
21. J. Park, M. Koh, J. Y. Koo, S. Lee, S. B. Park, *ACS Chem. Biol.* **11**, 44–52 (2016).
22. S. S. Ge *et al.*, *RSC Adv.* **8**, 29428–29454 (2018).
23. G. J. N. Wang *et al.*, *Chem. Mater.* **31**, 6465–6475 (2019).
24. L. Xiang *et al.*, *ACS Nano* **14**, 6449–6469 (2020).
25. B. O'Connor *et al.*, *Adv. Funct. Mater.* **21**, 3697–3705 (2011).
26. X. Zhang *et al.*, *Nat. Commun.* **4**, 2238 (2013).

ACKNOWLEDGMENTS

The GIXD measurements were performed at Advanced Light Source beamline 7.3.3 and SSRL 11-3. We thank Y. Ochiai, S. Tatsumi, and Y. Zheng for providing P3HT and DPP polymers. **Funding:** Supported by Stanford Catalyst for Collaborative Solutions. Part of this work was performed at the Stanford Nano Shared Facilities (SNSF), supported by NSF award ECCS-2026822. **Author contributions:** Y.-Q.Z., Y.L., and Z.B. designed the project and experiments; Y.-Q.Z. designed the diazirine crosslinker; Y.-Q.Z. and Y.L. developed the PhotoAssist fabrication method; Y.-Q.Z. and D.Z. fabricated the elastic circuits and carried out electrical characterization; D.Z. carried out the circuit design and simulation; Y.-Q.Z. and Y.L. did the conductivity measurement; Y.-Q.Z., S.L., and D.Z. performed the contact resistance measurement and data analysis; Z.Y. and D.L. synthesized the diazirine crosslinker; S.N. and H.-C.W. carried out GIXD characterization; Y.-Q.Z. and S.N. carried out the 3D profilometer mapping measurement and data analysis; S.L. helped with circuit design; S.N., S.L., and C.Z. helped with device and circuit measurements; J.L. helped to take device photographs; H.T. helped to prepare three-dimensional schematics; Y.-Q.Z., Y.L., Z.B., D.Z., and J.B.-H.T. wrote the manuscript; and all authors reviewed and commented on the manuscript. **Competing interests:** Y.-Q.Z., Y.L., and Z.B. are inventors on a patent application (no. 63/161,344) submitted by the Board of Trustees of Stanford University. **Data and materials availability:** All data are available in the main text or the supplementary materials.

SUPPLEMENTARY MATERIALS

science.sciencemag.org/content/373/6550/88/suppl/DC1
Materials and Methods
Figs. S1 to S43
Tables S1 and S2
References (*27*–*35*)

4 March 2021; accepted 26 May 2021
10.1126/science.abh3551

SPECTROSCOPY

Single-molecule laser nanospectroscopy with micro–electron volt energy resolution

Hiroshi Imada[1,2]*, Miyabi Imai-Imada[1], Kuniyuki Miwa[1,3], Hidemasa Yamane[4], Takeshi Iwasa[2,5,6], Yusuke Tanaka[7,8], Naoyuki Toriumi[8]†, Kensuke Kimura[1], Nobuhiko Yokoshi[4], Atsuya Muranaka[7,8], Masanobu Uchiyama[7,8], Tetsuya Taketsugu[5,6], Yuichiro K. Kato[9,10], Hajime Ishihara[4,11,12], Yousoo Kim[1]*

Ways to characterize and control excited states at the single-molecule and atomic levels are needed to exploit excitation-triggered energy-conversion processes. Here, we present a single-molecule spectroscopic method with micro–electron volt energy and submolecular-spatial resolution using laser driving of nanocavity plasmons to induce molecular luminescence in scanning tunneling microscopy. This tunable and monochromatic nanoprobe allows state-selective characterization of the energy levels and linewidths of individual electronic and vibrational quantum states of a single molecule. Moreover, we demonstrate that the energy levels of the states can be finely tuned by using the Stark effect and plasmon-exciton coupling in the tunneling junction. Our technique and findings open a route to the creation of designed energy-converting functions by using tuned energy levels of molecular systems.

The electronic excitation of molecules triggers diverse energy-conversion phenomena, including luminescence, photovoltaic effects, and various chemical dynamics (*1*–*3*). Understanding and controlling dynamic processes of molecules in excited states are of primary importance for creating new functions with organic materials. Optical spectroscopy has been widely used to investigate such electronic excited states (*4*, *5*). However, because of its limited spatial resolution, it cannot provide direct information about the local spatial distribution of molecular orbitals, which governs excitation. Conversely, atomic-resolution microscopy techniques such as electron microscopy and scanning probe microscopy can visualize local structure (*6*, *7*), but spectroscopic techniques that use such microscopes are very underdeveloped. Consequently, there have been few studies on electronic excitations and succeeding processes at the atomic or molecular level, and much remains to be learned about the associated energy conversions.

Methods involving spectroscopic measurement of electroluminescence (EL) induced by the tunneling current of a scanning tunneling microscope (STM-EL) (Fig. 1A) have advanced rapidly in recent years (*8*–*16*). These methods combine morphological and electronic characterization by means of STM with analysis of photon signals that provide information on charge and excitation dynamics. Although STM-EL is a distinctive and powerful technique for studying electronic excitations, it suffers from low state-selectivity during excitation. In contrast to the tunable lasers used in optical spectroscopy, the energy of the tunneling electrons is not well defined or monochromatic, which makes it particularly difficult to selectively excite a single quantum state by using the STM tunneling current. This has hindered elucidation of the intrinsic characteristics of individual excited states (such as energy levels and line widths) and precise state-to-state description of the subsequent dynamic processes.

In this work, we combined a narrow-line tunable laser with STM to achieve highly state-selective nanoscale excitation, enabling precise characterization of the electronic and vibrational states of single molecules with micro–electron volt energy resolution. As shown in Fig. 1B, nanocavity plasmons formed between the STM tip and the metal substrate were driven at a well-defined frequency by an external laser field that excited the molecule to induce photoluminescence (PL) (more details of the experimental setup are provided in fig. S1). To demonstrate the precision of STM-PL spectroscopy, free-base phthalocyanine (H_2Pc), a common luminescent molecule, and its deuterated derivative (D_2Pc) were deposited on atomically thin NaCl films grown on Ag(111) (Fig. 1C) (*7*). The ultrathin insulating film decoupled the molecules from the metal substrate, enabling single-molecule optical investigation (*8*, *11*–*14*, *16*, *17*).

As observed in previous STM-EL studies, H_2Pc on NaCl shows strong EL when holes are directly injected into the occupied molecular orbital from the STM tip (Fig. 1D, top blue curve) (*11*, *18*). The STM-EL spectrum showed a prominent peak at 1.817 eV. On the basis of Kasha's rule, this peak was previously assigned to the 0-0 transition from the vibrational ground state in the first singlet electronic excited state (S_1) to the vibrational ground state in the electronic ground state (S_0). The spectrum also showed small peaks of vibronic transitions at 1.60 to 1.75 eV (*19*).

The STM junction was then irradiated with the laser after tuning its energy to around 1.817 eV. The luminescence signal from the STM junction was filtered with a low-pass filter (LPF) to block the excitation laser light, and photons with energies below 1.77 eV were measured. Shown in Fig. 1D, the bottom four curves, are STM-PL spectra acquired at four STM tip positions with different distances from the molecule's center (Fig. 1C, bottom). When the tip was more than 5 nm away, the STM-PL spectrum showed almost no photon signal. As the tip approached the molecule, the photon signal rapidly grew, and the PL spectrum exhibited vibronic peaks that corresponded to peaks in the STM-EL spectrum on a one-to-one basis. The STM tip was placed outside the molecule, and excitation was induced solely through electromagnetic interaction without charge injection. The STM-PL spectra showed that the PL process was strongly enhanced by the local electromagnetic field of the nanocavity plasmon, and all the PL peaks originated from the single molecule under measurement (an additional description of the plasmon-molecule interaction is available in the supplementary materials). The total detected photon intensity (integrated over energy) exceeded 180,000 photons/s even at the very weak excitation power of 1 μW, indicating an efficiency several orders higher than those of tip-enhanced Raman spectroscopy (*20*–*22*) and STM-PL spectroscopy using a laser with a fixed energy (*17*). Additionally, the peaks in the STM-PL spectra were sharper than those in the corresponding STM-EL spectra, even though both measurements were done on the same molecule.

The line shape of resonances could be determined more precisely with PL excitation (PLE) spectroscopy, in which the excitation laser energy was swept throughout the time of monitoring the intensity of the red-shifted luminescence (Fig. 2A). A single-molecule PLE spectrum of H_2Pc is shown in Fig. 2B, which features an intense resonance at 1817.4 meV with a peak width of 0.5 meV and a small resonance on the higher-energy side. The precise spectral

[1]Surface and Interface Science Laboratory, RIKEN, Wako, Saitama 351-0198, Japan. [2]PRESTO, Japan Science and Technology Agency (JST), Kawaguchi, Saitama 332-0012, Japan. [3]Institute for Molecular Science, Myodaiji, Okazaki, Aichi 444-8585, Japan. [4]Department of Physics and Electronics, Osaka Prefecture University, Sakai, Osaka 599-8531, Japan. [5]Department of Chemistry, Faculty of Science, Hokkaido University, Sapporo, Hokkaido 060-0810, Japan. [6]Institute for Chemical Reaction Design and Discovery (WPI-ICReDD), Hokkaido University, Sapporo 060-0810, Japan. [7]Graduate School of Pharmaceutical Sciences, The University of Tokyo, 7-3-1 Hongo, Bunkyo-ku, Tokyo 113-0033, Japan. [8]Advanced Elements Chemistry Laboratory, RIKEN, Wako, Saitama 351-0198, Japan. [9]Nanoscale Quantum Photonics Laboratory, RIKEN, Wako, Saitama 351-0198, Japan. [10]Quantum Optoelectronics Research Team, RIKEN Center for Advanced Photonics, Wako, Saitama 351-0198, Japan. [11]Department of Materials Engineering Science, Osaka University, 1-3 Machikaneyama-cho, Toyonaka, Osaka 560-8531, Japan. [12]Center for Quantum Information and Quantum Biology, Osaka University 2-1 Yamada-oka, Suita, Osaka 565-0871, Japan.
***Corresponding author. Email: himada@riken.jp (H.I.); ykim@riken.jp (Y.K.).** †Present address: Department of Chemistry, School of Science, Tokyo Institute of Technology, Tokyo 152-8551, Japan.

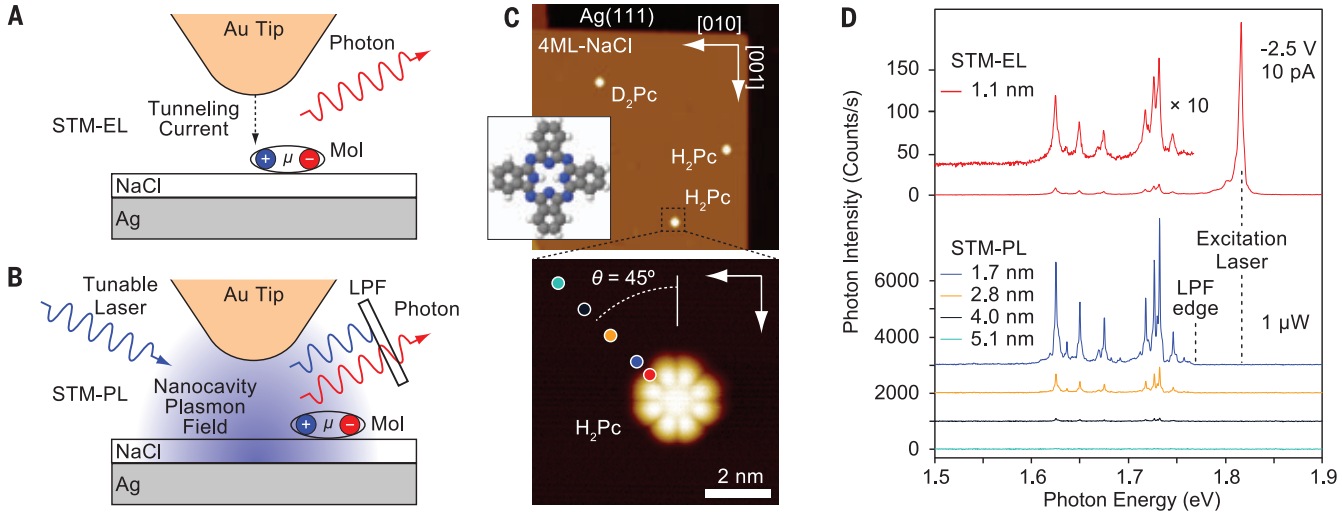

Fig. 1. STM-PL measurement in comparison with STM-EL. (**A** and **B**) Schematic depiction of STM-EL and STM-PL measurement. LPF, low-pass filter. The measurement system was based on a low-temperature ultrahigh-vacuum STM operating at 4.6 K and 5×10^{-11} torr. (**C**) (Top) An STM image of H_2Pc and D_2Pc on a four-monolayer-thick NaCl island grown on Ag(111) (sample bias voltage V_s = 1 V, tunneling current I = 3 pA, 70 × 70 nm^2). (Inset) The molecular structure of H_2Pc. (Bottom) A magnified STM image of a H_2Pc molecule (V_s = −2.5 V, I = 3 pA). The measurement tip positions for the spectra shown in (D) are indicated with circles whose color matches that of the corresponding spectrum. (**D**) STM PL and EL spectra of the same H_2Pc molecule. Measurement conditions for EL are V_s = −2.5 V, I = 10 pA, on the red dot, without laser irradiation, and for PL are laser energy = 1.817 eV, laser power = 1 μW, V_s = −2.5 V, I = 3 pA, at four tip-molecule distances. The spectra are offset for clarity.

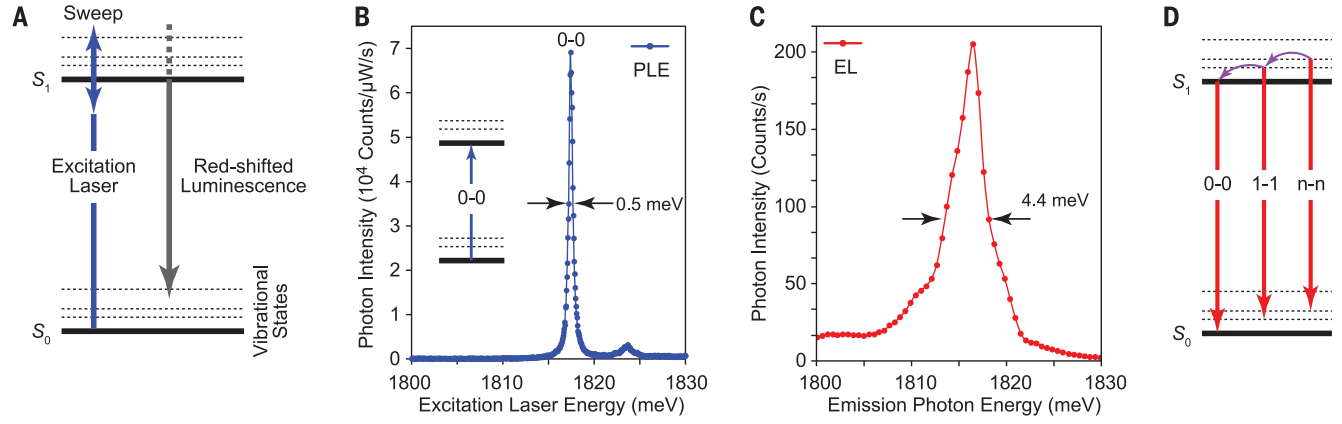

Fig. 2. Selective excitation of the 0-0 transition with PL excitation spectroscopy. (**A**) Energy diagram for PLE measurement. (**B**) A PLE spectrum of H_2Pc. The STM tip was placed 1.8 nm from the molecular center on a line at 45° to the molecular axis (V_s = −2.5 V, I = 3 pA). The laser energy was swept from 1800 to 1830 meV at 0.05-meV intervals, and the red-shifted luminescence intensity was measured for 0.5 s/point. (**C**) STM-EL spectrum of H_2Pc around the intense peak (a magnification of the STM-EL spectrum presented in Fig. 1D). (**D**) Energy diagram for the STM-EL emission process. Radiative transitions occur from vibrationally excited states in S_1, generating a broad and asymmetric peak.

characteristics (resonance energy and linewidth) can vary depending on both measurement and tip conditions. Because the initial state of the excitation at 4.6 K was the vibrational ground state in S_0, the lowest-energy transition at 1817.4 meV was assigned to the 0-0 transition from S_0 to S_1. The higher-energy peak was a transition accompanied by a low-energy excitation in the system. The strong STM-EL peak at 1817 meV was asymmetric and had a much greater peak width of 4.4 meV (Fig. 2C). Direct comparison of the STM-PLE and STM-EL spectra suggested that the peak in the STM-EL spectrum consisted of several overlapping electronic transitions from vibrationally excited states rather than a pure 0-0 transition (Fig. 2D). This breakdown of Kasha's rule was explained by the drastic plasmonic enhancement of radiative transition rates (*9*, *23*, *24*), which made the electronic transition rates comparable with the vibrational relaxation rates (further discussion is available in the supplementary materials). Similarly, the broad peak observed in the recently reported STM-PL spectrum (~10 meV) acquired with a fixed-energy laser (*17*) can be attributed to overlapping peaks of electronic transitions. This result shows that a tunable monochromatic probe is essential for characterizing individual quantum states in a plasmonic nanocavity.

A benefit of state-selective excitation of the 0-0 transition is that it substantially enhances the chemical sensitivity of the emission spectrum by narrowing the emission peaks of vibronic transitions (*19*). This feature can be seen by comparing the STM-PL spectra of H_2Pc and

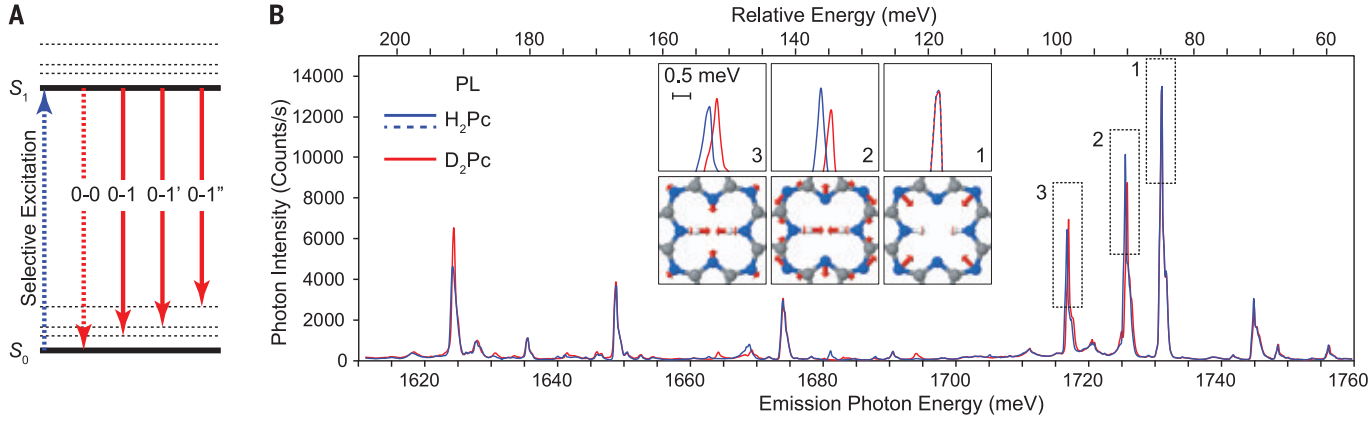

Fig. 3. Spectroscopic identification of H_2Pc and D_2Pc. (**A**) Energy diagram for the emission process in STM-PL after selective excitation of the 0-0 transition. 1, 1′, and 1″ denote the first vibrational excited states of different vibrational modes. (**B**) Direct comparison of STM-PL spectra of H_2Pc and D_2Pc acquired under identical experimental conditions. V_s = 1 V, I = 3 pA, r = 1.8 nm, θ = 45°, E_{ex} = 1817 meV. (Inset) Magnified peaks of modes 1, 2, and 3 and the corresponding atomic motions around the molecular center. White, hydrogen and deuterium; blue, nitrogen; gray, carbon.

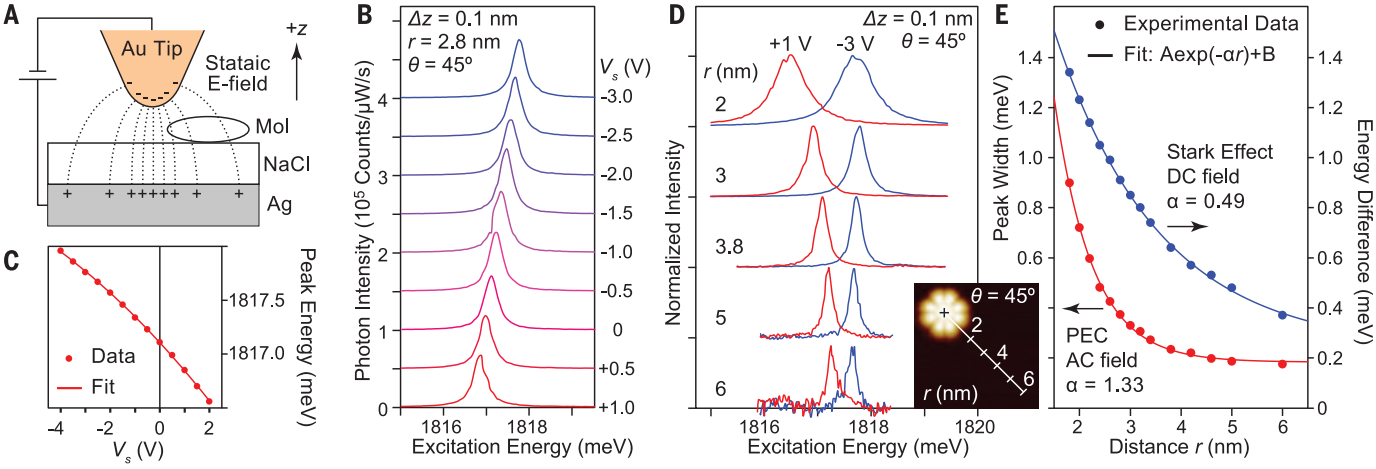

Fig. 4. Static electric field effect investigated by use of PLE. (**A**) Schematic depiction of the application of a local static electric field to the molecule by using the STM tip. In the following experiments described in (B) to (E), the tip height was carefully controlled to investigate the static electric field effect independent of other effects. (**B**) Bias voltage dependence of the 0-0 transition resonance of H_2Pc (r = 2.8 nm, θ = 45°). The series of the PLE spectra were measured with turning off the feedback control of STM to keep the three-dimensional tip position. The feedback loop was turned off at V_s = 1 V and I = 3 pA to define Δz = 0, followed by lifting the tip away from the substrate to Δz = +0.1 nm. (**C**) The peak position as a function of V_s. The experimental data points were fitted with a quadratic function. (**D**) PLE spectra acquired at two V_s values and various tip-molecule distances. The spectra were normalized to compare the spectral shapes. At each r, Δz = 0 was defined at V_s = 1 V and I = 3 pA, and the measurement was done at Δz = 0.1 nm. (**E**) Plot of the peak width and the peak energy difference in the PLE spectra as a function of the distance r.

D_2Pc presented in Fig. 3, which were acquired under identical experimental conditions. The overall spectral shapes were highly similar; there were only minor differences in peak positions and intensities from isotope effects. The differences were most pronounced for the three strong peaks at 1731, 1726, and 1717 meV, which we designated modes 1, 2, and 3, respectively. These peaks were all assigned to totally symmetric modes according to density functional theory (DFT) calculations (peak assignments are provided in fig. S4 and table S2). Expansions of each peak are shown in the insets of Fig. 3 together with diagrams that illustrate the atomic motions of the corresponding vibrational modes. Although the curves for H_2Pc and D_2Pc overlapped almost exactly for mode 1, modes 2 and 3 exhibited slight peak shifts and intensity differences.

The shift of the D_2Pc peaks to lower vibrational energies (higher photon energies) can be explained intuitively by considering the underlying atomic motions. Specifically, the two central hydrogen atoms of H_2Pc and deuterium atoms of D_2Pc and the nitrogen atoms bound to them move together in modes 2 and 3 but are almost stationary in mode 1. Deuteration is expected to reduce the energy of vibrational modes that involve appreciable movement of the hydrogen atoms (such as modes 2 and 3) because it increases the mass of the moving nuclei. Both the peak shifts and the intensity difference resulting from deuteration were consistent with the DFT calculations (fig. S4). These results show that STM-PL emission spectroscopy by using state-selective excitation achieved micro–electron volt energy resolution and was able to spectroscopically distinguish even closely related chemical species on the

basis of minute isotope effects. Our spectroscopic assignment of H_2Pc and D_2Pc was further supported with a measurement of current-induced tautomerization (fig. S6) (*25*).

Another substantial advantage of STM-PL is that because the tunneling current was not required for excitation, the STM tip could be used for other purposes. For example, we used the tip as a moving electrode to apply local static electric fields to manipulate individual quantum states in the nanocavity (Fig. 4A). The sample voltage (V_s) dependence of the 0-0 transition resonance measured with PLE is shown in Fig. 4B. As V_s decreased, the peak energy increased with a decreasing slope (Fig. 4C) and did not reach a maximum in the measured voltage range. This peak shift behavior was well fitted with a quadratic function, indicating that the peak shift induced by the static electric field involved both linear and quadratic terms. Shifting of the peak energy in this manner is referred to as the Stark effect.

The observation of a linear Stark effect here was unexpected for centrosymmetric molecules (*26*, *27*) such as phthalocyanines. The interaction energy of the charge distribution in a molecule $\rho(r)$ with an electrostatic potential $\phi(r)$ is $V_{int} = \int \rho(r)\phi(r)dv$. By expanding $\phi(r)$, we obtain $V_{int} = -\mu \cdot E(0) + \frac{1}{2}\sum_{i,j} Q_{ij} V_{ij}(0) + \cdots$ for a neutral molecule, where μ, Q_{ij}, $E(0)$, and $V_{ij}(0)$ represent the dipole moment vector and quadrupole moment tensor of the molecule, the electric field, and the electric field gradient at the molecular center ($r = 0$), respectively, and the indices (i and j) denote the Cartesian coordinate axes x, y, and z. Because a centrosymmetric molecule has no dipole moment, V_{int} is negligible under a uniform field [$V_{ij}(0) = 0$] within the first-order perturbation. Therefore, the linear Stark effect may be owing to submolecular variation of the static electric field that causes $V_{ij}(0)$ and higher terms to be nonzero (an explanation of the quadratic Stark effect is available in the supplementary materials). To substantiate this interpretation, we performed a first-principles theoretical study on a centrosymmetric H_2Pc molecule located in a nonuniform static field, including both first-order and higher-order perturbation effects. These calculations reproduced the observed linear and quadratic Stark effects reasonably well (fig. S7). The good agreement between experiment and theory suggests that the nonuniform field plays a crucial role in the induction of a Stark effect in nanocavity systems.

Last, we examined the spatial distribution of the nonuniform static (dc, $\omega = 0$) electric field in the nanocavity. Shown in Fig. 4D is how the 0-0 transition resonance evolved as a function of tip-molecule lateral distance at V_s values of +1 and –3 V (fig. S8). The peak width increased as the tip approached the molecule. This behavior was independent of the dc field and could be explained with plasmon-exciton coupling (PEC), which is an electromagnetic interaction in the optical frequency range ($\omega \sim$ 439 THz) (*24*). By contrast, the peak position was influenced by both PEC and the Stark effect. The peak position difference at each r, however, was induced solely by the Stark effect because for each r value, the tip position (which governs the strength of PEC) was kept constant in three dimensions, and only V_s was altered. Therefore, the peak position difference was free from the influence of PEC and could be a good indicator of the dc field strength.

The peak position difference (dc field effect) and peak width (ac field effect) both decayed exponentially as a function of the distance (Fig. 4E), with decay constants of 0.49 and 1.33 nm^{-1}, respectively. The considerably smaller decay constant of the dc field effect means that the dc field was more widely distributed around the tip apex than was the ac field. The stronger field confinement at the resonance frequency probably originated from self-interaction in the nanocavity (*28*). Despite its relatively wide distribution, the dc field was nonuniform over the molecular length scale and was able to explain the linear Stark effect. In addition, the different decay constants for the ac and dc fields reported here indicated that these field effects operated at different length scales. This insight will be critical for efforts to exert electrical control over chemical reactions (*29*), field-induced manipulation of molecules (*30*), intermolecular dipole coupling (*12*), and resonance energy transfer through electronic and vibrational states (*11*).

We have shown that the individual quantum states of a single molecule can be probed and controlled with excellent space-energy resolution by using a tunable laser combined with STM. The experimental results presented here agreed well with theoretical analyses. We believe that this result is because the use of STM allowed the measurement geometry (such as the position of the tip relative to the molecule, the molecule's adsorption site and angle, and the presence of impurities) to be controlled precisely, which has been difficult with other experimental techniques. The nanospectroscopy with high-energy resolution would play a major role in elucidating nature of molecular junctions where intrinsic molecular properties can be modified owing to spatially varying dielectric environment. Our experimental setup could be readily modified to perform time-resolved nanospectroscopy by using a pulsed rather than continuous laser. We anticipate that the combination of high-energy– and high-time–resolution nanospectroscopy with electromagnetic control of energy levels demonstrated here will create opportunities to better understand and efficiently exploit energy conversion dynamics.

REFERENCES AND NOTES

1. E. Romero, V. I. Novoderezhkin, R. van Grondelle, *Nature* **543**, 355–365 (2017).
2. H. Uoyama, K. Goushi, K. Shizu, H. Nomura, C. Adachi, *Nature* **492**, 234–238 (2012).
3. A. Mishra, P. Bäuerle, *Angew. Chem. Int. Ed.* **51**, 2020–2067 (2012).
4. C. Hettich *et al*., *Science* **298**, 385–389 (2002).
5. W. E. Moerner, M. Orrit, *Science* **283**, 1670–1676 (1999).
6. K. W. Urban, *Science* **321**, 506–510 (2008).
7. J. Repp, G. Meyer, S. M. Stojković, A. Gourdon, C. Joachim, *Phys. Rev. Lett.* **94**, 026803 (2005).
8. X. H. Qiu, G. V. Nazin, W. Ho, *Science* **299**, 542–546 (2003).
9. Z. C. Dong *et al*., *Nat. Photonics* **4**, 50–54 (2010).
10. P. Merino, C. Große, A. Rosławska, K. Kuhnke, K. Kern, *Nat. Commun.* **6**, 8461 (2015).
11. H. Imada *et al*., *Nature* **538**, 364–367 (2016).
12. Y. Zhang *et al*., *Nature* **531**, 623–627 (2016).
13. H. Imada *et al*., *Phys. Rev. Lett.* **119**, 013901 (2017).
14. B. Doppagne *et al*., *Science* **361**, 251–255 (2018).
15. K. Miwa *et al*., *Nano Lett.* **19**, 2803–2811 (2019).
16. K. Kimura *et al*., *Nature* **570**, 210–213 (2019).
17. B. Yang *et al*., *Nat. Photonics* **14**, 693 (2020).
18. G. Chen *et al*., *Phys. Rev. Lett.* **122**, 177401 (2019).
19. C. Murray *et al*., *Phys. Chem. Chem. Phys.* **13**, 17543–17554 (2011).
20. R. Zhang *et al*., *Nature* **498**, 82–86 (2013).
21. J. Lee, K. T. Crampton, N. Tallarida, V. A. Apkarian, *Nature* **568**, 78–82 (2019).
22. R. B. Jaculbia *et al*., *Nat. Nanotechnol.* **15**, 105–110 (2020).
23. R. Chikkaraddy *et al*., *Nature* **535**, 127–130 (2016).
24. T. Neuman, R. Esteban, D. Casanova, F. J. García-Vidal, J. Aizpurua, *Nano Lett.* **18**, 2358–2364 (2018).
25. P. Liljeroth, J. Repp, G. Meyer, *Science* **317**, 1203–1206 (2007).
26. C. Brunel, P. Tamarat, B. Lounis, J. C. Woehl, M. Orrit, *J. Phys. Chem. A* **103**, 2429–2434 (1999).
27. A. Moradi, Z. Ristanović, M. Orrit, I. Deperasińska, B. Kozankiewicz, *ChemPhysChem* **20**, 55–61 (2019).
28. C. Zhang, B. Q. Chen, Z. Y. Li, *J. Phys. Chem. C* **119**, 11858–11871 (2015).
29. X. Huang *et al*., *Sci. Adv.* **5**, eaaw3072 (2019).
30. M. Ohara, Y. Kim, M. Kawai, *Phys. Rev. B Condens. Matter Mater. Phys.* **78**, 201405 (2008).
31. H. Imada *et al*., Data for: Single-molecule laser nanospectroscopy with μeV energy resolution. Zenodo (2021); 10.5281/zenodo.4736415.

ACKNOWLEDGMENTS

We thank Y. Hasegawa, Y. Shimizu, and E. Kazuma for their technical support for tip fabrication and J. Takeda and I. Katayama for helpful discussions. The numerical calculations were performed in part with the use of the HOKUSAI supercomputer system at RIKEN. **Funding:** This work was financially supported in part by JST PRESTO [grants JPMJPR1862 (H.Im.) and JPMJPR20T1 (T.I.)] and by Japan Society for the Promotion of Science (JSPS) KAKENHI, grants JP19H04681 and JP 17H04796 (H.I.); JP 19K23591 (M.I.-I.); JP 18H05257 (Y.K.); JP17H06173 and JP17H05430 (M.U.); JP20H02728 (A.M.); and JP20K05412, JP20H04652, and JP20K05592 (T.I.). **Author contributions:** H.Im., M.I.-I., and Y.K. conceived the project and constructed the experimental setup, with the help of Y.K.K.; H.Im., M.I.-I., and K.K. performed the experiment using STM and analyzed the data. Y.T., N.T., A.M., and M.U. synthesized and characterized the D_2Pc molecule. K.M., H.Y., T.I., N.Y., T.T., and H.Is. provided the theoretical analyses. Y.K. directed the project. All authors discussed the results and wrote the manuscript. **Competing interests:** None declared. **Data and materials availability:** All data needed to evaluate the conclusions in the paper are present here or in the supplementary materials. Data for all figures presented in this study are available from Zenodo (*31*).

SUPPLEMENTARY MATERIALS

science.sciencemag.org/content/373/6550/95/suppl/DC1
Materials and Methods
Figs. S1 to S8
Tables S1 and S2
References (*32*–*40*)

2 February 2021; accepted 22 May 2021
10.1126/science.abg8790

APPLIED OPTICS

Laser soliton microcombs heterogeneously integrated on silicon

Chao Xiang[1]†, Junqiu Liu[2]†, Joel Guo[1], Lin Chang[1], Rui Ning Wang[2], Wenle Weng[2], Jonathan Peters[1], Weiqiang Xie[1], Zeyu Zhang[1], Johann Riemensberger[2], Jennifer Selvidge[3], Tobias J. Kippenberg[2]*, John E. Bowers[13]*

Silicon photonics enables wafer-scale integration of optical functionalities on chip. Silicon-based laser frequency combs can provide integrated sources of mutually coherent laser lines for terabit-per-second transceivers, parallel coherent light detection and ranging, or photonics-assisted signal processing. We report heterogeneously integrated laser soliton microcombs combining both indium phospide/silicon (InP/Si) semiconductor lasers and ultralow-loss silicon nitride (Si_3N_4) microresonators on a monolithic silicon substrate. Thousands of devices can be produced from a single wafer by using complementary metal-oxide-semiconductor–compatible techniques. With on-chip electrical control of the laser-microresonator relative optical phase, these devices can output single-soliton microcombs with a 100-gigahertz repetition rate. Furthermore, we observe laser frequency noise reduction due to self-injection locking of the InP/Si laser to the Si_3N_4 microresonator. Our approach provides a route for large-volume, low-cost manufacturing of narrow-linewidth, chip-based frequency combs for next-generation high-capacity transceivers, data centers, space and mobile platforms.

Optical frequency combs (OFCs) (*1*, *2*) have revolutionized timing, spectroscopy and metrology. Discovered a decade ago, OFCs can be generated in optical microresonators where bright dissipative Kerr solitons are formed (*3*). These types of OFCs are referred to as "soliton microcombs" and have already been used in system-level applications. In parallel, there has been substantial progress in photonic integrated platforms for microcomb generation, among which Si_3N_4 (*4*–*7*, *8*, *9*) has emerged as the most mature and widely used platform. Recent advances in fabrication of nonlinear, dispersion-engineered, Si_3N_4 photonic integrated circuits (PICs) have enabled optical losses below 1 dB/m (*8*, *9*), resulting in soliton formation with milliwatt threshold power levels that integrated lasers can provide and repetition rates in the microwave X-band (*10*). Combining with negligible thermal effects and Kerr-dominated frequency-dependent response (*9*), reliable soliton generation can be attained without complex or fast laser tuning. Additionally, laser self-injection locking (*11*–*14*) and hybrid integration of soliton microcombs with distributed feedback (DFB) lasers (*15*–*17*) and reflective semiconductor optical amplifiers (RSOAs) (*18*) allow for current-initiated and electrically controlled modules with low electrical power.

A long-standing goal is to monolithically integrate lasers and high-Q nonlinear microresonators onto a common silicon wafer. Heterogeneously integrated silicon photonics (*19*–*21*) offers a compelling solution using low-cost, industry-standard silicon substrates, aided by mature complementary metal-oxide-semiconductor (CMOS)–compatible fabrication facilities. High-performance, large-scale heterogeneous PICs with complete functionalities are disrupting optical interconnect technology and other applications (*22*, *23*). However, heterogeneous integration of high-power, narrow-linewidth semiconductor lasers with high-Q Si_3N_4 microresonators has not been demonstrated yet, because multiple material platforms (Si, Si_3N_4, and III-V) with appreciably different optical properties have to be deployed and combined. Here we overcome these challenges and present the first demonstration of heterogeneously integrated laser soliton microcombs. A chip-scale laser frequency comb (Fig. 1A, top) consists of three main parts: a DFB laser, a thermo-optic phase tuner, and a high-Q nonlinear microresonator, combined by leveraging multilayer heterogeneous integration (*24*). Here, the DFB laser, phase tuner, and nonlinear microresonator are built on InP/Si, Si, and Si_3N_4 layers, respectively (Fig. 1A, bottom inset). This vertical, multilayer structure is realized through sequential wafer bonding of a silicon-on-insulator (SOI) wafer and an InP multiple-quantum-well (InP MQW) epi wafer to a prepatterned Si_3N_4 substrate fabricated using the photonic Damascene process (*9*, *24*). Here we directly apply the heterogeneous integration on a 100-mm-diameter Si substrate and process the entire substrate on the wafer scale.

The continuous-wave laser output passes through a thermo-optic resistive heater (for optical phase control) and couples into a high-Q Si_3N_4 microring resonator where Kerr nonlinear four-wave mixing generates soliton microcombs. The Si_3N_4 microresonator exhibits anomalous group velocity dispersion (GVD) in the telecommunication C band and has a free spectral range (FSR) of 100 GHz. The laser directly pumps the microresonator without an intermediate optical isolator, and the entire device is electronically operated via laser current control and phase control. Laser self-injection locking (*11*, *12*, *13*, *14*) leverages the narrow-band optical feedback at desired phase relations from a high-Q microresonator to stabilize the pump laser and pulls the laser frequency toward the microring resonance. In this scenario, soliton microcombs can form when optimum laser-microresonator frequency detuning is reached. The DFB laser wavelength increases with increasing laser current, as the grating index increases as a result of injected electrical power heating. Consequently, certain gain currents trigger comb generation when the laser wavelength coincides with a microresonator resonance. The comb generation region resides where the laser is red-detuned to the resonance (Fig. 1B), and the phase of the Rayleigh backscattered light from the microresonator to the laser fulfills certain phase relations (*25*). Figure 1C shows photographs of the fabricated devices with difference scales.

Our fabrication process flow (Fig. 2A) starts with the photonic Damascene process (*7*, *9*) to fabricate the Si_3N_4 PIC on a Si substrate with 4-μm-thick thermal wet silicon dioxide (SiO_2). The PIC pattern is exposed with deep ultraviolet (DUV) stepper lithography and dry-etched into the SiO_2 substrate to form the waveguide preform. Stoichiometric Si_3N_4 is deposited on the patterned SiO_2 preform by using low-pressure chemical vapor deposition (LPCVD), filling the trenches and forming waveguide cores. Chemical-mechanical polishing (CMP) is used to remove excess Si_3N_4, planarize the wafer front surface, and control the Si_3N_4 waveguide height (780 nm). Afterward, spacer SiO_2 of 300-nm thickness is deposited on the Si_3N_4 substrate. The entire substrate is further annealed at 1200°C to drive out the residual hydrogen content in Si_3N_4 and SiO_2 and to densify the spacer SiO_2. A second CMP is performed to create a flat and smooth wafer surface. The measured root mean square (RMS) roughness of the wafer surface measured by atomic force microscopy (AFM) is 0.27 nm (Fig. 2B left), enabling direct substrate bonding with an SOI wafer.

To achieve high bonding yield, vertical channels for outgassing are etched before wafer bonding (*25*, *26*). Coarse alignment is required to bond blank films on the target areas of the

[1]Department of Electrical and Computer Engineering, University of California, Santa Barbara, Santa Barbara, CA 93106, USA. [2]Institute of Physics, Swiss Federal Institute of Technology Lausanne (EPFL), CH-1015 Lausanne, Switzerland. [3]Materials Department, University of California, Santa Barbara, Santa Barbara, CA 93106, USA.
*Corresponding author. Email: tobias.kippenberg@epfl.ch (T.J.K.); bowers@ece.ucsb.edu (J.E.B.)
†These authors contributed equally to this work.

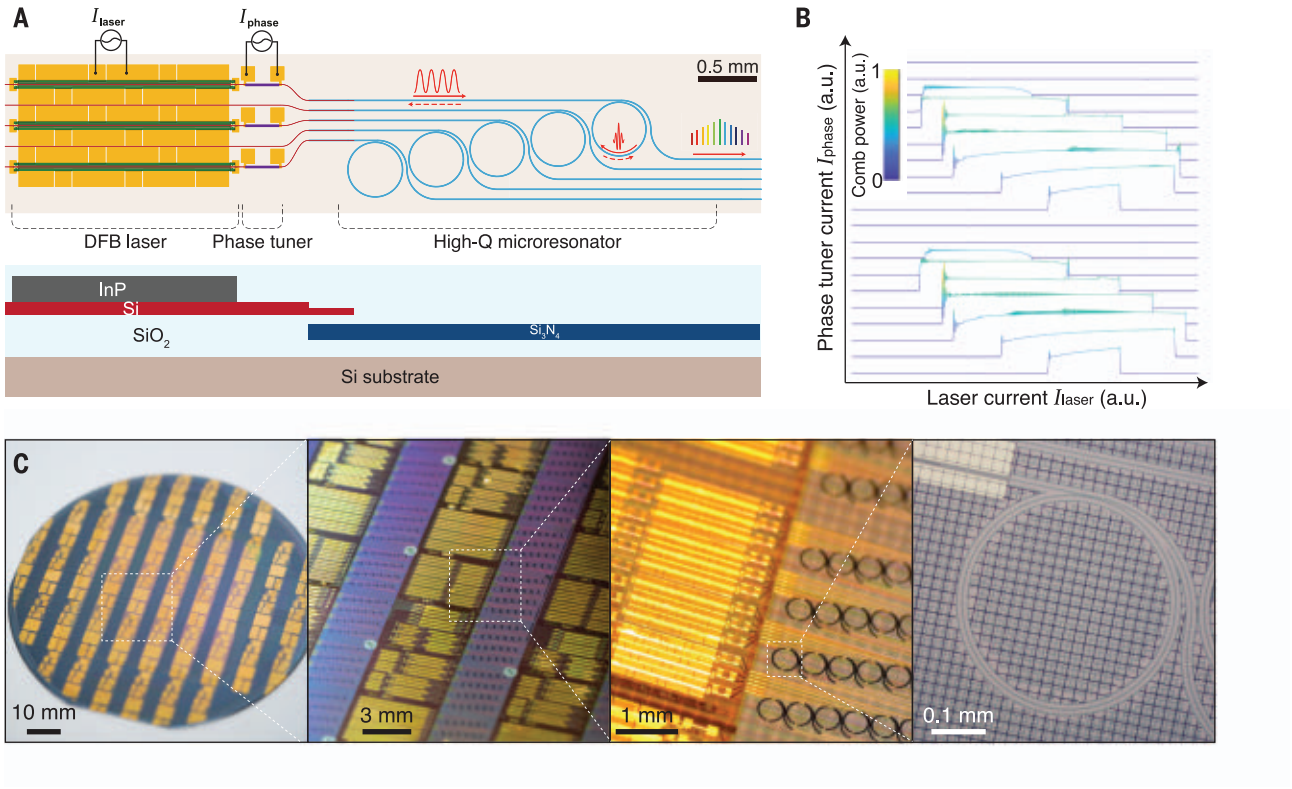

Fig. 1. Device schematic, images, and operation principle. (**A**) Schematic of laser soliton microcomb devices consisting of DFB lasers, phase tuners, and high-*Q* microresonators on a common substrate. A continuous-wave signal (solid red line) emitted from the laser is coupled into the microresonator and partially backscattered. The backscattered signal (dashed red line) to the laser triggers self-injection locking that assists soliton formation inside the microresonator. The locking is optimized by controlling the laser current I_{laser} and phase tuner current I_{phase}. The bottom inset shows the simplified device cross section. The laser is based on InP/Si, and the microresonator is based on Si_3N_4. The intermediate Si layer with two etch steps is used to deliver light from the InP/Si layer to the Si_3N_4 layer. (**B**) Schematic of the microcomb generation with sweeping laser current I_{laser} and varying phase tuner current I_{phase}, to control the optical phase of self-injection locking. This waterfall plot is based on a full nonlinear simulation (*25*). (**C**) Photographs showing the completed 100-mm-diameter wafer and zoom-in of multiple dies, and a microscopic image showing a Si_3N_4 microring resonator with Si/Si_3N_4 interface.

patterned substrate. Fine alignment of patterns on different layers with an accuracy within 100 nm is enabled by DUV stepper lithography. After removing the Si substrate and buried SiO_2 layer of the bonded SOI wafer, the Si device layer is processed to create waveguide structures with different etch depths, including shallow-etched Si rib waveguides for the lasers and phase tuners, fully etched hole structures for gratings (Fig. 2B, right), and thin Si tapers for mode conversion between the Si waveguide and underlying Si_3N_4 waveguide (*24*). InP-based MQW gain material is then bonded to the patterned Si device at the active regions. The InP process starts with InP substrate removal. InP mesa etches, including P-type InP, InAlGaAs MQW, and N-type InP, are performed by selective dry etching and wet etching. P- and N-type contact metals are deposited on the P-InGaAs layer and N-InP layer, respectively. The excess Si on top of Si_3N_4 microresonators is removed before laser passivation by hydrogen-free deuterated SiO_2 deposition (*27*). Vias are then etched for laser electrical contact, followed by proton implantation on the laser mesa structure to reduce electrical current leakage. Heater and probe metals are deposited at the end of the full process. Finally, the entire wafer is diced into dozens of dies or chips to facilitate testing. The InP/Si-to-Si rib waveguide transition loss is below 1 dB (*28*), and the Si-to-Si_3N_4 mode conversion efficiency is simulated to be above 90% (*25*). Assuming all devices share the same design, the overall device yield is determined primarily by the SOI bonding and InP bonding yields. In the current wafer, we have achieved bonding yields that enable thousands of complete laser-microresonator devices, each of which has a footprint as small as 1.6 mm^2 (*25*). Figure 2C shows the scanning electron microscopic (SEM) images of the device cross section, which is false-colored to illustrate the multilayer structure.

The experimental setup to characterize the final chip devices is shown in Fig. 3A. We first characterize the laser performance. The DFB laser is a high-power, single-longitudinal-mode pump source with a high side-mode suppression ratio (SMSR) such that the laser wavelength can be tuned to a microring resonance (*29*). Our laser has a 1.8-mm-long InP/Si gain section, and the grating is etched on both sides of the shallow-etched Si rib waveguide with a 170-nm gap separation from the Si waveguide core. The fully etched grating provides the optical resonant feedback for the pump laser and determines the lasing wavelength λ_{pump} by its pitch Λ ($\lambda_{pump} = 2n_{eff}\Lambda$). Here, $\Lambda = 238$ nm, n_{eff} ~3.26, and λ_{pump} ~1550 nm. A quarter-wavelength shift section is included at the grating length center to supply nondegenerate phase conditions favoring single-longitudinal-mode lasing. Figure 3B shows the measured light-current curves (solid blue), i.e., the laser output power versus stepped laser injection current, with 7-mA phase tuner current and 20°C stage temperature. The measured laser threshold current is 64 mA. The laser power is outcoupled from the Si_3N_4 waveguide inverse-taper to a lensed fiber. The maximum power in the output fiber is measured as 8 mW, and the corresponding on-chip power in the Si_3N_4 waveguide is ~20 mW. The center wavelength of the laser measured with a

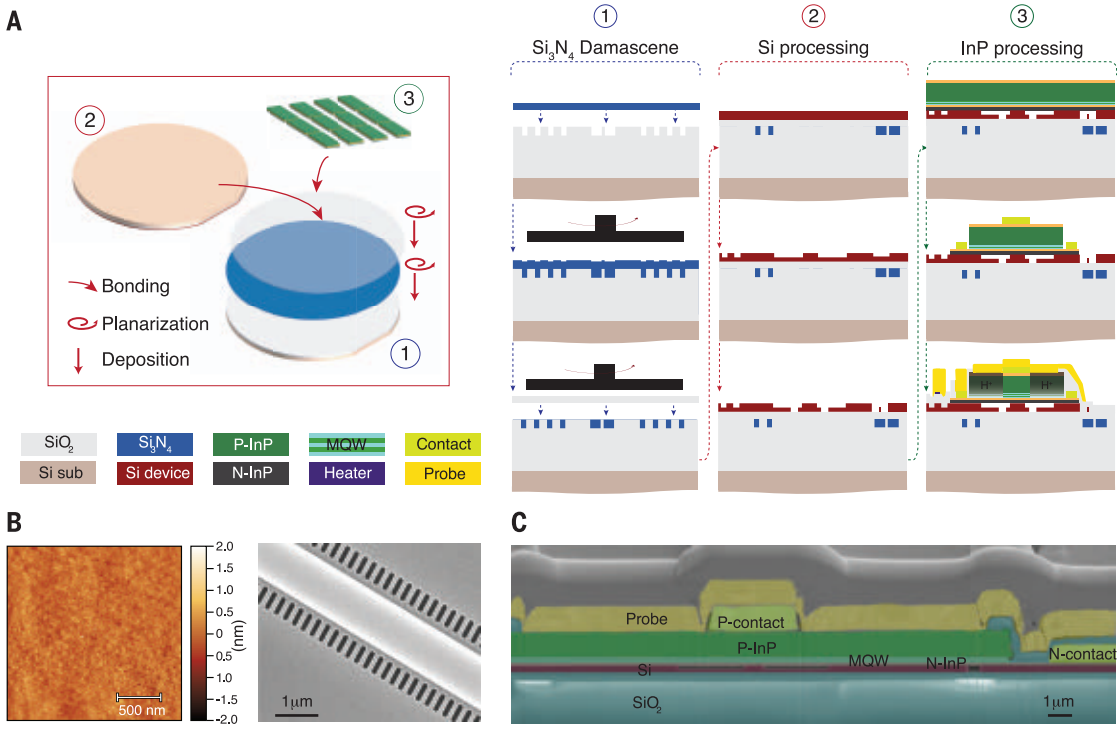

Fig. 2. Simplified wafer-scale fabrication process flow. (**A**) Multilayer heterogeneous integration process. Left panel shows that a prepatterned Si_3N_4 Damascene substrate is planarized and subsequently bonded with an SOI wafer and InP MQW epi pieces. Right panel shows selected key fabrication steps: (1) Si_3N_4 photonic Damascene process, including LPCVD Si_3N_4 deposition on the patterned SiO_2 substrate (top), excess Si_3N_4 removal and planarization via CMP (middle), and SiO_2 spacer deposition and polishing (bottom); (2) Si processing, including Si substrate removal (top), Si waveguide etch for laser and thermal tuner (middle) and for Si grating and Si-Si_3N_4 mode conversion taper (bottom); (3) InP processing, including InP substrate removal (top); InP mesa etch (middle); and excess Si removal, laser passivation, contact formation, vias open, heaters, and probe metal formation (bottom). All the photolithography steps are performed with a 248-nm DUV stepper, except that electron-beam lithography is used for the Si grating writing because of the required finer pattern resolution. Elements are not shown with the same scale so as to highlight the structures instead of the dimensions. (**B**) Left: Atomic force microscopy shows 0.27-nm RMS roughness of the Si_3N_4 wafer surface, after the second CMP on the SiO_2 spacer, before SOI bonding. Right: SEM image of Si grating for laser before InP bonding. (**C**) False-colored SEM image showing the cross section of the complete device in the laser area with multilayer structure.

wavelength meter is shown in Fig. 3B (dashed gray). Several dips on the light-current curve are observed at laser currents of 133.0, 231.0, 329.5, and 418.0 mA, where the laser wavelength coincides with microresonator resonances. These dips also verify the microresonator FSR of 100 GHz. A high-reflection coating is applied on the other side of the DFB laser to boost the laser output power. Future devices can avoid using this coating to yield mode-hop-free DFB lasers and linearized laser wavelength dependence on the laser current. The DFB laser has high SMSR at resonances #1 and #2, where high output powers are also obtained that are advantageous for comb generation. Figure 3C shows the single-longitudinal-mode laser spectra at two resonance wavelengths, with 60 and 57 dB SMSR, respectively.

Soliton microcomb is generated by aligning the laser frequency to the microresonator resonance via tuning the laser current, together with tuning the phase tuner current to control the relative forward to backward phase. As an optical isolator is absent between the laser and the Si_3N_4 microresonator, laser self-injection locking (*15*–*17*) occurs when the laser frequency coincides with a microresonator resonance. More information (*25*) about the phase dependence on comb generation is revealed by simulating the nonlinear self-injection locking process (*16*). In the critical coupling regime, the estimated Kerr parametric oscillation threshold is

$$P_{\mathrm{th}} = \frac{\pi n_0 \omega_{\mathrm{p}} A_{\mathrm{eff}}}{n_2 D_1 Q_0^2} \qquad (1)$$

where $\omega_{\mathrm{p}}/2\pi \approx 193$ THz is the optical frequency of the pump mode, $n_0 = 2.0$ is the refractive index of Si_3N_4, $n_2 = 2.4 \times 10^{-19}\,\mathrm{m^2/W}$ is the nonlinear index of Si_3N_4, $A_{\mathrm{eff}} \approx 1.6 \times 10^{-12}\mathrm{m^2}$ is the effective mode area, $D_1/2\pi$ is the microresonator FSR, and Q_0 is the microresonator intrinsic quality factor. For Si_3N_4 microresonators of $Q_0 \sim 7 \times 10^6$ (*25*) and 100-GHz FSR used in this work, we estimate $P_{\mathrm{th}} \approx 2$ mW.

With a laser current around 329 mA, the estimated on-chip laser power required to pump the Si_3N_4 microresonator exceeds 16 mW. Perfect soliton crystal states (*30*) are observed by fine-tuning the laser frequency and the optical phase between the forward laser output and backward reflected signal (Fig. 3D). The access to soliton crystal states indicates that the pump laser power just reaches the soliton formation threshold (*25*). We also observe soliton crystal states with decreasing crystallization orders when increasing the laser current (red detuning). Further increasing the laser gain current to ~418 mA generates a two-soliton crystal state with 200-GHz line spacing and a single-soliton state with 100-GHz repetition rate. The coherent soliton nature is revealed by photodetection of the low-intensity noise from the comb lines beating. Once generated, the soliton states can be stable for hours in standard laboratory environments without any external feedback control. This stability benefits from the monolithic nature of the chip device and the laser-microresonator coupling through laser self-injection locking.

To further characterize the laser self-injection locking, we measure the frequency noise spectra of the pump line and comb lines in the single-soliton state and laser free-running state (Fig. 4A). Leveraging a high-*Q* external cavity, self-injection locking exhibits frequency noise reduction, i.e., laser linewidth narrowing (*13*). The fundamental linewidth of the free-running DFB laser is ~60 kHz and is reduced to ~25 Hz in the self-injection–locked single soliton state. Noise reduction of 10 dB is observed at 1-kHz Fourier offset frequency and is more than 30 dB above the 300-kHz offset frequency. It has been revealed that the frequency noise of a self-injection–locked

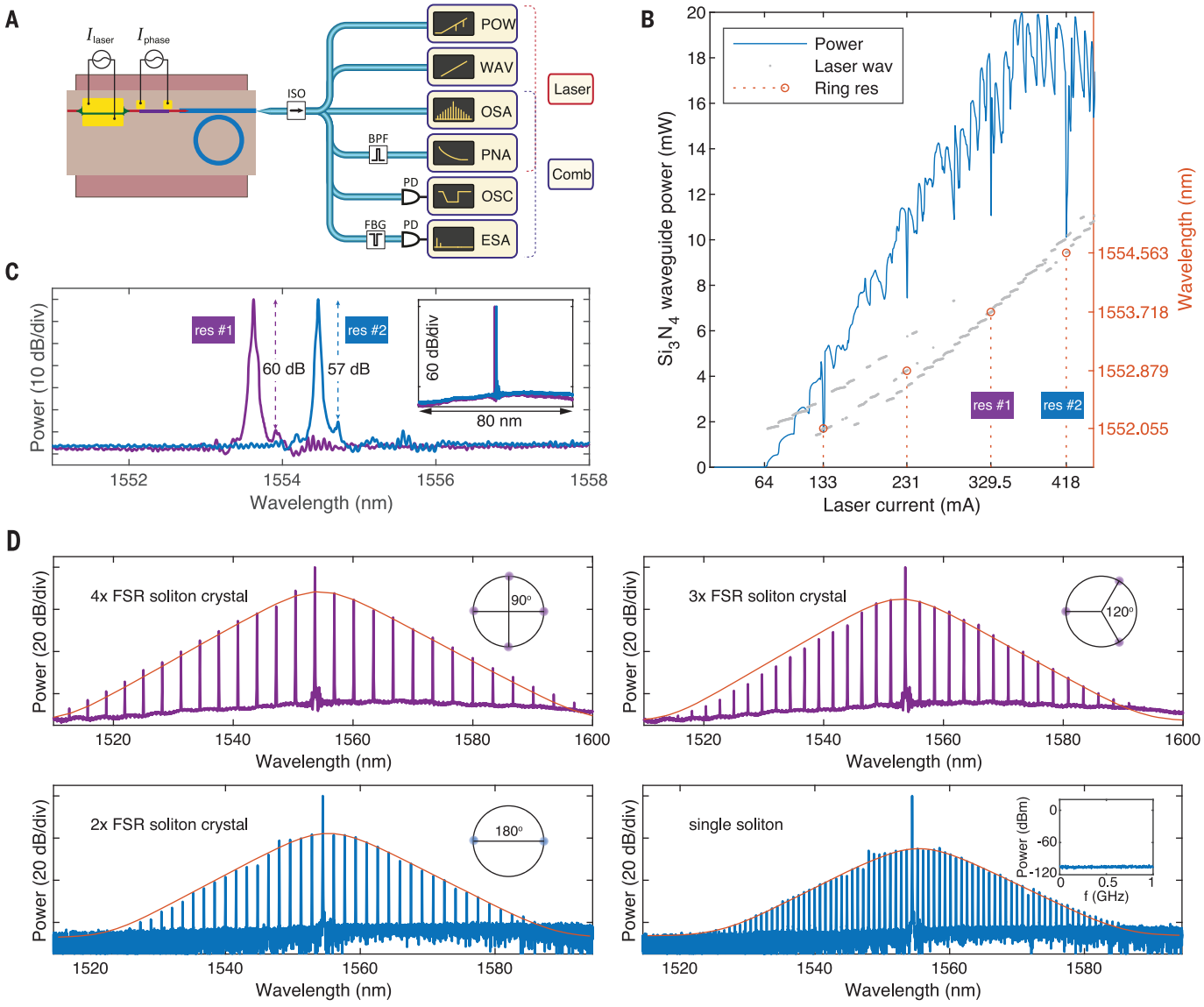

Fig. 3. Device characterization and experimental generation of soliton spectra. (**A**) Experimental setup for laser and soliton characterization. I_{laser} and I_{phase} are the current sources to drive the laser and the phase tuner. POW, power meter; WAV, wavelength meter; OSA, optical spectrum analyzer; PNA, phase noise analyzer; OSC, oscilloscope; ESA, electrical spectrum analyzer; ISO, isolator; BPF, band-pass filter; FBG, fiber Bragg grating; PD, photodetector. (**B**) Light-current sweep measurement with stepped laser current and fixed phase tuner current. Gray color shows the corresponding laser center wavelength as a function of the laser current. Red circles indicate the laser wavelength coinciding with microresonator resonances. Soliton microcombs are generated with laser currents and wavelengths at resonance #1 and resonance #2. (**C**) Single-mode DFB laser spectra at the wavelengths of resonance #1 and resonance #2. (**D**) Optical spectra of soliton states. Inset shows the relative position of multi-solitons circulating inside the microring resonator for four-, three-, and two-FSR soliton crystal states and low-frequency radio-frequency spectrum of the single-soliton state. The applied gain currents to generate these soliton states are shown in (B) for the corresponding resonances, and the phase tuner currents are 11.7 mA for four- and three-FSR states, 15.3 mA for two-FSR and single-soliton states. To switch the soliton state, the gain current is increased together with fine current tuning with 0.1-mA resolution.

laser to a high-Q Si_3N_4 microresonator can be dominantly limited by the thermo-refractive noise of the microresonator (*17*, *31*). Though the free-running linewidth of the DFB laser is broad, owing to the linewidth narrowing provided by self-injection locking, the laser can still directly generate soliton states, surpassing its intrinsic limitation of spectral impurity. Additionally, the coherence of the injection-locked pump line is transferred to other comb lines. For example, the first pair of neighboring comb lines, 100 GHz apart from the pump, have a fundamental linewidth around 200 to 300 Hz, and their frequency noise below 10-MHz offset frequency directly inherits that of the pump line. The self-injection locking scheme thus enables multiwavelength, narrow-linewidth laser sources. Our device represents the realization of a self-injection–locked, narrow-linewidth laser on Si.

Comb generation with self-injection locking relies critically on the phase relation between the forward signal (i.e., the laser emission to the microresonator) and backward signal (i.e., the backscattered light from the microresonator to the laser). In this case, comb generation is only allowed when the optical phase difference is within a certain optimized range. In previous works using hybrid integrated devices (*15*, *16*), controlling the phase difference

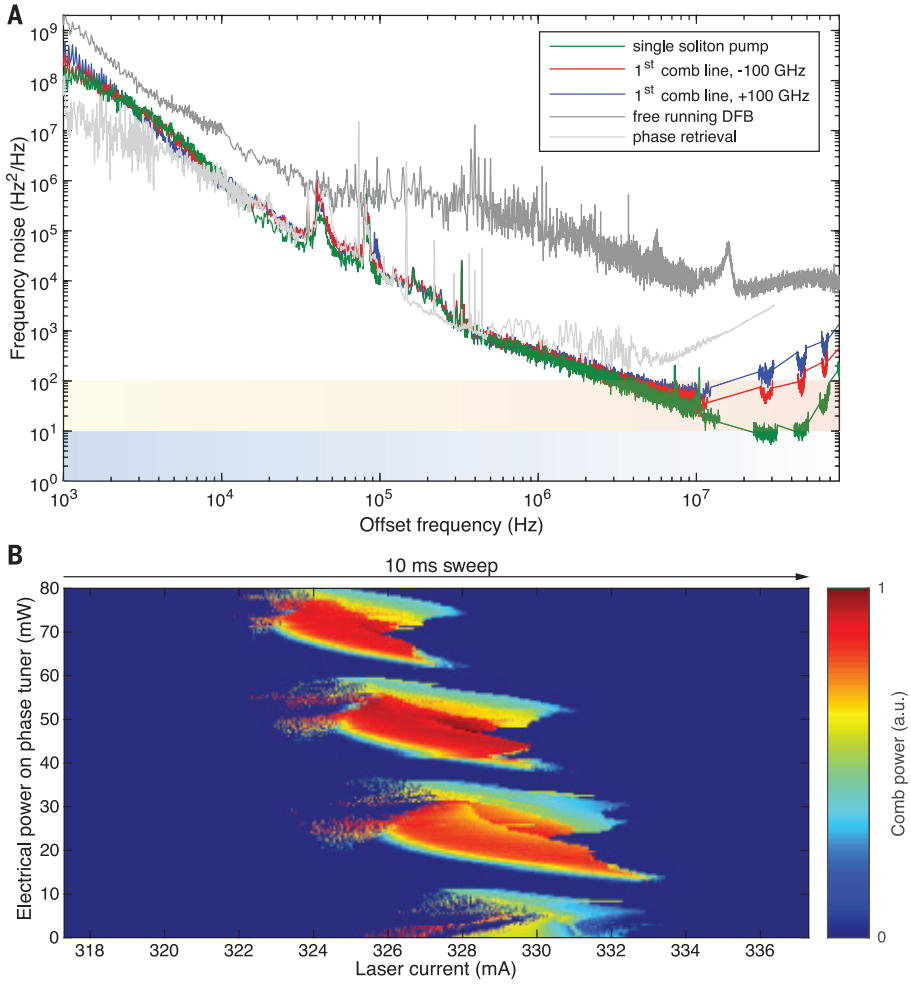

Fig. 4. Laser frequency noise spectra and comb generation with self-injection locking. (**A**) Frequency noise spectra of the self-injection–locked pump line (green), comb lines with ±100-GHz frequency offset to the pump (blue and red) in the single-soliton state, free-running single-mode DFB laser output without self-injection locking (dark gray), and comb line around 1550 nm for the two-FSR soliton crystal state using optical phase retrieval method (*25*). (**B**) Comb power evolution with sweeping laser current (10 ms sweep) under varying electrical power on the phase tuner.

was realized by varying the gap distance between the laser chip and Si_3N_4 chip, which, however, also caused the power coupling efficiency between these two chips to fluctuate. In our monolithic device, this optical phase difference can be directly controlled by varying the phase-tuner current. We experimentally study the comb formation with laser current sweep under different currents on the phase tuner. To exclude the interference from the mode-hop phenomenon when monitoring the power of the new frequency components, we sweep the laser current across the resonance #1 shown in Fig. 3B. Results shown in Fig. 4B reveal that the comb generation is only permitted with certain phase conditions. More study (*25*) indicates that the backscattered signal needs to be in phase with the forward signal. Additionally, the phase-altering effect is periodic and deterministic with the applied electrical power on the phase tuner. Thus, the allowed comb generation regime depends mainly on the pump power and the intensity of the backscattered light (*25*).

In sum, we have presented a heterogeneously integrated laser soliton microcomb on silicon. The device outputs a single soliton with a 100-GHz repetition rate and exhibits self-injection–locked laser performance with frequency noise reduction. More functions can be added into our current technology with other material platforms (*25*). Our process can be upgraded to 200- or 300-mm-diameter substrates by using modified CMOS foundry pilot lines and transfer heterogeneous integration to scalable production of chip-scale frequency combs for field-deployable applications.

REFERENCES AND NOTES

1. S. A. Diddams, K. Vahala, T. Udem, *Science* **369**, eaay3676 (2020).
2. T. Fortier, E. Baumann, *Commun. Phys.* **2**, 153 (2019).
3. T. J. Kippenberg, A. L. Gaeta, M. Lipson, M. L. Gorodetsky, *Science* **361**, eaan8083 (2018).
4. D. J. Moss, R. Morandotti, A. L. Gaeta, M. Lipson, *Nat. Photonics* **7**, 597–607 (2013).
5. A. L. Gaeta, M. Lipson, T. J. Kippenberg, *Nat. Photonics* **13**, 158–169 (2019).
6. Y. Xuan *et al.*, *Optica* **3**, 1171 (2016).
7. M. H. P. Pfeiffer *et al.*, *Optica* **3**, 20 (2016).
8. X. Ji *et al.*, *Optica* **4**, 619 (2017).
9. J. Liu *et al.*, *Nat. Commun.* **12**, 2236 (2021).
10. J. Liu *et al.*, *Nat. Photonics* **14**, 486–491 (2020).
11. L. Maleki *et al.*, *2010 IEEE International Frequency Control Symposium* (2010), pp. 558–563.
12. W. Liang *et al.*, *Nat. Commun.* **6**, 7957 (2015).
13. W. Liang *et al.*, *Nat. Commun.* **6**, 7371 (2015).
14. N. M. Kondratiev *et al.*, *Opt. Express* **25**, 28167 (2017).
15. B. Shen *et al.*, *Nature* **582**, 365–369 (2020).
16. A. S. Voloshin *et al.*, *Nat. Commun.* **12**, 235 (2021).
17. W. Jin *et al.*, *Nat. Photonics* **15**, 346–353 (2021).
18. B. Stern, X. Ji, Y. Okawachi, A. L. Gaeta, M. Lipson, *Nature* **562**, 401–405 (2018).
19. T. Komljenovic *et al.*, *J. Lightwave Technol.* **34**, 20–35 (2016).
20. J. Zhang *et al.*, *APL Photonics* **4**, 110803 (2019).
21. D. Liang, J. E. Bowers, *Light Adv. Manuf.* **2**, 5 (2021).
22. J. Sun, E. Timurdogan, A. Yaacobi, E. S. Hosseini, M. R. Watts, *Nature* **493**, 195–199 (2013).
23. R. Jones *et al.*, *IEEE Nanotechnol. Mag.* **13**, 17–26 (2019).
24. C. Xiang *et al.*, *Optica* **7**, 20 (2020).
25. See supplementary materials.
26. D. Liang, J. E. Bowers, *J. Vac. Sci. Technol. B Microelectron. Nanometer Struct. Process. Meas. Phenom.* **26**, 1560 (2008).
27. W. Jin *et al.*, *Opt. Lett.* **45**, 3340–3343 (2020).
28. M. L. Davenport *et al.*, *IEEE J. Sel. Top. Quantum Electron.* **22**, 78–88 (2016).
29. L. A. Coldren, S. W. Corzine, M. Mashanovitch, *Diode Lasers and Photonic Integrated Circuits* (Wiley, 2012).
30. M. Karpov *et al.*, *Nat. Phys.* **15**, 1071–1077 (2019).
31. G. Huang *et al.*, *Phys. Rev. A* **99**, 061801 (2019).
32. C. Xiang, J. Liu, Open data for "Laser soliton microcombs heterogeneously integrated on silicon,"version 1, Zenodo (2021); https://doi.org/10.5281/zenodo.4745864.

ACKNOWLEDGMENTS

We thank M. Dumont and J. He for help in device characterization and W. Jin for help in mode simulations. **Funding:** This publication was supported by the Defense Advanced Research Projects Agency (DARPA) under DODOS (HR0011-15-C-055) programs of the Microsystems Technology Office (MTO), by the Air Force Office of Scientific Research under Award no. FA8655-20-1-7009, and by the Swiss National Science Foundation under grant agreement no. 176563 (BRIDGE). J.R. acknowledges support from the EUs H2020 research and innovation program under the Marie Sklodowska-Curie IF grant agreement no. 846737 (CoSiLiS). **Author contributions:** C.X., J.L., and L.C. designed the wafer layout and process flow. J.L. and R.N.W. fabricated the Si_3N_4 substrate. C.X. and J.P. fabricated the heterogeneous InP/Si lasers and Si circuits with assistance from W.X. and Z.Z. C.X., J.G., and J.L. tested the final chips. C.X. and J.G. performed the laser soliton experiments with assistance from J.L. and J.R. W.W. performed the numerical simulations of self-injection locking. J.S. took the FIB-SEM image. C.X., J.L., and W.W. wrote the manuscript, with input from others. T.J.K. and J.E.B supervised the project. **Competing interests:** J.E.B.is a cofounder and shareholder of Nexus Photonics and Quintessent, startups in silicon photonics. T.J.K. is a cofounder and shareholder of LiGenTec SA, a start-up company that is engaged in making Si_3N_4 nonlinear photonic chips available through foundry service. **Data and materials availability:** The datasets are available through Zenodo (*32*).

SUPPLEMENTARY MATERIALS

science.sciencemag.org/content/373/3550/99/suppl/DC1
Materials and Methods
Supplementary Text
Figs. S1 to S7
Tables S1 and S2
References (*33*–*51*)

22 February 2021; accepted 20 May 2021
10.1126/science.abh2076

ZEOLITES

Synthesis of thermally stable SBT and SBS/SBT intergrowth zeolites

Hwajun Lee[1]†, Jiho Shin[2]†, Kyounghwan Lee[1], Hyun June Choi[1], Alvaro Mayoral[3,4,5], Na Young Kang[2], Suk Bong Hong[1]*

UCSB-6 (framework type SBS) and UCSB-10 (SBT), two three-dimensional phosphate-based molecular sieves with supercages accessible through 12-ring (circumscribed by 12 tetrahedral atoms) windows, are structurally similar to the hexagonal and cubic polytypes of faujasite or zeolite Y, an industrially relevant catalyst, but the cage structures are substantially different. Nonetheless, their inherent thermal instability has precluded any catalytic application so far. By using multiple inorganic cation and charge density mismatch approaches, we synthesized PST-32 and PST-2, a thermally stable aluminosilicate version of UCSB-10 and the hypothetical SBS/SBT intergrowth family member, respectively. This study suggests that many hypothetical cage-based zeolite structures with multidimensional channel systems can be synthesized as compositionally robust forms by systematically exploring the synergy effect of inorganic and organic structure–directing agents.

Zeolite Y (**FAU**), with a *fau* ($[4^{18}6^{4}12^{4}]$) cage (with a volume of 1.15 nm^3) accessible through four circular 12-ring (7.4 × 7.4 Å) windows, is used in 40% of petroleum conversion (*1*). EMC-2 (**EMT**), its hexagonal polytype, is the only other thermally robust aluminosilicate zeolite reported that has large cages and three-dimensional (3D) 12-ring channels in the protonated form (*2*, *3*). In the search for other cage-based large-pore materials, the **SBS** and **SBT** framework types, first described as UCSB-6 and UCSB-10 in 1998 (*4*), are attractive because the connection sequences in **SBS** and **SBT** composed of *can* ($[4^{6}6^{5}]$) cages as a basic building unit are essentially equivalent to those in **EMT** and **FAU**, respectively. However, the latter pair consists of *sod* ($[4^{6}6^{8}]$) cages, so there are intriguing differences in the 12-ring window size and shape, as well as in the cage structure and volume (Fig. 1) (*3*, *4*). Thus, **SBS** and **SBT** are of major importance as potential catalysts, especially for refining and petrochemical processes that use zeolite Y.

UCSB-6 and UCSB-10 have only been reported as phosphate-based compositions, with various framework metal atoms such as Co and Zn, that were designed following the host–guest charge density match approach (*4*). Linear flexible diamine-based molecules (e.g., 1,9-diaminononane and 4,7,10-trioxa-1,13-tridecanediamine), fully protonated to balance the negative framework charges created by transition metal substitution in the as-synthesized form, were intentionally selected as organic structure–directing agents (OSDAs). Unfortunately, UCSB-6 and UCSB-10 become amorphous upon OSDA removal, hindering their catalytic applications.

The charge density mismatch approach, conceptually different from the charge density match, is also a viable option for finding new stable aluminosilicate zeolites such as UZM-5 (**UFI**) (*5*, *6*). However, more than one type of alkali metal ions and sometimes alkaline earth ones as inorganic structure–directing agents (ISDAs) have often been used in the synthesis

[1]Center for Ordered Nanoporous Materials Synthesis, Division of Environmental Science and Engineering, POSTECH, Pohang 37673, Korea. [2]Petrochemical Catalyst Research Center, Korea Research Institute of Chemical Technology, Daejeon 34114, Korea. [3]Instituto de Nanociencia y Materiales de Aragon (INMA), CSIC, Universidad de Zaragoza, 50009 Zaragoza, Spain. [4]Laboratorio de Microscopias Avanzadas, Universidad de Zaragoza, 50018 Zaragoza, Spain. [5]Center for High-Resolution Electron Microscopy (ChEM), School of Physical Science and Technology, ShanghaiTech University, Shanghai 201210, China.
*Corresponding author. Email: sbhong@postech.ac.kr
†These authors contributed equally to this work.

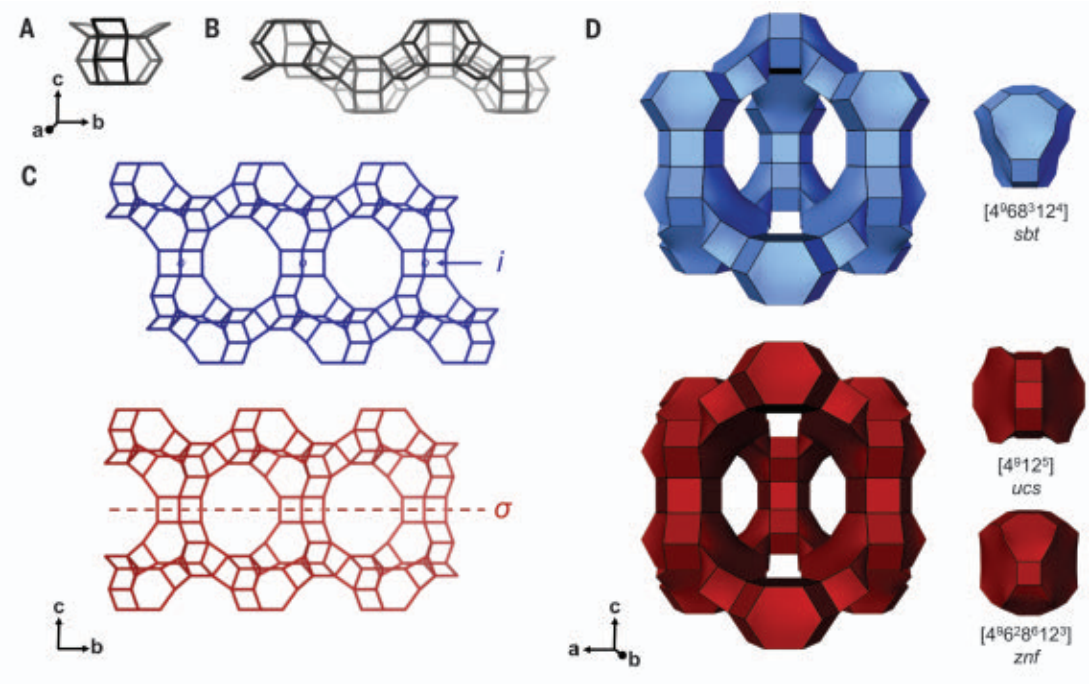

Fig. 1. SBS and SBT framework types. (**A**) Basic building unit, the *can* ($[4^{6}6^{5}]$) cage with six additional tetrahedral atoms. (**B**) Basic building layer along the *b* axis. Adjacent basic building units are linked by 4- and 8-rings to form a 2D building layer. (**C**) Connection modes of basic building layers in **SBS** (bottom) and **SBT** (top) along the *c* axis through double 6-ring units that have mirror (σ) and inversion (*i*) symmetries, respectively. (**D**) Cross-sectional views of **SBS** (bottom) and **SBT** (top) and their large cages. The **SBS** structure contains two types of supercages, one large *znf* cage (1.17 nm^3) with three 12-ring (7.0 × 6.9 Å) windows and the other considerably smaller *ucs* cage (0.68 nm^3) with three large (7.0 × 6.9 Å) and two slightly smaller (6.8 × 6.8 Å) 12-ring windows. The **SBT** structure has only one type of supercage (1.14 nm^3), the *sbt* cage interconnected by three large (7.8 × 7.3 Å) and one smaller (7.4 × 6.4 Å) 12-ring window.

of zeolites with Si/Al ratios generally <10 in the presence or absence of OSDAs (*7*). Recently, we have shown that the combined use of two different types of ISDAs with a specific OSDA is a practical alternative to new zeolite structures, possibly because of their cooperative structure direction effects or the preferential formation of particular building units by the particular type of ISDAs essential for the inorganic framework that is crystallizing (*8*–*10*).

Following the multiple inorganic cation approach, we synthesized PST-32, a thermally stable aluminosilicate (Si/Al = 4.0) version of UCSB-10, using Na^+ and Cs^+ as major and minor ISDAs, respectively, and *N*,*N*′-dimethyl-1,4-diazabicyclo[2.2.2]octane (Me_2-DABCO) as an OSDA (tables S1 and S2). We started PST-32 synthesis by replacing tetraethylammonium (TEA^+) ions in the synthesis gel with Si/Al = 5.0 containing Na^+, Cs^+, and TEA^+ ions, yielding zeolite rho (**RHO**) at 120°C (*10*) with various DABCO-based OSDAs while keeping the other synthesis parameters constant. The gel composition leading to PST-32 in the presence of Me_2-DABCO was narrow, as was the case of zeolites obtained using the same approach (*8*–*10*). For example, the absence of either Na^+ or Cs^+ in the synthesis mixture gave no PST-32.

Synchrotron powder x-ray diffraction (PXRD) and Rietveld analyses of the dehydrated protonated form of PST-32 (H-PST-32) confirmed that this zeolite had the **SBT** structure, a trigonal *R*-3*m* space group (Fig. 2A). A final reliability factor as low as R_{wp} = 2.0% and R_F^2 = 13.6% led to a goodness-of-fit of 2.6. The final lattice parameters were a = 17.28772(16) Å, c = 41.5378(11) Å, and α = β = 90°, γ = 120° (tables S3 to S5). Elemental and thermal analyses (fig. S3) indicated that PST-32 was synthesized at a unit cell composition of $|Na_{15.6}Cs_{11.3}(Me_2\text{-}DABCO)_{2.9}(OH)_{3.6}(H_2O)_{101.5}|[Al_{29}Si_{115}O_{288}]$. Thus, although enriched in Cs (Na/Cs = 1.4 versus 7.0) relative to its synthesis gel, both inorganic cations appeared to play a more important role in crystallizing this large-pore zeolite than Me_2-DABCO.

During the structure determination of PST-32, we noticed that its PXRD pattern was similar to that of PST-2, which we previously synthesized using the charge density mismatch approach at a relatively low framework Si/Al ratio (*5*, *6*), but were unable to solve the framework structure. We used TEA^+ as a charge density mismatch OSDA and Cs^+ as a crystallization ISDA at 100°C over a narrow crystallization field (tables S6 and S7). The PXRD pattern of as-synthesized PST-2 showed a sharp peak at 2θ ~ 5.7°, assignable to the 100 reflection of **SBS** (*3*), and peak broadening at 2θ ~ 6.4° (Fig. 2B). Furthermore, this material formed as long stacks of very thin, disk-like crystallites (Fig. 2C).

We applied spherical aberration corrected (C_s-corrected) scanning transmission electron microscopy (STEM) coupled with an annular dark field (ADF) detector (*11*) to evaluate the structure of PST-2 and determine whether it was a member of the hypothetical **SBS**/**SBT** intergrowth family (*3*). The close STEM-ADF inspection of a single PST-2 crystallite with a width of 10.2 nm, observed along the [100] direction, revealed an intergrown structure, which was enclosed by {001} and {010} (Fig. 2D). After evaluating >20 crystallites, the intergrowth between **SBS** and **SBT** was found in almost every case: Pure **SBS** phase was only once detected in a crystal 10 nm in width (fig. S1).

To gain more structural information, we delaminated PST-2 following the procedure for the preparation of ITQ-2, the calcined form of delaminated MCM-22 (**MWW**) precursor (*12*), and examined the disk structure on a perpendicular direction. The STEM-ADF images along [001] allowed us to observe not only the 12-rings but also the framework tetrahedral (T)-atoms (Fig. 2, E and F). Although the

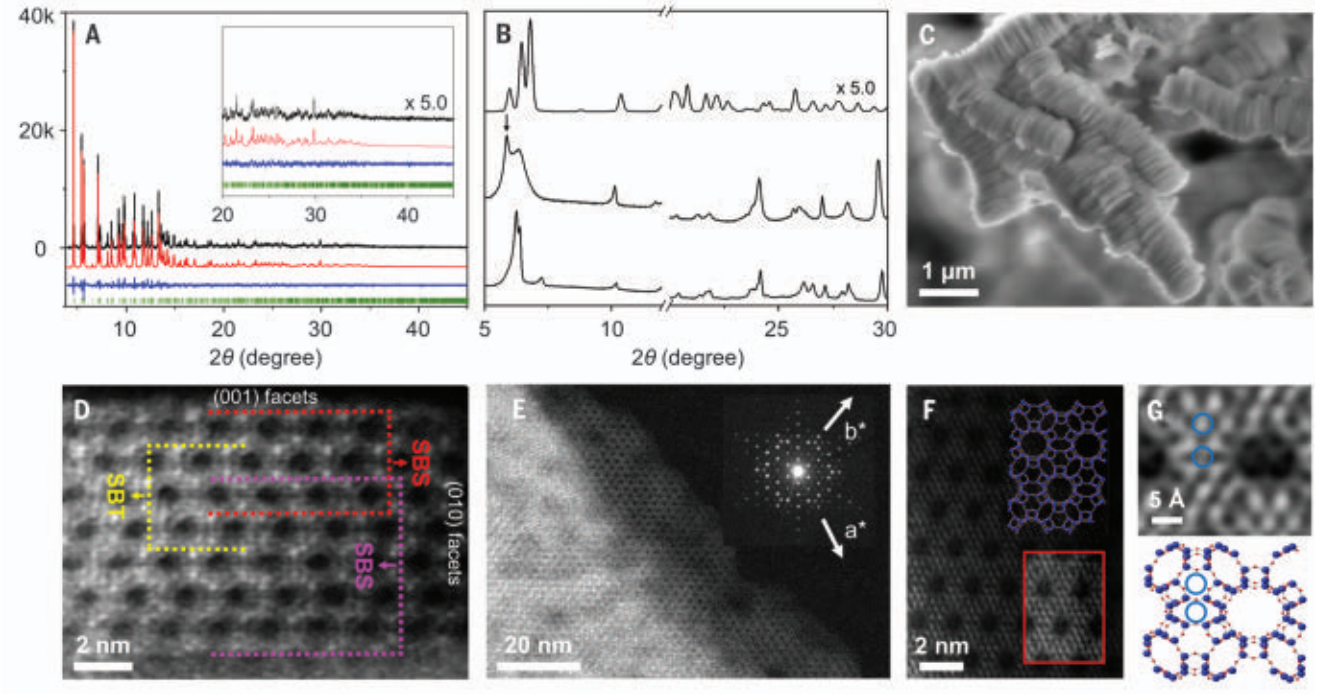

Fig. 2. Structural characterization of PST-32 and PST-2. (**A**) Rietveld plot for dehydrated H-PST-32: experimental (black), calculated (red), and difference (blue). The tick marks give the positions of allowed reflections. The first three low-angle x-ray peaks were excluded from the refinement because of peak shape problems. (**B**) Experimental PXRD patterns (Cu Kα radiation) of as-synthesized PST-32 (bottom) and PST-2 (middle) and simulated PXRD pattern of the **SBS** structure. The arrow indicates the (100) reflection in **SBS**. (**C**) SEM image of as-synthesized PST-2. (**D** and **E**) C_s-corrected STEM-ADF images of as-synthesized PST-2 along the [100] (D) and [001] (E) directions. The **SBS** and **SBT** regions in (D) are marked by dashed lines. The inset in (E) is the corresponding electron diffraction pattern. (**F** and **G**) Magnified STEM-ADF image (F) of the edge in (E), with the **SBS** structure model superimposed, and atomic visualization (G) of the **SBS** model with the corresponding schematic one. The differences between the experimental data and the framework are marked by blue circles.

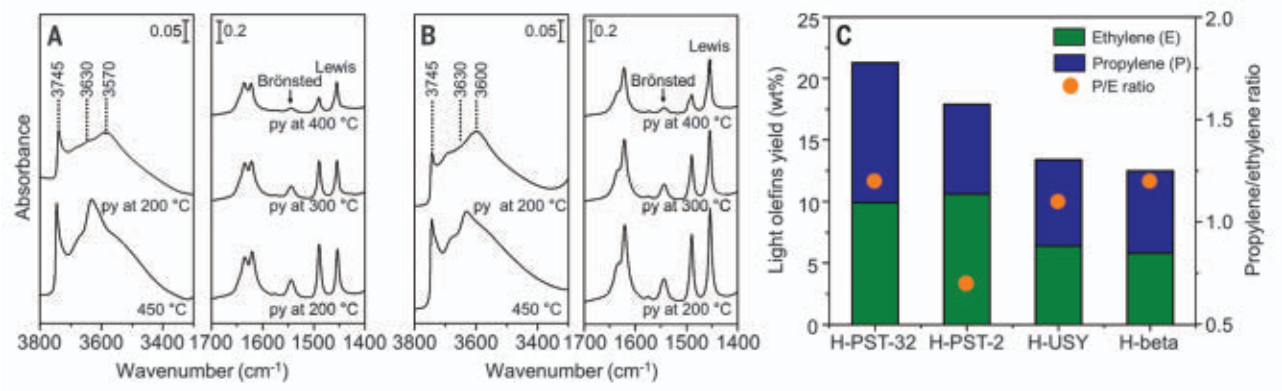

Fig. 3. Acidic and catalytic properties of PST-32 and PST-2. (**A** and **B**) IR spectra of H-PST-32 (A) and H-PST-2 (B) after dehydration at 450°C, pyridine adsorption at room temperature, and subsequent desorption at different temperatures. (**C**) Light olefins (ethylene and propylene) yield and propylene/ethylene ratio in diesel cracking over H-PST-32, H-PST-2, H-USY, and H-beta. Reaction conditions: 10 min on stream; 600°C; 100 mg of catalyst; 16 hours^{-1} weight hourly space velocity.

experimental data matched well with the **SBS** structure model, there were two additional extra-framework signals that would correspond to the Cs^+ ions located at the 6-rings of the *can* cage.

We quantified the topology and found an **SBS**/**SBT** ratio in PST-2 of 49:51 but with a considerably wide intergrowth distribution (15-100/0-85) in the crystallites studied, unlike the case of well-known beta and **FAU**/**EMT** intergrowth families (*13*, *14*), indicative of its smaller intergrowth formation energy. We analyzed the outermost layer in PST-2 along [001] and observed a zig-zag surface termination corresponding to the **SBS**/**SBT** building layer (fig. S2). The absence of any surface step implied that the formation rate of building layers was faster than their linking rate, hinting at the limited crystal growth through a layer-by-layer mechanism (*15*) along the *c* axis.

^{13}C and ^{27}Al magic-angle spinning (MAS) nuclear magnetic resonance (NMR) spectroscopy revealed that all OSDA cations and Al atoms in as-synthesized PST-32 and PST-2 remained intact and were present in framework T-atom sites, respectively (figs. S4 and S5). Deconvoluting their ^{29}Si MAS NMR spectra, we assumed that each observed resonance was a single Si environment. This gave $(Si/Al)_{NMR}$ ratios of 2.3 and 2.6, respectively (fig. S6), which are fairly lower than the Si/Al ratios (4.0 and 3.1, respectively) from elemental analysis, implying the wide Si-O-T angle range of various T-sites in PST-32 and PST-2.

The pore widths (6.7 and 6.4 Å, respectively) of H-PST-32 (Cs/Al = 0.06) and H-PST-2 (Cs/Al = 0.11) measured by Ar adsorption were essentially identical to and smaller than the pore width (6.8 Å) of ultrastable H-Y with Si/Al = 5.0 (H-USY), respectively (fig. S7). However, their micropore volumes (0.19 and 0.30 cm^3 g^{-1}) were smaller and larger than that (0.24 cm^3 g^{-1}) of H-USY, respectively. These results can be understood by considering the 12-ring window sizes of small *ucs* cages and the volume of larger *znf* cages in **SBS** (Fig. 1D) that occupies half the average proportion of PST-2.

The infrared (IR) spectra in the OH stretching region of dehydrated H-PST-32 and H-PST-2 showed that both zeolites exhibited two broad bands around 3630 and 3550 cm^{-1} (Fig. 3, A and B, and fig. S8), which could be assigned to Brönsted Si-OH-Al groups pointing into their supercages and *can* cages, respectively. The relative intensity ratio (about 1.2 versus 0.7) of high- to low-frequency Si-OH-Al bands being higher for H-PST-32 than for H-PST-2 suggested the preferential substitution of Al atoms for particular T-sites of their framework during the crystallization process. However, after pyridine adsorption, both zeolites exhibited the IR band at 1455 cm^{-1} in the C=C and C=N stretching region, indicative of pyridine adsorbed at Lewis sites (the extra-framework Al species). The band at 1545 cm^{-1} assigned to pyridinium cations remained after desorption at 400°C, indicating the presence of strong Brönsted acid sites in both H-PST-32 and H-PST-2.

From the competitive cracking of *n*-hexane/3-methylpentane, H-PST-32 and H-PST-2 were calculated to have constraint indices of 0.2 and 0.3, respectively, essentially the same as the values (0.2 to 0.5) observed for FAU-type zeolites (*16*). To assess their applicability as shape-selective catalysts in petroleum conversion, we studied the cracking of diesel (feed characteristics given in table S8) over H-PST-32 and H-PST-2. Comparing the catalytic results with those obtained from H-beta with Si/Al = 12.5, another commercial zeolite with a 3D large-pore system, as well as from H-USY (table S9), H-PST-32 showed the highest light olefins (ethylene and propylene) yield (21%) at similar diesel conversions (37-45%) (Fig. 3C and table S10). The light olefins yield (18%) on H-PST-2 was higher than the values (13% both) on H-USY and H-beta, whereas the former catalyst showed a rather low propylene/ethylene ratio (0.7 vs 1.1-1.2) compared with the other three catalysts. Unlike H-USY, in addition, H-PST-32 and H-PST-2 exhibited no noticeable decrease in light olefins yield during 100 min on stream even at a high-weight hourly space velocity of 48 hours^{-1} (fig. S9), revealing their high catalyst stability, which was probably due to the thin crystallite nature (Fig. 2C and table S9). These preliminary results showed that PST-32 and PST-2 have great potential for catalytic cracking applications.

As hypothesized for the **FAU**/**EMT** system (*17*), each building layer in **SBS**/**SBT** can also be connected in a strict alternating sequence of mirror and inversion symmetry planes down the *c* axis, creating a new zeolite structure containing *znf*, *ucs*, and *sbt* cages (figs. S10 and S11 and table S11). Although this structure, tentatively denoted as tss (the third polytype of the **SBS**/**SBT** family), does not exist in the current hypothetical member zeolite structure database (*18*, *19*), it has a framework energy of ~20 kJ (mol Si^{-1}) relative to α-quartz (*20*) and fulfills the local interatomic distances criteria (table S12) (*21*). Similar results were obtained for the "bst" structure composed of alternating **FAU** and **EMT** stackings (fig. S12 and table S12). This analysis suggests that the direct synthesis of tss and bst structures is in principle feasible. Indeed, the discovery of PST-32 and PST-2 demonstrates that many hypothetical 3D structures with large cages interconnected by 12-ring windows or even larger (*18*, *19*), which have important industrial implications, might be synthesized as thermally stable aluminosilicate compositions by promoting the synergistic cooperation between ISDAs and OSDAs. These cage-based large-pore materials also offer new opportunities for both fundamental research and applications, including catalysis, adsorption, and separations.

REFERENCES AND NOTES

1. W. Vermeiren, J.-P. Gilson, *Top. Catal.* **52**, 1131–1161 (2009).
2. F. Delprato, L. Delmotte, J. L. Guth, L. Huve, *Zeolites* **10**, 546–552 (1990).
3. C. Baerlocher, L. B. McCusker, "Database of zeolite structures" (2021); www.iza-structure.org/databases/.
4. X. Bu, P. Feng, G. D. Stucky, *Science* **278**, 2080–2085 (1997).
5. C. S. Blackwell *et al.*, *Angew. Chem. Int. Ed.* **42**, 1737–1740 (2003).
6. G. J. Lewis *et al.*, *Stud. Surf. Sci. Catal.* **154**, 364–372 (2004).
7. R. Szostak, *Handbook of Molecular Sieves* (Van Nostrand Reinhold, 1992).
8. J. Shin, D. Jo, S. B. Hong, *Acc. Chem. Res.* **52**, 1419–1427 (2019).
9. P. Guo *et al.*, *Nature* **524**, 74–78 (2015).
10. H. Lee, J. Shin, S. B. Hong, *ACS Mater. Lett.* **3**, 308–312 (2021).
11. A. Mayoral *et al.*, *Angew. Chem. Int. Ed.* **59**, 19510–19517 (2020).
12. A. Corma, V. Fornes, S. B. Pergher, Th. L. M. Maesen, J. G. Buglass, *Nature* **396**, 353–356 (1998).
13. M. M. J. Treacy, J. M. Newsam, *Nature* **332**, 249–251 (1988).
14. M. M. J. Treacy, D. E. W. Vaughan, K. G. Stromaier, J. M. Newsam, *Proc. R. Soc. London A* **452**, 813–840 (1996).
15. C. S. Cundy, P. A. Cox, *Microporous Mesoporous Mater.* **82**, 1–78 (2005).
16. J. Weitkamp, S. Ernst, *Catal. Today* **19**, 107–149 (1994).
17. J. M. Newsam, M. M. J. Treacy, D. E. W. Vaughan, K. G. Stromaier, M. T. Melchior, in *Molecular Sieves*, M. L. Occelli, H. E. Robson, Eds. (Van Nostrand Reinhold, 1992), pp. 454–472.
18. M. M. J. Treacy, I. Rivin, E. Balkovsky, K. H. Randall, M. D. Foster, *Microporous Mesoporous Mater.* **74**, 121–132 (2004).
19. M. D. Foster, M. M. J. Treacy, "A database of hypothetical zeolite structures" (2021); http://www.hypotheticalzeolites.net/.
20. M. D. Foster *et al.*, *Nat. Mater.* **3**, 234–238 (2004).
21. Y. Li, J. Yu, R. Xu, *Angew. Chem. Int. Ed.* **52**, 1673–1677 (2013).

ACKNOWLEDGMENTS

We thank D. Jo (KRICT) for DIFFaX simulations, Y. K. Park (KRICT) for helpful discussions, and the Pohang Accelerator Laboratory (PAL) for beam time at beamlines 2D (D. Moon), 5A (H. H. Lee), and 9B (D. C. Ahn). **Funding:** This work was supported by the National Creative Research Initiative Program (2012R1A3A2048833) through the National Research Foundation of Korea and by a grant from the Korea Research Institute of Chemical Technology (SI2112-10 and SI2161-114. A.M. acknowledges the Spanish Ministry of Science under the Ramon y Cajal Program (RYC2018-024561-I), the Regional Government of Aragon (DGA E13_20R), and the National Natural Science Foundation of China (NFSC-21850410448 and NSFC-21835002). **Author contributions:** Conceptualization: S.B.H.; Funding acquisition: S.B.H., A.M.; Investigation: H.L., J.S., K.L., H.J.C., A.M., N.Y.K.; Methodology: H.L., J.S., S.B.H.; Project administration: S.B.H.; Supervision: S.B.H.; Visualization: H.L., J.S., A.M., S.B.H.; Writing – original draft: H.L., J.S., A.M., S.B.H.; Writing – review and editing: H.L., J.S., A.M., S.B.H. **Competing interests:** Two Korean patents (application nos. 10-2019-0119315 and 10-2021-0047059), with S.B.H., J.S., and H.L. as co-inventors, have been filed by POSTECH. **Data and materials availability:** All data are available in the main text or the supplementary materials. Crystallographic parameters for the structure of H-PST-32 are archived at the Cambridge Crystallographic Data Center (www.ccdc.cam.ac.uk/) under reference no. CCDC 2083013.

SUPPLEMENTARY MATERIALS

science.sciencemag.org/content/373/6550/104/suppl/DC1
Materials and Methods
Supplementary Text
Figs. S1 to S12
Tables S1 to S12
References (*22*–*31*)

26 March 2021; accepted 19 May 2021
10.1126/science.abi7208

PLASTIC POLLUTION

The missing ocean plastic sink: Gone with the rivers

Lisa Weiss[1]*, Wolfgang Ludwig[1], Serge Heussner[1], Miquel Canals[2], Jean-François Ghiglione[3], Claude Estournel[4], Mel Constant[1]†, Philippe Kerhervé[1]

Plastic floating at the ocean surface, estimated at tens to hundreds of thousands of metric tons, represents only a small fraction of the estimated several million metric tons annually discharged by rivers. Such an imbalance promoted the search for a missing plastic sink that could explain the rapid removal of river-sourced plastics from the ocean surface. On the basis of an in-depth statistical reanalysis of updated data on microplastics—a size fraction for which both ocean and river sampling rely on equal techniques—we demonstrate that current river flux assessments are overestimated by two to three orders of magnitude. Accordingly, the average residence time of microplastics at the ocean surface rises from a few days to several years, strongly reducing the theoretical need for a missing sink.

In recent years, plastic pollution has become a growing concern that has attracted public awareness and fostered numerous studies to identify and quantify plastic waste sources, transport, and fate within terrestrial, coastal, and marine environments (*1*, *2*). A central issue has been the quantification of discharge to the global ocean, considered as a major sink for plastic debris (*3*). Leakage from waste generation and inadequate disposal on land—i.e., mismanaged plastic waste (MPW)—was initially identified as the main driver for plastic discharge to the ocean, with a potential annual transfer of 4.8 to 12.7 million metric tons (Mt) (*4*). Rivers are recognized as the principal conveyors in this transfer (*5*–*7*). Correlations between estimated river plastic fluxes and MPW in drainage basins confirmed, in subsequent studies, that maximum river fluxes of total plastics could reach 2.4 to 4.0 Mt year^{-1} (*8*, *9*). Among the different plastic size categories generally recognized, <5-mm microplastics (MPs) represent the size fraction for which both river flux and surface oceanic MP stock estimates rely on equal sampling techniques, thus allowing direct comparison (supplementary materials and methods section 3.1). Narrowing the figures to this better-documented category yields an average MP river input of 1.5 Mt year^{-1} (*10*). Furthermore, the amount of plastic—mainly MPs (*11*, *12*)—floating at the ocean surface is currently estimated at 14.4 thousand metric tons (kt) (*13*), 35.5 to 66.1 kt (*14*), or even 236 kt (*12*), depending on data availability, modeling approach, and the upper limit of particle size. So far, compelling evidence for rapid growth of the floating plastic stock in the ocean is missing (*15*, *16*). Therefore, dividing the relevant amount by the annual MP flux from rivers provides a conservative indication of the average residence time of MP debris at the ocean surface. A global river discharge in the range of a million metric tons per year accordingly implies an unrealistic short residence time (days to weeks) for MPs at the ocean surface.

As with the missing carbon sink concept (*17*) that fostered fundamental research on the global carbon cycle in the early 1990s, the idea of a missing ocean plastic sink emerged from such an overwhelming difference between the amount of MPs supposedly brought by rivers and the stocks accumulating at the ocean surface (*13*, *18*, *19*) and triggered research on the fate of plastic debris in the marine environment. Several processes have been proposed to be prime actors in the prevention of increased plastic accumulation at the ocean surface. Among these processes are rapid accumulation in living biomass (*20*), quick loss of buoyancy and settling to deeper water layers and the seabed (*21*–*25*), rapid stranding on beaches (*26*, *27*), degradation through physical fragmentation (*19*), microbial alteration (*28*), and photochemical dissolution (*29*). But none of these previous studies questioned the robustness of very short residence times of MPs at the ocean surface relative to those derived from the comparison between river fluxes and floating ocean stocks.

Contrary to measurements at sea, MP studies in rivers were scarce at the time of initial river flux estimates and disregarded differences in sampling techniques. However, recent studies on MPs in rivers allowed us to reassess river fluxes on the basis of a more exhaustive data compilation than previously made (Fig. 1 and table S1). We consequently identify three main methodological biases that magnified errors in the process leading from the quantification of plastic debris in individual rivers to the calculation of global river budgets. Correcting these errors leads to flux estimates that are orders of magnitude (OMs) smaller than previous values.

[1]CEFREM, UMR 5110 University of Perpignan–CNRS, F-66860 Perpignan Cedex, France. [2]CRG Marine Geosciences, Department of Earth and Ocean Dynamics, University of Barcelona, E-08028 Barcelona, Spain. [3]LOMIC, UMR 7621 Sorbonne University–CNRS, F-66650 Banyuls-sur-Mer, France. [4]LEGOS, UMR 5566 University Toulouse III–CNRS/CNES/IRD/UPS, F-31400 Toulouse, France.
***Corresponding author. Email: lisa.weiss@univ-perp.fr**
†Present address: IMT Lille Douai, GCE, F-59508 Douai, France.

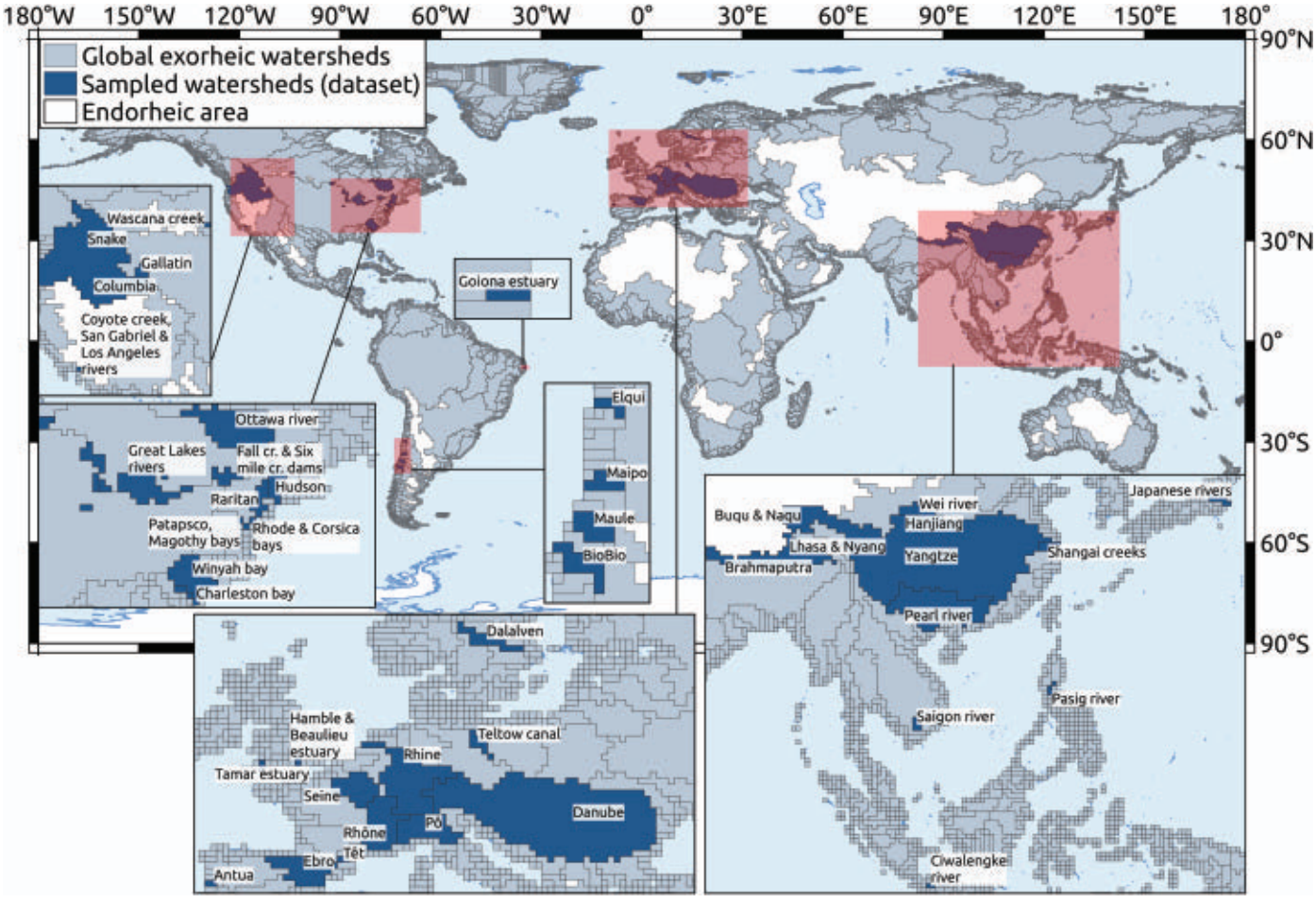

Fig. 1. Global watershed delineation and representation of the river catchments for which MP flux estimates can be established from the literature. These data represent 340 measurements at 127 sampling locations in 89 rivers and have been compiled from 42 published studies (table S1). With respect to the world overall, the 89 sampled rivers represent 14% of water discharge. Maps are shown at 0.5° × 0.5° grid cell resolution.

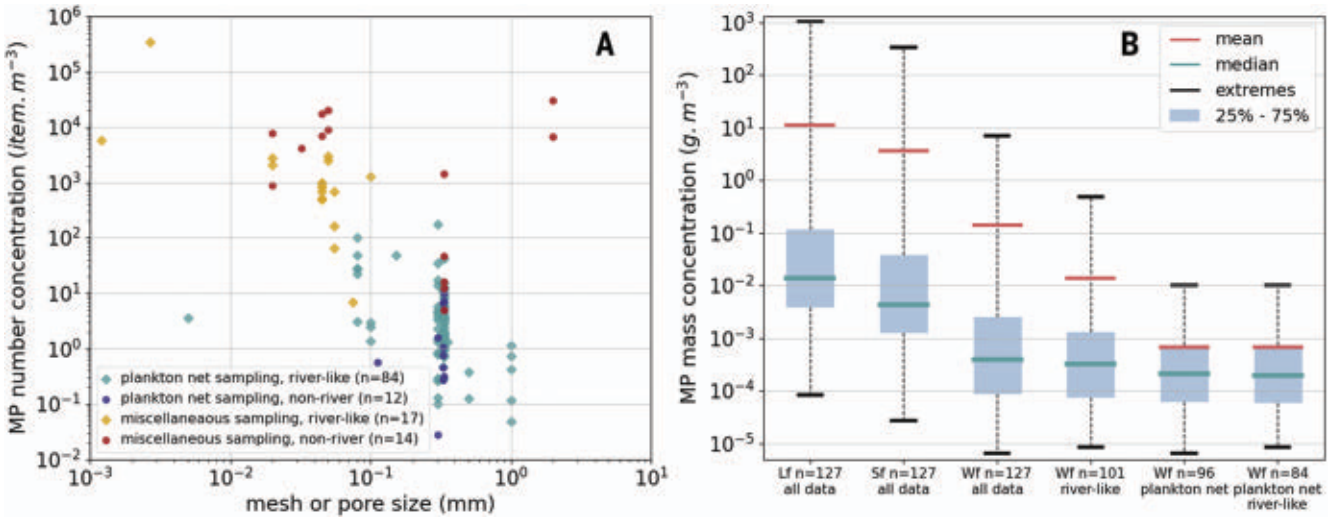

Fig. 2. MP concentration variability in rivers. (**A**) MP number concentrations (items per cubic meter) in different data subsets combining sampling techniques and study locations. Retention limits correspond to mesh (plankton net sampling) or filter pore sizes (miscellaneous sampling) used to retain MP particles according to the compiled studies. "River-like" sampling considers data obtained in rivers sensu stricto—i.e., excluding connected surface waters such as artificial canals, channelized streams, tidal estuaries, or bays (supplementary materials and methods 1.2). (**B**) Box plot representation of MP mass concentrations as a function of different combinations of sampling techniques and number-to-mass conversion factors (Lf, Sf, and Wf). The similarity of the two box plots at right (all plankton net data and plankton net data restricted to rivers) indicates that the high variability observed in the other box plots is mostly related to miscellaneous sampling.

The quest for a major missing plastic sink in the ocean then becomes needless.

The first source of error refers to the choice of a representative mass for MPs in rivers. Because most field studies only determined MP number concentrations, the accurate estimate of MP mass transport depends on knowing how to convert numbers to mass. On the basis of our extended dataset (n = 129 samples), a median mass of 0.23 mg per item [Weiss conversion factor 1 (Wf1)] for nonfiber MPs is obtained (supplementary materials and methods 1.3 and figs. S1 and S2). This value is substantially lower than those used in previous estimates—i.e., 3.0 mg per item (*8*) or 0.96 mg per item (*9*), referred to as Lf and Sf conversion factors hereafter [corresponding to the initial letters of the first authors' surnames in (*8*) and (*9*), respectively]. Our estimate for MP fibers is 0.75 μg per item (Wf2). Because bulk samples can be largely composed of fibers (up to >90%; table S1), composite MP mass (estimated using a composite Wf) often represents only a small fraction of Wf1, and Wf is frequently one to two OMs lower than Lf or Sf.

The second source of error results from the inappropriate mixing of data collected with different sampling techniques. MPs at sea are usually collected with plankton nets (*30*); this is also the most common sampling technique in rivers (*31*) (hereafter "plankton net sampling"). However, in a number of studies, MPs have been collected using other techniques (hereafter "miscellaneous sampling"), including filtration through pore sizes smaller than the minimum mesh size of plankton nets (80 μm). Our data clearly show that filtration collects much larger numbers of MPs (Fig. 2A) and, particularly, small-sized MPs, consistent with previous studies that found distributions of MPs sampled with this method skewed toward the lower size range in rivers (*32*), atmospheric deposits (*33*), and seawater (*34*). Major biases arise when such small plastic fragments are included in mass conversions using factors obtained from plankton net sampling. A notable example is the Yangtze River, for which miscellaneous sampling on filters (*35*) produced MP number concentrations three to four OMs larger than those obtained by sampling with plankton nets (*36*). The mass offset rises to almost five OMs when the number concentrations based on filtration are converted to mass concentrations by using Lf [as applied in (*8*)] and when the number concentrations based on plankton net sampling are converted by using Wf.

A box plot of MP mass concentrations highlights the combined effect of inappropriate conversion factors and misleading mixing of measurements from different sampling techniques (Fig. 2B). Uniformly applying the Lf factor to the reported number concentrations in our exhaustive dataset yields a mass concentration range encompassing seven OMs. In some cases, MP mass concentrations would be as low as those of natural trace metals during low-flow conditions (*37*), whereas in other cases they would be as high as total suspended sediment concentrations during flood conditions (*38*). Such an extended mass range has not been reported previously for any kind of particulate matter in rivers. However, use of the Wf factor lowers the median mass concentration by a factor of >30 and narrows its variability by one OM. Restricting the outcomes from field studies to those from plankton net sampling further lowers median concentrations and leads to the strongest reduction of variability. Values now stretch over just three OMs, which is more in line with the maximum seasonal variability for MP concentrations reported in case studies (*39*–*41*).

The third source of error concerns global MP flux estimates based on the relationship between MP river fluxes and MPW. Our calculations yield MP fluxes as high as millions of metric tons when using the above-mentioned Lf or Sf conversion factors (4610 and 1479 kt year^{-1}, respectively) and correlating river mass fluxes with MPW stocks in drainage basins (Table 1). Nevertheless, the associated values of the coefficient of determination are quite low (r^2 = 0.53), suggesting that the models are far from fully explaining the calculated river loads. Applying the composite factor Wf drops the global MP flux to 129 kt year^{-1} while r^2 increases to 0.59. Restricting the regression to the plankton net data subset further improves the correlation (r^2 = 0.66) and reduces the global flux to 31 kt year^{-1}. With this latter subset of data, MPW is no longer the best predictor of MP river loads, as the associated coefficient of determination is greater (r^2 = 0.69) when correlated with total basin population (Pop). Processing the large-scale extrapolations with the parametric equation based on regression with Pop instead of MPW still decreases the global MP flux by about one OM down to 3.5 kt year^{-1}. We also tested

Table 1. Regression models for observed MP river fluxes and potential controlling factors in the respective drainage basins. Information in this table pertains to the data subsets shown in Fig. 2. The resulting global MP fluxes are further detailed according to the main ocean basins to which they are discharged. The "Others" column includes discharges into the Mediterranean Sea, the Black Sea, and the Arctic Ocean.

Data subsets	Number of data	Regression parameters	Number-to-mass conversion factor	r^2	Global MP flux (kt year^{-1})	North Atlantic (%)	South Atlantic (%)	Indian Ocean (%)	North Pacific (%)	South Pacific (%)	Others (%)
All data	127	MPW	Lf	0.53	4,610	5.3	16.3	33.6	31.7	1.7	11.4
All data	127	MPW	Sf	0.53	1,479	5.3	16.3	33.6	31.7	1.7	11.4
All data	127	MPW	Wf	0.59	129	4.8	16.3	34.3	31.8	1.5	11.3
All data	127	Pop	Wf	0.49	15	12.6	10.1	33.4	30.2	3.3	10.4
River-like	101	MPW	Wf	0.57	56	6.1	16.3	32.3	31.7	2.1	11.5
River-like	101	Pop	Wf	0.45	7.2	15.4	10.5	29.0	29.3	4.9	10.9
Plankton net	96	MPW	Wf	0.66	31	5.7	16.3	32.9	31.7	1.9	11.5
Plankton net	96	Pop	Wf	0.69	3.5	13.3	10.2	32.3	30.0	3.7	10.5
Plankton net, river-like	84	MPW	Wf	0.66	29	6.0	16.3	32.4	31.7	2.1	11.5
Plankton net, river-like	84	Pop	Wf	0.69	3.6	13.8	10.3	31.5	29.8	4.0	10.6
Plankton net	96	sPop, sQ	Wf	0.80	6.1	23.1	12.0	21.6	27.7	11.0	4.6
Plankton net, river-like	84	sPop, sQ	Wf	0.80	6.6	23.3	12.0	21.4	27.6	11.0	4.7

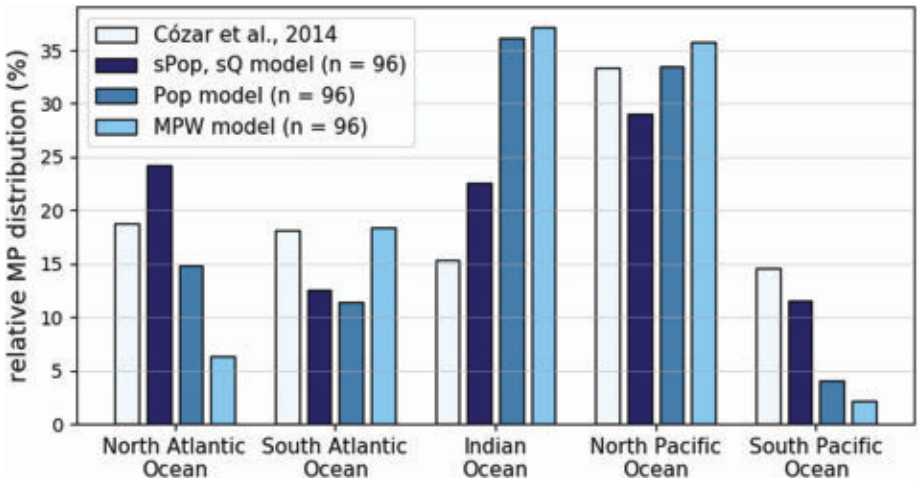

Fig. 3. Comparison between relative distribution of estimated MP stocks at the surface of the different ocean basins and relative distribution of riverine MP fluxes according to the plankton net sampling model outputs. Both surface ocean stocks for the listed ocean basins and river fluxes close at 100%. Extrapolations of MP river fluxes on the basis of Pop and/or sPop and sQ generally fit better with observed MPs accumulation at the ocean surface according to Cózar *et al*. (*13*) than extrapolation on the basis of MPW. Nevertheless, discrepancies exist, especially for the Indian Ocean in the Southern Hemisphere. The oceanic gyre is connected to the South Atlantic via the Agulhas Current leakage (*46*) and to the South Pacific via the Great Australian Bight and the Tasman Sea (*47*), suggesting that the stocks in these two ocean basins could be partly fed by MPs originating from the Indian Ocean. See Table 1 for plankton net sampling model outputs.

whether multiregression models can improve the statistics (supplementary materials and methods 2.2 and table S3). For the plankton net dataset, we identify a significant relationship between specific MP fluxes, population density (sPop), and drainage intensity (sQ). This relationship also increases the coefficient of determination to $r^2 = 0.80$ (Table 1), although global budgets change only moderately (6.1 kt year^{-1}). Regression analyses alone do not allow rejection of MPW as the best predictor for riverine MP fluxes, but the heterogeneity that MPW values implied in the spatial distribution of riverine MP discharges into the ocean does. Indeed, this heterogeneity does not match the observed accumulation patterns in the different ocean basins (Fig. 3). The discrepancy is particularly pronounced for the North Atlantic Ocean. Although this basin should have a MP concentration at least as large as that of the North Pacific Ocean (*13*, *34*, *42*), it always receives <6% of the global river inputs when extrapolations are calculated from MPW (Table 1). This is because MPW estimates for Europe and North America are quite low compared with estimates for Asia and Africa (fig. S3). Extrapolations based on Pop and/or on sPop and sQ fit more accurately with observed MP accumulation at the ocean surface (Fig. 3). Very recently, a modeling study (*7*) proposed a scenario of global river plastic fluxes on the basis of a human development index (HDI). Although the authors found clearly lower and spatially more equilibrated values compared with the results of previous studies (*8*, *9*), discrepancies still exist with regard to the accumulation patterns at the ocean surfaces. These inconsistencies are more important than in our approach, which does not weight HDI more heavily than Pop.

Lowering the global river plastic flux to a few thousand metric tons per year has major implications for our understanding of MP cycling in the sea. Conservatively dividing the oceanic stock of 14.4 kt (*13*) by our best MP flux estimate of 6.1 kt year^{-1} yields residence times around 2.4 years for the floating stock at the ocean surface. Although associated with significant uncertainties (supplementary materials and methods 3), such values support the idea that surface oceanic MP stocks result from rather slow accumulation processes, a notion that conflicts with the concept of ocean MPs being a highly reactive pool in terms of biological and chemical degradation and sequestration processes. Longer residence times are also in accordance with the observed long-distance transport of invasive species living on rafting plastics that may be part of the "plastisphere" (*28*, *43*). Slow accumulation does not exclude selective sorting and sequestration of MPs on their way from land to the oceanic gyres. The average mass of a floating oceanic MP is generally higher [between 0.97 and 7 mg (*11*, *13*, *14*, *19*, *42*)] than the value we found for nonfiber MPs in rivers and tends to increase in accumulation areas (supplementary materials and methods 3 and fig. S1). This difference may reflect selective sequestration of smaller MPs—for example, through turbulent dispersion in the water column (*34*) or ingestion by a wide range of organisms (*15*, *18*, *44*) and subsequent transfer to seafloor sediments where they form the bulk of plastic litter (*21*, *24*, *45*).

Our finding that MP river fluxes are much lower than previous estimates should not be misunderstood as an attempt to minimize the severity of the plastic pollution problem. On the contrary, it implies that even if riverine plastic inputs were to cease immediately, the floating MP stocks and their deleterious effects on the marine environment would persist for many years. Also, we do not claim that plastic cycling in the oceans is fully understood. There are many size classes, oceanic compartments and land-to-sea transfer processes on which further research is urgently needed to properly evaluate the exposure of marine biota to this novel type of pollution and to design cleaning strategies. Reliable mass quantification of plastic stocks and fluxes, at both the lower micrometer to nanometer scale and in the form of macroplastics, is atop the priority list for action. However, as we demonstrate with our results, all approaches should maximize efforts to develop standard sampling techniques and reliable extrapolation methods so as to avoid major errors in budget calculations that are uncritically accepted. We finally demonstrate that MP pollution in the world ocean is not restricted to MPW-designated hotspots in Asia or Africa. Collective initiatives that aim to reduce the ocean's MP load should therefore rely more on global land-based actions at much larger spatial scales than previously thought.

REFERENCES AND NOTES

1. D. K. Barnes, F. Galgani, R. C. Thompson, M. Barlaz, *Philos. Trans. R. Soc. B* **364**, 1985–1998 (2009).
2. C. M. Rochman, T. Hoellein, *Science* **368**, 1184–1185 (2020).
3. Group of Experts on the Scientific Aspects of Marine Protection (GESAMP), "Sources, fate and effects of microplastics in the marine environment: Part two of a global assessment," P.J. Kershaw, C. M. Rochman, Eds. (Rep. Stud. GESAMP no. 93, IMO/FAO/UNESCO-IOC/UNIDO/WMO/IAEA/UN/UNEP/UNDP Joint Group of Experts on the Scientific Aspects of Marine Environmental Protection, 2016); www.gesamp.org/publications/microplastics-in-the-marine-environment-part-2.
4. J. R. Jambeck *et al*., *Science* **347**, 768–771 (2015).
5. L. Lebreton, A. Andrady, *Palgrave Commun.* **5**, 6 (2019).
6. L. Lebreton, A. Andrady, Supplementary Data for "Future scenarios of global plastic waste generation and disposal," version 1, figshare (2019); https://doi.org/10.6084/m9.figshare.5900335.
7. L. Mai *et al*., *Environ. Sci. Technol.* **54**, 10049–10056 (2020).
8. L. C. M. Lebreton *et al*., *Nat. Commun.* **8**, 15611 (2017).
9. C. Schmidt, T. Krauth, S. Wagner, *Environ. Sci. Technol.* **51**, 12246–12253 (2017).
10. W. W. Y. Lau *et al*., *Science* **369**, 1455–1461 (2020).
11. S. Morét-Ferguson *et al*., *Mar. Pollut. Bull.* **60**, 1873–1878 (2010).
12. E. van Sebille *et al*., *Environ. Res. Lett.* **10**, 124006 (2015).

13. A. Cózar *et al*., *Proc. Natl. Acad. Sci. U.S.A.* **111**, 10239–10244 (2014).
14. M. Eriksen *et al*., *PLOS ONE* **9**, e111913 (2014).
15. K. L. Law *et al*., *Science* **329**, 1185–1188 (2010).
16. K. L. Law *et al*., *Environ. Sci. Technol.* **48**, 4732–4738 (2014).
17. C. D. Keeling, S. C. Piper, M. Heimann, in *Aspects of Climate Variability in the Pacific and the Western Americas*, D. H. Peterson, Ed. (AGU, 1989); https://doi.org/10.1029/GM055p0305.
18. R. C. Thompson *et al*., *Science* **304**, 838 (2004).
19. A. Ter Halle *et al*., *Environ. Sci. Technol.* **50**, 5668–5675 (2016).
20. P. Davison, R. G. Asch, *Mar. Ecol. Prog. Ser.* **432**, 173–180 (2011).
21. L. C. Woodall *et al*., *R. Soc. Open Sci.* **1**, 140317 (2014).
22. W. P. de Haan, A. Sanchez-Vidal, M. Canals; NUREIEV1 Shipboard Scientific Party, *Mar. Pollut. Bull.* **140**, 523–535 (2019).
23. K. Pabortsava, R. S. Lampitt, *Nat. Commun.* **11**, 4073 (2020).
24. I. A. Kane *et al*., *Science* **368**, 1140–1145 (2020).
25. J. Boucher, G Billard, *The Mediterranean: Mare plasticum* (IUCN, 2020).
26. S. Liubartseva, G. Coppini, R. Lecci, E. Clementi, *Mar. Pollut. Bull.* **129**, 151–162 (2018).
27. Y. Ourmières, J. Mansui, A. Molcard, F. Galgani, I. Poitou, *Cont. Shelf Res.* **155**, 11–20 (2018).
28. J. Jacquin *et al*., *Front. Microbiol.* **10**, 865 (2019).
29. L. Zhu, S. Zhao, T. B. Bittar, A. Stubbins, D. Li, *J. Hazard. Mater.* **383**, 121065 (2020).
30. V. Hidalgo-Ruz, L. Gutow, R. C. Thompson, M. Thiel, *Environ. Sci. Technol.* **46**, 3060–3075 (2012).
31. R. Dris *et al*., *Environ. Chem.* **12**, 539–550 (2015).
32. R. Dris *et al*., *Environ. Chem.* **12**, 592–599 (2015).
33. S. Allen *et al*., *Nat. Geosci.* **12**, 339–344 (2019).
34. M. Poulain *et al*., *Environ. Sci. Technol.* **53**, 1157–1164 (2019).
35. S. Zhao, L. Zhu, T. Wang, D. Li, *Mar. Pollut. Bull.* **86**, 562–568 (2014).
36. X. Xiong, C. Wu, J. J. Elser, Z. Mei, Y. Hao, *Sci. Total Environ.* **659**, 66–73 (2019).
37. J. M. Martin, M. Meybeck, *Mar. Chem.* **7**, 173–206 (1979).
38. M. Meybeck, L. Laroche, H. H. Dürr, J. P. M. Syvitski, *Global Planet. Change* **39**, 65–93 (2003).
39. M. Constant *et al*., *Sci. Total Environ.* **716**, 136984 (2020).
40. F. Faure, C. Demars, O. Wieser, M. Kunz, L. F. de Alencastro, *Environ. Chem.* **12**, 582–591 (2015).
41. A. Lechner *et al*., *Environ. Pollut.* **188**, 177–181 (2014).
42. L. Lebreton *et al*., *Sci. Rep.* **8**, 4666 (2018).
43. E. R. Zettler, T. J. Mincer, L. A. Amaral-Zettler, *Environ. Sci. Technol.* **47**, 7137–7146 (2013).
44. S. Deudero, C. Alomar, *Mar. Pollut. Bull.* **98**, 58–68 (2015).
45. W. Courtene-Jones, B. Quinn, S. F. Gary, A. O. M. Mogg, B. E. Narayanaswamy, *Environ. Pollut.* **231**, 271–280 (2017).
46. W. P. M. De Ruijter *et al*., *J. Geophys. Res.* **104**, 20885–20910 (1999).
47. C. Maes *et al*., *Geophys. Res. Lett.* **45**, 1915–1922 (2018).

ACKNOWLEDGMENTS

We thank the anonymous peer reviewers for their suggestions and comments, which improved this manuscript. We are indebted to P. Döll, who supplied the WATERGAP river-routing file in a 0.5° grid cell resolution, and to S. Pinel, who performed calculations with the bootstrap statistical method. **Funding:** This work was supported by doctorate school ED305 of the University of Perpignan Via Domitia through attribution of PhD grants to L.W. and M.Co. M.Ca. acknowledges support from Generalitat de Catalunya 2017 SGR 315 grant to GRC Marine Geosciences, Red Española sobre BAsuras MARinas (BAMAR, ref. CGL2016-81854-REDT), and Institut d'Estudis Catalans (IEC) I-MarCat grant (ref. PR2015-S06-CANALS). **Author contributions:** L.W. collected and assembled the river MP data from the literature, performed the statistics, implemented the river geographic information system, and extrapolated and analyzed the global MP fluxes. W.L. steered the study design, conducted the discussion, and contributed to data analysis. W.L., L.W., and S.H. wrote the manuscript, with substantial contributions from M.Ca., J.-F.G., and C.E. in their respective domains of expertise. M.Co. contributed to data mining from literature. M.Co., P.K., and M.Ca. supplied individual data on riverine MPs from previous studies. All authors discussed the results and commented on the manuscript. **Competing interests:** The authors declare no competing interests. **Data and materials availability:** The data frames used for the analyses are provided as table S1 and in the supplementary materials and methods; they are also freely available online at the links specified in the references. The code for statistical analyses is based on the *OLS statsmodels* and *scikit-learn* Python libraries (online documentation hosted at statsmodels.org and scikit-learn.org).

SUPPLEMENTARY MATERIALS

science.sciencemag.org/content/373/6550/107/suppl/DC1
Materials and Methods
Figs. S1 to S3
Tables S1 to S3
References (*48*–*97*)

27 July 2020; accepted 20 May 2021
10.1126/science.abe0290

SPATIAL GENETICS

Embryo-scale, single-cell spatial transcriptomics

Sanjay R. Srivatsan[1]†, Mary C. Regier[2,3]†, Eliza Barkan[1,4], Jennifer M. Franks[1], Jonathan S. Packer[5], Parker Grosjean[2], Madeleine Duran[1], Sarah Saxton[2], Jon J Ladd[6], Malte Spielmann[7,8], Carlos Lois[9], Paul D. Lampe[6], Jay Shendure[1,10,11,12]*, Kelly R. Stevens[2,3,12,13]*, Cole Trapnell[1,10,12]*

Spatial patterns of gene expression manifest at scales ranging from local (e.g., cell-cell interactions) to global (e.g., body axis patterning). However, current spatial transcriptomics methods either average local contexts or are restricted to limited fields of view. Here, we introduce sci-Space, which retains single-cell resolution while resolving spatial heterogeneity at larger scales. Applying sci-Space to developing mouse embryos, we captured approximate spatial coordinates and whole transcriptomes of about 120,000 nuclei. We identify thousands of genes exhibiting anatomically patterned expression, leverage spatial information to annotate cellular subtypes, show that cell types vary substantially in their extent of spatial patterning, and reveal correlations between pseudotime and the migratory patterns of differentiating neurons. Looking forward, we anticipate that sci-Space will facilitate the construction of spatially resolved single-cell atlases of mammalian development.

Single-cell methods have the potential to transform our understanding of organismal development. In diverse models of embryogenesis, we and others have performed "whole-organism" profiling of gene expression or chromatin accessibility at single-cell resolution (*1*–*7*), yielding a richer view of the emergence and trajectories of cell types than was previously available or possible (*8*, *9*).

Cells' spatial organization plays a central role in normal development and homeostasis, as well as in pathophysiology. However, a key limitation of most single-cell molecular profiling methods is that they operate on dissociated cells or nuclei. Although in situ methods can measure the expression of many or all genes while retaining spatial information (*10*), these methods also have limitations (fig. S1). Some, including the original "spatial transcriptomics" (*11*) and Slide-seq (*12*) methods, barcode and then count mRNAs derived from positions across patterned arrays. Although these methods can be implemented at a range of spatial scales, the boundaries of spots have no natural correspondence to the boundaries of cells. Therefore, they yield aggregate profiles of small regions encompassing multiple cells and/or portions of cells rather than truly resolving individual cells. Other methods, including MERFISH (*13*), seqFISH (*14*), and FISSEQ (*15*), rely on in situ hybridization or sequencing to measure the expression of many genes while retaining single-cell (or even subcellular) resolution within each field of view. However, such methods are typically limited by long image acquisition times and complex instrumentation requirements. In sum, existing techniques necessitate tradeoffs such that assaying the whole transcriptomes of individual cells over large territories remains impractical.

Spatial labeling of nuclei with hashing oligonucleotide

Previously, we developed sci-Plex, a method for labeling or "hashing" nuclei using unmodified DNA oligos before single-cell RNA sequencing with combinatorial indexing (sci-RNA-seq)

[1]Department of Genome Sciences, University of Washington, Seattle, WA, USA. [2]Department of Bioengineering. University of Washington, Seattle, WA, USA. [3]Institute for Stem Cell and Regenerative Medicine, Seattle, WA, USA. [4]Molecular and Cellular Biology Program, University of Washington, Seattle, WA, USA. [5]Foresite Labs, Boston, MA, USA. [6]Translational Research Program, Public Health Sciences, Fred Hutchinson Cancer Research Center, Seattle, WA, USA. [7]Institute of Human Genetics, University of Lübeck, Lübeck, Germany. [8]Human Molecular Genomics Group, Max Planck Institute for Molecular Genetics, Berlin, Germany. [9]Division of Biology and Biological Engineering, California Institute of Technology, Pasadena, CA, USA. [10]Allen Discovery Center for Cell Lineage Tracing, Seattle, WA, USA. [11]Howard Hughes Medical Institute, University of Washington, Seattle, WA, USA. [12]Brotman Baty Institute for Precision Medicine, Seattle, WA, USA. [13]Department of Laboratory Medicine and Pathology, Seattle, WA, USA.
***Corresponding author. Email: shendure@uw.edu (J.S.); ksteve@uw.edu (K.R.S.); coletrap@uw.edu (C.T.)**
†These authors contributed equally to this work.

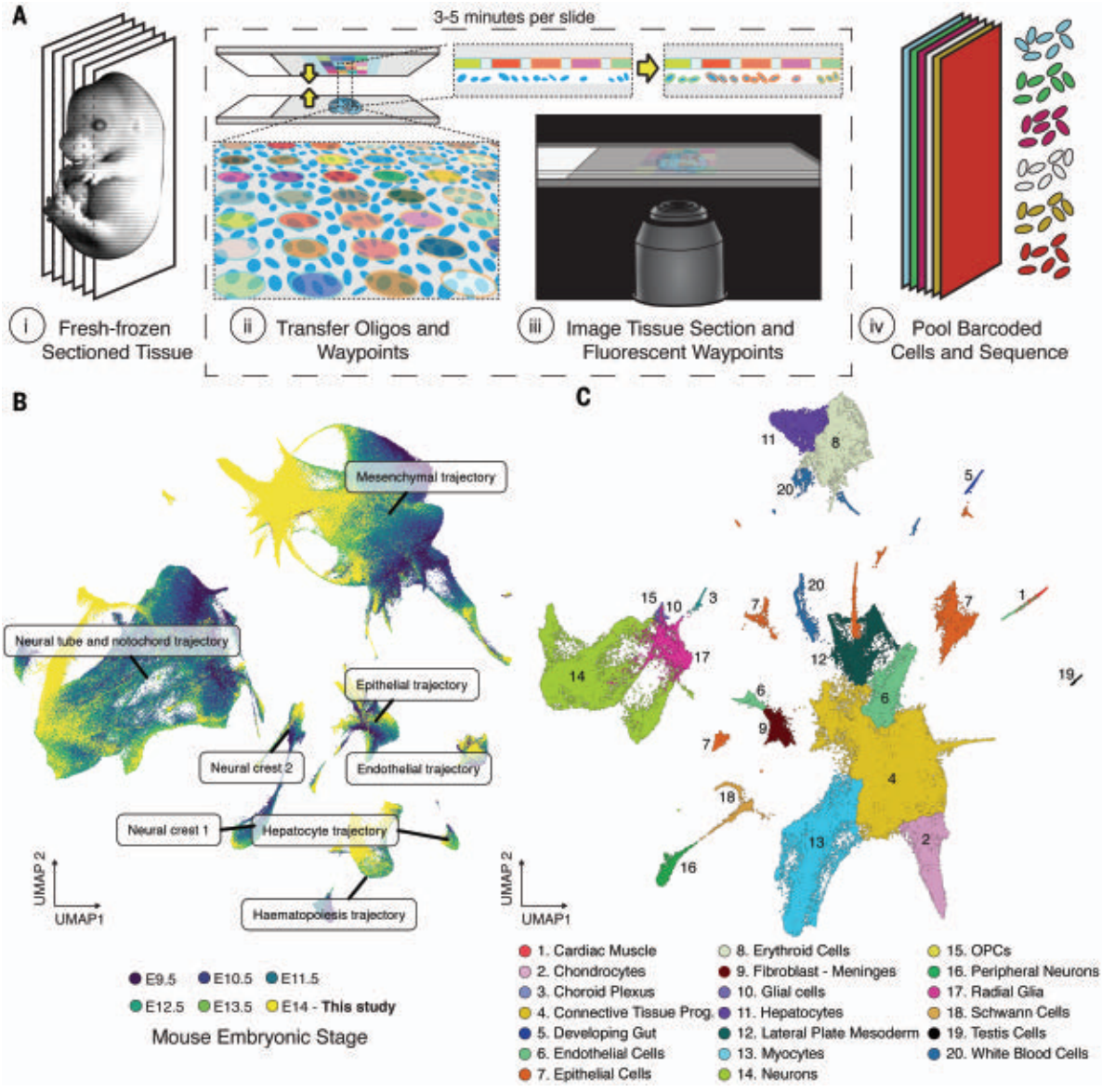

Fig. 1. s>ci-Space recovers single-cell transcriptomes while recording spatial coordinates. (**A**) Arrayed single-stranded oligos were transferred onto permeabilized nuclei in fresh-frozen tissue sections and imaged. Cells from each slide were also labeled with a section-identifying barcode so that multiple sections could be pooled before sci-RNA-seq. (**B**) Joint embedding of E14.0 single-cell transcriptomes from this study and published data spanning E9.5 to E13.5 (*1*). Major trajectories are labeled. (**C**) UMAP embedding of 121,909 cells from sectioned E14.0 mouse embryos. Cell types are denoted by color and number in legend.

(*16*). To leverage this workflow to capture spatial information, we spatially arrayed unique combinations of hashing oligos, and then transferred these oligos to nuclei within a tissue slice by diffusion (*17*). These hashing oligos, recovered in association with sci-RNA-seq profiles, capture each cell's approximate tissue coordinates upon sequencing.

As a proof of concept of this "sci-Space" approach, hashing oligos were spotted onto glass slides coated with dried agarose. These grids contained 7056 uniquely barcoded spots spanning a 18 mm by 18 mm area (mean radius of 73.2 ± 14.1 μm; mean spot-to-spot center distance of 222 ± 7.5 μm; fig. S2). About 5% of spots, constituting an identifiable pattern, were also loaded with SYBR green fluorescent dye. After transferring the oligos to the tissue, the grid could be registered with an image of the tissue using these concurrently imaged fluorescent fiduciaries (figs. S2 and S3). After optimization of hashing oligo concentrations and dissociation protocols (figs. S4 and S5), our protocol comprised four steps: (i) fresh-frozen tissue is sectioned; (ii) sectioned tissue is permeabilized with a solution containing a slide-specific oligo and physically juxtaposed to a glass slide bearing the spatially gridded hashing oligos; (iii) during oligo transfer, the assembly is imaged; and (iv) nuclei from the tissue on the slide are extracted, fixed, and subjected to sci-RNA-seq (Fig. 1A and figs. S6 and S7).

Spatially resolved single-cell sequencing of the mouse embryo

We applied sci-Space to profile 14 sagittal sections derived from two embryonic day 14 (E14.0) mouse embryos (C57BL/6N). After sequencing, quality filtering (*18*), and assignment of each cell to a slide (on the basis of its slide-specific hashing oligo), our dataset comprised

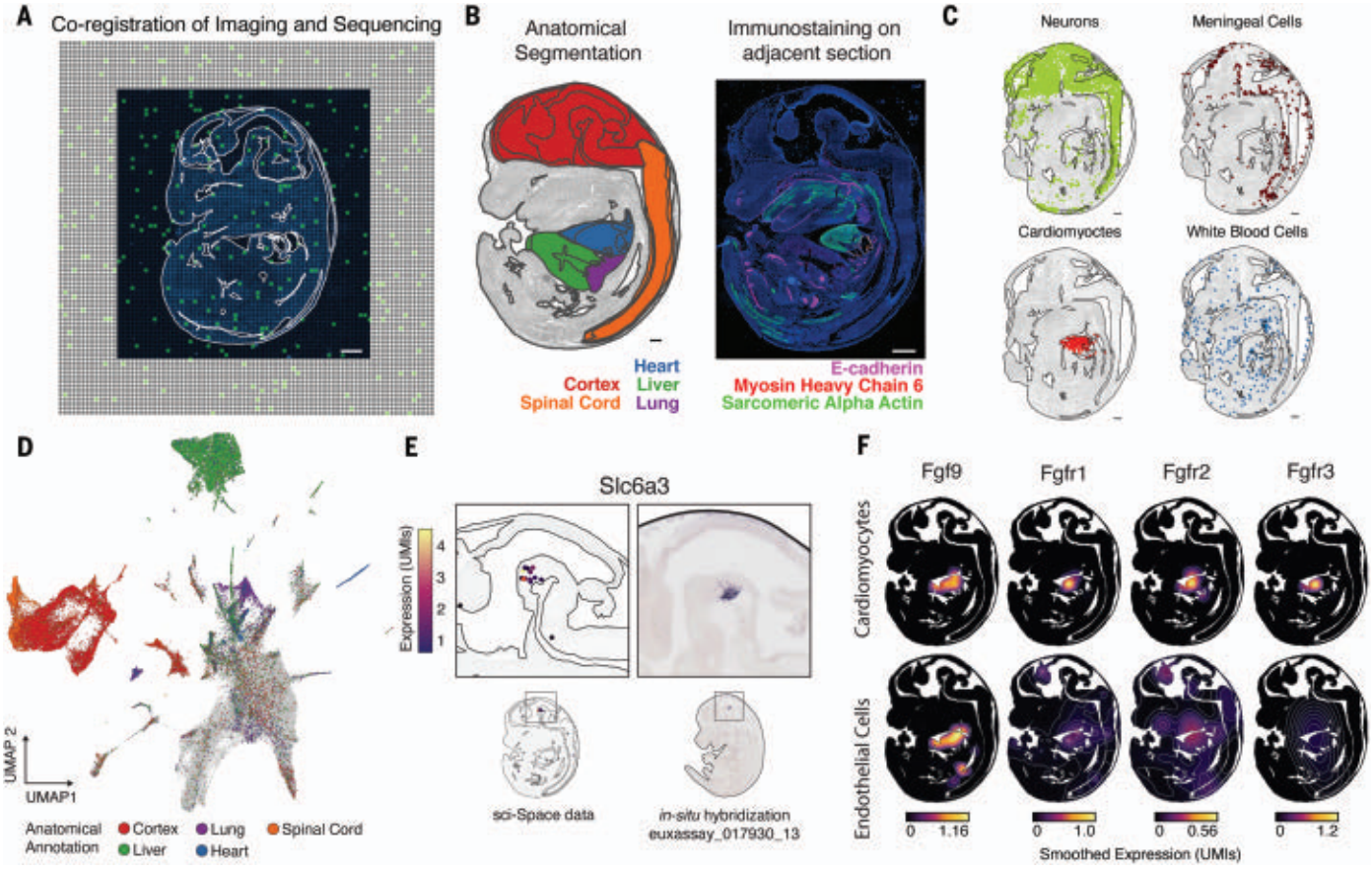

Fig. 2. sci-Space captures spatially and cell-type–resolved gene expression across the embryo. (**A**) Co-registered 4′,6-diamidino-2-phenylindole (DAPI)–stained section image and oligo array superimposed. SYBR waypoints are highlighted in green. (**B**) Anatomical regions of slide 1 (left) and an adjacent immunostained serial section aligned to slide 1 (right). (**C**) Highlighted cell types mapping to a single slide. (**D**) UMAP embedding colored by anatomical regions. (**E**) Gene expression of dopamine transporter *Slc6a3* from sci-Space data (left) and published (*27*) section/stage matched in situ (right). (**F**) Smoothed percentage of gene expression for *Fgf1*, *Fgfr1*, *Fgfr2*, and *Fgfr3* in cardiomyocytes (top) or endothelial cells (bottom). Color is scaled to maximum percentage within each gene. Scale bars in (A) to (C), 0.5 mm.

121,909 spatially resolved single-cell transcriptomes [mean 2514 unique molecular identifiers (UMIs) and mean 1231 genes detected per cell], without apparent batch effects between slides or embryos (figs. S8 and S9). This corresponds to capture of 164 nuclei/mm^2 of tissue on average, or sampling of 2.2% of the estimated nuclei present (fig. S10). Rather than annotating cell types ab initio, we co-embedded (*19*, *20*) these data with a published, nonspatial sci-RNA-seq mouse organogenesis cell atlas dataset spanning E9.5 to E13.5 (*1*) and cells from a developing mouse brain atlas (DMBA) spanning E13.5 to E14.5 (*21*). Reassuringly, these E14.0 data integrated well with both datasets (Figs. 1B and fig. S11). Draft cell type annotations, inferred by nearest-neighbor label transfer, were highly concordant with those recovered by Garnett (*22*), a semisupervised annotation algorithm (fig. S11). These annotations were then refined by manual inspection of differentially expressed genes (Fig. 1C and data file S1).

Images of sectioned embryos and sequencing data were co-registered using SYBR waypoints (*23*, *24*) (Fig. 2A and figs. S12 and S13). Each nucleus was mapped to the position matching its highest combination of spot and sector oligos within the imaged section. For ~9% of nuclei, the top assignment was not located near any other nuclei of the same cell type; for such "outliers," alternative mappings were considered. Altogether, nuclei were well localized (fig. S8, C to F) to one of 15,102 spatial positions across 14 sections; on average, each spatial position was assigned 8.1 nuclei (10.5 SD) (fig. S14). To quantify the anatomical distribution of cell type annotations, each section was segmented by organ (Fig. 2B and fig. S15), aided by immunostaining of adjacent sections (*25*) (fig. S16). Neurons mapped largely within the spinal cord and brain outlined by cells of the developing meninges, cardiomyocytes within the heart, and white blood cells throughout the organism (Fig. 2, C and D, and figs. S18 and S17). Analysis with Giotto (*26*), an unsupervised tool for segmenting spatial transcriptomic images into tissue "domains" of similar cell type composition, revealed 22 domains shared across sci-Space slides. In addition to detecting boundaries between major organs, Giotto was able to automatically recognize more complex domains with distributions extending throughout the embryo (e.g., mesenchymal tissue and cartilage) (fig. S19).

Finally, wherever cells are captured, sci-Space data enable the visualization of any gene in the transcriptome akin to an in situ hybridization, albeit at lower spatial resolution. For example, a sci-Space "digital in situ" of the dopamine transporter *Slc6a3* highlights a cluster of dopaminergic neurons at the midbrain-hindbrain boundary, consistent with stage- and section-matched whole-mount in situ data (*27*) (Fig. 2E and fig. S20). Unlike conventional in situ data, sci-Space data also resolve gene expression by cell type. For example, in the heart, both cardiomyocytes and endothelial cells express the growth factor *Fgf1*, whereas only

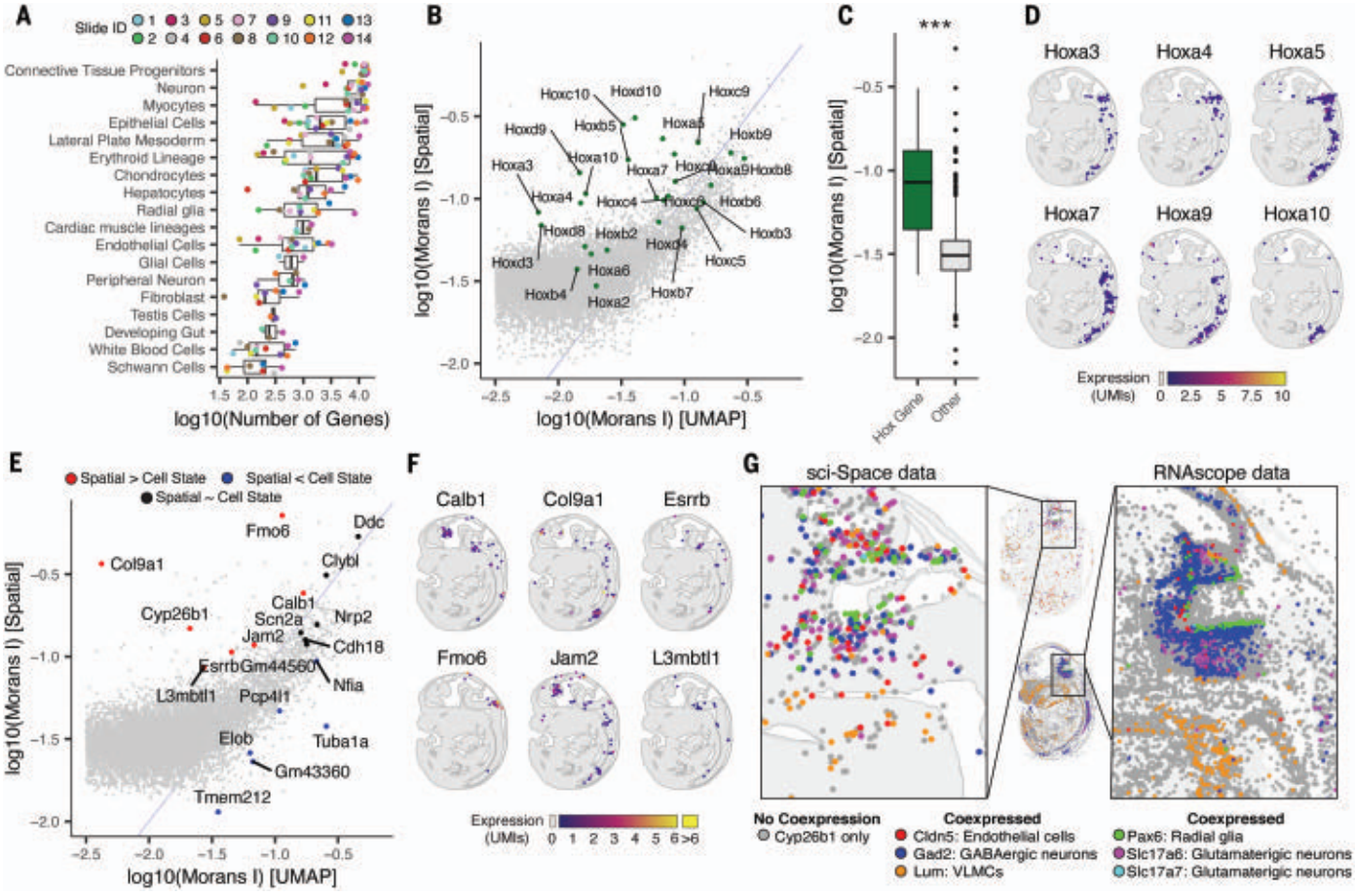

Fig. 3. Spatially restricted gene expression in developing neurons. (**A**) Number of spatially significant (Moran's test, FDR < 0.001) autocorrelated genes within each slide (color) and cell type. Only cell types with >50 cells per slide were included. (**B**) Log-log (log10) plot of autocorrelation in UMAP embedding (*x*-axis) versus autocorrelation in spatial coordinates (*y*-axis) for each gene computed on excitatory neurons from slide 1. Moran's I values close to 1 indicate perfect spatial correlation, and a value of 0 indicates a random spatial distribution. Hox genes are highlighted. (**C**) log10-scale boxplot of Moran's I statistic for Hox genes displayed in (B) versus all other expression level-matched genes ($P < 0.001$, two-sided *t* test). (**D**) Gene expression of HoxA cluster in slide 1. (**E**) Similar to (B), log-log (log10) plot of autocorrelation in UMAP embedding (*x*-axis) versus autocorrelation in spatial coordinates (*y*-axis) for each gene with genes in different regimes highlighted for slide 1. (**F**) Expression patterns across slide 1 for other spatially restricted genes that are not restricted to a single neuron subcluster. (**G**) Comparison of sci-Space (slide 14)– and RNA FISH (RNAscope)–detected *Cyp26b1* patterns of expression (gray) and coexpression with markers (colors as indicated in key) for neuronal and supportive cell types.

cardiomyocytes express the growth factor receptors *Fgfr1*, *Fgfr2*, and *Fgfr3* (Fig. 2F).

Contrasting sci-Space and spatial transcriptome capture (STC) methods

A key distinction between sci-Space and STC methods (fig. S1, left) is that because STC methods capture transcripts from lysed tissue sections (*11*, *12*), each spot can include RNA from multiple cells and/or portions of cells. As such, STC methods are limited in their ability to resolve gene expression variation within individual cells or cell types. To quantify the consequences of this limitation, we spatially aggregated transcriptomes from sci-Space nuclei, effectively creating a "mock-STC" dataset. Cell types and clusters readily discernible in the single-cell data were challenging to resolve in the mock-STC data (fig. S21, A to C). One approach to ameliorating this limitation involves mapping cells profiled by nonspatial single-cell RNA-seq onto a STC "scaffold", thereby imputing cellular locations within a tissue (*20*, *28*). To assess the viability of this approach, we applied such imputation to mock STC data and compared it with the single-nucleus data used to derive it (fig. S21, D and E). The mean distance between a nucleus' imputed position and its measured position was 11.6 spots (~2.5 mm), a measure that varied by cell type (fig. S21F). Thus, despite sampling fewer transcripts than STC methods (fig. S21, G to I), sci-Space's single-cell resolution—that is, its ability to unambiguously ascertain sets of transcripts expressed in the same cell—represents a key advantage over STC methods.

Analogously, we posited that sci-Space data could serve as a scaffold for the imputation of locations of cells profiled by nonspatial single-cell RNA-seq but with the advantage of matching single-cell transcriptomes. To test this, we aligned neurons from sci-Space and the DMBA. Transfer of dissection-based DMBA anatomic annotations were consistent with sci-Space coordinates (fig. S23). Furthermore, this alignment mapped hundreds of DMBA transcriptional clusters to specific positions, many spatially restricted (fig. S23). For example, of 193 transcriptomic clusters from La Manno et al. (*21*) that mapped to slides 13 and 14, 94 and 115 clusters displayed statistically significant focal enrichment, respectively [false discovery rate (FDR) < 0.01; Getis-Ord Local G].

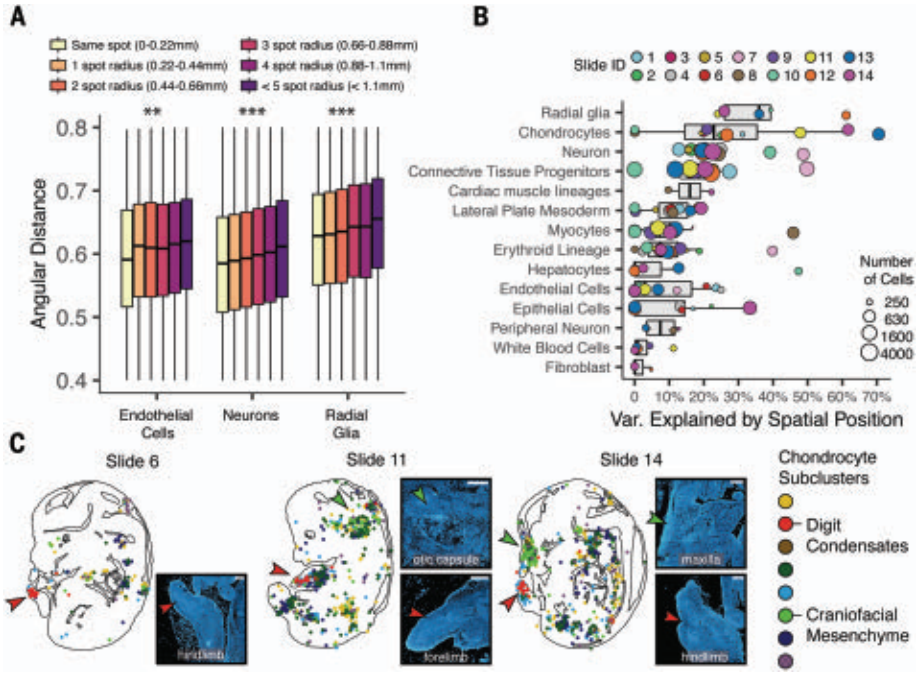

Fig. 4. Quantifying the variance in gene expression attributable to spatial position. (**A**) Pairwise angular distance (radians) between global transcriptomes of cells of the indicated cell types. Cell pairs are grouped by distance on the physical array (millimeters) (**P < 0.001, ***P < 0.0001, Wald linear regression test). (**B**) Proportion of nontechnical variance explained within cells of each type by spatial position. Point size indicates number of cells and point color indicates the slide of origin. (**C**) Recovered positions of chondrocytes from slides 6, 11, and 14 colored by subcluster. Arrows indicate focal concentrations of craniofacial mesenchyme (green) and digit condensate subclusters (red). Insets to the right of each plot show parts of each image with similarly positioned arrows. White text of each inset labels the anatomic structure displayed. Scale bars in (C), 0.25 mm.

Spatial patterns of gene expression across cell types

To systematically examine these data for spatially patterned, cell-type–specific gene expression across the E14.0 embryo, we quantified spatial autocorrelation, the degree to which the cells expressing a given gene are spatially proximate. Testing each annotated cell type separately, we identified hundreds to thousands of genes exhibiting positive spatial autocorrelation per cell type (see the supplementary materials, file S2; Moran's test, FDR < 0.001). Among the cell types analyzed, connective tissue progenitors and neurons had the most spatially autocorrelated genes detected (Fig. 3A; mean 12,150 ± 2270 and 8623 ± 3846 genes per slide, respectively).

One explanation for such spatial autocorrelation of genes within a cell type would be the presence of spatially restricted, unannotated cell subtypes. For example, upon subclustering of connective tissue progenitors, we can indeed find spatially restricted cell subtypes (fig. S24, A and B), such that the genes defining these subtypes are expected to be spatially autocorrelated. Alternatively, a gene's spatial pattern of expression could arise from spatially restricted gene expression contributed by multiple cell subtypes. To distinguish between these scenarios, we calculated each gene's spatial autocorrelation (spatial Moran's I) and compared this value with its autocorrelation in UMAP space (UMAP Moran's I), a proxy for gene expression driven by a single-cell subtype. Across all genes, the two measures were reasonably well correlated (Pearson's rho 0.49, $P < 2 \times 10^{-16}$). However, a subset of genes, particularly in neurons, displayed higher spatial autocorrelation in the tissue context than in UMAP space (Fig. 3B and fig. S25, A and B). For example, Hox genes, a class of homeotic transcription factors that specify the body plan, featured prominently in this subset, consistent with spatial patterning that could not be explained solely by spatial restriction of a single-cell subtype (Fig. 3, B and C, and fig. S25, A to D). Expression of HoxA cluster genes paralleled the establishment of the spinal cord's anterior-posterior axis (*29*) (Fig. 3D and fig. S25), with no cell subtype restriction observed across datasets (*30*) or modalities (fig. S26, A to C).

Additional non-Hox genes also displayed excess spatial autocorrelation (Fig. 3, E and F, and fig. S26D). One such gene, *Cyp26b1*, encodes an enzyme that metabolizes the developmental morphogen retinoic acid. The spatial distribution of morphogens such as retinoic acid can play a critical role in tissue patterning (*29*). sci-Space data localized the focal expression of *Cyp26b1* to the brainstem with expression observed in multiple neuronal subclusters (figs. S25, A and B, and S26, A and B). This result was validated by RNA fluorescence in situ hybridization (FISH) for *Cyp26b1* and neuronal subtype–specific genes (Fig. 3G and fig. S26C). Together, these data identify *Cyp26b1* expression both in progenitors (radial glia) lining the hindbrain and in their progeny, spatially adjacent postmitotic neurons, suggesting that the expression of *Cyp26b1* is retained as these cells differentiate. This example illustrates how sci-Space can distinguish between spatial patterns of gene expression driven by a single-cell type from those present across multiple cell types.

Quantifying the explanatory power of spatial position

To investigate how each cell type's transcriptome varied globally across the embryo, we calculated the angular distance between the transcriptomes of pairs of cells of the same type separated by varying distances. For many cell types, as the physical distance between cells increased, so did the angular distance between their transcriptomes. However, this trend varied considerably, e.g., it was particularly pronounced in radial glia, neurons, and endothelial cells (Fig. 4A and fig. S27, A and B).

To quantify the contribution of spatial context to variation in gene expression across individual cells, we developed a statistical approach. Briefly, we first partitioned cells into groups on the basis of cell type and spatial location. Then, we computed the angular distance between each cell and the average expression profile for cells of that same type in the same spatial bin. After estimating and subtracting the technical variance attributable to data sparsity, we quantified how much of the remaining biological variance was due to each cell's type and/or spatial position. To validate this approach, we decomposed the variance attributed to lineage in the developing *Caenorhabditis elegans* embryo, where there is a relationship between two cells' lineage relationship and their observed gene expression variance (*2*). We found that our variance decomposition approach followed the law of total variance (fig. S28C) and, in agreement

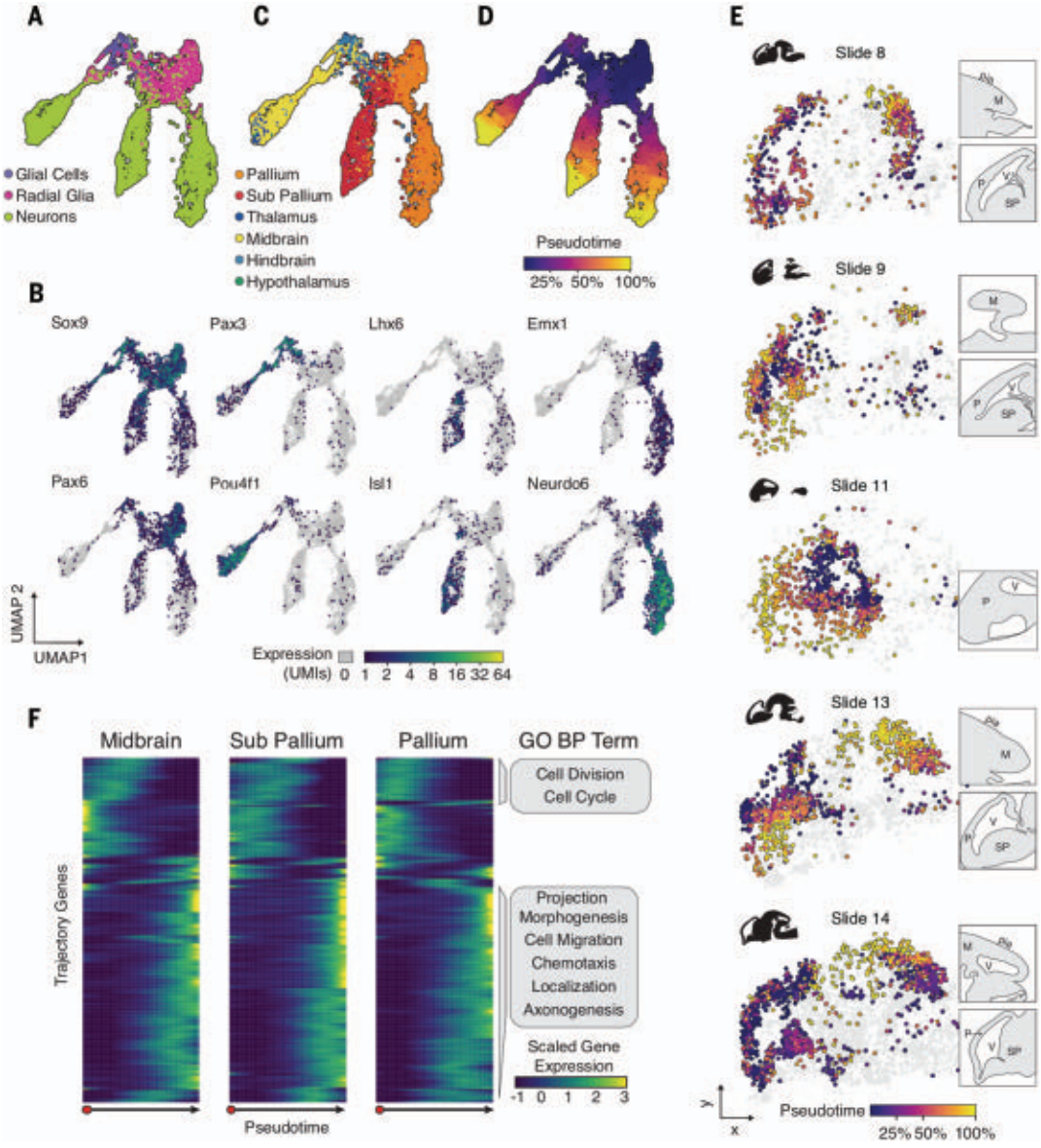

Fig. 5. Pseudotemporal spatial trajectories capture migratory patterns in the developing brain. (**A** to **D**) UMAP embedding displaying the neural trajectories colored by cell type (A), specific gene expression (B), cortical region (C), or pseudotime (D). (**E**) Neurons and radial glia in the cortex are colored by pseudotime or are otherwise colored gray. Insets of caudal (top) and rostral (bottom) brain outlines are shown to the right of each slide. M, midbrain; P, pallium; SP, subpallium; V, ventricle). (**F**) Scaled and centered gene expression for genes (rows) significantly varying over pseudotime in all three trajectories. Enriched Gene Ontology Biological Processes terms (GO BP) are displayed next to clustered genes.

with Packer *et al.* (*2*), showed that variance attributable to a cell's lineage relationship peaked around generation 7 (fig. S28D).

Applying this variance decomposition approach to the sci-Space data, we estimated that sparse UMI sampling accounted for 95.1% of the observed variance in global gene expression across cells and in subsequent analyses, we focused on the remaining 4.9% "nonsampling" variance. Of this nonsampling variance in global gene expression, cell type alone accounted for 19%. However, a joint model that included both cell type and spatial position accounted for 50% (fig. S29). The implication, that spatial information explains as much, if not more, of nonsampling gene expression variance as major cell type, was supported by the recovery of cell type and spatial gene modules of similar size and composition (fig. S30). However, some cell types' transcriptomes appeared more sensitive to spatial position than others (Fig. 4B). For example, chondrocytes were influenced by position within the embryo, reflecting the ongoing development of various connective tissue lineages at E14.0, and explained at least in part by subclusters that appear to correspond to digit condensates and craniofacial mesenchyme (Fig. 4C and fig. S31). Other such cell types included neurons and their precursors, the radial glia.

Pseudotemporal sci-Space trajectories reflect neuronal migration dynamics

To explore how spatial context might relate to gene expression heterogeneity in a developing cell lineage, we focused on radial glia and neurons. In particular, we hypothesized that we might be able to detect and localize the coordinated processes of neuronal differentiation and migration (*31*). UMAP dimensionality reduction of these cell types revealed the presence of three distinct trajectories originating in radial glia and leading to neurons (Fig. 5A). Gene expression dynamics along these three branches were consistent with neuronal differentiation, the up-regulation of cell cycle genes followed by expression of genes involved in migration (fig. S32). Each branch was strongly enriched for subtype-specific marker gene expression, Pou4f1^{+}/Pax3^{+} tectal neurons, Isl1^{+}/Lhx6^{+} cortical interneurons, and Emx1^{+}/Neurod6^{+} cortical pyramidal neurons, indicating that the embedding captures their specification from radial glia (Fig. 5B). We examined how these trajectories were anatomically distributed by segmenting the brain from each section using the Allen Institute's Anatomical Reference Brain

Atlas (http://atlas.brain-map.org/) as a guide. Cells from each trajectory overwhelmingly occupied a distinct brain region (Fig. 5C). To quantify progression through differentiation, we calculated pseudotime for each branch using radial glia as the root (Fig. 5D and fig. S32). Intersecting pseudotime and spatial information, we observed that cells early in differentiation clustered around the ventricles in the forebrain and developing midbrain, whereas those farther away exhibited a more differentiated transcriptome (Fig. 5E and fig. S33).

The spatial gradients of cellular maturity estimated with sci-Space data are consistent with well-documented coordination of cellular differentiation and neuronal migration. In the pallium, immature neurons migrate and differentiate radially outward, leading to the inside-out development of the cortical layers (*31*). In the subpallium, cortical interneurons born in the ganglionic eminences migrate tangentially to populate the developing cortex and olfactory bulb (*32*). Our data also identify a third major pattern of migration in which precursors emanate from the dorsal aspect of the ventricular zone in the developing midbrain. These midbrain neurons seem to migrate both radially, toward the pial surface, and tangentially, parallel to the pial surface, to populate this region (Fig. 5E, slides 8, 13, and 14, and fig. S33, slides 4 and 7). Although radial and tangential migration are generally discussed as being mutually exclusive phenomena, our data, consistent with some prior work (*33*, *34*), suggest otherwise in the developing midbrain. Furthermore, these cells share a common transcriptional program with differentiating and migrating neurons in the pallium and subpallium (Fig. 5F and data file S3).

Discussion

sci-Space is a method for spatial transcriptomics that retains single-cell resolution while capturing spatial information at a scale specified by a patterned array of cell hashing oligos. As a proof of concept, we applied sci-Space to retrieve the approximate spatial coordinates of transcriptionally profiled cells across whole-mount sections from E14.0 mouse embryos. The sci-Space data are readily integrated with nonspatial single-cell RNA-seq data collected from mouse embryos at adjacent time points (*1*, *21*), enabling rapid annotation of diverse cell types and visualization of cell-type–specific, spatially patterned gene expression, i.e., digital in situs. We identify examples, some expected and others unexpected, of genes expressed in an anatomically patterned manner within cells of a given type.

The spatial resolution of sci-Space is presently limited by the patterned array of hashing oligos, here to ~200 μm. Although increasing spot density and decreasing spot size are a straightforward path to increasing resolution, sci-Space is unlikely to detect effects arising from interactions between adjacent cells. This is limited by recovery of only a fraction of cells from each serial section such that we obtain a "survey" rather than achieving dense measurements. Nonetheless, sci-Space fills a need not addressed by other technologies. Like other STC methods (e.g., Slide-seq), sci-Space can be applied routinely and efficiently to large regions, e.g., whole-embryo serial sections. However, unlike these methods, sci-Space recovers single-cell transcriptomes. It can therefore capture patterns of spatial gene regulation private to specific cell types and estimate the contribution of each cell type to the expression of morphogens and other signaling molecules, both within and across anatomical regions. Moreover, sci-Space data can serve as a spatial "scaffold" for conventional, nonspatial single-cell RNA-seq atlases, which may be more challenging to map onto tissues profiled by spatial profiling methods that lack single-cell resolution.

Finally, using these spatially resolved single-cell data, we developed a statistical approach to identify cell types in the developing embryo that exhibit spatially regulated gene expression. Closer analysis of radial glia and neurons revealed gradients of developmental maturity in different regions of the brain indicative of known and new patterns of neuronal migration. Together with data from complementary technologies, we anticipate that the further application of sci-Space to serial sections spanning entire embryos from many time points will facilitate the construction of a set of highly time- and space-resolved four-dimensional atlases of gene expression across mammalian development.

REFERENCES AND NOTES

1. J. Cao *et al*., *Nature* **566**, 496–502 (2019).
2. J. S. Packer *et al*., *Science* **365**, eaax1971 (2019).
3. J. A. Briggs *et al*., *Science* **360**, eaar5780 (2018).
4. B. Pijuan-Sala *et al*., *Nature* **566**, 490–495 (2019).
5. J. A. Farrell *et al*., *Science* **360**, eaar3131 (2018).
6. N. Karaiskos *et al*., *Science* **358**, 194–199 (2017).
7. D. A. Cusanovich *et al*., *Nature* **555**, 538–542 (2018).
8. P. P. L. Tam, J. W. K. Ho, *Development* **147**, dev179788 (2020).
9. X. Qiu *et al*., *Nat. Methods* **14**, 979–982 (2017).
10. J. Liao, X. Lu, X. Shao, L. Zhu, X. Fan, *Trends Biotechnol.* **39**, 43–58 (2021).
11. P. L. Ståhl *et al*., *Science* **353**, 78–82 (2016).
12. S. G. Rodriques *et al*., *Science* **363**, 1463–1467 (2019).
13. K. H. Chen, A. N. Boettiger, J. R. Moffitt, S. Wang, X. Zhuang, *Science* **348**, aaa6090 (2015).
14. S. Shah, E. Lubeck, W. Zhou, L. Cai, *Neuron* **92**, 342–357 (2016).
15. J. H. Lee *et al*., *Science* **343**, 1360–1363 (2014).
16. S. R. Srivatsan *et al*., *Science* **367**, 45–51 (2020).
17. M. C. Regier *et al*., *Lab Chip* **19**, 2114–2126 (2019).
18. S. L. Wolock, R. Lopez, A. M. Klein, *Cell Syst.* **8**, 281–291.e9 (2019).
19. L. Haghverdi, A. T. L. Lun, M. D. Morgan, J. C. Marioni, *Nat. Biotechnol.* **36**, 421–427 (2018).
20. T. Stuart *et al*., *Cell* **177**, 1888–1902.e21 (2019).
21. G. La Manno, bioRxiv 184051 [Preprint]. 3 July 2020. https://doi.org/10.1101/2020.07.02.184051.
22. H. A. Pliner, J. Shendure, C. Trapnell, *Nat. Methods* **16**, 983–986 (2019).
23. T. Pietzsch, S. Saalfeld, S. Preibisch, P. Tomancak, *Nat. Methods* **12**, 481–483 (2015).
24. J. Schindelin *et al*., *Nat. Methods* **9**, 676–682 (2012).
25. P. Thévenaz, U. E. Ruttimann, M. Unser, *IEEE Trans. Image Process.* **7**, 27–41 (1998).
26. R. Dries *et al*., bioRxiv 701680 [Preprint]. 13 July 2019. https://doi.org/10.1101/701680.
27. G. Diez-Roux *et al*., *PLOS Biol.* **9**, e1000582 (2011).
28. D. Fawkner-Corbett *et al*., *Cell* **184**, 810–826.e23 (2021).
29. A. Sagner, J. Briscoe, *Development* **146**, dev182154 (2019).
30. J. Delile *et al*., *Development* **146**, dev.173807 (2019).
31. B. Nadarajah, J. E. Brunstrom, J. Grutzendler, R. O. Wong, A. L. Pearlman, *Nat. Neurosci.* **4**, 143–150 (2001).
32. M. Turrero García, C. C. Harwell, *FEBS Lett.* **591**, 3942–3959 (2017).
33. S.-S. Tan, H. Valcanis, M. Kalloniatis, A. Harvey, *Dev. Biol.* **241**, 117–131 (2002).
34. Y. Watanabe, C. Sakuma, H. Yaginuma, *Dev. Biol.* **437**, 131–139 (2018).
35. S. R. Srivatsan, M. Regier, Cole-trapnell-lab/sci-Space: Initial release, Zenodo (2021); https://doi.org/10.5281/ZENODO.4698159.
36. S. Srivatsan, M. Regier, Creating sci-space grids for spatial barcoding v1 (protocols.Io.Bm64k9gw), Protocols.io (2020); https://doi.org/10.17504/protocols.io.bm64k9gw.
37. S. Srivatsan, M. Regier, Spatial transfer of oligonucleotides and imaging v2 (protocols.Io.Btw5npg6), Protocols.io (2021); https://doi.org/10.17504/protocols.io.btw5npg6.
38. S. Srivatsan, J. Cao, Single cell RNA sequencing library preparation v1 (2-level sci-RNA-seq) (protocols.io.bquamwse), Protocols.io (2020); https://doi.org/10.17504/protocols.io.bquamwse.

ACKNOWLEDGMENTS

We thank members of the Lampe, Stevens, Shendure, and Trapnell laboratories for critical discussions and feedback, particularly V. M. Rachleff, E. Nichols, R. Daza, J. Cao, V. Ramani, and L. Saunders. **Funding:** Aspects of this work were supported by the NIH (1U54HL145611 to C.T. and J.S.; UM1HG011586 to C.T. and J.S.; 1R01HG010632 to C.T. and J.S.; DP2HL137188 to K.R.S.; and T32EB1650 to S.S.), the Deutsche Forschungsgemeinschaft (SP1532/3-1;4-1;5-1 to M.S), the Brotman Baty Institute for Precision Medicine, the Paul G. Allen Frontiers Foundation (Allen Discovery Center grant to J.S. and C.T.), and the Washington Research Foundation (postdoctoral fellowship to M.C.R.). J.S. is an investigator of the Howard Hughes Medical Institute. **Author contributions:** S.R.S. and M.C.R. conceptualized and performed the experiments. J.L. aided in sci-Space slide fabrication with support from P.L. S.R.S. and M.C.R. performed the computational analyses with assistance from E.B., P.G., J.F., M.D., and J.P. and under the supervision of C.T. M.S. and C.L. provided critical feedback on the project. S.R.S., M.C.R., C.T., K.R.S., and J.S. wrote the manuscript with input from all authors. K.R.S., J.S., and C.T. supervised the project. **Competing interests:** One or more embodiments of one or more patents and patent applications filed by the University of Washington may encompass the methods, reagents, and data disclosed in this manuscript. **Data and materials availability:** Processed and raw data can be downloaded from the National Center for Biotechnology Information (NCBI) under GSE166692. Code used to reproduce the presented analyses is indexed on Zenodo (*35*). Laboratory protocols can be found on protocols.io (*36*–*38*).

SUPPLEMENTARY MATERIALS

science.sciencemag.org/content/373/6550/111/suppl/DC1
Materials and Methods
Figs. S1 to S33
Tables S1 and S2
References (*39*–*42*)
Data Files S1 to S3
MDAR Reproducibility Checklist

30 March 2020; resubmitted 13 February 2021
Accepted 24 May 2021
10.1126/science.abb9536

ENZYME STRUCTURE

Crystal structure of a key enzyme for anaerobic ethane activation

Cedric J. Hahn[1]†, Olivier N. Lemaire[1]†, Jörg Kahnt[2], Sylvain Engilberge[3]‡, Gunter Wegener[1,4,5]*, Tristan Wagner[1]*

Ethane, the second most abundant hydrocarbon gas in the seafloor, is efficiently oxidized by anaerobic archaea in syntrophy with sulfate-reducing bacteria. Here, we report the 0.99-angstrom-resolution structure of the proposed ethane-activating enzyme and describe the specific traits that distinguish it from methane-generating and -consuming methyl-coenzyme M reductases. The widened catalytic chamber, harboring a dimethylated nickel-containing F_{430} cofactor, would adapt the chemistry of methyl-coenzyme M reductases for a two-carbon substrate. A sulfur from methionine replaces the oxygen from a canonical glutamine as the nickel lower-axial ligand, a feature conserved in thermophilic ethanotrophs. Specific loop extensions, a four-helix bundle dilatation, and posttranslational methylations result in the formation of a 33-angstrom-long hydrophobic tunnel, which guides the ethane to the buried active site as confirmed with xenon pressurization experiments.

Natural seeps perfuse the marine seafloor with a variety of different hydrocarbons, including alkane gases (*1*, *2*). Most of the volatile fraction is consumed within the sediment by a process coupled to the reduction of sulfate (*2*–*6*), which is mainly carried out by consortia of anaerobic alkane–oxidizing archaea and sulfate-reducing bacteria (*5*–*11*). The oxidation of the generated sulfide represents the basis of light-independent ecosystems in the deep sea (*6*–*10*, *12*). Ethane is the second-most abundant gaseous alkane, but its natural emissions from sediments are estimated to be rather low (*2*). This low emission results from efficient metabolism of microorganisms that consume the ethane within the seafloor. Recent discoveries pointed out two archaeal species that activate and completely oxidize ethane under anoxic conditions: *Candidatus* Argoarchaeum ethanivorans (*7*) and *Candidatus* Ethanoperedens thermophilum (*8*). These two closely related species belonging to the GoM-Arc1 clade are widely present in marine subsurface sediments (*5*, *7*, *8*). Analogously to the anaerobic oxidation of methane (AOM), the ethanotrophs generate ethyl-coenzyme M from ethane and coenzyme M (HS-CoM). It has been proposed that such activation works in the same fashion in other alkane-oxidizing archaea (*5*, *11*, *13*). It is assumed that ethyl-CoM is further metabolized to acetyl-coenzyme A (acetyl-CoA) by a so-far-unknown process (*7*, *8*). The acetyl-CoA decarbonylase–synthase complex turns acetyl-CoA into CO_2 and methyl-H_4MPT, and the methyl group is oxidized to CO_2. These organisms depend on ethane as substrate and are incapable of metabolizing other alkanes (*7*, *8*). Generated electrons are transferred to the partner bacteria, supposedly through external cytochromes, nanowires, or diffusible sulfur species, as already discussed for consortia performing the AOM (*7*, *8*, *14*, *15*).

The central enzyme for alkane-activation in ethanotrophs was proposed to be the methyl-CoM reductase (MCR) (*7*, *8*, *16*–*18*). Extensively studied in methanogens, MCR harbors a specific Ni-porphinoid F_{430} cofactor that catalyzes the reduction of a CoM-bound methyl group with coenzyme B (HS-CoB), forming methane and the heterodisulfide CoM-S-S-CoB (*16*, *19*, *20*). The anaerobic methane–oxidizing archaea (ANME) reverse the methanogenesis pathway, using MCR to activate methane, forming methyl-CoM and HS-CoB (*21*, *22*). MCR produced by the ANME-2 clade contains the canonical F_{430} cofactor, whereas a methylthio-F_{430}-cofactor was found in MCR from the ANME-1 clade (*23*–*25*). The MCR-homolog from ethanotrophs would capture ethane and generate ethyl-CoM and HS-CoB. This hypothesis is corroborated by three observations: (i) genes coding for the three subunits of the MCR-homolog are among the most expressed (*7*, *8*); (ii) ethyl-CoM was formed during anaerobic oxidation of ethane (AOE) by the consortium when incubated in the presence of ethane (*7*, *8*); and (iii) MCR from methanogenic archaea was shown to generate ethane from ethyl-CoM and HS-CoB, yet with rates much lower than for methane generation from methyl-CoM (*26*, *27*). The alkane capture machinery in *Ca.* E. thermophilum appears to be specialized for ethane; ethyl-CoM was the only detectable alkyl-CoM in cells incubated with a mixture of different alkanes (*8*). Moreover, in ethanotrophs the protein sequences of the MCR subunits are substantially different from methanogenic MCRs, with large insertions and substitutions of canonical residues (fig. S1 and table S1). Understanding the specific structural features of this enzyme may explain how MCR was adapted to accommodate ethane.

To obtain material for MCR-homolog structure determination, we used a thermophilic AOE enrichment cultured from sediments collected at the Guaymas Basin hydrothermal vents (*8*). The culture has a doubling time of only 7 days (*8*), which is notable compared with thermophilic AOM cultures isolated from the same site that exhibit doubling times of 50 days (*10*). *Ca.* E. thermophilum and its sulfate-reducing bacterial partner, *Candidatus* Desulfofervidus auxilii, constitute most of the active population of the enrichment (*8*). When we amended the culture medium with the methyl-CoM analog 2-bromoethane sulfonate (BES), a known inhibitor of alkyl-CoM reductases (*16*), both ethane consumption and sulfide production decreased, dependent on the amount of BES (Fig. 1A and fig. S2). A control ANME culture showed the same sensitivity at similar BES concentrations (Fig. 1A). The results corroborate the hypothesis of an MCR-like enzyme performing ethane activation.

MCR relative abundance in cell extracts from hydrogenotrophic and methylotrophic methanogens as well as ANME-1, ANME-2, and *Ca.* E. thermophilum were compared (Fig. 1B). Native gel profiles of all methanogens indicate an intense band at a size corresponding to isolated MCR. As expected from previous reports (*23*, *24*), the methanotrophic enrichments exhibit a band attributed as MCR with much stronger intensity compared with that of methanogens, resulting from the overproduction of MCR that characterizes these consortia (*28*, *29*). The profile of *Ca.* E. thermophilum contained a protein at a similar position on the native gel that we confirmed with mass spectrometry to be the MCR-homolog (supplementary materials, materials and methods). Compared with the high relative abundance of MCR in ANME enrichments, the cell extract profile of AOE enrichment appears to have a stronger background, similar to that of pure cultures of methanogens. Such lower MCR abundance could result from the lower energy required for the activation of CH bonds of ethane than of methane (*16*, *26*). This, and the overall higher energy yield of sulfate-dependent ethane oxidation (*7*, *30*), may explain the observed faster growth as compared with those of respective methane-oxidizing cultures.

We purified (fig. S3) and crystallized anaerobically the native MCR from *Ca.* E. thermophilum. The x-ray crystal structure was solved

[1]Max Planck Institute for Marine Microbiology, Bremen 28359, Germany. [2]Max Planck Institute for Terrestrial Microbiology, Marburg, Germany. [3]Paul Scherrer Institute (PSI), Villigen PSI, Villigen, Switzerland. [4]Center for Marine Environmental Sciences (MARUM), University of Bremen, Bremen, Germany. [5]Alfred Wegener Institute Helmholtz Center for Polar and Marine Research, Bremerhaven, Germany.
*Corresponding author. Email: gwegener@mpi-bremen.de (G.W.); twagner@mpi-bremen.de (T.W.)
†These authors contributed equally to the work.
‡Present address: European Synchrotron Radiation Facility (ESRF), Grenoble, France.

and refined to 0.99-Å resolution (table S2) and presents an organization similar to the eight structurally characterized homologs of MCR from methanogens and ANME-1 (Fig. 2A and table S1). The MCR of *Ca.* E. thermophilum has the canonical 2(αβγ) organization and is 20 kDa larger as compared with *Methanothermobacter marburgensis*, resulting from insertions (α10-18, α90-111, α330-340, β70-95, and γ227-240) found in all three subunits. These insertions are present in the enzymes from other ethanotrophs but absent in those of methanogens and methanotrophs (fig. S4). The insertions are located in the same area of the protein surface and redesign the surface charges without interfering with the HS-CoB tunnel, a hydrophilic cavity that connects the bulk solvent to the catalytic center containing HS-CoM and F_{430} (Fig. 2B and fig. S5). The active site organization and coenzymes position indicate a Ni(II)-inactive state. HS-CoM and HS-CoB are present at full occupancy. Most of the residues involved in HS-CoM and HS-CoB binding are conserved with other MCRs, with the exception of the $\alpha'Ala^{259}$ and γTyr^{120}, which are perfectly conserved in ethanotrophs, replacing the canonical arginine and leucine to position the carboxy-group of HS-CoB and sulfonate-group of HS-CoM, respectively (figs. S1, S4, and S6).

The core of the enzyme embeds the Ni-porphinoid F_{430}-cofactor, exhibiting two methylations of the carbon backbone according to the unambiguous electron density (Fig. 2C). Mass spectrometry and hydrolytic profile confirmed the presence and the position of these methylations (figs. S7 and S8). A gene (locus FHEFKHOI_00788) annotated as a putative uroporphyrinogen-III C methyltransferase and accompanying the coding sequence of the cofactor F_{430} synthetase (*cfbE*) (*31*, *32*) could be a candidate for the methylation of F_{430} (fig. S9). Sequence alignment and phylogenetic analysis indicate that this gene is an additional copy of the *cobM* gene, which is specific to ethanotrophs (fig. S9C). The protein encoded by the locus FHEFKHOI_00788 groups in a distinct branch of the CobM methyltransferase phylogenetic tree (fig. S9C). The second homolog branches with CobM sequences from other alkanotrophs and methanogens.

The ultraviolet (UV)–visible spectrum of the purified protein exhibits a different pattern with a maximal absorption peak at 441.5 nm, compared with 424.0 nm for a methanogenic MCR (Fig. 2D). We extracted the dimethylated-F_{430} from the protein to evaluate whether the differences in the spectra are due to the cofactor modifications or a specific protein environment. The extracted dimethylated-F_{430} showed a maximal absorbance at 432.6 nm, thus shifted compared with the classical F_{430}, which has a maximum at 430.4 nm (Fig. 2E). Hence, the observed shift of protein-bound F_{430} mostly

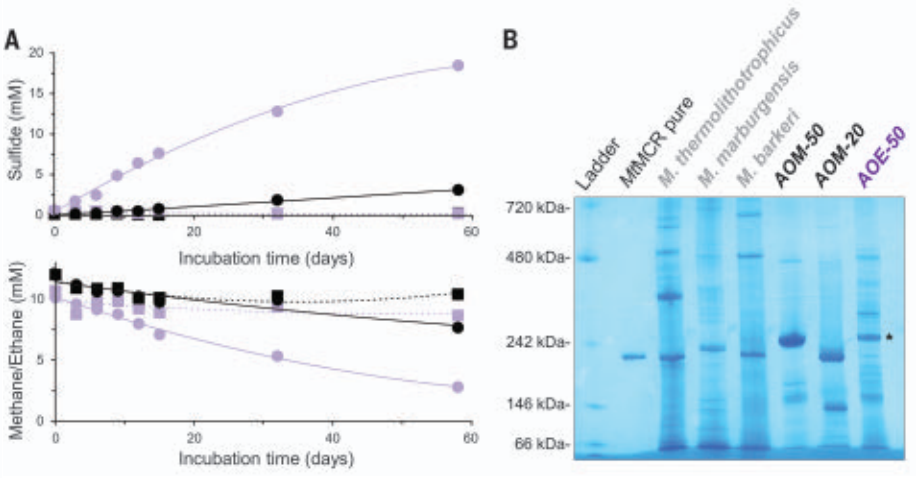

Fig. 1. Inhibition of AOE and comparison of cell extracts from methanogen cultures and methanotrophic and ethanotrophic enrichments. (**A**) Sulfide generation and alkane degradation in AOM (black) and AOE (purple) cultures incubated at 50°C, in the absence (circles, full lines) or presence (squares, dashed lines) of the MCR-specific inhibitor 2-bromoethane sulfonate at 10 mM (fig. S2). (**B**) High-resolution clear native polyacrylamide gel electrophoresis of purified MCR from *M. thermolithotrophicus* (*Mt*MCR, 1.5 μg) and soluble extracts from hydrogenotrophic (*M. thermolithotrophicus* and *M. marburgensis*) and methylotrophic (*Methanosarcina barkeri*) methanogens, AOM and AOE enrichments (10 μg each). The asterisk indicates the position of the MCR homolog from *Ca.* E. thermophilum.

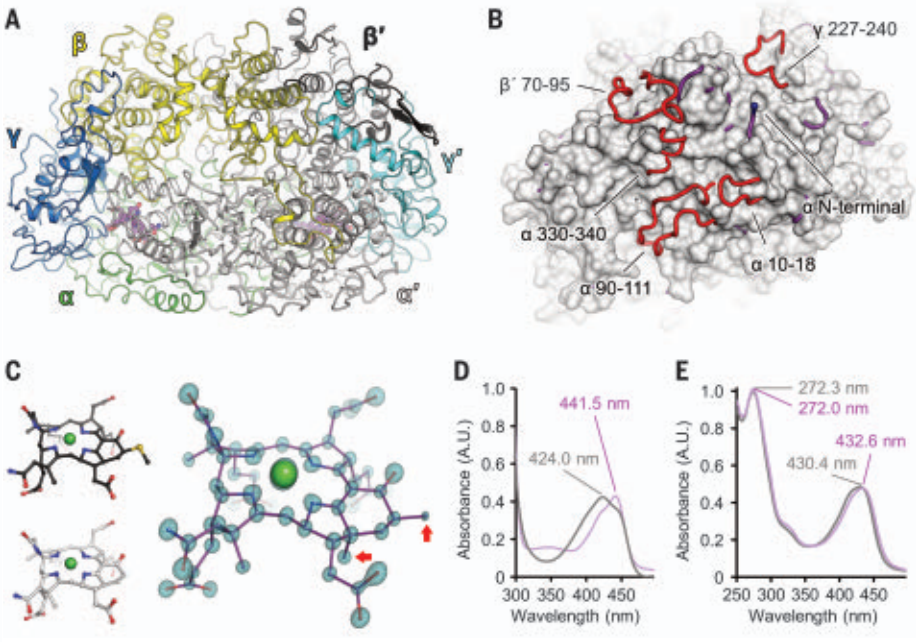

Fig. 2. Structure of the MCR from *Ca.* E. thermophilum and its dimethylated F_{430}-cofactor. (**A**) Overall structural organization of the MCR-homolog from *Ca.* E. thermophilum (PDB 7B1S) represented in cartoon where each subunit harbors a different color code. Prime symbols correspond to the opposing monomers. (**B**) Superposition of MCR from *Ca.* E. thermophilum (purple) and MCR type I from *M. marburgensis* (PDB 5A0Y, white surface) (*33*). The additional loops in *Ca.* E. thermophilum (red) are protruding from the *M. marburgensis* surface. (**C**) Structure of the cofactor F_{430} from *M. marburgensis* (white) (*33*), the methylthio-F_{430} of ANME-1 from Black Sea mats (PDB 3SQG, black) (*23*), and the dimethylated-F_{430} from *Ca.* E. thermophilum (purple). The green ball represents nickel, and the methylations are indicated with red arrows. The $2F_o$-F_c map is contoured at 6σ and shown as a transparent blue surface with a black mesh. (**D**) UV-visible spectra of MCRs (both at 78 μM concentration) and (**E**) the extracted F_{430} (normalized for comparison) from *Ca.* E. thermophilum (purple) and *M. thermolithotrophicus* (gray).

results from differences in its coordination in the enzyme rather than its methylations.

Contrary to all structurally characterized MCRs, the enzyme from *Ca.* E. thermophilum coordinates the nickel by means of a methionine instead of the canonical glutamine. The sulfur from the methionine interacts with the nickel without disturbing the metal position in the porphinoid ring (Fig. 3, A and B, and fig. S10). The methionine substitution cannot be considered as a prerequisite for ethane activation because the canonical glutamine is conserved in the MCR of the ethane oxidizer *Ca.* A. ethanivorans and relatives from cold seep environments (figs. S1 and S4). MCRs from methanogens and ANME archaea have virtually identical active sites, illustrating the selective pressure on the residues necessary for this complicated reaction (fig. S11, A and B) (*16*, *23*). It is therefore noteworthy to observe a different composition of the active site in the MCR-homolog from ethane oxidizers (Fig. 3C). The most notable differences are in the loop α367-374, carrying the bulky αTrp^{373} that replaces the canonical phenylalanine. This loop displaced the porphinoid ring owing to hydrogen bond network from the αAsn^{375} and accompanied by a clamping effect from αTyr^{376} and αPhe^{441}, causing a tilting of the ring by 11.4° compared with other MCRs (Fig. 3C and fig. S11B). As a result, the distance between the thiol groups of HS-CoM and HS-CoB is the longest reported so far in inactive Ni(II) structures of MCRs, with 6.6 Å compared with the 6.3 Å on average (Fig. 3, A and B). The catalytic chamber gains in volume (Fig. 3, D and E, and fig. S11, C and D), allowing ethane binding through appropriate van der Waals interactions. The chamber widening could impair the correct positioning of a classic cofactor F_{430} on the protein scaffold (Fig. 3, C to E, and fig. S11). However, the additional methylations on the F_{430} would structurally overcome this issue by maintaining its correct position and the integrity of the porphinoid planarity. We propose that these methylations accommodate the cofactor in this dilated active site and assure its appropriate environment to maintain its reactivity (Fig. 3, C to E).

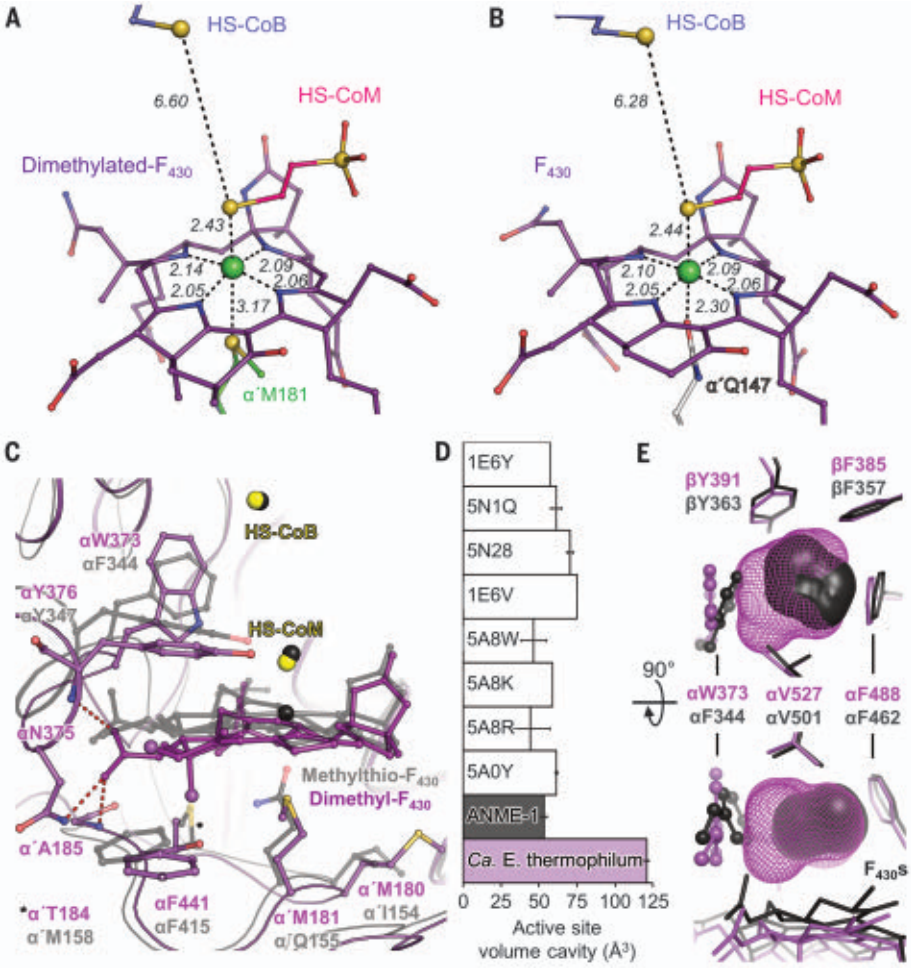

Fig. 3. A widened active site to accommodate ethane. (**A** and **B**) Nickel coordination in atomic resolution structures of *Ca.* E. thermophilum [(A), PDB 7B1S] and MCR type I from *M. marburgensis* [(B), PDB 5A0Y]. Distances between the nickel (green ball) and its surrounding atoms are indicated with dashes and given in angstroms. (**C**) Cartoon representation of MCR from ANME-1 (transparent black, with nickel as ball, PDB 3SQG) superposed on the C terminus of the α-subunit of *Ca.* E. thermophilum (purple). HS-CoM, HS-CoB reactive thiols are shown as balls. F_{430}s and residues involved in the tilting of the dimethylated-F_{430} are shown as balls and sticks, and hydrogen bonds are indicated with red dashes. Most ethanoic and propanoic groups of the F_{430}s and water network were omitted for clarity. (**D**) Volume of each of the catalytic cavities in MCR structures from methanogens (white, indicated by PDB codes) (supplementary materials, materials and methods), methanotroph (black), and ethanotroph (purple) are reported on the histogram. (**E**) Comparison of the catalytic cavity volume between MCR from ANME-1 (black surface) and *Ca.* E. thermophilum (purple mesh). Surrounding residues are shown as sticks. The αTrp^{373} position is indicated with balls and sticks.

The structure of MCR from *M. marburgensis* revealed a spherical electron density between the thiols of HS-CoM and HS-CoB (*16*). Similarly, the MCR of *Ca.* E. thermophilum has a weak elongated electron density at this position. The modeling of a diatomic molecule such as ethane would be preferred to a water molecule, albeit static disorder in the cavity could also lead to the observed density (fig. S12). To confirm the ethane-binding site and characterize a putative path inside the enzyme, we performed a xenon-pressurization experiment. Across the whole MCR from *Ca.* E. thermophilum, 16 Xe sites were unambiguously detected (fig. S13 and table S3). The major Xe site was found at the ethane site, between the two coenzymes, without interfering with the thiol groups. A second site was detected in a hydrophobic cavity located between the active site and the surface. Computational analysis confirmed that this cavity is part of an extended tunnel of 33 Å length (Fig. 4). According to the atomic-resolution structure, the tunnel is devoid of water molecules, attesting to its hydrophobic properties, which are ideal for the diffusion of hydrophobic gases such as ethane. All other Xe sites were found on the surface in hydrophobic pockets. No Xe was detected in the coenzyme tunnel because the proteins in the crystal systematically contain both HS-CoM and HS-CoB, preventing Xe diffusion into the tunnel. A similar computational analysis did not detect a similar tunnel in MCRs from *M. marburgensis* and ANME-1.

The MCR from *M. marburgensis* can generate ethane from ethyl-CoM and HS-CoB, albeit with low affinity and activity compared with methane production (*26*, *27*). Xenon-pressurization of crystals from *M. marburgensis* MCR isoform I [named type I, in reference to (*33*)] revealed 12 Xe sites exclusively located

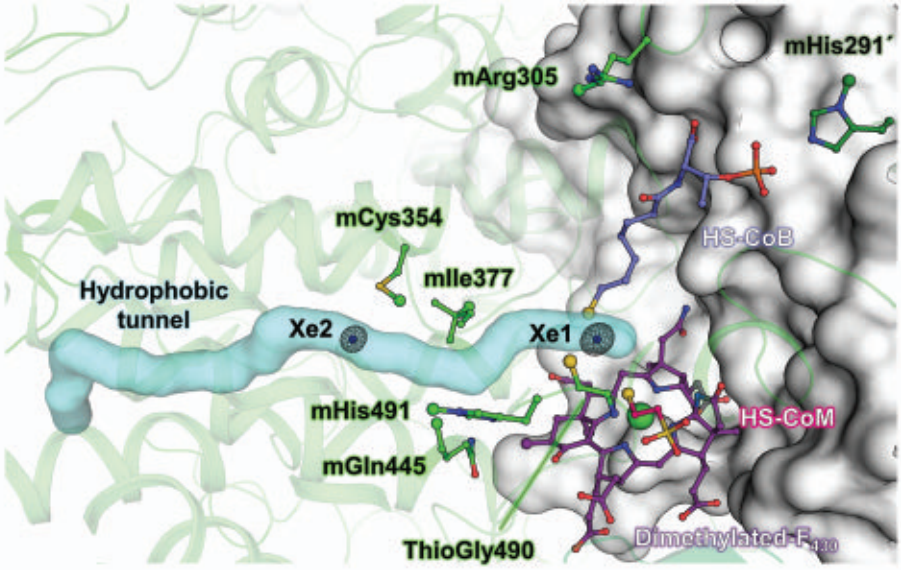

Fig. 4. Ethane tunnel supporting gas diffusion toward the catalytic chamber. The protein is displayed in cartoon, with the α′-subunit as white surface. Posttranslational modifications, cofactor, and coenzymes are shown in sticks, with additional methyls and sulfurs as green and yellow balls, respectively. The hydrophobic tunnel calculated by the CAVER program (*34*) creating a route for the substrate to the catalytic center of the enzyme is shown as a cyan surface. The anomalous Fourier map contoured at 15σ shown as black mesh indicates the position of Xe atoms obtained with xenon-pressurization experiment (PDB 7B2C), indicated with dark blue spheres.

at the surface of the enzyme in hydrophobic pockets (fig. S14 and table S3), and no Xe could be detected in the catalytic chamber. These results suggest that the internal tunnel is specific to ethane oxidizers and could allow for efficient transport of ethane to the catalytic center. In *Ca.* E. thermophilum, the tunnel is formed at the interface of a four-helix bundle from the α subunit (helices 340-367, 373-382, 443-463, and 527-544). It is covered and flanked at the outer surface by the specific additional loops and the helix 385-401 (fig. S15). The opposite side of the tunnel, opening in the active site, is covered with posttranslationally modified residues: S-methylcysteine-354, 3-methylisoleucine-377, 2(*S*)-methylglutamine-445, and N^2-methylhistidine-491 (Fig. 4 and figs. S15 and S16). The N^2-methylhistidine-491 is of particular interest because this residue is a tyrosine or phenylalanine in all other MCRs (figs. S1 and S4). Installation of these modifications would require a specific machinery that will need further investigation. Other modifications systematically found in methane-releasing MCRs were detected in the electron density and confirmed with mass spectrometry (fig. S16).

Our results reveal specific structural features harbored by the MCR-homolog of the ethane oxidizer *Ca.* E. thermophilum, which favors ethane consumption over methane or larger alkanes (*8*). We propose to rename this enzyme, which is the entry point for anaerobic oxidation of ethane, to ethyl-CoM reductase (ECR). Assuming a similar organization of the active Ni(I) enzyme, the larger volume of the catalytic cavity would likely impair correct positioning of methane. The chamber volume would not be sufficient to accommodate alkanes larger than ethane, especially in the heterodisulfide-containing enzyme. Moreover, the hydrophobic tunnel inner diameter (average bottleneck radius 1.02 Å) would already prevent more voluminous alkanes such as propane from accessing the active site. Future investigations should resolve how the ECR active site constrains a particular reactive state of the ethane, allowing its exclusive and efficient capture.

REFERENCES AND NOTES

1. J. F. Clark, L. Washburn, J. S. Hornafius, B. P. Luyendyk, *J. Geophys. Res.* **105** (C5), 11509–11522 (2000).
2. G. Etiope, P. Ciccioli, *Science* **323**, 478–478 (2009).
3. S. B. Joye *et al.*, *Chem. Geol.* **205**, 219–238 (2004).
4. V. Mastalerz, G. J. de Lange, A. Dahlmann, *Geochim. Cosmochim. Acta* **73**, 3849–3863 (2009).
5. R. Laso-Pérez *et al.*, *mBio* **10**, e01814–e01819 (2019).
6. A. Boetius *et al.*, *Nature* **407**, 623–626 (2000).
7. S. C. Chen *et al.*, *Nature* **568**, 108–111 (2019).
8. C. J. Hahn *et al.*, *mBio* **11**, e00600–e00620 (2020).
9. V. J. Orphan, C. H. House, K. U. Hinrichs, K. D. McKeegan, E. F. DeLong, *Science* **293**, 484–487 (2001).
10. T. Holler *et al.*, *ISME J.* **5**, 1946–1956 (2011).
11. R. Laso-Pérez *et al.*, *Nature* **539**, 396–401 (2016).
12. M. Sibuet, K. Olu, *Deep Sea Res. Part II Top. Stud. Oceanogr.* **45**, 517–567 (1998).
13. G. Borrel *et al.*, *Nat. Microbiol.* **4**, 603–613 (2019).
14. S. E. McGlynn, G. L. Chadwick, C. P. Kempes, V. J. Orphan, *Nature* **526**, 531–535 (2015).
15. G. Wegener, V. Krukenberg, D. Riedel, H. E. Tegetmeyer, A. Boetius, *Nature* **526**, 587–590 (2015).
16. R. K. Thauer, *Biochemistry* **58**, 5198–5220 (2019).
17. D. V. Miller, S. J. Booker, *Biochemistry* **58**, 4269–4271 (2019).
18. Y. Wang, G. Wegener, S. E. Ruff, F. Wang, *Environ. Microbiol.* **23**, 530–541 (2021).
19. U. Ermler, W. Grabarse, S. Shima, M. Goubeaud, R. K. Thauer, *Science* **278**, 1457–1462 (1997).
20. T. Wongnate *et al.*, *Science* **352**, 953–958 (2016).
21. S. J. Hallam *et al.*, *Science* **305**, 1457–1462 (2004).
22. A. Meyerdierks *et al.*, *Environ. Microbiol.* **12**, 422–439 (2010).
23. S. Shima *et al.*, *Nature* **481**, 98–101 (2011).
24. M. Krüger *et al.*, *Nature* **426**, 878–881 (2003).
25. M. Kaneko *et al.*, *Anal. Chem.* **86**, 3633–3638 (2014).
26. S. Scheller, M. Goenrich, R. K. Thauer, B. Jaun, *J. Am. Chem. Soc.* **135**, 14985–14995 (2013).
27. R. P. Gunsalus, J. A. Romesser, R. S. Wolfe, *Biochemistry* **17**, 2374–2377 (1978).
28. F. P. Wang *et al.*, *ISME J.* **8**, 1069–1078 (2014).
29. V. Krukenberg *et al.*, *Environ. Microbiol.* **20**, 1651–1666 (2018).
30. R. K. Thauer, *Curr. Opin. Microbiol.* **14**, 292–299 (2011).
31. K. Zheng, P. D. Ngo, V. L. Owens, X. P. Yang, S. O. Mansoorabadi, *Science* **354**, 339–342 (2016).
32. S. J. Moore *et al.*, *Nature* **543**, 78–82 (2017).
33. T. Wagner, J. Kahnt, U. Ermler, S. Shima, *Angew. Chem. Int. Ed.* **55**, 10630–10633 (2016).
34. E. Chovancova *et al.*, *PLOS Comput. Biol.* **8**, e1002708 (2012).
35. Hahn *et al.*, X-ray crystallography and mass spectrometry raw and processed data accompanying the manuscript "Crystal structure of a key enzyme for anaerobic ethane activation". Zenodo (2021).

ACKNOWLEDGMENTS

We thank the Max Planck Institute for Marine Microbiology and the Max-Planck-Society for continuous support. We thank the SOLEIL and SLS synchrotrons for beam time allocation and the respective beamline staffs of Proxima-1 and X06DA for assistance with data collection, with specific regards to P. Legrand. We also acknowledge C. Probian and R. Appel for their continuous support in the Microbial Metabolism laboratory. We are thankful to R. Amann and R. K. Thauer for their critical views on the manuscript and their stimulating discussions. We thank K. Knittel for her inputs during a regular exchange. We thank A. Teske for organizing the sampling campaign of the Guaymas Basin hydrothermal vents (NSF grant 1357238). **Funding:** Additional funds came from the Deutsche Forschungsgemeinschaft funding the Cluster of Excellence "The Ocean Floor—Earth's Uncharted Interface" (EXC-2077–390741603) at MARUM, University Bremen. S.E. was granted by SNF grant 200021_182369. **Author contributions:** C.J.H., O.N.L., G.W., and T.W. designed the research. C.J.H., O.N.L., and G.W. performed cultivation and culture experiments. C.J.H., O.N.L., and T.W. purified and crystallized the proteins. S.E., O.N.L., and T.W. collected x-ray data and built the models. O.N.L. and T.W. analyzed the structures. S.E. and T.W. performed and analyzed the xenon-pressurization experiments. J.K., O.N.L., and T.W. analyzed the F_{430} cofactor and posttranslational modifications. C.J.H., O.N.L., G.W., and T.W. interpreted the data and wrote the paper, with contributions and final approval of all co-authors. **Competing interests:** The authors declare no competing interests. **Data and materials availability:** All structures were validated and deposited in the Protein Data Bank (PDB) under the following accession numbers: 7B1S, native ethyl-coenzyme M reductase from *Ca.* E. thermophilum; 7B2C, Xenon-pressurized ethyl-coenzyme M reductase from *Ca.* E. thermophilum and 7B2H, Xenon-pressurized methyl-coenzyme M reductase from *M. marburgensis*. Raw and processed data for x-ray crystallography and mass spectrometry experiments are hosted at Zenodo (*35*). All other data are available in the manuscript or the supplementary materials.

SUPPLEMENTARY MATERIALS

science.sciencemag.org/content/373/6550/118/suppl/DC1
Materials and Methods
Supplementary Text
Figs. S1 to S16
Tables S1 to S3
References (*36*–*58*)

15 December 2020; accepted 28 May 2021
10.1126/science.abg1765

ScienceCareers online @sciencecareers.org

Science Careers helps you advance your career. Learn how!

- Register for a free online account on **ScienceCareers.org**.
- Search hundreds of job postings and find your perfect job.
- Sign up to receive e-mail alerts about job postings that match your criteria.
- Upload your resume into our database and connect with employers.
- Watch one of our many webinars on different career topics such as job searching, networking, and more.
- Download our career booklets, including Career Basics, Careers Beyond the Bench, and Developing Your Skills.
- Complete an interactive, personalized career plan at "my IDP."
- Visit our Employer Profiles to learn more about prospective employers.
- Read relevant career advice articles from our library of thousands.

Visit **ScienceCareers.org** today — all resources are free

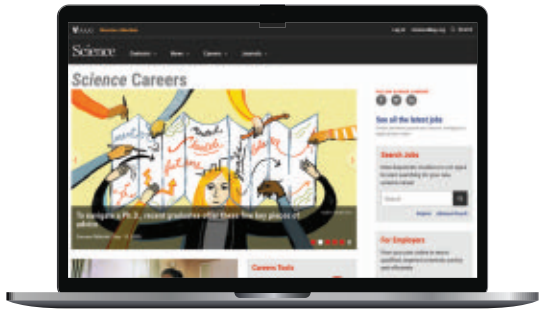

SCIENCECAREERS.ORG

ScienceCareers
FROM THE JOURNAL SCIENCE AAAS

Technische Universität Braunschweig

Zertifikat seit 2007 audit familiengerechte hochschule

The **Faculty of Electrical Engineering, Information Technology, Physics**, Institute of Condensed Matter Physics, offers a

Junior Professorship (m/f/d) for „Experimental Physics, Quantum Materials“ Salary-Gr. W1 TT W2

The junior professor should represent physics in its entire breadth in teaching and the field of solid state physics in research. Possible research focuses could be in the following areas:

- Analysis of 2D materials
- Special quantization effects
- Topological states
- Coupling phenomena on surfaces and boundary surfaces

Vacancy offer:
https://www.tu-braunschweig.de/en/vacancies

Please send your application until August 31st 2021 using the **online form** of the TU Braunschweig.

Shenzhen Institute of Advanced Technology
Chinese Academy of Sciences

Established in partnership between the Chinese Academy of Sciences and the Shenzhen Municipal Government, the Shenzhen Institute of Advanced Technology (SIAT) is a newly-created university with an objective to become the world's preeminent institute for emerging science and engineering programs. SIAT is equipped with state-of-art teaching and research facilities and is dedicated to cultivating international, visionary, and interdisciplinary talents while delivering research support to pursue innovation-driven development.

SIAT is located in Shenzhen, also known as the “Silicon Valley of China,” a modern, clean, and green city, well-known for its stunning architecture, vibrant economy, and its status as a leading global technology hub. SIAT is seeking applications for faculty positions of all ranks in the following academic programs: Computer Science and Engineering, Bioinformatics, Robotics, Life Sciences, Material Science and Engineering, Biomedical Engineering, Pharmaceutical Sciences, Synthetic Biology, Neurosciences, etc. SIAT seeks individuals with a strong record of scholarship who possess the ability to develop and lead high-quality teaching and research programs. SIAT offers a comprehensive benefits package and is committed to faculty success throughout the academic career trajectory, providing support for ambitious and world-class research projects and innovative, interactive teaching methods.

Further information:
http://english.siat.cas.cn/DP/Va/

For your career in science, there's only one Science

Features in myIDP include:

- Exercises to help you examine your skills, interests, and values.
- A list of 20 scientific career paths with a prediction of which ones best fit your skills and interests.

myIDP

Visit the website and start planning today!
myIDP.sciencecareers.org

Science Careers | AAAS In partnership with:

FASEB Federation of American Societies for Experimental Biology
University of Massachusetts Medical School
UCSF University of California San Francisco
UIC
BURROUGHS WELLCOME FUND

FIND YOUR HAPPIER PLACE.

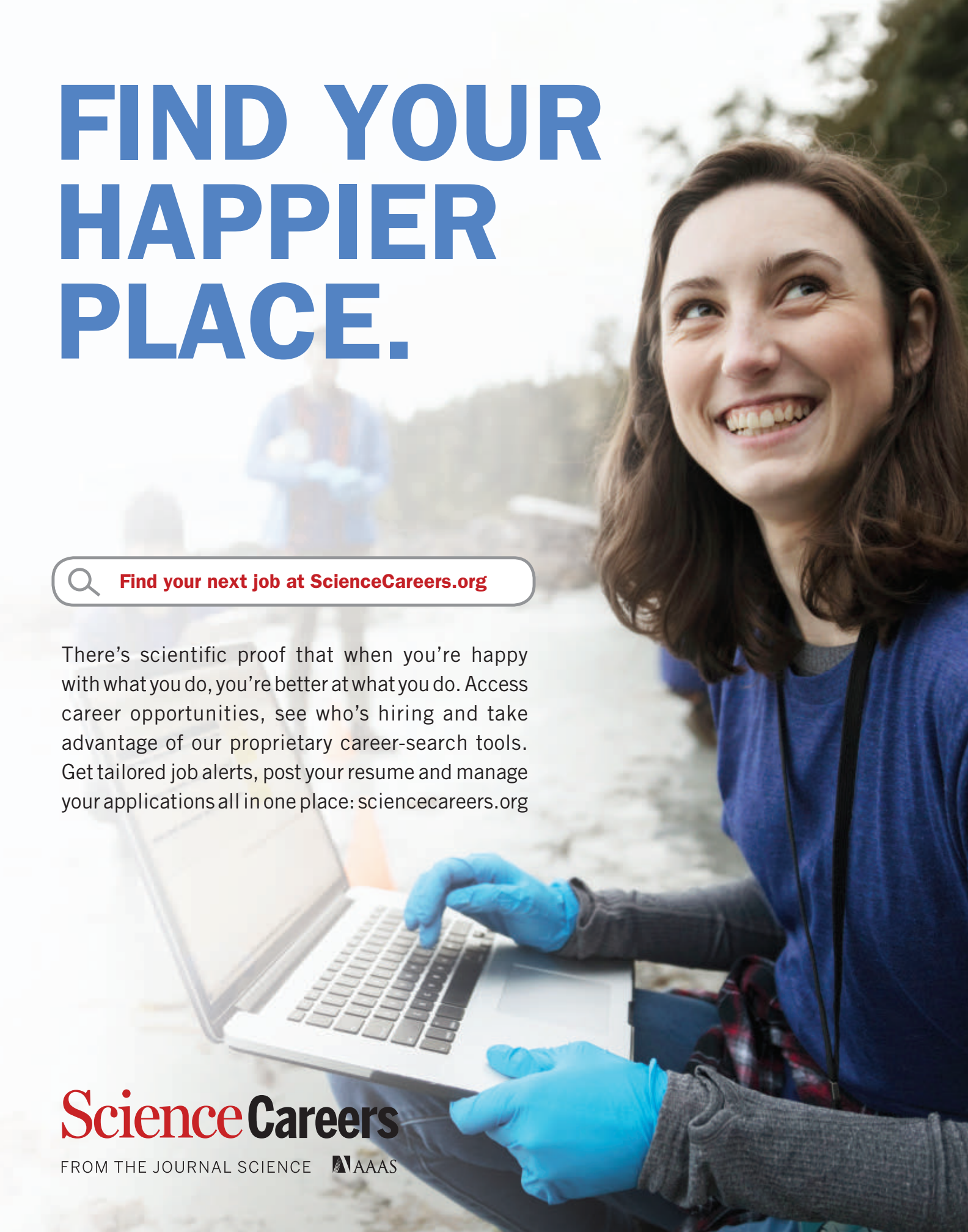

Find your next job at ScienceCareers.org

There's scientific proof that when you're happy with what you do, you're better at what you do. Access career opportunities, see who's hiring and take advantage of our proprietary career-search tools. Get tailored job alerts, post your resume and manage your applications all in one place: sciencecareers.org

ScienceCareers

FROM THE JOURNAL SCIENCE AAAS

Who's the top employer for 2020?

Science Careers' annual survey reveals the top companies in biotech & pharma voted on by *Science* readers.

Read the article and employer profiles at sciencecareers.org/topemployers

Science 2020
TOP EMPLOYER

By **Sheila Teves**

Embracing my roots

One day, in the before-COVID times, I was traveling to deliver a seminar. As I walked down to breakfast in the hotel lobby, another guest waylaid me with a complaint: "The oatmeal is out." The tone was arrogant, demanding, and dismissive. It took me a second to realize that she had mistaken me for a hotel employee. A flash of hot indignation washed through me. I have come a long way from the Filipina immigrant girl working part time as a food server during high school, I thought to myself; now I was a professor running my own research lab. Later I realized there was another reason the encounter stung so much.

As Filipino immigrants living in the United States, many of my family members and I started out as "essential workers"—and some still are. My mom was a fast food cashier. My grandmother, aunt, and cousin worked as caregivers; my grandfather washed dishes in a restaurant. My family did honest and hard work. But when I was younger, I was self-conscious about it. All I wanted was to escape the shame of being poor. I didn't want to shop with food stamps anymore or be in the free lunch line at school.

My mom, wanting a better life for me and my brother, believed in education. So under her direction, I studied hard while my family cooked, cleaned, and cared for others. When I received a full scholarship for college, it felt like a golden ticket out of poverty not just for me, but for my family, too. And when I was accepted into graduate school, getting paid to study and train to be a scientist felt like a luxury. For the first time, I had enough money to live on my own and even help my family once in a while. I felt I had finally found an escape.

"The melding of ... my identities wasn't always smooth."

Leaving home and entering the academic world took me further and further from my immigrant working-class roots. Every so often, though, I would meet other Filipino immigrants working in the university as janitors, building maintenance staff, shipping and receiving workers, and lab aides. When I interacted with them, I would seamlessly revert to my younger immigrant self, speaking Tagalog, the Philippines's national language, and behaving more deferentially. When I stepped back into my academic role, I would play the confident and assertive scientist. At some point I realized I only stopped to talk with the other Filipino immigrants when I was alone, which made me feel guilty. But I convinced myself that I was just being sensitive to my lab mates; after all, it would be rude to converse in another language when they were around. I wasn't ready to admit that part of me was ashamed of my working-class background.

While I was in grad school, reminders of my roots were rare, but this changed when I started my postdoc. There, I met two Filipina immigrant women working as aides in our lab. For 20 years they had taken care of essential but unglamorous work—cleaning, dishwashing, autoclaving, media prep—to support the researchers and their work. After hearing them speak Tagalog, I shyly approached them to introduce myself. They embraced me immediately, and I started to have lunch with them almost daily. They would always bring Filipino food to share, reminding me of home.

Eventually, other lab members started to join us for lunch. At first it felt awkward. Scientists usually default to talking science, whereas I almost never talked science with the Filipinas. And I wasn't sure I was ready for my scientific colleagues to see this other side of me. The melding of our groups—and my identities—wasn't always smooth. But in time, we found common ground in food, sharing and exchanging dishes from our diverse cultures. I became the bridge between the scientists and the Filipina lab aides, and my immigrant roots slowly re-emerged and became comfortably fused with my academic identity. I realized they never had to be separate in the first place.

Looking back at that hotel experience, I now realize that being mistaken as a hotel server is not really what stung. Whether I am a hotel server or a professor, I—like my family members and all the other essential workers—deserve to be treated with respect and dignity, not belittled and dismissed. ■

Sheila Teves is an assistant professor of biochemistry and molecular biology at the University of British Columbia, Vancouver, and a 2020 Wall Scholar at the Peter Wall Institute for Advanced Studies.

ILLUSTRATION: ROBERT NEUBECKER

AAAS.ORG/COMMUNITY

AAAS' Member Community is a one-stop destination for scientists and STEM enthusiasts alike. It's "Where Science Gets Social": a community where facts matter, ideas are big and there's always a reason to come hang out, share, discuss and explore.

Member COMMUNITY
AAAS

AMERICAN ASSOCIATION FOR THE ADVANCEMENT OF SCIENCE

REVEALING THE NEXT BREAKTHROUGH IN IMMUNOLOGY

APPLY NOW FOR THE $30,000 GRAND PRIZE

APPLICATIONS DUE: OCTOBER 1, 2021

The Michelson Philanthropies & ***Science*** Prize for Immunology recognizes research that will have a significant impact on vaccine and immunotherapy development. Together with AAAS/***Science***, Michelson Philanthropies awards breakthrough research from the past three years. The applications are judged on innovation and potential impact.

With these prizes, scientists (35 and younger) have the opportunity to advance their research projects, are provided with a renowned platform in ***Science*** to publish their work and connect them with other innovators through the Michelson Prizes alumni network.

Young researchers from a wide range of disciplines are encouraged to apply.

APPLY TODAY:
www.sciencemag.org/michelson

MICHELSON PHILANTHROPIES & Science
PRIZE FOR IMMUNOLOGY